THE OLIGO-MIOCENE TURBIDITES AND ASSOCIATED FACIES OF THE CAMPOS BASIN, OFFSHORE BRAZIL

by

Nilo Chagas de Azambuja Filho

July 1990

Thesis submitted in fulfilment of PhD degree of the University of London and for the Diploma of Membership of the Imperial College.

L
LO
UN

ABSTRACT

The Oligocene-Miocene succession in the Campos Basin, an Atlantic-type continental marginal basin, is dominated by upper bathyal foraminiferal-nanofossil marlstones, siliciclastic mudstones and sand-rich turbidites. It consists of a basal thin Oligocene section, where the turbidites are concentrated, overlain by a thick offlapping slope/shelf sequence up to the present. The turbidites are characterized by thick (40-120 m) amalgamated fine/coarse-grained massive sandstones with box-like wireline log patterns, good areal continuity, excellent reservoir characteristics, and showing hummocky clinoforms seismic patterns. They are interpreted as being generated by high concentration turbidity currents, probably induced by littoral drift cells during periods of relative lowering of sea-levels. These are considered to be deposited in the broad lows created by the collapse of the underlying Aptian evaporites. The periodicity of the turbiditic events appears to have been linked with the resonance of climatic and probably tectonic periodicities producing the lowering of sea level.

The clay mineral compositions of the mudrocks are mainly detrital in origin. However, there is some evidence of illitization of illite-smectite in the most deeply buried mudrocks (~123°C, ~3850 m). Framboidal pyrite, dolomite, calcite, kaolinite, and locally feldspar alteration and chlorite are the most common diagenetic phases in the mudrocks.

The turbidite sandstones are predominantly subarkoses and arkoses (Pettijohn et al., 1973), but bioclasts (shallow- and deep-water species) are also common (average 5%). Widespread early calcite cementation associated with bioclast rich intervals, generation of secondary porosity by dissolution of calcite and feldspars, replacement of feldspar and mica by kaolinite are the most common diagenetic processes in the sandstones. The generation of the diagenetic phases and secondary porosity in the sandstones appears to have been caused by fluids originating from deeply buried successions ascending along growth faults.

to my parents Nilo and Luiza, and wife Ludmila

London, July 1990

Department of Geology

Imperial College

Nilo Chagas de Azambuja Filho

ACKNOWLEDGEMENTS

I thank Petrobrás for financial sponsorship throughout the research period, and the assistance and technical support provided by the staff at the Petrobrás Research Centre, CENPES, and Headquarters, in Rio de Janeiro, Brazil, and the logistic support provided by ESLON and BRASOIL in London. I am grateful to Drs. Milton Romeu Franke, Guilherme Estrella, Heitor Chagas and Manoel Figueiredo of Petrobrás for the opportunity to do this work. I wish to thank also Mrs. Eva Zylberglejd and Margot Rope for their logistic support.

An integrated study like this would never have been possible without the contribution of several people involved in different activities. I am very grateful to Drs. E. A. M. Koutsoukos, Marcio Rocha Mello, Messrs. E. Souza Cruz, Vitor Abreu, Hernani Chaves, Mrs. Lourdes de Fatima, and others that directly or indirectly have contributed data for this research. I am particular grateful to Dr. Corfield for the oxygen and carbon stable isotope analysis carried out at Oxford University and also to Dr. Alfredo Arche, from Madrid University, for his assistance during my field work in the South Pyrenean Basin.

I would like to thank very especially Drs. Harry Shaw and Graham Evans together with Dr. Joe Cartwright for their assistance and advice throughout this study and their critical reviews of the manuscript.

I am also grateful to my colleagues Renato Azevedo, Joao Keller, Alvaro Crosta, Claudio Porto, Qianyu Li and Jeremy Greenwood for stimulating discussions and their help during my stay at Imperial College. I would like to thank: Mathew Owen-Huges, Ian Gilbert and Dr. John Ferguson for their contribution in the study of the sedimentary cycles; Messrs. Paul Grant, Martin Gill, Dick Giddens, Adolfo Cash and Grace Lau for their technical help.

Finally, I would like to thank my wife Ludmila Abrahao Azambuja for all the encouragement, emotional support and cooperation that she has given me during this research.

CONTENTS

CHAPTER 1

OUTLINE OF THE THESIS Pg.

1.1 Introduction..... 20

1.2 Aims of the research and methods employed..... 20

1.3 General outline of the thesis..... 22

CHAPTER 2

REGIONAL GEOLOGY

2.1 Introduction..... 24

2.2 Lithostratigraphy of the southeast Brazil 24

2.3 The onshore sedimentary basins in the provenance area 28

CHAPTER 3

GEOLOGICAL EVOLUTION OF THE CAMPOS BASIN

3.1 The tectonic evolution of the Campos Basin..... 31

3.2 Stratigraphy of the Campos Basin..... 38

3.2.1 Stratigraphic evolution and depositional environments of the offshore Campos Basin..... 38

3.2.1.1 Igneas Básicas: 130-120 MY (Rio da Serra)..... 38

3.2.1.2 The Lagoa Feia Formation: Barremian-Aptian..... 39

3.2.1.3 The Macaé Formation: Albian-Lower Turonian..... 42

3.2.1.4 The Campos Formation: Coniacian-Recent..... 46

3.2.1.5 The Embore Formation: Tertiary-Recent..... 47

3.2.2 Stratigraphic evolution and depositional environments of the onshore Campos Basin..... 48

CHAPTER 4

METHODOLOGY

4.1 Introduction..... 50

4.2 Facies analysis..... 50

4.2.1 Lithofacies..... 50

4.2.1.1 Lithofacies definitions and descriptions..... 50

4.2.1.2 Equivalent outcrop lithofacies..... 52

4.2.2 Electrofacies..... 53

4.3 Petrological analysis..... 55

4.3.1 Optical petrography..... 55
4.3.2 Scanning electron microscopy (S.E.M.)..... 56
4.3.2.1 Emissive mode..... 56
4.3.2.1.1 Secondary electron imaging (S.E.I.)..... 56
4.3.2.1.2 Backscattered electron imaging (B.S.I.)..... 58
4.3.2.2 Cathodoluminescence (C.L.)..... 58
4.3.2.3 Energy dispersive x-ray analysis (EDAX)..... 59
4.3.3 X.R.D. analysis..... 59
4.3.3.1 Sample preparation and diffractometer parameters 59
4.3.3.2 Interpretation of diffractograms..... 61
4.4 Geochemical analysis..... 62
4.4.1 Total organic carbon..... 62
4.4.2 Calcium carbonate content..... 62
4.4.3 Stable isotopes..... 63
4.5 Palaeontological analysis..... 63
4.6 Static down hole formation temperature..... 64
4.7 Sequence stratigraphy..... 65
4.8 Cyclicity..... 68

CHAPTER 5
FACIES ANALYSIS
5.1 Introduction..... 77
5.2 Facies classification..... 78
5.3 Electrofacies and lithofacies characteristics..... 82
5.3.1 Gravelly Sandstone Electrofacies (GvS)..... 82
5.3.1.1 Gravelly Sandstone Lithofacies GvS..... 82
5.3.1.2 Geophysical characteristics..... 83
5.3.1.2.1 Wireline logs..... 83
5.3.1.2.2 Seismic response..... 83
5.3.1.3 Interpretation of the Electrofacies (GvS)..... 83
5.3.2 Gravelly Sandstone with Mudclast
Electrofacies (GvSm)..... 87
5.3.2.1 Gravelly Sandstone with Mudclast
Lithofacies GvSm..... 87
5.3.2.2 Geophysical characteristics 88
5.3.2.2.1 Wireline logs responses..... 88
5.3.2.2.2 Seismic response..... 88
5.3.2.3 Interpretation of the Electrofacies (GvSm)..... 91

5.3.3 Diamictite Electrofacies (DMT)..... 91
5.3.3.1 Muddy Gravels/Gravelly Mudstone Lithofacies DMT. 91
5.3.3.2 Geophysical characteristics 92
5.3.3.2.1 Wireline logs responses..... 92
5.3.3.2.2 Seismic response..... 95
5.3.3.3 Interpretation of the Electrofacies (DMT)..... 95
5.3.4 Amalgamated Sandstone Electrofacies (AmS)..... 95
5.3.4.1 Very Coarse/Coarse Sandstone Lithofacies VcS.... 96
5.3.4.2 Amalgamated Coarse/fine Sandstone
Lithofacies (AmS)..... 98
5.3.4.3 Geophysical characteristics..... 101
5.3.4.3.1 Wireline log responses..... 101
5.3.4.3.2 Seismic responses..... 105
5.3.4.4 Interpretation of the Electrofacies (AmS)..... 106
5.3.5 Thick-bedded Sandstone Electrofacies (FTab)..... 107
5.3.5.1 Medium/fine Sandstone Lithofacies FTab..... 107
5.3.5.2 Amalgamated Fine/very fine Lithofacies FTb..... 108
5.3.5.3 Geophysical characteristics..... 112
5.3.5.3.1 Wireline log responses..... 112
5.3.5.3.2 Seismic responses..... 116
5.3.5.4 Interpretation of the Electrofacies (FTab)..... 116
5.3.6 Muddy Thin-bedded Sand-mud Couplet
Electrofacies (FTb-e)..... 117
5.3.6.1 Thin/very Thin-bedded Sandstone/Mudstone
Lithofacies FTb-e..... 117
5.3.6.2 Millimetric Rhythmic Siltstone Lithofacies FTde. 118
5.3.6.3 Geophysical characteristics..... 124
5.3.6.3.1 Wireline log responses..... 124
5.3.6.3.2 Seismic responses..... 125
5.3.6.4 Interpretation of the Electrofacies (FTb-e)..... 125
5.3.7 Sandy Thin-bedded Sand-Mud Couplet
Electrofacies (E)..... 125
5.3.7.1 Thin-bedded Fine-Sandstone Lithofacies Fla..... 126
5.3.7.2 Thin/very Thin-bedded fine-sandstone
Lithofacies Wav..... 130
5.3.7.3 Very Thin-bedded Fine/very fine-sandstone
Lithofacies Rip..... 133
5.3.7.4 Geophysical characteristics 134

5.3.7.4.1 Wireline log responses..... 134
5.3.7.4.2 Seismic responses 137
5.3.7.5 Interpretation of the Electrofacies (E)..... 137
5.3.8 "Chaotic" Electrofacies (F)..... 138
5.3.8.1 "Chaotic" Lithofacies F..... 138
5.3.8.2 Geophysical characteristics..... 139
5.3.8.2.1 Wireline log responses 139
5.3.8.2.2 Seismic responses..... 142
5.3.8.3 Interpretation of Electrofacies (F)..... 142
5.3.9 Carbonate Mudstones/Marlstone Electrofacies (G1/G2)..... 142
5.3.9.1 Chalk or Biogenic Carbonate Mudstone Lithofacies G1..... 142
5.3.9.2 Hemipelagic Marlstone Lithofacies G2..... 143
5.3.9.3 Geophysical characteristic 147
5.3.9.3.1 Wireline log responses..... 147
5.3.9.3.2 Seismic responses..... 150
5.3.9.4 Interpretation of the Electrofacies (G1/G2)..... 151
5.3.10 Mudstone Electrofacies (G3/G4)..... 151
5.3.10.1 Calcareous Mudstone Lithofacies G3..... 151
5.3.10.2 Siliciclastic Mudstone Lithofacies G4..... 152
5.3.10.3 Geophysical characteristics..... 153
5.3.10.3.1 Wireline log responses..... 153
5.3.10.3.2 Seismic responses..... 156
5.3.10.4 Interpretation of the Electrofacies (G3/G4).... 156
5.3.11 Mottled Mudstone Electrofacies (MM/MS)..... 156
5.3.11.1 Mottled Mudstone/Muddy Sandstone Lithofacies MM/MS..... 157
5.3.11.2 Geophysical characteristics..... 165
5.3.11.2.1 Wireline log responses..... 165
5.3.11.2.2 Seismic responses..... 165
5.3.11.3 Interpretation of the Electrofacies (MM/MS).... 166
5.3.12 Thin-bedded Bioturbated Sandy Siltstone Electrofacies (BS1)..... 166
5.3.12.1 Thin-bedded Bioturbated Sandy Siltstone Lithofacies BS1..... 166
5.3.12.2 Geophysical characteristics 167
5.3.12.2.1 Wireline log responses..... 167

5.3.12.2.2 Seismic responses..... 170
5.3.12.3 Interpretation of the Electrofacies (BS1)..... 170
5.4 Electrofacies association and distribution..... 171
5.4.1 Hemipelagites Electrofacies Association (I)..... 171
5.4.2 Channel Electrofacies Association (II)..... 172
5.4.3 Channel-Lobe Transition Electrofacies
Association (III)..... 173
5.4.4 Proximal-Lobes Electrofacies Association (IV)..... 175
5.4.5 Contourites Electrofacies Association (V)..... 183
5.5 Conclusions..... 186

CHAPTER 6
SEQUENCE STRATIGRAPHY AND DEPOSITIONAL MODEL
6.1 Introduction..... 188
6.2 Oligocene-Recent succession..... 189
6.2.1 Depositional sequence 1 or Basal sequence..... 195
6.2.1.1 Sequences 1a and 1b..... 197
6.2.1.2 Sequence 1c..... 198
6.2.2 Depositional sequence 2..... 204
6.2.3 Depositional sequence 3..... 204
6.2.4 Depositional sequences 4 to 8..... 206
6.3 Discussion:modern and ancient submarine environments 208
6.3.1 Modern submarine environments and fans..... 208
6.3.1.1 Southern Brazilian continental margin..... 208
6.3.1.2 Modern fans..... 212
6.3.2 Ancient submarine fans..... 214
6.4 Controls in the turbidites deposition..... 216
6.5 Conclusions and depositional model..... 222

CHAPTER 7
SEDIMENTARY CYCLES
7.1 Oligocene-Miocene sedimentary cycles..... 229
7.2 The nature and origin of cycles..... 235
7.3 Possible causes of cyclicity..... 238
7.4 Time series or spectral analysis of sedimentary
cycles.....242
7.5 Stable isotopes..... 262
7.5.1 Stable isotope results..... 262

7.5.2 Interpretation and discussion of the isotope signature.....263
7.6 Conclusions.....270

CHAPTER 8
MUDROCK PETROLOGY
8.1 Introduction and previous work..... 272
8.2 Sampling 273
8.3 Composition of the Oligocene-Lower Miocene mudrocks 276
8.3.1 Whole-rock mineralogy 277
8.3.2 Clay mineralogy..... 277
8.3.2.1 Composition of the clay fraction (< 2 μm) in the mudrocks 277
8.3.2.2 Clay mineral compositions of the mudrocks and the sandstones 282
8.4 Clay mineral compositions of the various lithofacies 292
8.5 Diagenesis of the mudrocks..... 301
8.5.1 Interstratified illite-smectite..... 301
8.5.2 Early diagenesis: framboidal pyrite and dolomite.. 308
8.5.2.1 Framboidal pyrite..... 309
8.5.2.2 Dolomite.....310
8.5.3 Feldspar diagenesis..... 318
8.5.4 Authigenic clay minerals..... 323
8.5.5 Calcite dissolution..... 331
8.6 Discussion and conclusions..... 336

CHAPTER 9
SANDSTONE COMPOSITION AND DIAGENESIS
9.1 Introduction.....339
9.2 Sandstone composition..... 339
9.2.1 Framework composition..... 339
9.2.2 Sandstones matrix..... 347
9.3 Sandstone classification..... 353
9.4 Provenance of the sandstones..... 357
9.5 Sandstone diagenesis..... 362
9.5.1 Pseudomatrix or compaction matrix..... 363
9.5.2 Framboidal pyrite..... 370
9.5.3 Microquartz.....370

9.5.4 Early feldspar overgrowths..... 376
9.5.5 Smectite coating 376
9.5.6 Ankerite..... 379
9.5.7 Early calcite..... 379
9.5.8 Secondary porosity..... 383
9.5.9 Kaolinite..... 388
9.5.10 Dolomite..... 389
9.5.11 Chlorite..... 400
9.5.12 Quartz and feldspar overgrowths..... 400
9.13 Pyrite..... 401
9.5.14 Euhedral calcite..... 401
9.5.15 Fibrous illite 408
9.6 Paragenesis-discussion..... 409
9.6.1 Microquartz cement 410
5.6.2 Calcite cement..... 410
9.6.3 Secondary porosity..... 416
9.6.4 Late diagenetic phases in the deepest sample..... 423
9.7 Conclusions..... 423

CHAPTER 10

SUMMARY AND CONCLUSIONS..... 425

REFERENCES.....432

LIST OF FIGURES, TABLES AND PLATES

Pg.

Fig. 1.1 Location of the study area..... 21

Fig. 2.1 Geotectonic map of the southeast of Brazil..... 26
Fig. 2.2 Distribution of the granitoid bodies in the southeast of Brazil..... 28
Fig. 2.3 Location of the Sao Paulo, Taubaté and Resende Basins..... 29

Fig. 3.1 Location and boundaries of the Campos Basin and the study area..... 32
Fig. 3.2 Geological evolution of the Brazilian Continental Margin..... 33
Fig. 3.3 Simplified structures of the southeast Brazil.. 35
Table 3.1..... 36
Fig. 3.4 A detached growing fault soling-out on the Aptian evaporites with activity up to the Recent..... 37
Fig. 3.5 Lithostratigraphic column of the Campos Basin.. 40
Fig. 3.6 Schematic section showing the lithostratigraphic units and structural features of the Campos Basin..... 41
Table 3.2..... 43
Fig. 3.7 Distribution of the evaporites in the South Atlantic during the Aptian..... 44
Fig. 3.8 The South Atlantic during the Albian..... 45
Fig. 3.9 The modern Paraíba do Sul Delta..... 49

Fig. 4.1 Studied area with the location of wells and seismic sections (also in the pocket at the back of the thesis) 51
Fig. 4.2 Ideal sequence of sedimentary structures in a turbidite bed "the Bouma Sequence"..... 52
Fig. 4.3 Dipmeter patterns and geological anomalies commonly associated with them..... 54

Fig. 4.4 S.E.M. operation modes..... 57
Fig. 4.5 An example of extrapolation to determine static bottom hole temperature..... 64
Fig. 4.6 An example of vertical seismic profile and synthetic seismogram computed with sonic log..... 66
Fig. 4.7 Seismic reflection patterns and terminations... 68
Table 4.1..... 72
Fig. 4.8 Waves 1, 2 and combined, an example..... 73
Fig. 4.9 Periodogram of waves 1, 2, and combined wave 3 74
Fig. 4.10 Wave 4 with its corresponding periodogram..... 76

Table 5.1 Electrofacies.....(pocket)
Plate 5.1 Gravelly Sandstone Electrofacies (GvS)
Plate 5.1a Composite log..... 84
Plate 5.1b Photos..... 85
Plate 5.1c Explanation of the symbols used in the logs.. 86
Plate 5.2 Gravelly Sandstone with Mudclasts Electrofacies (GvSm)
Plate 5.2a Composite log..... 89
Plate 5.2b Photos..... 90
Plate 5.3 Diamictite Electrofacies (DMT)
Plate 5.3a Composite log..... 93
Plate 5.3b Photos..... 94
Fig. 5.1 and 5.2 Grain-size distribution of a sample from the Very Coarse-Sandstone Lithofacies VcS..... 97
Plate 5.4 Very Coarse Sandstone Lithofacies VcS
Plate 5.4a Composite log..... 99
Plate 5.4b Photos..... 100
Fig. 5.3 and 5.4 Grain-size distribution of a sample from the Amalgamated Sandstone Lithofacies AmS..... 102
Plate 5.5 Amalgamated Sandstone Lithofacies AmS
Plate 5.5a Composite log 103
Plate 5.5b Photos..... 104
Fig. 5.5 and 5.6 Grain-size distribution of a sample from Lithofacies FTab..... 109
Plate 5.6 Thick-bedded Sandstone Lithofacies FTab
Plate 5.6a Composite log..... 110
Plate 5.6b Photos..... 111

Fig. 5.7 and 5.8 Grain-size distribution of a sample from Lithofacies **FTb**..... 113

Plate 5.7 Thick-bedded Sandstone Lithofacies **FTb**
Plate 5.7a Composite log..... 114
Plate 5.7b Photo..... 115
Plate 5.8 Muddy Thin-bedded Sand-Mud Couplet Electrofacies (**FTb-e**)
Plate 5.8a Composite log..... 119
Plate 5.8b Photo..... 120
Plate 5.9 Muddy Thin-bedded Sand-Mud Couplet Electrofacies (**FTb-e**)
Plate 5.9a Composite log..... 121
Plate 5.9b Photo..... 122
Fig. 5.9 and 5.10 Grain-size distribution of a sample from Lithofacies **Fla**..... 127
Plate 5.10 Thin-bedded Fine-Sandstone with Flaser-bedding Lithofacies **Fla**
Plate 5.10a Composite log 128
Plate 5.10b Photo..... 129
Plate 5.11 Thin-bedded Fine-sandstone with Wavy-bedding Lithofacies **Wav**
Plate 5.11a Composite log 131
Plate 5.11b Photo..... 132
Plate 5.12 Very thin-bedded Very fine/Fine-Sandstone Lithofacies **Rip**
Plate 5.12a Composite log 135
Plate 5.12b Photo..... 136
Plate 5.13 "Chaotic" Electrofacies (**F**)
Plate 5.13a Composite log 140
Plate 5.13b Photo..... 141
Plate 5.14 Chalk/Carbonate Mudstone Lithofacies **G1**
Plate 5.14a Composite log 144
Plate 5.14b Photo..... 145
Plate 5.15 Marlstone Lithofacies **G2**
Plate 5.15a Composite log 148
Plate 5.15b Photo..... 149
Plate 5.16 Siliciclastic Mudstone Lithofacies **G4**

Plate 5.16a Composite log 154
Plate 5.16b Photo..... 155
Plate 5.17 Mottled Mudstone Electrofacies (MM/MS)
Plate 5.17a Composite log 159
Plate 5.17b Photo..... 160
Plate 5.18 Plate Mottled Mudstone Electrofacies (MM/MS)
Plate 5.18a Composite log 161
Plate 5.18b Photo..... 162
Plate 5.19 Mottled Sandstone Lithofacies MS
Plate 5.19a Composite log 163
Plate 5.19b Photo..... 164
Plate 5.20 Bioturbated Sandy Siltstone Electrofacies (BS1)
Plate 5.20a Composite log 168
Plate 5.20b Photo..... 169
5.11a Explanation for the stratigraphic sections..... 176
Fig. 5.11b Stratigraphic section A-B..... 177
Fig. 5.12 Stratigraphic section C-D..... 178
Fig. 5.13 Stratigraphic section E-F..... 179
Fig. 5.14 Stratigraphic section G-H..... 180
Fig. 5.15 Stratigraphic section I-J..... 181
Fig. 5.16 Stratigraphic section K-L..... 182
Fig. 5.17 Schematic depositional model for the Mottled Mudstone Electrofacies (MM/MS)..... 185

Fig. 6.1 Dip-oriented regional geological section of the northeast part of the Campos Basin.....190/191
Table 6.1 Comparison between the Martini (1971) nannofossil zones and the zonation used by Petrobrás..... 193
Fig. 6.2 Seismic section T-T' and interpretation - pocket
Fig. 6.3 Seismic section U-U' and interpretation - pocket
Fig. 6.4 Seismic section V-V' and interpretation - pocket
Fig. 6.5 Seismic section X-X' and interpretation - pocket
Fig. 6.6 Seismic section Y-Y' and interpretation - pocket
Fig. 6.7 Seismic section Z-Z' and interpretation - pocket
Fig. 6.8 Chart showing the depositional sequences and their turbidite fans correlated with Haq et al. (1987).. 194
Fig. 6.9 Sandstone isoliths of the fans a and b..... 200

Fig. 6.10 Sandstone isoliths of the fans c+d+e in (A), and f+g+h in (B)..... 201
Fig. 6.11 Strike-oriented seismic sections (A and B) in the channelized area and their interpretations.....202/203
Fig. 6.12 Systems tracts, after Vail (1987)..... 206
Fig. 6.13 Physiography of the southeast part of the Brazilian continental margin..... 210
Fig. 6.14 Occurrence of Siri carbonates, the Blue Marker, and the main Oligocene canyons..... 217
Fig. 6.15 Integration of the sandstone isoliths of all the Oligocene-Lower Miocene fans in the study area..... 218
Fig. 6.16 Integration of the occurrence of the Siri carbonates and the Oligocene canyons with a simplified map of Oligocene-Lower Miocene fans..... 219
Fig. 6.17 Schematic depositional model for the Oligocene-Lower Miocene turbidites and associated facies.....225/226
Fig. 6.18 Schematic evolutional model for the Oligocene-Lower Miocene complex 227/228

Fig. 7.1 Characteristics of the cyclic sedimentation in core and wireline logs of well MRL-4..... 230
Fig. 7.2 Characteristics of the Oligocene-Lower Miocene cyclic sedimentation in wireline logs of well 344..... 233
Fig. 7.3 Characteristics of the Oligocene cyclic sedimentation in wireline logs of well 342..... 234
Fig. 7.4 Current in the oceans of the Southern Hemisphere during the Tertiary..... 241
Fig. 7.5 Variations of CaCO3% with depth, its frequencies and corresponding wavelengths..... 243
Fig. 7.6 Wavelengths of the cyclicity obtained from cores and wireline logs of wells 330 and MRL-4..... 244
Fig. 7.7 Variations of the wave lengths of the CaCO3% cycles with depth in the cored interval (well 330)..... 246
Fig. 7.8 Smoothed curve for CaCO3% and corresponding frequencies and calculated wavelengths..... 247
Table 7.1A Frequencies of cycles (wells 330 and MRL-4).. 249
Table 7.1B Frequencies of cycles (wells MRL-4 and 342).. 250
Table 7.2 Sedimentation rate per nannofossil zone..... 251

Table 7.3 Ratio of orbital periodicities..... 251
Table 7.4A Periodicity of the sedimentary cycles per nannofossil zones of wells 330, 344, MRL-4..... 252
Table 7.4B continuation..... 253
Table 7.4C continuation..... 254
Table 7.5 Periodicities between sandstones in zone N-545 of well 344..... 255
Fig. 7.9 Frequencies and corresponding wavelengths of the cycles between sandstones in nannofossil zone N-545..... 256
Fig. 7.10 Frequencies derived from well 342..... 258
Fig. 7.11 Frequencies from the basal interval of the zone N-550, derived from neutron log, well 344..... 260
Table 7.6 Stable isotopes of benthonic foraminifera..... 264
Fig. 7.12 Oxygen and carbon stable isotopes of benthonic foraminifera (Cibicidoides sp.) from well 330..... 265
Fig. 7.13 Oxygen, carbon isotopes and CaCO3% plotted against depth of the total interval..... 266
Fig. 7.14 Variations in the CaCO3% in relation to the oxygen and carbon stable isotopes in well 330..... 267

Fig. 8.1 Relationship of the temperatures with sample depth from the sea surface..... 274
Fig. 8.2 Variations of the temperature at 2700 m from the sea-surface in relation to the water depth of the wells. 275
Table 8.1 Clay minerals of the mudrocks..... 278
Fig. 8.3 XRD traces of randomly oriented powder samples from Marlstone G2 and Mudstone G4..... 280
Fig. 8.4 Comparison between XRD glycolated traces from Anjos (1986) and from the present study..... 281
Table 8.2 Clay minerals of the sandstones..... 283
Fig. 8.5 XRD traces of the Lithofacies MM..... 284/285
Fig. 8.6 XRD traces of the Lithofacies FTab..... 286/287
Fig. 8.7 XRD traces of the Lithofacies FTa..... 288/289
Fig. 8.8 XRD traces of the Lithofacies GvS..... 290/291
Fig. 8.9 XRD Relative percentages of the main clay minerals presented in the various lithofacies..... 293
Fig. 8.10 XRD traces of the Lithofacies G2..... 294/295
Fig. 8.11 XRD traces of the Lithofacies G4..... 296/297

Fig. 8.12 XRD traces showing a comparison between the typical reflections of the different lithofacies..... 298
Fig. 8.13 Relationship between percentages of kaolinite and illite-smectite in the different lithofacies..... 299
Fig. 8.14 Relationship between illite-smectite/illite and kaolinite/illite ratios versus lithofacies..... 300
Fig. 8.15 Relationship between the percentages of kaolinite versus illite-smectite in different lithofacies from 2400-2950 m and 3850-3860 m..... 302
Fig. 8.16 XRD glycolated and heated 550°C traces showing the variation of illite-smectite with depth..... 303
Fig. 8.17 - Behaviour of the illite-smectite X.R.D. traces of this study compared with those of Anjos (1986)..... 305
Fig. 8.18 XRD glycolated traces showing variations of the illite-smectite with depth from random to ordered..... 306
Fig. 8.19 Variations of the percentages of illite-smectite with temperature 307
Table 8.3 Early diagenesis depth zonation..... 309
Plate 8.1 ..... 312/313
Plate 8.2 ..... 314/315
Plate 8.3 ..... 316/317
Plate 8.4 ..... 321/322
Plate 8.5 ..... 324/325
Plate 8.6 ..... 326/327
Fig. 8.20 "Finger print" showing the composition of the illite-smectite cement inside foraminifera..... 328
Plate 8.7..... 329/330
Fig. 8.21 XRD glycolated traces showing the behaviour of the calcite in relation to lithofacies and depth..... 333
Plate 8.8..... 334/335

Plate 9.1..... 342/343
Plate 9.2..... 344/345
Table 9.1 Lithofacies average composition..... 348
Fig. 9.1 Relative composition of the Rock Fragment (RF) components in the sandstone lithofacies..... 349
Plate 9.3..... 350/351

Fig. 9.2 Relative percentages of clay minerals in the rocks of the sandstone lithofacies..... 352
Fig. 9.3 Classification of the terrigenous sandstone from Pettijohn et al. (1973)..... 354
Fig. 9.4 Composition of the rocks of the various sandstone lithofacies..... 355
Fig. 9.5 Classification of the sandstone lithofacies in relation to their bioclast content..... 356
Fig. 9.6 Sandstone average composition compared with Savage et al. (1988) and Moraes (1989)..... 359
Plate 9.4..... 364/365
Plate 9.5..... 366/367
Plate 9.6..... 368/369
Plate 9.7..... 372/373
Plate 9.8..... 374/375
Plate 9.9..... 377/378
Plate 9.10..... 380/381
Plate 9.11..... 384/385
Plate 9.12..... 386/387
Plate 9.13..... 390/391
Plate 9.14..... 392/393
Plate 9.15..... 394/395
Plate 9.16..... 396/397
Plate 9.17..... 398/399
Plate 9.18..... 402/403
Plate 9.19..... 404/405
Plate 9.20..... 406/407
Table 9.2 Diagenetic evolution of the sandstones..... 409
Fig. 9.7 Profiles of δ^{13} C from pore waters in five DSDP sites..... 412
Table 9.3 Carbon and oxygen carbon isotopes of bulk calcite cement of the sandstones..... 414
Fig. 9.8 Distribution of the temperature of the samples in the analyzed sandstones..... 419
Fig. 9.9 General model of the subsidence curves for the Campos Basin 420

CHAPTER 1

OUTLINE OF THE THESIS

1.1 INTRODUCTION

The Campos Basin accounts for more than 60% of the present-day Brazilian oil production. It is situated off the southeast coast of Brazil on the continental shelf of the state of Rio de Janeiro. The exploratory activity was initiated in shallow-water parts of the basin in the early 70's. In 1974 the first accumulation of hydrocarbon was discovered in Albian limestones. During the 80's exploratory began in the deeper waters (>500 m) in the northeastern region of the Campos Basin. As a result, two giant oil fields (Albacora and Marlim) were discovered in sand-rich turbidite-type reservoirs of Upper Cretaceous and Oligocene-Miocene age.

1.2 AIMS OF THE RESEARCH AND METHODS EMPLOYED

The aim of the research reported in this thesis was to use an integrated approach to gain a better understanding of the characteristics and distribution of the Oligocene-Miocene sedimentary facies in the Campos Basin and their diagenetic evolution. The study area is a rectangle of 5,000 km^2 in the northeastern part of the Campos Basin, at water depths of between 100 and 2,000 m (**Fig. 1.1**). Data and sample material was provided by Petrobrás-Petróleo Brasileiro S.A., the Brazilian National oil company and included core samples (490 m), wireline logs (50 wells) and 800 Km of seismic sections (**Fig. 1.1**). Fieldwork has also been carried out in the Pyrenean Basin in the regions of Ainsa-Broto and San Sebastian, northeastern Spain, to study similar sedimentary facies found in the Oligocene-Miocene successions of the Campos Basin. This Basin was selected for

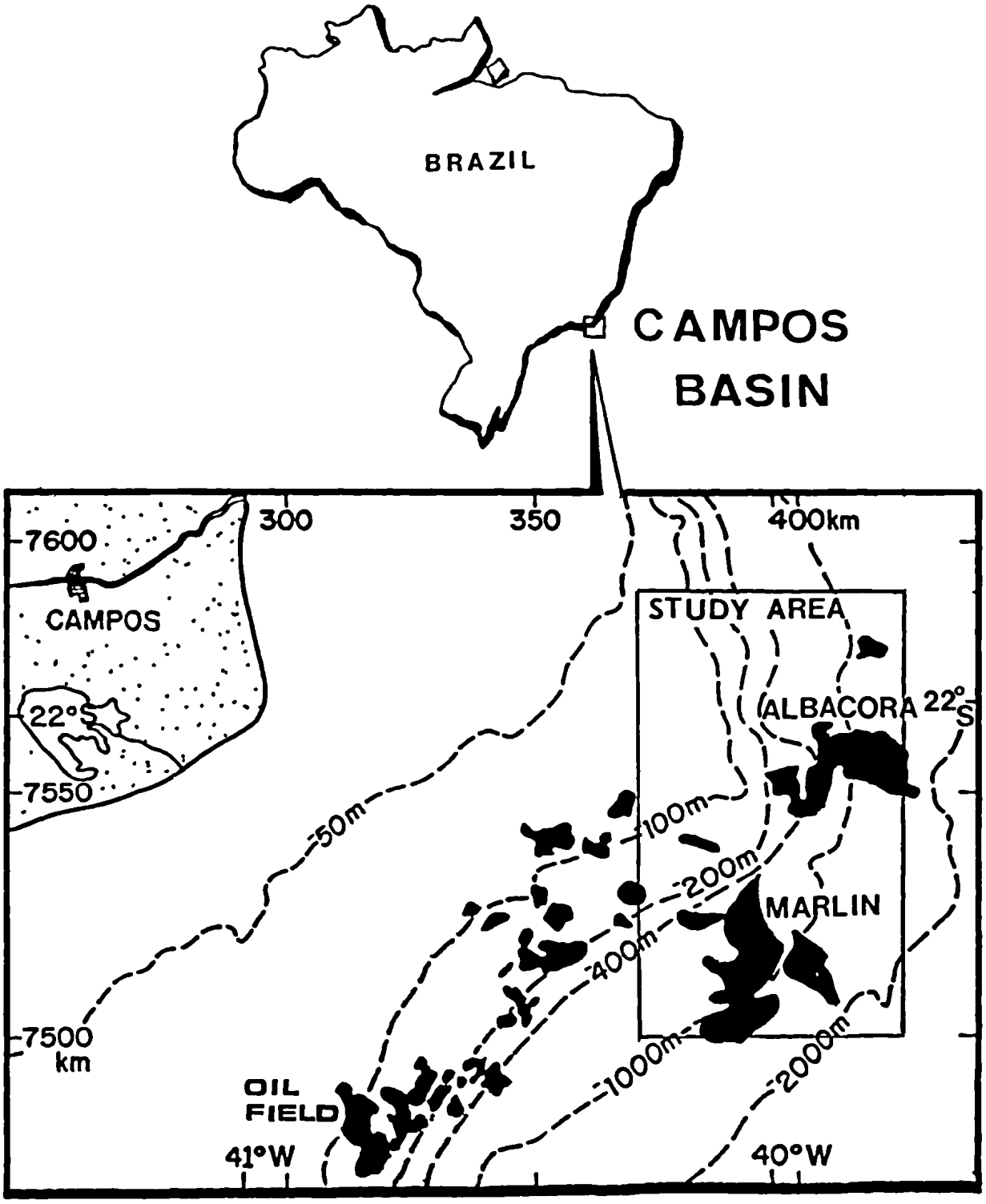


Fig. 1.1 Location of the study area within the Campos Basin.

comparison because of its excellent outcrops and its importance in the literature as the basis for turbidite-facies classifications and depositional models of deep-sea fans (Mutti & Ricchi Lucchi, 1975; Mutti, 1977 and 1985; Mutti et al., 1985; Kruit et al., 1972 and 1975; Crimes, 1973 and 1976).

The sedimentological data were integrated with wireline logs and seismic sections to provide a better understanding of the sedimentary facies and the factors controlling their distribution. Detailed petrological studies were carried out to better understand the nature and formation of potential hydrocarbon reservoirs and adjacent facies.

The following analytical techniques have been used in this study:

1 - sedimentological core description
2 - sedimentological outcrop/core description
3 - interpretation of wireline logs
4 - facies analysis
5 - seismic stratigraphical analysis
6 - spectral analysis of rhythmic bedding
7 - optical microscopy
8 - scanning electron microscopy
    a - secondary electron imaging
    b - backscattered electron imaging
9 - whole rock and clay mineral x-ray diffraction
10 - integration of the above data with reference to current modern literature.

1.3 GENERAL OUTLINE OF THE THESIS

The thesis has an introductory part describing the general regional geology of southeast Brazil including the major tectonic controls on the formation of the Basin (Chapter 2). This is followed by a discussion of the stratigraphy and geological history of the Campos Basin (Chapter 3). Chapter 4 describes in detail all the analytical methods used in this study. The sedimentological studies and facies analysis are presented in Chapter 5, followed by an integration of the facies analysis with the

seismic data in Chapter 6. Here the depositional sequences are defined and the distribution of the main sand-rich turbidite systems are presented. The sedimentary cycles observed in the Oligocene-Miocene succession are discussed in Chapter 7 together with their potential as a complementary tool in the interpretation of deep-water sediments. The petrological and diagenetic evolution of the mudrocks and sandstones are described in chapters 8 and 9, respectively. Finally, in Chapter 10 conclusions of this research are summarised.

CHAPTER 2

REGIONAL GEOLOGY

2.1 INTRODUCTION

The geology of southeast Brazil is characterized by the Serra do Mar Mountains which consist of Precambrian metamorphic and igneous rocks and the Paraná, Resende, Sao Paulo and Taubaté sedimentary basins. The offshore region is characterized by the Campos, Santos and Espirito Santo basins.

The regional tectonic pattern of southeast Brazil and the formation of the Campos Basin was controlled by major Precambrian crustal discontinuities (Almeida et al., 1976 and 1981; Brenner et al., 1980; and Haralyi and Hasui, 1982).

The principal geotectonic units of this region show the same orientation as the main structural lineaments of the rifts (NE/SW) that controlled the Early Mesozoic phase of development of the passive-marginal basins of Brazil (**Fig. 2.1**).

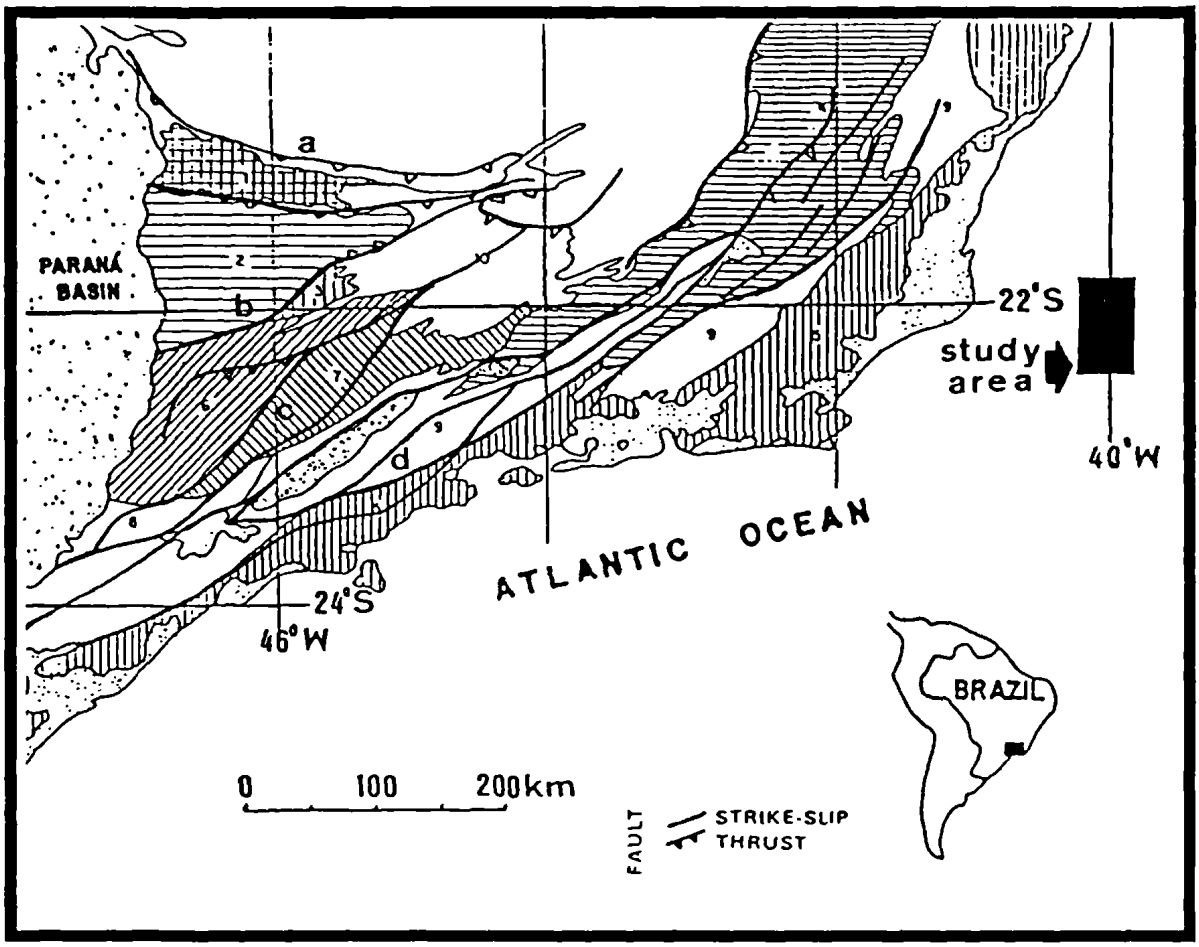
The linearity of the Paraíba do Sul River, the largest modern river in the region, between Sao Paulo and Rio de Janeiro, reflects a zone of weakness associated with transcurrent faulting (NE/SW). A complementary system of NW/SE trending faults also controls the main drainage kinks of the Paraíba do Sul River (Mohriak, 1988).

2.2 LITHOSTRATIGRAPHY OF THE SOUTHEAST BRAZIL

The lithostratigraphy of the southeast of Brazil, adjacent to the Campos Basin, is briefly described below (based on DNPM, 1978; and Radambrasil, 1983):

CENOZOIC sandstones, shales, limestones, localized alkaline igneous rocks;

MESOZOIC	sandstones, shales, limestones, localized alkaline igneous rocks; widespread basaltic volcanism in the Campos Basin and Paraná Basin in the interval 140-120 MyrBP;
PALAEOZOIC	sandstones, shales, limestones of the Paraná Basin; meta-sediments of the Lower Palaeozoic Pouso Alegre, Castro, Camarinha, Guaratubinha, Campo Alegre Basins;
PRECAMBRIAN G (500-640 Myr)	Granites of the Brazilian Orogeny;
PRECAMBRIAN A (570-1000 Myr)	Sao Roque Group (meta-sediments); Bambuí Group (siliciclastic and carbonate sediments); Coastal Belt Complex (granitoids, gneisses, migmatites and charnockites); Sao Joao del Rey/Andrelandia Groups (meta-sediments and gneisses);
PRECAMBRIAN B C (1000-2500 Myr)	Minas Supergroup/Canastra Group (siliciclastic and carbonate meta-sediments);
PRECAMBRIAN C (1800-2500 Myr)	Juiz de Fora Complex (gneisses and charnockites); Varginha-Guaxupé Complex, Amparo Group (gneisses, schists and migmatites);
PRECAMBRIAN D (>2500 Myr)	Divinópolis Complex (migmatites); Rio das Velhas Group (meta-sediments); Barbacena Group (migmatites, gneisses).



GEOTECTONIC UNITS:

1 Campos Gerais Complex
2 Varginha-Guaxupé Complex
3 Silvianópolis Complex
4 Juiz de Fora Complex
5 Costal Complex
6 Amparo Complex
7 Paraíba do Sul Complex
8 Sao Roque Group
9 Açungui Group
10 S.J.D. Rey/Andrelandia g.
Phanerozoic cover

SHEAR ZONES THRUSTS:

a - Campo do Meio
b - Ouro Fino
c - Sao Paulo-Paraíba do Sul
d - Camanducaia

Fig. 2.1 - Simplified geotectonic map of the southeast of Brazil (modified from Hasui and Oliveira, 1984).

The most likely provenance for the Campos Basin sediments were those of the Coastal Complex, Açungui/Sao Roque Group, Juiz de Fora Complex, Paraíba do Sul Complex, Amparo Complex and the Granitoid rocks (**Fig 2.1**), whose characteristics are briefly described below (Cordani and Bittencourt, 1967; Cordani and Kawashita, 1971; Cordani et al., 1972).

a) The **Coastal Complex** - homogeneous and heterogeneous migmatites, kinzigitic gneisses[1], granites, rocks of charnockitic[2] association, basic and alkaline rocks. b) The **Açungui and Sao Roque Groups** - schists, phyllites and gneisses of greenschist/amphibolite metamorphic facies, widespread granitoid bodies (quartz-microcline-plagioclase-biotite/hornblende gneisses) and several quartz-dioritic granites.

c) The **Juiz de Fora Complex** - granulites, charnockites, enderbites[3], pyroxene-granulites, gneisses, amphibolites and migmatites.

d) The **Paraíba do Sul Complex** - gneisses, schists and migmatites.

e) The **Amparo Complex** - para-gneisses and migmatites produced by metamorphism of siliciclastic sediments, tuffs, and basic igneous rocks to an amphibolite/granulite facies.

f) The **Granitoid Rocks** of southeast Brazil (**Fig. 2.2**) are quartz-dioritic to quartz-granitic in composition and are distributed mainly in a NE/SW trend. These rocks are associated with the Sao Paulo - Vale do Paraíba shear zone, and some are clearly controlled by strike-slip faults and probably owe their emplacement to an extensional stress tectonic regime (Mohriak, 1988).

---

[1] A coarsely granulose gneiss formed by the metamorphism of sedimentary rock and essentially composed of garnet, orthoclase, oligoclase, muscovite, graphite and cordierite or sillimanite (Tomkeieff, 1983).

[2] A series of rocks, resembling the pyroxene-granulites of Saxony, ranging from hypersthene-granite (charnockite) through norite-like types of pyroxenite, and characterized throughout by presence of hypersthene (Tomkeieff, 1983).

[3] A medium-grained rock with a faint foliation, composed of antiperthite, blue quartz, hypersthene and magnetite. Claimed to be an acid member of the charnockite series (Tomkeieff, 1983).

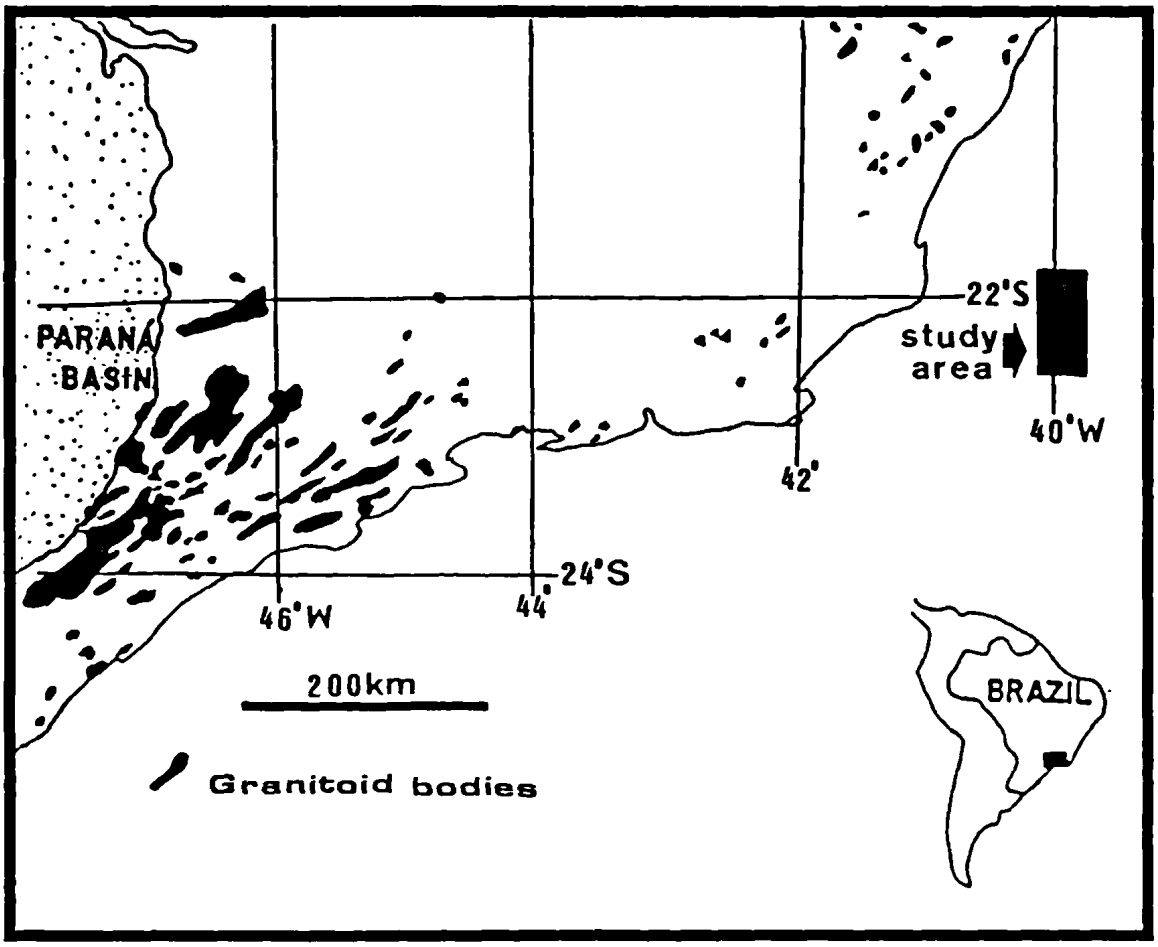


Fig. 2.2 - Distribution of the granitoid bodies in southeast Brazil (from Hasui and Oliveira, 1984). The study area is represented by the black rectangle offshore.

2.3 THE ONSHORE SEDIMENTARY BASINS IN THE PROVENANCE AREA

During the Tertiary there was a general epeirogenic uplift in the continental region of SE Brazil, resulting in regional erosion. Renewed tectonic activity is indicated by reactivation of Precambrian transcurrent faults as block-bounded normal faults. This was possibly associated with isostatic readjustment due to denudation and uplift of the blocks, causing the formation of small sedimentary basins infilled with continental sediments (the Taubaté, Resende and Sao Paulo Basins (Mohriak, 1988)). These basins are located near the border between the states of Sao Paulo and Rio de Janeiro (Fig. 2.3).

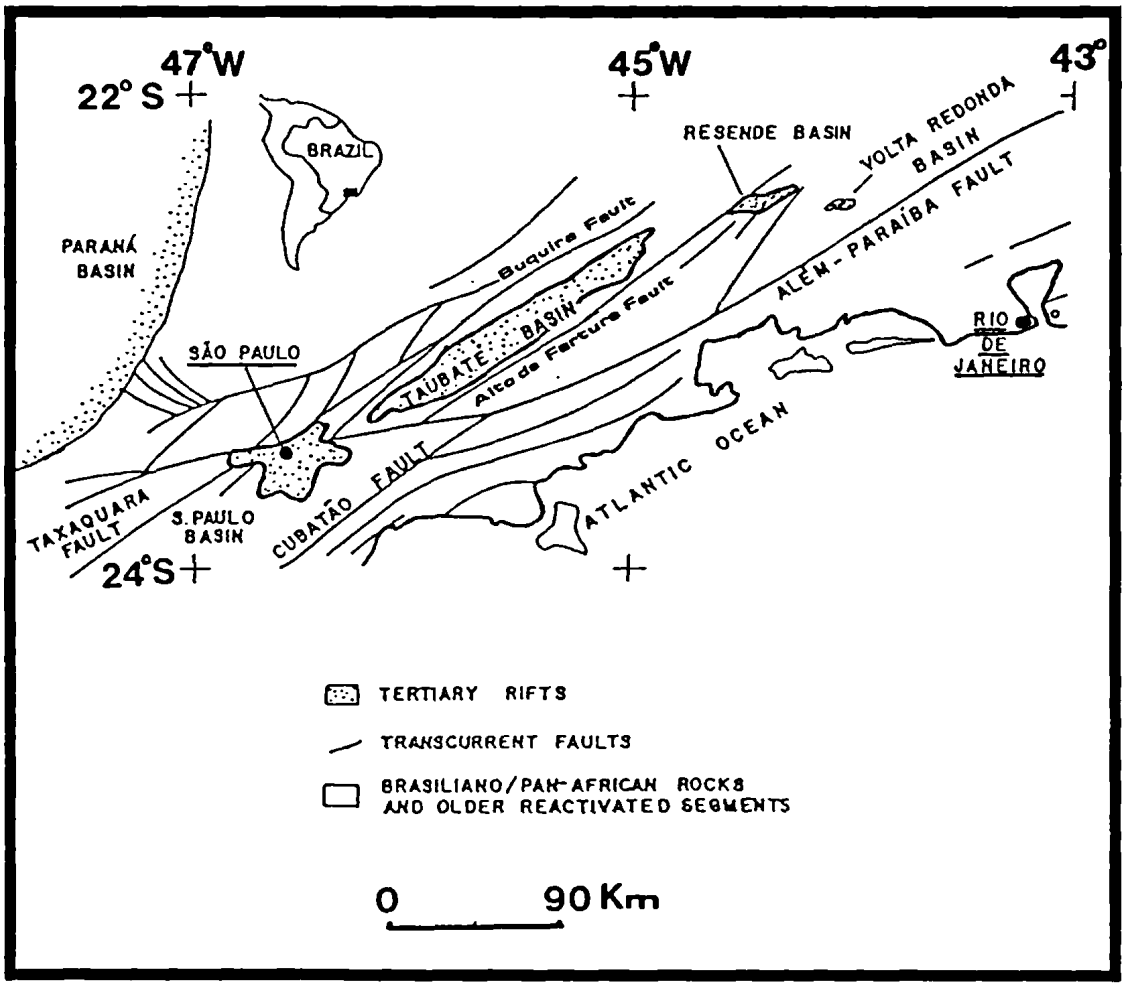


Fig. 2.3 - The location of the Sao Paulo, Taubaté and Resende basins and some of the main structural lineaments of the region (modified from Riccomini et al., 1989).

The Taubaté Basin is a half-graben elongated in the SW-NE direction, 170 km by 20 km, and covering an area of about 2400 km^2. It is bounded to the north by the Buquira Fault, a large Precambrian shear zone, and to the south by the Alto da Fartura transcurrent fault. The sedimentary strata show a regional NW tilt towards the fault planes as

result of subsequent reactivations of these faults.

The tectonic activity was penecontemporaneous with the deposition of about 800 m of sandstones, shales and marlstones. The lower part of the sequence, the Tremembé Fm. of Oligocene-Miocene age, is dominated by lacustrine mudrock facies while the upper part is dominated by fluvial sandstone facies, the Caçapava Fm. of Pleistocene age (Couto and Mezzalira, 1971; Hasui and Poncano, 1978).

Towards the NE, near Rio de Janeiro State, the Resende Basin (**Fig. 2.3**) shows similar lithologies but of younger ages, probably equivalent to the deposits that infill the Sao Paulo Basin (Plio-Pleistocene).

The development of the Sao Paulo, Taubaté and Resende Basins probably allowed them to act as traps for part of the sediment load, causing a decrease in the siliciclastic input from this region into the more seaward Campos Basin during the Tertiary (see Chapter 6).

The region adjacent to the Campos Basin was the most likely source area for the sediments which infilled the Campos Basin and the topography during the Tertiary seems to have been similar to that of today. It is highly probable that the ancient drainage pattern was controlled by the Precambrian regional lineaments which also control the course of the modern Paraíba do Sul River.

CHAPTER 3

GEOLOGICAL EVOLUTION OF THE CAMPOS BASIN

3.1 THE TECTONIC EVOLUTION OF THE CAMPOS BASIN

The Campos Basin is bounded to the north by the Vitória Arch and to the south by the Cabo Frio Arch (**Fig. 3.1**). The western limit of the basin is marked by the Precambrian rocks that crop out near the city of Campos. The Basin extends eastwards into the abyssal plain and its eastern "limit" has been defined only on the basis of its economic interest. The Basin occupies an area of 30,000 Km^2 as far as the 200 m isobath and there is a further 70,000 Km^2 if the Basin is considered to extend to a depth limit of 3,400 m (**Fig. 3.1**). The floor of the Campos Basin consists of basic igneous rocks of the Serra Geral Formation and they have been dated at 140-120 Myr (Amaral, 1966).

The most important event in the evolution of the Campos Basin was the Mesozoic rifting characterized by the emplacement of oceanic crust between the South American and the African continents (Nairn and Stehli, 1973), and the formation of several basins in which sedimentation occurred associated with different stages of this tectonic evolution: the Intracratonic or pre-rift phase, Rift phase, Evaporitic phase and Marine phase (Asmus and Porto, 1972; 1980; Asmus, 1982; Ponte et al., 1980) (**Fig. 3.2**). However, according to Mohriak et al. (1990) the geological data now available do not support this model of domal uplift and block faulting towards the axis (**Fig. 3.2**). Instead, they proposed a model for the evolution of the Campos Basin based on the divergent motion between South America and Africa with crustal thinning and vertical isostatic adjustments characterized by an initial fault-control phase of subsidence followed by a phase of thermal subsidence.

The formation of the Campos Basin was controlled by the development of the Cabo Frio and Vitória Arches arising from differential subsidence. These basement highs (Bacoccoli & Morales, 1973) are structures transverse to the coast and parallel to the trend of the main E-W transform faults of the region (Rezende, 1978). The setting of these highs were controlled by these main oceanic fracture zones (Francheteau & Le Pichon, 1972).

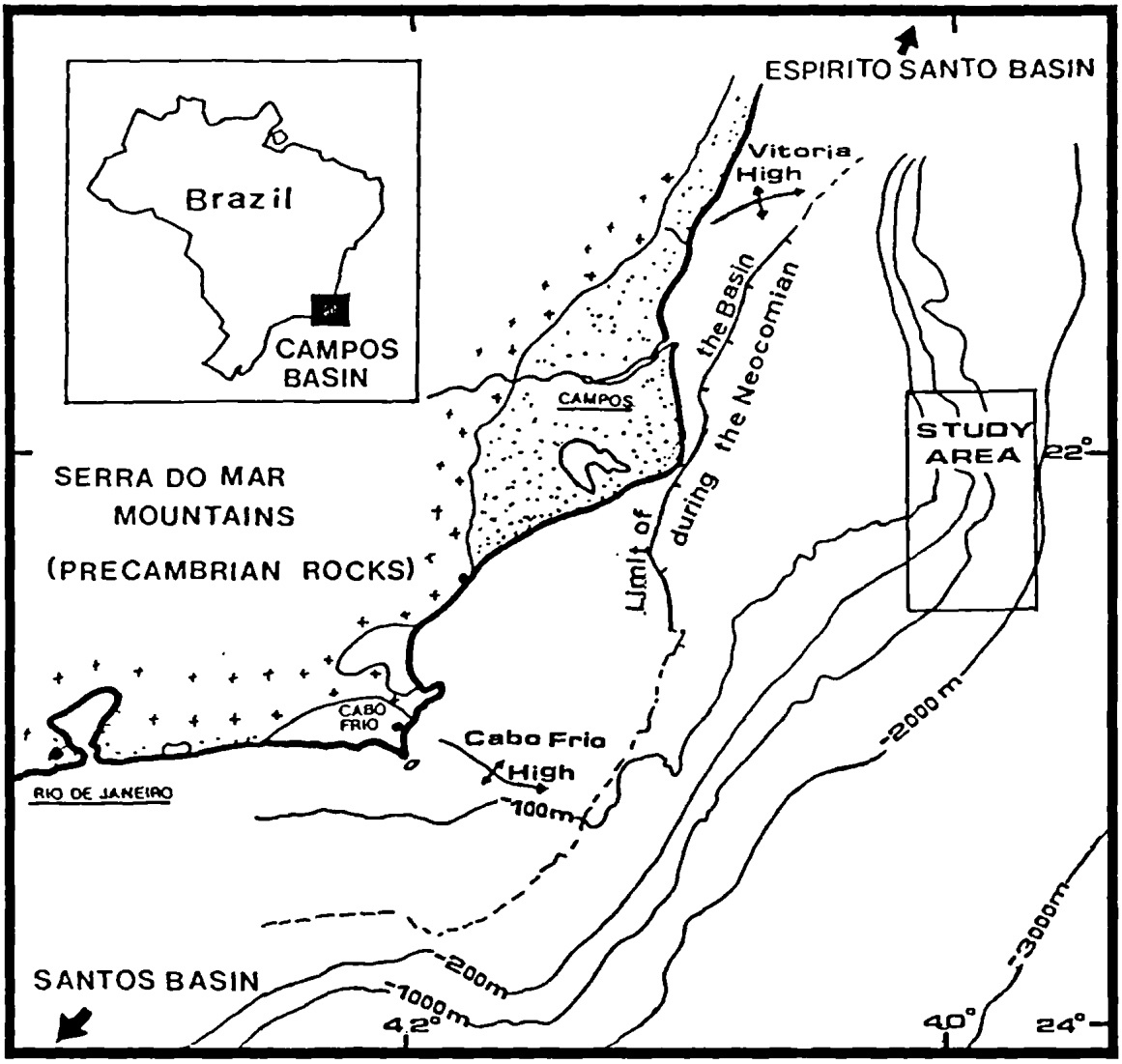


Fig. 3.1 - Location and boundaries of the Campos Basin and the study area.

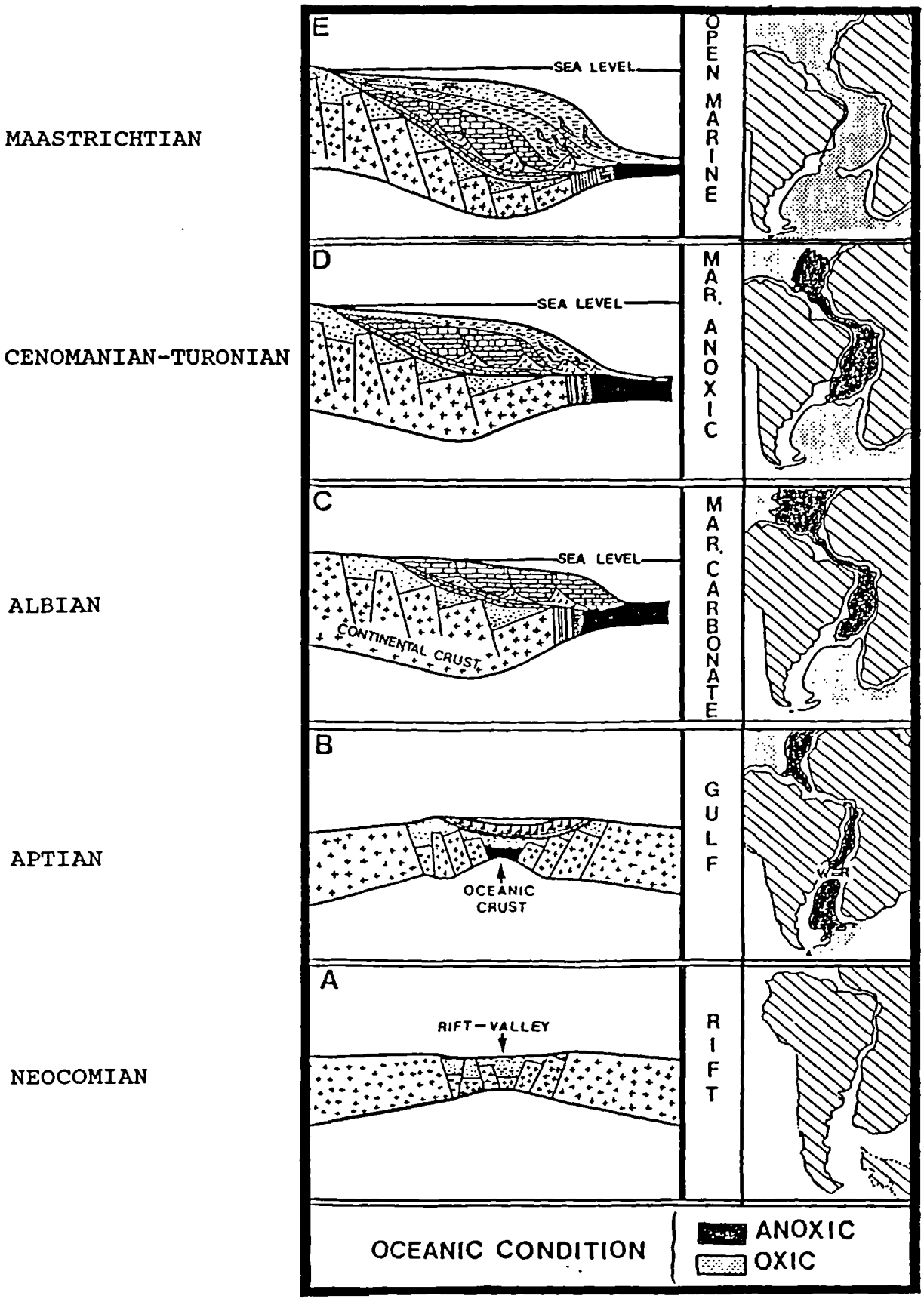


Fig. 3.2 - Geological evolution of the Brazilian Continental Margin during the Cretaceous (modified from Ponte et al., 1980; Tissot et al, 1980; and Mello, 1988).

With the onset of rifting during the Neocomian, sediments accumulated in a type III basin (Klemme, 1971) or tafrogeosyncline (Dewey and Bird, 1970). During this stage fault-controlled grabens were rapidly infilled with siliciclastic sediments. The active faults during this period were mainly normal faults. The downthrown block was usually on the basinward side, but examples of antithetic faulting were observed in the seismic sections. These were active mainly during the Neocomian (Mohriak, 1988).

The Campos Basin can be classified as a divergent, mature, Atlantic-type continental marginal basin (Ponte & Asmus, 1978; Ojeda, 1982). Using the basin classification of Kingston et al. (1983) the Campos Basin formula, according Figueiredo & Gabaglia (1986), can be written as: IF 12L/IS 12M/(MS 12M/Lc/MS 2M3) Lb basin. The symbols used in this formula are defined as:

IF = internal fracture;
IS = internal sag;
MS = marginal sag;
L = lacustrine environment;
M = marine environment;
1 = pre-transgressive continental sediments;
2 = marine or lacustrine sediments;
3 = regressive continental sediments;

modifying tectonic:

Lb = weak, associated with halokinetic movements;
Lc = moderate strike-slip movements and normal faulting reactivation.

The grabens and horsts of the Campos Basin are bounded by several systems of faults, often parallel to the main Precambrian structures (**Fig. 3.3**). The hinge-lines, characterized by an increase in the dip of the basin floor towards the basin centre, are also parallel to the main Precambrian lineaments. It is also possible to recognize the synthetic and antithetic faults that produced the main horsts and grabens during the rift-stage (**Fig 3.3 B**).

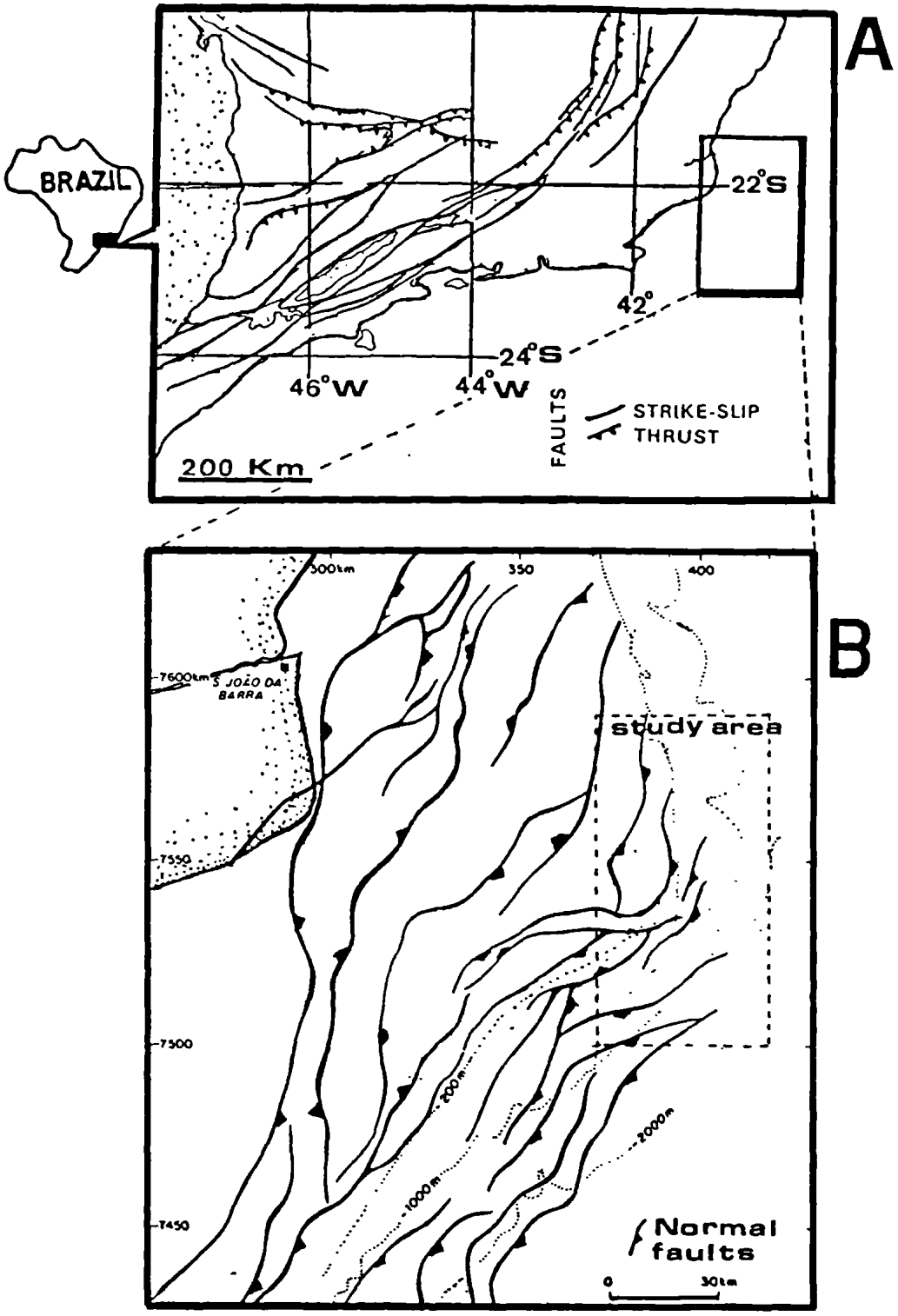


Fig. 3.3 - (A) The simplified structures of southeast Brazil showing the main shear zones and thrusts (modified from Hasui and Oliveira, 1984); (B) The faults affecting the Campos Basin basement (modified from Dias et al., 1987).

The Neocomian rift sequence in the Brazilian basins has been divided into several stages by Petrobrás palaeontologists based on ostracod biozones and their approximate absolute ages are shown in **Table 3.1** (after Beurlen, 1981).

TABLE 3.1

Alagoas	(108 - 115 Myr)	APTIAN
Jiquiá	(115 -)	
Buracica	(- 120 Myr)	
Aratu	(120 - 125 Myr)	NEOCOMIAN
Rio da Serra	(125 - 130 Myr)	

The rift-stage in the Campos Basin is represented by the Lagoa Feia Formation and consists of thick (>2,000 m) siliciclastic and carbonate sequences, deposited in a basin with an irregular floor of alternating horsts, grabens and half-grabens. The syn-tectonic alluvial-lacustrine sedimentation shows rapid facies variations (Schaller, 1973; Castro and Azambuja Filho, 1980; Bertani and Carozzi, 1984).

The rifting-phase ceased once sea-floor spreading started and the first marine incursions into this coastal basin took place during the Aptian. This transgression gave rise to extensive deposition of evaporites (Asmus, 1975).

During the Albian both seafloor spreading and thermal subsidence of the continental margin produced more normal marine environments than in the restricted pre-Albian environments. This change was accompanied by the deposition of marine platform and slope carbonates when there was little tectonic activity. As the Basin started to tilt seaward in response to thermal subsidence at the end of Albian, there was gravity induced movement of slabs of carbonate on the evaporitic layers producing growth faults.

From the Upper Cretaceous to the Recent open-marine

sedimentation was controlled by thermal subsidence and tilting of the Basin and was predominantly siliciclastic in nature (Campos, 1980; Mohriak, 1988). Continuous tilting and piling up of sediments on the underlying carbonates and evaporites caused increased movement of the evaporites and growth faults became more common. Some detached faults soling out on the evaporites are active up to the Recent (**Fig. 3.4**) (Carminatti, 1987). The rate of sedimentation associated with some of these faults was very high with more than 2,000 m of sediments being deposited during the Miocene alone.

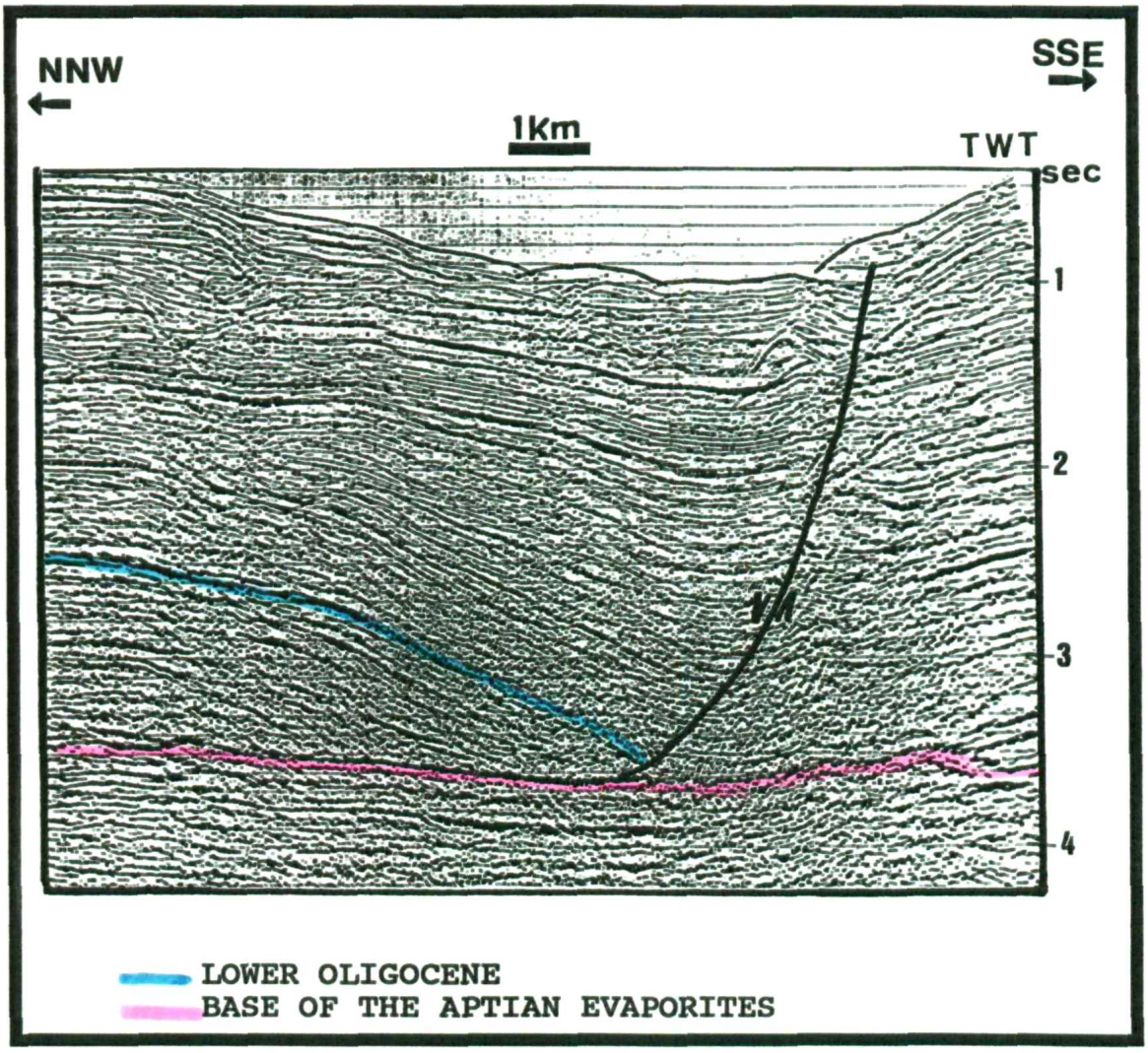


Fig. 3.4 - A detached growth fault soling out on the Aptian evaporites with activity up to the Recent.

There is evidence of some igneous activity in the Campos Basin during the Upper Cretaceous (90-80 Myr) and the Lower Tertiary (60-40 Myr) represented by tuffs and diabase sills, which can be related to extensional movements probably associated with E-W transform faults (Carminatti, 1987; Mohriak, 1988).

3.2 STRATIGRAPHY OF THE CAMPOS BASIN

The Campos Basin stratigraphy can be conveniently divided into that of the offshore and onshore areas. The offshore area will be discussed in more detail as the majority of the data comes from this area because of its economic relevance. The stratigraphy of the onshore region will be described more briefly, because this area consists mainly of sandstones with little palaeontological data. The ages of the rocks in the onshore area were obtained mainly through correlation with the corresponding offshore interval.

3.2.1 STRATIGRAPHIC EVOLUTION AND DEPOSITIONAL ENVIRONMENTS OF THE OFFSHORE CAMPOS BASIN

The lithostratigraphy (**Fig. 3. 5**) of the Campos Basin has the following units: Igneas Básicas, Lagoa Feia Formation, Macaé Formation, Campos Formation and Embore Formation (Schaller, 1973). The total thickness of these sediments is commonly more than 4,000 m.

A regional schematic section in time, based on a seismic line extending from the northwest of the basin into deep water, shows the main lithological units and structural elements of the Campos Basin (**Fig. 3.6**). It also shows well developed roll-over structures at the shelf-edge associated with listric faulting that soles-out on the Aptian evaporites.

3.2.1.1 IGNEAS BÁSICAS: 130-120 Myr (RIO DA SERRA)

The Igneas Básicas unit consists of basic igneous rocks that are assumed to constitute the basement for the Neocomian sequence. Several radiometric dates for these

rocks indicate ages varying from 130 to 120 MyrBP (Asmus and Guazelli, 1981), corresponding approximately to the Rio da Serra/Aratu stages (see **Table 3.1**).

3.2.1.2 THE LAGOA FEIA FORMATION: BARREMIAN-APTIAN

The Lagoa Feia Formation includes the sediments deposited during the Rift and Proto-Oceanic stages of the basin development during the Lower Cretaceous. It consists of conglomerates, lithic (volcaniclastic) sandstones, siltstones, shales and carbonates, overlain by anhydrite and halite. The lower contact with the extrusive basic igneous rocks of the Igneas Basicas (120-130 Myr), is considered to be discordant throughout the area (**Fig. 3.5**) (SECASU, 1980; and Guardado et al., 1990). However, according to Bertani & Carozzi (1984) this discordance is probably only present on the paleohighs. Within the lows, the overlying sediments are concordant and the contact is considered to be transitional, characterized by basic volcaniclastics with small dikes.

Castro & Azambuja Filho (1980) divided the entire Lagoa Feia Formation into four sedimentary cycles. Each cycle is composed of basal coarse-grained sediments (conglomerates and sandstones) deposited in alluvial plain or lake-margin environments followed by lacustrine shales, locally black and rich in organic matter (T.O.C. up to 9 weight%, Pereira et al., 1984), non-marine coquinas of bivalves and ostracods and marlstones. Each cycle represents a regressive facies succession followed by a transgressive sequence, reflecting periodic contraction and expansion of the lacustrine environments.

The biota found in this Formation consists mainly of non-marine ostracods with thick reticulated shells (secreted in saline waters), bivalves, gastropods, as well as pollen and spores. The palaeontological and the sedimentological evidence indicate that the rocks of the Lagoa Feia Formation were deposited in a generally shallow saline lacustrine environment (Castro et al, 1981; Bertani & Carozzi, 1984).

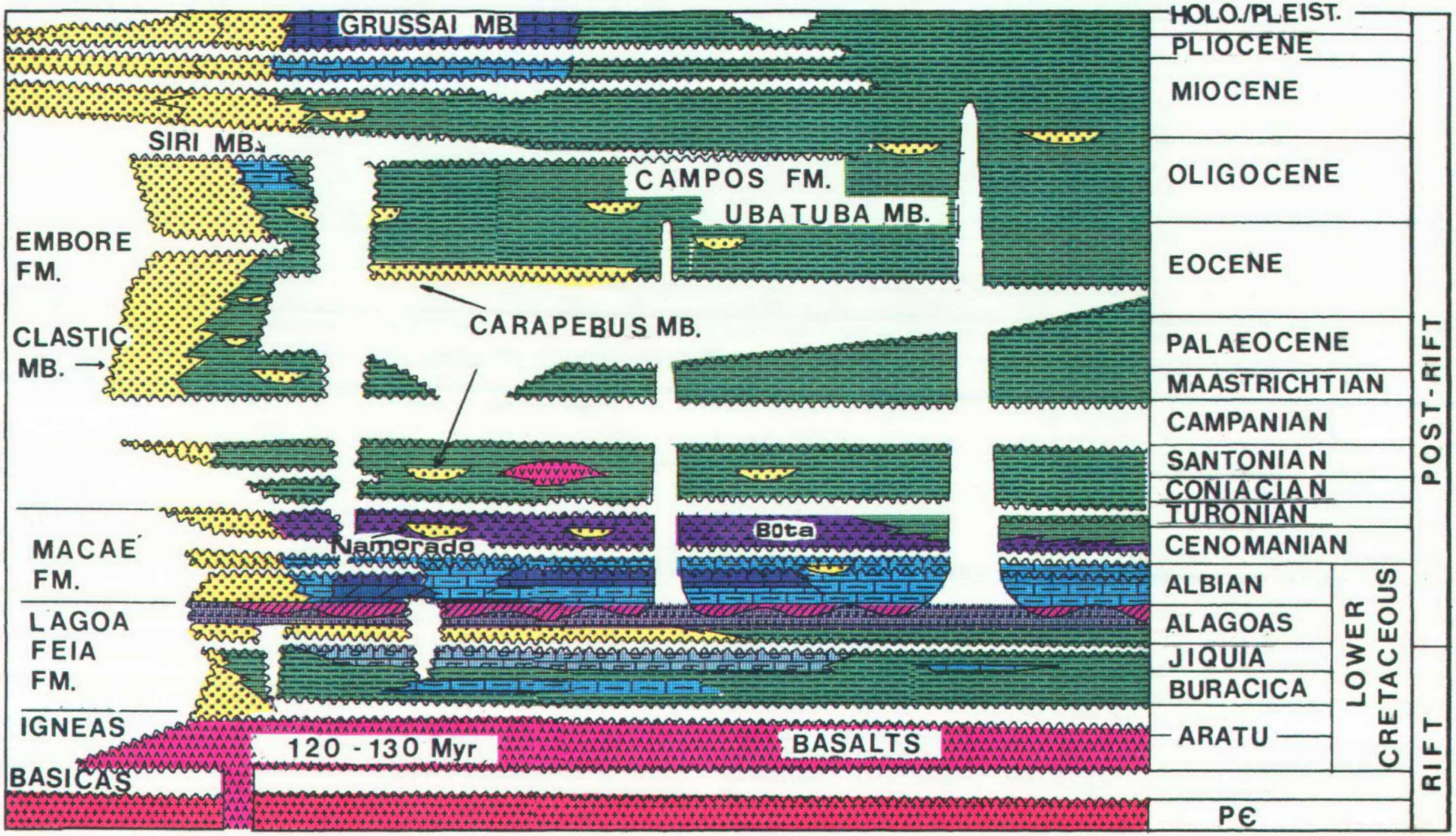


Fig. 3.5 Lithostratigraphic column of the Campos Basin (modified from Guardado et al., 1990).

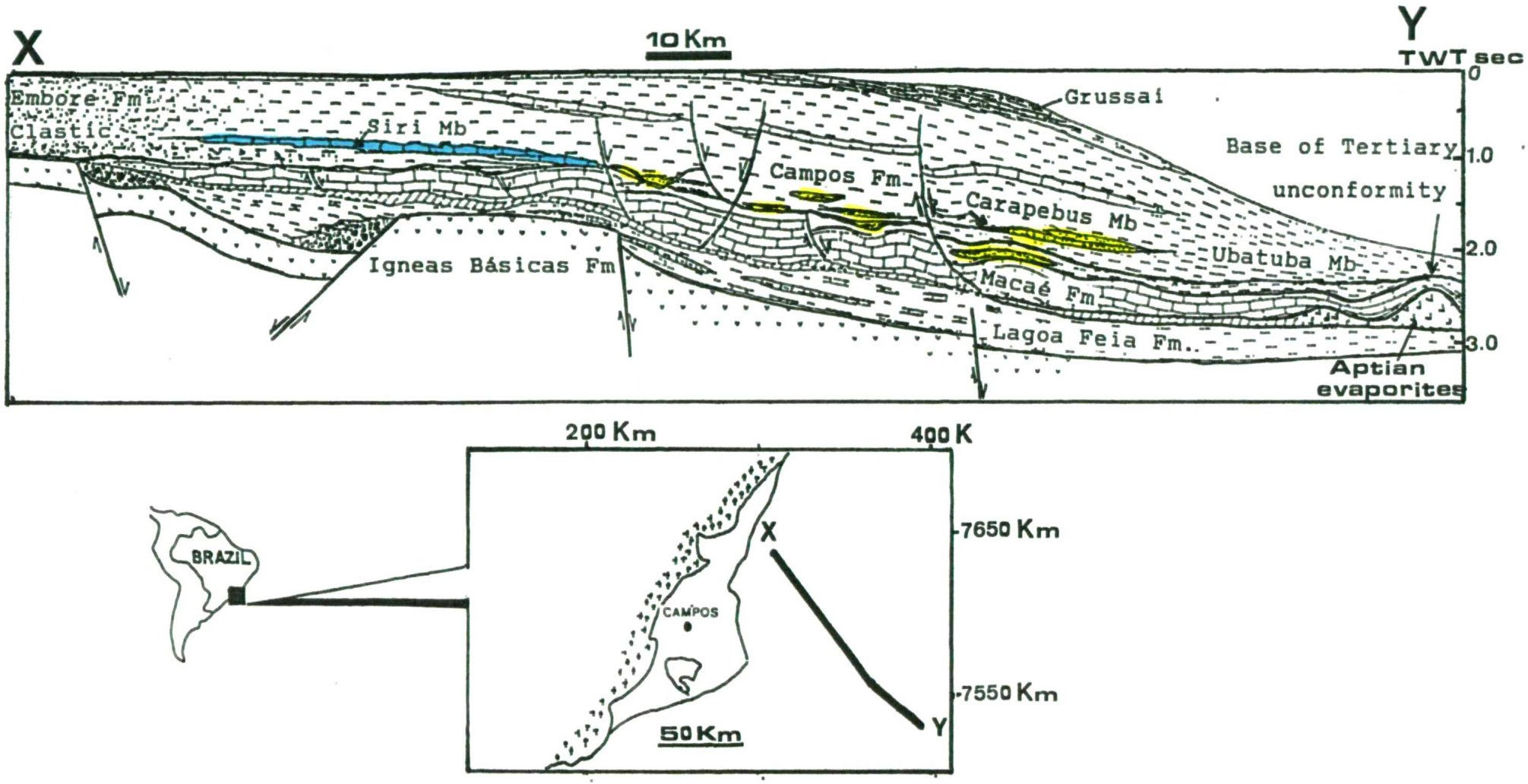


Fig. 3.6: Schematic section in two-way travel time (TWT) showing the main lithostratigraphic units and structural features of the Campos Basin (modified from Mohriak, 1988).

The occurrence of gypsum and anhydrite nodules, early diagenetic trioctahedral smectites, dolomite, zeolites of the heulandite-clinoptilolite type and authigenic minerals kerolite and sepiolite reinforce this interpretation of deposition in a shallow saline-alkaline lake (Bertani & Carozzi, 1984).

The laminated calcareous black shales and marlstones of the upper part of the cycles are the source rocks for the hydrocarbons in the Campos Basin. Their biomarker characteristics indicate deposition in a saline alkaline lake (Mello et al., 1988).

During Aptian times a thick pile of evaporite was deposited over the Neocomian sediments coincident with the first incursion of the sea. This was accompanied by little tectonic activity, a hot climate and the basin topography being restricted by the Walvis Ridge to the south. These conditions provided an environment conducive to the widespread deposition of evaporites. This evaporitic event is well documented in the Brazilian marginal basins and in the western marginal basins of Africa, indicating that deposition occurred on a continental scale (**Fig. 3.7**).

There is a predominance of anhydrite, halite and dolomite in the southern basins (Santos, Campos and Espirito Santos) whilst in the Sergipe Basin of northeast Brazil there was deposition of more soluble salts such as sylvite, carnallite and taquidrite. This reinforces the view that at this time the opening of the Atlantic Ocean was to the South.

3.2.1.3 THE MACAÉ FORMATION: ALBIAN-LOWER TURONIAN

The Macaé Formation consists of a thick sequence of marine carbonates and contemporaneous fluvio-deltaic sandstones and shales, and has been divided into a Lower (Albian) and an Upper Macaé Formation (Cenomanian/Lower Turonian), the latter also informally called the "Bota" (see **Table 3.2** and **Fig. 3.5**) (Falkenhein et al., 1981).

TABLE 3.2

UPPER MACAÉ FORMATION OR "BOTA"
(Cenomanian/Lower Turonian)
slope carbonate/calcareous mudstones and
siliciclastic turbidites (the Namorado Sandstone)
LOWER MACAÉ FORMATION (Albian)
platform carbonates facies (grain/pack/wackestones)
upper part = less restricted fauna
lower part = restricted fauna

The basal part of the Lower Macaé Formation consists of shallow water siliciclastic sediments interbedded with oolitic grainstones characterized by a restricted fauna of benthic and planktonic foraminifera, suggesting an inner-neritic hypersaline environment. With an increase in the subsidence of the Walvis Ridge there was a gradual opening of the basin to the south and the environment become less restricted creating conditions for widespread carbonate sedimentation (**Fig. 3.8**). The deposition of oolitic/oncolitic grainstones/packstones and carbonate mudstones[4] took place in a middle to deep-neritic (30-200 m) environment with a greater diversity of foraminiferal species and an abundance of planktonic forms, but still with some evidence of a restricted environment.

The Upper Macaé Formation is composed mainly of carbonate mudstones, marlstones and shales and some siliciclastic turbidites (the Namorado Sandstone). The marlstones and shales are rich in planktonic foraminifera, calcispheres and radiolaria.

[4] Carbonate mudstones according to Dunham (1962).

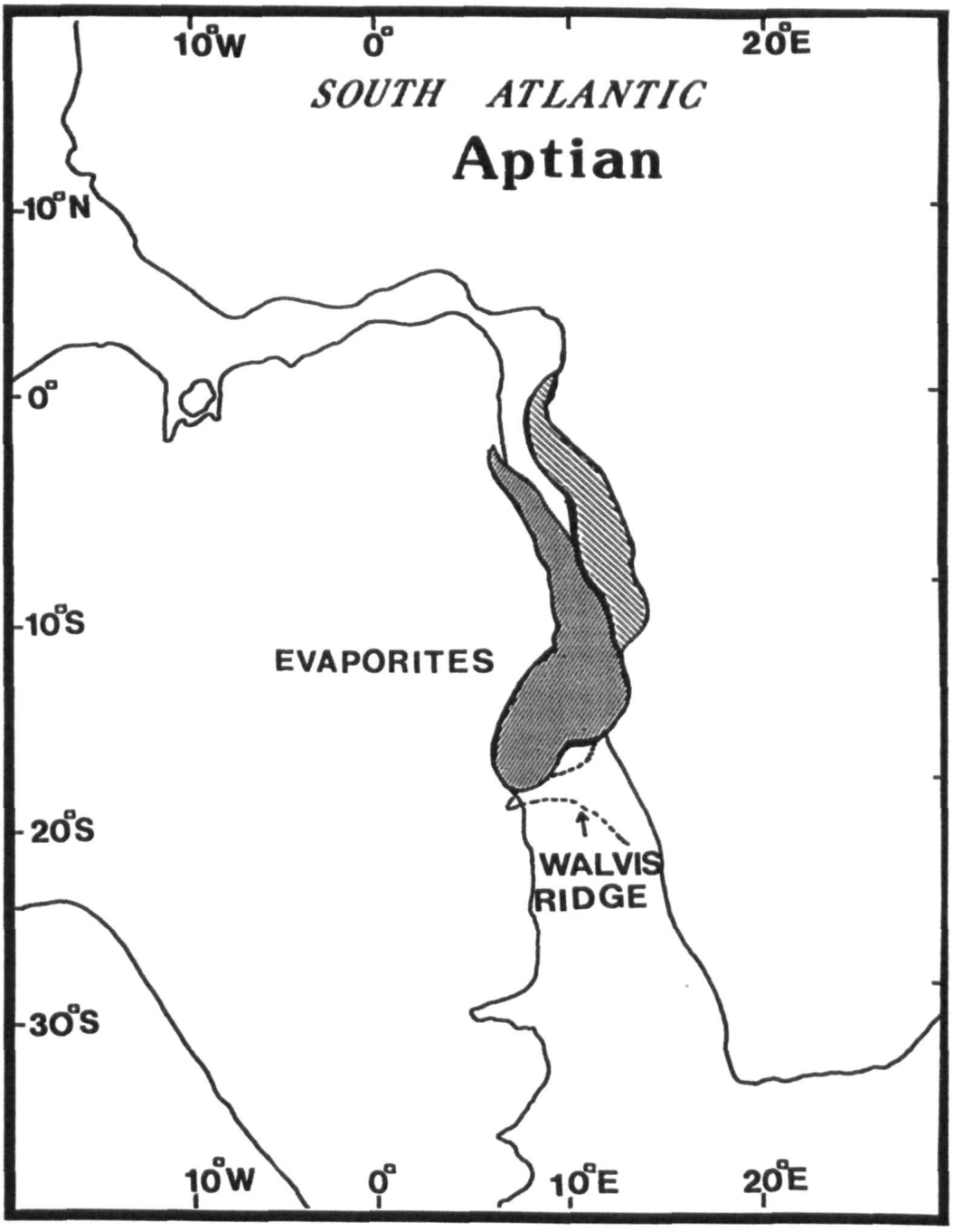


Fig. 3.7 - The distribution of the evaporites in the South Atlantic during the Aptian (modified from Leyden et al., 1976).

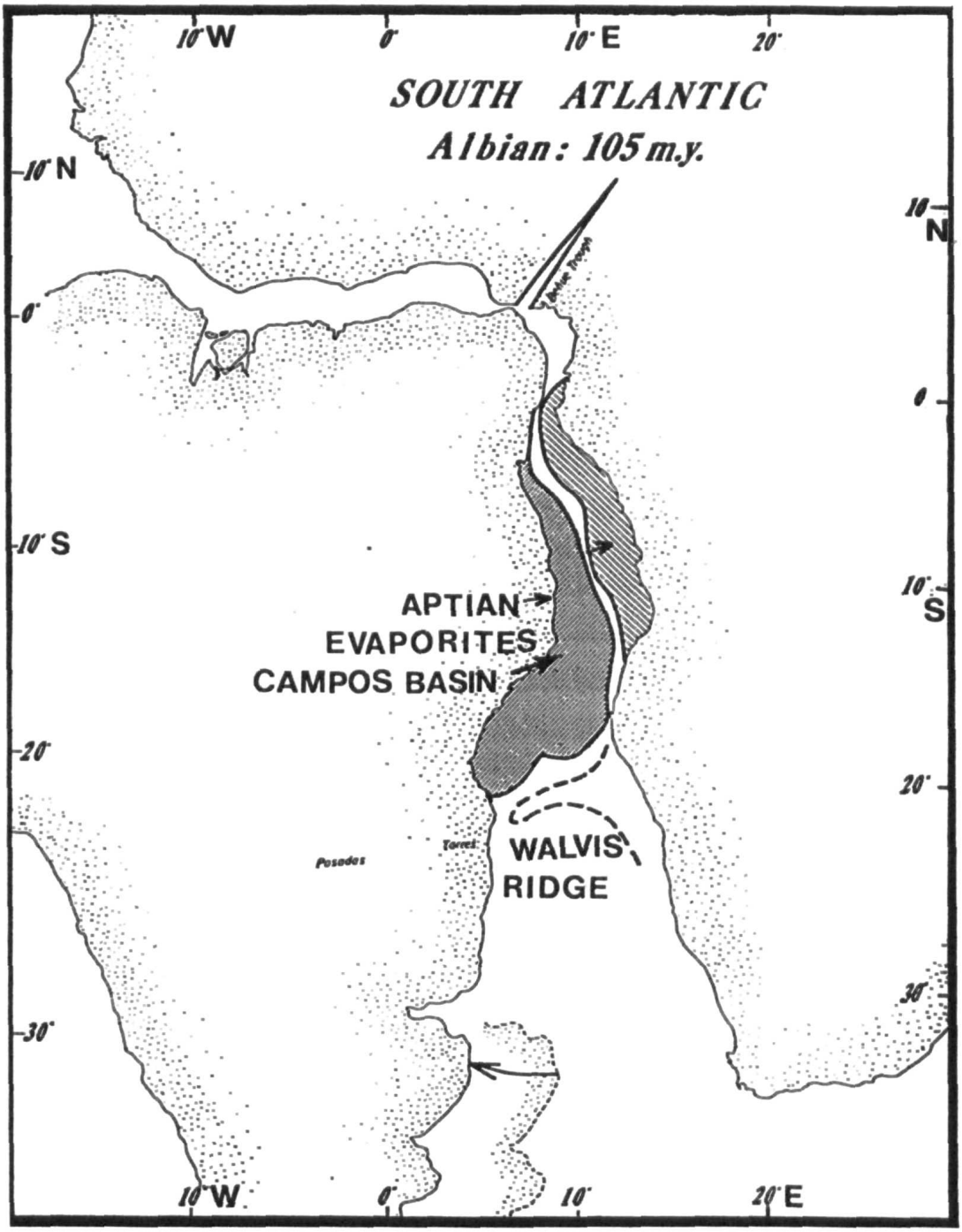


Fig. 3.8 - The South Atlantic during the Albian showing the opening of the Walvis Ridge (modified from Leyden et al., 1976).

According to Koutsoukos (1984, 1985) Koutsoukos & Dias-Brito (1987) the Macaé Formation was generally deposited in shallow neritic to upper bathyal environments within a narrow epicontinental sea. The evolution of the facies was topographically controlled by the continuous tilting of the basin seaward and the development of growth faults, associated with the movement of underlying Aptian evaporites, with deposition of grainstones and packstones on the tectonic highs which were within the wave-base level (Falkenhein et al., 1981).

3.2.1.4 THE CAMPOS FORMATION: CONIACIAN-RECENT

The Campos and Embore Formations are the result of the continuous tilting and subsidence of the basin from the Cenomanian to Holocene. These two Formations have an overall thickness of about 4,000 m in the eastern part of the basin.

The Campos Formation consists of deep-water siliciclastic mudstones, marlstones, carbonate mudstones (Ubatuba Member), and siliciclastic turbidites (Carapebus Member). The siliciclastic turbidites occur mainly at three distinct stratigraphic levels (Barros, 1980): Upper Cretaceous, Eocene and Oligocene-Miocene (**Fig. 3.5** and **3.6**).

The Coniacian to Maastrichtian sequence is characterized by a progressive deepening of the basin with maximum water depths occurring in the Maastrichtian when bathyal/abyssal conditions were established in more distal areas. Sedimentation was characterized by siliciclastic mudstones, marlstones, carbonate mudstones (Ubatuba Member) and siliciclastic turbidites (Cretaceous Carapebus Member). The troughs created during the collapse of the underlying evaporites provided the main pathways for the turbidites (Guardado & Arso, 1985).

The Cenomanian section is missing in some areas of the basin (**Fig. 3.5**). This hiatus has been interpreted by some authors (Koutsoukos, 1984; 1987; Dias Brito, 1987) to be a consequence of a global erosional/non-depositional event. This was the result of a tectonic change which led to the complete linking of North and South Atlantic, sometime

during the Cenomanian and Turonian.

The Tertiary units are characterized by a thick progradational sequence of deep-water siliciclastic mudstones, marlstones, and carbonate mudstones with intercalations of siliciclastic turbidites (Tertiary Carapebus Member) deposited in a bathyal well-oxygenated, open-marine environment (Koutsoukos, 1987; Mello et al., 1988c). A regional unconformity is indicated by the generalized absence of the Palaeocene and Lower Eocene deposits in the basin. During the Middle-Eocene, a thick sequence of clastic turbidites was deposited throughout the basin. The Oligocene is characterized by the predominance of mudstones, marlstones and some sandstone intercalations. The Miocene is characterized by the progradation of a siliciclastic shelf/slope unit with some carbonate intercalations. The seismic expression of the Miocene unit is that of a typical offlap depositional sequence. The Upper Tertiary sedimentation rates greatly exceeded the subsidence rates and the deep-water environments were replaced by progressively shallower-water sedimentary environments characterized by a general progradation of deltaic and platform facies onto the slope. These greater accumulation rates were a response to the uplift of the Serra do Mar Mountains with consequent increase in the sediment supply into the Campos Basin.

Particulary during the middle Eocene, late Oligocene and the early Miocene several canyons were cut in the shelf and slope sediments and these were the pathways for the subsequent gravity flows that deposited the Tertiary Carapebus Member (Barros, 1980; Della Favera, 1975; Gamboa et al., 1986; Guardado & Arso, 1985; Mutti et al., 1979; Sonoki, 1987).

3.2.1.5 THE EMBORE FORMATION: TERTIARY-RECENT

The Embore Formation consists of the Siri, Grussaí, and Clastic Facies Members.

The Siri Member was deposited during the Oligocene as shallow-water platform bioclastic carbonates and passes

transitionally into pelagic-marlstones and carbonate mudstones in the deeper parts of the basin.

The Grussaí Member is characterized by coarse-bioclastic platform-carbonates deposited from the Miocene to the Recent.

The Clastic Facies Member is characterized by proximal fluvio-deltaic sandstones that pass gradually into mudstones in the deeper water environments.

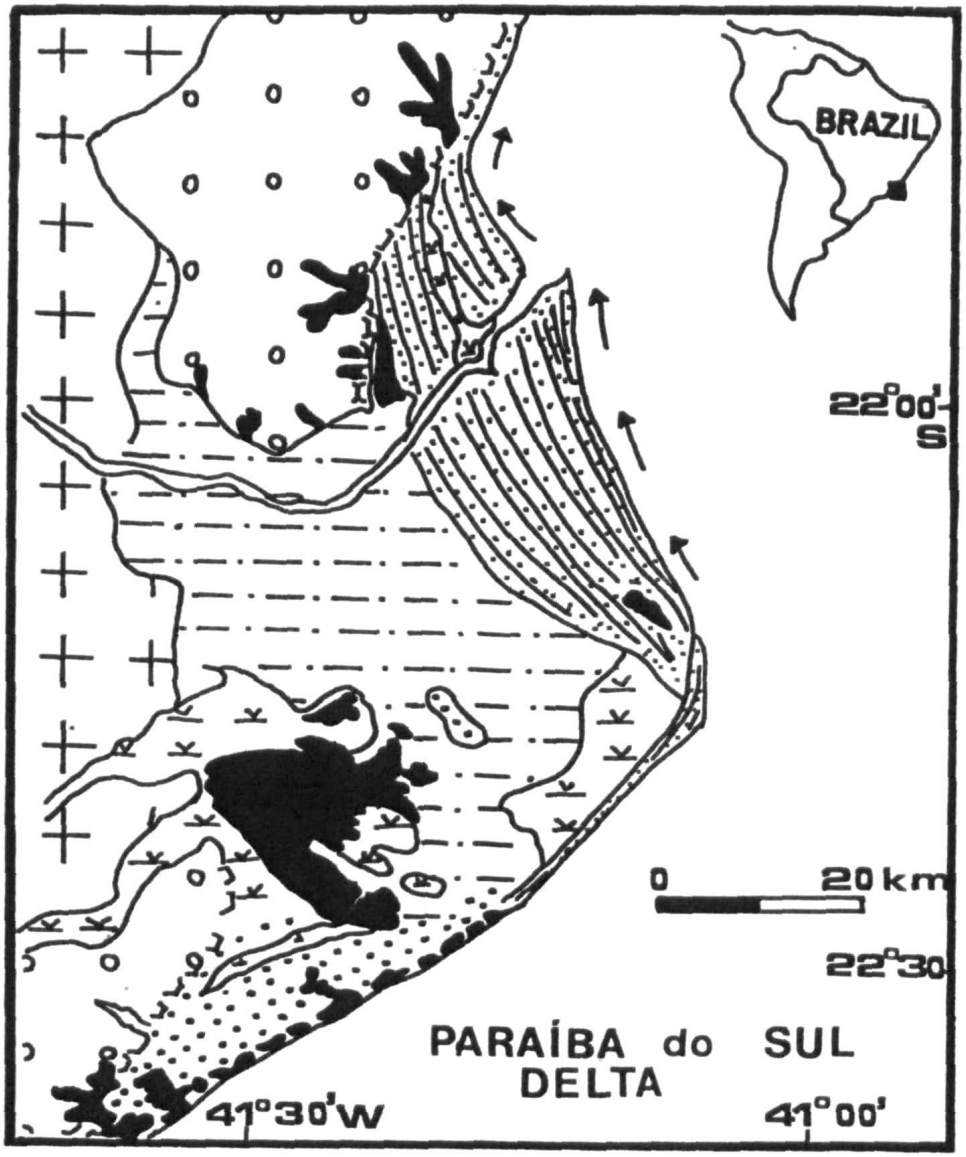
The Embore Formation reflects by coastal/shelf sedimentation while the Campos Formation formed in deeper water environments (mudstones-Ubatuba Member) into which siliciclastic turbidites (Carapebus Member) were introduced.

3.2.2 STRATIGRAPHIC EVOLUTION AND DEPOSITIONAL ENVIRONMENTS OF THE ONSHORE CAMPOS BASIN

The onshore part of the Campos Basin consists of a small area (500 Km^2) of sandy siliciclastic sediments overlying igneous and metamorphic rocks. The first borehole in the basin (CST-10) drilled through about 2000 m of Tertiary sediments (Embore Formation) overlying 600 m of basaltic rocks (Igneas Básicas Formation) before reaching the Precambrian basement. The faults that cut the basement also clearly offset the sedimentary deposits. In the area around the Lagoa Feia (a modern lagoon), west of this borehole, the basement is only a few tens of meters below the surface (Mohriak, 1984).

The extrapolation of palaeontological data from the offshore exploratory wells into the onshore section, using seismic data, indicates that sedimentation occurred mainly in the Tertiary (Mohriak, 1988).

In the Lagoa Feia region the sequence is dominated by the Holocene sediments of the Rio Paraíba do Sul deltaic plain (Araujo and Beurlen, 1975). The modern Paraíba do Sul delta as other modern deltas on the Brazilian coast can be classified as a wave-dominated delta (Bacoccoli, 1971) According to Dominguez at al. (1987) the distribution of the coastal facies have been strongly influenced by high-frequency sea-level oscillations (200-300 yr) during the



lake

freshwater swamp

fluvial

Precambrian basement

Barreiras Fm.- Tertiary

Holocene beach-ridge terrace

Pleistocene beach-ridge terrace

beach-ridge alignment

wave-generated longshore drift direction

Fig. 3.9: The modern Paraíba do Sul Delta (modified from Dominguez et al., 1987).

BIBL. INDIA UNIV

CHAPTER 4

METHODOLOGY

4.1 INTRODUCTION

The sample material and data for this research project came from an offshore area of 5,000 Km^2 in the northeastern part of the Campos Basin, Brazil. These consist of wireline logs from 50 exploratory wells, 490 m of cores from 28 wells, and 800 Km of seismic lines of which 550 Km are inside and 250 Km outside the area. The latter are extensions of regional lines that cross the study area (**Fig. 4.1**).

4.2 FACIES ANALYSIS

4.2.1 LITHOFACIES

4.2.1.1 LITHOFACIES DEFINITIONS AND DESCRIPTIONS

The definition of the lithofacies was based on sedimentological descriptions of core samples combined with their wireline log responses and comparisons with pertinent literature (Bouma, 1962 and 1964; Mutti & Ricci Lucchi, 1975; Mutti, 1977 and 1985; Mutti et al. 1985; Kruit et al. 1972 and 1975; Crimes, 1973 and 1976; and Pickering et al., 1986 and 1989). The Bouma Sequence, complete (Tabcde) or incomplete, has been used to differentiate and interpret the lithofacies generated by turbidity currents (**Fig. 4.2**)

The cores were initially described on a scale of 1:25 and then converted to 1:200, which is more suitable for comparisons with wireline logs. The cores were also logged with the surface gamma ray (GR) on a scale of 1:200. The surface GR logs were very useful to relate the cored interval with the wireline logs.

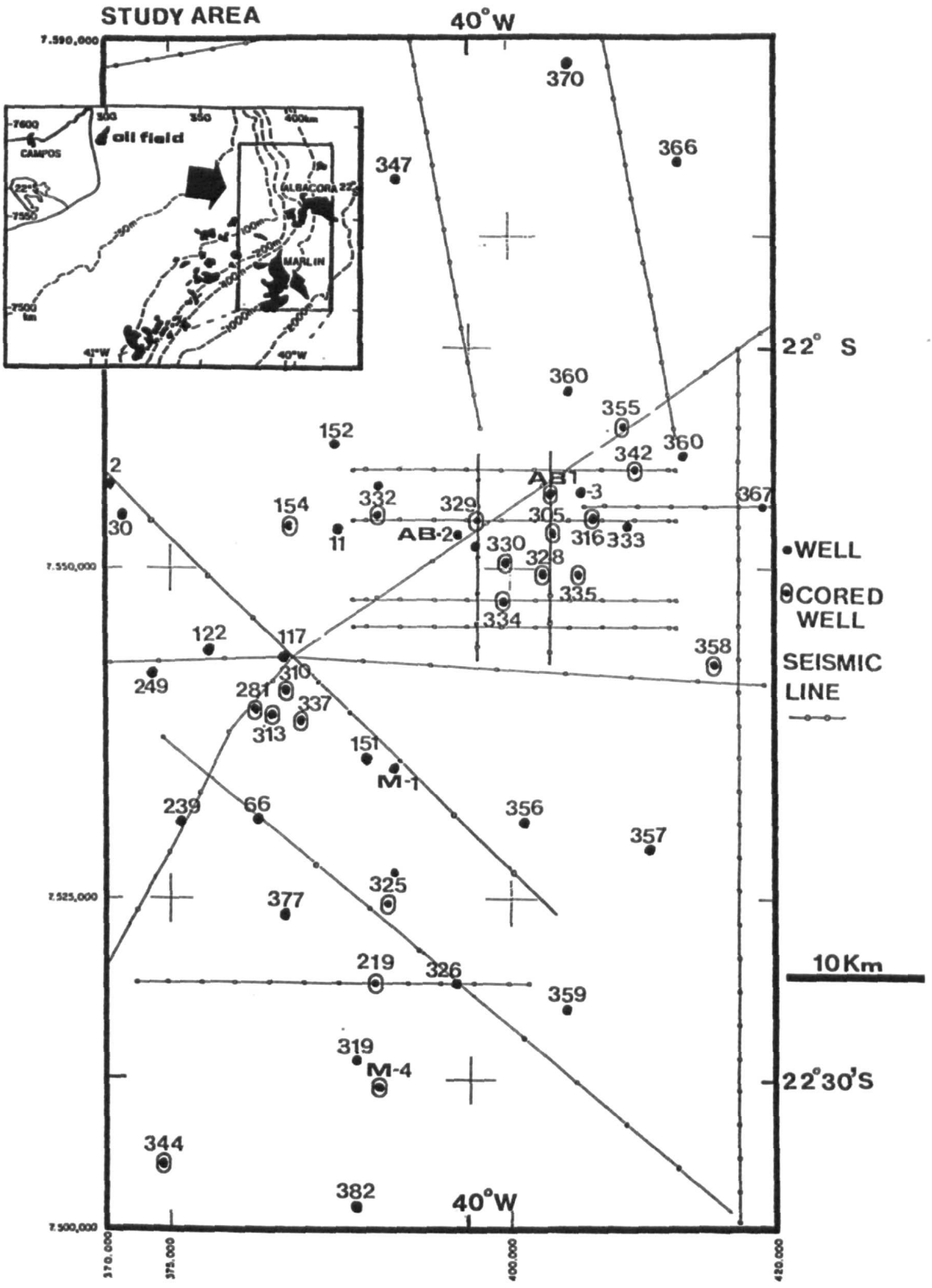


Fig. 4.1 - Studied area with the location of wells and seismic sections. The same figure but including stratigraphic and schematic sections is located in the pocket at the back of the thesis.



GRAIN SIZE	BOUMA (1962) DIVISIONS	INTERPRETATION
Mud	E Laminated to homogeneous mud	Deposition from low-density tail of turbidity current ± settling of pelagic or hemipelagic particles
Silt	D Upper mud/silt laminae	Shear sorting of grains & flocs
Sand	C Ripples, climbing ripples, wavy or convolute laminae	Lower part of lower flow regime of Simons *et al* (1965)
	B Plane laminae	Upper flow regime plane bed
Coarse Sand	A Structureless or graded sand to granule	Rapid deposition with no traction transport, possible quick (liquefied) bed

Fig. 4.2 Ideal sequence of sedimentary structures in a turbidite bed "the Bouma Sequence" (after Bouma 1962, with interpretations after Harms & Fahnestock 1965, Walker 1965, Middleton 1967, Walton 1967, Stow & Bowen 1980).

4.2.1.2 EQUIVALENT OUTCROP LITHOFACIES

The study of rocks of sedimentary facies in outcrops and their correlation with similar cored sediments is a usual technique to overcome interpretative difficulties related to facies geometry and facies variations. For this reason, the well exposed turbidite facies at the Pyrenean basin, north Spain, were selected for comparison with the subsurface data. There, rocks of turbidite facies were studied in the outcrops of the Eocene Hecho Group (Ainsa-Broto) and in the Eocene Jaizkibel Fan (San Sebastian), respectively eastern and western parts of the Pyrenean Basin. The rocks of the turbidite facies that occur in this Basin have been used as examples for classifications of deep-water facies and to develop submarine fan depositional models for (Mutti & Ricci Lucchi, 1975; Mutti, 1977 and 1985; Mutti et al. 1985; Kruit et al. 1972 and 1975; Crimes,

1973 and 1976; and Pickering et al., 1986 and 1989).

Although the size and the tectonic style of the Pyrenean Basin (small active-margin basin) differs significantly from the Campos Basin (large passive-margin basin) these differences were taken into account when the comparisons were made.

4.2.2 ELECTROFACIES

The wireline-log responses of rocks of the various lithofacies (i.e. electrofacies) are very useful in subsurface facies analysis and together with the seismic data they are the most widely available subsurface data. The definition of the electrofacies was made using core calibrated wireline logs. Each electrofacies is composed of one or several distinct lithofacies which simply or in various combinations produced the particular wireline log response of that electrofacies. Additionally, those electrofacies that occur frequently associated were called electrofacies associations.

For this project the following kinds of wireline logs were available (not necessarily in all wells):
a) Conventional gamma ray (°API); natural gamma ray spectometry (NGS) consisting of total gamma ray (SGR in °API), computed gamma ray (CGR) = SGR - uranium content (°API). The individual curves for thorium and uranium are scaled in ppm, and potassium is scaled as weight%;
b) Surface gamma ray (°API); c) Resistivity - induction spherically focussed (ISF), and spherically focussed log (SFLU) ($OHM.m^2/m$); d) Sonic (BHC) - borehole compensated sonic log ($\mu sec/ft$); e) Density (FDC) - formation density compensated (g/cm^3); f) Neutron (CNL) - compensated neutron log, scaled in limestone porosity units (p.u.) for the corresponding porosity value of an ideal sandstone 4 p.u. needed to be added to these values); h) Dipmeter - high resolution dipmeter tool (HDT) or stratigraphic high resolution dipmeter tool (SHDT) is presented as 4 or 8 microconductivity curves respectively, and as a computed display being the "tadpole" plot the most common.

The lithologies were best characterized by density and neutron logs. The relative behaviour of the two curves indicates the characteristics of the various lithofacies. The sonic and resistivity logs were also helpful when density and neutron logs were not available.

The gamma ray log aided the interpretation, but due to the presence of mica and k-feldspars in the mudrocks and in the sandstones individual lithofacies could not be very precisely identified from gamma ray log. However, when the NGS log was available it was possible to monitor variations of uranium, thorium and potassium and correlate them to the lithofacies.

The most common processed presentation form of the dipmeter log is the "tadpole plot", represented by arrows whose heads indicate the dip angle and the "tail" points to the azimuth. The interpretation of the "tadpole" patterns (**Fig. 4.3**) was carried out using the principles described in the Schlumberger dipmeter interpretation manual (1981), plus examples and case histories from the literature (e.g. Selley, 1978 and 1979; and Ricci Lucchi, 1984).

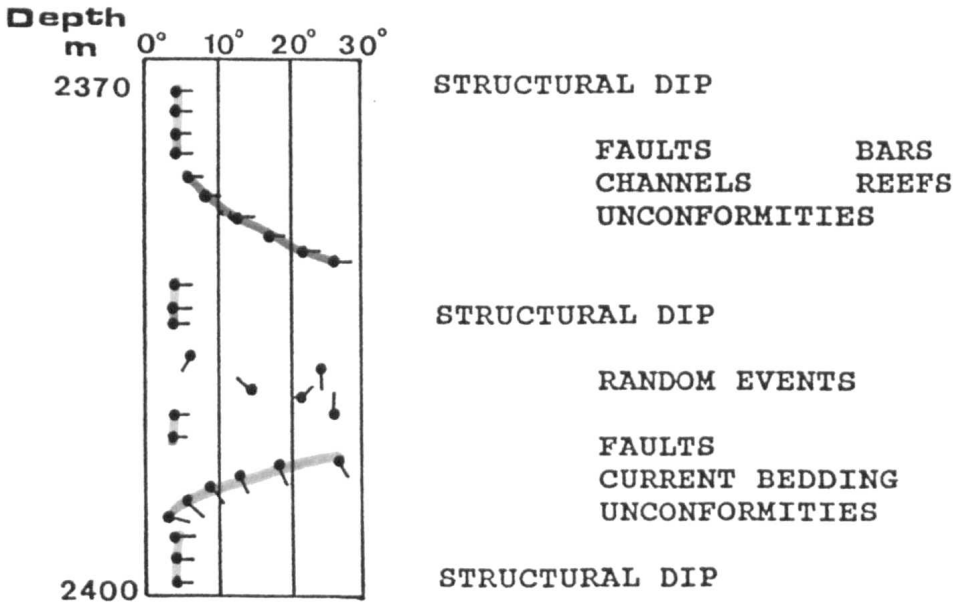


Fig. 4.3 Dipmeter patterns and geologic anomalies commonly associated with them (Schlumberger, 1981).

As the resolution of the dipmeter is 1-2 centimetres, whilst for the other logs it is 60 cm, the microconductivity curves were used as an additional and important source of information to identify thin-bedding, massive sandstones, slumped intervals and thin tight cemented intervals.

4.3 PETROLOGICAL ANALYSIS

Petrological studies of the cored samples were made using optical microscopy, scanning electron microscopy (S.E.M.) and x-ray powder diffraction (X.R.D.).

4.3.1 OPTICAL PETROGRAPHY

A petrographic description sheet was prepared for each sample. Grain-size, shape and sorting were described with reference to visual comparison charts (Powers, 1953; Scholle, 1979). The composition of the sandstone was determined by visual estimations and point counting. A ten memory Swift automatic point counter fitted with a mechanical click stop stage was used to count 300 points in each thin-section. Due to discrepancies found between the visual estimates and point counting analysis in some heterogeneous very fine or pebbly sandstones, a further 500 points were counted for these lithologies.

The system of sandstone classification used in this study was that of Pettijohn et al. (1973). This classification was generally appropriate although not ideal. The major problem was the large proportion of bioclastic framework grains in some of the sandstones, exceeding 20 % of the total in some cases. The term "bioclastic" was applied when the percentage of bioclasts was more than 10%. In general, the sandstones can be classified as arkoses or subarkoses. Additionally, the rock fragment component was redefined for this study and includes bioclasts, and mafic minerals.

Porosity estimations were only made visually and the criteria used for defining the types of porosity were based on those of Schmidt and Mcdonald (1979).

4.3.2 SCANNING ELECTRON MICROSCOPY (S.E.M.)

The various modes of operation of an S.E.M. depend on the different ways in which the electron beam interacts with the specimen. Three modes of operation were used in this study: a) the emissive mode (both backscattered and secondary); b) the cathodo-luminescent mode; and c) the x-ray analytical mode. The electron microscope used in this study was the Hitatchi S-2500 model.

4.3.2.1 EMISSIVE MODE

The scattered electrons produced by the interaction of the electron beam with the specimen are of two types: a) low energy (<50 ev), produced by inelastic collisions from the top 50-500 Å of the specimen; b) higher energy backscattered electrons are produced by elastic collisions (**Fig. 4.4**, for more details see White et al., 1980; and Goldstein et al., 1981).

4.3.2.1.1 SECONDARY ELECTRON IMAGING (S.E.I.)

Secondary electron imaging provides information about the surface topography of the specimen and is used to produce images of fractured surfaces. However, this type of imaging has proved less successful in the study of fine-grained argillaceous rocks, because there is less topographic contrast in fractured specimens of these rocks. It is also difficult to make direct comparisons between thin-section observations and the secondary electron images obtained from the fractured surfaces. Such comparisons are better made with backscattered electron images of polished thin section specimens.

The sample preparation for S.E.I. consists of mounting a sample of about 1 cm^2 with a freshly fractured surface on an aluminium stub and coated with a 300 Å thick gold film applied in a sputter coater.

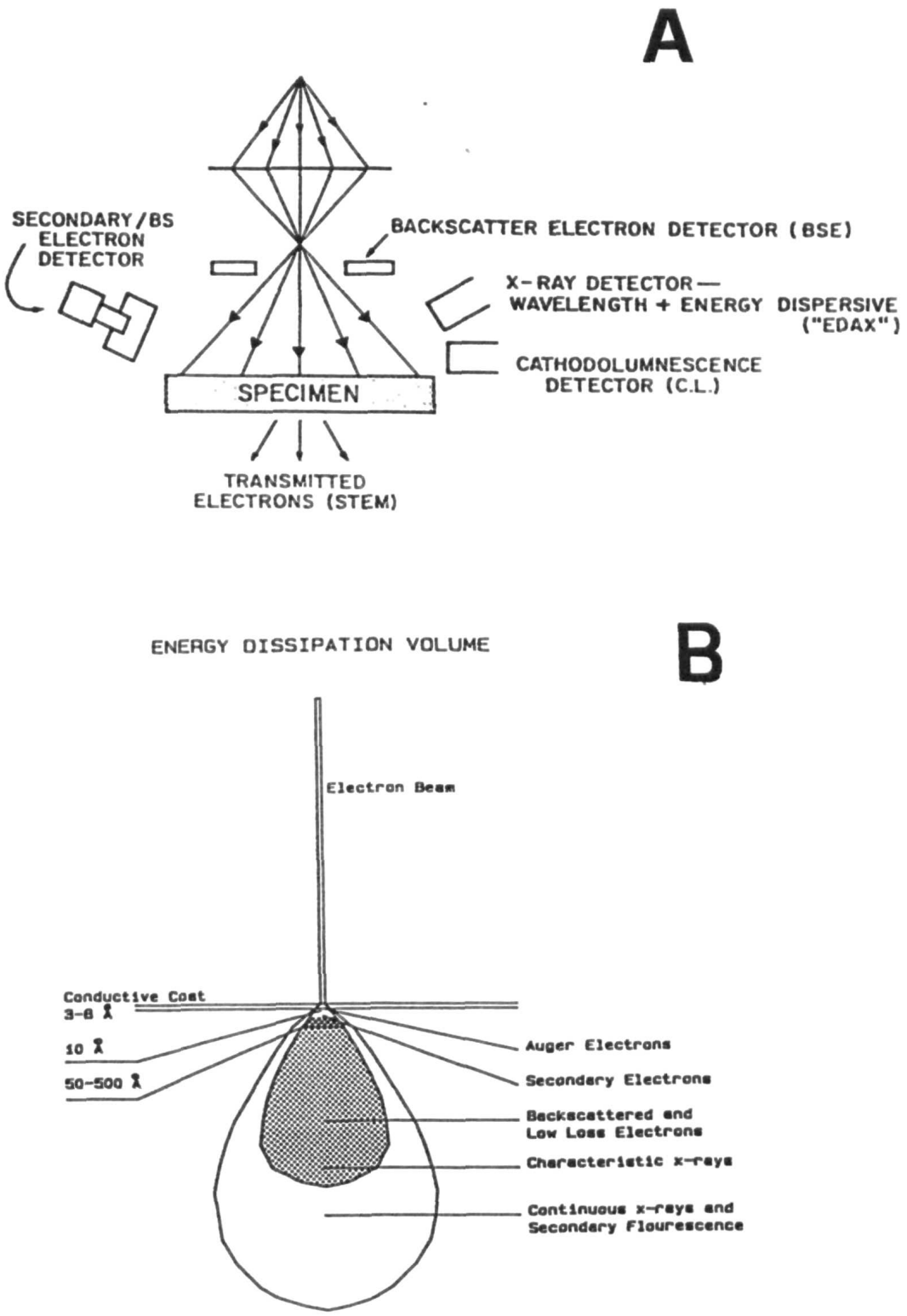


Fig. 4.4 A) Operation modes of an electron microscope (Shaw, 1987); and B) the energy dissipation volume of an electron beam striking a specimen (Goldstein et al., 1981).

4.3.2.1.2 BACKSCATTERED ELECTRON IMAGING (B.S.I.)

For backscattered imaging the secondary electrons are excluded either by biasing the backscattered electron (BSE) detector with a sufficiently high negative potential to repel the lower energy secondary electrons or by having a BSE detector insensitive to the secondary electrons. The degree of backscattering is measured in terms of the BSE coefficient (η).

$$\eta = \frac{\text{number of backscattered electrons}}{\text{number of incident electrons}}$$

The BSE coefficient is a function of the mean atomic number of the specimen and the higher the mean atomic number the brighter is the backscattered image. This is referred to as compositional contrast. It is possible to differentiate minerals with only a difference of 0.1 in their mean atomic number (Lloyd and Hall, 1981) which is very useful for compositional analysis. Because the intensity of the backscattered electron signal is also a function of the angle of tilt producing topographic contrast, to examine the compositional contrast alone polished block and thin-section specimens need to be used.

The sample preparation consists either of making thicker than normal thin-sections, then polishing them down to 30 μm or for polished blocks, setting small pieces of rock in resin which are then cut and polished. A conductive carbon coat was applied to the surface prior to examination.

4.3.2.2 CATHODOLUMINESCENCE (C.L.)

Cathodoluminescence (C.L.) is the emission of the visible light spectrum when a mineral is bombarded with electrons. Details of the mechanism for production of C.L. images using an S.E.M. are given by Goldstein et al. (1981). The spectrum of light emitted is a function of the composition of the minerals being irradiated. The C.L. (S.E.M.) method is useful for analyzing quartz or feldspars, but for carbonates the intensity of the emitted light is so great that it saturates the detector and does not allow imaging contrasts. Because of this limitation the C.L.

(S.E.M.) method was less useful during this study, because the majority of the analyzed samples have calcite as the principal cement and only a few specimens have quartz and feldspar overgrowths.

An alternative C.L. method for carbonate analysis was to use a cold stage cathodoluminescence source (Technosyn model 8200 MK II) connected to an optical microscope.

The same polished thin sections utilized for the S.E.M. analyses can be used for both C.L. imaging processes, but without carbon coating.

4.3.2.3 ENERGY DISPERSIVE X-RAY ANALYSIS (EDAX)

The energy dispersive x-ray analytical facility (EDAX) on an S.E.M. utilizes the fluorescent x-rays produced by the elements in a mineral when an electron beam strikes the specimen. The fluorescent x-rays are characteristic and proportional to the concentration of the elements in the specimen. A stationary electron beam of variable size is used for this type of analysis and chemical composition can be obtained from grains down to 5 μm (Shaw, 1987). It is not possible to detect elements lighter the Na^{+} using EDAX.

Qualitative EDAX analyses were carried out routinely to help confirm identification of the observed mineral phases. For more precise analyses of specific minerals quantitative analysis were carried out using a Link System 869 analyzer with a ZAF4 software and a cobalt standard. The technique used to calculate structural formulae from these quantitative analyses was the "last element by difference" assuming the number of oxygen atoms for the mineral being analyzed. Details of quantitative energy dispersive x-ray analysis are given by Goldstein et al. (1981).

4.3.3 X.R.D. ANALYSIS

4.3.3.1 SAMPLE PREPARATION AND DIFFRACTOMETER PARAMETERS

Samples of core material and cuttings were analyzed using x-ray powder diffraction methods. The analyses were performed using a Philips 1830 diffractometer employing monochromated Cu Kα radiation generated at 40 kV and 50 mA.

The diffractometer had an automatic divergence slit assembly but the data could be converted to equivalent 1° fixed divergence slit data by the APD 1700 Software.

For whole-rock analysis the selected specimens were ground in an agate Teema mill. The powder was packed in aluminium sample holders and analyzed under the following conditions: step size of 0.040° 2θ, sample time of 3 seconds, at a scanning rate of 75 s/deg 2θ, from 5° to 75° 2θ. The data were subsequently converted from an automatic to a fixed (1 deg) divergence slit in order to compare with existing JCPDS mineral identification tables.

The clay fractions (<2 μm) of the samples were prepared by first washing the powdered samples in distilled water to remove any salt and adding a few drops of ammonia as a deflocculant. The <2 μm fractions were obtained by centrifuging the samples in distilled water for 5 minutes at 1000 rpm and then decanting off the <2 μm material which remained in suspension. Part of the <2 μm fraction was then saturated with $MgCl_2$ to produce Mg-saturated clays for analysis. The clay fractions were prepared as oriented specimens required for the X.R.D. analysis by the suction-onto-ceramic-tile method (Shaw, 1970).

The discs were dried out in a desiccator containing silica-gel. The clay fraction (<2 μm) of the samples were analyzed in the x-ray diffractometer air-dried, glycolated and heated at 400°C and 500°C.

To verify whether the expandable clays were vermiculites or not the samples treated with $MgCl_2$ were also solvated with glycerol. Vermiculites show a diffraction peak of about 14.5 Å, after this treatment and the smectites a diffraction peak of about 18 Å (Walker, 1957 and 1958).

The diffractometer conditions used for the analysis of the clays in the air dry state were: variable divergence slit converted to a fixed 1° slit ; scanning step size of 0.015 2θ; scanning angle range of 2°-40° 2θ; scanning rate 66.67 sec/°2θ; monochromated CuKα radiation. The glycolated and heated specimens were analyzed with the same parameters except the scanning range was 2° - 25.5° 2θ. The $MgCl_2$

treated samples (air-dried and glycolated) were analyzed under the same conditions except the scanning range was 2º to 50º 2θ, in order to investigate reflections in higher angles. The samples treated with $MgCl_2$ and solvated with glycerol were run only from 2º to 10º 2θ, to compare the patterns with those treated with ethylene glycol.

4.3.3.2 INTERPRETATION OF DIFFRACTOGRAMS

The interpretation of the whole rock and clay fraction diffractograms was based on an integrated approach, including comparisons with the literature (Hower et al., 1976; Bailey, 1980; Brindley and Brown, 1980; Reynolds and Hower 1970; Reynolds, 1980; Srodon, 1980, 1981, 1984; Shaw 1987; and Eslinger & Pevear 1988).

The relative abundance of the clay minerals was computed semi-quantitatively using the relative intensities of the peaks obtained from the glycolated samples and those heated to 400ºC. The amount of kaolinite (K), discrete illite (I), illite-smectite (I/S) and chlorite (Ch), when present, were estimated using the following formulae (Weaver, 1958; Brown and Brindley (1980); Brindley, 1980):

$$\%K = \frac{7.15\text{-}7.18\ \text{Å}/2\ (\text{H400ºC})}{10\text{Å}\ (\text{H400ºC}) + 7.15\text{-}7.18\text{Å}/2 + 7.07\text{-}7.09\text{Å}/2\ (\text{H400ºC})}$$

$$\%I = \frac{10\ \text{Å}\ (\text{glycolated})}{10\text{Å}\ (\text{H400ºC}) + 7.15\text{-}7.18\text{Å}/2 + 7.07\text{-}7.09\text{Å}/2\ (\text{H400ºC})}$$

$$\%(I+I/S) = \frac{10\ \text{Å}\ (\text{H400 ºC})}{10\text{Å}\ (\text{H400ºC}) + 7.15\text{-}7.18\text{Å}/2 + 7.07\text{-}7.09\text{Å}/2\ (\text{H400ºC})}$$

and % I/S = % (I+I/S) - % I;

where H means heated.

$$\%Ch = \frac{7.07\text{-}7.09Å/2 \text{ (chlorite peak, H400°C)}}{10Å \text{ (H400°C)} + 7.15\text{-}7.18Å/2 + 7.07\text{-}7.09Å/2 \text{ (H400°C)}}$$

The determination of the relative amount of smectite in the mixed-layer illite-smectite and the degree of ordering was based on the methods described in Srodon (1980, 1981 and 1984), Reynolds and Hower (1970), and Reynolds (1980). The amounts of smectite estimated by these different methods gave variations of up to 32%, but, on average, the differences are around 10%. These discrepancies may be due to variations in the ethylene glycol-clay complex thickness that can lead to as much as 30% of error in estimating the amount of smectite in a mixed-layer illite-smectite mineral (Srodon, 1980).

4.4 GEOCHEMICAL ANALYSIS

4.4.1 TOTAL ORGANIC CARBON

Organic geochemical analysis (T.O.C., type of organic matter and hydrogen index) was carried out on seven samples of mudstones. The total organic carbon (T.O.C.) was determined on the residue of powdered rock (0.5 g) after treatment with warm hydrochloric acid. The analyses were made using a WR-12 LECO carbon analyzer.

4.4.2 CALCIUM CARBONATE CONTENT

The calcium carbonate content of the samples was estimated by dissolving the crushed sample in 10% hydrochloric acid and recording the produced volume of CO_2.

There were two main objectives in estimating the calcium carbonate contents: a) to determine the calcium carbonate of the mudrocks; and b) to confirm the cyclic variations in calcium carbonate contents (i.e. mudstone/marlstone couplets) observed visually in cores and wireline logs. The analyses to check the presence of cycles in the calcium carbonate contents of the mudrocks were made on 273 samples from two continuous cores of well 330 with a 10 cm sampling interval.

4.4.3 STABLE ISOTOPES

Determination of the oxygen and carbon stable isotopes in the calcite cements were carried out by the Geochemistry section of the Petrobrás Research Centre (CENPES) at Rio de Janeiro, Brazil, using standard techniques established by Craig (1957). The results were reported as δ^{13} C ‰PDB and δ^{18} O ‰PDB (Pee Dee Belemnite), where:

$$\delta^{18}O = \frac{^{18}O/^{16}O_{sample} - ^{18}O/^{16}O_{std}}{^{18}O/^{16}O_{std}} \times 1000$$

$$\delta^{13}C = \frac{^{13}C/^{12}C_{sample} - ^{13}C/^{12}C_{std}}{^{13}C/^{12}C_{std}} \times 1000$$

The analyses were carried out using a Varian MAT-230 mass spectrometer.

Additionally, the oxygen and carbon stable isotopes compositions of benthonic foraminifera were analyzed by Dr. Richard Corfield at Oxford University. Of the 29 samples analyzed 25 were of Cibicidoides sp. and 4 of Florilus sp.. The samples of Florilus sp. were from the same depths of the Cibicidoides sp. and were analyzed to check possible differences in the composition between these species.

4.5 PALAEONTOLOGICAL ANALYSIS

To palaeontologically characterize the principal fine-grained lithofacies, 20 samples of mudstones, siltstones, marlstones, diamictites and very fine-grained sandstones were selected. Sample preparation involved reducing the sample into small pieces and then boiling them in distilled water until the fossils were freed from the matrix. The foraminifera were separated using a 62 μm sieve, then dried and mounted on aluminium stubs for S.E.M. analysis. The identification of the foraminifera was carried out with the assistance of Dr. Eduardo Koutsoukos at Plymouth Polytechnic.

4.6 STATIC DOWN HOLE FORMATION TEMPERATURE

Static down hole formation temperature is an important working parameter for many purposes but particularly for diagenetic studies. Due to circulation cooling effects the recorded maximum bottom hole temperatures can be 4°C. to 24°C lower than the true static formation temperature. Fertl & Wichmann (1977) proposed an analytical extrapolation technique (the Horner-plot) to obtain true static temperature at any particular depth using two or more maximum downhole temperature (BHT) readings recorded while running conventional logs.

This method requires information on the maximum recorded borehole temperature, the time after each log run (t) and circulation time, prior to the logging (t).

There is a straight-line relationship between maximum recorded temperature (BHT in °F) and the ratio of:

$$\frac{\Delta t}{t + \Delta t}$$

(Δt = time after circulation stopped, in hours)

(t = circulating time, in hours)

Extrapolation of this straight line to a time ratio of:

$$\frac{\Delta t}{t + \Delta t} = 1 \quad \text{i.e. } t = 0$$

will define the true static formation temperature (Fig.4.5).

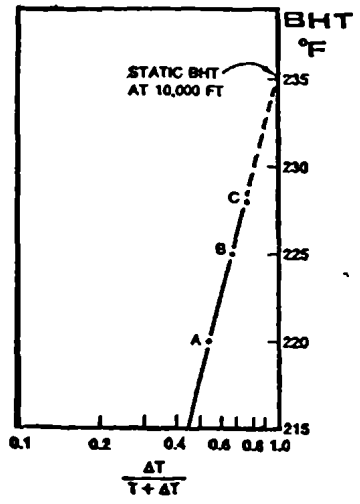


Fig. 4.5 An example of extrapolation to determine static bottom hole temperature (Fertl & Wichmann, 1977).

When only one value of BHT was available at a given depth, a mean correction was applied as suggested by Nwachukwu (1976), using the correction graph presented by Carstens and Finstad (1981, Fig.4).

There are several sources of inaccuracy in the determination of the true static formation temperature from bottom hole temperature measurements (Carstens and Finstad, 1981), but in the analyzed wells the most important was the influence of the water depth which varies from 90 m to 1565 m. The solution used was to estimate the bottom water temperature using the data from Riley and Chester (1971, Fig. 3.5) and consider it as the initial temperature, rather than use the mean surface temperature as normally done. For the wells in deeper waters the initial 1,000 m are relatively cooler than wells in shallower water. This correction may overcompensate and make the temperatures lower than they should be, but it avoids the greater error if the sea-surface temperature was taken as the initial reference temperature.

4.7 SEQUENCE STRATIGRAPHY

The principles used for seismic stratigraphy analysis are well described in papers by Vail (1977, 1987), Vail et al. (1977, 1981, 1984, 1987), Mitchum (1977, 1985), Mitchum et al. (1977), and in Wilgus et al. (1988).

To trace the reflections more precisely some of the seismic sections were enlarged using a photocopying machine. The best way would have been to use special seismic processing such as acoustic impedance and velocity analysis, but this processing was not available for this study.

Correlations, using wireline logs of wells along the seismic sections were carried out to identify the distribution of the main facies and their seismic responses. The correlation of facies with seismic reflectors was made using synthetic seismograms and vertical seismic profiles computed from well-log data made available by Petrobrás **(Fig. 4.6)**.

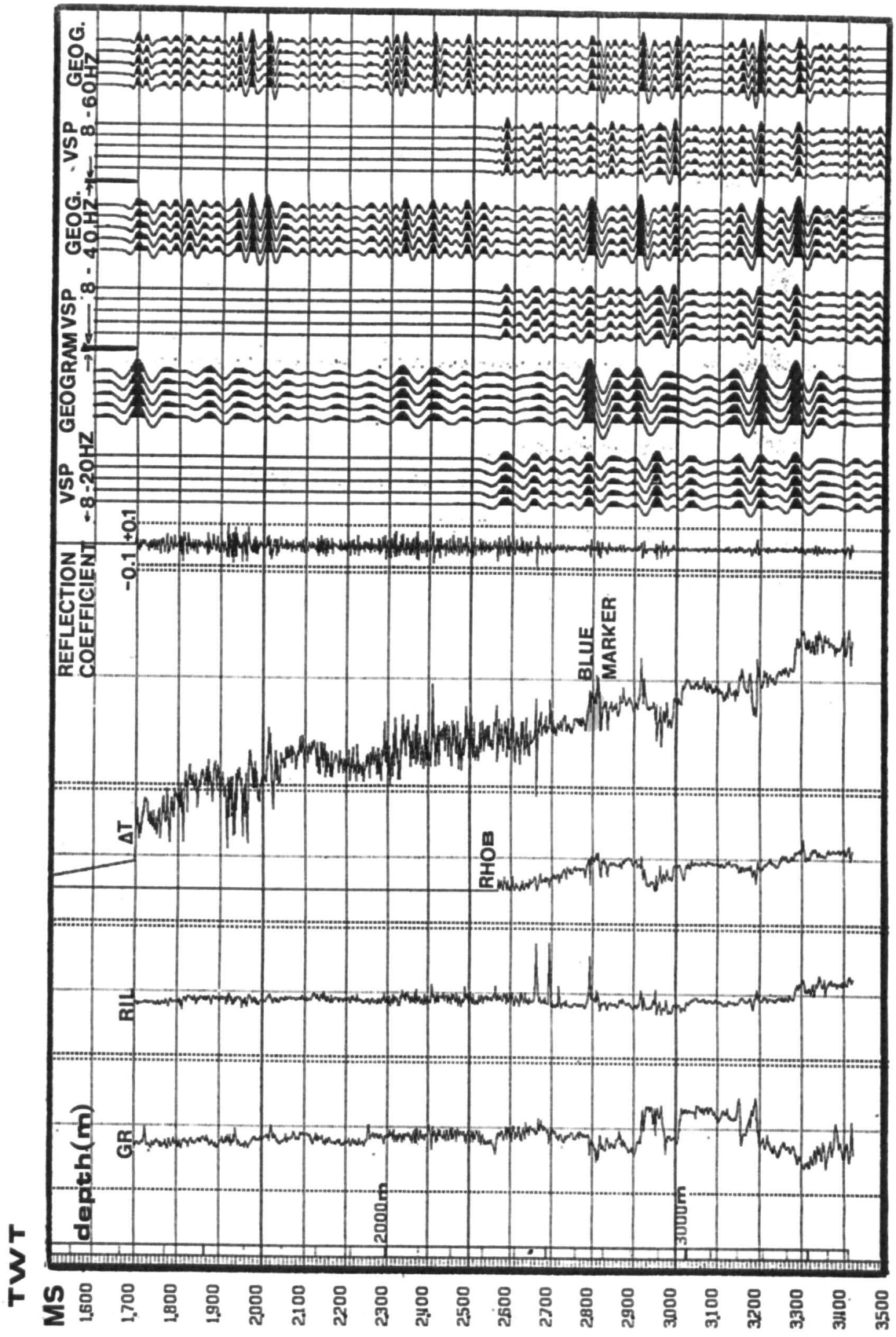


Fig. 4.6 An example of vertical seismic profile and synthetic seismogram computed with sonic log and which have been used to correlate the facies with seismic sections.

The Oligocene-Recent succession was divided into 8 major depositional sequences[5] based on their principal unconformities[6] and correlative conformities[7], identified by reflection terminations (top lap, onlap or downlap) and configurations or seismic facies patterns[8] (**Fig 4.7**). The major sequence-boundaries have been correlated with the local nannofossil biozones, defined by Petrobrás. The basal sequence (Sequence 1) embodies the majority of the sand-rich turbidites and, in some parts of the studied area, can be divided into three sequences (Seq. 1a, 1b and 1c). This division was carried out using the base of the sandstones of the basin-floor fans[9] (Type 1 sequence boundary[10]) up to the base of the next fan or, where there were no sandstone bodies, the identification of the individual sequences was made using condensed sections[11]. The most important condensed section is represented by the "Blue Marker" (Gamboa et al., 1986), an interval of about 30 m of chalk/marlstone beds overlying low velocity mudstones. It was used as a marker because of its regional distribution and its relationship with the basin-floor fans, which were deposited above this marker.

---

[5] A sequence is a relatively conformable succession of genetically related strata bounded by unconformities and their correlative conformities (Mitchum, 1977).

[6] A surface of erosion or non-deposition that separates younger from older rocks and represents a significant hiatus (Mitchum et al., 1977).

[7] A conformity is a bedding surface separating younger from older strata, along which there is no evidence of erosion (either subaerial or submarine) or nondeposition, and along which no significant hiatus is indicated. It includes surfaces onto which there is very slow deposition, with long periods of geologic time represented by very thin deposits (Wagoner et al., 1988).

[8] Mitchum, Vail and Sangree (1977).

[9] The basin-floor fan is characterized by deposition of submarine fans on the lower slope or basin floor (Wagoner et al., 1988).

[10] A Type 1 sequence boundary is characterized by subaerial exposure and concurrent subaerial erosion associated with stream rejuvenation, a basinward shift of facies, a downward shift in coastal onlap, and onlap of overlying strata (Wagoner et al., 1988).

[11] Condensed sections are thin marine stratigraphic units consisting of pelagic to hemipelagic sediments characterized by very low-sedimentation rates. They are areally most extensive at the time of maximum regional transgression of the shore line (Loutit et al., 1988).

Isopach maps of the sand-rich basin floor-fans were made using both well and seismic data. The net of seismic lines did not equally cover all parts of the studied area, consequently, some of the limits and thicknesses of the sandstones bodies had to be estimated by extrapolation. There is no doubt that with a better net of seismic lines (i.e. a 3D survey) these maps would be considerably improved.

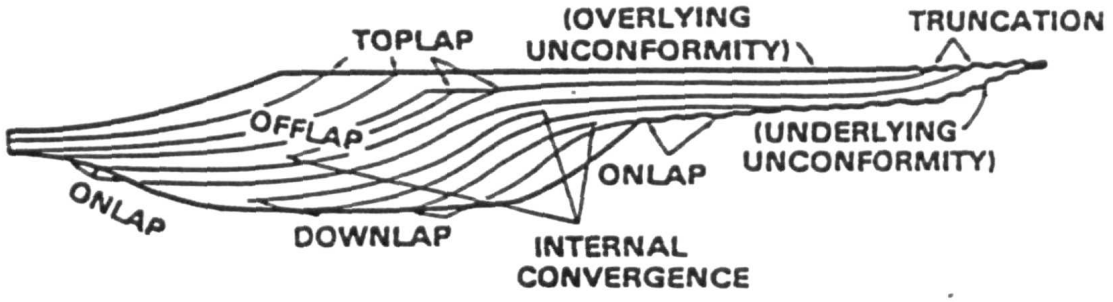


Fig. 4.7 Seismic reflections patterns and their terminations (Mitchum, Vail and Sangree, 1977).

4.8 CYCLICITY

There are many methods of quantifying cyclicity and time series analysis is one of them. A time series is a collection of observations made sequentially in time. Time series analysis is a method in which values in a series are compared with a moving average value (i.e. the average value changes for different increments along the series). According to Chatfield (1984) the natural model for a time series that contains a periodic component of a given frequency can be represented by $X_t = R \cos (Wt + \theta) Z_t$, where X_t is the observation at time t, W is the frequency of the periodic variation in radians per unit of time, R is the amplitude of the variation, θ is the phase, and Z_t denotes

some stationary random series (i.e. a series that does not show a mean systematic change). The angle (Wt + θ) is measured in radians. Since W = number of radians per unit time it is sometimes called the angular frequency. However, some authors (e.g. Jenkins and Watts, 1968) defined frequency as $f = W/(2\pi)$, the number of cycles per unit of time, and the period of a sinusoidal cycle (i.e. wavelength) is $2\pi/W$ or $1/f$. This defines the form of frequency from a physical point of view, but in the mathematical formulae Chatfield (1984) uses angular frequency (W), though to interpret the data he uses $f = W/(2\pi)$.

Time series analysis and power-spectral density studies both quantify the periodicity of a sequence. Spectral analysis is the name given to methods of estimating the spectral density function of a given series. It is essentially a modification of Fourier analysis to make it suitable for stochastic (i.e. values can only be partially predicted by past values) rather than deterministic functions of time (i.e. when a time series can be predicted). Fourier analysis is basically concerned with approximating a function of sine and cosine terms called the Fourier series representation:

$$X_t = a_0 + \sum_{p=1}^{N/2-1} [a_p \cos(2\pi pt/N) + b_p \sin(2\pi pt/N)] + a_{N/2} \cos \pi t$$

for $t = 1, 2, \ldots\ldots, N$; where (a_p, b_p) are :

$a_0 = \bar{X}$, $a_{N/2} = \sum(-1)^t X_t/N$,

$a_p = 2[\sum X_t \cos(2\pi pt/N)]/N$ }

$b_p = 2[\sum X_t \sin(2\pi pt/N)]/N$ } --- $p = 1, \ldots., N/2-1$.

The overall effect of Fourier analysis is to partition the variability of a series into components at frequencies $2\pi/N$, $4\pi/N$, ..., π.

The components of frequency $W_p = 2\pi/N$ is often called p^{th} harmonic. For $p \neq N/2$ it is often useful to write the p^{th} harmonic in the (equivalent) form:

$a_p \cos W_p t + b_p \sin W_t = R_p \cos(W_p t + \emptyset_p)$, where

R_p = amplitude of p^{th} harmonic = $\sqrt{(a^2_p + b^2_p)}$ and

$\emptyset_p$ = phase of p^{th} harmonic = $\tan^{-1}(-b_p/a_p)$

Each harmonic is represented by a sequence of sine and cosine terms, each representing individual wavelengths.

For $p \neq N/2$ the contribution of the p^{th} harmonic to the total sum of squares is given by $N(a^2_p + b^2_p)/2$ which is equal to $NR^2_p/2$. The value given for each harmonic is called its power spectrum and measures the importance of each harmonic. If $R^2_p/2$ is regarded as the contribution to the variance in the range $W_p \pm \pi/N$, it is possible to plot a histogram whose height in the range $W_p \pm \pi/N$ is such that $R^2_p/2$ = area of histogram = height of histogram x $2\pi/N$. Thus the height of the histogram is given by $I(W_p) = NR^2_p/4\pi$. The plot of $I(W)$ $(= NR^2_p/4\pi)$ against W is called the **periodogram** even though $I(W)$ is a function of frequency rather than the period. As each harmonic represents a particular wavelength so those harmonics with high power spectrum values (high importance level) are selected, their wavelengths calculated and used to determine the periodicity of the sequence. Only those wavelengths which are represented by a particular harmonic with a high power spectrum value and harmonics with moderately high power spectrum values corresponding to multiples of the original wavelength, are considered to represent cyclicity.

The data used in this study has been grouped into two types of core and wireline log data. The core data included the percentage of CaCO3 of 274 samples spaced 10 cm intervals, from the well 330 and core photos from wells 330 and MRL-4. The lithologies of these cores were codified as: sandstones = -1, mudstones = 1, calcareous mudstones = 2 and marlstones = 3. The wireline log data included dipmeter logs, scaled at 1/40 and 1/200, sampled at 10 and 40 cm respectively, neutron logs, scaled at 1/200, and sampled at 20 cm intervals and the sonic log, scaled at 1/1000, sampled at 20, 50 and 100 cm. Part of the wireline log data was available on disk and other parts had to be digitized manually.

Initially, to test the existence of cycles in the studied succession a set of data from wells 330 and MRL-4 was supplied to Messrs Owen-Hughes and Gilbert to use in an

undergraduate geostatistics project. They used a Fourier transform program supplied by Dr. John Ferguson to analyze the data.

The determination of cyclicities and their periodicities in this study were obtained from periodograms produced by the STATGRAPHICS computer package. The periodogram plots the squared amplitudes of the sinusoids (power-spectrum density) in the ordinates against frequency of the harmonic oscillations in the abscissa represented by cycles/sampling interval. For more details see STATGRAPHICS user's Guide (1988) and Chatfield (1984). The wavelength or period of each significant frequency (i.e. high power density) is obtained by dividing the sampling interval by the number of cycles, which is listed by the program (e.g. **Table 4.1**).

To illustrate the data produced by the periodogram using the STATGRAPHICS program lets us consider two hypothetical simple waves and a combined wave (wave 1 + wave 2). Wave 1 has a wavelength of 7.2 m and an amplitude of 60 (e.g major variations in CaCO3%), wave 2 has a wavelength of 1.8 m and an amplitude of 10 (e.g. minor variations in CaCO3%), and the combined wave (3) has a wave length of 7.2 m and an amplitude of 68. The total interval sampled was 18 m with samples taken every 10 cm (see **Fig. 4.8 a, b** and **c** respectively). The periodograms for wave 1, wave 2 and the combined wave 3 are shown in **Figure 4.9 a, b** and **c**, respectively. Additionally, the frequencies of the harmonic oscillations and corresponding power-spectrum densities for the combined wave are shown in **Table 4.1.** The periodograms for waves 1 and 2 show periodicities with a very high power density, while the periodogram for the combined wave shows a significant periodicity which coincides with the one from wave 1 but it shows a very low power density for the superimposed wave 2 because of the relatively lower when combined amplitude. The discrepancy found between the actual wavelength of wave 1 and the one computed by the periodogram can be explained by the fact that the representation of the higher frequencies is affected by the sampling interval,

while the representation of the lower frequencies depends on the total interval covered by the series (Craddock, 1968). Consequently, the total sampling interval for wave 1 should have been much longer and did not required such a high sampling density.

The limitations of the 640 K bite RAM memory of available IBM PC compatible computers restricted the processing to about 200 points per analyzed interval. However, if the data have been previously smoothed this can be increased to more than 750 points.

TABLE 4.1 - Estimated periodogram ordinates (power-spectrum density) for the frequencies of the harmonic oscillations of the combined wave (wave 1 + wave 2)

Frequency	Ordinate	Frequency	Ordinate	Frequency	Ordinate
0.00000	0.00000	0.00556	7440.74	0.01111	40437.8
0.01667	27306.9	0.02222	2161.28	0.02778	596.186
0.03333	235.841	0.03889	106.393	0.04444	64.8761
0.05000	37.2395	0.05556	2271.64	0.06111	17.3227
0.06667	8.97144	0.07222	6.20684	0.07778	5.62522
0.08333	2.83917	0.08889	3.35007	0.09444	2.87740
0.10000	1.24610	0.10556	1.88567	0.11111	0.98185
0.11667	0.65809	0.12222	1.62986	0.12778	0.83080
0.13333	1.06907	0.13889	1.35460	0.14444	0.29951
0.15000	0.76735	0.15556	0.99744	0.16111	0.31598
0.16667	1.17305	0.17222	0.75147	0.17778	0.18275
0.18333	0.68656	0.18889	0.37824	0.19444	0.15700
0.20000	0.82753	0.20556	0.19925	0.21111	0.19856
0.21667	0.29872	0.22222	0.08697	0.22778	0.08574
0.23333	0.34499	0.23889	0.00653	0.24444	0.23050
0.25000	0.05234	0.25556	0.18670	0.26111	0.08093
0.26667	0.07597	0.27222	0.17889	0.27778	0.26260
0.28333	0.04314	0.28889	0.47751	0.29444	0.10055
0.30000	0.06740	0.30556	0.40853	0.31111	0.24573
0.31667	0.18543	0.32222	0.65416	0.32778	0.05168
0.33333	0.13201	0.33889	0.51300	0.34444	0.14406
0.35000	0.29223	0.35556	0.53090	0.36111	0.01777
0.36667	0.17117	0.37222	0.38580	0.37778	0.07201
0.38333	0.26435	0.38889	0.28802	0.39444	0.07087
0.40000	0.10177	0.40556	0.27499	0.41111	0.10705
0.41667	0.17086	0.42222	0.12610	0.42778	0.26119
0.43333	0.04671	0.43889	0.29441	0.44444	0.20982
0.45000	0.07349	0.45556	0.16478	0.46111	0.47031
0.46667	0.01258	0.47222	0.43325	0.47778	0.32004
0.48333	0.02304	0.48889	0.26011	0.49444	0.54583
0.50000	0.00123				

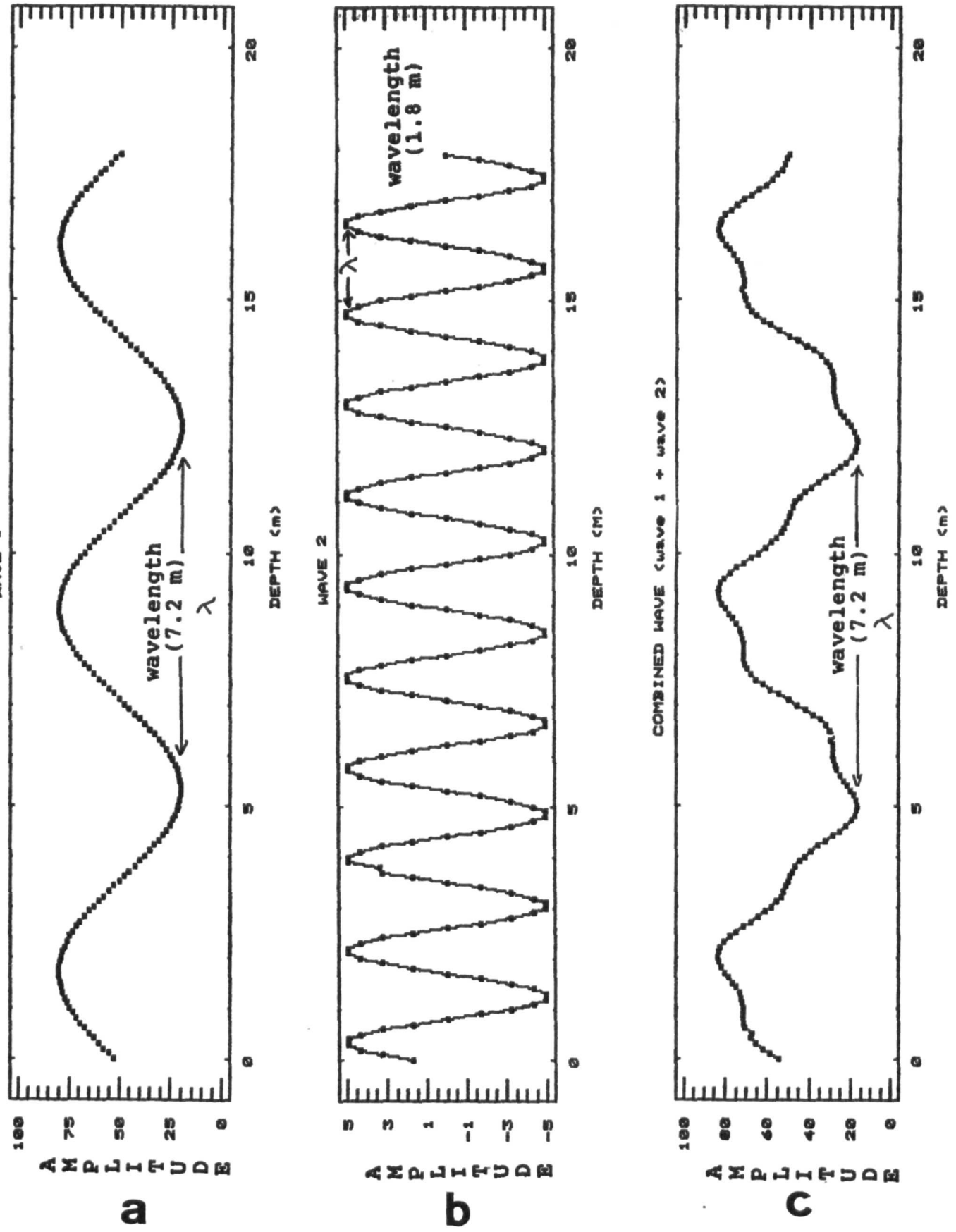


Fig. 4.8 Waves 1 and 2 and combined wave (wave 1 + wave 2).

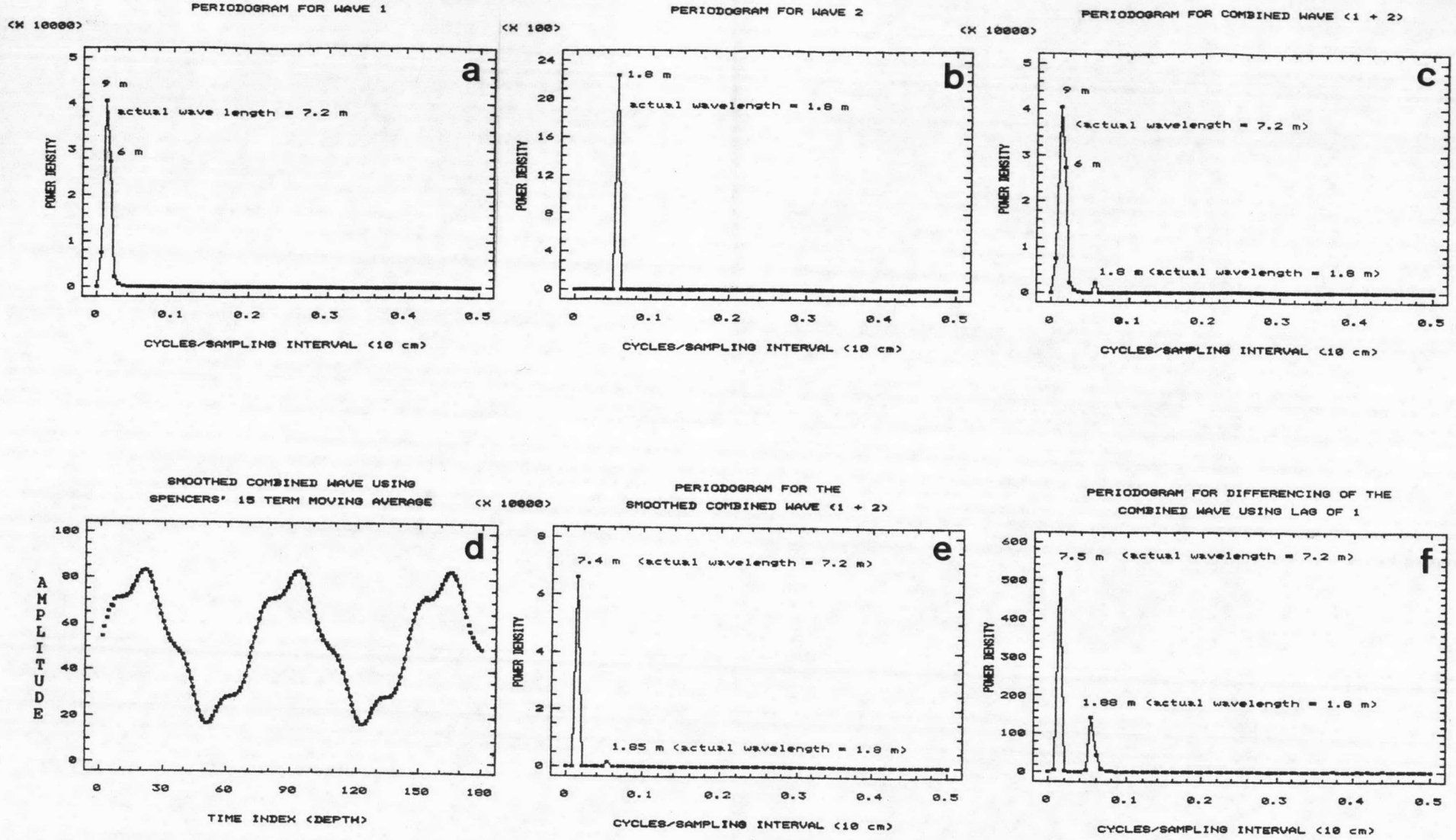


Fig. 4.9 Periodograms **a**, **b**, and **c** are respectively from waves 1, 2 and the combined wave, while **e** and **f** are from the smoothed (**d**) and the differencing values of the combined wave.

Smoothing and differencing are two pre-treatments that can be used to improve the definition of the lower and the higher frequencies (see Terra Nova v. 1, nº5, 1989). To improve the definition of the lower frequencies Spencer's 15-term moving average formulae was used (see **Fig. 4.9 d** and **e**). For more details about smoothing (i.e. time-trend analysis) see Harbaugh & Merriam (1968, p. 53-59). For high frequencies of small amplitude a simple differencing method using a lag of 1 (i.e. between consecutive values) was used to improve their definition. Differencing involves comparing adjacent values but using the difference between pair of values rather than the values themselves. This enhances local contrasts and produces better defined periodicities for small variations (**Fig 4.9 f**). Both methods are available in the STATGRAPHICS program.

An additional option to improve the results of those frequencies associated with small variations is to cube the values, this enhances the differences without greatly changing the data or reducing the number of points. Using these pre-treatments the resulting data were reanalysed with the periodogram. The results obtained by these pre-treatments are similar to those obtained with non-treated data which gives some confidence in the use of these methods (see **Fig. 4.9**). However, it is not uncommon to find that the power spectra which contain a preferred frequency, for example W, also show maxima representing the harmonics of this frequency as multiples at intervals of ...3W, 2W, W, W/2, W/3... and so on. This is because very few periodic or oscillating time series will have the precise shape of a sine wave (e.g. wave 1 and wave 2) and it follows that they must contain a certain number of frequencies that are themselves harmonics to the fundamental frequency (Schwarzacher, 1975). This can be illustrated with wave 4, a non sine wave, and its corresponding periodogram (**Fig. 4.10**). It can be seen that in addition to the fundamental frequency (4.5 m) there are at least two other significant frequencies (2.25 m and 1.12 m), which represent harmonics (i.e multiples).

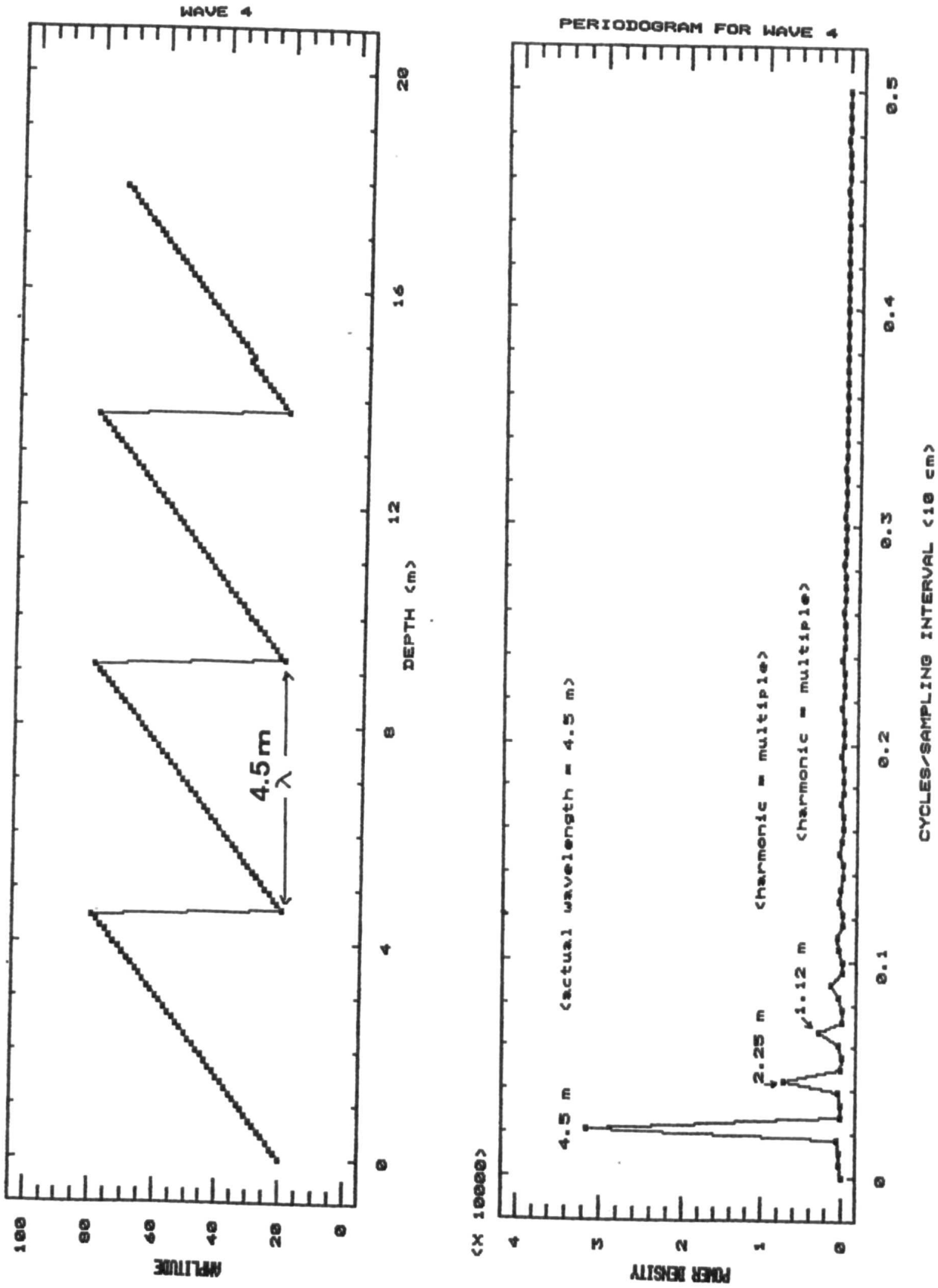


Fig. 4.10 Wave 4 with its corresponding periodogram.

CHAPTER 5

FACIES ANALYSIS

5.1 INTRODUCTION

In the study area the Oligocene-Miocene succession of the Campos Basin is composed of siliciclastic mudstones, marlstones and sandstones. These sandstones consist mainly of fine/medium sand-grade siliciclastics intermixed with varying amounts of calcareous skeletal remains (most of it bioclastic) of neritic or/and bathyal organisms. They are always interbedded with mudrocks which contain a bathyal fauna. There are two principal types of sandstones: the most abundant are thick (40 m) amalgamated, massive or normally graded, fine/medium-grained sandstones; the other, thin- to thick-bedded gravelly/fine-grained sandstones frequently displaying normal grading, parallel-laminations or even climbing-ripples (Tabc, Tbc or Tcd Bouma sequences) commonly interbedded with mudstones, diamictites and slumped deposits. In seismic sections it is possible to identify these sandstones at the base of the prograding Miocene slope succession, indicating deposition in a relatively deep-water marine environment. These characteristics indicate that the sandstones were derived from shallow water and resedimented into deeper water.

Similar type of deposits have been classified in the literature as turbidite deposits, especially since Bouma (1962), and interpreted as formed by gravity induced flows. The definition and description of this type of sedimentary accumulation has been mainly based on the facies classification published by Mutti & Ricci Lucchi (1972, 1975). More recently, Pickering et al. (1986; 1989) published a facies classification scheme for modern and ancient deep-water sediments, which is a modified version of the original scheme proposed by Mutti & Ricci Lucchi (1972,

1975). The classification of Pickering et al. (1986) seems to be too complex to be used routinely and too complicated to apply in the field (Shanmugam & Moiola, 1988).

Depositional models for these deep-water deposits have received a great deal of attention, with those published by Normark (1970), Mutti & Ricci Lucchi (1975) and Walker (1978) being the most widely applied.

Despite the detailed studies of these types of sediments there are still many doubts concerning their facies, facies associations and distribution. According to Mutti and Normark (1987) comparison of modern and ancient fans can only provide valid results when the scale of observations are similar. Additional problems can result from interpretations using data with different degrees of resolution and different terminology. The application of depositional models to modern and ancient examples have been widely discussed and criticized (Mutti & Normark, 1987; and Shanmugam & Moiola, 1988).

5.2 FACIES CLASSIFICATION

The cored rocks studied in this project have been classified into 20 LITHOFACIES based on sedimentological analysis, comparisons with similar rocks observed at outcrops in the Eocene strata in the South Pyrenean Basin (Ainsa-Broto and San Sebastian regions), Spain and those reported in the literature.

Twelve ELECTROFACIES were distinguished using core calibrated wireline log analysis. Each electrofacies is composed of one or more distinct lithofacies which alone or in various combinations produced the characteristic wireline log response of that electrofacies.

Additionally, the ELECTROFACIES (12) and their corresponding LITHOFACIES (20) have been assembled into eight GROUPS (**A-H**) based on their general sedimentological and wireline log similarities (**Table 5.1**). These groups resemble the facies classification presented by Mutti & Ricci Lucchi (1972, 1975). However, the latter is sometimes too restricted to adequately describe all the variations

observed in the analyzed sediments, but provides a useful framework. The facies classification of Pickering et al. (1986, 1989) has also been used, but on the other hand, it has more complex facies subdivisions than those of this study. Also, these classifications are of limited use when making comparisons with ancient subsurface data because they are mainly based on outcrop descriptions and modern depositional environments.

The eight groups of electrofacies with their corresponding lithofacies are presented below. A summary of the main characteristics of the electrofacies is presented in **Table 5.1** at the back of the thesis.

GROUP A

(GvS) - GRAVELLY-SANDSTONE ELECTROFACIES/LITHOFACIES

(GvSm) - GRAVELLY-SANDSTONE WITH MUDCLASTS ELECTROFACIES/LITHOFACIES

Similar to Facies A1 of Mutti & Ricci Lucchi (1975).

(DMT) - DIAMICTITE ELECTROFACIES/LITHOFACIES

Similar to Facies A2 of Mutti & Ricci Lucchi (1975).

GROUP B

(AmS) - AMALGAMATED SANDSTONES ELECTROFACIES, including:

VcS - Very coarse/fine Sandstone Lithofacies either with Ta[1] or massive.

AmS - Amalgamated Massive Coarse/fine Sandstone Lithofacies

Similar to Facies B1 of Mutti & Ricci Lucchi (1975).

[1] Ta meaning the basal interval of the Bouma sequence (see Chapter 4).

GROUP C

(FTab)[2]- THICK-BEDDED SANDSTONE ELECTROFACIES, including:

FTab - Medium/fine Sandstone Lithofacies with Tab or Tabc.
Similar to Facies C1 of Mutti & Ricci Lucchi (1975).

FTb - Parallel-laminated Fine/very fine-grained Amalgamated Sandstone Lithofacies with Tb or locally Tbc.
Similar to Facies C2 of Mutti & Ricci Lucchi (1975).

GROUP D

(FTb-e)- MUDDY THIN-BEDDED SAND-MUD COUPLET ELECTROFACIES, including:

FTb-e - Thin/very thin-bedded Sandstone/Mudstone Lithofacies with sandstone:shale <1, the sandstones show Tbcde, Tbc, Tcde and local Tacde and Tade.
Similar to Facies C2/D1-2 of Mutti & Ricci Lucchi (1975).

FTde - Millimetric Rhythmic (Tde) Siltstone Lithofacies.
Similar to Facies D3 of Mutti & Ricci Lucchi (1975).

GROUP E

(E) - SANDY THIN-BEDDED SAND-MUD COUPLET ELECTROFACIES, including:

Fla - Thin-bedded Fine-grained Sandstone Lithofacies with Flaser-bedding and Faint Ripple Cross-laminations.

Wav - Thin/very thin-bedded Fine/very fine-grained Sandstone Lithofacies with Wavy-bedding and Ripple Cross-laminations.

Rip - Very thin-bedded Very fine-grained Sandstone Lithofacies with Lenticular bedding, Climbing-ripples/or ripple-drifts presenting erosion on the stoss-side.

Similar to Facies E of Mutti & Ricci Lucchi (1975).

---

[2]**Remarks:** FTab represents a lithofacies composed of beds showing mainly the Tab part of the Bouma sequence.

GROUP F

(F) - "CHAOTIC" ELECTROFACIES

F - "Chaotic" Lithofacies, includes contorted coherent/ semi-coherent strata, brecciated and balled strata.

Similar to Facies F of Mutti & Ricci Lucchi (1975).

GROUP G

(G1/G2)- CARBONATE MUDSTONE/MARLSTONE ELECTROFACIES, including:

G 1 - Chalk or Biogenic Carbonate Mudstone Lithofacies.

G 2 - Hemipelagic Marlstone Lithofacies.

Similar to Facies G of Mutti & Ricci Lucchi (1975).

(G3/G4)- MUDSTONE ELECTROFACIES, including:

G 3 - Calcareous Siliciclastic Mudstone Lithofacies.

G 4 - Siliciclastic Mudstone Lithofacies.

Similar to Facies G of Mutti & Ricci Lucchi (1975).

GROUP H

(MM/MS)- MOTTLED MUDSTONE/SANDSTONE ELECTROFACIES, including:

MM - Mottled Mudstone (medium/thick-bedded) Lithofacies

MS - Mottled Muddy Sandstone Lithofacies

Not specified by Mutti & Ricci Lucchi (1975).

(BS1) - THIN-BEDDED BIOTURBATED SANDY SILTSTONE ELECTROFACIES

BS1 - Thin-bedded Bioturbated Sandy Siltstone Lithofacies

Not specified by Mutti & Ricci Lucchi (1975).

5.3 ELECTROFACIES AND LITHOFACIES CHARACTERISTICS

GROUP A

5.3.1 - GRAVELLY SANDSTONE ELECTROFACIES (GvS)

This electrofacies is composed of lithofacies **GvS**.

5.3.1.1 GRAVELLY-SANDSTONE LITHOFACIES GvS

Recognition and sedimentary structures: This lithofacies is composed of very poorly sorted[3] conglomeratic sandstones with cobbles, pebbles and granules (30%) in a matrix of fine sand-sized grains. Poorly defined or no detectable sedimentary fabric in the recovered core intervals.

Thickness: This lithofacies varies from a few decimeters (30 cm) to a few meters (2 m).

Contacts: (for simplification the lithofacies will be represented by their symbols) 1) The top is abrupt with the **VcS** or with the **FTab** Lithofacies; 2) The base is erosional with the **FTde** Lithofacies.

Composition[4]: calcareous lithic arenite.

The composition of the gravels can be divided into two groups. The pebbles/cobbles consist of calcareous bioclastic sandstones, mudstones, siltstones, recrystallized carbonate mudstones and packstones (Dunham, 1962). The granular material is: quartz, feldspar, granitic rock fragments, bioclasts (red algae, macroforaminifera, bryozoa and bivalve). Calcite cementation (poikilotopic and equant) is common making rocks of this lithofacies very tight.

Reservoir characteristics: POOR[5] due to the extensive calcite cementation.

---

[3] Sorting = after Folk and Ward, 1957.

[4] The composition of the sandstones was based on a modified version of the Pettijohn et al. (1973) classification, in which the rock fragment component was redefined and includes rock fragments (sedimentary/metamorphic/igneous), mica and bioclasts. For more details see Chapter 9, section 9.3.

[5] The terms poor, moderate, and good/excellent have been used for porosities values as follow: poor = less than 10%,
moderate = between 10 and 20%, good/excellent between 20 and 33%.

Example: The wireline log characteristics and the corresponding lithofacies are shown in the **photos A** and **C** of **Plate 5.1.** An outcrop of the Eocene Hecho Group turbidites near Arro Village, Spain (**photo B of Plate 5.1**), shows a channel-fill with lenses of conglomerate and gravelly sandstones similar to this lithofacies.

5.3.1.2 GEOPHYSICAL CHARACTERISTICS OF ELECTROFACIES (GvS)

5.3.1.2.1 Wireline logs

The rocks of this electrofacies have very low porosity, high resistivity, low GR due to calcite cementation. This electrofacies can be easily distinguished using the microresistivity curves of the dipmeter log by its higher resistivity values. The tadpole plot of the dipmeter log shows the "bag of nails" pattern, however there is local evidence for "red" patterns.

The rocks of this electrofacies have the following mean wireline log values: GR = 46° API, ISF = 4.5 OHMS.m^2/m, SFLU = 30.0 OHMS.m_2/m (OIL ZONE), DELTAT = 59 μsec/ft, RHOB = 2.62 g/cc and ΦN= 17 p.u.

5.3.1.2.2 Seismic response

Depending on their thickness and degree of calcite cementation, the rocks of this electrofacies can produce a high amplitude lateral discontinuous reflector. The existence of tightly cemented zones can influence the characteristics of the type of reflector so care must be taken in the interpretation.

5.3.1.3 INTERPRETATION OF THE ELECTROFACIES (GvS)

The rocks of this electrofacies are a residual deposit from a high-concentration turbidity current, forming the basal part of a channel-fill deposit. Similar characteristics were observed in the Eocene channel-fill facies from the Hecho Group near Ainsa, Spain, where imbricated lenses of conglomerate lay disconformably over thin-bedded turbidites and diamictites as result of lateral migration of the channel axis (see **Plate 5.1b**, photo B).

PLATE 5.1a

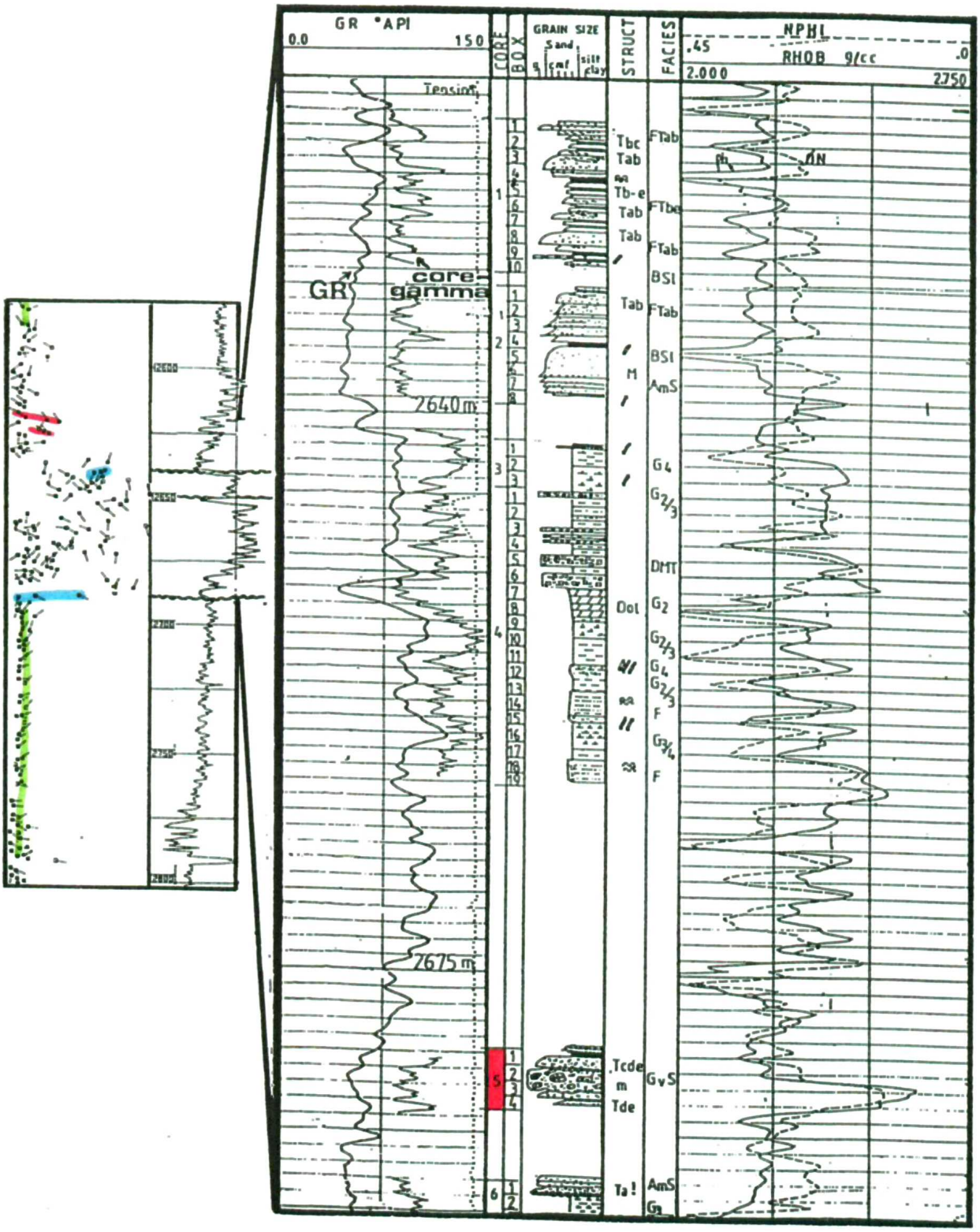


Plate 5.1 - Gravelly Sandstone Electrofacies (GvS). Composite log (5.1a) and corresponding cored interval (core 5) in 5.1b (A) and (C). For comparison an outcrop of similar lithofacies from the Eocene Hecho Group near Arro Village, Spain, is shown in photo B (Scale encircled hammer).

PLATE 5.1b

A



B



C

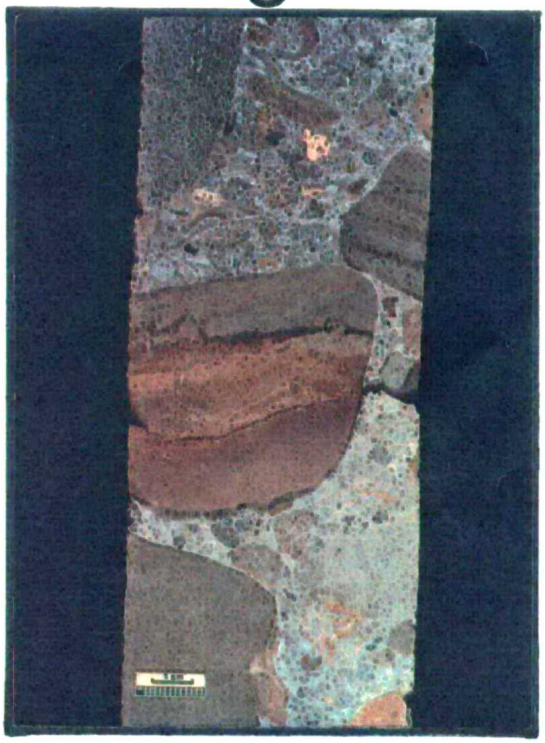


Plate 5.1c - Explanation for the lithology and sedimentary structures symbols used in the composite logs.

The rocks of this electrofacies (GvS) are similar to those of Facies A1 described by Mutti & Ricci Lucchi (1972, 1975), but much thinner. In the classification of Pickering et al. (1986) it is similar to the Disorganized Pebbly Sand Facies - A1.4 or less probably the Normally Graded Pebbly Sand Facies - A2.7.

From now on the Mutti & Ricci Lucchi (1972, 1975) and Pickering et al. (1986) classifications will be represented by **MRL** and **PCK**, respectively.

5.3.2 - GRAVELLY SANDSTONE WITH MUDCLAST ELECTROFACIES (GvSm)

This electrofacies is composed of the lithofacies **GvSm**.

5.3.2.1 - GRAVELLY SANDSTONE WITH MUDCLAST LITHOFACIES GvSm

Recognition and sedimentary structures: This lithofacies is composed of pebble-sized rip-up mudstone clasts in a moderately sorted fine/medium-grained sandy "matrix"[6]. The mudclasts commonly show a crude sub-horizontal orientation due to their platy morphology.

Thickness: It varies from a few decimeters to a few meters thick.

Contacts: 1) The top is abrupt with the **MM** or with the **AmS** Lithofacies. 2) The base is erosional with the **MM** Lithofacies or itself.

Composition: sublitharenite/lithic arenite

The sandstones of this lithofacies consist of fine/medium quartz, feldspar, bioclasts (benthonic > planktonic foraminifera, and echinoids), muscovite and a high percentages of mudstone rip-up clasts. The mudstone clasts consist of a muddy matrix with up to 40% of foraminifera (benthonic > planktonic) and 20% silt-sized quartz grains. Due to compaction the mudstone clasts have been deformed and squeezed between and penetrated by quartz/feldspar grains creating a pseudomatrix (see **Chapter 9** for more details).

[6] Sandy "matrix" is here used to describe the sand grade material enclosing the coarser clasts.

Reservoir characteristics: POOR to moderate. The reduction in porosity is entirely due to the compaction matrix rather than in the rocks of the Gravelly Sandstone Electrofacies (GvS) where porosity has been effectively obliterated by the intense calcite cementation.

Example: The wireline log characteristics of this electrofacies and the corresponding cored interval are shown in **Plate 5.2.** An outcrop of the Eocene Jaizkibel Fan in Punta Turrilla, Spain, shows a similar lithofacies with rip-up mudstone clasts occurring at the base of shallow scours infilled by very coarse/fine-grained sandstones (**photo B**).

5.3.2.2 GEOPHYSICAL CHARACTERISTICS OF THE ELECTROFACIES (GvSm)

5.3.2.2.1 Wireline logs responses

The rocks of this electrofacies occur at the base of some sand bodies. They have a high content of rip-up-mudstone clasts which results in GR and neutron values similar to those of the diamictites and mudstone electrofacies and requires careful analysis to allow them to be differentiated.

The rocks of this electrofacies have the following mean wireline log values: GR = 65 ª API, ISF = 7.0 OHMS. m^2/m (OIL ZONE), SFLU = 15.0 OHMS. m^2/m (OIL ZONE), DELTAT = 114 μsec/ft, RHOB = 2.22-2.30 g/cc, average: 2.25 g/cc, ΦN = 36-39 p.u. (see **Plate 5.2a**).

5.3.2.2.2 Seismic response

There is no typical seismic response for the rocks of this electrofacies because of its small thickness. However, it is likely to be found associated with weak discontinuous reflectors at the base of slope channels (see **Chapter 6**).

PLATE 5.2a

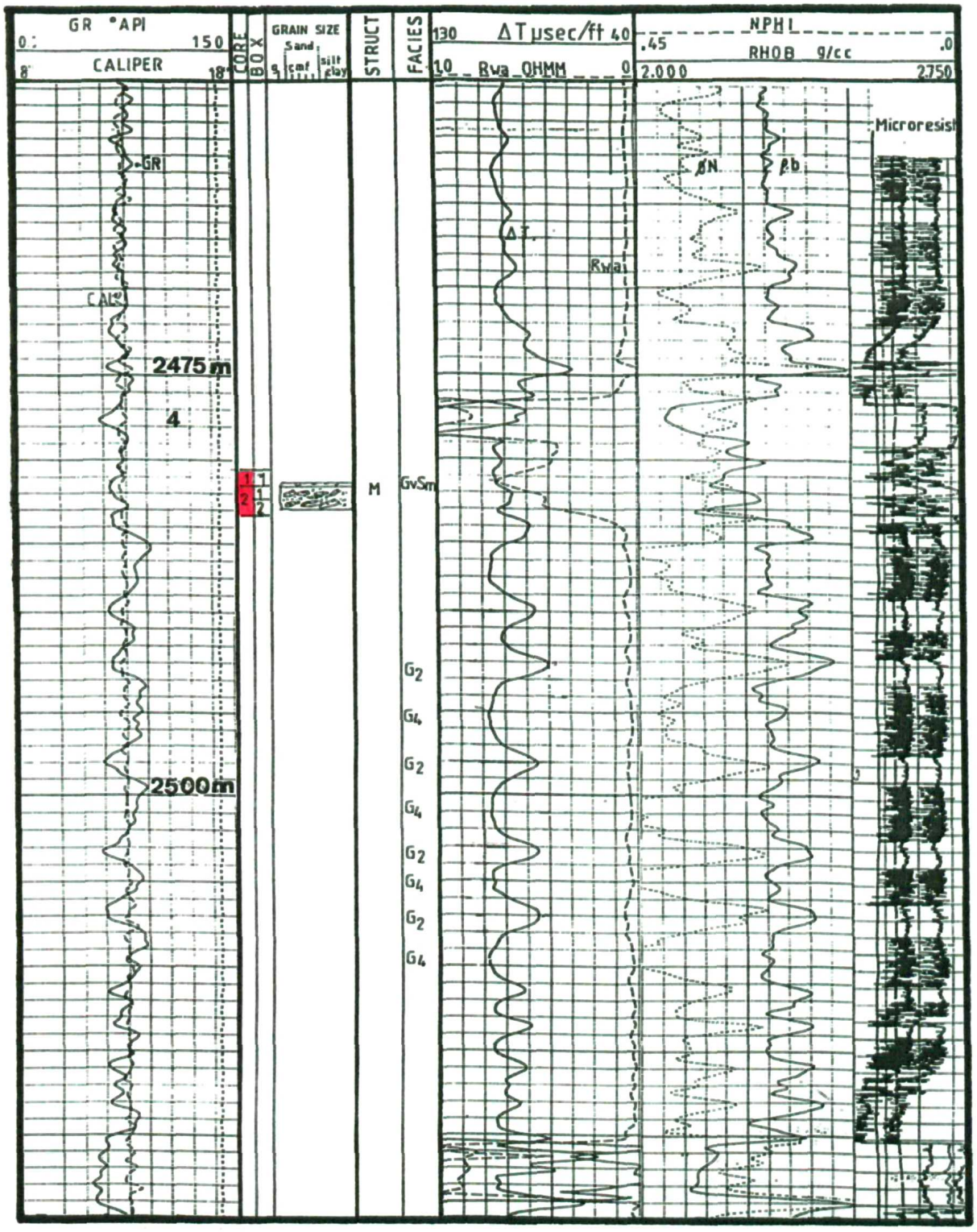


Plate 5.2 - **Gravelly-Sandstone with Mudclasts Electrofacies (GvSm)**. Composite log (5.2a) and the corresponding cored interval, cores 1 and 2 (5.2b). In photo B is shown a similar lithofacies from the Eocene turbidites that crop out at Punta Turrilla near San Sebastian, Spain. (At the based of box 02/02 the coiled object is foam for core protection).

PLATE 5.2b

A



B



C



5.3.2.3 INTERPRETATION OF THE ELECTROFACIES (GvSm)

The presence of moderately sorted sand-sized grains together with rip-up mudstone clasts indicates that these rocks have been formed from material derived from shallow- and deep-water sedimentary environments, respectively. This facies is interpreted as having formed by the short-medium distance transport of a high concentration turbidity current, loaded with moderately sorted fine/medium sand-sized grains. This caused erosion and incorporation of the slope mudstones and, in the final stages, rapid collective deposition. Similar rip-up mudclast lithofacies have been observed in the Eocene turbidites of the Jaizkibel Fan that crop out near San Sebastian, Spain (**Plate 5.2b, photo B**).

The rocks of this electrofacies can be compared with those of Facies A1 of the **MRL** but they are much thinner and more localized, and to the Disorganized Pebbly, Mud-flake Breccia Facies of the **PCK**.

5.3.3 DIAMICTITE ELECTROFACIES (DMT)

This electrofacies is composed of the lithofacies **DMT**.

5.3.3.1 MUDDY GRAVELS/GRAVELLY MUDSTONE LITHOFACIES DMT

Recognition and sedimentary structures: The rocks of this lithofacies are composed of matrix-supported structureless muddy gravels/gravelly mudstones, with locally oriented platy/mudclasts, but no evidence of grading.

Thickness: The average thickness of individual beds is 60 cm but, the whole interval including the interbedded Mudstones Electrofacies **(G3/G4)**, can be tens of metres thick, usually around 20 m.

Contacts: 1) The top is abrupt with the **(G3/G4)** and the **(MM/MS)** Electrofacies. 2) The base is abrupt or erosional with **(G3/G4)** and **(MM/MS)** Electrofacies.

Composition: lithic graywacke

This lithofacies consists of rocks containing up to 10% gravel-sized grains whose composition is mainly mudstone (10-70 mm), quartz and feldspar (2-10 mm). The sand-sized population (quartz and feldspar) is bimodal: one medium and the other very fine sand-sized grains (**Plate 5.3b**, photo C).

The latter, is more abundant than the former and is widespread in the muddy matrix together with some biotite and muscovite, benthonic > planktonic foraminifera, echinoids, and bivalve fragments. This lithofacies is characterized by a middle/deep neritic foraminifera assemblage represented by calcareous-hyaline benthonic foraminifera (Nodosaria sp. A, Eponides sp., Brizalina sp., Cibicides sp., Cassidulina sp.) and calcareous-porcellanous benthonic foraminifera (Milliolids sp.; and by the planktonic foraminifera Globigerina tripartita) (Azambuja Filho & Koutsoukos, 1990; in preparation).

Reservoir characteristics: The rocks of this lithofacies are not reservoir rocks.

Example: See **Plate 5.3.**

5.3.3.2 GEOPHYSICAL CHARACTERISTICS OF ELECTROFACIES (DMT)

5.3.3.2.1 Wireline logs responses:

The rocks of this electrofacies have high GR values and relatively low neutron porosity values. The curves of the latter touch or cross the respective density log curves. Usually the interbedded mudstones show relatively higher neutron values. The whole interval that contains this Electrofacies (**DMT**) has higher GR values compared with adjacent electrofacies such as the Amalgamated Sandstones (**AmS**) or the Marlstone (**G1/G2**). The tadpole plot of the dipmeter log shows the "bag of nails" pattern indicative of "chaotic" dips. The microresistivity curves of the dipmeter log provide a good definition of the diamictites because they have higher resistivity values when interbedded with mudstones.

The rocks of this electrofacies have the following mean range of wireline log values: GR = 65-70 °API, ISF = 2.0-2.8 OHMS. m^2/m, SFLU = 2.5-2.8 OHMS. m^2/m, DELTAT = 78-90 μsec/ft, RHOB = 2.37-2.38 g/cc and ΦN = 19-20 p.u..

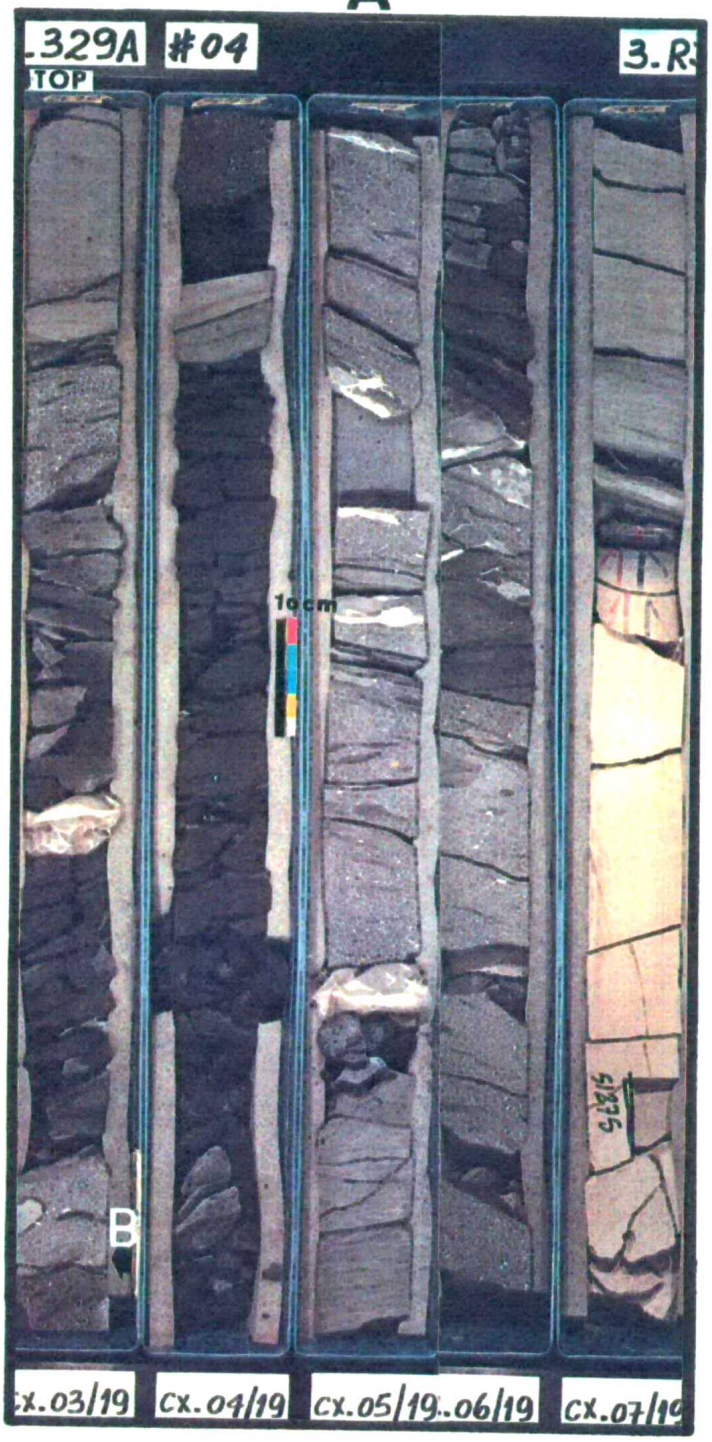
PLATE 5.3a



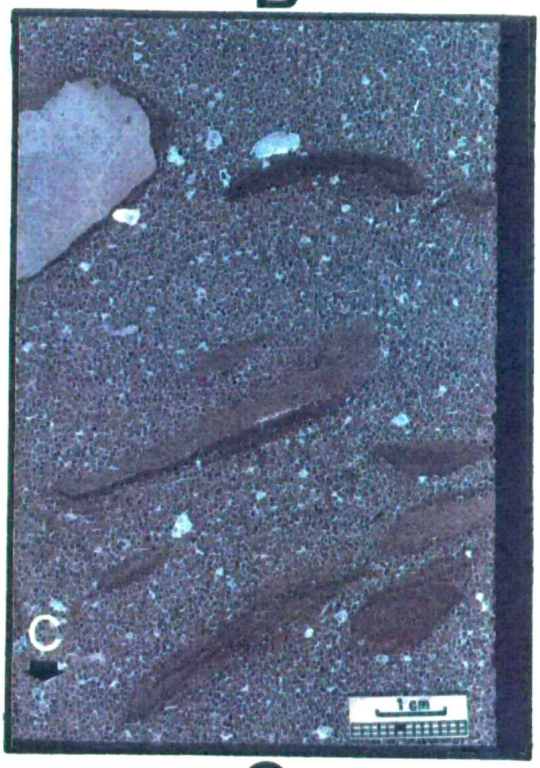
Plate 5.3 - **Diamictite Electrofacies (DMT)**. Composite log (5.3a) and its corresponding cored interval, core 4 (5.3b). The photomicrograph C shows the composition and the textural characteristics of a rock of this electrofacies.

PLATE 5.3b

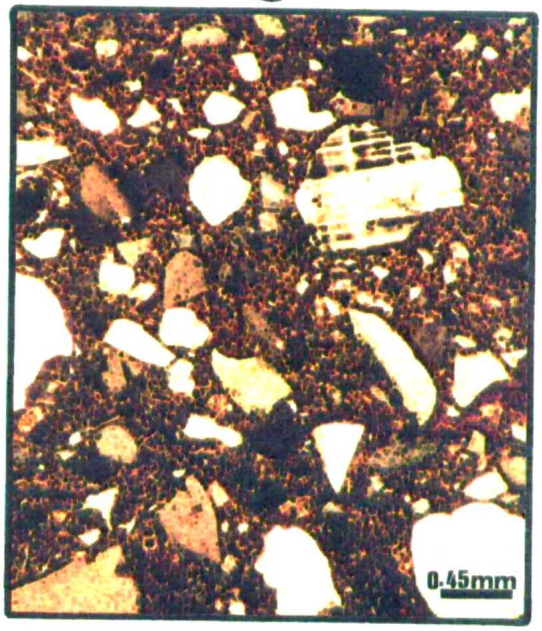
A



B



C



5.3.3.2.2 Seismic response

This electrofacies when embodies the more conglomeratic lithologies and is interbedded with the Mudstone Electrofacies (**G3/G4**) can produce a relatively continuous and high amplitude reflector.

5.3.3.3 INTERPRETATION OF THE ELECTROFACIES (DMT)

The rocks of this electrofacies are the result of deposition by debris-flows and occur most frequently associated with channel-fill deposits (Electrofacies **GvS, AmS, FTab** and **FTb-e, see Plate 5.3a**). Their fauna indicate that some of the material has been transported from environments at least as shallow as middle-neritic. These debris flows must therefore have travelled a reasonable distance before they were deposited in a bathyal environment. These rocks can be seen disconformably overlying a dolomitized marlstone (pelagic/hemipelagic sedimentation) representing an abrupt change in the depositional processes at this site (**Plate 5.3b, photo A, box 07/19**).

This electrofacies has some characteristics very similar to those of the "Chaotic" Electrofacies (**F**) and their differentiation, based only on wireline logs, is very difficult. They could be considered as one electrofacies, despite their genetic differences. However, in some instances it is useful to try and differentiate them to refine the interpretation.

The rocks of this electrofacies are similar to those of Facies A2 of the **MRL** and the Disorganized Gravelly Mud Facies- A1.3 of the **PCK**.

GROUP B

5.3.4 AMALGAMATED SANDSTONE ELECTROFACIES (AmS)

This electrofacies is composed of rocks of lithofacies **VcS** and **AmS**.

5.3.4.1 NORMALLY GRADED OR MASSIVE VERY COARSE/COARSE-SANDSTONE LITHOFACIES VcS

Recognition and sedimentary structures: This lithofacies is composed of amalgamated thick-bedded poorly sorted pebbly/fine-sandstone which may show normal grading.

Thickness: The average thickness of individual beds is 50 cm, but due to amalgamation it can be up to 7 m thick.

Contacts: 1) The top is erosional or amalgamated with itself (**VcS**) or with the (**FTab**) Electrofacies; it may also be abrupt or slightly transitional to the (**AmS**), the (**FTab**) and to the (**BSl**) Electrofacies. 2) The base is erosional with itself, (**G3/G4**), (**BSl**), (**AmS**), and (**FTab**) Electrofacies.

Composition: calcareous bioclastic subarkose

These sandstones consist of two main grain size populations: one of granules/coarse-grained sand and another of medium/fine-grained sand. The mean grain size varies from 1.3 to 2.4 phi with an average around 2.0 phi and sorting between 1.2 and 1.8 phi standard deviation (from now on designated as **std**) with an average around 1.4 phi **std**. The fine tail observed in the cumulative curve and represented by the positive skewness values (0.30 and 1.95, with an average of 1.2) together with the kurtosis values (4 - 8, with an average of 5.9) characterize the relatively wide range of grain sizes, reflecting also its poor sorting (**Fig 5.1** and **5.2**).

The sand-sized clasts consist of quartz, feldspar (microcline > plagioclase), bioclasts (red algae, bryozoa, macro-foraminifera, benthonic and rare planktonic foraminifera), biotite and muscovite, and some intraclasts of mudstones and recrystallized carbonate mudstones. When the rocks of this lithofacies are rich in bioclasts, they are usually tightly cemented by poikilotopic calcite (see **Chapter 9** for more details).

Reservoir characteristics: These are GOOD TO EXCELLENT, when not cemented. The cemented intervals are very tight, and consequently have poor reservoirs properties. Secondary porosity caused by dissolution of calcite cement improves

FIGURE 5.1

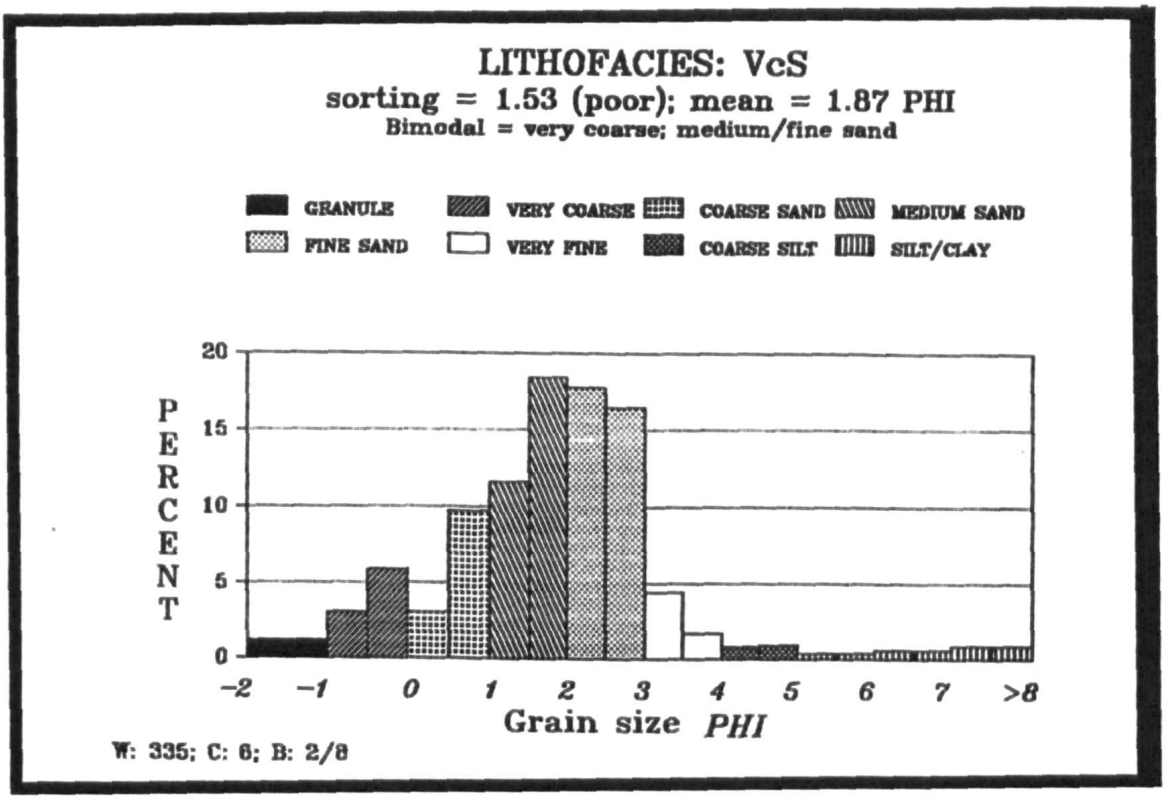
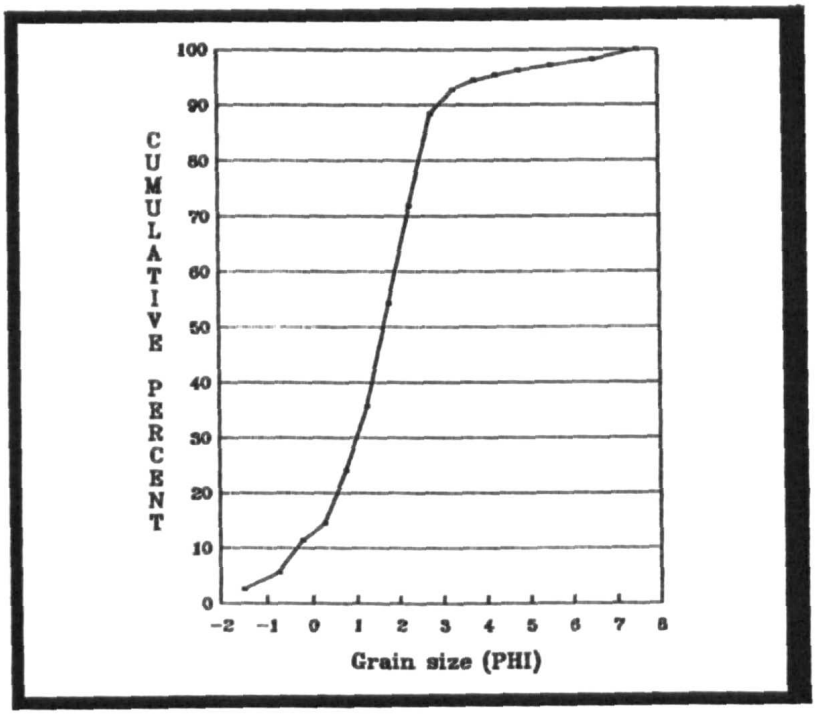


FIGURE 5.2



Figures 5.1 and 5.2 - Grain-size distribution of a sample from the Very Coarse Sandstone Lithofacies VcS.

the reservoir characteristics in some of the cemented horizons. In spite of these cemented intervals being only a few decimeters thick they act as effective local permeability barriers.

Example: Plate 5.4. Similar rocks to this lithofacies were found in the outcrops of the Eocene Jaizkibel Fan, Punta Turrilla, near San Sebastian, Spain, where very coarse-grained sandstones frequently disconformably overlie fine-grained sandstones **(Plate 5.4b photo C).**

5.3.4.2 AMALGAMATED COARSE/FINE-SANDSTONE (EITHER MASSIVE OR WITH POOR NORMAL GRADING) LITHOFACIES, AmS

Recognition and sedimentary structures: The rocks of this lithofacies are composed of thick/medium-bedded coarse/fine-sandstone, commonly amalgamated and with a general lack of sedimentary structures. However, locally poor normal grading due to a coarse tail was observed. This lithofacies has poor core recovery and usually occurs as loose sand in the cores making it difficult or impossible to identify sedimentary structures. The differences between this lithofacies **(AmS)** and the Medium/fine-Sandstone Lithofacies **FTab** are the lack of muddy intercalations separating the sandstones and the general lack of sedimentary structures in the former, indicative of a relatively faster deposition by the "freezing" of the flow. When this lithofacies **(AmS)** is compared with the Very Coarse-Sandstone Lithofacies **VcS** the main difference is its finer average grain size. There is almost a continuum between the Very Coarse-Sandstone Lithofacies **VcS** and the Medium/fine-Sandstone Lithofacies **FTab**, probably as a result of the transition from a grain-flow to a turbidity current dominated regime. The expected fluid escape structures were not observed, probably due to the poor core recovery.

Thickness: The individual beds are 40 cm thick, but as they are commonly amalgamated, the whole interval can be tens of meters thick, with minor intercalations of other lithofacies.

PLATE 5.4a

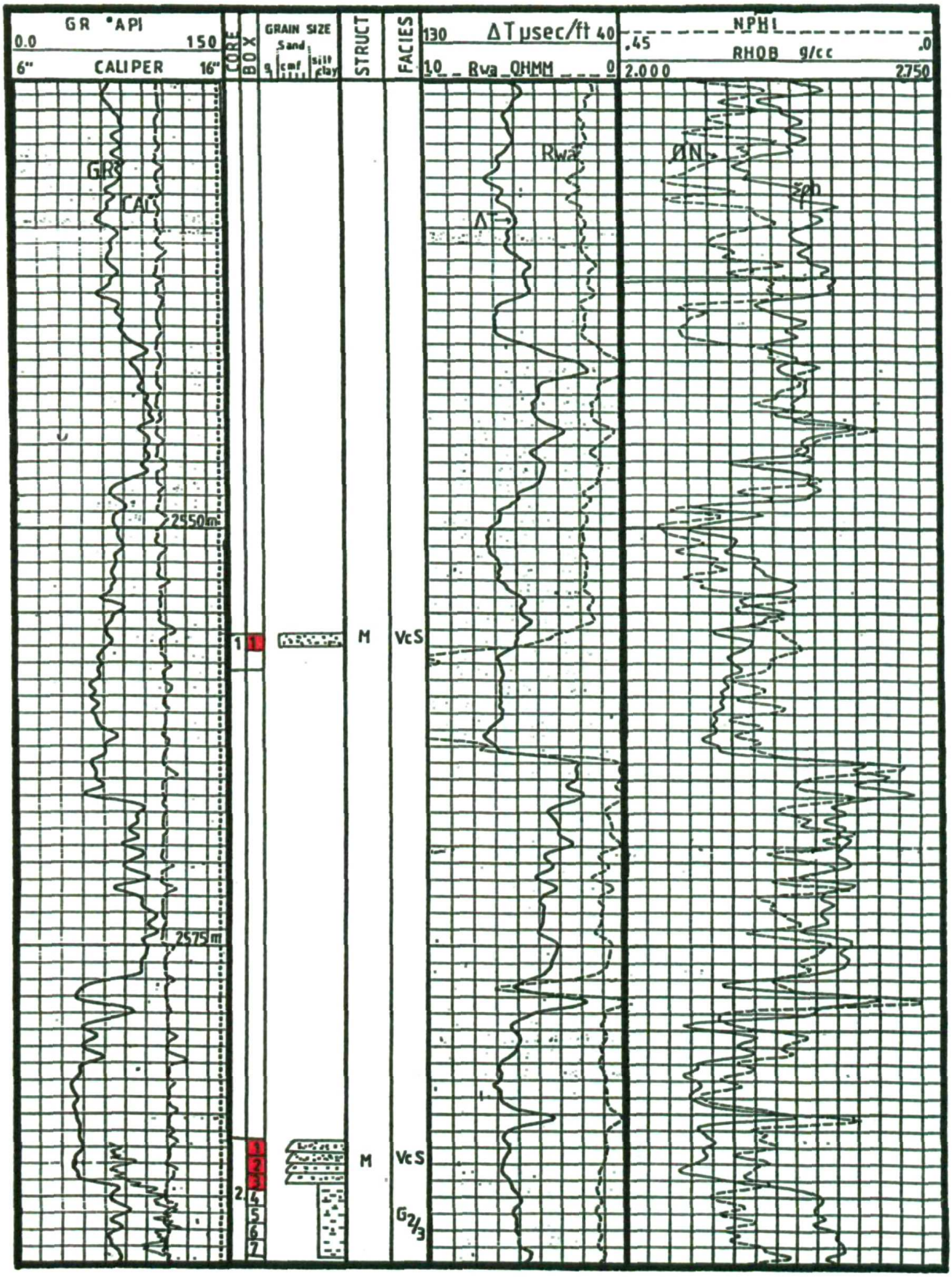
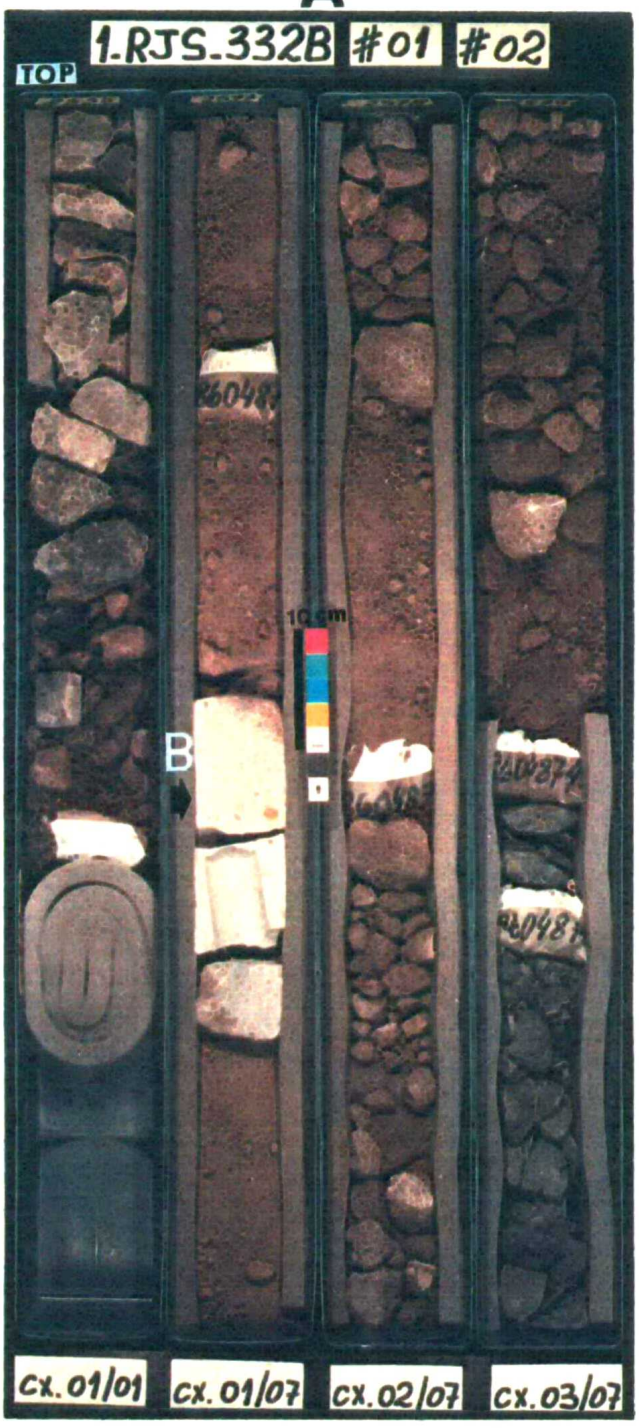


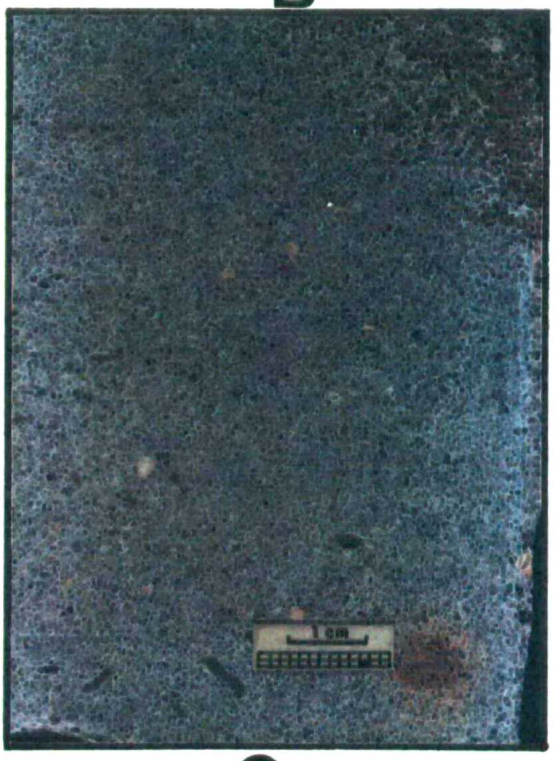
Plate 5.4 - Very Coarse Sandstone Lithofacies VcS of the Amalgamated Sandstone Electrofacies (AmS). Composite log (5.4a) and corresponding cored interval, cores 1, 2 (5.4b). Observe the poor normal grading at photo B. Outcrop of similar rocks from the Eocene turbidites at Punta Turrilla (San Sebastian, Spain), are shown in photo C.

PLATE 5.4b

A



B



C



Contacts: 1) The top is abrupt or amalgamated with itself (**AmS**); abrupt with **VcS**, **FTab** and with **BSl** Lithofacies. 2) The basal is abrupt or amalgamated with itself (**AmS**); abrupt with **BSl**, **G3**, and with **VcS** Lithofacies.

Composition: subarkose/arkose

The rocks of this lithofacies are characterized by a bimodal distribution of coarse/medium and fine-sand showing a wide range of grain size (1.35-3.1 phi, with an average around 2.6 phi), and poor sorting (2-1.05 phi **std**, with an average of 1.5 phi **std**). In contrast to the **VcS** Lithofacies, there is either little or no coarse tail in this lithofacies (**Fig. 5.3** and **5.4**), but the fine tail is better developed and is represented by the positive skewness (0.5-2.3, with an average of 1.25) and relatively high percentages of fines (5- >8 phi=10%).

The sand grains have the following compositions quartz, microcline > plagioclase, bioclast (echinoids, benthonic and planktonic foraminifera and bryozoa), glauconite, biotite and muscovite, mudclasts (with siderite), and heavy minerals (opaques, zircon, tourmaline, garnet).

The rocks of this lithofacies can have up to 35% calcite cement usually associated with bioclast rich intervals, but these cemented horizons are normally only a few decimeters thick (see **Chapter 9**).

Reservoir characteristics: GOOD/EXCELLENT. However, it sometimes embodies thin (30 cm) very tight cemented intervals.

Example: See **Plate 5.5**. A similar lithofacies was seen in the outcrops of the Eocene Jaizkibel Fan, at Cabo Higuer, Spain, where scours up to 4 m deep can be frequently seen (**photos B and C**).

5.3.4.3 GEOPHYSICAL CHARACTERISTICS OF THE ELECTROFACIES (AmS)

5.3.4.3.1 Wireline log responses

The rocks of this electrofacies are characterized by high porosity values, good separation of the neutron and density log curves and low GR, indicative of a porous and

FIGURE 5.3

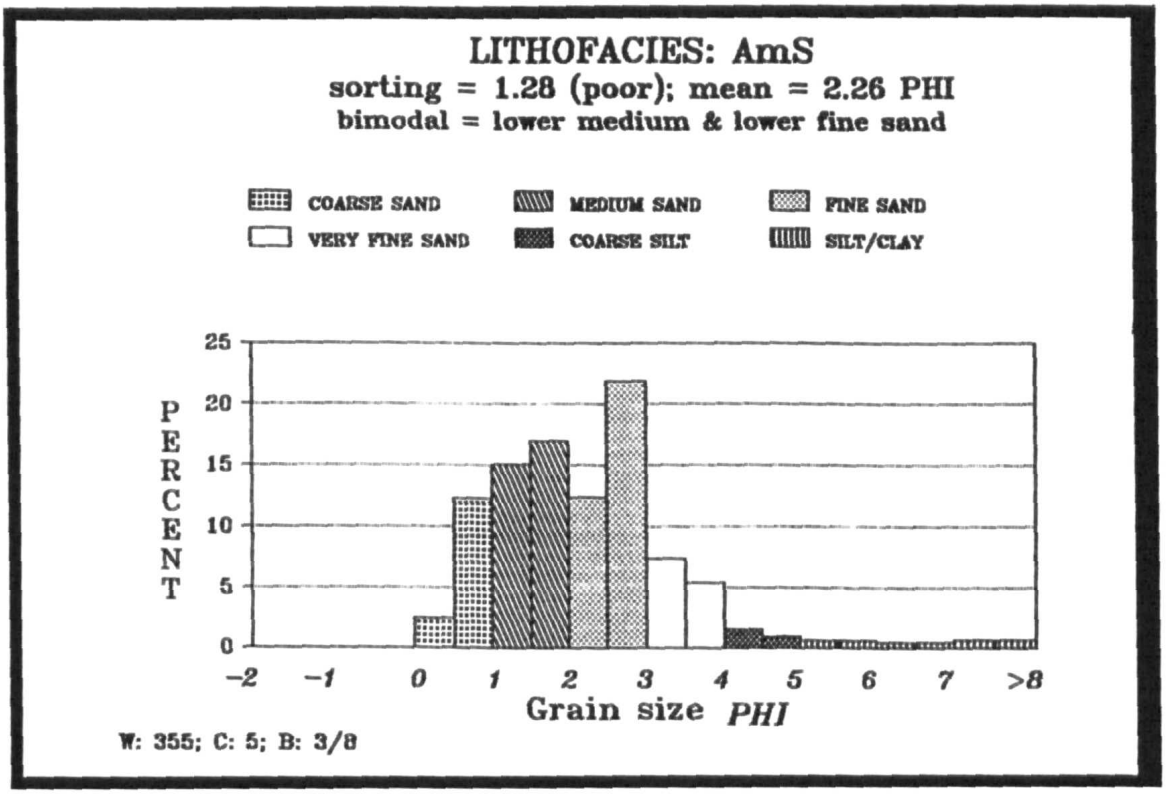
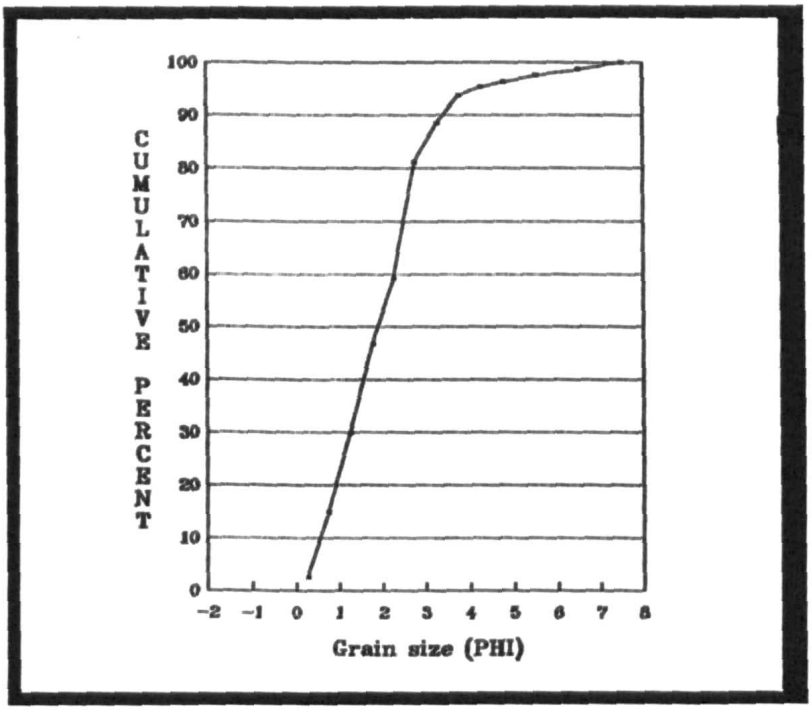


FIGURE 5.4



Figures 5.3 and 5.4 - Grain-size distribution of a sample from the Amalgamated Sandstone Lithofacies AmS.

PLATE 5.5a

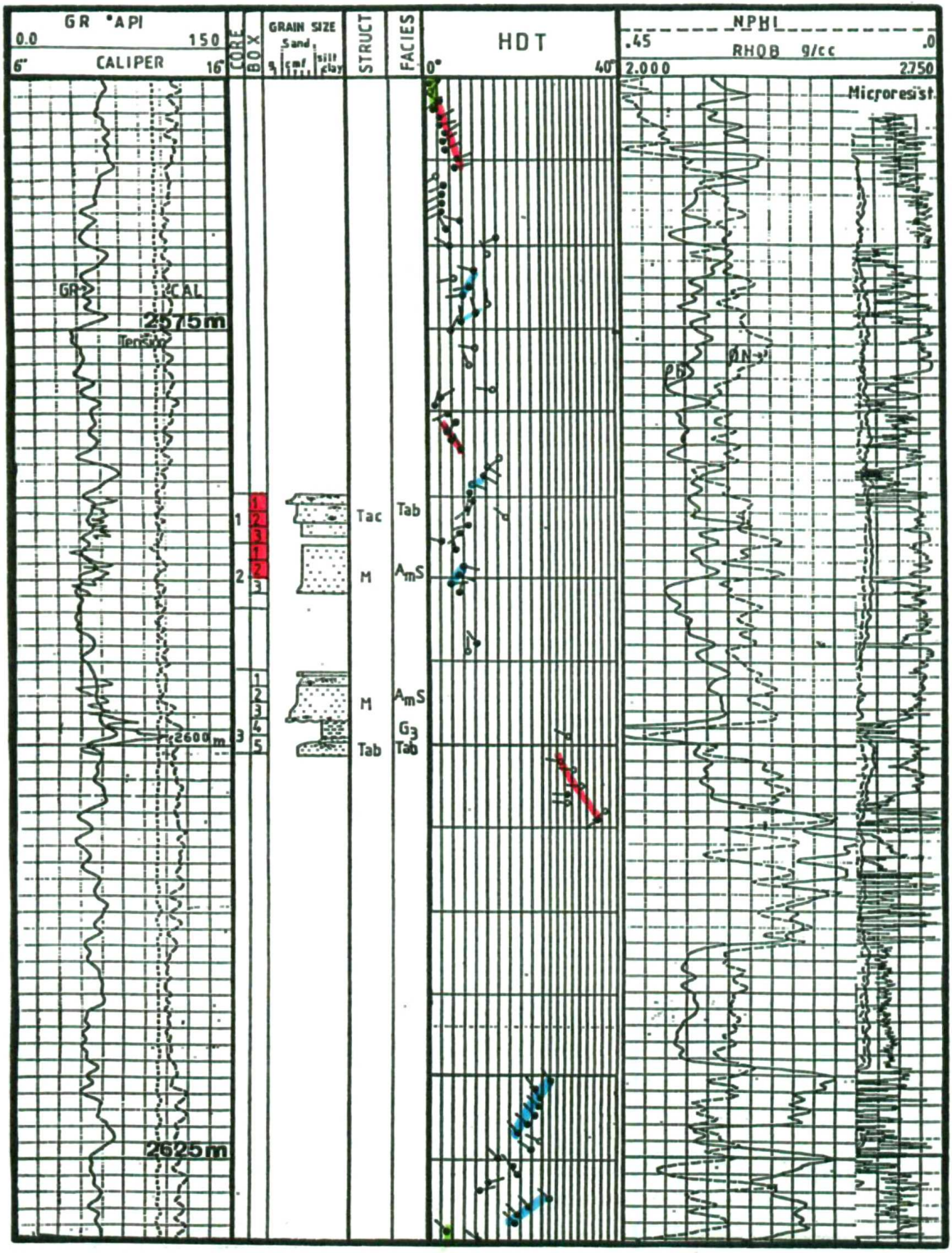
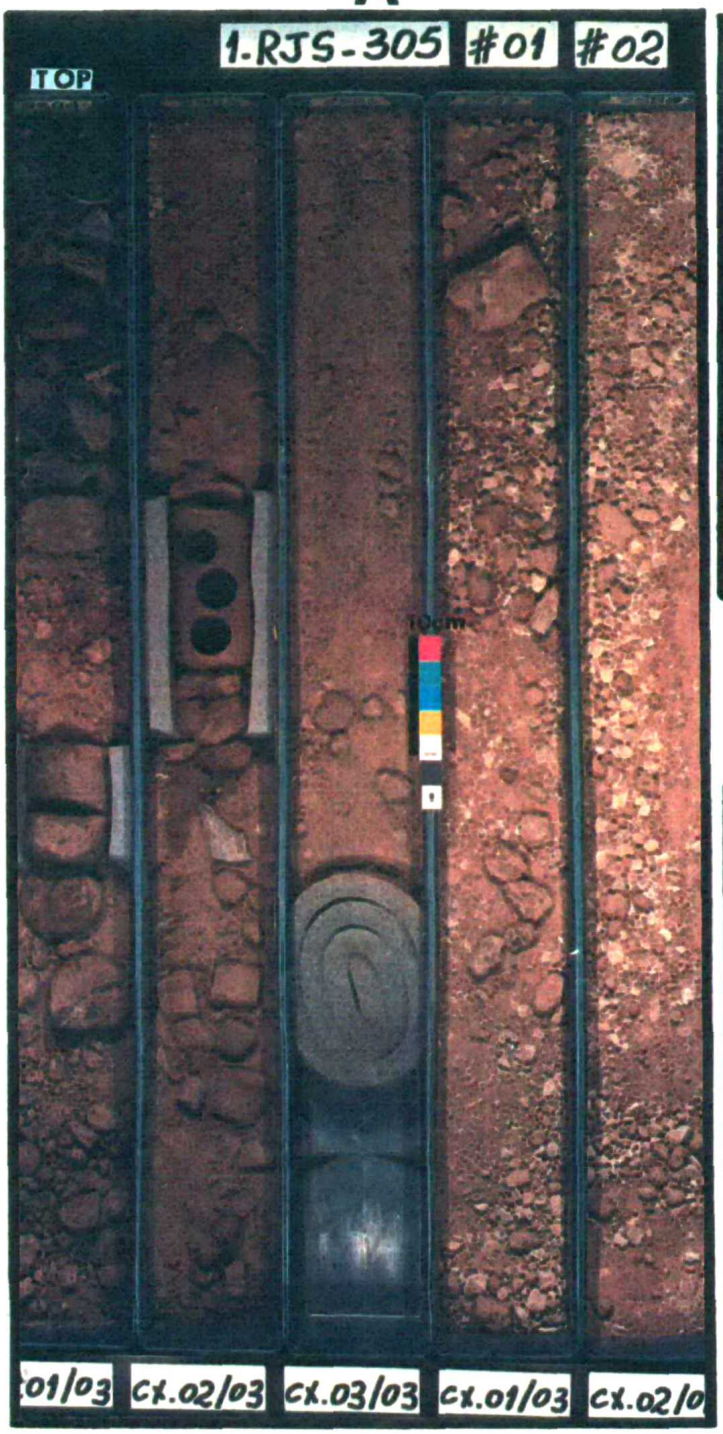


Plate 5.5 - **Amalgamated Sandstone Lithofacies** of the **Electrofacies (AmS)**. Composite log (5.5a) and corresponding cored interval, cores 1 and 2 (5.5b). A similar facies from the Eocene turbidites from Cabo Higuer near San Sebastian, Spain, is also shown. Observe the scours. (The black stripes are caused by weathering and were originally vertical. This photo has been tilted to put the bedding horizontal).

PLATE 5.5b

A



B



C



clean sandstone. The microconductivity curves of the dipmeter presents monotonous curves, representing a "homogeneous" lithology. As a result the computed dips are scattered and with only a few reliable values. The tadpole plot shows scattered arrows with angles varying from 14-31º and pointing towards several directions (SW, SE, NW, N). Locally there are some "red" or "blue" patterns (**Plate 5.5a**), that could be interpreted as the infilling of scours. However, these values are not enough to provide a good interpretation, and reprocessing would be necessary to improve the results. As this electrofacies is represented by massive sandstones the only reliable dips are those associated with contacts at muddy or cemented intervals.

In spite of the danger of using cemented levels for correlation, it is possible to correlate them with the coarser cemented intervals in the core samples of this electrofacies. A high frequency of these coarse-grained cemented intervals could be used to infer main flow pathways and their orientation interpreted from dipmeter logs.

The rocks of this electrofacies have the following mean range of wireline log values:
a) NON CEMENTED: GR = 38-45º API, ISF = 0.9-1.0 OHMS.m^2/m (water zone and not cemented), SFLU = 0.8-1.0 OHMS.m^2/m, DELTAT= 96-120 μsec/ft, RHOB = 2.10-2.20 g/cc (porosity ~33-27 %, using 2.65 g/cc for RHOB matrix), ΦN = 27-29 p.u.;
b) CEMENTED: GR = 40-55º API, ISF = 6.5-30 OHMS.m^2/m (oil zone), ISF = 0.7-0.9 OHMS.m^2/m (water zone), SFLU = 2.25-5.5 OHMS.m^2/m (oil zone), SFLU = 1.2-1.4 OHMS.m^2/m (water zone), DELTAT = 60-80 μsec/ft, RHOB = 2.25-2.52 g/cc, ΦN = 7-21 p.u..

5.3.4.3.2 Seismic responses:

The rocks of this electrofacies can produce a high amplitude ("anomalous") reflector provided it is of sufficient thickness and either overlying or underlying the Carbonate Mudstones/Marlstones Electrofacies (**G1/G2**). This situation is quite common in the Oligocene succession. When this electrofacies has frequent coarse-grained and cemented

sandstones it produces high amplitude discontinuous reflectors, which can be used as an indication of channelized regions. Additionally, when the interval that contains this electrofacies is very thick it is possible to identify, in strike-oriented seismic sections, hummocky clinoforms patterns[7].

5.3.4.4 INTERPRETATION OF THE ELECTROFACIES (AmS)

The rocks of this electrofacies are the result of rapid grain deposition from high-concentration turbidity currents by "freezing" of a dense cohesionless suspension, probably in broad channels of the middle fan. In the analyzed wells, the **VcS** lithofacies normally constitutes the basal portion of the sand-bodies, which, by comparison with outcrops of the Jaizkibel Fan, near San Sebastian, Spain, have a cut-and-fill pattern with scours at their base, generally cutting rocks of finer-grained lithofacies.

The **VcS** Lithofacies grades upward into the **AmS** Lithofacies and together they form the Amalgamated Sandstones Electrofacies (**AmS**). The core, wireline logs and field evidence suggests that this electrofacies is the result of a deposition by multistacked shallow channels, whose channel-fill sequences pass upwards transitionally into the rocks of the Thick-bedded Sandstone Electrofacies (**FTab**) and the Muddy Thin-bedded Sand-mud Couplet Electrofacies (**FTb-e**) and Mudstone Electrofacies (**G3/G4**). Usually this transition occurs over only a few meters or even may have an abrupt boundary (see **Plate 5.5a**). In seismic sections this electrofacies is represented by reflectors showing hummocky clinoforms and incline reflections which can be interpreted as a combination of the lateral migration of shallow (~50 m) channels and interfingering lobes. This seismic pattern is more frequently found in broad gentle lows, where the flows have deposited the majority of their sand load. This electrofacies is similar to the facies described for the

---

[7] Mitchum, Vail and Sangree (1977).

suprafan depositional lobe of Normark (1970) and the channel-lobe transition or Type II fan (low-efficiency or sand-rich fan) of the Mutti (1985).

The rocks of this electrofacies (**AmS**) are comparable to the B1 Facies of **MRL**, and to the B1.1 Thick/medium-bedded Disorganized Sands Facies or the B2.1 Parallel-stratified Sands Facies of **PCK**. It is very difficult to identify possible parallel-stratifications to differentiate between the facies B1.1 and B2.1 of the latter classification because of the poor recovery of the cores and the lack of x-radiographs of the rocks of these sequences.

GROUP C

5.3.5 THICK-BEDDED SANDSTONE ELECTROFACIES (FTab)

This electrofacies is composed of rocks of the lithofacies **FTab** and **FTb**.

5.3.5.1 MEDIUM/FINE-SANDSTONE LITHOFACIES FTab

Recognition and sedimentary structures: The rocks of this lithofacies are composed of very thick/thick-bedded medium/fine-grained sandstone, locally very coarse (Ta) at the base, with well developed normal grading and faint parallel-laminations or may even pass upward into ripple cross-laminations (Tc). The intercalated muddy intervals are frequently heavily bioturbated by horizontal burrows up to 1.5 cm in diameter and correspond to the Bioturbated Sandy Siltstone Electrofacies (**BSl**). Amalgamation can also occur and become more common towards the base when passing transitionally into the rocks of the Amalgamated Sandstone Electrofacies (**AmS**).

Thickness: Individual beds are about 40 cm thick, but the whole interval can be a few meters thick.

Contacts: 1) The top is transitional to the (**BSl**) Electrofacies and the (**FTb-e**) Electrofacies, but abrupt with itself (**FTab**) and with the **AmS** Electrofacies. 2) The basal is abrupt with itself (**FTab**), the (**BSl**), the (**AmS**), and with

the (FTb-e) Electrofacies.

Composition: subarkose/arkose

The rocks of this lithofacies are medium/fine-sandstones with a mode of lower fine sand (the mean varies from 2.0 to 3.3 phi, with an average around 2.7 phi), and a poor/moderate sorting (1.6-0.95 phi **std**, with an average around 1.3 phi **std**). There is only a small coarse tail and it probably represents the **Ta** part of the Bouma sequence. The fine tail is similar to that found in the (**AmS**) Electrofacies and is represented by the positive skewness (1.26-2.76, with an average around 1.68) and moderate percentages of fines (5- >8 phi = 8 %; see **Fig. 5.5** and **5.6**).

The composition of the grains are: quartz, microcline >plagioclase, biotite and muscovite, carbonaceous detritus, rare bioclasts (planktonic foraminifera), and rare heavy minerals (zircon and tourmaline). Locally there are calcite cemented intervals.

Reservoir characteristics: GOOD/EXCELLENT, especially because of its amalgamated nature.

Examples: See **Plate 5.6.**

5.3.5.2 PARALLEL-LAMINATED FINE/VERY FINE-GRAINED AMALGAMATED SANDSTONE LITHOFACIES FTb

Recognition and sedimentary structures: This lithofacies is characterized by amalgamated fine/medium-grained sandstone beds with well developed parallel-laminations and also some climbing-ripples or ripple-drift showing evidence of traction currents. A similar facies was observed in the outcrops near San Sebastian, Spain, where thick intervals of sandstone have very similar characteristics to those found in this lithofacies (**FTb**).

Thickness: The individual beds are only a 10-20 cm thick, but when amalgamated they can be 4 m thick.

Contacts: 1) The top is transitional to the **Wav** Lithofacies of (**E**) Electrofacies; abrupt with itself. 2) The base is abrupt with itself (**FTb**), the **Wav**, **VcS**, **FTab**, or the **G3** Lithofacies.

FIGURE 5.5

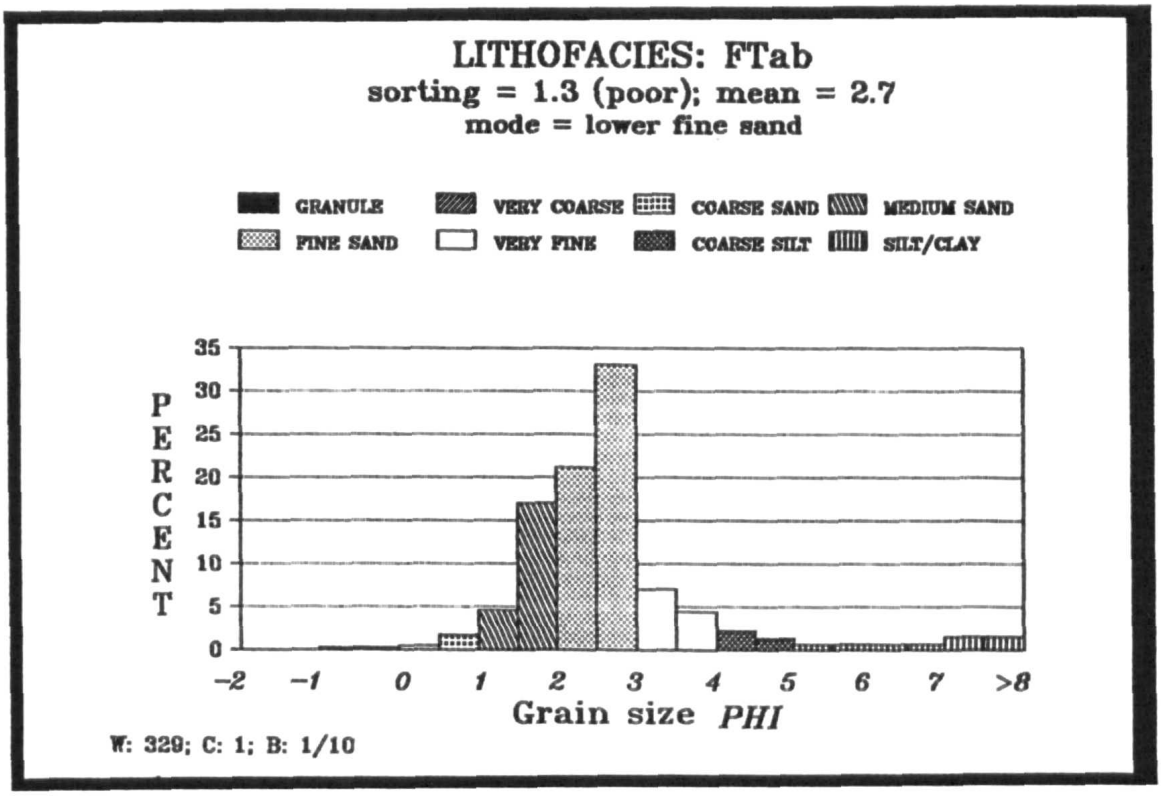
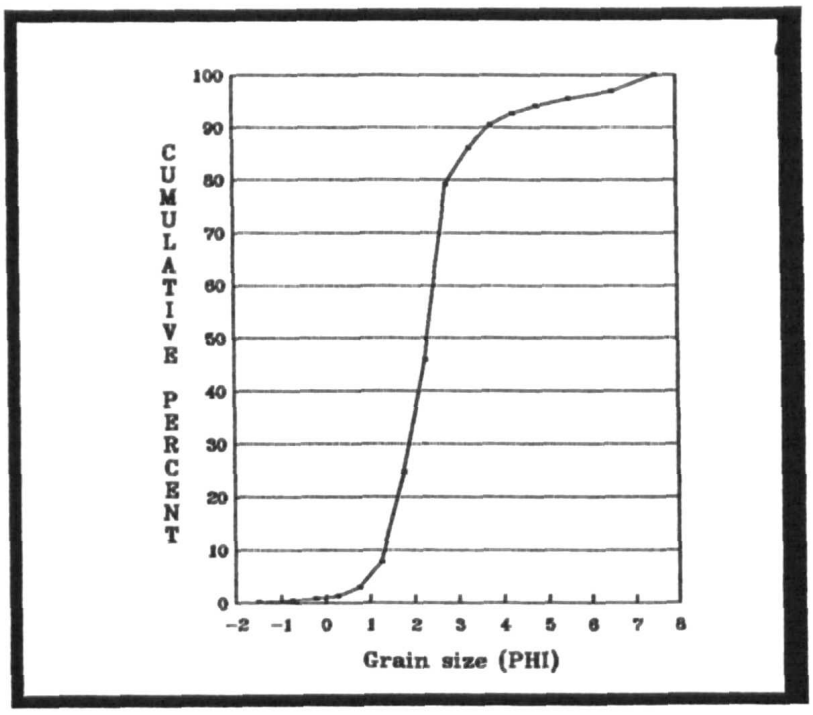


FIGURE 5.6



Figures 5.5 and 5.6 - Grain-size distribution of a sample from the Medium/fine-normal graded Sandstone Lithofacies FTab.

PLATE 5.6a

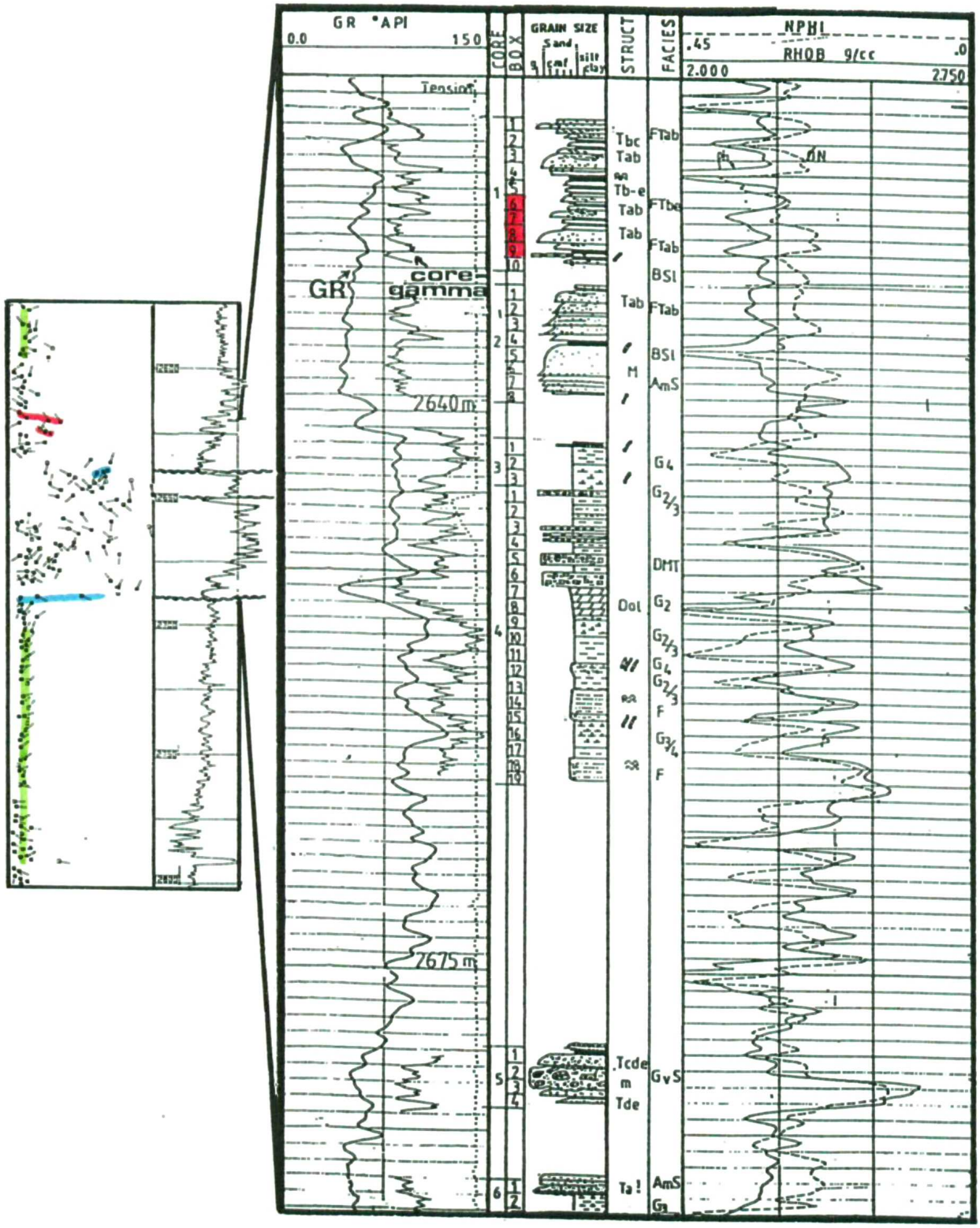
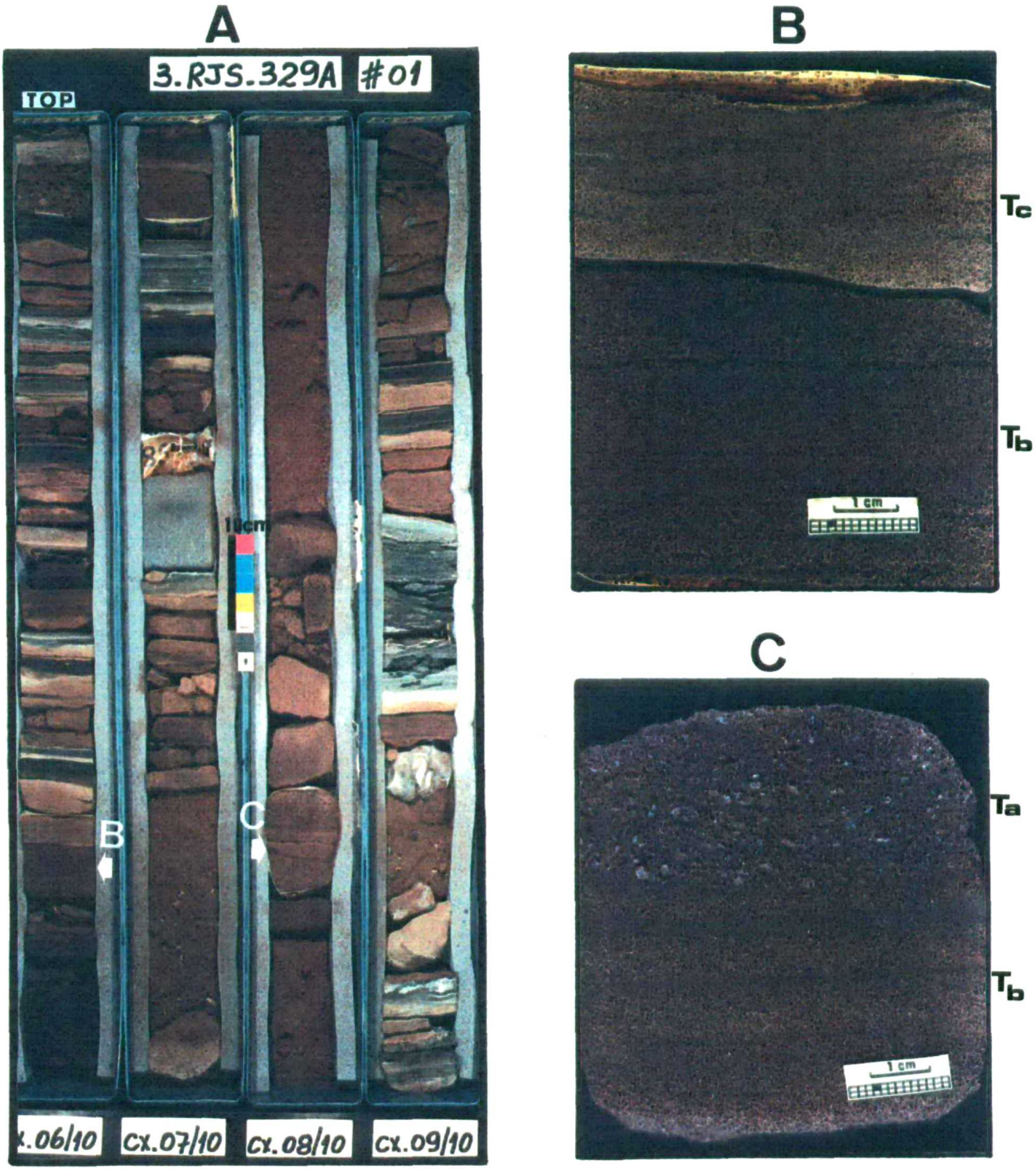


Plate 5.6 - Lithofacies FTab of the Thick-bedded Sandstone Electrofacies (FTab). Core 1 shows a transition downward and upward respectively to the **AmS** and **FTb-e** Lithofacies (5.6a and 5.6b). The close ups show Tabc (B) and Ta part of the Bouma sequence with an erosional contact over a Tb (C).

PLATE 5.6b


A
3.RJS.329A #01
TOP
10cm
B
C
cx.06/10
cx.07/10
cx.08/10
cx.09/10
B
Tc
Tb
1 cm
C
Ta
Tb
1 cm

Composition: subarkose

The rocks of this lithofacies consist of fine/very fine-grained sandstones, with a mode of lower fine sand-grade (the mean varies from 3.3 to 3.7 phi, with an average around 3.5 phi), and a poor/moderate sorting (1.0-1.4 phi **std**, with an average around 1.2 phi **std**). There is no coarse tail, which would be expected from the dominance of the parallel-laminations. The fine tail is similar to that found in rocks of **FTab** Lithofacies but with a greater proportion of very fine sand-sized grains represented by its slightly greater positive skewness values (1.3-2.7, with an average around 1.9). The percentage of fines (5- >8 phi = 8%) is similar to **FTab** Lithofacies (**Fig 5.7, 5.8**).

The clast composition is mainly of quartz, plagioclase>microcline, bioclasts (benthonic>planktonic foraminifera = 1%), heavy minerals (opaques, tourmaline, and zircon), and rare mica. Locally, due to the presence of faint ripple cross-laminations there is an increase in the amount of heavy minerals and mica.

Reservoir characteristics: GOOD/EXCELLENT.

Example: See **Plate 5.7.**

5.3.5.3 GEOPHYSICAL CHARACTERISTICS OF ELECTROFACIES (FTab)

5.3.5.3.1 Wireline log responses

Recognition: This electrofacies consists of cycles about one meter thick, characterized by a large separation of the density and neutron logs curves at the base of the interval, indicative of a clean sandstone, and a crossing of the curves at the top, indicative of the Bioturbated Siltstones Electrofacies (**BSl**). The general vertical GR and density/neutron curve patterns indicate a well defined fining and thinning upwards (see **Plate 5.7a**).

The rocks of this electrofacies have the following mean range of wireline log values: GR = 50-63°API; NGS/CGR = 60°API, SGR = 46°API, Th = 3.000 ppm, Ur = 1800 ppm, K = 0.20 p. (weight%), ISF = 7-35 OHMS.m^2/m (OIL ZONE), SFLU = 6-20 OHMS.m^2/m (OIL ZONE), DELTAT = 95-112 μsec/ft, RHOB = 2.15-2.27 g/cc, ΦN = 29-35 p.u..

FIGURE 5.7

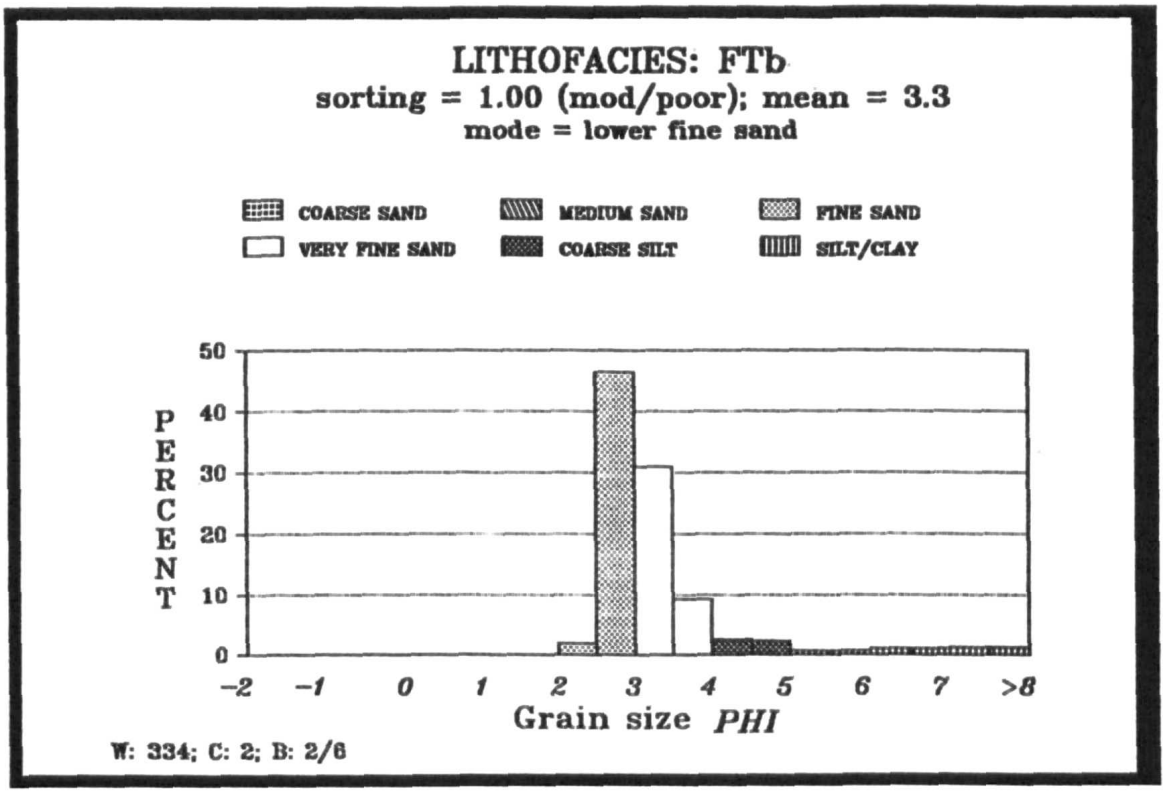
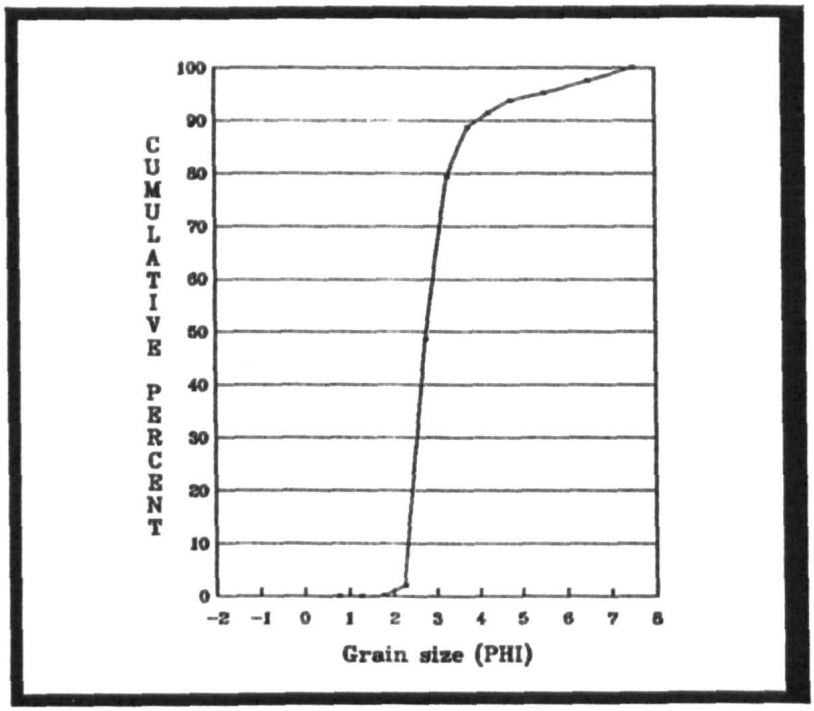


FIGURE 5.8



Figures 5.7 and 5.8 - Grain-size distribution of a sample from the Parallel-laminated Fine/very fine Sandstone Lithofacies **FTb**.

PLATE 5.7a

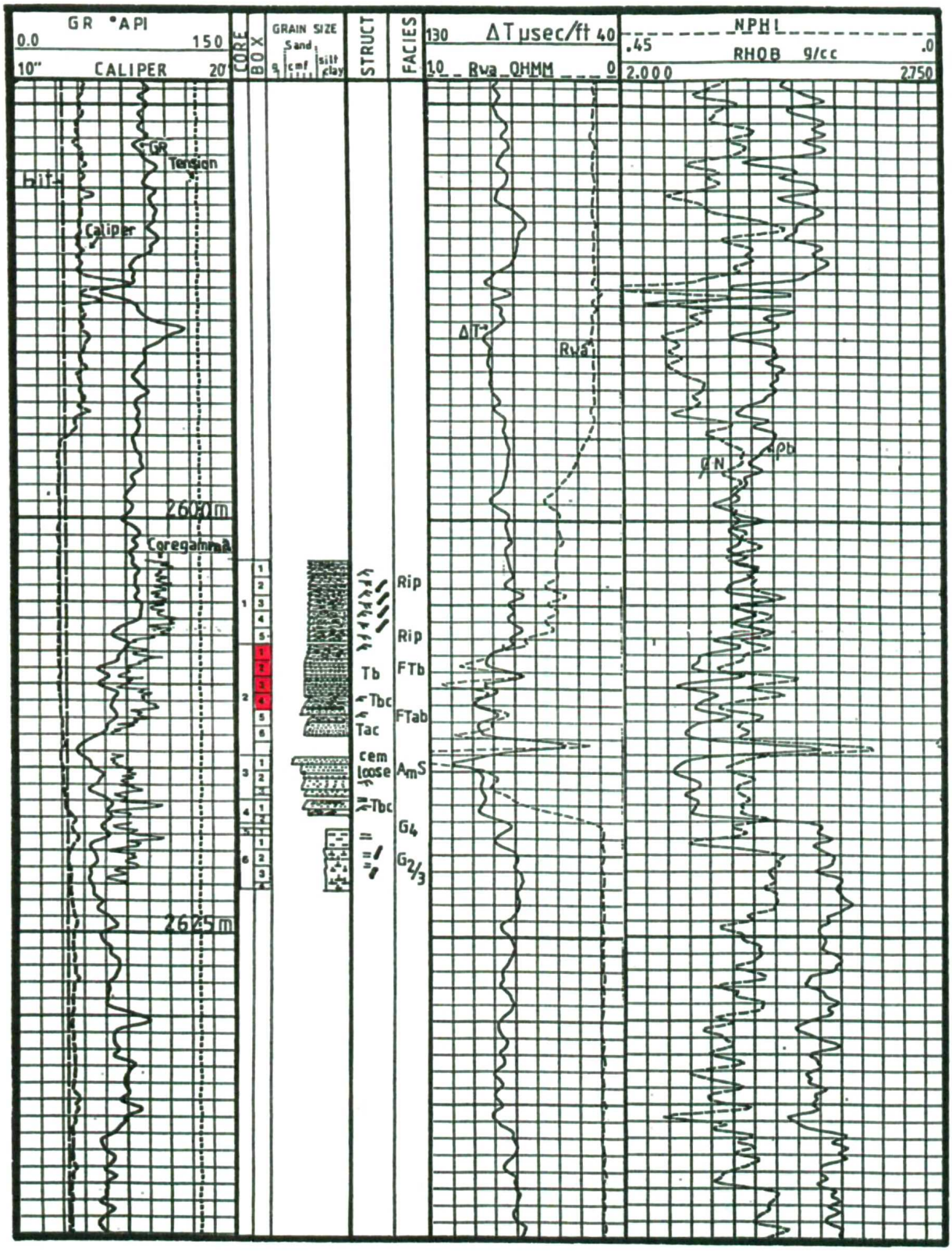
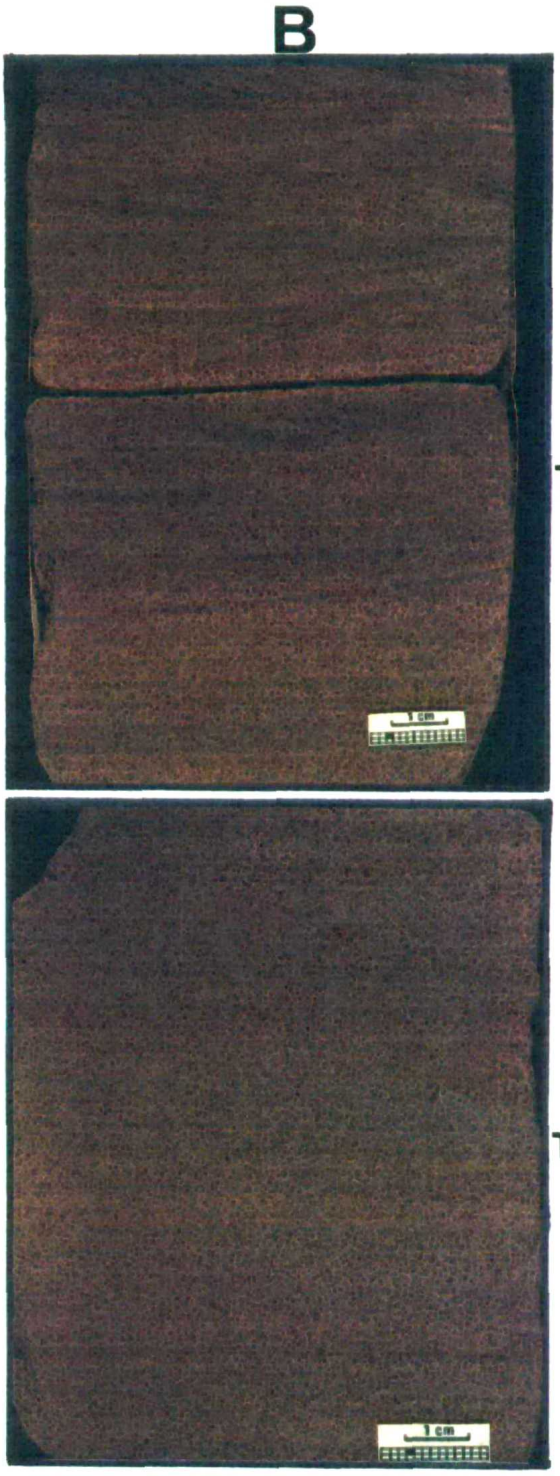


Plate 5.7 - Lithofacies FTb of the Thick-bedded Sandstone Electrofacies (FTab). Composite log (5.7a) of this Electrofacies with its corresponding cored interval showing Tb and some Tbc of Bouma sequences in **A, B** and **C** (5.7b).

PLATE 5.7b


A
3.RJS.334
#2
TOP
B
C
cx. 01/06
cx. 02/06
cx. 03/06
cx. 04/06


B
C
Tbc
Tb
1 cm
1 cm

5.3.5.3.2 Seismic responses

The rocks of this electrofacies do not have a specific seismic character but as it frequently occurs associated with the Amalgamated Sandstone Electrofacies (**AmS**) it can be assumed that it contributes to the hummocky clinoform characteristics of the **AmS** Electrofacies.

5.3.5.4 INTERPRETATION OF THE ELECTROFACIES (FTab)

The rocks of this electrofacies are the result of deposition from high to medium concentration turbidity currents. The better developed parallel-laminations in the **FTb** Lithofacies is the result of more dilute traction currents than those that resulted in the deposition of the **FTab** Lithofacies. The rocks of this electrofacies have similar sedimentological characteristics to those of the Facies C of **MRL** and Very thick and Thick-bedded Sand-mud Couplet of Facies C2.1 and the Medium bedded Sand-mud Couplets of Facies C2.2 in the **PCK** classification.

In the upper part of the sequences, there is a frequent association of this electrofacies with the coarser-grained electrofacies (**GvS** and **AmS**) at their base, and the Thin-bedded Sand-mud Couplets Electrofacies (**FTb-e**) and the Mudstone Electrofacies (**G3/G4**) at the top, showing a general thinning and fining upward pattern. This indicates that this facies is part of a channel-fill sequence rather than part of a typical "depositional lobe" (Mutti & Ricci Lucchi, 1972, 1975; Mutti, 1977, 1985; Mutti and Normark,1987; and Shanmugam & Moiola, 1988) which conversely is characterized by a thickening and coarsening upward sequence. However, as the **FTb** Lithofacies has very well defined parallel-laminations, more typical of "depositional lobe" sediments such as Facies C of **MRL**, there is a possibility that this electrofacies has been deposited in a region dominated by channel-fill facies sediments but representing a late depositional phase during the abandonment of a turbidite system.

GROUPS D and E

THIN-BEDDED SAND-MUD COUPLETS ELECTROFACIES

There are two groups of electrofacies characterized by thin-bedded sand-mud couplets and the grain size of these sandstone beds varies from medium sand to silt-sized with a mode of very fine sand. The difference between the lithofacies (**FTb-e** and **FTde**) from Group **D** and the lithofacies (**Fla, Wav** and **Rip**) from Group **E** is based on the more tractional character of the sedimentary structures in the latter, represented by erosion on the stoss-side of the ripples, the bed geometry and a higher sand/mud ratio (usually > 1).

GROUP D

5.3.6 MUDDY THIN-BEDDED SAND-MUD COUPLETS ELECTROFACIES (FTb-e)

This electrofacies is composed of the lithofacies **FTb-e** and **FTde.**

5.3.6.1 THIN/VERY THIN-BEDDED SANDSTONE/MUDSTONE LITHOFACIES FTb-e - SANDSTONE:SHALE <1, AND THE SANDSTONES WITH Tbcde, Tbc, Tcde, Tade, local Tacde and Tade.

Recognition and sedimentary structures: This lithofacies consists of rhythmic alternations of thin-bedded fine/very fine-grained sandstone with mudstones. The sandstone beds have normal grading (lower fine to very fine sand-sized grains), and faint parallel-laminations and climbing-ripples at the top, where the grain size is fine enough to allow it. Bioturbation is a common feature and is represented by horizontal sand-filled burrows that vary from a few mm up to 15 mm in diameter.

Thickness: These sandstone beds vary in thickness from 1 cm (only Tc) to up 10 cm thick (Tabcde) with an average of 5 cm (Tbc). The whole interval is more than 10 m thick.

Contacts: 1) The top is transitional to the **FTde**

Lithofacies; and abrupt/erosional with the (**FTab**) Electrofacies. 2) The base is either transitional or abrupt with (**FTb-e**) or (**FTab**) Electrofacies.

Composition: subarkose

The sandstones of this lithofacies consist of poorly/moderately sorted fine/very fine sand-sized grains. Their grain composition is: quartz, plagioclase=microcline (15%), bioclasts (benthonic=planktonic foraminifera, and ostracods), minor amounts of mica (biotite and muscovite), opaques, mudclasts, and carbonaceous detritus. There is matrix only in the bioturbated upper part of the sandstone beds and with a higher proportion of foraminifera. Calcite cementation is very restricted, associated with the bioturbated finer grained sandstones.

Reservoir characteristics: MODERATE/POOR. This is mainly due to the limited thickness of the sandstone beds and the high frequency of interbedded mudstones which act as vertical permeability barriers.

Examples: Two examples of this lithofacies are shown, one with a general thinning and fining upward sequence overlying coarse-grained electrofacies forming the upper part of a channel sequence (**Plate 5.8**) and the other interbedded with hemipelagic sediments with no vertical relationship with coarse-grained electrofacies (**Plate 5.9**).

5.3.6.2 MILLIMETRIC RHYTHMIC SILTSTONE LITHOFACIES FTde

Recognition and sedimentary structure: This lithofacies is characterized by very thin (1-15 mm) rhythmic interbedding of graded coarse silt-mud couplets (Tde). The main distinctive characteristic is its well defined parallel-laminations, although occasionally they appear slightly lenticular. The silt laminae show a sharp basal contact and frequently grade upwards transitionally into the Mudstone Electrofacies (**G3/G4**). Bioturbation is common and can destroy the laminations. The most common trace fossils found in the core samples are: Zoophycos, Planolites (2 mm in diameter), and Thalassinoides (with 10 mm in diameter).

PLATE 5.8a

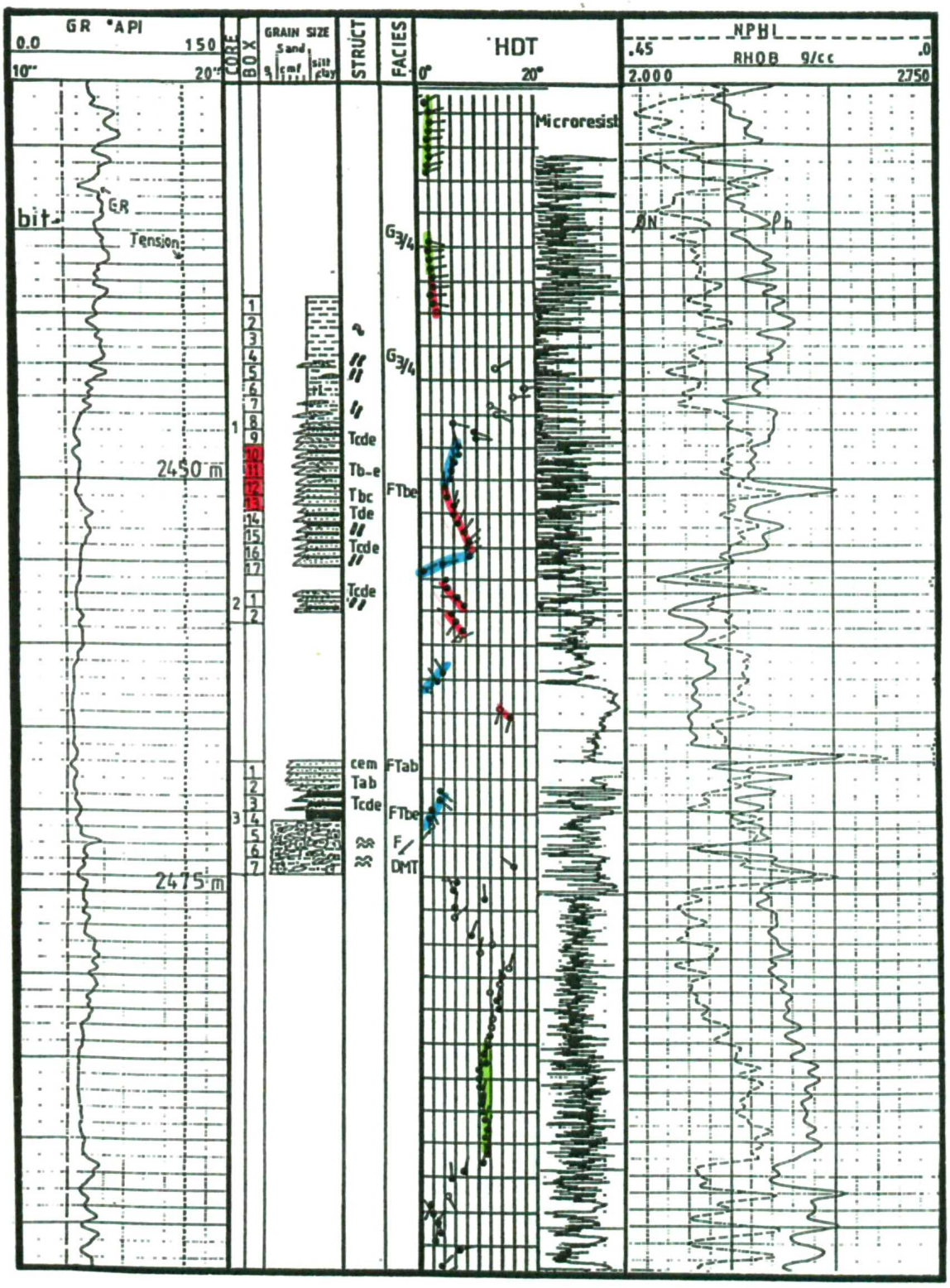


Plate 5.8 - Muddy Thin-bedded Sand-Mud Couplet Electrofacies (FTb-e). Composite log (5.8a) with its corresponding cored interval (5.8b). A similar channel-fill facies of the Hecho Group from an outcrop near Arro Village, Spain, is shown in photo (B). A close-up of the cored couplets shows faint normal grading and ripple cross-laminations (photo C).

PLATE 5.8b

A



B



C

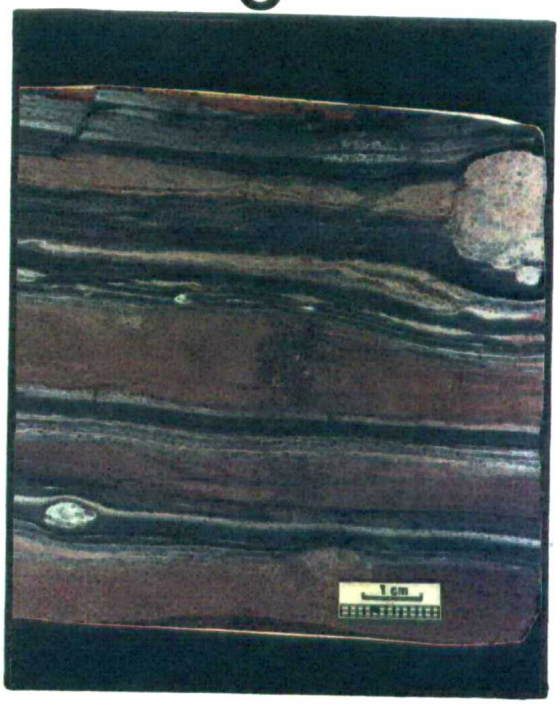


PLATE 5.9a

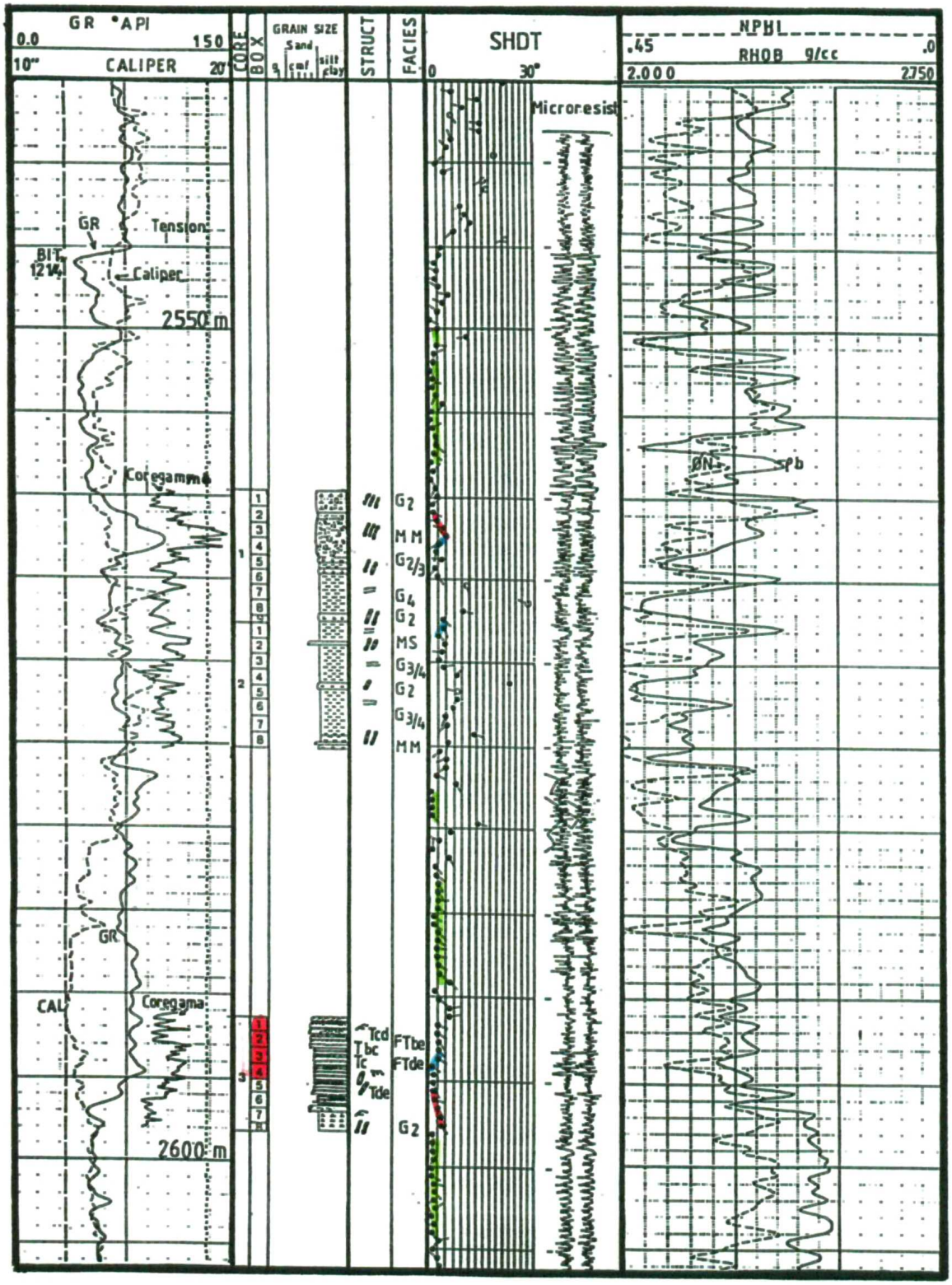


Plate 5.9 - Muddy Thin-bedded Sand-Mud Couplet Electrofacies (FTb-e). Composite log (5.9a) and its corresponding cored interval (5.9b). Observe the high frequency of millimetric intercalations (photo A) of very fine-grained sandstones and mudstones. Thicker sandstone beds show well developed Tbc Bouma sequence (B and C).

PLATE 5.9b


A
3.RJS.316 #03
TOP
B
C
10 cm
cx.01/08
cx.02/08
cx.03/08
cx.04/08
B
Tbc
1 cm
C
Tcd
Tc
Tb
1 cm

Thickness: The individual siltstone beds or laminae are only few millimetres thick (1-15 mm) but the whole interval can be a few meters thick.

Contacts: 1) The top is transitional to **G4, FTb-e** Lithofacies; abrupt with **FTab, FTb-e,** and **GvS** Lithofacies. 2) The base is transitional to the **FTb-e;** abrupt with **F, MM, FTab** Lithofacies.

Composition:

The rocks of this lithofacies consist of coarse silt grains whose composition is mainly of quartz, feldspar (microcline>plagioclase), mica, bioclasts (benthonic > planktonic foraminifera), and organic matter distributed in a mud-matrix. The clay fraction of the mud-matrix consists of smectite-rich (90% SM) mixed-layer illite-smectite (48%), kaolinite (23%) and illite (29%) (for more details of the clay fraction composition see **Chapter 8**).

This lithofacies is characterized by a deep neritic to upper bathyal assemblage represented by calcareous-hyaline benthonic foraminifera (Gyroidina sp., Nodosaria sp. A, Lenticulina sp. A, Dentalina sp. A, Melonis sp. A, Cibicides sp., Bolivina sp.) and planktonic foraminifera (Globigerinoides g. primordius, Globigerinoides immaturus, Globorotalia Kugleri, Globigerina sp. A) (Azambuja Filho & Koutsoukos, 1990; in preparation).

Proportionally there are more microfossils and organic matter in the mudstones compared with the sandy/silty layers. Bioturbation in this lithofacies is frequently represented by burrows infilled with sand-sized grains.

Reservoir characteristics: The rocks of this lithofacies do not form a reservoir.

Example: This lithofacies is commonly interbedded with thin-bedded turbidites (**FTb-e** Lithofacies) exemplifying its very well defined parallel-stratifications due to the alternations of sandy and muddy laminae (**Plate 5.8**).

5.3.6.3 GEOPHYSICAL CHARACTERISTICS OF THE ELECTROFACIES (FTb-e)

5.3.6.3.1 Wireline log responses

The rocks of this electrofacies are characterized by very thin interbeds of sandstones and mudstones and the GR log shows a saw-tooth pattern with values intermediate between those of sandstones and mudstones. The combination of the density-neutron log curves is a very good tool to identify this interfingering pattern typified by the convergence, divergence and intercrossing of the two curves in decimeter intervals. Additionally, the neutron log values show an increase upwards, indicative of an increase in the clay content (fining upwards). This facies has usually higher neutron log values than the Sandy Thin-bedded Sand-Mud Couplet Electrofacies (E) staying most of the time to the left of the density log curve, which is the converse of what happens for (E) Electrofacies. The microresistivity curves of the dipmeter log display a well defined thin-interbedding, and the tadpole plot shows good results. When this electrofacies is associated with the top of coarser-grained sequences it displays a general "red" pattern with relatively low angles, varying from 8º at the base to 2º at the top, with minor "blue" (4º-7º) and "red" (10º-6º) patterns (see **Fig 5.8a**). The general "red" pattern passes transitionally upwards into a "green" (2º) pattern characteristic of the Mudstone Electrofacies (**G3/G4**). In the example shown in the **Plate 5.9**, where there is no vertically associated coarser-grained electrofacies, the dipmeter shows very low angles (1º-2º) close to a "green" pattern, but with slight increases characterizing very gentle "blue" patterns, due to the presence of thicker sandstone beds (**Plate 5.9**).

The rocks of this electrofacies have the following mean range of wireline log values: GR = 90-95º API, ISF = 1.9-3.2 OHMS.m^2/m (OIL ZONE), SFLU = 2-3.7 OHMS.m^2/m (OIL ZONE), DELTAT = 96-109 μsec/ft, RHOB = 2.25-2.31 g/cc, and ΦN = 30-35 p.u..

5.3.6.3.2 Seismic responses

This electrofacies does not have a particular seismic response probably because of its commonly reduced thickness.

5.3.6.4 INTERPRETATION OF THE ELECTROFACIES (FTb-e)

The rocks of this electrofacies show a high frequency of sand-mud interbeds which are interpreted as reflecting deposition from relatively low-concentration turbidity currents. The graded silty beds could be the result of sorting of silt grains and clay flocs in the viscous sub-layer of the turbidity flow (Stow and Bowen, 1980).

The existence of examples where this electrofacies is either vertically (**Plate 5.8a**) or laterally associated with coarse-grained sandstones of channel-fill deposits (see **section 5.4**, Fig. 5.11 at the level of the sandstones C and D) it is possible to interpret this electrofacies as channel-fill/overbank deposits. The deposition of this electrofacies probably occurred in channels during their abandonment/lateral migration or as overbank/crevasse splay deposits. The former when vertically associated with coarser-grained sandstones and the latter when laterally associated with coarser-grained electrofacies.

The rocks of this electrofacies are comparable to those of Facies D2/D3 of the **MRL**. The lithofacies **FTb-e** and **FTde** correspond to C2.2 and C2.3 Facies, and to D2.1 and D2.3 Facies of the **PCK** classification.

<u>GROUP E</u>

5.3.7 SANDY THIN-BEDDED SAND-MUD COUPLETS ELECTROFACIES (E)

This electrofacies is composed of the lithofacies: **Fla**, **Wav** and **Rip**. These lithofacies have a higher sandstone:shale ratio than those of the lithofacies FTb-e and FTde (Electrofacies **FTb-e**), usually >1, and ripples showing erosion on the stoss-side, which provides evidence of traction. The grain-size varies from fine-sand to silt/clay with a mode of lower very fine-sand.

5.3.7.1 THIN-BEDDED FINE-SANDSTONE WITH FLASER-BEDDING AND FAINT RIPPLE-CROSS-LAMINATION LITHOFACIES Fla

Recognition sedimentary structure: This lithofacies is characterized by fine/very fine-grained sandstones with faint ripple cross-laminations and some flaser-bedding. The high frequency of amalgamation and the lack of muddy layers between the fine/very fine-grained sandstones are the main distinctive features of this lithofacies compared with the lithofacies **Wav** and **Rip.**

Thickness: The thickness of this lithofacies varies from a few centimetres up to 4 m.

Contacts: 1) The top is transitional to the **Rip** Lithofacies. 2) The basal is transitional to the **Rip** Lithofacies and abrupt with the **(MM/MS)** Electrofacies.

Composition: subarkose

The rocks of this lithofacies are characterized by a fine/very fine-grained sandstone with a mode of very fine-sand (the mean varies from 3.4 to 4.16 phi, with an average around 3.8 phi), and poor/moderate sorting (0.94-1.36 phi **std**, with an average around 1.17 phi **std**). The fine tail is better developed than in the rocks of the other lithofacies. There is a greater proportion of coarse silt-sized grains compared to the **FTb** Lithofacies, but with very similar positive skewness values (1.28-2.58, and an average around 1.8). The rocks of lithofacies have very high percentages of fines (5- >8 phi) with values up to 20% **(Fig. 5.9** and **5.10).**

The sand-sized grains consist of quartz, feldspar, and mudclasts with siderite, heavy minerals and carbonaceous debris.

Reservoir characteristics: MODERATE TO GOOD. The good reservoir quality reflects the high amalgamation frequency of the sandstones, which eliminates permeability barriers (mud-drapes) and consequently gives it better reservoir qualities than the rocks of lithofacies **Wav** and **Rip.**

Example: See **Plate 5.10.**

FIGURE 5.9

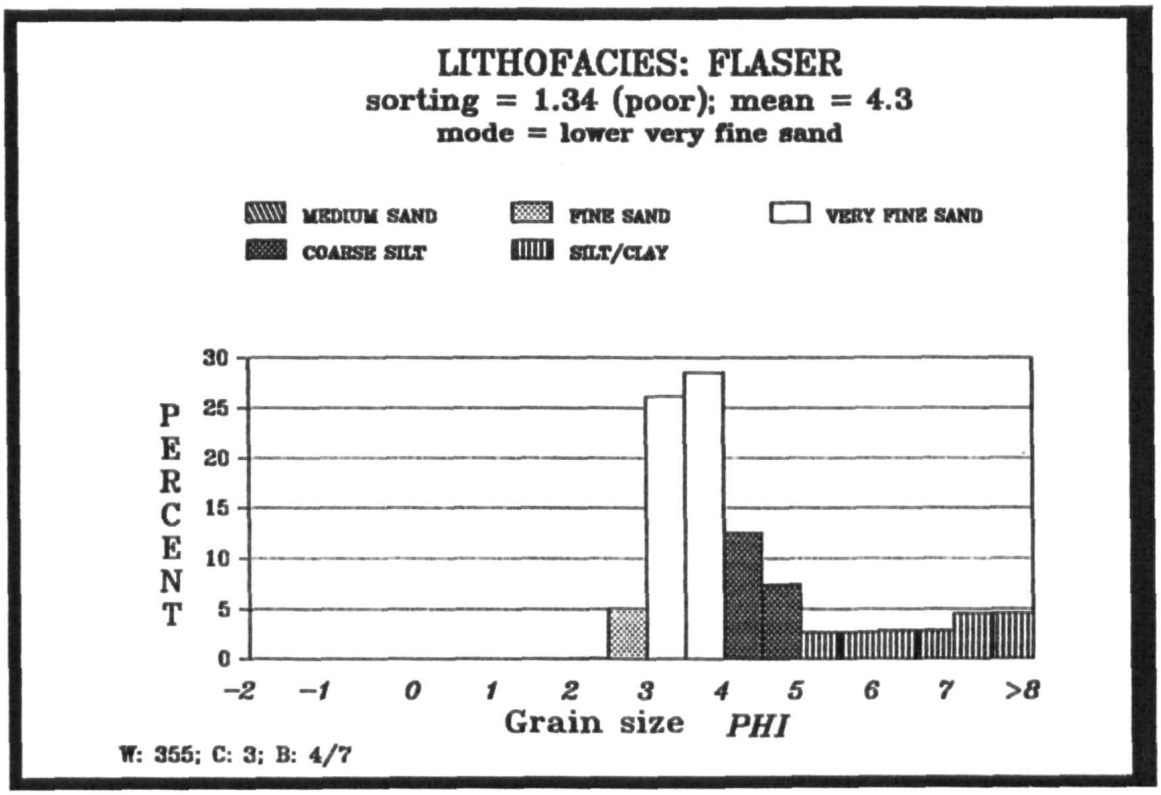
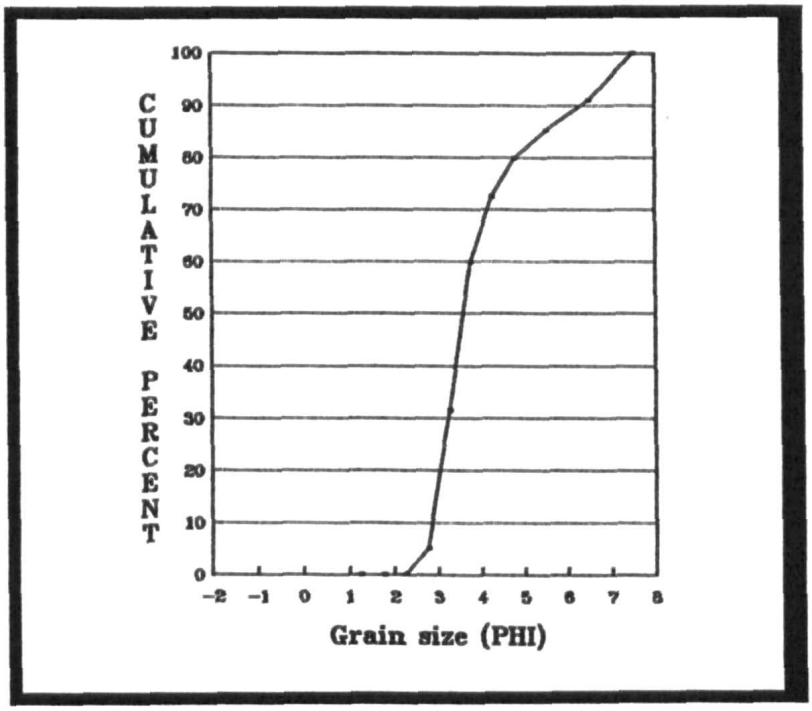


FIGURE 5.10



Figures 5.9 and 5.10 - Grain-size distribution of a sample from the Thin-bedded Very fine-Sandstone with Flaser-bedding Lithofacies **Fla.**

PLATE 5.10a

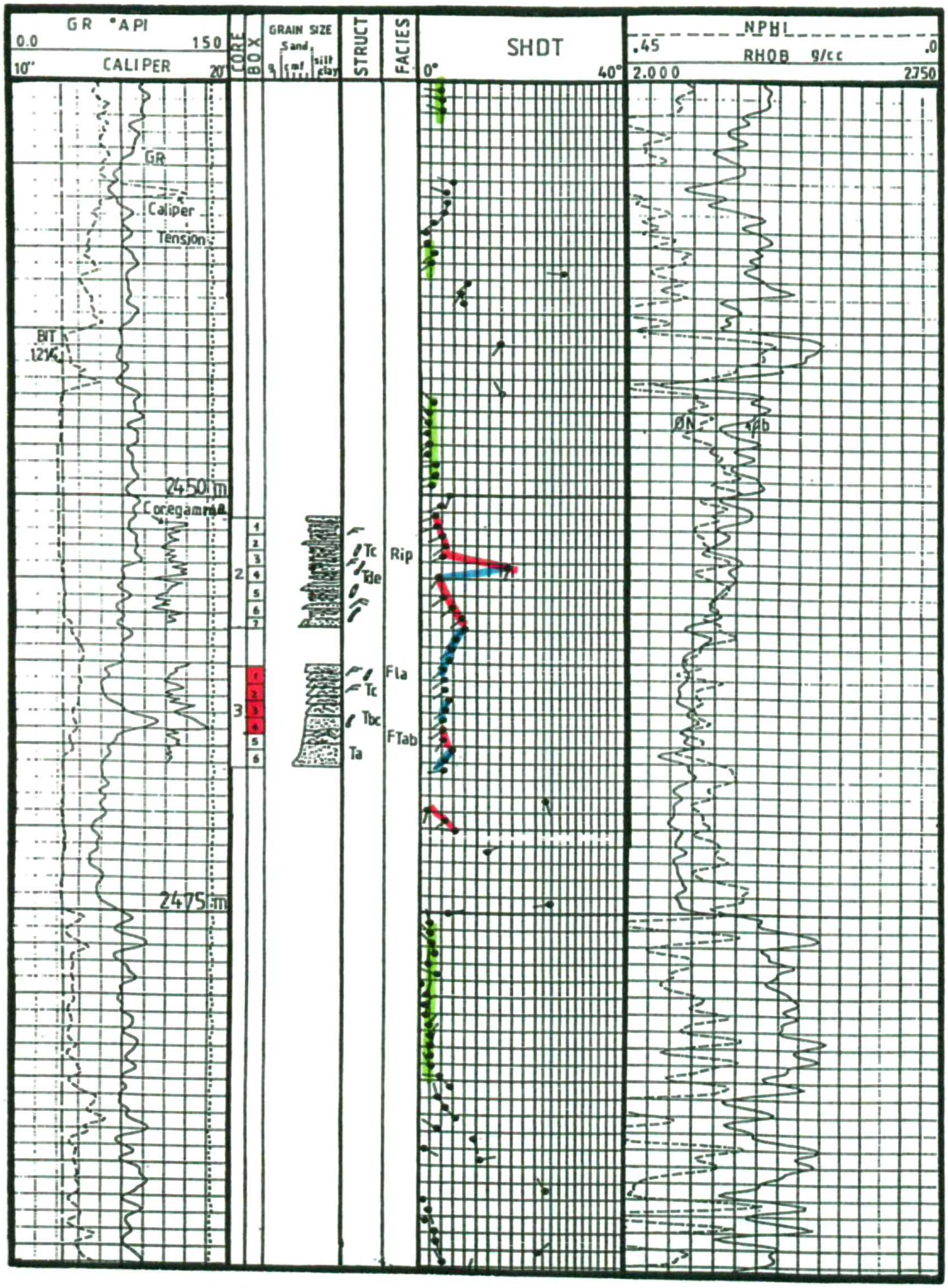
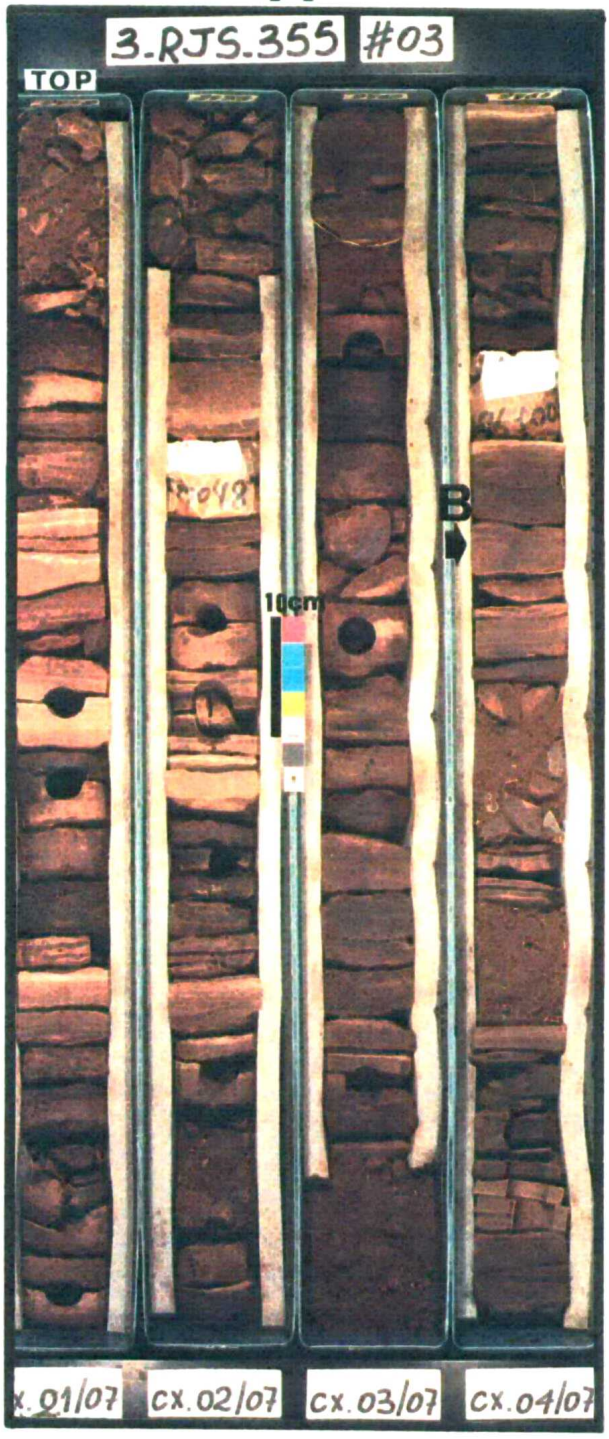


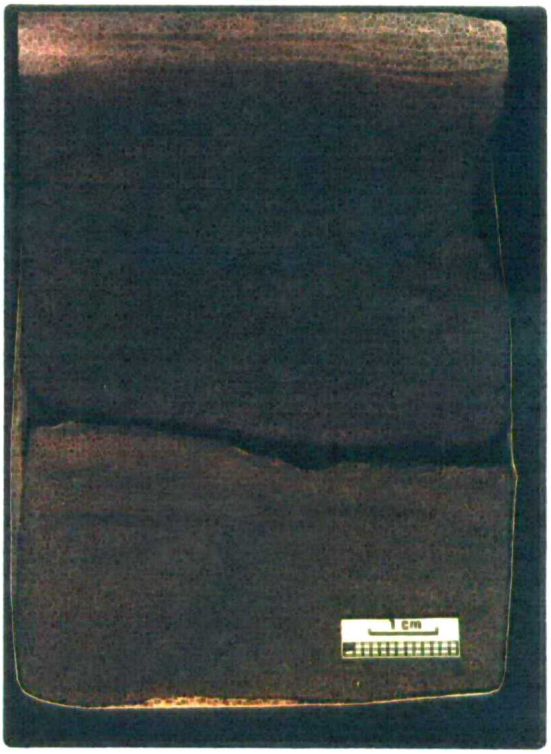
Plate 5.10 - Thin-bedded Fine-sandstone with Flaser-bedding Lithofacies Fla of the Electrofacies (E). Composite log (5.10a) and its corresponding cored interval (5.10b). The high degree of amalgamation, small thickness of individual beds, and discontinuous muddy laminae have characteristics that resemble flaser-bedding in this example (5.10b).

PLATE 5.10b

A



B



5.3.7.2 THIN/VERY THIN-BEDDED FINE-SANDSTONE WITH WAVY-BEDDING AND FAINT RIPPLE-CROSS-LAMINATIONS LITHOFACIES Wav

Recognition and sedimentary structures: The rocks of this lithofacies are characterized by thin/very thin-bedded (3 cm) fine/very fine-grained sandstones with wavy-bedding and local flaser-bedding with mud-drapes of about 1-3 mm of thickness. The internal structures show normal grading and faint ripple cross-laminations. However, when the grain sizes were fine enough (lower very fine sand) climbing-ripples have developed. It is common to find ripples with evidences of erosion on the stoss-side and preservation under the mud-drapes. Bioturbation is frequently present in this lithofacies and indicated by small (2 mm, but can be as big as 10 mm) horizontal or inclined unidentified burrows and Zoophycos. The main differences between this lithofacies and the **Rip** Lithofacies are thicker sandstone beds, coarser grain-size (fine-sand), and less well defined ripple cross-laminations.

Thickness: The thickness of this lithofacies varies from a few centimetres up to 6 m.

Contacts: 1) The top is transitional to the **Rip** or to **G4** Lithofacies, the latter inferred from logs (i.e. **G3/G4** Electrofacies). 2) The basal is abrupt with **(G3/G4)** Electrofacies, and with the **FTb** Lithofacies.

Composition: subarkose/bioclastic subarkose

The rocks of this lithofacies are characterized by poorly/moderately sorted, fine/very fine sand-sized grains of quartz, feldspar, bioclasts (planktonic>benthonic foraminifera) locally up to 20%, mudclasts with siderite, heavy minerals, glauconite and carbonaceous debris. In the intervals with more bioclasts and bioturbations the calcite cementation is more intense.

Reservoir characteristics: This lithofacies has MODERATE reservoir characteristics.

Example: For comparison an example of channel-margin deposits from the Hecho Group near Ainsa, Spain, **Facies E** of **MRL**, and Mutti et al. (1985) is shown in **Plate 5.11.**

PLATE 5.11a

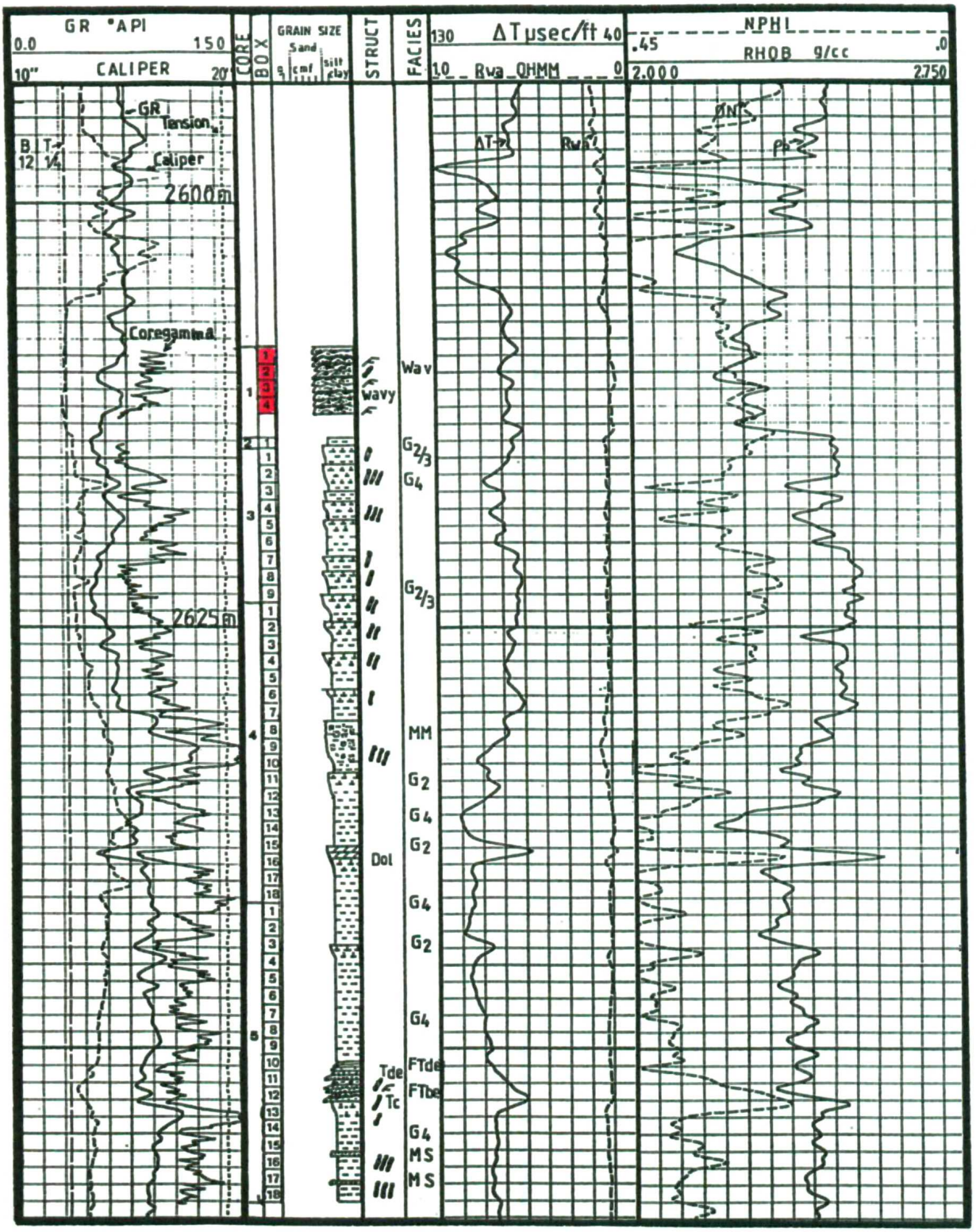
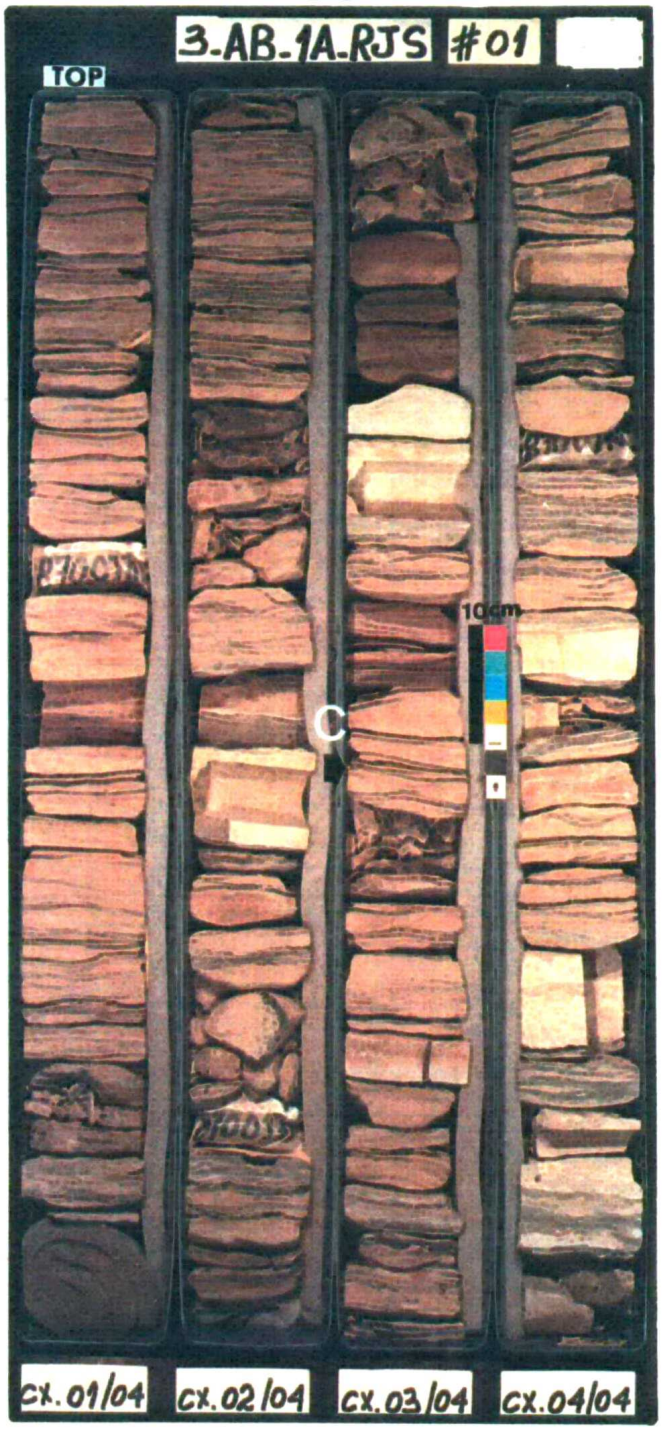


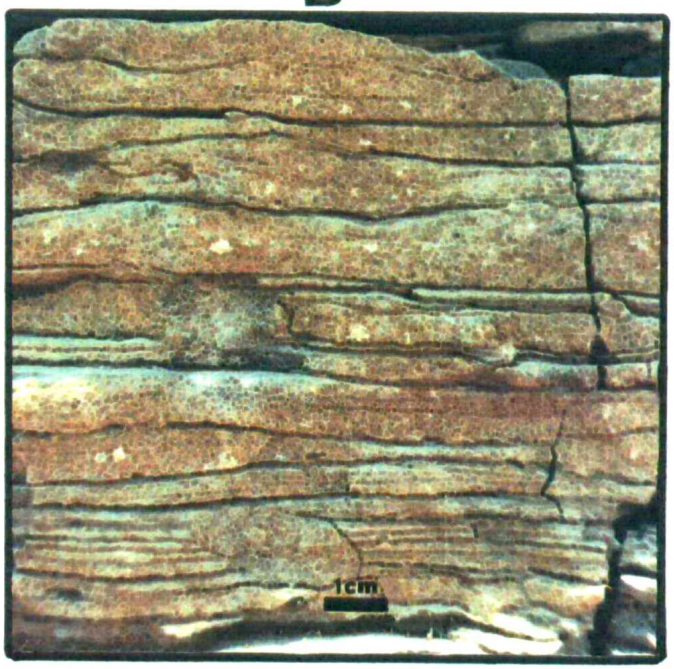
Plate 5.11 Thin-bedded Fine-Sandstone with Wavy-bedding Lithofacies Wav of Electrofacies (E). Composite log (5.11a) and its corresponding cored interval (5.11b). A similar facies of channel-margin deposits (E Facies of MRL) from the Hecho Group, near Ainsa, Spain, is shown in photo B. For comparison a close-up of the core is shown in C.

PLATE 5.11b

A



B



C



5.3.7.3 VERY THIN-BEDDED FINE/VERY FINE-SANDSTONE LITHOFACIES Rip, showing lenticular bedding with climbing-ripples and ripple-drifts.

Recognition and sedimentary structure: The rocks of this lithofacies are characterized by very thin-interbeds of very fine-grained sandstones and siltstones (heterolithic stratification). The sandstones have climbing-ripples with erosion on the stoss-side. When the sandstones have a higher sand:mud ratio, ripple-drift is the predominant sedimentary structure. The ripples have a single preferential direction of migration, but occasionally there are indications of divergent directions. Preservation of the ripple morphology is common because of the mud-drapes. Bioturbation is a common feature in this lithofacies and appears as small (1-2 mm in diameter) horizontal and inclined burrows. Locally, there are some larger (10 mm) horizontal burrows. In some places the bioturbation is pervasive and has destroyed the ripple cross-lamination.

Thickness: The thickness of this lithofacies varies from a few centimetres to 5 m.

Contacts: 1) The top is transitional to (G3/G4) Electrofacies and abrupt with **FTb** Lithofacies. 2) The base is transitional as a whole to the **FTb** Lithofacies.

Composition: subarkose/bioclastic subarkose

The rocks of this lithofacies are composed of very fine poorly/moderately sorted sand grains with the following composition: quartz, feldspars, bioclasts (benthonic ~ planktonic foraminifera = 15%, but locally in the muddy bioturbated zones up to 40%), biotite and muscovite, organic matter, and mudclasts with siderite. Locally, these sandstones can have up to 35 % calcite cement, especially in the bioturbated zones. The foraminifera assemblage is characterized by a slope (deep neritic-upper bathyal derived fauna) represented mainly by calcareous-hyaline benthonic foraminifera (Brizalina sp., Cassidulina sp. Cibicides sp., Cibicidoides tuxpamensis (Cole), Globocassidulina sp. A, Gyroidinoides sp. A, Lenticulina sp. A, Melonis ex gr. pompilioides, Hanzawaia cushmani (Nuttall), Neoeponides sp.

A, Uvigerina sp. A) and planktonic foraminifera (Globorotalia Kugleri and Globigerinoides quadrilobatus immaturus) (Azambuja Filho & Koutsoukos, 1990; in preparation).

The interbedded silty-laminae consist of a mixture of smectite-rich (90% SM) mixed-layer illite-smectite, kaolinite, illite, and abundant biotite, muscovite, carbonaceous detritus and foraminifera.

Reservoir characteristics: The rocks of this lithofacies have MODERATE TO POOR reservoir characteristics. Its quality depends on the frequency and the abundance of mud-drapes.

Examples: See **Plate 5.12.** For comparison an example of the channel-margin deposits of the Eocene Hecho Group, near Ainsa, **Facies E** of **MRL**, Mutti (1977) and Mutti et al. (1985) is also shown.

5.3.7.4 GEOPHYSICAL CHARACTERISTICS OF ELECTROFACIES (E)

5.3.7.4.1 Wireline log responses

This electrofacies is characterized by a very thin-interbeds of sandstones and mudstones, and the GR log shows a saw-tooth pattern with intermediate values between those of the sandstones and the mudstones. The density-neutron log curves show an interfingering pattern similar to that of the (FTb-e) Electrofacies but with lower neutron porosity values indicative of a more sandy lithology. The neutron log curve has a tendency to stay to the left of the density log curve. Another common feature is the existence of "spikes" in the logs as result of very thin tightly cemented intervals, which correlate with greater abundances of foraminifera.

The rocks of this electrofacies show a fining upward pattern and the microresistivity curves of the dipmeter log display a thin-interbedding. This is expressed in the tadpole plot as a general "red" pattern with low angle dips (8°-2°), but also with local "blue" patterns (see **Plate 5.10a**). The interpretation of the dipmeter log indicates that the rocks dip towards the axis of a channel (see Fig. 5.14, in **section 5.4** for more details).

PLATE 5.12a

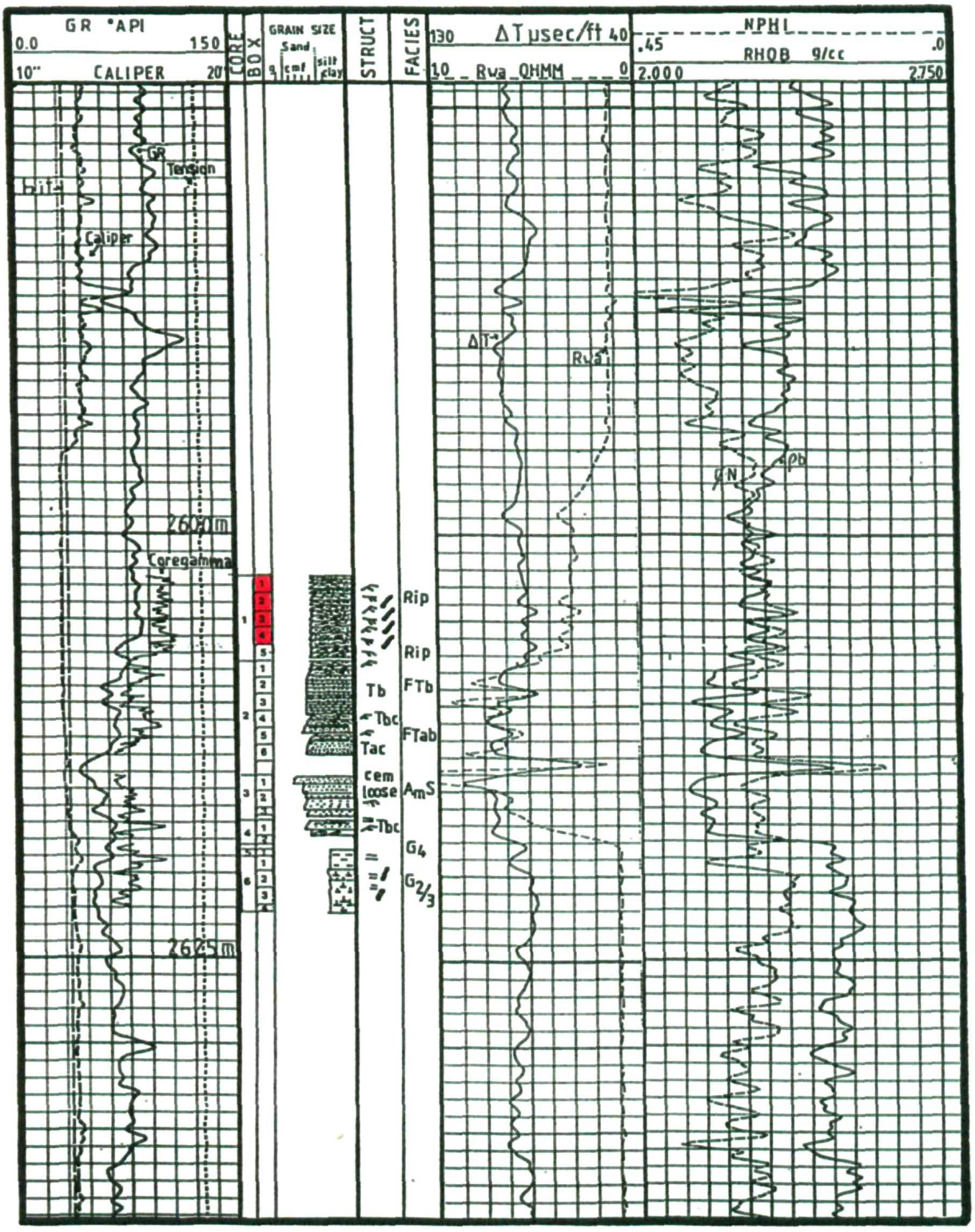
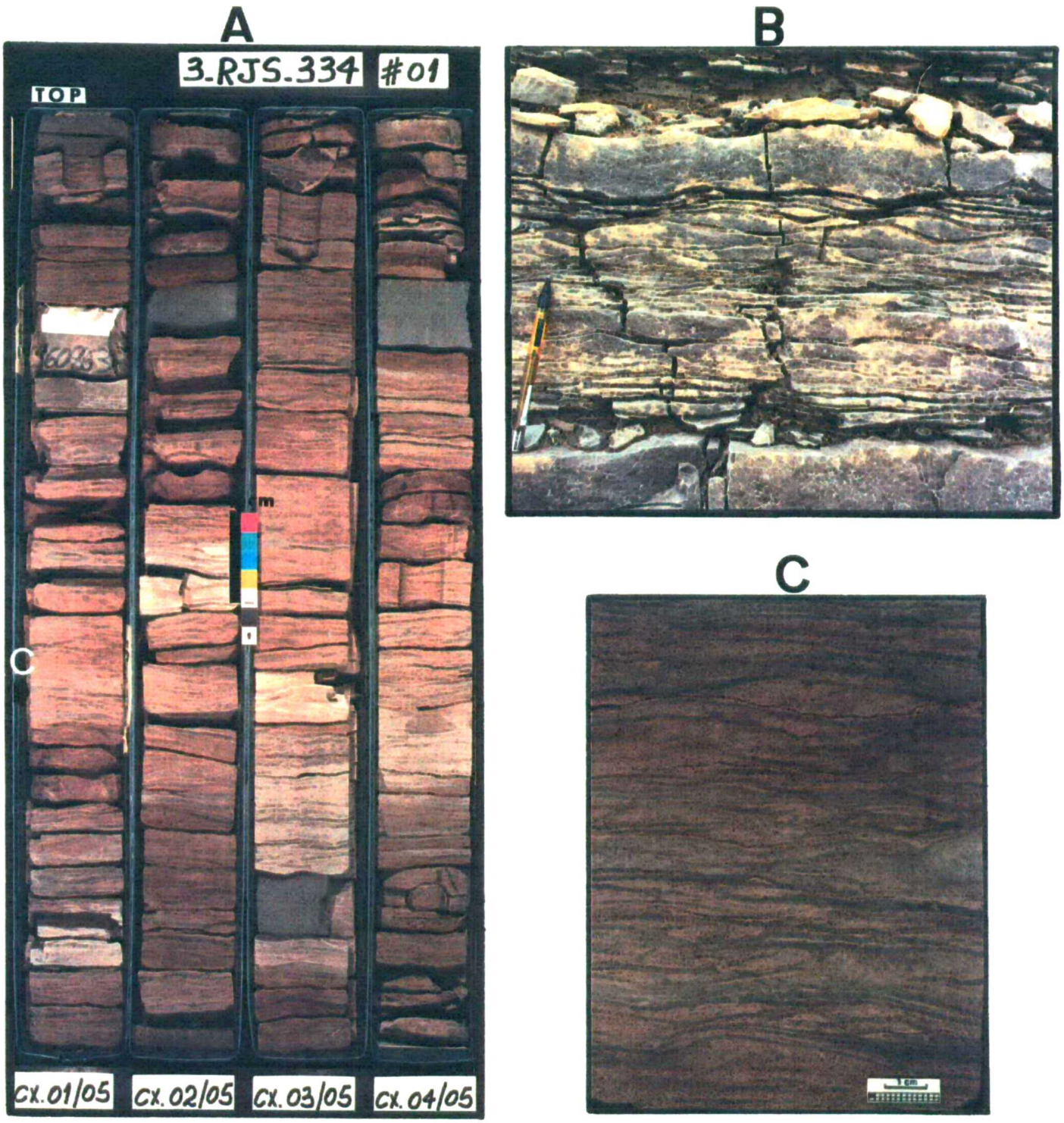


Plate 5.12 - Very thin-bedded Fine/very Fine-grained Sandstone Lithofacies Rip of Electrofacies (E). Composite log (5.12a) and its corresponding cored interval (5.12b). For comparison similar rocks of the Eocene Hecho Group that crops out near Ainsa, Facies E of MRL and Mutti et al. (1985) are shown. Compare with the close-up (photo C).

PLATE 5.12b



The rocks of this electrofacies have the following mean range wireline log values: GR = 50º-85º API (lithofacies **Fla** = SGR = 83º-87 ºAPI, CGR = 43º-45º API, Th = 4,000 ppm, Ur = 4,300-5,000 ppm, K = 15-18 %), ISF = 1.0-30 OHMS.m^2/m (transition/oil zone), SFLU = 1.0-30 OHMS.m^2/m (transition/oil zone), DELTAT = 86-123 μsec/ft, RHOB = 2.14-2.35 g/cc, ΦN = 26-33 p.u. (sandy and cemented - muddy).

5.3.7.4.2 Seismic responses

This facies does not have a visible expression on the seismic sections because of its reduced thickness.

5.3.7.5 INTERPRETATION OF THE ELECTROFACIES (E)

The rocks of this electrofacies are the result of deposition from low concentration turbidity currents with a higher proportion of traction than fall-out (Jopling and Walker, 1968) and the high frequency of mud-drapes is indicative of intermittent turbidity flows. In the rocks of this electrofacies there are some intervals that have up to 40% of benthonic and planktonic foraminifera that could be explained by segregation and concentration of these lighter grains (foraminifera chambers) in the finer fraction (very fine sand/silt-sized grains) during deposition from low concentration turbidity currents. Similar high concentrations of bioclasts were observed in thin-sections of samples from the channel-margin facies of the Hecho Group (Facies E of MRL, Mutti, 1977, and Mutti et al., 1985) near Ainsa, Spain. Concentrations of foraminifera have also have been found in "sand-waves and longitudinal bars" inside the main channel of the modern Mississippi fan (Stelting et al., 1985).

The customary association of this (E) Electrofacies with the upper part of fining upward sequences, the dips towards the sandstone body axis, their fauna and similarity with those facies observed in the channel-margin deposits of the Hecho Group, near by Ainsa, Spain (Facies E of Mutti et al., 1985), suggests that a channel-margin setting is the most likely origin for the rocks of this electrofacies.

An alternative interpretation for this electrofacies could be the winnowing by bottom currents (i.e. they are contourites) as suggested by Souza Cruz et al. (1987). Mutti et al. (1979), studying the Eocene of the Campos Basin, have interpreted the frequent absence of the top part of the Bouma sequence in the turbidites and the existence of heavily bioturbated muddy sandstones as the product of reworking of the fines by bottom currents (contourites).

The main problem in interpreting the rocks of this electrofacies as contourites is the absence of any peculiarities in the composition or fauna which could indicate a contour current deposit. The fauna found in this electrofacies is more suggestive of down-slope transport rather than from deeper regions. Additionally, the rocks of this electrofacies do not have the characteristics of contourites described by Mutti et al. (1979) and found in the Mottled Mudstone/Muddy Sandstone Electrofacies (MM/MS) (see section 5.3.11).

GROUP F

5.3.8 "CHAOTIC" ELECTROFACIES (F)

This electrofacies is composed of rocks of the "Chaotic" Lithofacies F.

5.3.8.1 "CHAOTIC" LITHOFACIES F

Recognition and sedimentary structure: The rocks of this lithofacies are characterized by silt/clay-rich sediments with contorted coherent/semi-coherent, internally dislocated, brecciated and balled and pinched strata.

Thickness: The thickness of this lithofacies varies from a few centimetres up to several meters (> 7 m).

Contacts: 1) The top is abrupt with the (G3/G4) and the (MM/MS) Electrofacies; erosional with the (AmS) Electrofacies; or transitional to the (G3/G4) Electrofacies. 2) The base is abrupt with the (FTb-e), the (MM/MS), and the (G1/G2) Electrofacies.

Composition: lithic wackestone

Prior to deformation the rocks of this lithofacies could have similar to the Mottled Mudstone Electrofacies (**MM/MS**), Mudstone Electrofacies (**G3/G4**) or Muddy Thin-bedded Sand-mud Couplet Electrofacies (**FTb-e**). When brecciated, the layers consist of a fine-grained sandy-mudstone matrix with deformed mudstone clasts of different sizes which are sometimes transitional to the Diamictite Electrofacies (**DMT**). The fossil assemblage varies according to the nature of the original sediments that have been deformed. An example of this lithofacies has middle-deep neritic foraminifera assemblage represented by calcareous-hyaline benthonic foraminifera (Brizalina sp., Cibicides, sp., Bolivina sp., and Uvigerina pergrina) and planktonic foraminifera (Globigerinoides g. primordius, Globigerinoides immaturus, Globigerina tripartita) (Azambuja Filho & Koutsoukos, 1990; in preparation).

Reservoir characteristics: The rocks of this lithofacies are not reservoir rocks.

Examples: See **Plate 5.13.**

5.3.8.2 GEOPHYSICAL CHARACTERISTICS OF THE ELECTROFACIES (F)

5.3.8.2.1 Wireline log responses

The rocks of this electrofacies are characterized in wireline logs by GR values similar to those of the Mudstone Electrofacies (**G3/G4**), but with higher density and velocity values. The tadpole plot of the dipmeter log shows a random pattern ("bag of nails") indicative of a random dip distribution compatible with the lithology observed in the cores.

The rocks of this electrofacies have the following mean range of wireline log values: GR = 70-90° API, ISF = 2.0-3.5 OHMS.m^2/m, SFLU = 2.2-5.5 OHMS.m^2/m (oil zone), DELTAT = 76-106 μsec/ft, RHOB = 2.25-2.46 g/cc, ΦN = 15-33 p.u..

PLATE 5.13a

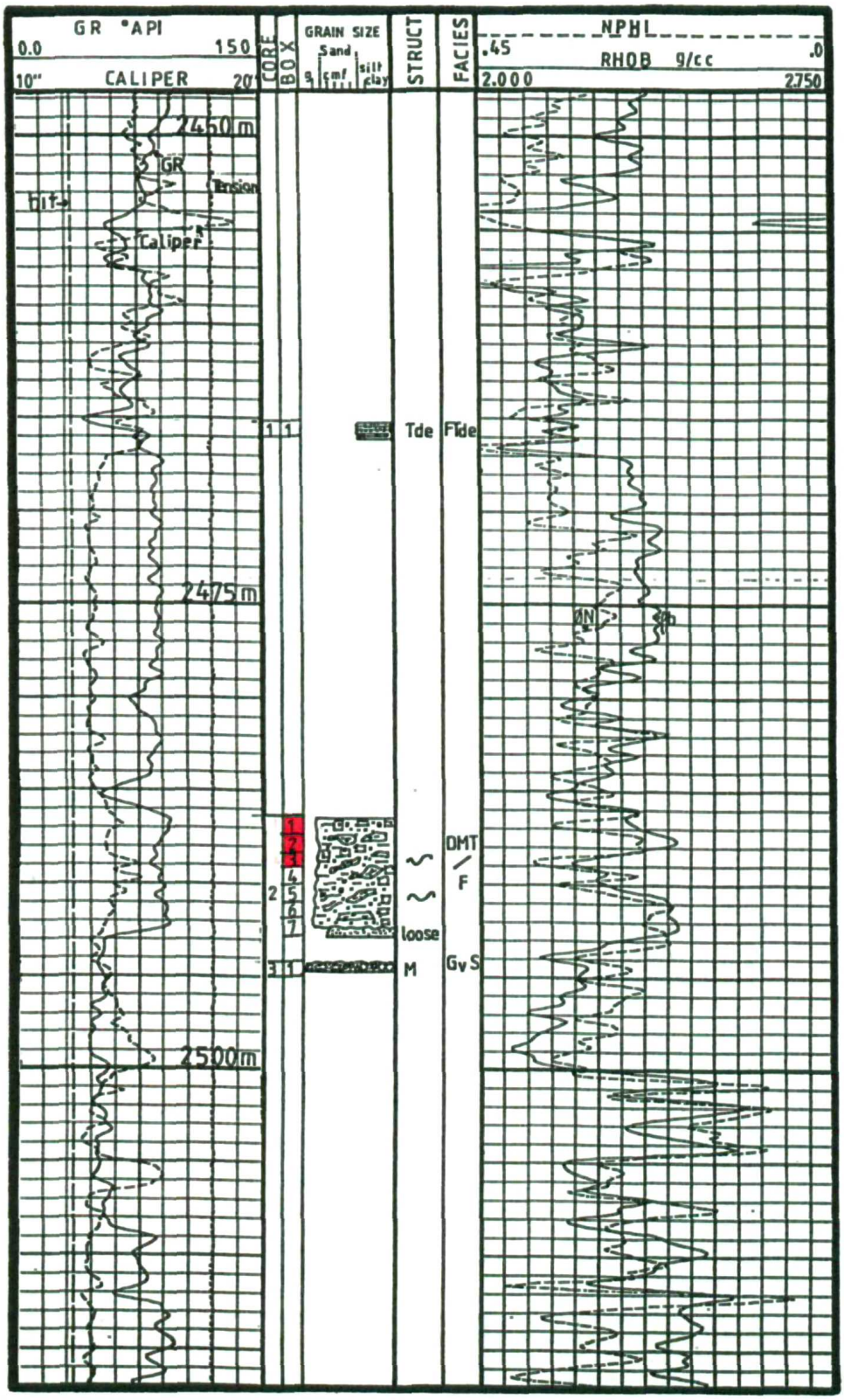
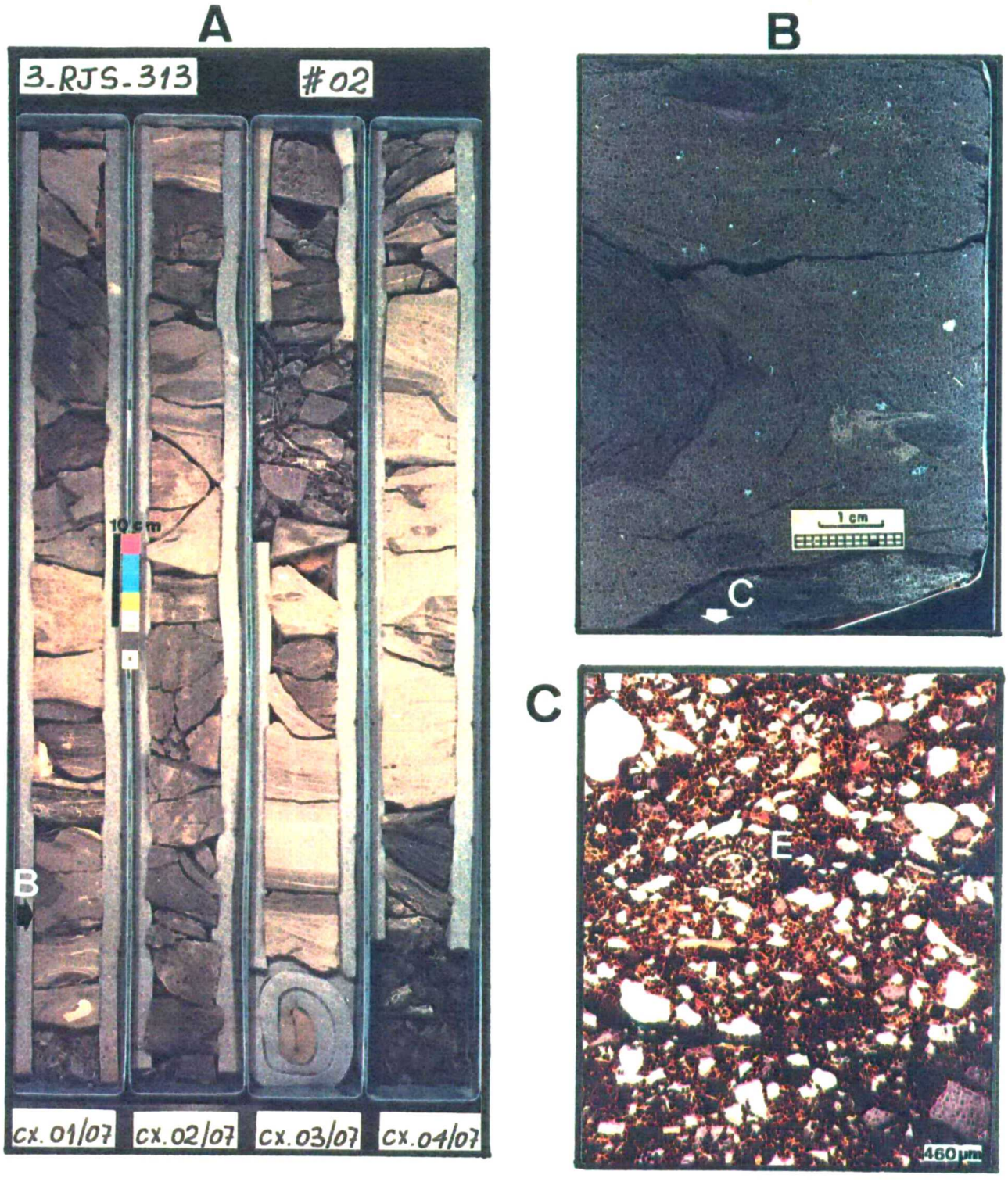


Plate 5.13 "Chaotic" Electrofacies (F). Composite log (5.13a) and its corresponding sampled interval (5.13b). Observe the brecciation features, the texture and composition of these rocks (photos **A, B, C**). Additionally, in photo **C** can be seen a spine of an echinoid (**E**).

PLATE 5.13b


A
3-RJS-313
#02
10 cm
B
cx. 01/07
cx. 02/07
cx. 03/07
cx. 04/07
B
1 cm
C
C
E
460 µm

5.3.8.2.2 Seismic responses

The rocks of this electrofacies commonly show high amplitude and relatively continuous reflectors due to the their higher density and velocity values when interbedded with mudstones (G3/G4 Electrofacies).

5.3.8.3 INTERPRETATION OF ELECTROFACIES (F)

The rocks of this electrofacies are the result of gravity-induced sliding and slumping in which the shear strength of the sediment has been exceeded, causing deformation and brecciation of strata. The formation of this facies could have taken place at any time once the instability of part of the slope or overbank deposits was reached. However, the occurrence of this electrofacies appears to be controlled by the rate of sedimentation, causing over steepening and consequently slope-instability.

The rocks of this electrofacies F are similar to the F Facies of MRL, and the Class F Facies of PCK classification.

GROUP G

5.3.9 CARBONATE MUDSTONES/MARLSTONE ELECTROFACIES (G1/G2)

This electrofacies is composed of the rocks of lithofacies G1 and G2.

5.3.9.1 CHALK/BIOGENIC CARBONATE MUDSTONE LITHOFACIES G1

Recognition and sedimentary structure: The rocks of this lithofacies are characterized by having more than 75 % calcareous biogenic material, mainly coccoliths and foraminifera, with no visible primary sedimentary structures, but often pervasively bioturbated. The most common types of trace fossils are Zoophycos, Chondrites and Planolites. There are other kinds of bioturbations but they are indistinct. The burrows vary from less than 1 mm to more than 10 mm in diameter. Bioturbation frequently causes a local increase in the amount of the siliciclastic clay content. This indicates that some burrows must have been

deep enough to have started in overlying muddy siliciclastic strata and burrowed down into the rocks of this lithofacies.

Thickness: Individual bed thickness varies from a few cm up to 1 m, and the whole interval can reach 30 m, when interbedded with the Mudstone Electrofacies (**G3/G4**).

Contacts: 1) The top is transitional to the **G2** and abrupt with the **G4** Lithofacies. 2) The base is abrupt with **G4** or with **G2** and transitional to the **G2** Lithofacies.

Composition: chalk or carbonate mudstone

The rocks of this lithofacies consist mainly of coccoliths, especially Braarudosphaera sp. (Shimabukuro et al., 1987), and some planktonic foraminifera. The abundance of foraminifera increases with the siliciclastic clay content.

Reservoir characteristics: The rocks of this lithofacies are generally not reservoir rocks. However, in one core sample (**Plate 5.14, box 2/6**) of this lithofacies there were a few open fractures with dissolution features which are oil stained. This suggests that locally fracture porosity could be significant.

Example: See **Plate 5.14.** Observe in the composite log (Plate 5.14a) the high frequency of intercalations of carbonate mudstones/marlstones and mudstones that vary from 3 to 1 per metre. The thicker ones (1 m) correspond to this **G1** Lithofacies (see corresponding **photo A** in 5.14b).

5.3.9.2 HEMIPELAGIC MARLSTONE LITHOFACIES G 2

Recognition and sedimentary structure: This lithofacies has decimeter (10-100 cm) beds containing 25 to 75% calcareous biogenic and siliciclastic clay/silt-sized material. The high foraminifera content gives a coarse silty texture to the rock. The marlstone beds show a gradual upward increase in the abundance of biogenic material and a rapid decrease in the last top few cm. The most common types of trace fossils are Zoophycos, Chondrites and Planolites. Iron sulphide filaments (mycelia) are also common. The bioturbation is intense and the burrows in the rocks of this lithofacies are better developed than in the lithofacies **G1**,

PLATE 5.14a

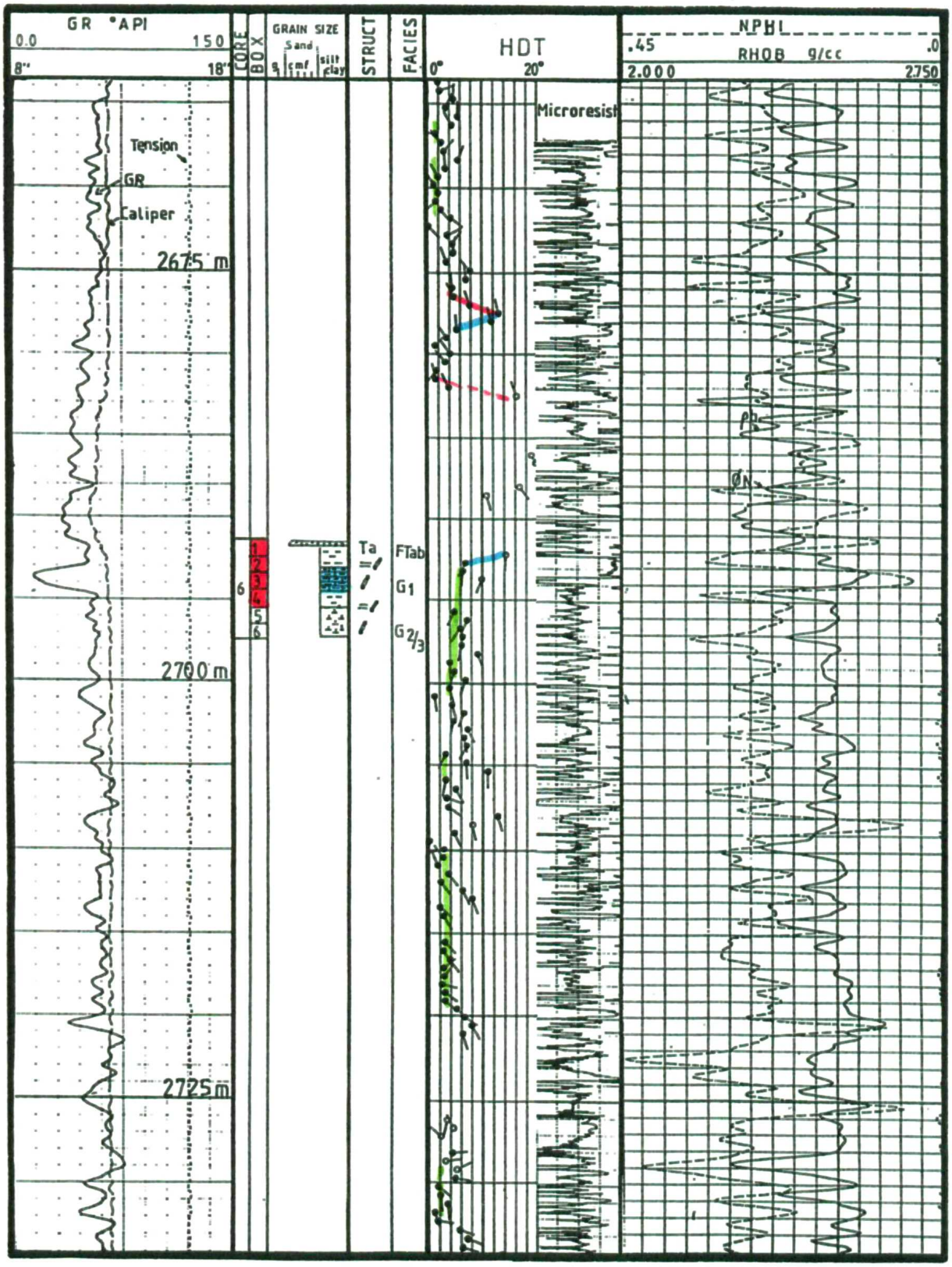
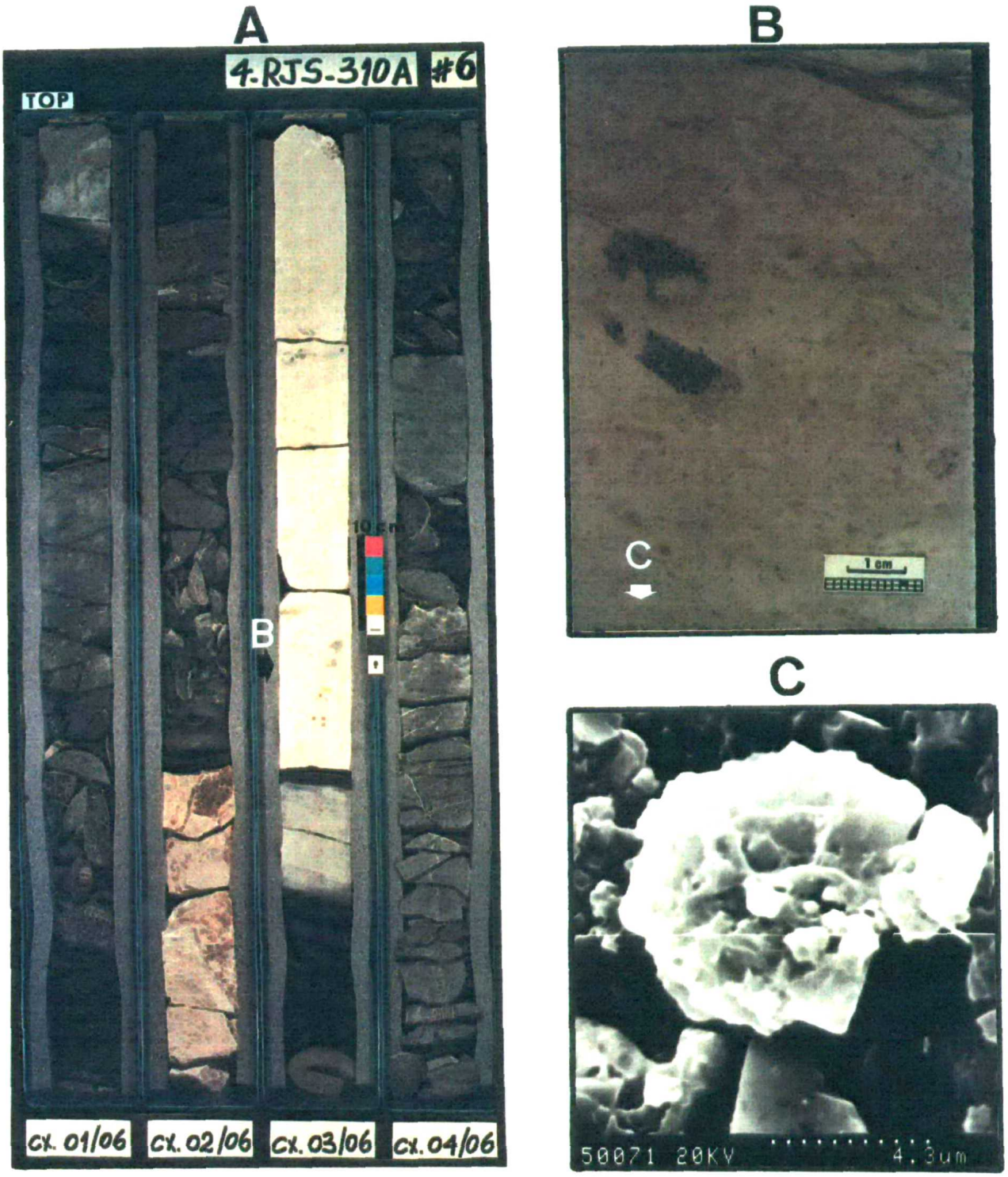


Plate 5.14 - Chalk Lithofacies G1. Composite log (5.14) and its corresponding cored interval (5.14b). Oil stained fractures can be seen in box 2/6 (photo A). The burrows are difficult to identify because of the lack of siliciclastic mud (photo B). An example of the commonly found coccolith Braarudosphaera sp. is shown in the S.E.I. photomicrograph C.

PLATE 5.14b


A
4-RJS-310A #6
TOP
B
cx. 01/06
cx. 02/06
cx. 03/06
cx. 04/06
B
C
1 cm
C
50071 20KV
4.3um

because of their higher siliciclastic clay/silt content. The bioturbation is more frequent towards the top of the beds, and together with their mud infilling this is an indication that the preserved burrows started in overlying siliciclastic muds and penetrated deep into the sediment. This confirms the observations of Wetzel (1984) that Zoophycos and Chondrites are trace fossils of deep-burrowing forms.

Thickness: The thickness of individual beds varies from 10 up to 100 cm thick, but the whole interval including the interbedded Calcareous Mudstone Lithofacies (**G3**) can be tens of meters.

Contacts: 1) The top is transitional to Chalk (**G1**) or **G3** Lithofacies; abrupt with **G4** Lithofacies or erosional with coarser electrofacies (**AmS**, **GvS** or **DMT**). 2) The base is transitional to the **G3** Lithofacies.

Composition: hemipelagic marlstone

There is a continuum from coccolith-rich carbonate mudstones with more than 75% calcareous biogenic material to the calcareous siliciclastic mudstone which has more than 10% biogenic material. The clay fraction is represented by smectite-rich (90% SM) mixed-layer illite-smectite (58%), kaolinite (19%) and illite (23%). The rocks of this lithofacies are characterized by their high abundance of foraminifera which are mainly of middle bathyal calcareous-hyaline benthonic foraminifera (Gyroidinoides ssp., Lenticulina ssp., Brizalina sp. A, Nodosaria sp. A, Cibicidoides tuxpamensis (Cole), Uvigerina sp. A, Siphonina sp. A, Gavelinella sp., Lagena sp. A), agglutinated foraminifera (Ammodiscus glabratus (Cushman & Jarvis), Ammodiscus sp., Bathysiphon ex gr. vitta, and Rhizammina ex gr. indivisa Brandy) and planktonic foraminifera (Orbulina universa, Globigerina nitida, Catapsydrax unicavus, Globigerinatheka sp. A) (Azambuja Filho & Koutsoukos, 1990; in preparation).

An important localized phenomenon associated with this lithofacies is the occurrence of dolomite. This was observed in marlstone beds interbedded with the rocks of the thick

Mudstones Lithofacies (G4). The dolomitization is the result of replacement of the microfossils by dolomite. This was most frequently found in the thick Mudstones Electrofacies (G3/G4) which normally overlie the Carbonate Mudstone/Marlstone Electrofacies (G1/G2) (see Lithofacies G4 and **Plate 5.16, photos A** and B).

Reservoir characteristics: The rocks of this lithofacies are not reservoir rocks.

Example: See **Plate 5.15.**

5.3.9.3 GEOPHYSICAL CHARACTERISTIC OF ELECTROFACIES (G1/G2)

5.3.9.3.1 Wireline log responses

This electrofacies is composed of two end members, the Chalk Lithofacies G1 and the Hemipelagic Marlstone Lithofacies G2. The Chalk (G1) beds are characterized by very low GR, and very low neutron, density and sonic porosity values. The curve of the neutron log usually crosses to the right of the density curve, while in the Hemipelagic Marlstones Lithofacies G2 it stays close but to its left side indicating a higher clay content in the G2 Lithofacies. The microresistivity curves of the dipmeter log display well defined high and low resistivity beds characteristics of the rhythmic interbedding of Carbonate Mudstone/Marlstone Electrofacies (G1/G2) and Mudstone Electrofacies (G3/G4). The tadpole plot usually shows low dip angles (~2°) characteristic of the "green" pattern (**Plate 5.14a**). An interesting feature observed in the computed plot, using local dip correlation (Schlumberger program), is the presence of dips with similar values but dipping in opposite directions, at the base and top of the more resistive beds. These dips can be interpreted as the result of wavy bedding, probably an effect of lateral differential compaction, producing a type of mega-wispy structure.

The microresistivity curves of the dipmeter logs from this electrofacies, especially in the lower part of the succession define cycles of interbedded marlstones and mudstones only a few decimeters thick (**Plate 5.14a** and

PLATE 5.15a

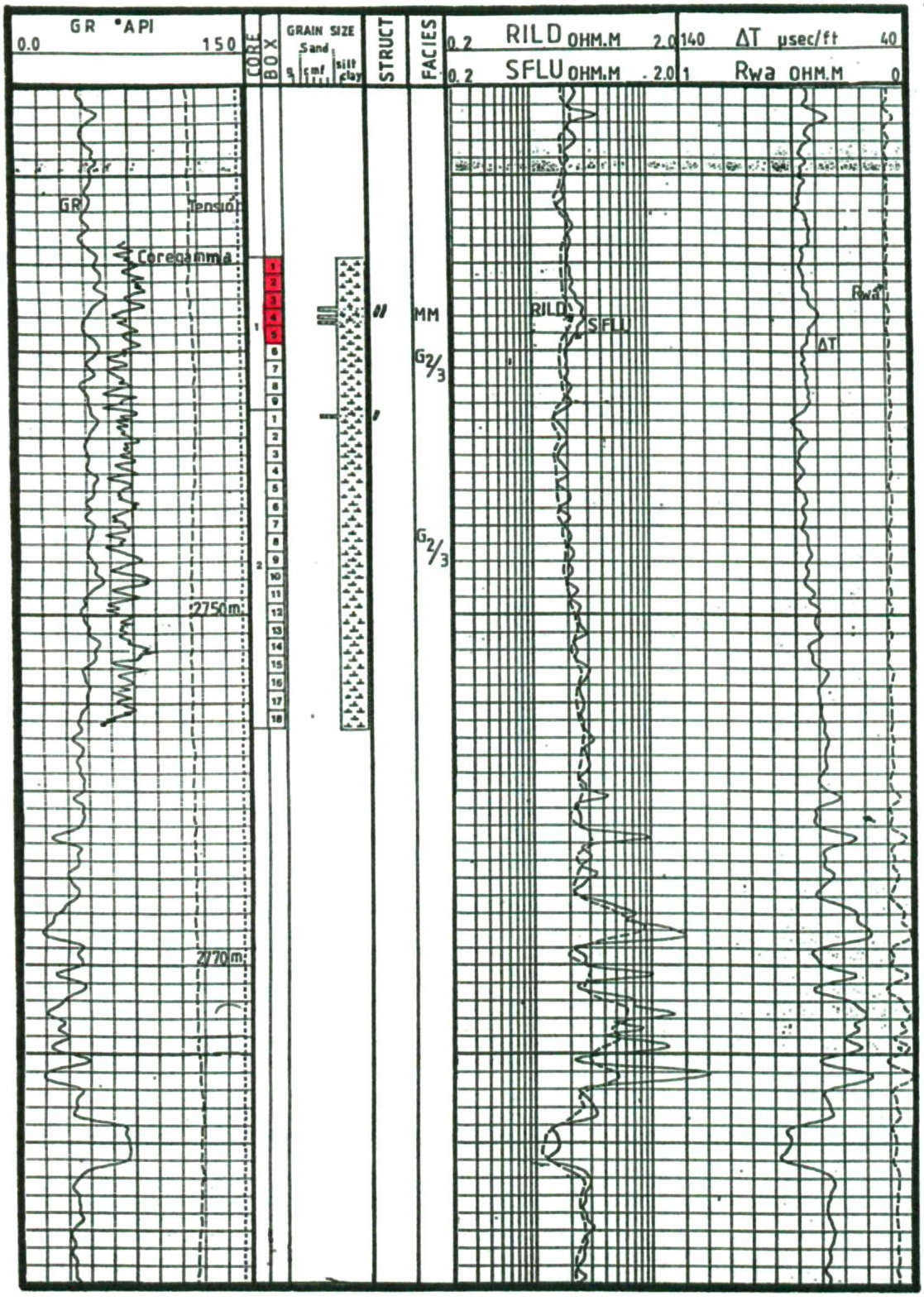
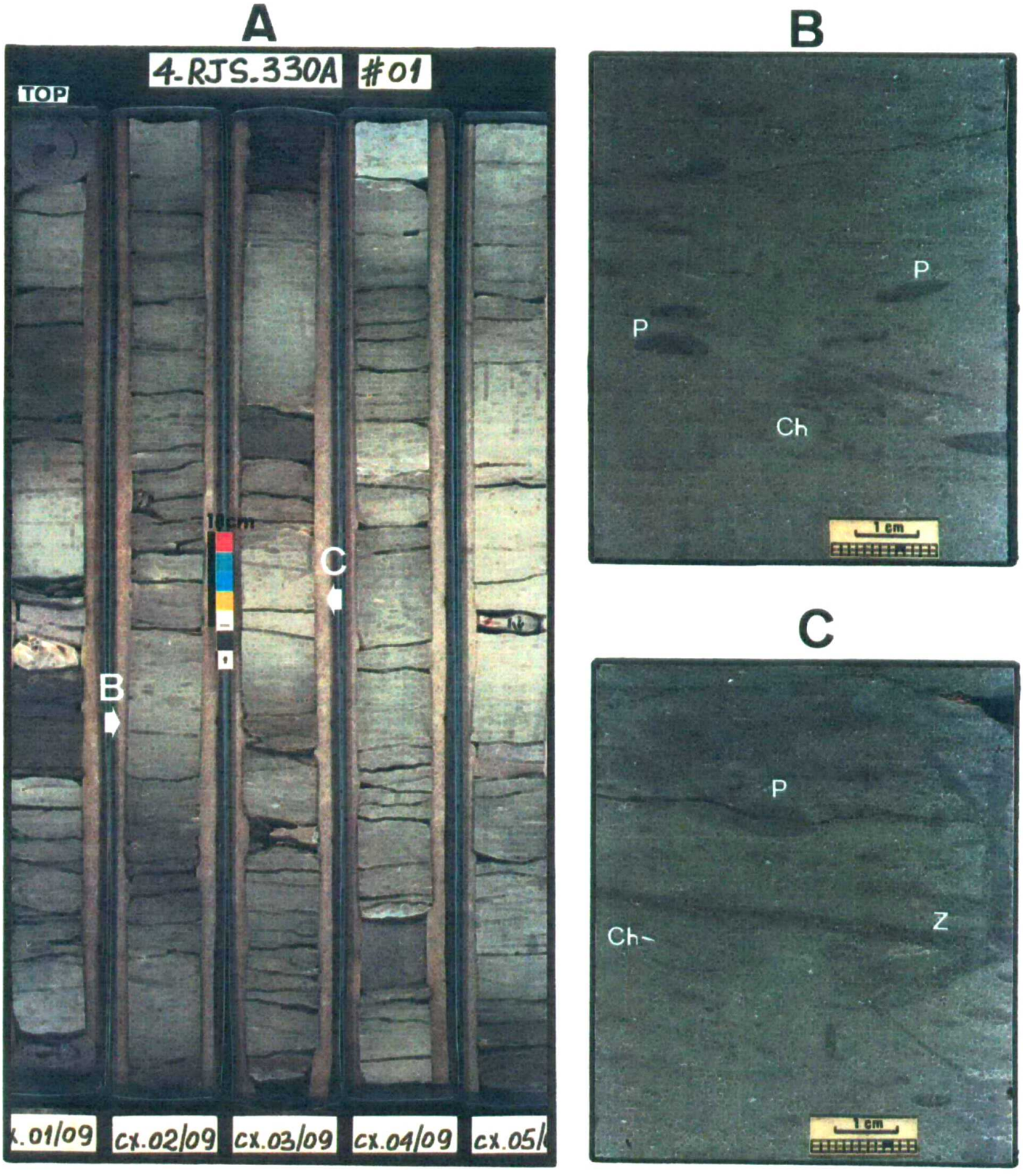


Plate 5.15 - Marlstone Lithofacies G2. Composite log (5.15) and its corresponding cored interval (5.15b). Observe the rhythmic characteristic of this lithofacies (photo **A**). Planolites (P), Chondrites (Ch) and Zoophycos (Z) are the most common observed trace fossils (photos **B** and **C**).

PLATE 5.15b


A
4-RJS-330A #01
TOP
10cm
B
C
cx.01/09
cx.02/09
cx.03/09
cx.04/09
cx.05/
B
P
P
Ch
1 cm
C
P
Ch
Z
1 cm

5.15b). The dipmeter is the only log able to differentiate this bedding, because of its 2 cm vertical resolution, whilst the other wireline logs have resolutions of only 50-60 cm. As the marlstones usually occur as 3 or 4 beds of 10-30 cm thick interbedded with very thin mudstones or vice versa, they appear from neutron-density logs to be interbedded marlstones and mudstones each about 1 m thick.

The rocks of this electrofacies have the following mean range of wireline log values:
GR = 15°-50° API, ISF = 1.3-5.0 OHMS.m^2/m, SFLU = 2.0-20.0 OHMS.m^2/m (oil zone), DELTAT = 57-100 μsec/ft, RHOB = 2.36-2.57 g/cc, ΦN = 4-27 p.u..

5.3.9.3.2 Seismic responses

The rocks of this Carbonate Mudstone/Marlstone Electrofacies (G1/G2) have a very good impedance contrast in relation the rocks of the adjacent thick Mudstone Electrofacies (G3/G4), and this produces high amplitude and continuous seismic reflectors. Based on core/wireline log/seismic correlations it is possible to show that the rocks of the (G1/G2) Electrofacies are the source of the regional reflector present in the Lower Oligocene succession of the Campos Basin (the "Blue Marker" of Gamboa et al., 1986). This reflector represents an interval with a general low rate of sediment accumulation and a low siliciclastic input, producing a 30 m interval of predominantly chalk beds overlying an interval dominated by the Mudstone Electrofacies (G3/G4) which has very low density and sonic velocity.

The rocks of this electrofacies correspond to the G Facies of MRL, whilst the Chalk or Carbonate Mudstone Lithofacies (G1) and the Hemipelagic Marlstones Lithofacies (G2) correspond respectively to the G1.1 and G1.2 Facies of the PCK classification.

5.3.9.4 INTERPRETATION OF THE ELECTROFACIES (G1/G2)

The rocks of this electrofacies are the result of a slow deposition (i.e. 1 mm to 3 cm/Kyr, Stow & Piper, 1984) of nanoplankton, foraminifera and terrigenous material by vertical settling, with some contribution from terrestrial run-off and some bottom-water currents. The calculated average rate of deposition for the sediments of this facies during the Oligocene is around 1.5 cm/Kyr (undecompacted, see **Chapter 6**). Similar figures (2-3 cm/Kyr uncompacted) were reported by Wetzel (1984) for the modern abyssal plain of NW African continental margin. This indicates that this facies had a low sedimentation rate and characterized a period when the Campos Basin in the study area was starved of siliciclastic sediments, during non turbiditic intervals.

5.3.10 MUDSTONE ELECTROFACIES (G3/G4)

This electrofacies is composed of rocks of the lithofacies **G3** and **G4**.

5.3.10.1 CALCAREOUS MUDSTONE LITHOFACIES G 3

Recognition and sedimentary structure: The rocks of this lithofacies consist of a calcareous mudstone with abundant foraminifera. When compared with the lithofacies **G1** and **G2** they differ in their higher mud content and darker colour. Bioturbation is not very well developed as in the rocks of the Hemipelagic Marlstones Lithofacies (**G2**) but can be locally important, in the form of indistinct small subhorizontal burrows, Planolites, Chondrites and Zoophycos.

Thickness: The average individual bed thickness is around 15 cm but the whole interval including the Carbonate Mudstone/Marlstone Electrofacies (**G1/G2**) can be several metres thick.

Contacts: The top is transitional to the (**G1/G2**) Electrofacies; abrupt to the **G4** Lithofacies; and erosional with coarser-grained (**AmS**), (**GvS**), (**DMT**) Electrofacies. The base is transitional to the **G2** or **G4** Lithofacies.

Composition: calcareous siliciclastic mudstone

The rocks of this lithofacies consist of siliciclastic

clay and silt-sized mica (biotite and muscovite) with up to 25-30% planktonic and benthonic foraminifera whose chambers vary from less than 88 μm up to 350 μm. The clay fraction is represented by smectite-rich (90%) mixed-layer illite-smectite (53%), kaolinite (24%) and illite (23%). Pyrite is commonly found inside the fossils chambers or in the matrix. The quartz grains are silt-sized and make up less than 10% of the total rock. The matrix is rich in coccoliths but proportionally less than in the Carbonate Mudstone/Marlstone Electrofacies (**G1/G2**).

Reservoir characteristics: The rocks of this lithofacies are not reservoir rocks.

Examples: The rocks of this lithofacies can be distinguished from those of the Marlstone Lithofacies (**G2**) by its darker colour and higher percentage of siliciclastic mud (**Plate 5.15**).

5.3.10.2 SILICICLASTIC MUDSTONES LITHOFACIES G 4

Recognition sedimentary structure: The rocks of this lithofacies are composed of dark grey-green structureless muds without significant planktonic or other biogenic material. Usually this mudstone starts to split apart spontaneously in the cores forming small clay chips. Bioturbation is not a common feature and when present is represented by indistinct small subhorizontal burrows.

Thickness: The rocks of this lithofacies vary in thickness from a few decimeters up to >4 m (**Plate 5.2a**), but is usually about 2 m thick. In some cases there are intervals up to 30 m thick dominated by this lithofacies.

Contacts: 1) The top is transitional to the **G3** Lithofacies; abrupt with the coarser-grained (**GvS, AmS, DMT**) Electrofacies or with the (**MM/MS**) Electrofacies. 2) The base is transitional to **G3, FTde, Rip** Lithofacies and abrupt with **G2, F** Lithofacies.

Composition: The rocks of this lithofacies are composed of clay minerals, mica (biotite and muscovite), microfossils (coccoliths and foraminifera) and organic matter. The clay grade fraction contains relatively large (53%) amounts of

smectite-rich (90% SM) mixed-layer illite-smectite, kaolinite (24%) and illite (23%). The siliciclastic silt-sized grains consist of quartz and feldspar and some heavy minerals. Frequently when thick (~1 m) marlstone intervals are interbedded with very thick (~4 m) siliciclastic mudstones, the marlstones are dolomitized (**Plate 5.16b**, photomicrograph **B**). In the siliciclastic mudstones only rare rhombs of dolomite were found (Plate 5.16b, photomicrograph **C**; for more details of this type of dolomitization see **Chapter 8**).

The rocks of this lithofacies contain upper to middle bathyal calcareous-hyaline benthonic foraminifera (Gyroidina sp. A and G. ssp., Dentalina sp. A, Pseudonodosaria obesa and P. sp. A, Bulimina espinata and B. sp. A, Cibicidoides sp. A, Uvigerina "spinosa", Stilostomella lepidula, Oridorsalis umbonatus, Melonis pompilioides), agglutinated foraminifera (Ammodiscus glabratus (Cushman & Jarvis), Ammodiscus sp. A and Rhizammina indivisa Brandy) and planktonic foraminifera (Globigerinoides g. primordius, Globigerina tripartita, Catapsydrax stainforthi, Globigerina venezuelana, Globorotalia kugleri and Catapsydrax dissimilis) (Azambuja Filho & Koutsoukos, 1990; in preparation).

Reservoir characteristics: The rocks of this lithofacies are not reservoir rocks.

Example: See **Plate 5.16.**

5.3.10.3 GEOPHYSICAL CHARACTERISTICS OF THE ELECTROFACIES (G3/G4)

5.3.10.3.1 Wireline log responses

The rocks of this electrofacies are easily recognized by their relatively high GR, very high neutron, density and sonic porosities. The microresistivity curves of the dipmeter log display a typical pattern that can be easily identified by its very high frequency of oscillations, contrasting with the low frequency and almost constant values of the cyclic interbedded Marlstones (G2). This pattern is very well illustrated in the composite log

PLATE 5.16a

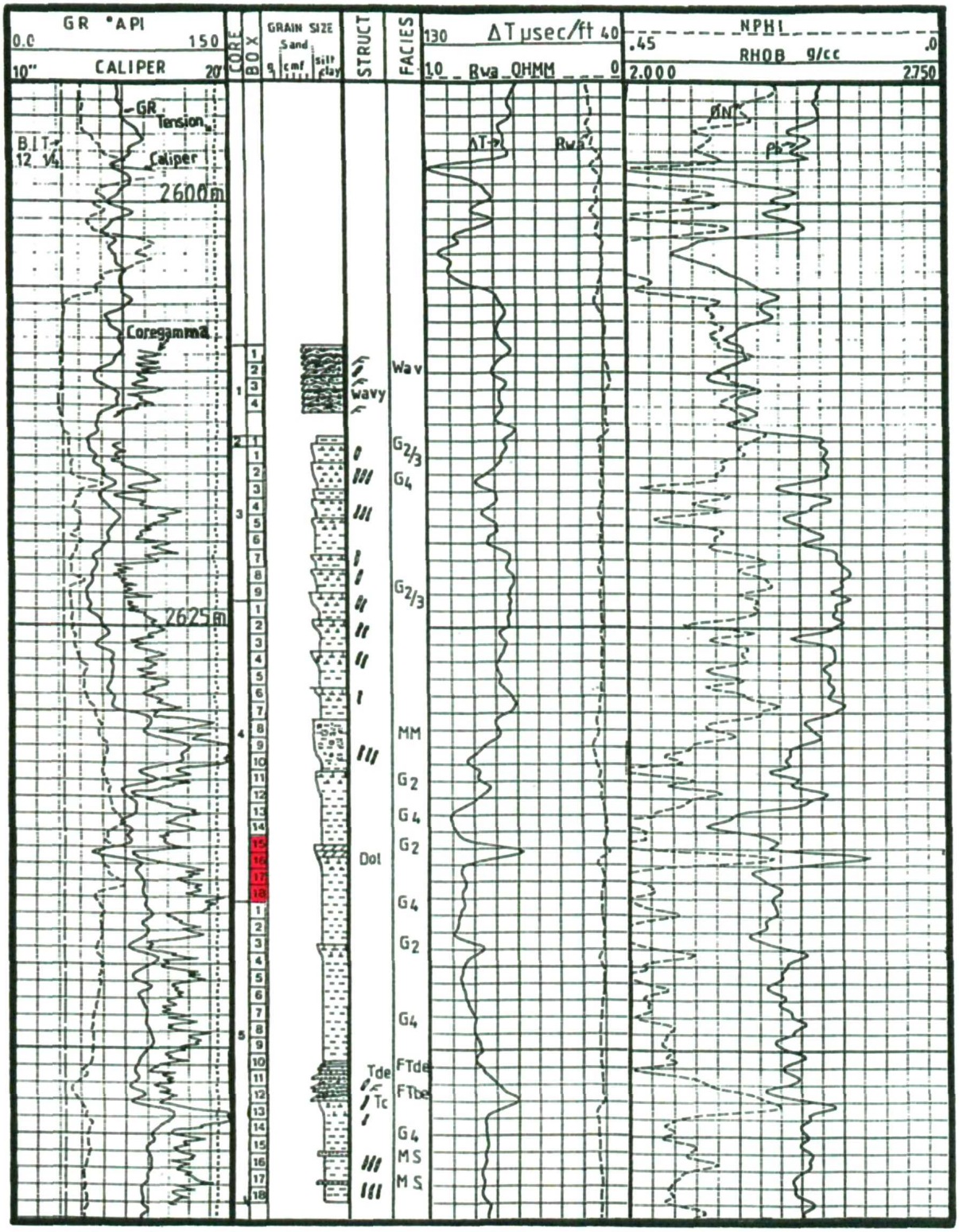
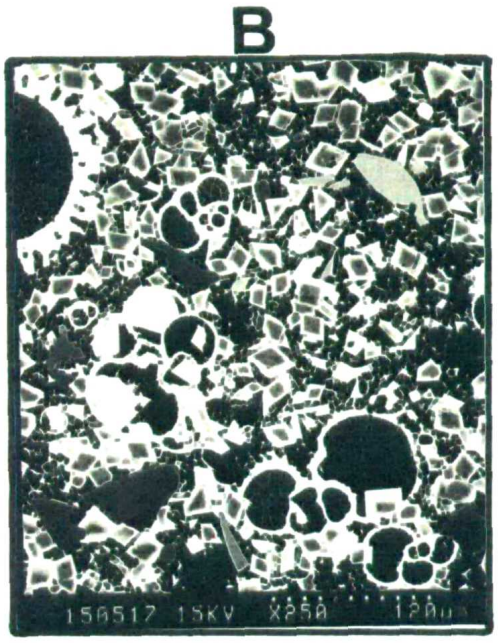


Plate 5.16 - Siliciclastic Mudstones Lithofacies G4. Composite log (5.16a) and corresponding cored interval (5.16b). Darker grey/black colour, very high porosity and characteristic clay chips in core samples. Compare the differences in the composition of dolomitized marlstones (G2 Lithofacies) with the one of this lithofacies, respectively shown in the S.E.M (B.S.I.) photomicrographs B and C.

PLATE 5.16b







(**plates 5.2a** and **5.8a**). The corresponding tadpole plot displays low dip angles characteristics of the "green" pattern representing the local structural dip (**Plate 5.8a**).

The rocks of this electrofacies have the following range of wireline log values: GR = 65-85° API, ISF = 0.8-2.0 OHMS.m^2/m, SFLU = 1.0 -2.4 OHMS.m^2/m, DELTAT = 90-120 μsec/ft, RHOB = 2.28-2.45 g/cc, ΦN = 27-45 p.u..

5.3.10.3.2 Seismic responses

The rocks of this electrofacies are of great importance in seismic sections due to their relatively very low sonic velocity and very low density values, and its association with the Carbonate Mudstone/Marlstone Electrofacies (**G1/G2**) (see **section 5.3.9.3.2**).

5.3.10.4. INTERPRETATION OF THE ELECTROFACIES (G3/G4)

This electrofacies consists of two end member mudstones: one is thinner and richer in calcareous microfossils (**G3**) and the other is thicker and with less biogenic material (**G4**). The thinner calcareous mudstones (**G3**) represent the relative slow accumulation of foraminifera and coccoliths and mud-grade siliciclastic material by vertical settling, with substantial contribution from run-off and probably some lateral transfer by weak mid- and bottom-water currents. The thicker mudstones, **G4** Lithofacies, are the result of relatively more rapid deposition of clay and silt-sized grains from low density mud-dominated turbidity currents.

The rocks of this electrofacies are comparable to the G Facies of **MRL**. The Calcareous Mudstone Lithofacies (**G3**) and the Siliciclastic Mudstones (**G4**) correspond respectively to the G2.1 and E1.1 Facies of the **PCK** classification.

GROUP H

5.3.11 MOTTLED MUDSTONE/SANDSTONE ELECTROFACIES (MM/MS)

This electrofacies is composed of rocks of the lithofacies **MM** and **MS** and represent a continuum between a muddy and sandy mottled lithologies.

5.3.11.1 MOTTLED MUDSTONE/MUDDY SANDSTONE (MEDIUM/THICK-BEDDED) LITHOFACIES MM/MS

Recognition and sedimentary structure: There are variable thickness intervals characterized by mudstones or muddy sandstones with pervasive (mottled) bioturbation. The bioturbation has produced sandy siliciclastic mudstones or a muddy sandstones and destroyed any other primary sedimentary structure. Only locally is it still possible to identify a faint irregular lamination. The thin bioturbated sandstone beds (~5-10 cm thick) found in the middle of thick sequences of hemipelagic marlstones have some ripple cross-laminations, but generally obscured by the bioturbation and intensive cementation.

The most commonly identified trace fossils in the rocks of this lithofacies were Chondrites, Zoophycos, Planolites and possibly some Teichichnus and Scolicia.

Thickness: The thickness of this electrofacies varies from a few centimetres up to several metres (~ 50 m).

Contacts: The top is transitional the **(G3/G4)** Electrofacies and abrupt to the **G2** Lithofacies. The base is transitional/abrupt with the **(G3/G4)** Electrofacies, and erosional with the **G2** Lithofacies.

Composition: bioclastic arkosic/subarkosic wackestone.

There are two main types of sandstone composition: 1) muddy mottled sandstone characterized by a very poorly sorted mixture of siliciclastic very-fine sand/silt-sized grains (quartz, feldspar and heavy minerals) and calcareous bioclasts (foraminifera) concentrated in clusters and distributed in the clay matrix; 2) fine/very fine-sandstones with anomalous amounts of heavy minerals (see B.E.I. photomicrograph **C** in the **Plate 5.19**) cemented by chert and a later calcite (see **Plate 9.7** in the **Chapter 9**).

The composition of the clay-grade fractions of the mottled siltstones is kaolinite (34%), illite (24%) and smectite-rich (90% SM) mixed-layer illite-smectite (42%). The relatively higher percentage of kaolinite is partially diagenetic (see **Chapter 8**). Biotite, muscovite and organic matter (type III in the Tissot et al., 1974, classification)

are also common constituents.

The fauna found in the mottled mudstones are characterized by a deep neritic/middle bathyal calcareous-hyaline benthonic foraminifera assemblage (Eponides sp., Gyroidina sp. A, G. ssp., Lenticulina sp. A, Nonionellina sp., Dentalina sp. A, Pseudonodosaria obesa, P. sp. A, Uvigerina sp., Bulimina espinata, B. sp. A, Gyroidinoides sp., Valvulinella sp.), and planktonic foraminifera (Globigerinoides g. primordius, Globigerinoides immaturus and Globorotalia sp.) (Azambuja Filho & Koutsoukos, 1990; in preparation).

An interesting feature is the coincidence of anomalous GR values (102°API) and relatively high total organic carbon content (TOC) of 1.7 weight% plus the absence of calcareous microfossils and only the presence of agglutinated foraminifera in an interval from well 316 (photo C in the **Plate 5.18b**). These fauna represent a low oxygen tolerant assemblage characteristic of upper/middle bathyal environments: Trochammina globigerinifomis (Parker & Jones) and Recurvoides ex. gr. deflexiformis (North) (Azambuja Filho & Koutsoukos, 1990; in preparation).

Reservoir characteristics: The rocks of this electrofacies either are not reservoir rocks or they only have very poor reservoir properties.

Examples: In **Plates 5.17, 5.18** and **5.19** are shown examples of: 1) relatively thick (>4 m) and; 2) thin (~1 m) mottled silty-sandy siliciclastic intervals; and 3) thin cemented sandstones. An example of mottled siltstones/muddy sandstones from an interval about 50 m thick, generally coarsening upwards and with a sharp top is shown in **Plate 5.17**. This interval is composed of smaller units about 1-2 m thick and they resemble the model (shown in 5.17b) of a "typical" arrangement of contourite facies with negatively to positively graded couplets (Stow & Piper, 1984; Gonthier et al., 1984). Additionally, can be seen that some of these mottled intervals have high GR values (**Plate 5.18a**) and that the burrows have been infilled with sand-sized grains and later cemented by calcite (**Plate 5.18b**, photos B and C).

PLATE 5.17a

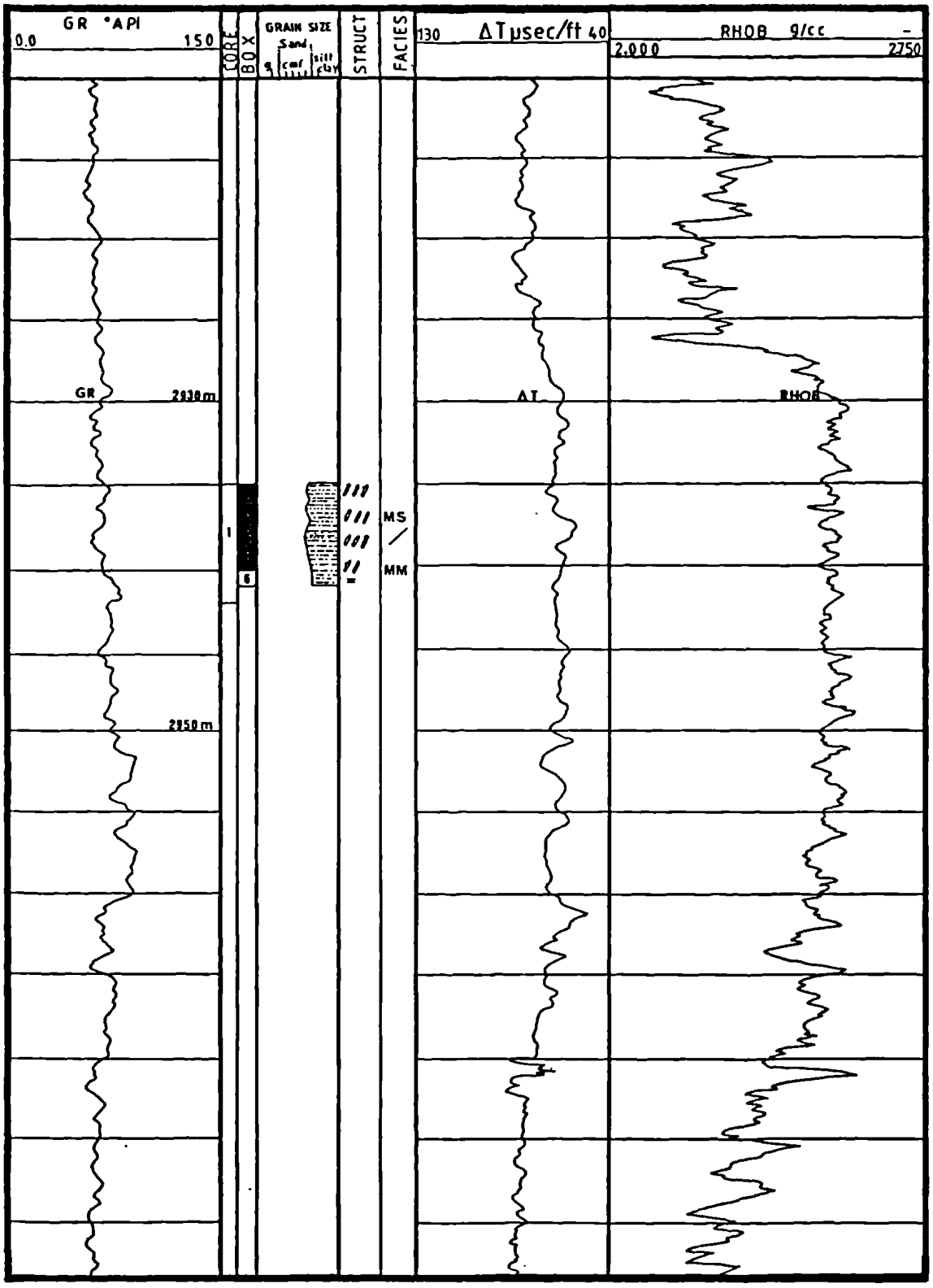
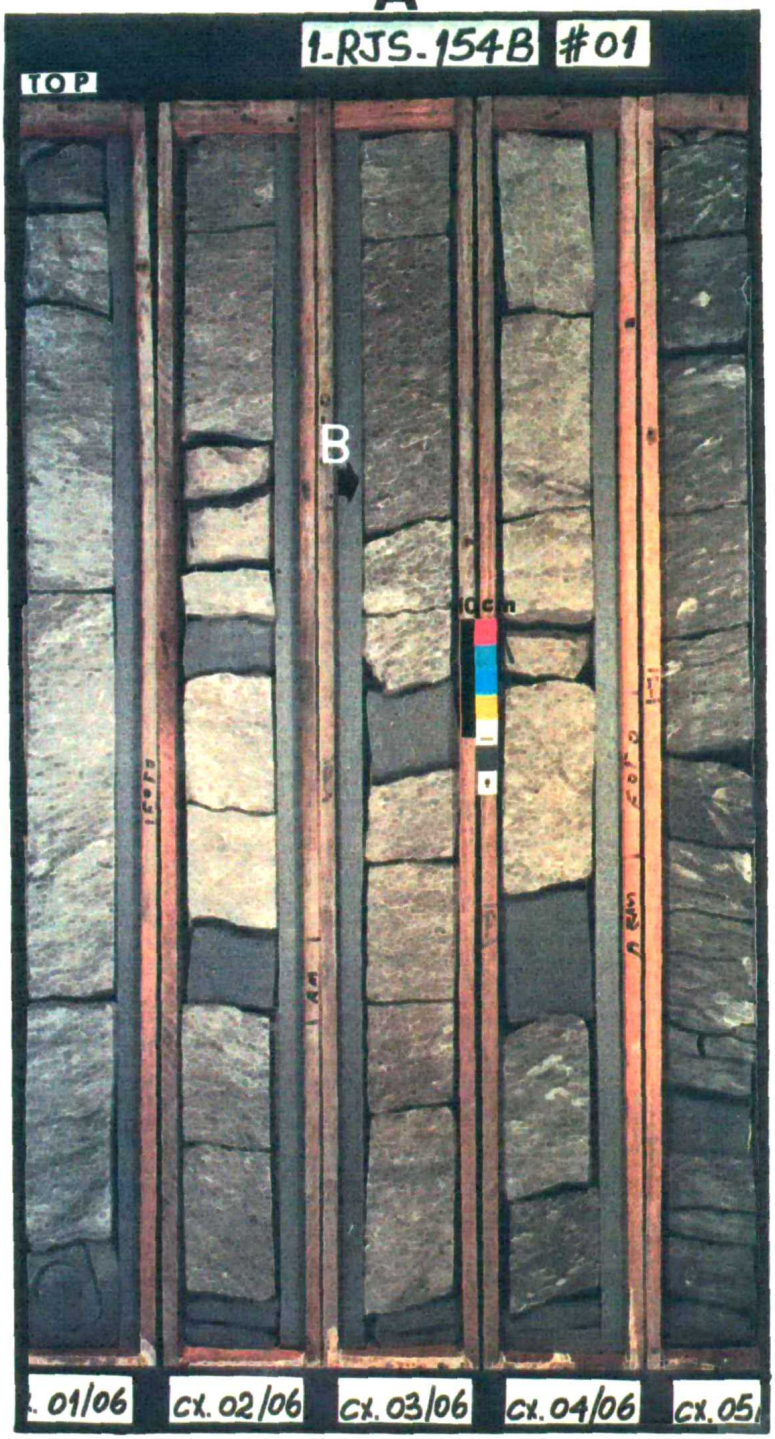


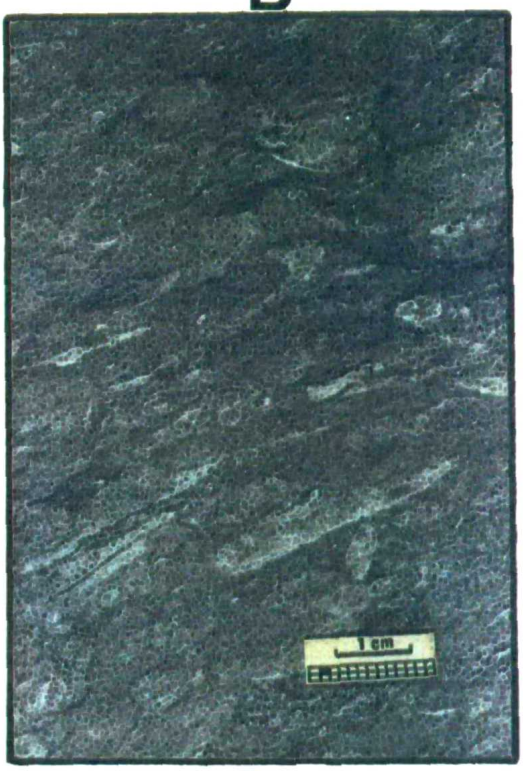
Plate 5.17 Mottled Mudstones Electrofacies (MM/MS). Composite log (5.17a) and corresponding cored interval (5.17b). A "typical" arrangement of contourite facies in Plate 5.17b, C (from Stow and Piper, 1984; after Gonthier et al., 1984) is also shown for comparison.

PLATE 5.17b

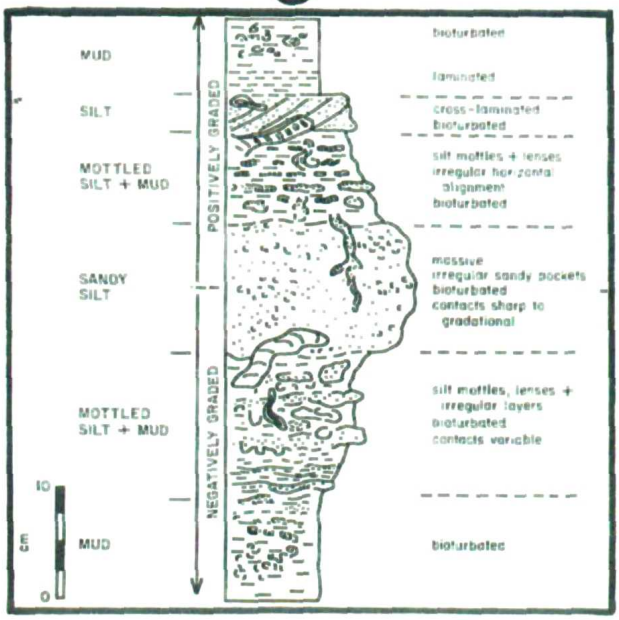
A



B



C



Typical arrangement of contourite facies (from Stow and Piper, 1984, after Gonthier et al. 1984)

PLATE 5.18a

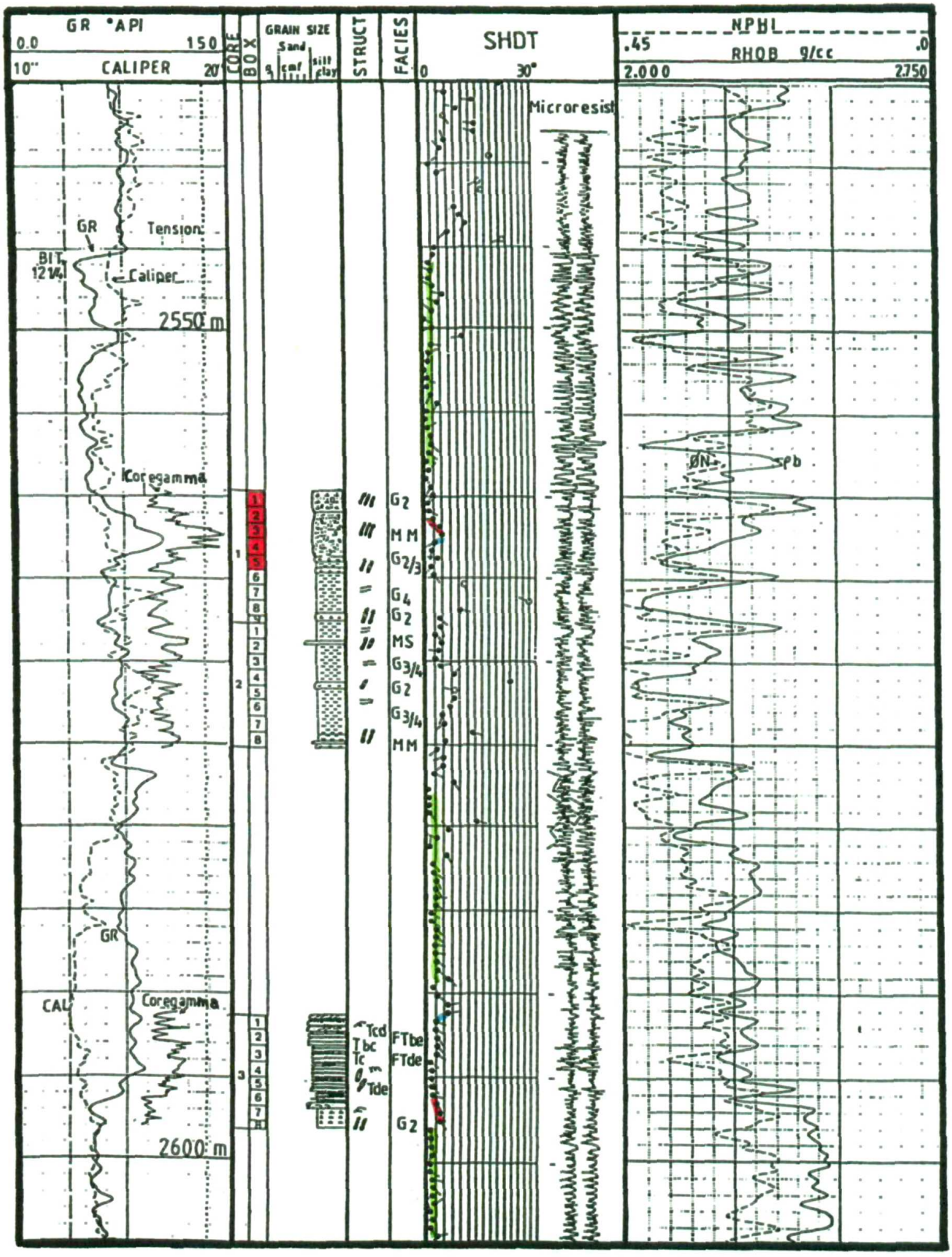
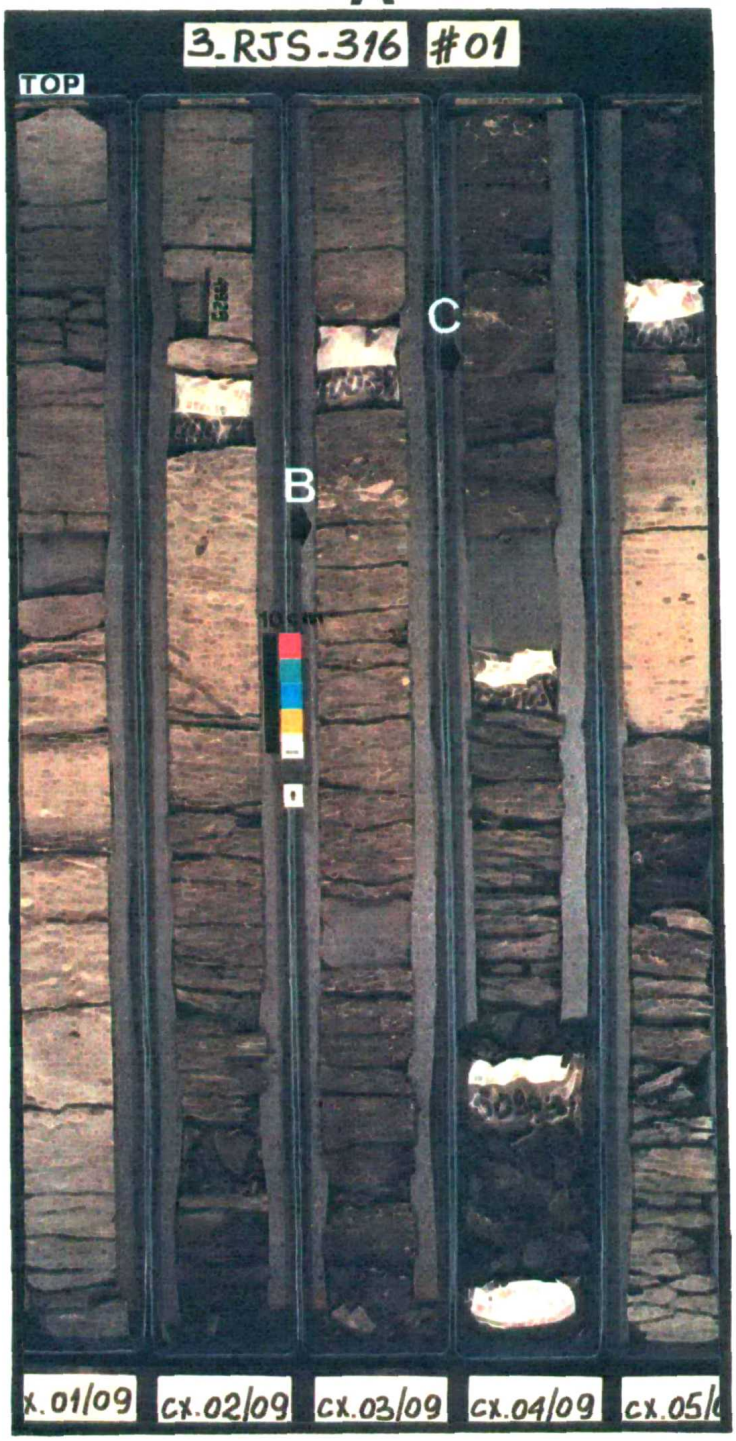


Plate 5.18 - Mottled Mudstone Electrofacies (MM/MS). Composite log (5.18a) and corresponding cored interval (5.18b). Close-ups B and C show burrows infilled with sand-sized grains and cemented by calcite, lighter areas.

PLATE 5.18b

A



B



C



PLATE 5.19a

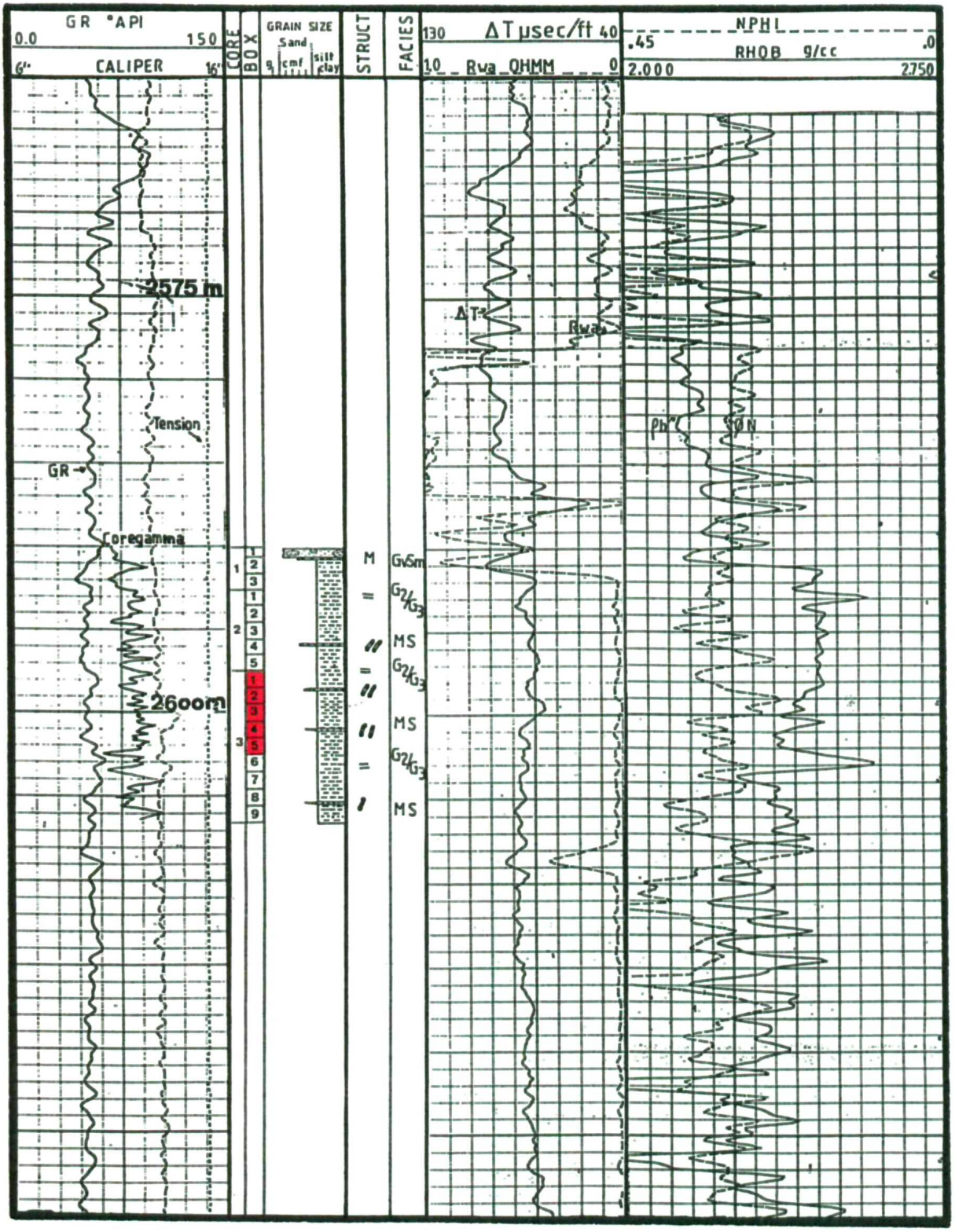
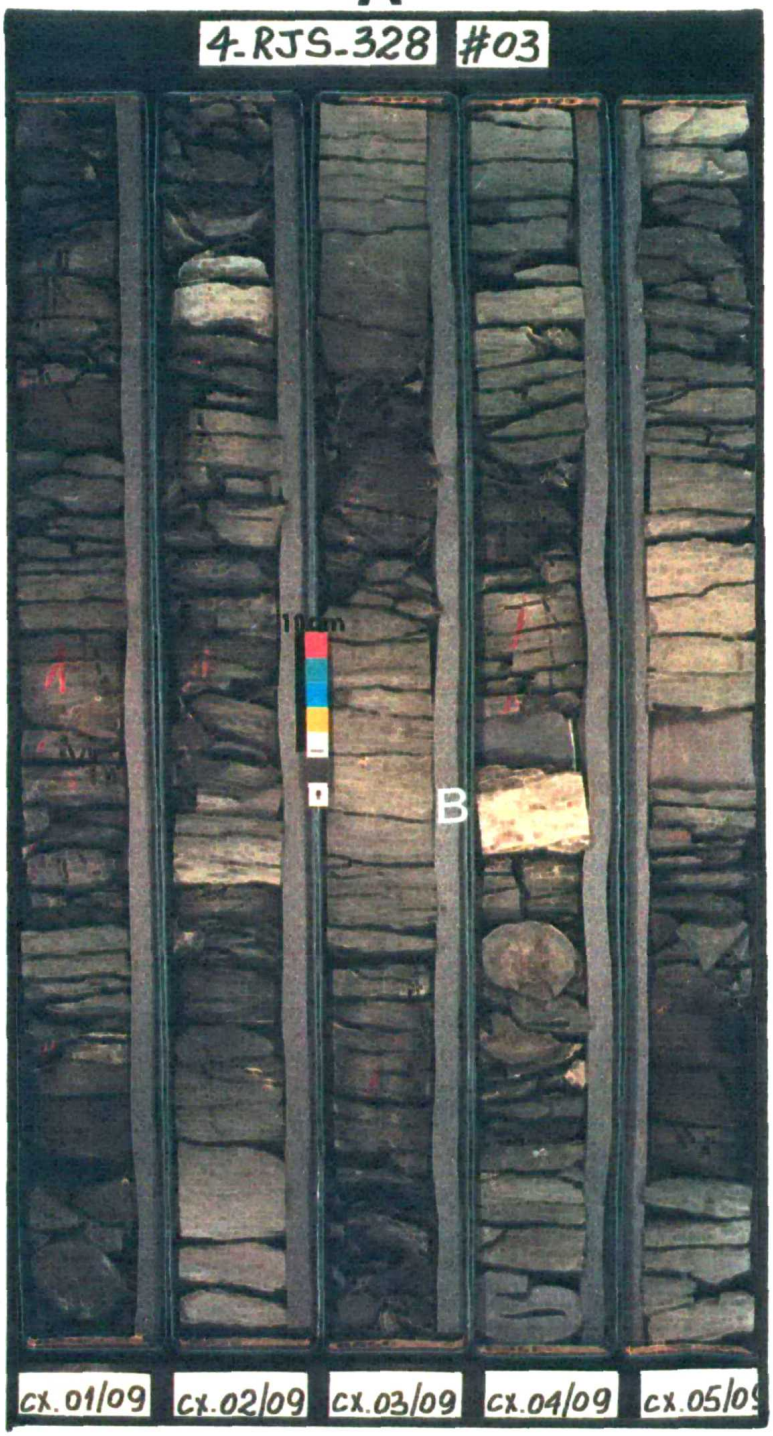


Plate 5.19 Mottled Sandstone Lithofacies MS of the (MM/MS) Electrofacies. Composite log (5.19a) and corresponding cored interval (5.19b). The B.S.I. photomicrograph (C) shows the high amounts of heavy minerals (brighter grains).

PLATE 5.19b

A



B



C



5.3.11.2 GEOPHYSICAL CHARACTERISTICS OF THE ELECTROFACIES (MM/MS)

5.3.11.2.1 Wireline log responses

The rocks of this electrofacies are characterized by high to very high GR values in the more muddy intervals and medium to high in sandier intervals. The local very high GR values reflect high uranium contents associated with relatively higher organic carbon contents (~1.5 weight% of TOC). These features support the interpretation that these intervals with very high GR values represent more reducing depositional conditions with lower oxygen content as suggested from the faunal evidence described above.

The neutron and density logs of this electrofacies are intermediate between the Mudstones Electrofacies (**G3/G4**) and the Hemipelagic Marlstones Electrofacies (**G1/G2**). The microresistivity curves of the dipmeter log do not differentiate individual beds but only show similar resistivity intervals without well defined beds. The tadpole plots for this electrofacies show slightly higher dip values than the surrounding mudstones. For example the tadpole plot of the muddy-sandstones from well 316 displays a poorly defined "red" pattern with dip angles of about 4 ° at the base of the cored interval and less than 2° at the top (**Plate 5.18a**).

The rocks of this electrofacies have the following mean range of wireline log values: GR = 70° (sandy) - 120° API (radioactive), ISF = 1.2-1.8 OHMS.m^2/m and 5.0 OHMS.m^2/m (oil zone), SFLU = 1.6-1.8 OHMS.m^2/m and 4.0 OHMS.m^2/m (oil zone), DELTAT = 65 (cemented) - 103 μsec/ft, RHOB = 2.20-2.24 g/cc and 2.40-2.55 g/cc (sandy cemented), ΦN = 31-40 p.u.. The neutron values are only related to the Mottled Sandy Mudstones Lithofacies **MM** because there is no available neutron log adjacent to the Mottled Muddy Sandstone Lithofacies **MS**.

5.3.11.2.2 Seismic responses

There are no typical or different seismic features associated with this electrofacies.

5.3.11.3 INTERPRETATION OF THE ELECTROFACIES (MM/MS)

The rocks of this electrofacies are probably the result of deposition from bottom currents over prolonged periods of time or from low-concentration turbidity currents, with pervasive bioturbation destroying much of the original structure.

There is no equivalent specific facies in the **MRL** classification, but in the **PCK** classification there are three similar facies to the Mottled Mudstone Electrofacies **(MM/MS)**. They also represent a continuum from more sandy to more muddy facies, C1.2, D1.3 and E1.3, which correspond respectively to the Mottled Muddy Sandstone Lithofacies **MS** and Mottled Sandy Mudstone Lithofacies **MM**. Stow & Piper (1984) have called this type of facies sandy and muddy contourites, respectively, and they have used the vertical schematic sequences from the Faro Drift (Gonthier et al., 1984) to represent the ideal vertical sequences for these contourites (see **Plate 5.17b**).

5.3.12 THIN-BEDDED BIOTURBATED SANDY SILTSTONE ELECTROFACIES (BSl)

5.3.12.1 THIN-BEDDED BIOTURBATED SANDY SILTSTONE LITHOFACIES BSl

Recognition and sedimentary structure: The rocks of this electrofacies consist of poorly laminated greyish green sandy siltstone. Bioturbation is a common feature and occurs as horizontal burrows of about 1-1.5 cm in diameter infilled with sand-sized grains.

Thickness: This electrofacies varies from a few centimetres up to 2 m thick.

Contacts: 1) The top is abrupt (erosional) with the **AmS, VcS, MM** Lithofacies; transitional to **G3** Lithofacies. 2) The base is abrupt with **(AmS), (G3/G4)** Electrofacies and transitional to the **(MM/MS)** Electrofacies.

Composition: Its composition is similar to those of the Calcareous Mudstone Lithofacies **G3** but with more silt and sand-sized grains (see **section 5.3.10.1**). The sandy burrows are usually cemented by calcite.

Reservoir characteristics: The rocks of this electrofacies are not reservoir rocks.

Example: The rocks of this electrofacies commonly occur interbedded with the Amalgamated Sandstones Electrofacies **(AmS) (Plate 5.20).** A similar bioturbated siltstone from the channels of the Eocene Hecho Group near Ainsa, Spain, is also shown in **photo C.**

5.3.12.2 GEOPHYSICAL CHARACTERISTICS OF ELECTROFACIES (BSl)

5.3.12.2.1 Wireline log responses

The rocks of this electrofacies have an average thickness of one meter and occur interbedded with coarser-grained **(AmS)** Electrofacies. The combination of the GR, neutron and density log curves is a useful tool to identify this electrofacies which is generally characterized by intermediate characteristics between the sandstones and the mudstones. Usually the neutron log curve stays to the left of the density curve, but close to it. The microresistivity curves of the dipmeter log detect with accuracy these thin siltstones intervals, **(BSl)** Electrofacies, and the tadpole plot shows these to have isolated dips with low angles. These siltstones occur as kind of mud-drapes and are thought to define sandstone packages deposited as infills of shallow scours formed within the main channel complex. These dips can be used to identify trends in sandstone-body geometry because the mud-drapes were preferentially deposited and preserved in depressions. However, for better results it is necessary to reprocess the data using a correlation interval of about 2 m, rather than the usual processing interval of 1 m. The objective of doing this is to establish only the main breaks, which would be the most reliable dips for interpreting orientation of sand bodies.

The rocks of this electrofacies have the following mean range of wireline logs values: GR = 50-80° API, ISF = 0.3-0.4 OHMS.m^2/m (non cemented) and 0.9-1.0 OHMS.m^2/m (cemented), SFLU = 0.8-0.9 OHMS.m^2/m (non cemented) and 2.8-3.0 OHMS.m^2/m (cemented), DELTAT = 105-110 μsec/ft (non

PLATE 5.20a

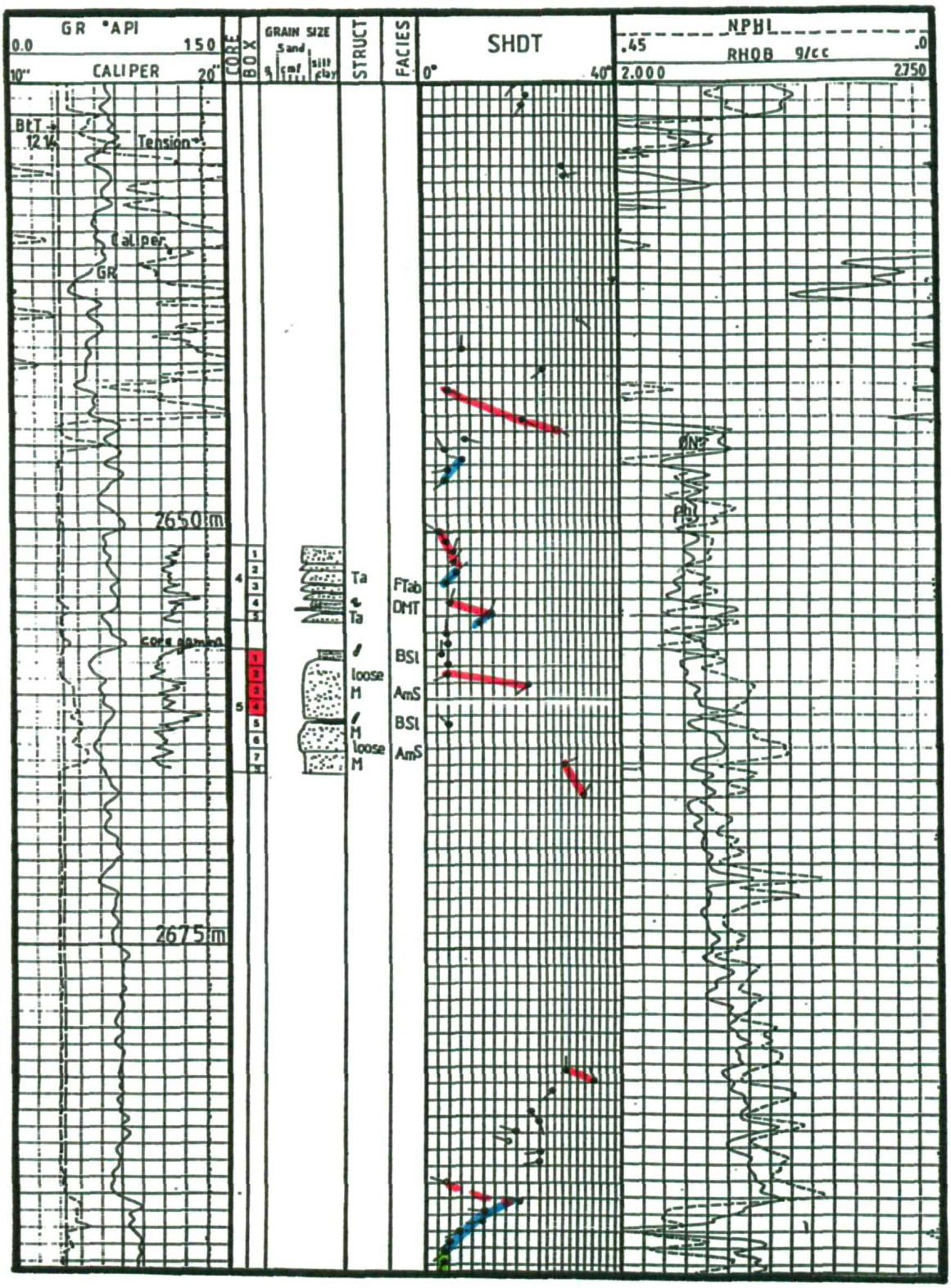


Plate 5.20 - Bioturbated Sandy Siltstone Electrofacies (BSl). Composite log (5.20a) and corresponding cored interval (5.20b). Close-up (B) shows burrows infilled with sand. Similar features can be seen in the photo C from bioturbated siltstones in the channels of the Eocene Hecho Group, near Ainsa, Spain.

PLATE 5.20b

A



B



C



cemented) and 87-88 μsec/ft (cemented), RHOB = 2.19-2.23 g/cc (non cemented) and 2.44 g/cc (cemented), ΦN = 33-39 p.u. (non cemented) and 19 p.u. (cemented).

5.3.12.2.2 Seismic responses

The rocks of this electrofacies do not have enough thickness to be identified in seismic sections.

5.3.12.3 INTERPRETATION OF THE ELECTROFACIES (BS1)

The rocks of this electrofacies are the result of slow deposition from diluted turbidity currents and intensive bioturbation. There is a transition from the sandstones to the siltstones and the interval is usually heavily bioturbated with irregular laminations. Some of these transitional intervals could be interpreted as the result of reworking by bottom currents and bioturbation.

This type of electrofacies is commonly found in outcrops of channel-fill facies of the Eocene Hecho Group, Ainsa, and are characterised by intense bioturbation, especially the horizontal sandy burrows, Thalassinoides (photo C in the **Plate 5.20**).

There is no specific facies in the MRL classification to compare with the rocks of this electrofacies. In the PCK classification the rocks of this electrofacies correspond to the Facies D1.3 - Mottled silt and mud, which is also the nearest equivalent to the Mottled Mudstone Electrofacies (MM/MS), which has different characteristics and associations.

5.4 ELECTROFACIES ASSOCIATION[8] AND DISTRIBUTION

Five main electrofacies associations have been identified:

I - HEMIPELAGITES;
II - CHANNEL RELATED DEPOSITS:
IIa - CHANNEL-FILL;
IIb - CHANNEL-MARGIN;
III - CHANNEL-LOBE TRANSITION
IV - PROXIMAL LOBES
V - CONTOURITES

5.4.1 HEMIPELAGITES ELECTROFACIES ASSOCIATION (I)

This electrofacies association is characterized by the rhythmic interbedding of the pelagic/hemipelagic Chalk/Marlstone Electrofacies (**G1/G2**) and the Mudstone Electrofacies (**G3/G4**). Usually they are arranged in cycles that start with the siliciclastic mudstones at the base and becoming more calcareous upwards and passing transitionally into the marlstones or chalks with a concomitant decrease in the siliciclastic mud content. The siliciclastic mudstones (**G4**) represent periods of higher sediment influx as fine-grained turbidity currents compared to the times of marlstone (**G2**) deposition which may reflect climatic variations or even represent minor sea-level fluctuations. The siliciclastic mudstones (**G4**) are frequently found at the top of coarse-grained turbidite sequences indicative of a related genesis.

The Hemipelagites Electrofacies Association (I) represents the highstand deposits of the Oligocene-Lower Miocene turbidite complex[9] and the mudstone/marlstones couplets could represent oscillations in climatic conditions (see **plates 5.14, 5.15** and **5.16**). The "BLUE MARKER" of Gamboa et al. (1986) is an example of this type of electrofacies association. This pelagic/hemipelagic

---

[8] Facies or electrofacies association are groups of facies that occur together and are considered to be genetically or environmentally related (Reading, 1986).

[9] A turbidite complex refers to a basin-fill succession and is composed of several turbidite systems that are stacked one upon the other (Mutti & Normark, 1987)

electrofacies association has a widespread distribution and can be used to separate turbidite systems[10]. In the northern part of the studied area eight sand-rich turbidite systems (**a, b, c/d, e, f,** and **g/h**) have been identified. The turbidite systems **a, b** and **c/d** are the most important. The separation of the systems **c/d** and **g/h** is only locally possible, particularly in areas further offshore where amalgamation is less frequent (stratigraphic sections **A-B, C-D, E-D** and **G-H**, respectively, **figures 5.11, 5.12, 5.13** and **5.14**). The estimated position in time and the areal distribution of these turbidite events will be thoroughly discussed in **Chapter 6**.

5.4.2 CHANNEL ELECTROFACIES ASSOCIATION (II)

The channel electrofacies association (II) can be divided into: channel-fill (**IIa**) and channel-margin/overbank (**IIb**) electrofacies association.

The **Channel-fill electrofacies association (IIa)** consists of two subfacies associations. One resembles the "mixed" channel-fill deposits of Mutti & Normark (1987) and is characterized by the following electrofacies: Gravelly Sandstones (**GvS**), Gravelly Sandstone with Mudclasts (**GvSm**), Amalgamated Sandstone (**AmS**, mainly represented by the Very Coarse Sandstone Lithofacies **VcS**), Diamictites (**DMT**), Chaotic (**F**), the Thick-bedded (**FTab**) and Muddy Thin-bedded (**FTb-e**) sand-mud couplets. Examples of this electrofacies association were cored in wells 281, 313 and 329 (see **plates:** 5.1, 5.2, 5.3, 5.4, 5.8, and 5.13). The other is similar to the "depositional" channel-fill sequence of Mutti & Normark (1987) and is characterized by the following electrofacies: Amalgamated sandstone (**AmS**), Thick- and Thin-bedded Sandstones (**FTab**) and (**FTb-e**). Examples of this electrofacies association were cored in wells 305 and 332 (**plates 5.4**, and **5.5**).

---

[10] A turbidite system is a body of genetically related mass-flow sediments deposited in stratigraphic continuity and are commonly bounded, above and below by mudstones (reflecting high stands of sea level) or by submarine erosional unconformities (Mutti & Normark, 1987). A turbidite system is part of a depositional sequence in the sense of Vail et al. (1977) and will commonly occur at the base of a sequence initiated during a relatively low stand of sea level.

The **Channel-margin/overbank electrofacies association (IIb)** is mainly represented by the Sandy Thin-bedded Sand-mud Couplet Electrofacies (**E**) and the Mudstone Electrofacies (**G3/G4**). This association was cored in wells 281, 316, 329, 334, 355 and AB-1 (**plates: 5.8, 5.9, 5.10, 5.11,** and **5.12**).

The Channel Electrofacies Association (**II**) is frequently found in wells located in relatively more onshore positions (wells: AB-1, AB-3, 281, 297, 310, 313, 329, 330 and 332). However, the Diamictite Electrofacies (**DMT**), usually associated with the former wells, has also been observed in the most offshore well, 367 (see level "**d**" in the stratigraphic sections **A-B** and **C-D**, respectively **figures 5.11** and **5.12**). This electrofacies association presents a channelized geometry with relatively rapid vertical and lateral variations (strike-oriented stratigraphic section **G-H**, **Figure 5.14**, based on wireline log correlations). The dimensions of these channelized features are around 50 m deep and 1-5 Km wide. The channels have been infilled in several stages and with some shift of their depositional axis. As will be seen in **Chapter 6** this type of channels has a very low relief due to their shallow depth and the absence of thick overbank deposits that make their identification in seismic sections rather difficult. The period of time for the infilling of these channel systems can be estimated by stratigraphic correlations as about 1 million years.

5.4.3 CHANNEL-LOBE TRANSITION[11] ELECTROFACIES ASSOCIATION III

This electrofacies association is characterized by relatively areal continuous and amalgamated sandstones with "blocky" patterns in the wireline logs, and thicknesses that vary from 30 up to 120 m. The most abundant constituent of this association is the Amalgamated Sandstone Electrofacies (***AmS***), composed of the Very Coarse-Sandstone Lithofacies (***VcS***), commonly with thin bioclast-rich cemented intervals,

[11] The channel-lobe transition term is being used here as described by Mutti & Normark (1987) for sand-rich turbidites or "poorly efficient" (Mutti, 1979) and that correspond to the "suprafan" type lobe of Normark (1970).

and the Amalgamated Coarse/fine-Sandstone Lithofacies **AmS**. Usually towards the top of this association are the Thick-bedded Sandstones Electrofacies (**FTab**), that shows a fining and thinning upwards motifs.

The tadpole plot of the dip meter log for this facies association shows only scattered dip readings, which represent mudstone intercalations, (**BSl**) Electrofacies, or cemented intervals. However, towards the top of the sandstone bodies more thinly interbedded sandstones/ mudstones become common with a decrease in the frequency of amalgamations occurs and as a result a clear "red" pattern of dips is developed.

Variations from the typical Channel Electrofacies Association (**II**) with the Diamictites Electrofacies (**DMT**) and the Chaotic Electrofacies (**F**), to the amalgamated and more continuous sandstones of the Channel-Lobe transition Association (**III**) can be seen in the dip-oriented stratigraphic section **A-B** (**Fig. 5.11**).

The combined characteristics of this electrofacies association with two different turbidite systems brought into contact through the erosion of the Hemipelagites (**I**) can be seen in wells 333 and 342 of the stratigraphic section **E-F** (**Fig 5.13**). Further offshore the sandstone bodies are more continuous and separated by Hemipelagites (**I**) suggesting a decrease in the importance of the channels (**Fig. 5.12**). In the relatively more onshore setting the corresponding intervals containing the sandstones (**a to d**) become enriched in diamictites and poorer in amalgamated sandstones (**Fig. 5.14**).

The upper three (**f**, **g**, and **h**) sandstone levels of the northern sector (see section **C-D**, **Fig. 5.12**) have a slightly different electrofacies association. They are also characterized by Amalgamated Sandstones Electrofacies (**AmS**) but with very fine/medium sands and more developed fining and upward thinning sequences. They are characterized by the Thick-bedded Sandstone Electrofacies (**FTab**) and the Sandy Thin-bedded Sand-mud Couplet Electrofacies (**E**) with characteristic "red" patterns in the dipmeter logs (**Plate**

10). In the section C-D (Fig. 5.12) at the level of the sandstones (g) and (h) it is possible to interpret a lateral migration of the channel in well 360 to well 355. This type of migration could be due to channel meandering or abandonment, which could be the cause of the very well developed fining and thinning upward sequences of these younger turbidite systems.

5.4.4 PROXIMAL LOBES[12] ELECTROFACIES ASSOCIATION (IV)

This electrofacies association is characterized by the following electrofacies: Amalgamated Sandstones (AmS), Thick- and Thin-Bedded Sand-Mud Couplets (FTab and FTb-e), Bioturbated Sandy Siltstone (BSl) and Mudstone (G3/G4). The distinction of this electrofacies association from the Channel-lobe transition association (III) is difficult, because they have similar electrofacies. However, the Proximal Lobe Electrofacies Association (IV) has a relatively higher frequency of mudstone (G3/G4 Electrofacies) intercalations. The most important characteristic of this association is its widespread areal continuity. In the southern part of the studied area, sandstones bodies can be correlated over an extensive area of several kilometres (sections I-J and K-L, figures 5.15 and 5.16). However, this does not necessarily imply that they are continuous throughout the region, but they appear to have a very good regional distribution. To confirm their continuity a 3D seismic survey is needed, but this was not available for the present study. The wireline log characteristics of the wells in this region indicate the predominance of the Amalgamated Sandstone Electrofacies (AmS) with some small channels in the more onshore wells (377, 219, 326), while in well 359 there seem to be fewer channels (15-20 m) and less amalgamations which was tentatively interpreted as proximal lobe facies.

[12] According to Mutti & Normark (1987) lobe deposits are a depositional element composed of non-channelized sandstone bodies that occur downstream of channel-fill sediment and of the channel-lobe transition.

EXPLANATION FOR THE STRATIGRAPHIC SECTIONS



ELECTROFACIES ASSOCIATION:

Hemipelagites	I
Channel-fill	IIa
Channel-margin	IIb
Channel-lobe transition	III
Proximal Lobe	IV

CONTACTS:

EROSIONAL OR CORRELATIVE
TRANSITIONAL

MARKER = "BLUE" MARKER

TURBIDITE SYSTEMS:
a, b, c, d, e, f, g and h.

WIRELINE LOGS:
GR = Gamma Ray;
RILD = Resistivity log

N-540 NANOFOSSIL ZONES
(used by Petrobrás)

Figure 5.11a - Explanation for the stratigraphic sections.

FIG. 5.11

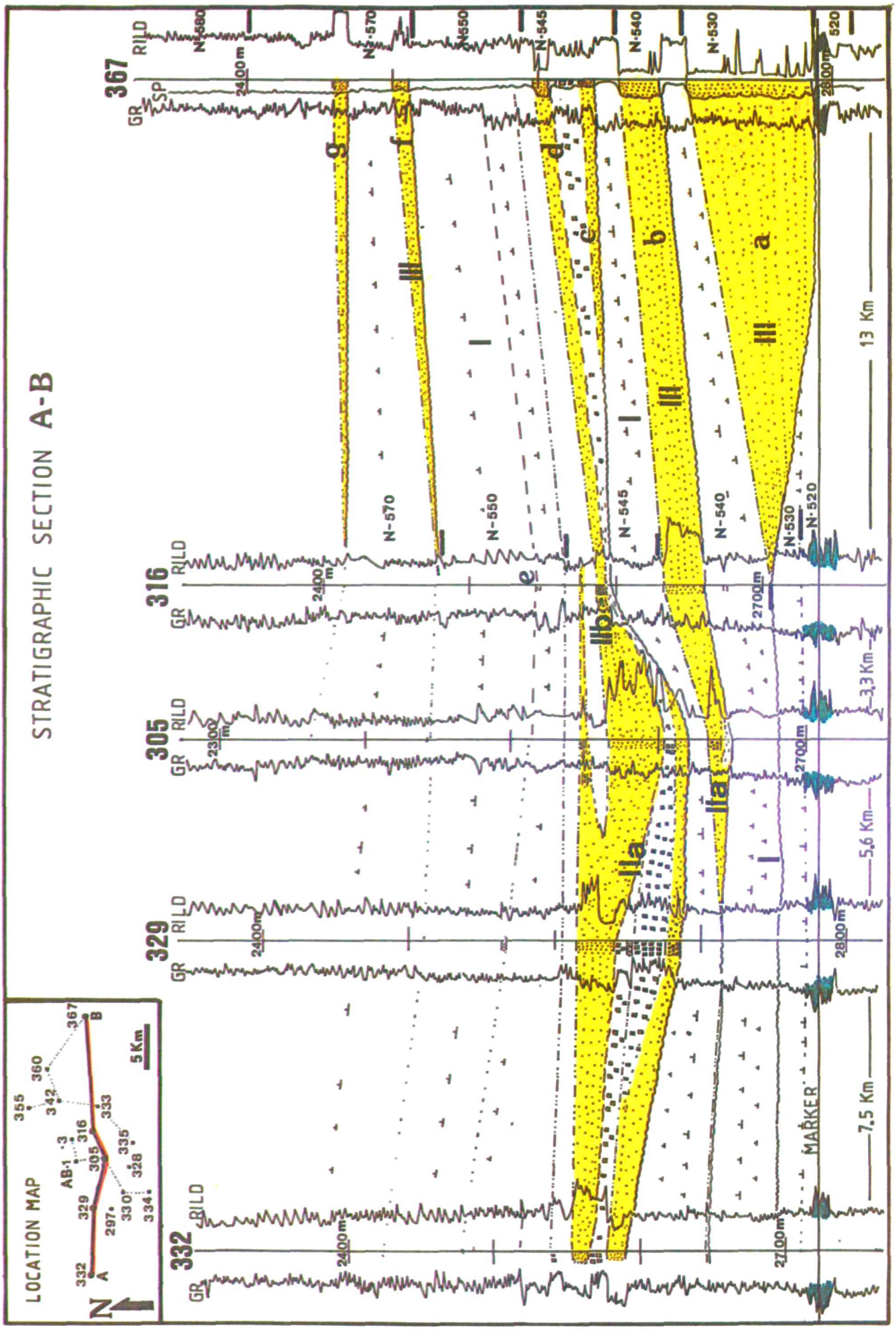
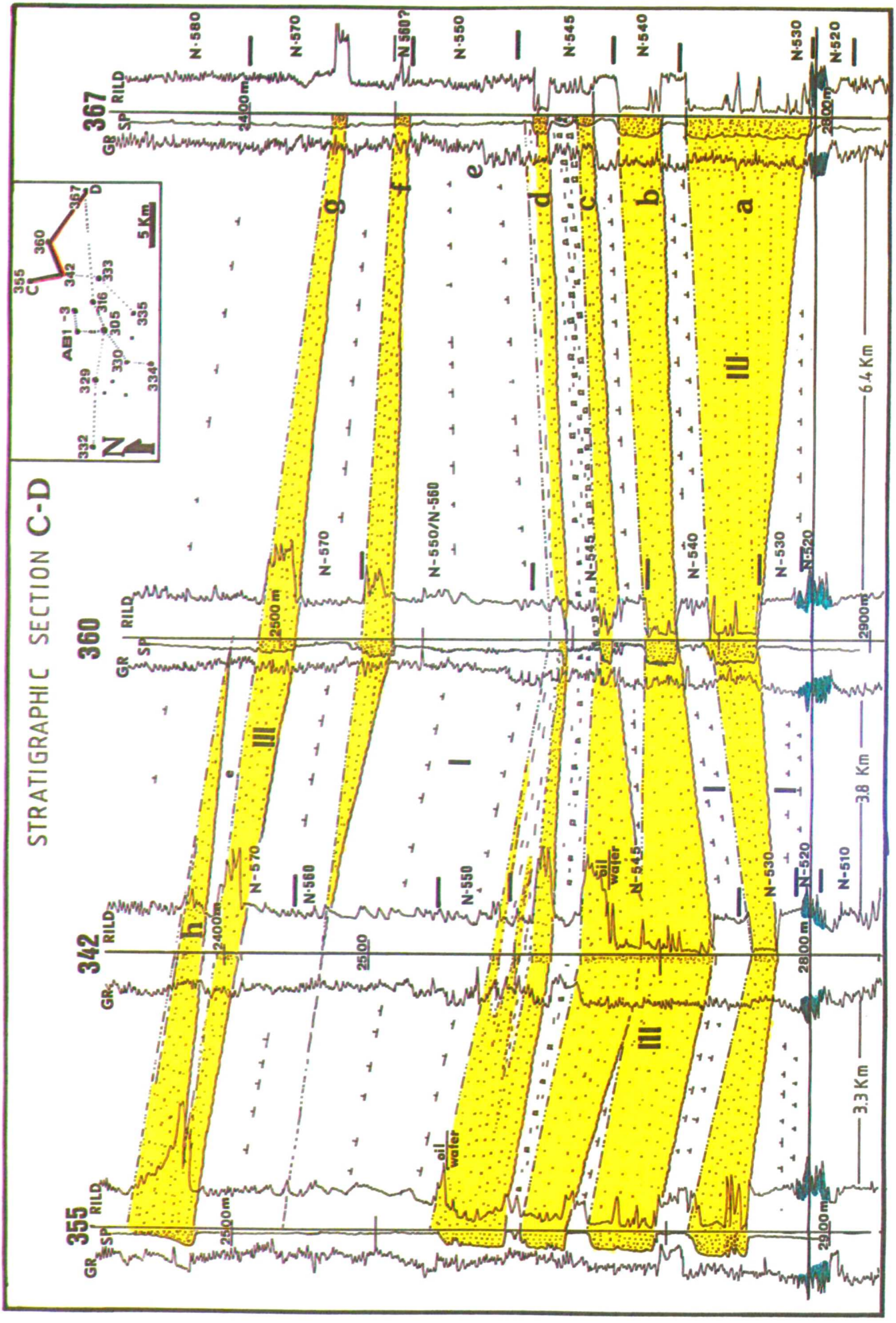

STRATIGRAPHIC SECTION A-B
LOCATION MAP
N
5 Km
367
316
305
329
332
RILD
GR
SP
2400 m
2700m
2800m
N-580
N-570
N-550
N-545
N-540
N-530
N-520
13 Km
3.3 Km
5.6 Km
7.5 Km
MARKER
a
b
c
d
e
f
g
I
II
IIa
IIb
III

FIG. 5.12


STRATIGRAPHIC SECTION C-D
367
360
342
355
RILD
SP
GR
N-580
N-570
N-560?
N-550
N-545
N-540
N-530
N-520
N-510
2400m
2500m
2600m
2800m
2900m
a
b
c
d
e
f
g
h
I
II
III
oil
water
6.4 Km
3.8 Km
3.3 Km
5 Km
N-550/N-560
C
D
355
360
342
367
AB1 -3
329
330
305
316
333
335
334
332

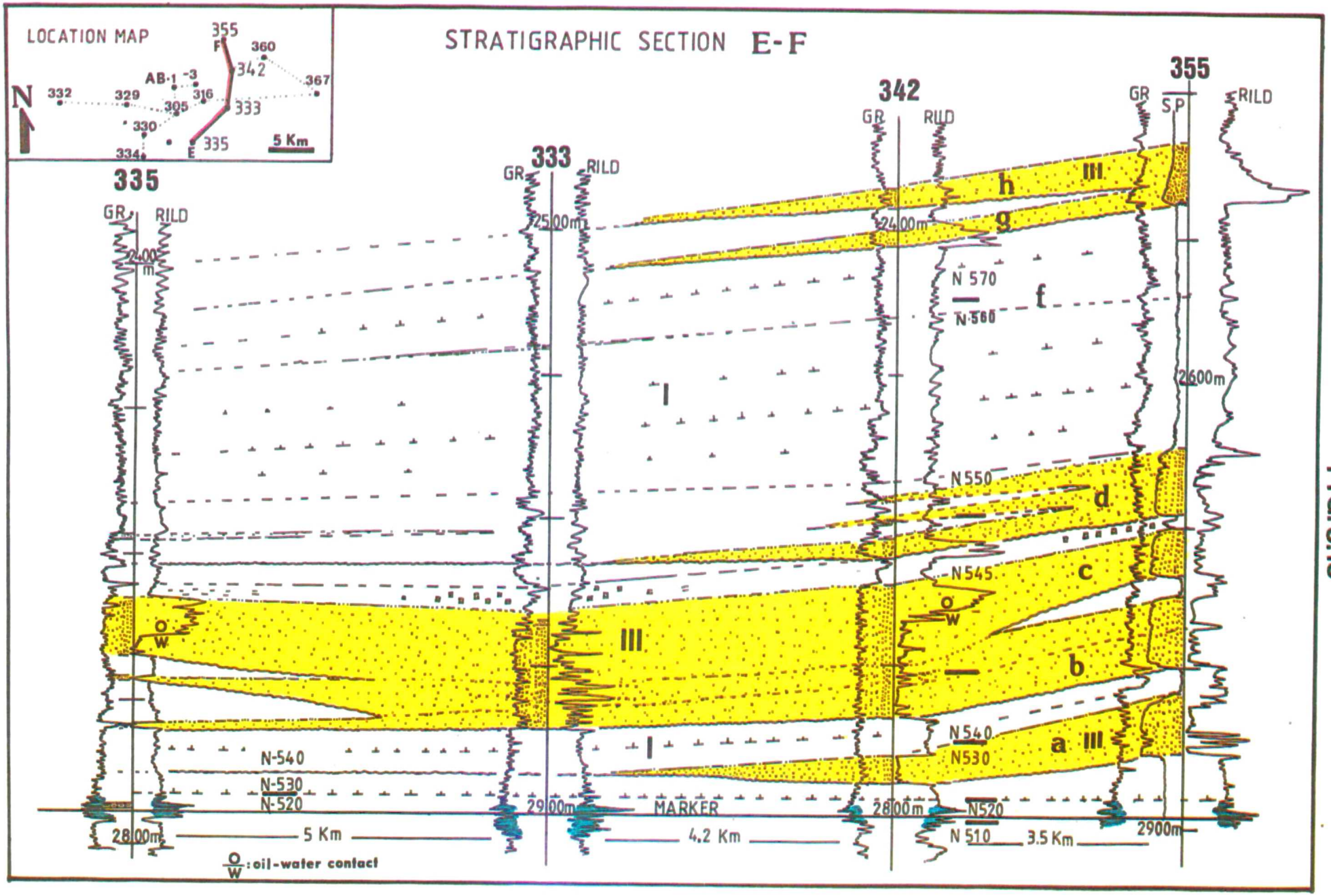

LOCATION MAP
N
355
F
360
342
367
AB-1
-3
332
329
316
333
330
335
E
334
5 Km
STRATIGRAPHIC SECTION E-F
335
333
342
355
GR
RILD
SP
2400m
2500m
2600m
2900m
2800m
h
g
f
d
c
b
a
III
I
N 570
N 560
N550
N545
N540
N530
N520
N510
O
W
N-540
N-530
N-520
MARKER
5 Km
4.2 Km
3.5 Km
O/W : oil-water contact

FIG. 5.13

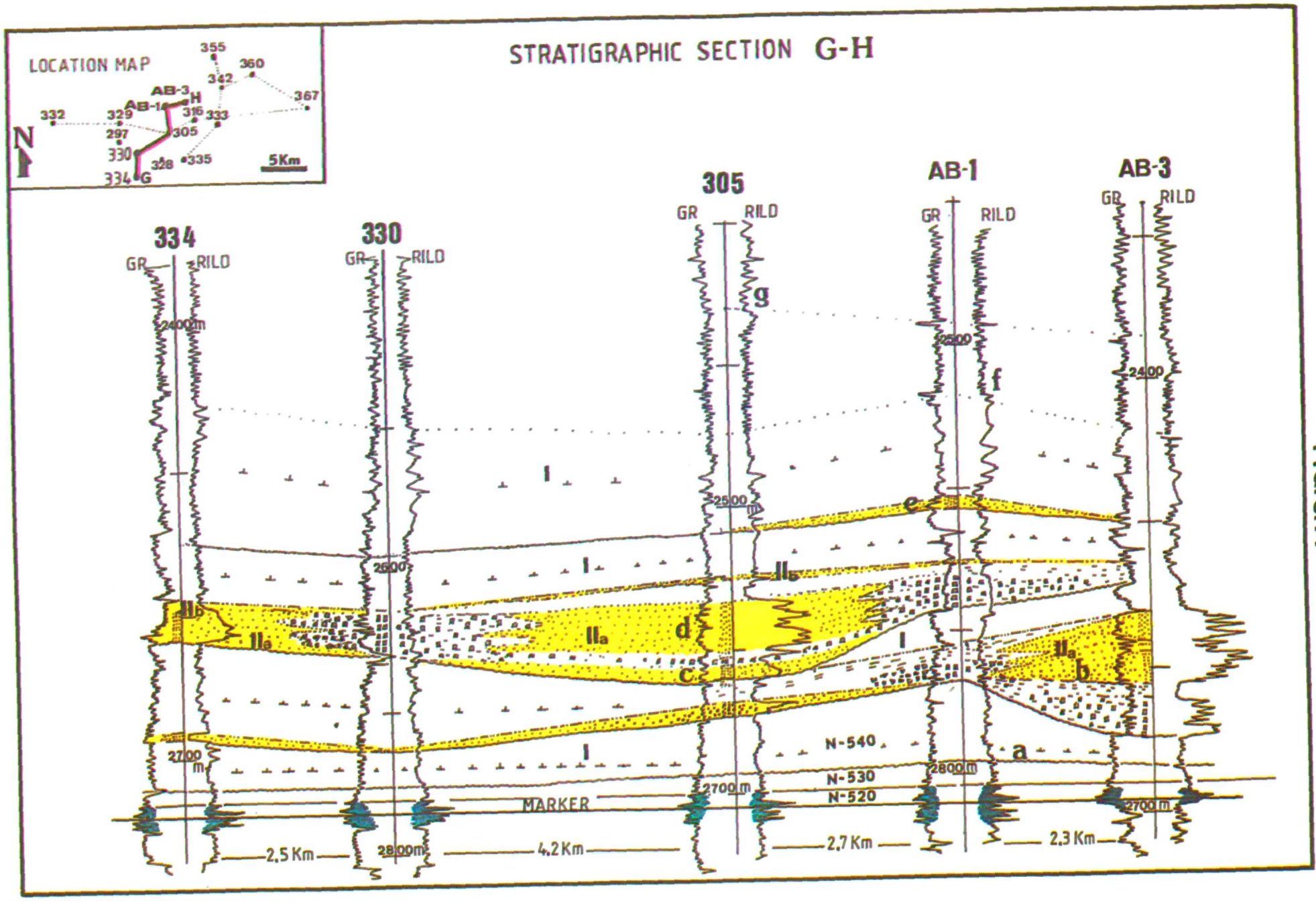
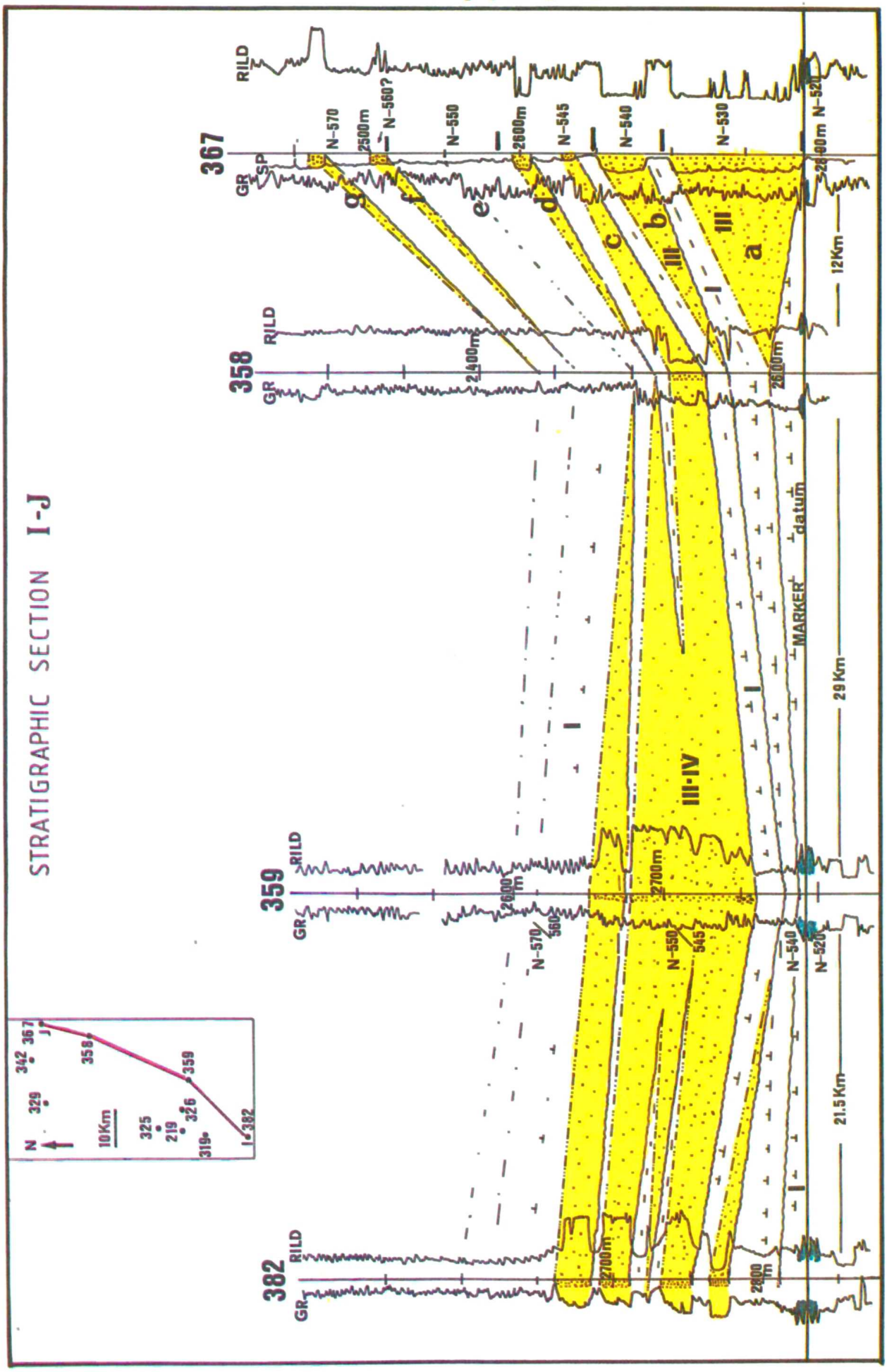

STRATIGRAPHIC SECTION G-H
LOCATION MAP
355
360
342
367
AB-3
H
AB-1
332
329
316
333
297
305
330
328
335
334
G
5Km
N
334
330
305
AB-1
AB-3
GR
RILD
2400m
2500
2600
2700 m
2800m
I
IIb
IIa
g
e
d
c
f
b
a
N-540
N-530
N-520
MARKER
2,5 Km
4,2 Km
2,7 Km
2,3 Km

FIG. 5.14

FIG. 5.15


STRATIGRAPHIC SECTION I-J
RILD
GR
SP
367
358
359
382
N-570
N-560?
N-550
N-545
N-540
N-530
N-520
2500m
2600m
2400m
2700m
MARKER
datum
12Km
29 Km
21.5Km
10Km
N
342
329
325
219
319
326
382

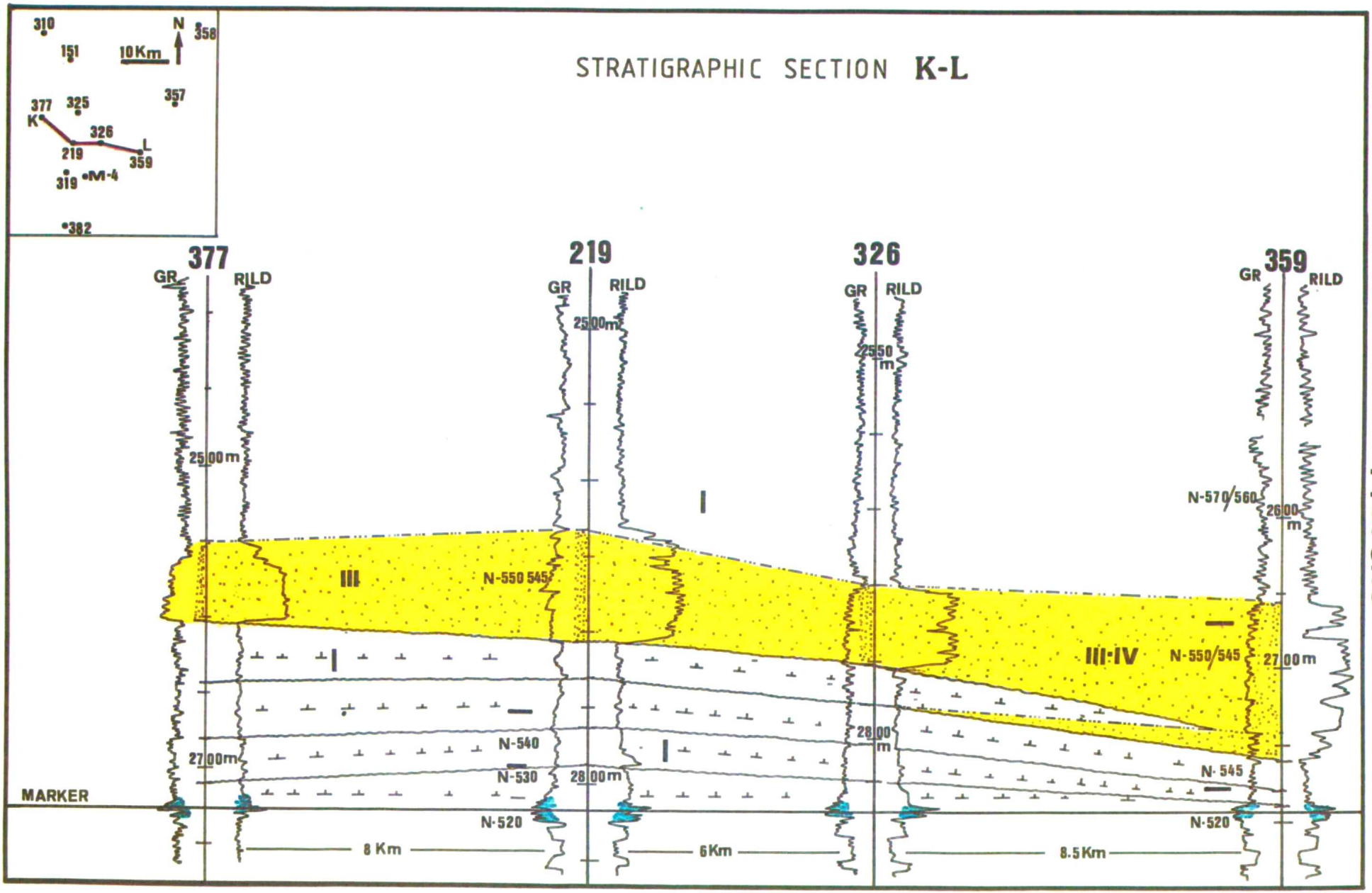

STRATIGRAPHIC SECTION K-L
310
151
10Km
N
358
357
377
325
K
326
219
L
359
319
M-4
382
377
219
326
359
GR
RILD
25.00m
27.00m
28.00m
26.00m
I
III
III:IV
N-550 545
N-550/545
N-570/560
N-540
N-530
N-545
N-520
MARKER
8 Km
6Km
8.5Km

FIG. 5.16

5.4.5 CONTOURITES ELECTROFACIES ASSOCIATION (V)

A contourite was originally defined as the sediment deposited from thermohaline-driven bottom currents flowing parallel to bathymetric contours (Heezen et al., 1966). According to Pickering at al. (1989) recent definitions of a contourite are as follows: a) a bed deposited or significantly reworked by a current that is persistent in time and space and flows along the slope in relatively deep water; or b) a sediment reworked or redeposited by bottom currents, which are commonly geostrophic and contour-following, but which may be either fast or sluggish (Robertson & Ogg, 1986).

Descriptions of ancient examples of contourites in the literature are very scarce and dubious. According to Pickering et al. (1989) only one of 30 successions in which there appears to be contour-current deposition has been considered sufficiently convincing to form the basis of a case study (the Talme Yafe Formation, deposited in the Cretaceous Tethys Sea, off the Arabian craton, Bein & Weiler, 1976).

Mutti et al. (1979 and 1980) have interpreted the mottled muddy sandstones and the absence of fines at the top of the Eocene turbidites in the Campos Basin as the product of reworking by bottom currents. However, apart from these characteristics there is no further evidence to support this interpretation.

In the succession analyzed during this study, the most likely sediments to be interpreted as having been reworked by bottom currents and shows pervasive contemporaneous bioturbation (i.e. contourites) can be separated into two subelectrofacies associations characterized by the following lithofacies: 1) very thick intervals of Mottled Mudstone **MM** and Mottled Muddy Sandstone **MS** rich in foraminifera and interbedded with Siliciclastic Mudstone **G4** and 2) thin/ medium-thick intervals of Mottled Mudstone **MM** or thin cemented Mottled Sandstone **MS** interbedded with Marlstone (**G2**) (**plates 5.17, 5.18** and **5.19**, respectively). The thick mottled intervals are composed of negative and positive,

less developed, graded couplets (1-2 m) similar to the "typical" arrangement of contourite facies described by Stow & Piper (1984). The thick Mottled Mudstone Electrofacies (MM/MS) is better developed in well 154, which is located on the hanging wall of a growth fault created during the Aptian salt collapse. The creation and evolution of this regional depression has probable caused an increase in sedimentation rate at this site to about 30 cm/kyr, which represents at least twice the average sedimentation rate during the Lower Miocene. This depression is very likely to have acted as focus for the currents in the area and produced similar deposits to those described from deep-sea sediment drifts (e.g. Gonthier et al., 1984; Chough and Hesse, 1985). **Fig. 5.17** shows a schematic diagram for the location of this structural low. Conversely, in the other wells the thickness of these deposits are only a few decimeters-metres thick indicating that reworking by bottom currents has occurred in some intervals but their deposits were only significant when associated with regional structural lows. There this type of current could have been funnelled and reached velocities high enough to transport reasonable volumes of sediments. In samples of the thin-mottled cemented sandstones have been found anomalous amounts (~5%) of heavy minerals and chert cements (respectively, **Plate 5.19** in this chapter and **Plate 9.7** in Chapter 9). These sandstones could probably represent residual deposits of contour currents.

Souza Cruz et al. (1987) interpreted the very fine-sandstones with ripple-drift-laminations (Rip Lithofacies) sampled in core 1 in well 334 as contourites (**Plate 5.12**). In this study it was thought that this interval because of its characteristics, vertical association and similarities to the channel-margin/overbank deposits of the Eocene Hecho Group (Ainsa, Spain), can be better related to channel-margin/overbank deposits rather than to contourites.

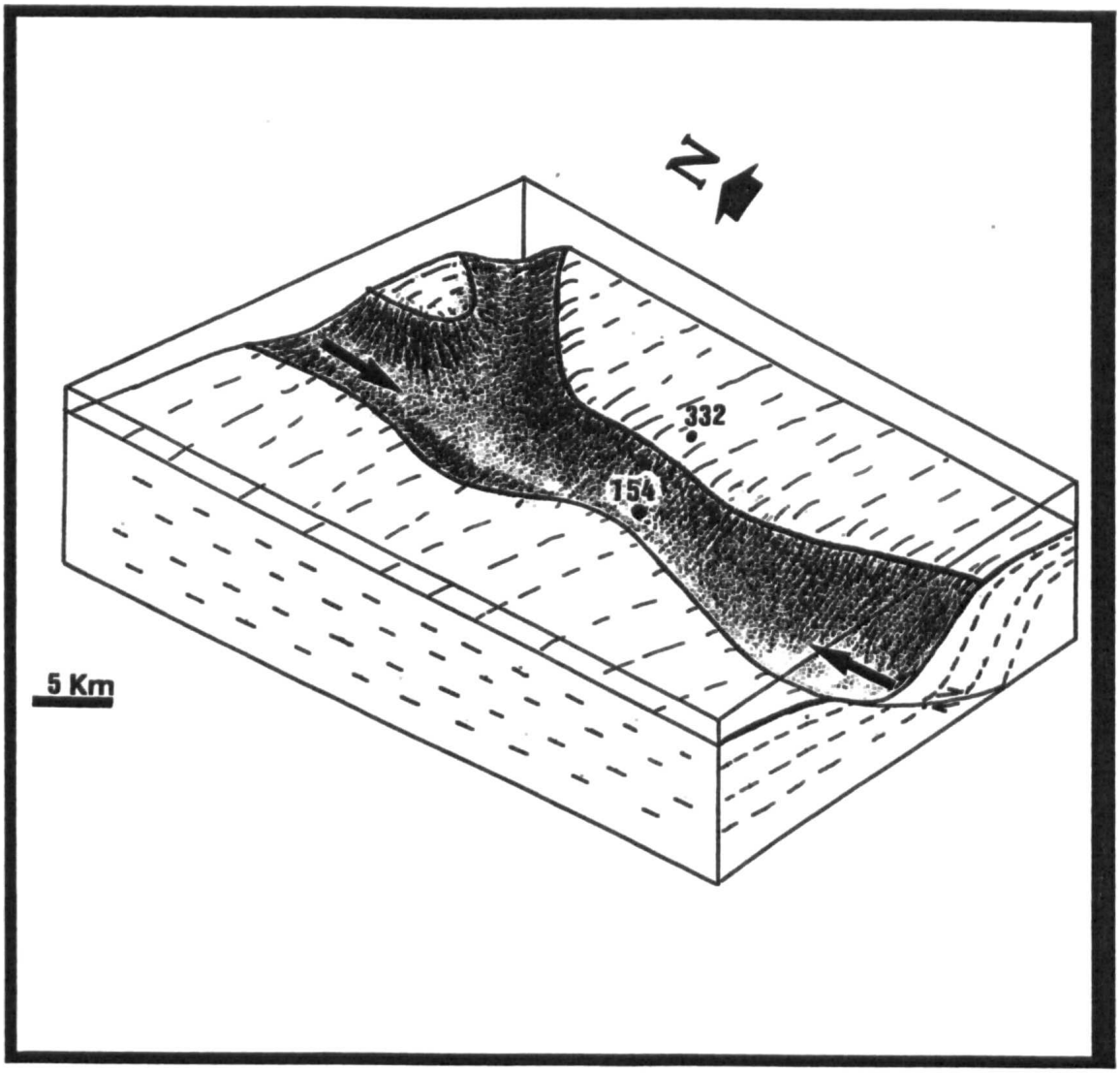


Figure 5.17 - Schematic depositional model for the rocks of the thick Mottled Mudstones Electrofacies (MM/MS) in the area of well 154, where a structural low formed by the withdrawal of the underlying Aptian evaporites would have controlled the deposition of these rocks.

5.5 CONCLUSIONS

The cored lithologies have been classified into 20 lithofacies based on their sedimentological characteristics and comparisons with similar sequences observed at outcrop in the Eocene strata of the South Pyrenean Basin, Ainsa-Broto and San Sebastian regions, Spain, and the pertinent literature. Those lithofacies with similar wireline log and, in some cases, seismic responses have been organized into 12 electrofacies. Additionally these electrofacies were assembled into eight groups, based on their wireline log responses, textural, sedimentary structures and bed thickness similarities. These electrofacies groups are generally similar to those of the facies classification of Mutti & Ricci Lucchi (1972, 1975), but there are some exceptions e.g. the Mottled Mudstone Electrofacies (MM/MS) and Bioturbated Sandy Siltstones Electrofacies (BS1).

Five main electrofacies associations have been identified: Hemipelagites (I), Channel-Fill/Margin (II), Channel-Lobe transition (III), Proximal Lobes (IV) and Contourites (V). The stratigraphic correlations of the electrofacies associations using calibrated[13] wireline logs (i.e. electrofacies) allowed eight turbidite systems (**a, b, c/d, e, f, g/h**), to be identified, with **e** and **f** the less important events.

The sediments analyzed in this study can be divided into two main groups: one represented by pelagic/ hemipelagic marlstones and siliciclastic mudstones (Hemipelagite Electrofacies Association - I) characterizing the deposits of a relative highstand of sea level; and another characterized by siliciclastic sandstones, some diamictites and siliciclastic mudstones (electrofacies associations II, III and IV) representing deposits of a relative lowstand of sea level.

The Contourite Electrofacies Association (V) represented by Mottled Mudstones Electrofacies (MM/MS) is only locally important. It is associated with structural

[13]The calibration of wireline logs was made using the cored lithofacies and their resulting electrofacies plus the palaeontological data.

lows and its interpretation as contourites appears to be the most adequate. However, the Very thin-bedded Very fine-Sandstones with Ripple-drift Lithofacies (**Rip**) that has been interpreted as contourites by Souza Cruz et al. (1987) is interpreted as being more related to channel-margin/ overbank deposits than to contourites.

The Oligocene-Lower Miocene turbidite systems are characterized by thick amalgamated sandstones bodies, very high sand:mud ratios and electrofacies associations dominated by amalgamated channelized or proximal lobe electrofacies separated by pelagic/hemipelagic electrofacies. These general characteristics are very similar to those of sand-rich fan system models such as the "suprafan" lobes of Normark (1970) or the "poorly efficient"/Type II of Mutti (1979; 1985). In **Chapter 6** more detailed comparisons with such depositional models using additional seismic data will be made.

CHAPTER 6

SEQUENCE STRATIGRAPHY AND DEPOSITIONAL MODEL

6.1 INTRODUCTION

In order to better understand the spatial and temporal relationships of the Oligocene-Miocene sedimentary facies described in the previous chapter, an integration of the lithostratigraphic, chronostratigraphic and seismic data was carried out using the seismic stratigraphy approach (Vail et al., 1977; Vail, 1987; and Posamentier & Vail, 1988; Posamentier et al., 1988). In spite of possible pitfalls involved in breaking down a succession into stratigraphic sequences this kind of analysis is still the best way to determine the three dimensional distribution of sedimentary sequences and to predict the occurrence and characteristics of specific sedimentary deposits.

The definition of the stratigraphic sequences was carried out in three steps. Firstly, facies analysis was used to interpret the cored lithologies with concomitant wireline log and palaeontological calibrations and well correlations (Chapter 5). Secondly, the calibrated wireline logs were correlated with seismic sections using synthetic seismograms, such correlations were also used to define the resolution of seismic data in the studied area. Finally, the Oligocene-Recent succession was broken down into depositional sequences using sequence stratigraphy[1] (reflection terminations, configurations and geometries), attempting to identify in seismic lines the most important markers, sand-rich turbidite deposits and sedimentary hiatus identified with well data and vice versa (see Chapter 4).

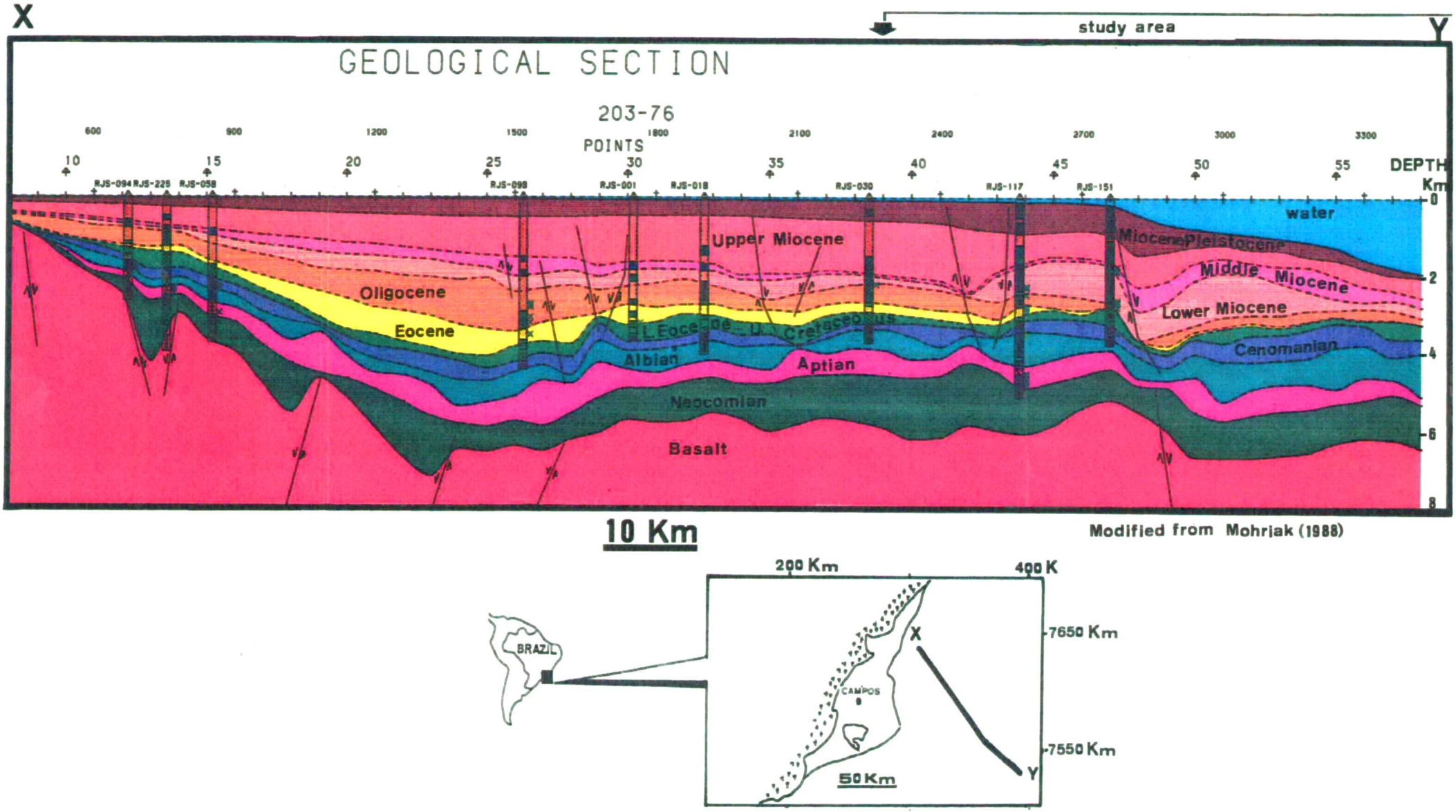
[1] Sequence Stratigraphy is the study of rock relationships within a chronostratigraphic framework wherein the succession of rocks is cyclic and is composed of genetically related stratal units (Posamentier et al., 1988).

6.2 OLIGOCENE-RECENT SUCCESSION

The Oligocene-Recent succession of the Campos Basin clearly shows a lenticular geometry in a depositional dip-oriented geological section (**Fig. 6.1**). Its basal portion consists of an Oligocene succession which has a tabular-lens shaped geometry. Locally, in its proximal half (near well RJS-98), there is an increase in thickness which can be, in part, related to higher subsidence reflecting deeper structural controls. The upper portion consists of a Miocene-Recent succession which is represented by a thick progradational lens. The thicker parts of this succession are associated with growth faults and roll-over structures, especially near the shelf-edge, where it thins relatively rapidly towards deep water. This fault zone can be related to older faults associated with the Neocomian rift phase (**Fig.6.1**). The offlapping character of the Miocene-Recent succession arises because the rate of sedimentation is greater than the rates of thermal subsidence (**Fig. 6.2**). The increased sediment supply reflected the Tertiary isostatic uplift of the source area, the Serra do Mar Mountains (Mohriak, 1988). However, as these Miocene sediments have not undergone significant compaction their thicknesses have to be used with care when comparing them with older and more compacted successions.

The Oligocene-Recent succession can be divided into eight depositional sequences, the lower datum is the Lower Oligocene "Blue Marker", and the upper one is the present sea floor. The "Blue Marker" is an easily distinguishable very high amplitude and continuous seismic reflector at the base of the Miocene progradational megasequence, in the northeastern part of the Campos Basin (Gamboa et al., 1986). It represents the distal equivalent to the Siri carbonate platform sediments whose transition was characterized by a ramp morphology rather than steep gradients. This marker is composed of Braarudosphaera-rich chalk beds and has been interpreted as being deposited in an upper/middle bathyal environment about 32-33 Myr ago (Gamboa, 1986; and Shimabukuro, 1987).

Fig.6.1 - Dip-oriented regional geological section of the northeast part of the Campos Basin.


X
study area
Y
GEOLOGICAL SECTION
203-76
POINTS
600
900
1200
1500
1800
2100
2400
2700
3000
3300
10
15
20
25
30
35
40
45
50
55
DEPTH
Km
RJS-094
RJS-225
RJS-058
RJS-098
RJS-001
RJS-018
RJS-030
RJS-117
RJS-151
water
Miocene
Pleistocene
Upper Miocene
Middle Miocene
Lower Miocene
Oligocene
Eocene
L. Eocene
U. Cretaceous
Cenomanian
Albian
Aptian
Neocomian
Basalt
0
2
4
6
8
10 Km
Modified from Mohriak (1988)
200 Km
400 K
7650 Km
7550 Km
BRAZIL
CAMPOS
X
Y
50 Km

The sequences are characterized by a succession of genetically related strata bounded by unconformities or correlative conformities (Vail et al., 1977) (see also Chapter 4). The intrasequence boundaries were established using onlap, downlap or erosional truncations of the seismic reflectors and their correlative conformities (see **sections T-T', U-U', V-V', X-X', Y-Y'** and **Z-Z'**, respectively **figures 6.2, 6.3, 6.4, 6.5, 6.6, 6.7****[2]). These boundaries show a reasonable correlation with the local nannofossil zonation used by Petrobrás (**Table 6.1**), based on Richter (1985) and which has been correlated with Martini (1971). Correlation of the local nannofossil zones with the chronostratigraphic chart of Haq et al. (1987) (after Martini, 1971) was made using correlations from the biostratigraphic chart of the Campos Basin (Beurlen et al., 1988). However, there are several points where the nannofossil zones do not coincide (e. g. zone T. Carinatus) (see **Fig. 6.8**).

The estimated time span involved for deposition of these sequences varies from less than 1 to about 3 million years, but this also depends on the degree of definition. This indicates the need for a better "tuning" between these biostratigraphic charts for detailed work.

The sequences **1, 2,** and **3** are those that embody the sand-rich turbidite deposits, that are the main concern for this study. Consequently, these sequences will receive more attention than the younger ones (**4, 5, 6, 7,** and **8**) in the following descriptions. Five main turbidite systems or "fans", locally up to eight (**a-h**), were identified within sequences 1, 2 and 3 (**Fig. 6.8**). The turbidite were interpreted as being deposited respectively during the zones N-530 (**a**), N-540 (**b**), N-545 (**c** and **d**)/N-550 (**e**), N-560 (**f**) and N-570 (**g** and **h**).

---

[2] **These figures are located in the back cover pocket. They consists of uninterpreted seismic sections and sketches of the main reflectors, with their termination patterns and the sequence boundaries. For better visualization of the distribution of the figures see the location map in Fig. 4.1, also in the pocket.

TABLE 6.1

Nannofossil Biozone		Series		Sequences
Local - modified from Richter (1985)	Martini (1971)			
G. oceanica (N-720)	NN-21 NN-20 NN-19	Holocene-Pleistocene		8
D. brouweri (N-670)	NN-18 NN-17 NN-16	Upper	MIOCENE	**********
R. pseudoumbilica (N-650)	NN-15 NN-14 NN-13 NN-12	Upper	MIOCENE	7c
D. quinqueramus (N-640)	NN-11 NN-10	Upper	MIOCENE	7b
D. hamatus/ Micrantholithus ssp. (N-630)	NN-9 NN-8 NN-7	Upper / Middle	MIOCENE	7a
C. floridanus (N-590)	NN-6	Middle	MIOCENE	********** c_____ 6 b_____ a
S. heteromorphus (N-580)	NN-5	Middle	MIOCENE	********** 5 b_____ a
H. ampliaperta (N-570)	NN- 4	Middle / Lower	MIOCENE	** 4 ******* ********** 3 b_____ a
S. belemnos (N-560)	NN- 3	Lower	MIOCENE	********** 2 **********
T. carinatus (N-550)	NN- 2	Lower	MIOCENE	Basal 1 c
H. recta (N-545)	NN- 1	Lower	MIOCENE	Seq. 1 b --------- 1 a
S. ciperoensis (N-540)	NP-25	U.	OLIGOCENE	**********
S. predistentus (N-530)	NP-24	Lower	OLIGOCENE	---------- Blue Marker ----------
S. pseudoradians (N-520)	NP-23	Lower	OLIGOCENE	
R. umbilica (N-510)	NP-22 NP-21	Lower	OLIGOCENE	

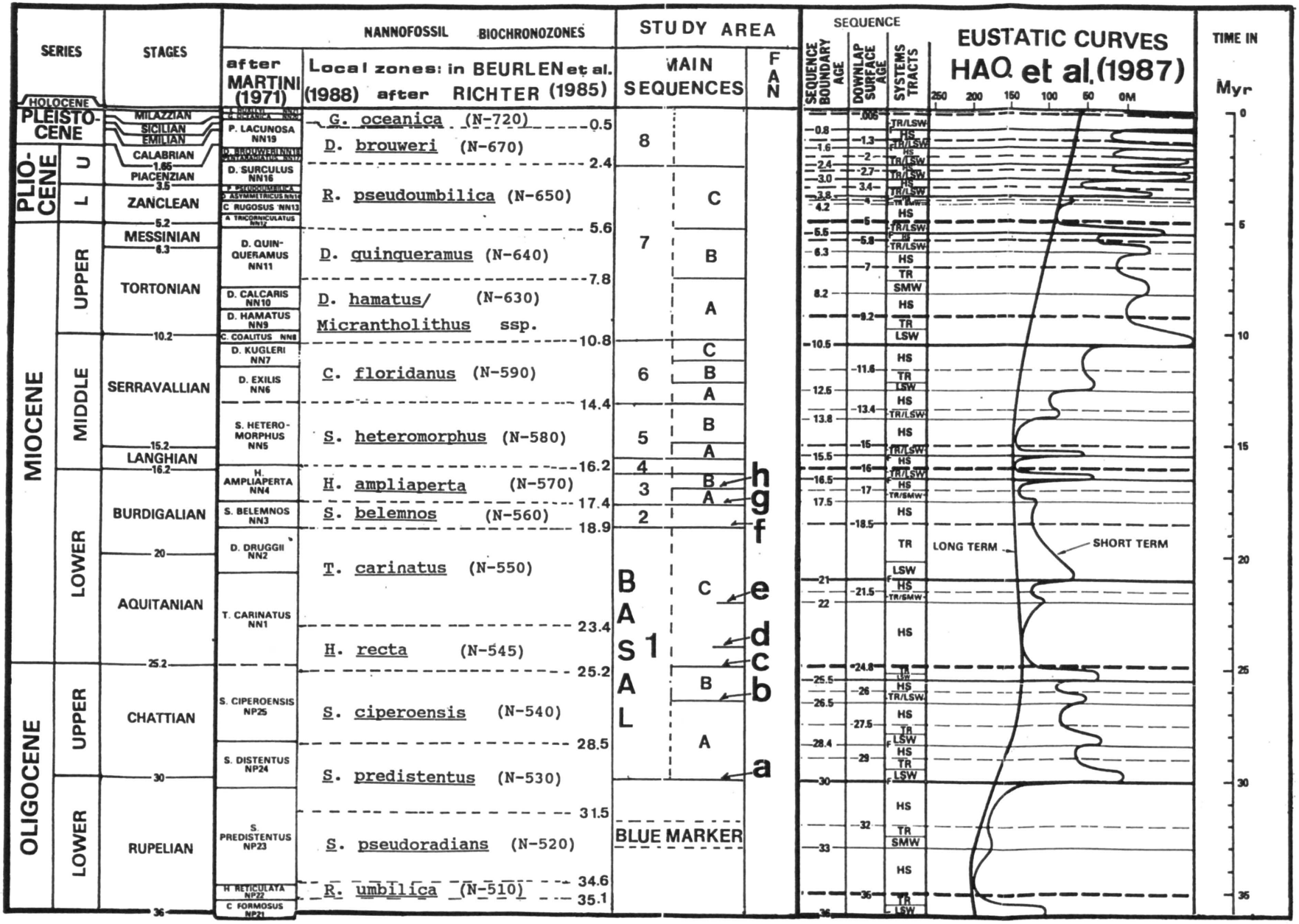


Fig. 6.8 - Correlation of the local nannofossil zones (Richter, 1985; and Beurlen, 1988) with Haq et al. (1987) showing the distribution in time of the turbidite fans and the depositional sequences.

The thick (~50 m) turbidite sandstones appear in seismic sections as high amplitude reflectors. This is due to their low sonic velocity compared to the adjacent marlstones, which have high sonic velocity, resulting in a good impedance contrast. This contrast is amplified when sandstones are hydrocarbon bearing (see **sections U-U', X-X'** near wells 342 and 219).

Tentative correlations of the age of the sequences and their turbidite systems with eustatic curves of Haq et al. (1987) are shown in **Fig. 6.8.** There is a remarkable coincidence between the first occurrence of the turbidites of Sequence **1a** and the major sea-level fall of 30 Myr (Chattian) shown on their chart (**Fig. 6.8**). However, the other turbidite systems of sequences (**1b, 1c, 2, 3a** and 3b) do not show the same relationship with other lowstands of sea level on their chart. These correlations are subjected to the resolution limitations of the available nannofossil dating (i.e. 1.2 to 4.5 Myr). The time span of the local nannofossil zones used is far greater than would be required (i.e. <500 Kyr) for an accurate correlation between the occurrence of these turbidite events and the short term sea level changes proposed by Haq et al. (1987) (see **Fig. 6.8**). Furthermore, there is no absolute dating available in the studied interval and only palaeontological dating could be used to calibrate such correlations. An auxiliary method using Climatic Cycles can also be used to improve these correlations (see Chapter 7).

6.2.1 DEPOSITIONAL SEQUENCE 1 OR BASAL SEQUENCE

Depositional Sequence **1** or the "Basal Sequence" has a wedge-like seismic profile with a tabular-lens shaped toe in the more offshore areas, especially in the northern sector of the studied area (see **section T-T', Fig. 6.2**). Its basal contact is erosional (**Fig. 5.11, sections T-T', U-U', Y-Y'**) and is probably a Type 1[3] sequence boundary according Van

[3] Type 1 sequence boundary are characterized by subaerial exposure and concurrent subaerial erosion associated with stream rejuvenation, a basinward shift of facies, a downward shift in coastal onlap, and onlap of overlying strata (Van Wagoner et al., 1988).

Wagoner et al., (1988). The internal reflections show a sigmoidal pattern. However, because the studied area is located further offshore the majority seismic sections available show mainly the thin distal portions of such a sigmoidal pattern (sections **T-T'**, **U-U'**, **V-V'**). However, in a seismic section closer to coastline (section **X-X'**), in the southern part of the area, this sequence is relatively thicker due to its relatively more proximal position and the existence of a growth fault dipping shorewards.

The age of this sequence has been estimated using local nannofossil zonation (Richter, 1985) as varying from the middle (?) of the N-530 to the middle (?) of the N-560 zones (**Table 6.1** and **Fig. 6.8**).

Usually the "Basal Sequence" is represented in seismic sections only by 0.1 to 0.2 seconds and in the study area its corresponding stratigraphic interval consists mainly of sand-rich turbidites (or basin-floor fans[4]) and hemipelagites. The seismic facies patterns of the thicker sandstones are characterized by hummocky clinoforms or high amplitude and relatively continuous reflectors. The hemipelagites are characterized by a low accumulation rate (**chapters 5** and **7**) and were deposited during non-turbiditic periods. Stratigraphic intervals such as this that incorporate slowly accumulating sediments (hemipelagites), laid down in the distal parts of both the transgressive and the highstand[5] deposits, are called condensed sections[6] (Loutit et al., 1988). The chalks and marlstone beds that form the Blue Marker represent the most important condensed section in the Oligocene-Miocene of the study area (see **Chapter 5** for details of its composition). The condensed sections are characterized by high amplitude and continuous seismic reflectors (e.g. the Blue Marker). Sequences 1

---

[4]The basin-floor fan is characterized by deposition of submarine fans on the lower slope or basin floor (Wagoner et al., 1988).

[5]Vail et al. (1977) and Wagoner et al. (1988).

[6]Condensed sections are thin marine stratigraphic units consisting of pelagic to hemipelagic sediments characterized by very low-sedimentation rates. They are areally most extensive at the time of maximum regional transgression of the shore line (Loutit et al., 1988).

and 2 in the study area are thinner than the younger ones. This is the result of the progradational character of the Miocene sediments and the consequent increase in the accumulation rates progressively further offshore.

The subdivision of Sequence 1 into minor sequences (1a, 1b, and 1c), because of its general reduced thickness, was made using the base of the sandstones (Type 1 sequence boundary) plus downlaps and onlaps in the seismic sections, whenever they existed (see sections T-T' and X-X'). In those places where there was no sandstone-body their separation was made using their correlative horizons and condensed sections (see sections T-T', Y-Y', near well 367). Sometimes the subdivision into sequences 1a, 1b and 1c can be made (sections T-T', U-U', X-X' and Y-Y'), and their estimated ages vary respectively between the local nannofossil zones N-530/N-540, N-540/N-545 and N-545/N-560 (Table 6.1 and Fig. 6.8). However in other places, it is difficult or even impossible to make such subdivision either due to amalgamated or reduced thicknesses falling below the seismic resolution (sections T-T', U-U', Y-Y', Z-Z').
In spite of these limitations three main turbidite systems (a, b and c/d/e) were identified in Sequence 1 using calibrated wireline logs (i.e electrofacies and palaeotology) and seismic data (Fig. 6.8).

6.2.1.1 SEQUENCES 1a AND 1b

There were two main depositional sites for the sand-rich fans a (N-530) and b (N-540), in sequence 1 (Fig. 6.9). The most important depositional site is in the region of wells 342, 355, 360 and 367 (85 m thick) and the other in well 370 (40 m thick) (see stratigraphic section A-B, Fig. 5.11 in Chapter 5 and figures 6.2, and 6.9). The deposition of these sand-rich turbidites appears to have been controlled by the inflection of the topographic gradient associated with the fault zone near wells 316, 342 and 335, respectively in sections T-T', U-U', V-V'). The present difference in depth between wells 316 and 333, using the Blue Marker as a datum, is 170 m, reflecting the influence

of this fault zone during the deposition of these sandstones (for more details compare the section **T - T'** with the stratigraphic section **A-B** of the Fig. 11 in **Chapter 5**). The turbidite systems **a** and **b** become thicker further offshore and pinch out (onlap) towards onshore regions off wells 316, 305 and 335 (respectively in sections **T-T', U-U', V-V'**). The turbidite systems from sequence **1c** (**c/d/e**) are better developed in wells 305, 355, 335 and 333 (**Fig. 5.11, 5.12** and **5.13**), indicating that the sequence **1c** shows a retrogradational relationship with sequences **1a** and **1b**. This relationship can also be observed in the sandstone isolith maps (**Fig. 6.9** and **6.10**).

The turbidite sandstones in the northernmost-part of the studied area do not show such tectonic control. They have a general geometry similar to a mound and pinch out towards the north-end of the section, beyond well 370 (section **Z - Z'** and **Fig. 6.9**). However, additional seismic sections are needed to better define their depositional controllers. In the southern sector of the area there was no significant development of sandstones from sequences **1a** and **1b** and those found in wells 344 and 382 are probably related to another depositional system to the south of the study area (**Fig. 6.9**).

6.2.1.2 SEQUENCE 1c

Sequence **1c** is composed of two main turbidite systems (**c** and **d**), both within the nannofossil zone N-545 and one minor (**e**) in zone N-550. The latter is represented in the north by Channel-Margin/Over bank Electrofacies Association (IIb) in well AB-1 (see section **G-H, Fig 5.14**), but appears to be more important in the southern sector of the studied area (section **I-J, Fig. 5.16**). Nevertheless, more detailed palaeontological studies are needed to confirm these correlations particularly with respect to system **e**. Frequently the distinction between the sandstones of the turbidite systems **c**, **d**, and **e** is rather difficult due to amalgamation, especially in those regions dominated by either the Channel-Fill (II), Channel-Lobe Transition (III)

or Proximal Lobes (IV) electrofacies association (see stratigraphic section **A-B, G-H** and **I-J, Fig. 5.11, 5.14** and **5.16**). For practical reasons the thicknesses of these sandstones have been combined on the isolith maps (**Fig. 6.10A**).

The sandstones of Sequence **1c** in the northern sector of the area are closer to the coastline than those of sequences **1a** and **1b** (**Fig. 6.10A**), where they are characterized mainly by the Channel-Fill Electrofacies Association (II) (stratigraphic sections **A-B, G-H**, respectively **Fig. 5.11** and **5.14**). Their main depocentre has also been shifted towards the northwest relative to the previous systems (i.e. well 355 with 75 m thick). The feeders (channels) of these sandstones can be traced towards the east where they are more frequently associated with diamictites, gravelly sandstones and thin-bedded turbidites (wells 329, 297 330, see also **figures 5.11** and **5.14**). However, in the strike-oriented seismic sections passing through this region no major deep incisions (channels) can be seen (**Fig. 6.11 A** and **B**). The sandstones can be traced in the strike-oriented seismic sections for about 0.5 to 2 Km. The estimated topographic relief from the base of the sandstone up to the channel margins after compaction is about 50 m.

In the northernmost part of the area strike-oriented sections (**Z -Z'**) show a channel-fill feature of about 3 Km wide that has been infilled with sandstones of Sequence **1c** which are at least 35 m thick in well 366. However, the most important deposition of sands in Sequence **1c** occurred towards the south, where wells 325 and 357 penetrated 112 m and 125 m of amalgamated sandstones, respectively (**Fig. 6.10A**).

Sonoki (1987) identified 4 main turbidite bodies within a sequence that completely infilled the Enchova Canyon in the southern part of Campos Basin. This sequence was within zone N-545 and thus coincides with the period which Sequence **1c** was deposited.

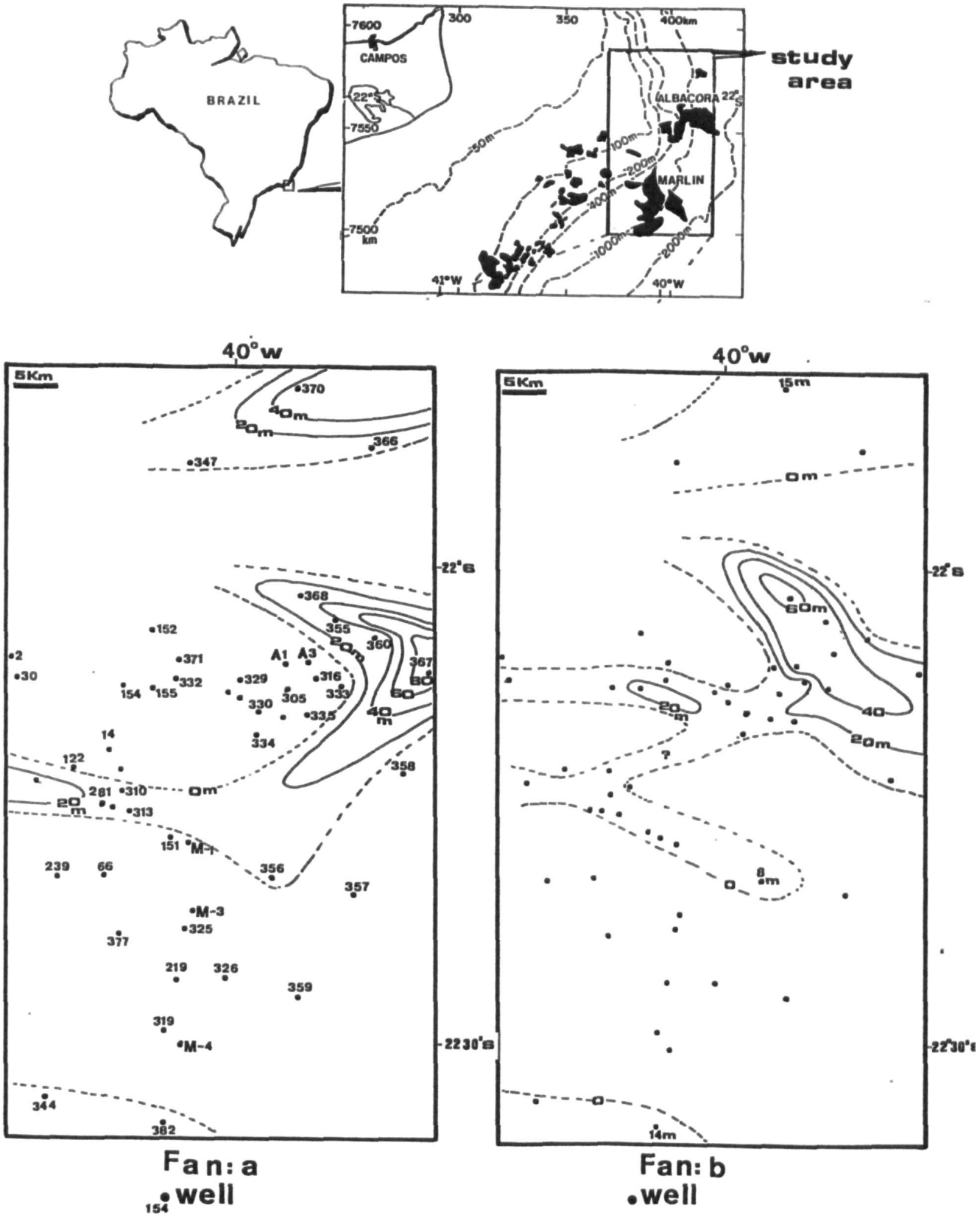


Fig. 6.9 - Sandstone isoliths of the fans a and b.

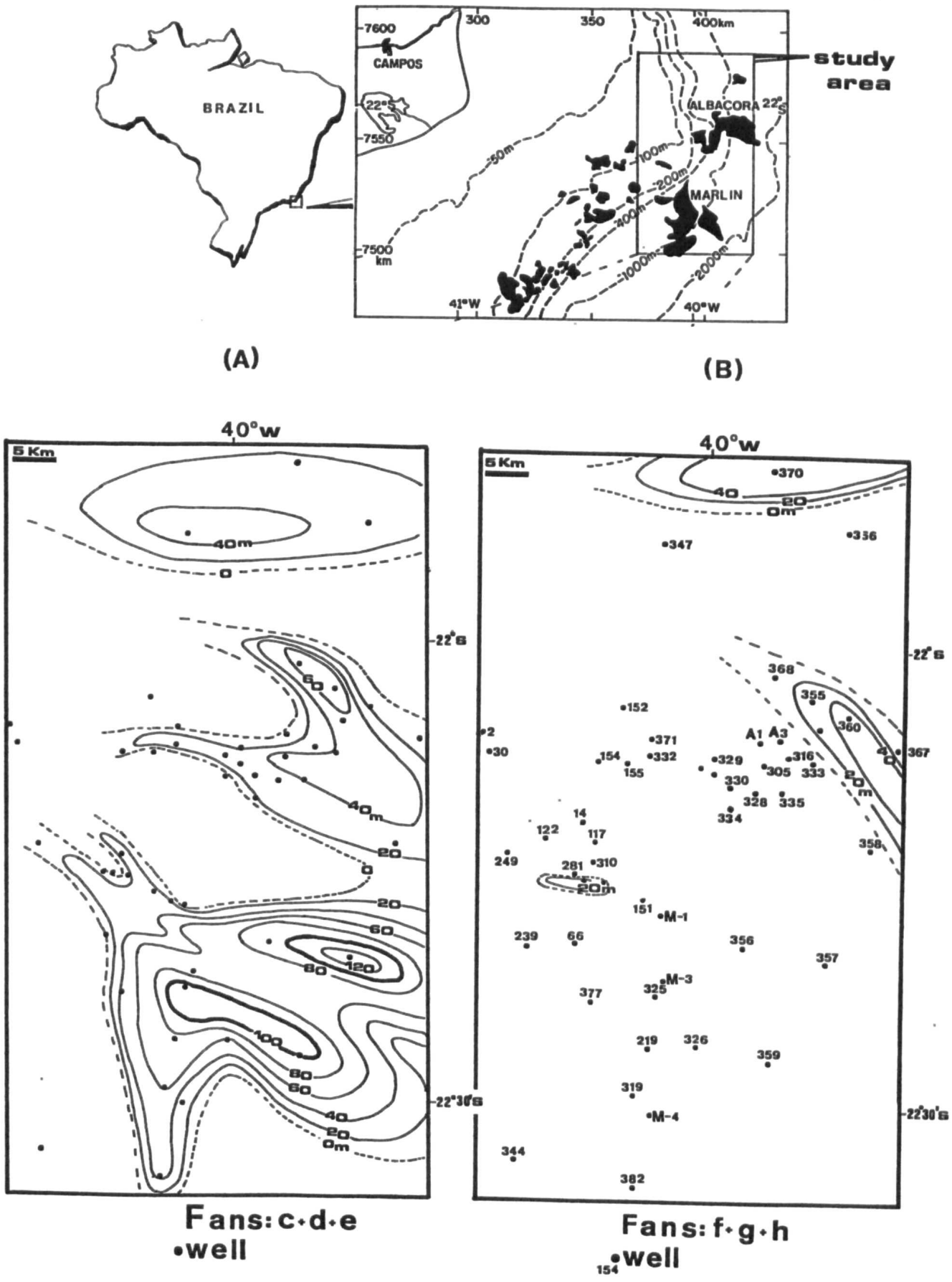
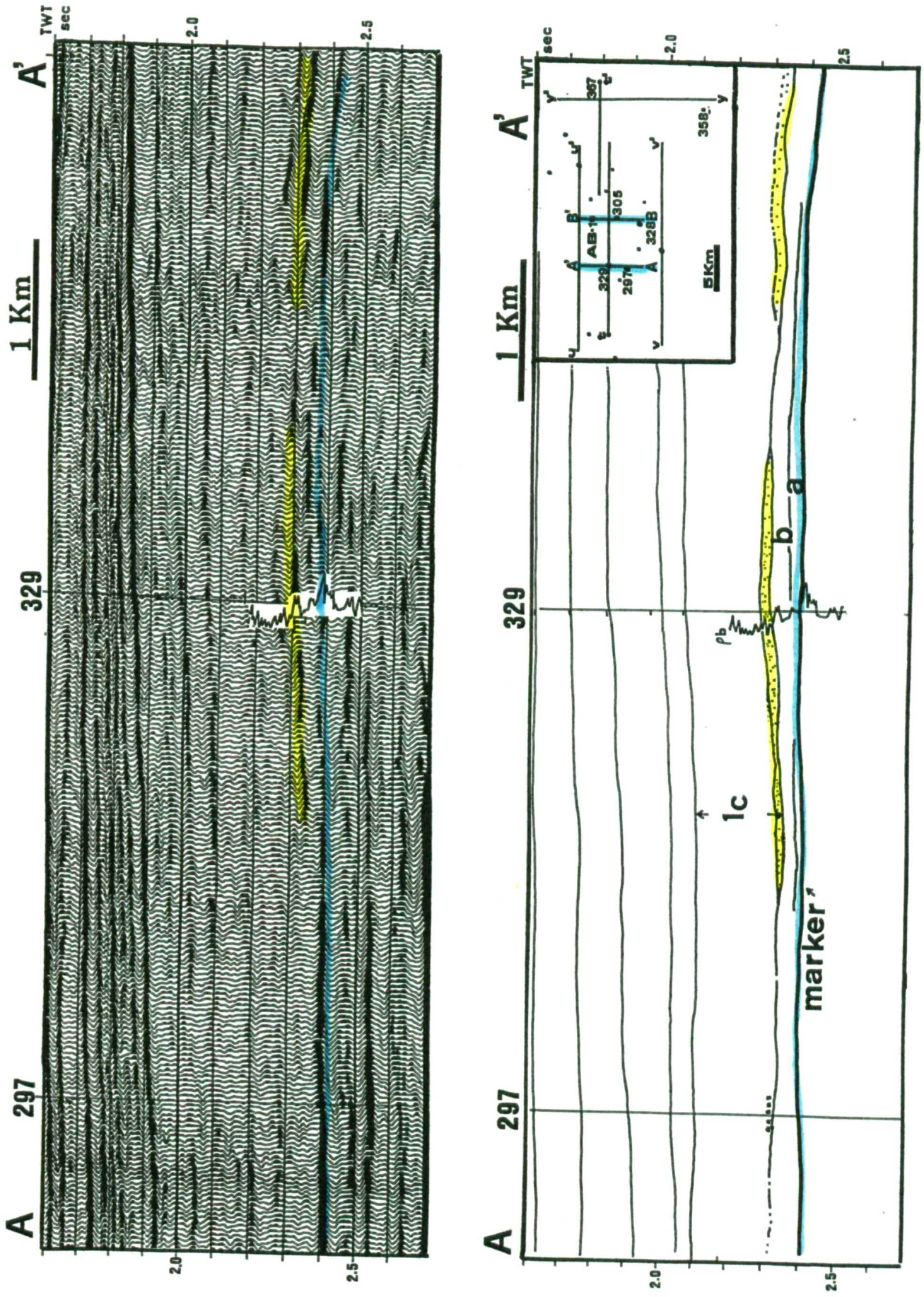


Fig. 6.10 - Sandstone isoliths of the fans c+d+e in (A), and f+g+h in (B).



Seismic section A.

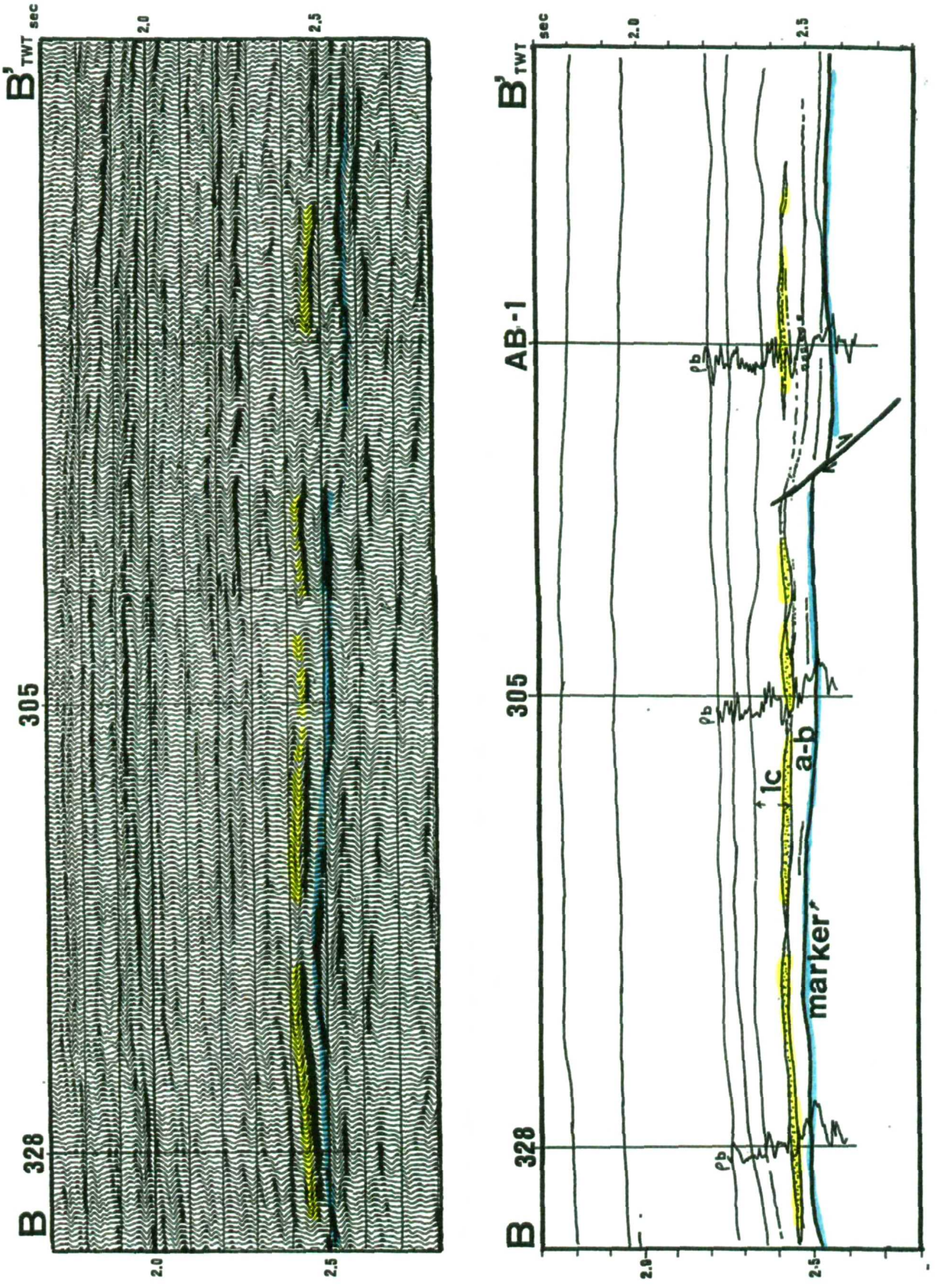


Fig. 6.11 - Strike-oriented seismic sections (A and B) in the channelized area and their interpretations.

Sequence **1c** is the most important sand-rich turbidite-bearing sequence in the studied area and this is probably also true for other parts of the Campos Basin. However, Sequence **1a** is potentially equally important, especially in areas further offshore.

6.2.2 DEPOSITIONAL SEQUENCE 2

Depositional Sequence **2** consists of a very thin (~50-100 m) wedge in the toe of which turbidites have been deposited. It is differentiated by the presence of downlaps over the sequence **1** and downlaps of the overlying sequence **3** (sections **T-T'**, **X-X'**). Locally its upper boundary is characterized by erosional truncations (sections **T-T'**, **U-U'**, **V-V'**, respectively shorewards from wells 329, 342, and 334). The occurrence of sandstones in this unit is restricted to the area around wells 360 and 367 where they have thicknesses of 25 m and 7 m, respectively. The age of this sequence varies from the end of zone N-550 and the beginning of zone N-570. Because of its small thickness it is very difficult to trace into deeper water, but it can be easily identified in more onshore areas (see section **X-X'**).

The sandstones deposited in this sequence have been assigned to turbidite system **f** (see **figures 5.11** and **5.12** in the Chapter 5). Coincidently these sandstones have also been found together with turbidite systems **g** and **h** of Sequence **3**. Hence their total thickness and occurrence are presented together in the same isolith map (**Fig. 6.10 B**).

6.2.3 DEPOSITIONAL SEQUENCE 3

Depositional Sequence **3** was deposited within the nannofossil zone N-570 (Fig. 6.8). It has a lens-like shape and in its thicker parts can be subdivided into sequences **3a** and **3b**, based on seismic and stratigraphic characteristics. The basal boundaries of these sequences are characterized by well defined downlap and onlap terminations of the seismic reflectors (see sections **U - U'**, **V-V'**, respectively **figures 6.3, 6.4**). The geometry and reflection patterns are similar

to the pattern of a lowstand wedge[7] (Vail, 1987 and 1988; and Posamentier et al., 1988), see **Fig. 6.12**. The older sequences do not have such a characteristic geometry probably because, as mentioned by Gamboa et al. (1986) and observed in regional seismic lines out side of the studied area, the transition from the shelf into the slope was characterized by a gentle ramp rather than a steep shelf break. As a result the corresponding lowstand wedge deposits were distributed more evenly and prograded and aggraded as a characteristic lowstand wedge associated with a shelf break (compare **Fig. 6.12** with section **T-T'**). The higher accumulation rates of this sequence, compared with sequences **1** and **2**, was probably a very important factor in controlling its geometry. The same also occurred in the younger depositional sequences. However, further regional sequence stratigraphic studies are needed to confirm those geometric differences.

Two turbidite sandstone bodies occur in the toe of sequences **3a** and **3b**. They are relatively thin (16 m and 12 m in well 342) and have been defined as turbidite systems **g** and **h** (see **Fig. 5.12** in Chapter 5). They are represented in seismic sections as high amplitude onlapping reflectors on the basal boundaries of these sequences (**3a** and **3b**) and are overlain by downlapping seismic reflectors. However, frequently these sandstones are represented by only one reflector because their individual thicknesses are below the seismic resolution (section **U-U'**), or because they occur amalgamated, as seen in well 355 (**Fig. 5.12**).

There are two main depositional sites for the sandstones of depositional sequences **2**, **3a** and **3b**: one is in the region of the wells 355, 360, 367 and the other in the far north (well 370). Locally, in the eastern part of the middle of the area (well 313) turbidite sandstones belonging to these sequences have also been found but they appear to be areally restricted (**Fig. 6.10 B**).

---

[7] A lowstand wedge is characterized on the shelf by incised-valley fill, which commonly onlaps onto the sequence boundary, and on the slope by progradational fill with wedge geometry overlying and commonly downlapping onto the basin-floor fan or the slope fan. It is composed of progradational to aggradational parasequence sets (Van Wagoner et al., 1988).

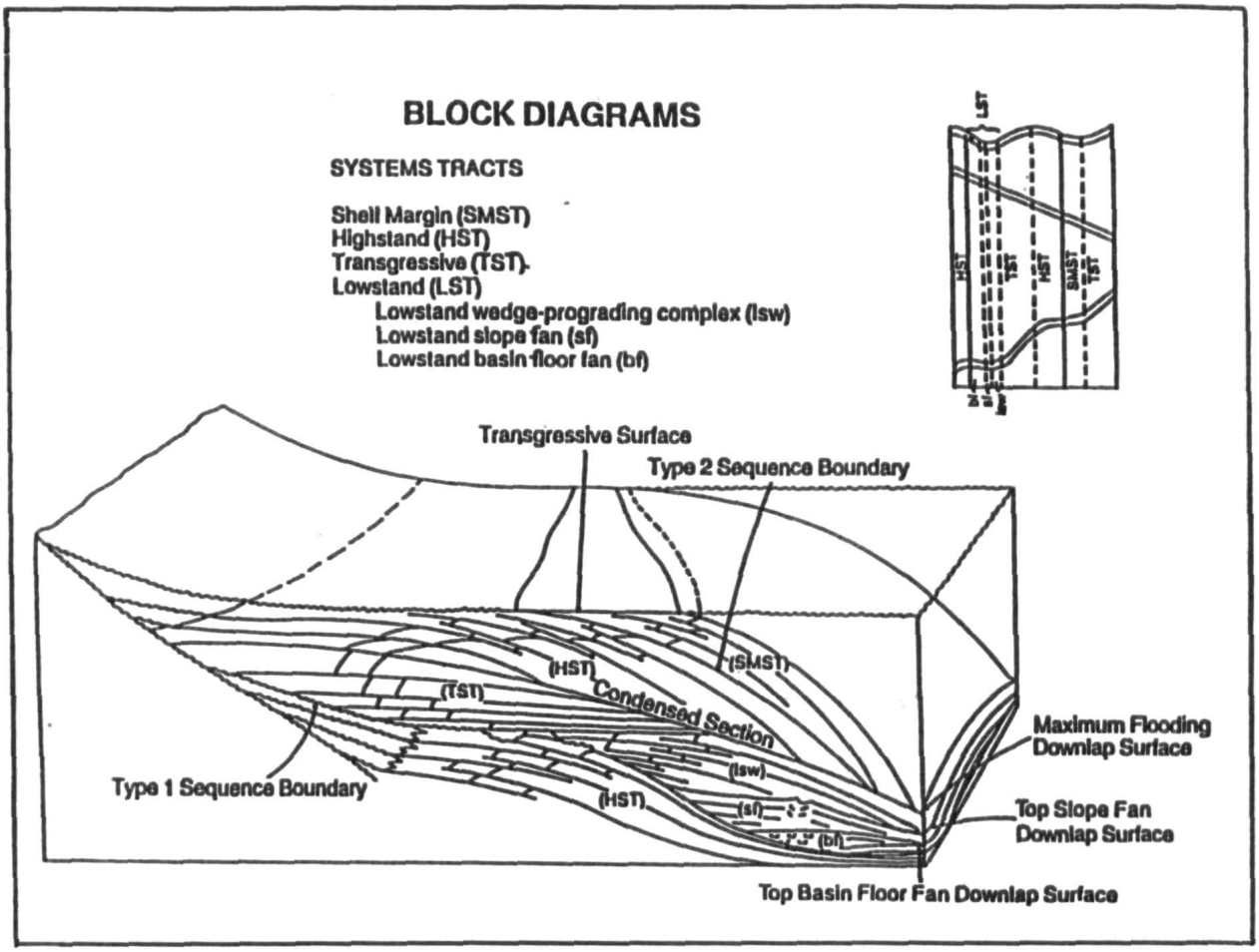


Fig. 6.12 Systems tracts deposited in a basin with a shelf break (after Vail 1987).

6.2.4 DEPOSITIONAL SEQUENCES 4 TO 8

Sequences 4 to 8 are marked by a continuous progradational character up to the end of the Pliocene (section T-T', Fig. 6.2). This pattern reflects that the rate of thermal subsidence was exceeded by the rate of sediment accumulation. There is no record of sand-rich turbidites in these sequences in the study area.

The sequence 4 has a general tabular shape shorewards with some evidence of erosional truncation at its top and onlap at its base (T-T', U-U', V-V'). Towards further offshore it shows a lenticular shape with downlaps, while its top is marked by the downlaps of the base of Sequence 5 (section V-V').

The Sequence 5 has similar features to Sequence 4, however thicker, what allows it subdivision locally into two sequences **5a** and **5b** based on downlaps and onlaps (see section **V-V'**).

The Sequence 6, shorewards, is bounded at its base by downlaps over an erosional surface (**T-T'**, near well 329) and further offshore by downlaps, where it reaches maximum thicknesses of ~0.5 seconds (**T-T'**, between wells 333 and 367). This Sequence 6 can be divided into three others (**6a**, **6b** and **6c**) in this thicker region, based on their reflection patterns (see **T-T'**, **U-U'**, **V-V'**, **Y-Y'**).

Sequence 7 has similar characteristics to those of Sequence 6. However, its basal boundary is characterized by a widespread erosional surface clearly seen in all seismic sections. It can also be locally divided into three sequences (**7a**, **7b**, and **7c**) using downlap, onlap and erosional truncations (see **T-T'**, **Z-Z'**).

Sequence 8 is also characterized by a widespread erosional base and has been considerably displaced shorewards in relation to the others, but has kept a similar progradational profile to those from the Sequence 4 to the 7 (see **T-T'**). At its base localised incisions can also be identified (see sections **U-U'**, **V-V'**, **Z-Z'**). In the southern sector of the studied area, this uppermost sequence is thinner indicating preferential sedimentation towards the north during this period (see sections **X - X'**, **Y-Y'**).

The boundaries of these upper sequences coincide roughly with those of the nannofossil zones (**Fig 6.8**). The non-occurrence or non-identification of zones in some wells can be easily explained when the depositional sequences are identified and correlated between such sites. The absence of particular zones indicates the pinch-out of a sequence or a very reduced thickness.

It is possible to identify two main incisions associated with the boundaries of these upper sequences, one at the base of the Sequence 4 and another at the base of the Sequence 7b, respectively deposited in the upper part of the zone N-570 and in the zone N-640 (section **Z - Z'**, **Fig. 6.7**).

However, towards the south only a minor incision can be seen at the base of the Sequence 7a, within zone N-630 (Fig.6.6).

The predictive model (Fig. 6.12) proposed by Vail (1987) and Posamentier et al. (1988) appears to be consistent with the results obtained in this study. This is particulary well illustrated by Sequence 3, where the sand-rich turbidites, or basin floor fans in their terminology, occur at the base of a progradational seismic configuration (see section U-U'). As the upper sequences (4 to 8) show a general progradational pattern, but do not have sand-rich turbidites in the study area, it would be expected from this model to find them in further offshore regions. However to confirm this additional seismic data from further offshore regions are needed.

6.3 DISCUSSION: MODERN AND ANCIENT SUBMARINE ENVIRONMENTS

Comparisons with examples from modern and ancient submarine sedimentary environments have been made to better understand the seismic facies characteristics, distribution and related sedimentary facies of the studied area.

Firstly, data from the study area will be compared with similar modern sedimentary sequences from the southeast Brazilian continental margin and those of the Amazon, Mississippi and Indus fans. Secondly, comparisons will also be made with ancient sand-rich fans described from the subsurface, Tertiary North Sea, and outcrops, of the Eocene Jaizkibel Fan, Northern Spain.

6.3.1 MODERN SUBMARINE ENVIRONMENTS AND FANS

6.3.1.1 SOUTHERN BRAZILIAN CONTINENTAL MARGIN

Two types of modern slopes have been identified in the southeast Brazilian continental margin between the Abrollos Bank and the Cabo Frio. There is a steep one associated with a narrow shelf and with several ravinements. The other, towards the south, is characterized by a progradational slope and associated with the Paraíba do Sul delta (Brehme, 1984).

In the study area, the modern continental slope is characterized by a convex upward profile with an average gradient of 1:36, cut by several canyons. The base of the slope occurs at water depth of about 2,000 m (see **Fig. 6.13** and sections **T-T', Z-Z'**). Brehme (1984) related these modern canyons to migratory stages of the Paraíba do Sul River (**Fig. 6.13**).

The largest canyons are associated with structural lows and faults generated by the movement of the underlying Aptian salt (see **Fig. 6.7** and **Fig. 3.4**). However, the other canyons and channels do not show any apparent connection with these structural features seen in the strike-oriented seismic sections (see section **Fig. 6.7**, near wells 366 and 370). The sediments transported through these canyons were responsible for the development of the modern Paraíba do Sul Fan (**Fig. 6.13**).

Brehme (1984) identified two major deep-sea channels, one in the north and the other in the south, whose extensions have been mapped for more than 1,000 Km. The southern one formed during the Oligocene, while the northern one has been eroded only since the Oligocene. The erosional event responsible for the formation of these Oligocene deep-sea channels described by Brehme (1984) was probably that responsible for the formation of the Oligocene canyons mapped by Gamboa et al. (1986) (**Fig. 6.14**). If so the gravity flows and turbidity currents assumed responsible for such erosions must have travelled very log distances (>1,000 m, see **Fig. 6.13**). This erosional event in the study area possibly could be correlated with the basal boundary of Sequence **1**, which has been interpreted as a Type 1 sequence boundary (section 6.2.1). The large volumes of sand-rich turbidites deposited within Sequence **1** (fans **a, b, c/d/e**) can be interpreted as the result of the coarse-grained sedimentary load being deposited during the passage of these turbidity current (**Fig. 6.9, 6.10, 6.13**).

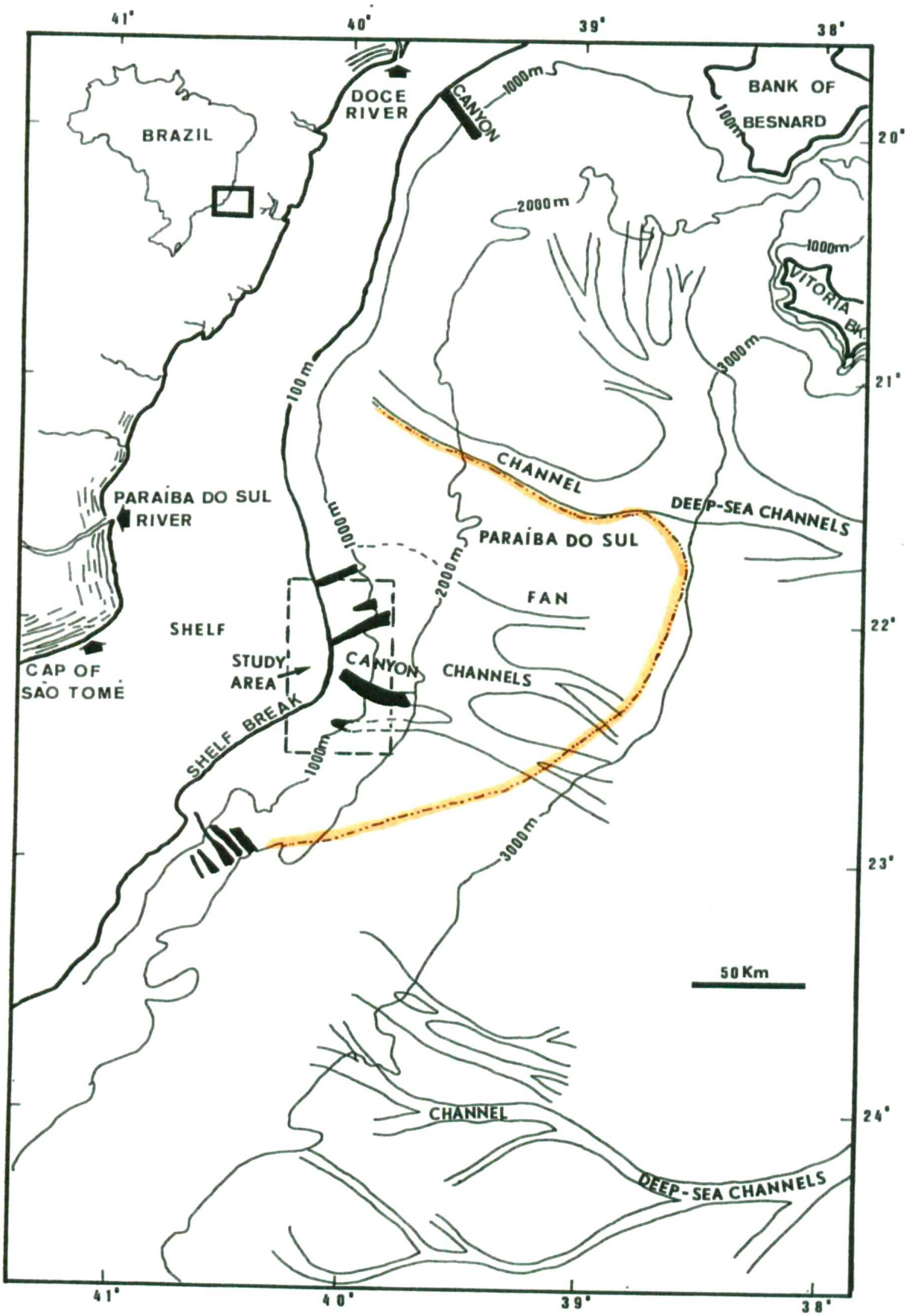


Fig. 6.13 Physiography of the southeast part of the Brazilian continental margin (modified from Brehme, 1984).

Four kinds of channels were identified in the sequences of the study area, two in the Basal Sequence 1 and two in the upper sequences. One of the two types of channels in the Basal Sequence 1 is represented by small to medium channels with relief of about 50 m of relief and 0.5 - 1.5 Km wide occurring in relatively onshore areas. They are associated with Diamictites (DMT), Gravelly Sandstones (GvS) electrofacies and are poorly defined in seismic sections (**Fig. 6.11**). The other type is characterized by larger (50-100 m relief x 1 - 2 Km wide) channels which occur further offshore. They are associated with Amalgamated Sandstones Electrofacies (AmS) and characterized by weak inclined and discontinuous seismic reflectors (sections Y-Y', Z-Z').

The two types of channels in the upper sequences are better developed probably because of higher sedimentation rates during the Middle/Upper Miocene and less compaction. One type is characterized by erosional features 2-4 km wide and 50-250 m deep whose infill is distinguished by slightly inclined reflectors that gradually become horizontal, parallel and more continuous upwards. The other type is characterized by narrower channels (1 Km wide and about 150-200 m deep) infilled with a few weak and random reflections at the base and slightly inclined reflectors towards the top (**Fig. 6.7**). Similar seismic features can be observed in modern channels of the study area, where one type is characterized by an unfilled box-like shape and the other by a "V" shape in cross-section. Both channels have smooth margins due to erosion and aggradation (**Fig. 6.7**).

According to Brehme (1984) these modern canyons have lengths between 10-30 Km. Further offshore of the studied area they become a large shallow erosional feature which develops into short deep-sea channels (see **Fig. 6.13**).

Unfortunately, the modern Paraíba do Sul fan occurs offshore of the study area and no direct comparison with the seismic sections could be made, because of the lack of seismic sections across the modern fan. However, such comparisons could be made with other well studied modern fans.

6.3.1.2 MODERN FANS

Studies of the modern Amazon, Indus and Mississippi fans show that there is a clear relationship between the sea floor gradient and the sedimentological features relating to the deposition of the deep-sea deposits.

Upper- and middle-fans, as described by many authors (Bouma & Coleman, 1985; Damuth et al., 1983; Kolla & Coumes, 1987; Appi et al., 1987; and Shanmugan et al., 1988), are characterized by morphological features of several hundred meters. They are the result of aggradation of large channel-levee complexes.

The lower fan has a smooth relief with channels and levees of relatively small dimensions (5-30 m) and an overall low gradient. It is characterized by being a sand-rich region and is distinguished by its parallel reflectors. The sands found in the lower fan region of the Mississippi fan were called "sand sheets" by O'Connell (1985) and are characterized by several discontinuous and weak seismic reflectors, resembling small lateral migrating channels. Shanmugan et al. (1988) concluded that the lower Mississippi Fan is characterized by relatively small channels with lithofacies similar to those defined by Mutti & Ricci Lucchi (1975) as A, B, and F facies, but there is no depositional lobe facies (C and D Facies of Mutti & Ricci Lucchi, 1975).

A seismic section along the strike of the Indus fan, presented by Kolla & Coumes (1987), shows a clear progradation of the channel-levee system over the middle/lower fan and its contrasting seismic properties. In the Amazon and the Mississippi fans the same features of similar size are present.

The Oligocene-Recent succession in the study area shows a similar general progradational pattern to the Indus Fan, but conversely it does not show thick levee deposits. A possible explanation for the lack of thick levee deposits could be both a higher sand:mud ratio in the wave-dominated platform sediments of the Campos Basin and the absence of a major river such as the Indus or the Amazon. A modern fan with similar high energy wave-dominated shelf environments

is the Navy Fan, offshore the western coast of North America. It is characterized by a very high sand:mud and by shallow channels on the "suprafan" depositional lobe (Normark, 1970). Unfortunately, because of the lack of seismic sections on the Navy Fan reported in the literature no direct comparisons could be made. Conversely, there are good seismic data sets published for the Mississippi and the Indus fans, but they also have unique sizes and very high sedimentation rates. Consequently, their characteristics must only be used with care when comparing with smaller fans.

Sequences **1**, **2** and **3** show similar features to those observed by O'Connell (1985) and Shanmugan et al. (1988). The vertical facies sequence of the turbidites show characteristics that resemble more a channel-fill (i.e. fining and thinning upward or "box-like" with fining upward at the top, see **figures 5.11** to **5.16**) rather than a depositional lobe (i.e. coarsening and thickening upward). This can be partially explained by the relative "proximal" position of the analyzed wells, which are characterized by thick amalgamated sandstones deposited in shallow channels, where the Channel-Lobe Transition Electrofacies (III) grades laterally into a more continuous and probably non-channelized system (see also sections **T-T'**, **Y-Y'**, **Z-Z'**). As can be seen on the sandstone isolith map for Sequence **1a**, more turbidite sandstones would be expected further offshore areas associated with the "depositional lobes" (**Fig. 6.9A**).

In spite of the areal limitations of this study and the absence of seismic sections on the modern Paraíba do Sul Fan, it is possible to use the general modern slope profile and relate this configuration to older profiles observed in sequences such as Sequence **3**. In this sequence the turbidite systems (**g** and **h**) have been deposited at the base of the slope, which is characterized by a decrease in the gradient (section **U-U'**). This slope/basin-floor fan relationship is reminiscent of the model of Vail (1987) and can be used as a predictive model for sequences with similar features. As the younger sequences (**4** to **8**) have a similar progradational

character to that of the sequence 3 their probably basin-floor fans would be expected to occur progressively further offshore (see section T-T'). This can be exemplified with the modern Paraíba do Sul Fan which occurs further offshore of the study area (**Fig. 6.13**).

6.3.2 ANCIENT SUBMARINE FANS

The Palaeogene fans of the North Sea and the Eocene Jaizkibel Fan, Spain are sand-rich, and as such provide interesting subsurface and outcrop comparison with the Oligocene-Lower Miocene sand-rich turbidites systems.

The Early Tertiary North Sea fan systems consist of a large number of thick (30-300 m) amalgamated siliciclastic turbidites frequently with "box-like" wireline log features similar to the Amalgamated Sandstones Electrofacies (AmS) or Facies B of Mutti & Ricci Lucchi (1975).

The Oligocene-Lower Miocene fans of the Campos Basin have many characteristics in common with those of the North Sea Tertiary sands: high sand:mud ratios, similar sedimentary facies (i.e. thick amalgamated sandstones), shifting of the depositional site of the fans, the temporary trap of sands in a wave-dominated platform, the presence of multiple source points for the fans (**Fig. 6.16**), the uplift of the Serra do Mar Mountains during the Tertiary. Additionally, the lower datum for the Early Palaeocene sediments of the North Sea is the top of the Cretaceous chalk, which can be traced as a seismic marker throughout the North Sea (Stewart, 1987), reminiscent of the Blue Marker relationship in the Campos Basin.

Cox (1984) considered that some Early Tertiary fans of the North Sea were only active for short specific times, while others were active over longer periods of time. Similar activity patterns are thought to have occurred in the fans from the study area. Those from the north have been active during all the eight turbiditic events, while the one at the south was mainly active during the zone N-545 (**Fig. 6.15**).

The Eocene Jaizkibel Fan that crops out in North Spain also shows similarities with the facies observed in the Campos Basin. The sedimentary facies of this fan have been described by Kruit et al. (1972 and 1975) and Crimes (1973 and 1976). The author had the opportunity to study these outcrops and compare them with the facies from the Oligocene-Lower Miocene of the Campos Basin (see Chapter 5).

In this area of Spain (Cabo Higuer-Monte Jaizkibel-Pasajes-San Sebastian-Zaruz-Zumaya) there is a complete succession of sedimentary facies varying from "proximal" sand-rich amalgamated sandstones with large scours, to "intermediate" thickly-bedded sand-mud couplets with coarsening and thickening upward sequences in intermediate position, up to a "distal" thinly-bedded sand-mud couplets interbedded with hemipelagic marlstones. In the Oligocene-Lower Miocene of the Campos Basin only the facies associations similar to those of the "proximal" settings (Cabo Higuer and Monte Jaizkibel) of the Jaizkibel Fan were recorded. The reason for this can be interpreted from the map of **Fig. 6.15** showing that the wells drilled up to now are all in the relatively "proximal" positions of the fans, and consequently the facies association found in these wells generally reflect what would be expected.

One of the most important similarities was observed at Cabo Higuer and the Monte Jaizkibel, where very massive amalgamated sandstones reach thicknesses of 1000 m and appear to be equivalent to the Amalgamated Sandstones (**AmS**) and Very Coarse Sandstone (**VcS**) lithofacies (i.e. Electrofacies **AmS**) in the Campos Basin. The greater thickness of these sandstones compared to those found in the turbidite systems of the Campos Basin, reflects their different tectonic setting. The Campos Basin is a passive margin basin while this region of Spain was part of an active margin basin.

6.4 CONTROLS ON TURBIDITE DEPOSITION

The preference for the deposition of the turbidites in some sites can be in part related to the collapse of the underlying Aptian evaporites which created gentle lows into which the turbidity currents preferentially flowed (sections **T-T'** and **Y-Y'**, respectively dip- and strike-oriented[8]). The sandstones of the depositional sequence **1a** and **1b** pinch out before well 358 (section **Y-Y'**). The greater thicknesses of sandstones in Sequence **1c** between wells 358 and 367 can be interpreted as indicative of differential subsidence probably controlled by underlying salt movement triggered by an increase in the sedimentary load. This differential subsidence has been operative at least up to the base of the Sequence **5** (see section **Y-Y'**).

In **Fig. 6.16** is presented an integration of the distribution of these submarine fans (**6.15**) with the regional map (**Fig. 6.14**) presented by Gamboa et al. (1986). This shows the preserved shallow-water Oligocene carbonate platform (Siri Member) with its corresponding distal facies (Blue Marker), and the location of the principal Oligocene canyons. There is a very good agreement between the proposed location of the canyons and the possible source areas for individual fans interpreted from the isolith maps (**Fig. 6.15**, and **6.16**). Based on this relationship it is possible to predict the occurrence of similar sand-rich turbidites to the south of the study area, offshore of the Oligocene canyons mapped by Gamboa et al. (1986) (see **Fig. 6.16**).

As canyons can be more readily recognized, they can be used to trace unconformities towards relatively deeper water in order to predict the location of sand-rich submarine-fans. However, one would expect to find sand-rich fans more frequently in basins with sand-rich and wave-dominated shelves. The waves and associated drift cells would winnow the sediments during the highstands and supply them to the canyon heads during the falling sea levels thus triggering turbidity currents.

---

[8]The intersection point in the section T - T' is shown by an arrow and the letters Y-Y', while in the section Y - Y' it is the same site of the well 367.

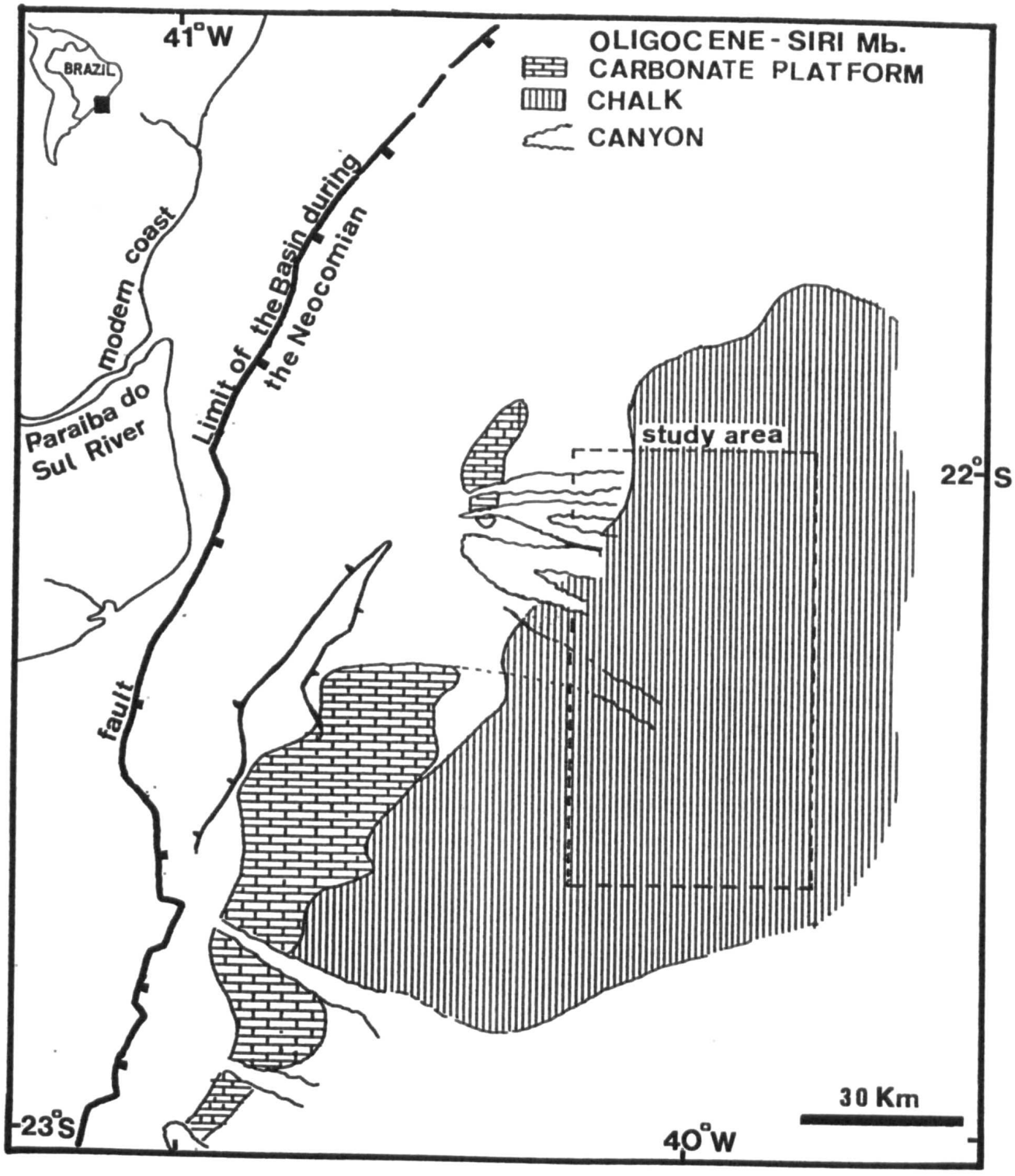


Fig. 6.14 - Occurrence of the Siri platform carbonate with its corresponding deep-water chalk facies, the Blue Marker, and the position of the main Oligocene canyons (modified from Gamboa, 1986).

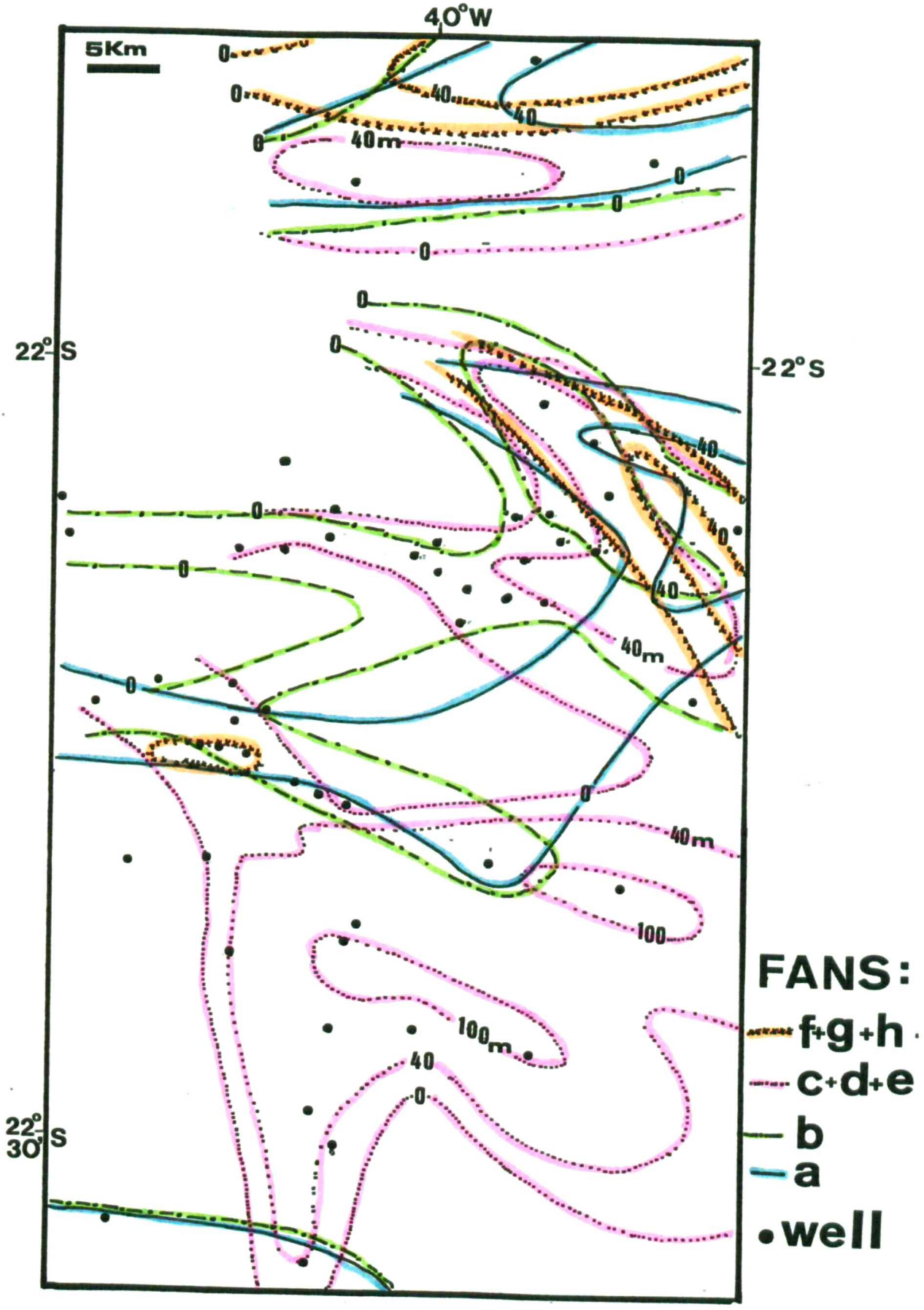


Fig. 6.15 - Integration of the sandstone isoliths of all the Oligocene-Lower Miocene fans in the study area.

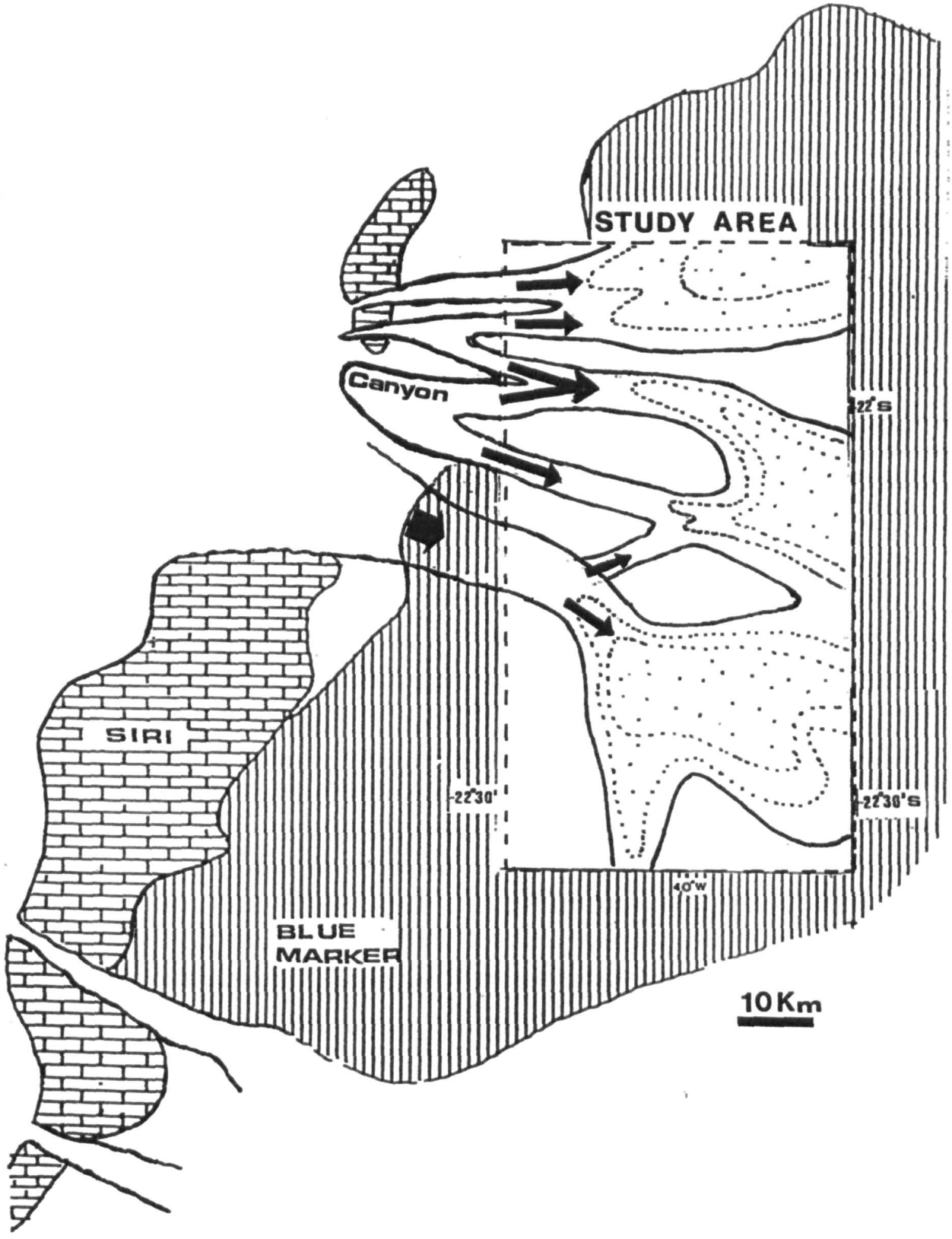


Fig. 6.16 - Integration of the occurrence of the Siri carbonates and the Oligocene canyons (from Gamboa et al., 1986) with a simplified map of Oligocene-Lower Miocene fans derived from Fig. 6.15.

The phenomenon that initiated all these interconnected events (i.e. erosion of canyons and deep-sea channels, deposition of the sands-rich turbidites and triggered the Aptian salt movement in those sites which have received larger sedimentary loads) could either be caused by a large fall in the sea level (eustatic) or tectonic in origin or even a combination of the two (i.e. a relative sea-level fall).

According to Haq et al. (1987) there is a large eustatic sea-level fall at the beginning of the Chattian and the first occurrence of sand-rich turbidites, after the deposition of the Blue Marker in this part of the Campos Basin, correlates with this major fall in the sea-level at about 30 Myr[9] (**Fig. 6.8**). However, an isostatic uplift of the source area of the Campos Basin, the Serra do Mar Mountains, also occurred during the Tertiary with the concomitant formation of the Taubaté, Resende and Sao Paulo sedimentary basins (Mohriak, 1988). The Tertiary isostatic uplift of the Serra do Mar Mountains caused an increase in the sediment supply into the Campos Basin, as is clearly shown by the shallowing upward pattern of the Miocene-Recent succession (see section **T-T'**). The condensed nature of the Oligocene succession in the study area indicates that this increase in the sediment supply, excluding the sand-rich turbidites, only occurred in this region from the base of the nannofossil zone N-545 (Lower Miocene) upwards (section **T-T'** and **Fig. 5.11**, for more details see **tables 7.2, 7.4, 7.5 and Fig. 7.2** in Chapter 7).

The Lower Oligocene chalk/marlstone deposits (N-520/ N-530) represented by the Blue Marker and the platform carbonates of the Siri Member characterize a period of low siliciclastic deposition and can be interpreted as either the result of a relative high sea highstand of sea level, when the sediments were trapped in the source and coastal areas of the Basin or a decrease in the sediment supply. The remarkable coincidence of these carbonates with the Lower

[9] See chapter 7 for further refinements of the age of the first sandstone occurrence above the Blue Marker.

Oligocene high sea level stand according to Haq et al. (1987) can be used to emphasize the importance of eustatic control (see **Fig. 6.8**).

As discussed above, the subsequent sea-level fall at 30 Myr also coincides with the first occurrence of sand-rich turbidites in the study area, which can be just a coincidence or a real phenomenon. However, it is also necessary to have at least two major relative sea-level falls to explain the deposition of the turbidite systems **a** (N-530) and **b** (N-540). The hemipelagites that lie below and above these turbidite systems represent low sedimentation rates (see **Fig. 5.11**, and for more details see **tables 7.2** and **7.4** in Chapter 7). A relative sea-level fall would therefore be the most effective way to create an environment with sufficient energy to resediment large volumes of siliciclastic sands into deep-water and allow for the deposition of the interbedded thick hemipelagites during subsequent periods.

Alternatively the formation of the onshore rift basins (i.e. Taubaté, Resende and Sao Paulo) during the Oligocene (see Chapter 2) could also have played an important role in controlling the sediment supply to the Campos Basin by trapping coarse siliciclastic sediments in these basins and favouring the deposition of carbonates (Siri Member) in the Campos Basin. However, the basal section (Oligocene) of the Taubaté Basin is characterized mainly by lacustrine mudrocks and only in its upper section (Pleistocene) have coarse-grained fluvial facies been deposited (see Chapter 2), suggesting that probably they were not of great importance in trapping coarse sediments. Additionally, these basins are much smaller than the Campos Basin. However, these onshore basins are poorly known and require further studies concerning their possible role in the control of the sediment supply to the Campos Basin.

6.5 CONCLUSIONS AND DEPOSITIONAL MODEL

The Oligocene-Recent succession has been divided into eight depositional sequences. Five main sand-rich turbidite systems have being identified and they occur in the three basal sequences (**1**, **2** and **3**). The most important turbidite systems belong to Sequence **1** (N-530/N-560). These sandstones are characterized by either hummocky clinoform seismic facies or high amplitude and relatively continuous reflectors.

There were three main depocentres, two in the north of the study area, where all the turbidite-fans systems were deposited, and one in the south where mainly the fans **c/d/e** (N-545/550) were deposited. The deposition of the turbidites was partially controlled by structural lows and associated faults possibly related to the collapse of the underlying Aptian evaporites.

The high sand:mud ratio of these fans can be linked to similar high sand:mud ratios observed in the shelf areas. This high sand:mud ratio was probably the response of a combined increase in the supply of the coarse-grained siliciclastic sediments into the Basin due to an isostatic uplift of the source area, the Serra do Mar Mountains, and the existence of a wave-dominated shelf environment. The Oligocene canyons mapped by Gamboa et al. (1986) were the main pathways for these shallow water sediments during their transport into deep water (upper/middle bathyal). The chalk beds of the Blue Marker were the substratum over which the Oligocene-Lower Miocene sand-rich basin-floor fans were deposited.

A depositional model for the Oligocene-Lower Miocene succession (depositional sequences 1 - 3) in the northeast part of the Campos Basin has been constructed by integrating the results of this study with regional data from previous studies of the Basin (**Fig. 6.17**).

Stage I schematically represents a relative highstand of sea level. The energy on the outer shelf was very low and only fine-grained sediments and oozes (nannofossil and foraminifera) were deposited in deep water. The chalk beds,

of the Blue Marker were formed under such conditions, while their equivalent shallow-water carbonates (Siri Member) were deposited on the shelf. The coast/shelf environments acted as a temporary siliciclastic storage area, where sands were winnowed and mixed with shallow-water skeletal carbonates.

Stage II is illustrated with two diagrams: one representing the coastal/shelf/upper slope and the other the corresponding deep-water environments. With the relative lowering of sea level during the Oligocene the shelf became gradually exposed, causing a lowering in the erosional base-level and concomitant increase in the energy on the outer shelf. As a result huge volumes of coarse-grained sediments were transferred through wave action, longshore currents and rivers into deep-water environments. This material was preferentially captured at canyon heads and then transported as high density turbidity currents to form the sand-rich fans in gentle topographic lows created by the collapse of the underlying Aptian salt. This preferential sedimentation was enhanced even more in these structural lows.

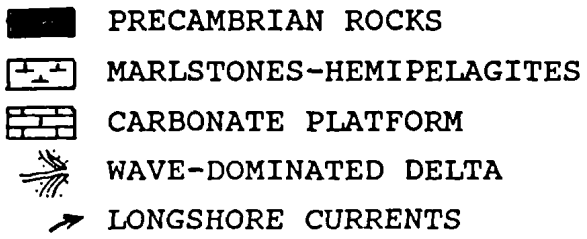
This schematic depositional model for the Oligocene-Lower Miocene turbidites resembles the suprafan of Normark (1970) and the sand-rich "poorly efficient"/ Type II (Mutti, 1979/1985) or the Channel-lobe transition of Mutti & Normark (1987). The diagram only represents the relatively proximal areas of the fans because they correspond most closely to the portion observed in the study area.

The evolution model for the Oligocene-Lower Miocene turbidite complex (**Fig. 6.18**) shows the general onlap of the turbidite systems and local depositional control by faulting causing an increase of the sea floor gradient and frequent erosional features (well 316). Further onshore of this faulting the electrofacies associations are characterized by channel-fill deposits with diamictites (i.e IIa of section 5.4, see well 329 in **Fig 5.11**), while in offshore the dominant facies association is the channel-lobe transition (i.e. III of section 5.4) with thick amalgamated and relatively continuous sandstones (well 367, see **Fig. 5.11**). The later progradational pattern of the Miocene slope

deposits concludes the evolution model. This model resembles the turbidite evolution model of Mutti (1985), but differs by the absence of his Type I fans.

Correlations with the eustatic curves of Haq et al. (1987) sea-level are difficult, but there is a remarkable coincidence between the first occurrence of the turbidites of Sequence **1a** and the major sea-level fall of 30 Myr (Chattian) shown on their chart (**Fig. 6.8**). However, the other turbidite systems of sequences (**1b, 1c, 2, 3a** and **3b**) do not show an relationship with other lowstands of sea level. A higher resolution chronostratigraphy is required before it can be said with confidence whether these turbidite events can generally be correlated with eustatic fluctuations. The resolution needed is of a few hundred thousand years, and the ideal would be 100 Kyr. Besides the conventional dating methods (palaeontological, radiometric and magnetometric) isotopic curves, especially for oxygen, calibrated with orbital cycles using spectral analysis would be of extreme value. Similar procedures have been used effectively by Feeley et al. (1990) in the Mississippi Fan, and the author has also tried to apply similar methodology in Chapter 7.

Fig. 6.17 - Schematic depositional model for the Oligocene-Lower Miocene turbidites and associated facies.



DEPOSITIONAL MODEL

OLIGOCENE

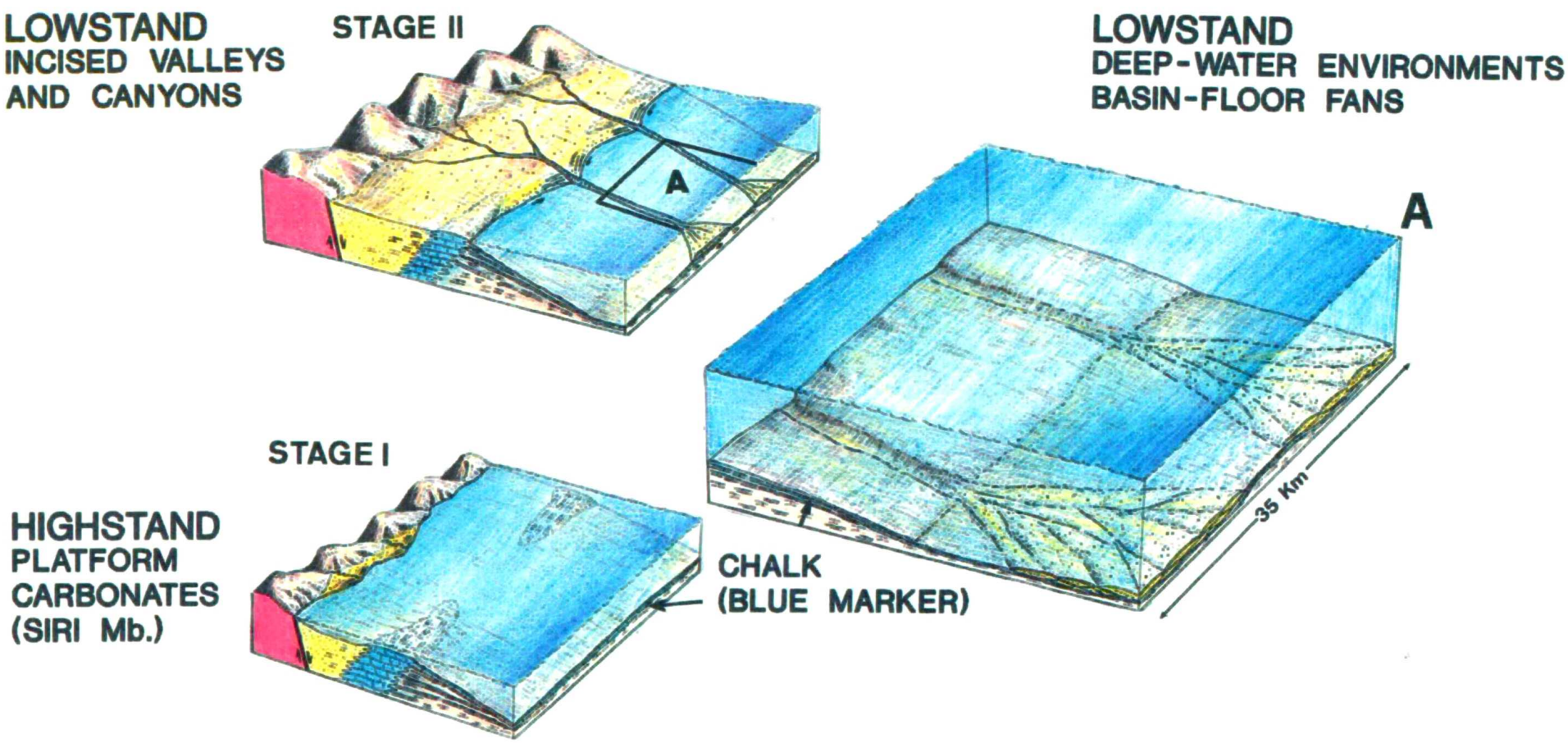
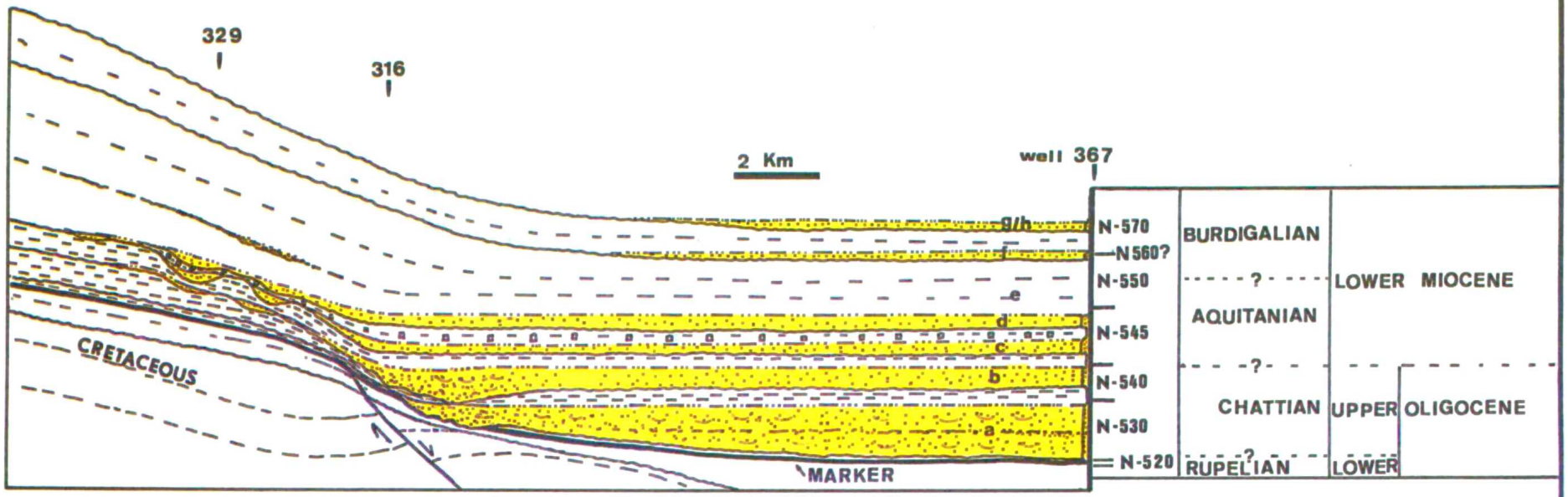


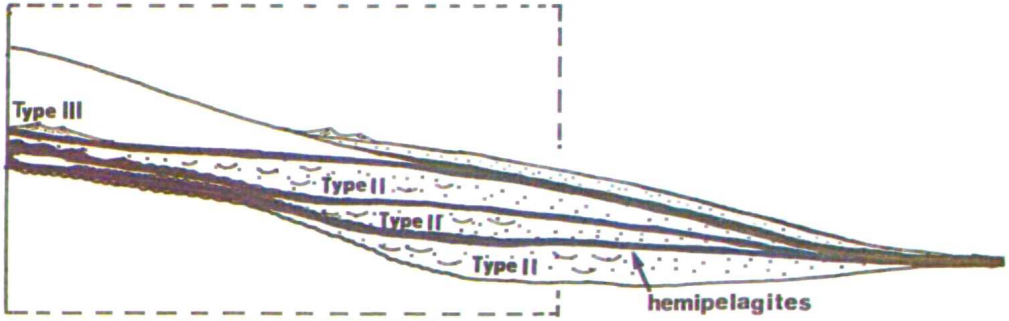
FIG. 6.17

Fig. 6.18 - Schematic evolutional model for the Oligocene-Lower Miocene complex in the northern part of the study area (based on section T-T').

OLIGO-LOWER MIOCENE TURBIDITE COMPLEX



SCHEMATIC EVOLUTION BASED ON MUTTI (1985)



EQUIVALENT TO THE STUDIED AREA

FIG. 6.18

CHAPTER 7

SEDIMENTARY CYCLES

7.1 OLIGOCENE-MIOCENE SEDIMENTARY CYCLES

There is a conspicuous cyclicity or rhythms of marlstones (**G1/G2 Electrofacies**) and mudstones (**G3/G4 Electrofacies**) in the Oligocene-Miocene succession, especially in those cored intervals that correspond to the nannofossil zones N-530 and N-540. The average thickness of individual marlstone-mudstone couplets is 25 cm, but there are variations, mainly reflecting an increase in the siliciclastic mudstone bed thickness. When the cores were examined and correlated with their corresponding wireline logs the existence of cyclic interbedding of marlstones and mudstone-rich intervals was confirmed (see **Fig 7.1**, and **Fig. 5.14** and **5.15** in Chapter 5). These intervals consist of 3 or 4 marlstone beds with very thin mudstones or vice versa, forming marlstone-rich or mudstone-rich bundles. These bundles in their turn are arranged frequently into asymmetric cycles from carbonate-poor to carbonate-rich megabundles (**Fig. 7.1**).

The wireline log responses in the Carbonate Mudstone/Marlstone Electrofacies (**G1/G2**) and Mudstone Electrofacies (**G3/G4**), as described in the Chapter 5, are well defined. However, not all wireline logs differentiate beds of a few centimetres thick and so it is important to take into account the magnitude of bed-thickness and to choose the most suitable kind of wireline log to identify them. The only wireline log which differentiates very thin/thin beds (5-40 cm) is the dipmeter log. This log is able to detect the very high frequency cycles of thin marlstone-mudstone couplets. On the other hand, to identify

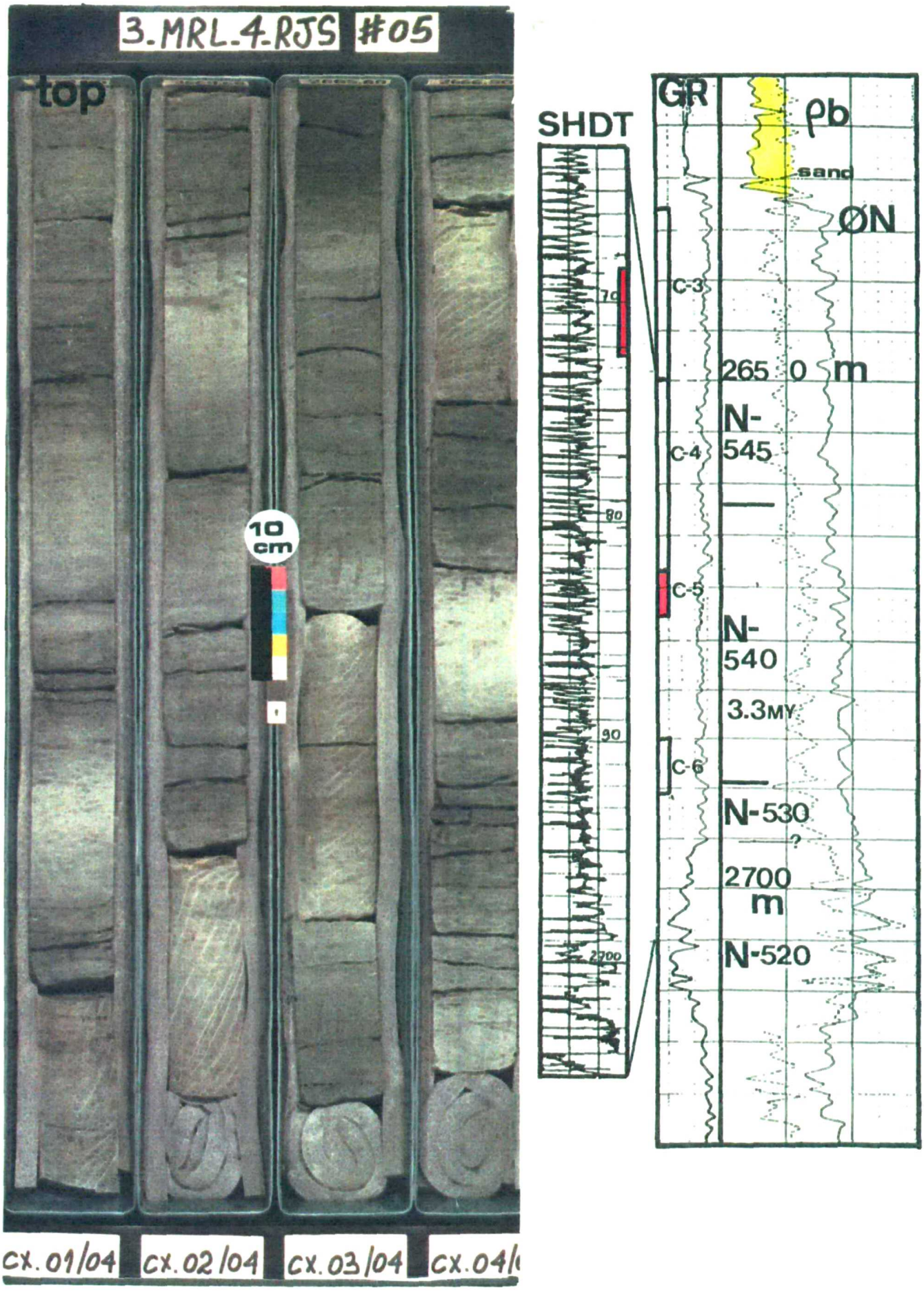


Fig. 7.1 Characteristics of the cyclic sedimentation in core and wireline logs (GR/FDC/CNL and SHDT).

the marlstone-rich or mudstone-rich bundles a combination of the neutron-density log curves is the most effective. The digitized values are recorded every 20 cm but the vertical resolution of these logs is only 50-60 cm. This resolution is ideal to represent the average properties of bundles composed of 2 to 4 individual marlstone-mudstone couplets of about 10-35 cm thick. The wireline log responses to these groups of couplets are alternating density or porosity values whose corresponding intervals vary in thickness from about 0.8 m to more than 1.5 m. The neutron-density logs peaks can be found organized into bundles of 3 or 4 peaks, which in their turn can be grouped into marlstone-rich intervals composed of about 15-24 peaks (see **Fig 7.1**). There are cases where one lithology dominates and the distinction of individual peaks is not possible, instead a peak representing an average value appears. In this case some of the bundles of 3 peaks occur as two or even only one peak (**Fig 7.1**, see also enlargements in **Fig. 7.2 c** and **d**). Also in the intervals that correspond to the nannofossil zones N-520/N-530 the individual siliciclastic mudstones beds are thinner than those of the N-540 zone, reflecting the relatively higher proportion of marlstones in the former. In the younger Miocene successions the siliciclastic mudstones are relatively thicker than those of the interbedded marlstones. The gradual transition from the Oligocene to the Miocene succession is characterized by an increase in the thickness of individual mudstone beds and a concomitant increase in the thickness of the whole interval belonging to the nannofossil zones N-545 and N-550 (compare the variations in thickness in **Fig 7.2 a, b** and **c**). This reflects an increase in the sedimentation rate and can be attributed to an increase in siliciclastic input, because the marlstones although relatively thicker are still much thinner than the interbedded mudstones. The average rate of sedimentation (undecompacted) varies from about 1-2 cm/Kyr[1]

[1] Sedimentation rate: the calculate average of the undecompacted sedimentation rate was carried out by dividing the total thickness of an interval by its corresponding time span (nannofossil zone duration). The absolute ages for the duration of a single nannofossil zones were obtained from the Biostratigraphic Chart of Beurlen et al. (1988).

in the lower sections (N-520/540) to about 17 cm/Kyr at the top (N-550), thus explaining the increase in mudstone thickness between the marlstone peaks. This phenomenon was also seen in the seismic sections from the Miocene succession where the offlapping pattern of the seismic reflectors indicates that a major progradation of the slope facies occurred during this period with a consequent increase in the average sedimentation rate. Probably the most important observation concerning these cycles is the occurrence of sandstone (turbidite) intervals in the Oligocene-Miocene succession. These turbidites also seem to have a cyclicity, but of a lower frequency. This can be seen in wells 344 and 342 (**Fig. 7.2** and **7.3**). As the marlstone-mudstone couplets represent sedimentation in an upper/middle bathyal environment (see Chapter 5) this cyclic sedimentation can be interpreted as a regional phenomenon. Furthermore, if we assume the time span during the deposition of each couplet to be "constant", thickness variations would reflect changes in the sedimentation rate. Consequently, these cycles could be used to establish local variations in the sedimentation rates by improving correlations. Alternatively, these cycles could be used to define more accurately the time-span of depositional events and thus better understand their possible mechanisms, as will be seen later in section 7.4.

In Chapter 6 tentative correlations were made between the data of the present study and that of Haq et al. (1987). The results were not totally satisfactory, indicating that improved palaeontological dating and correlations are required. A major problem is the resolution of the palaeontological tool i.e. the time span of each nannofossil zone. In the studied interval the nannofossil zones used by Petrobrás vary between 1.8 Myr (N-545) to 4.5 Myr (N-550) (Beurlen et al., 1988). It should be possible to improve the resolution of the dating using the sedimentary cycles in the sequence. However, before discussing how this can be achieved a few questions need to be answered in relation to sedimentary cycles such as: 1) the kind of mechanisms

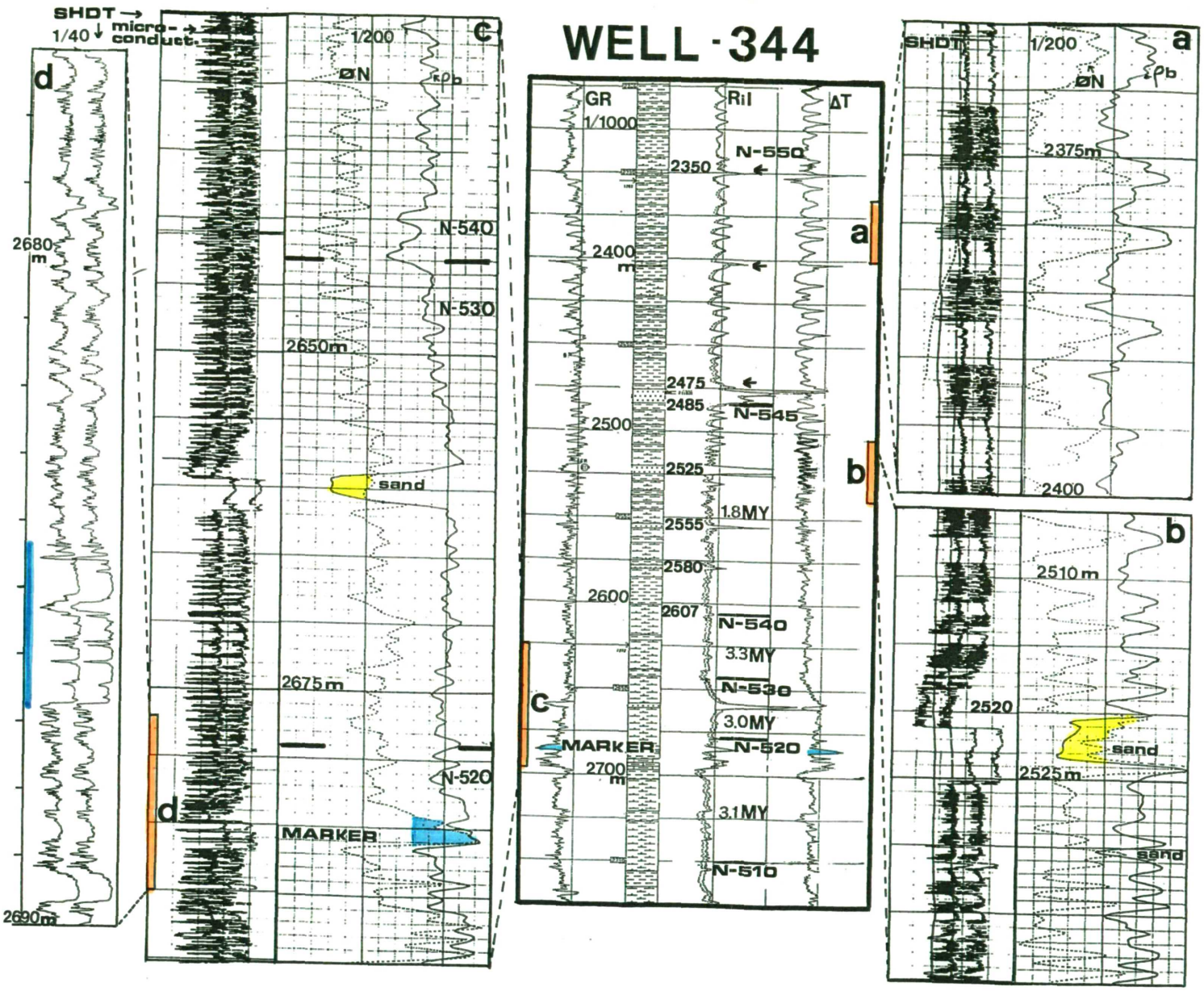


Fig. 7.2 Characteristics of the Oligocene-Lower Miocene cyclic sedimentation in wireline logs of well 344, originally scaled as 1:1000. Enlargements a, b, and c show FDC/CNL and SHDT curves scaled at 1:200. Enlargement d shows SHDT scale at 1:40

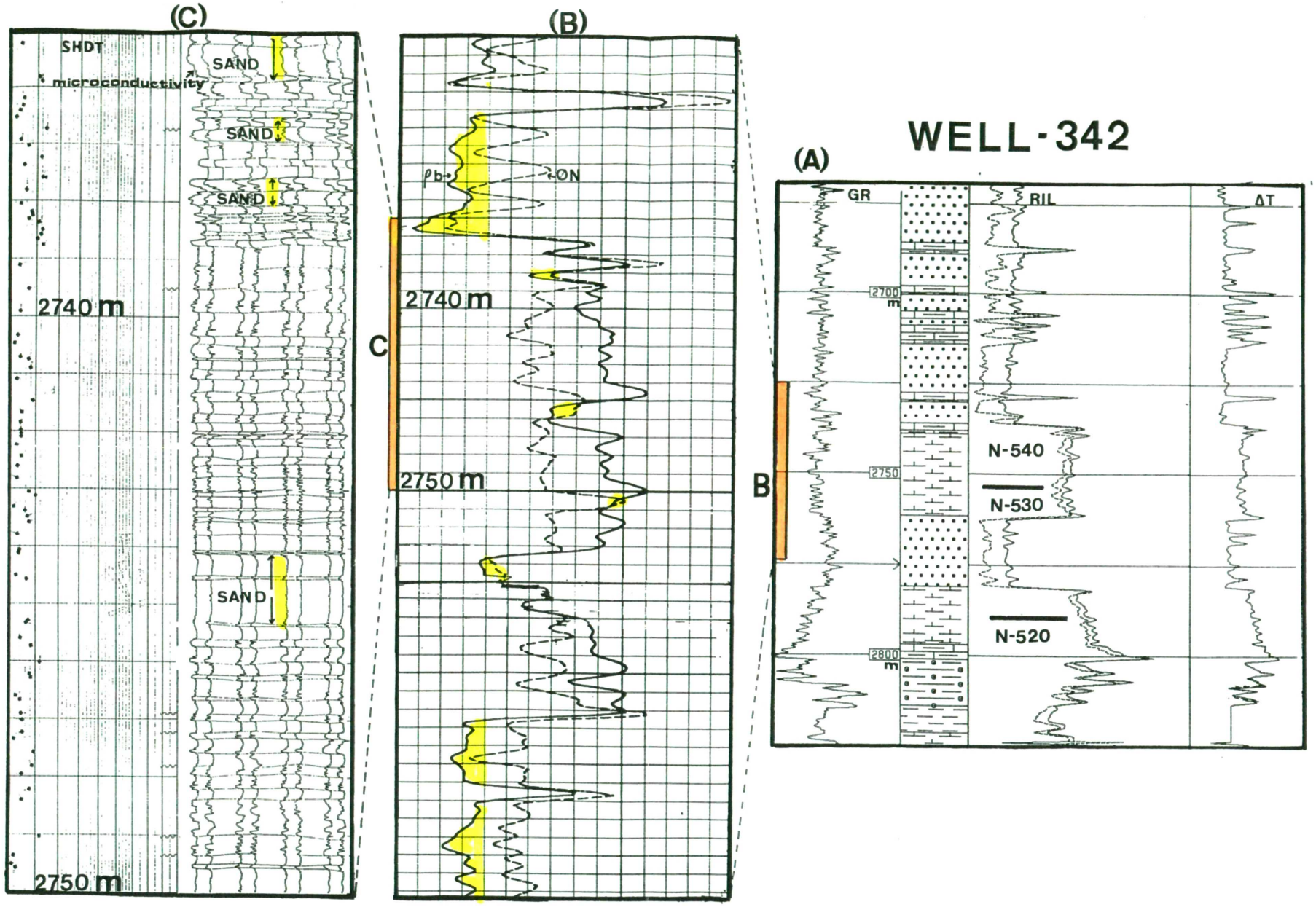


Fig. 7.3 Characteristics of the Oligocene cyclic sedimentation in wireline logs. (A) Composite log originally scaled 1:1000; (B) FDC/CNL, 1:200; (C) SHDT, 1:40.

causing this type of regional cyclicity; 2) their frequencies and predictability; and 3) the nature of the sedimentary processes influencing large areas in a cyclical and relatively uniform way.

7.2 THE NATURE AND ORIGIN OF CYCLES

Cycles can be autocyclic (Beerbower, 1964), resulting from a local sedimentary process such as the shift of a channel or a delta lobe, or be due to allocyclic oscillations that reflect rhythmical changes in climate, atmosphere and ocean.

Pelagic/hemipelagic sedimentation reflects changes in oceanographic factors including availability of nutrients and turbidity of the water, which affect the abundance of zooplankton and phytoplankton in these environments. Oligotrophic environments are characterized by clean nutrient-deficient waters with small amounts of phytoplankton and long complex food chains of great diversity (polytaxism). Under these conditions there is a predominance of carbonate sedimentation (calcareous foraminifera and nannofossil). Conversely, during eutrophic periods nutrients are abundant with large amounts of phytoplankton and consequently reduced biotic diversity (Oligotaxism). The preservation potential of oligotrophic biotas is greater because calcareous taxa are predominant and calcium carbonate is less dissolved due to lower amounts of organic matter produced during oligotrophic conditions (Hallock, 1987).

According to Hallock (1987) important fluctuations in the trophic resource continuum[2] in the euphotic zones of the world's oceans coincide with periods of transgression and regression, respectively corresponding with oligotrophic and eutrophic environments.

---

[2] The trophic resource continuum in euphotic zones of the world's oceans is the spectrum of conditions from the richest runoff and upwelling areas to the most deficient subtropical seas (Hallock, 1987).

Bé et al. (1976), studying changes in the western equatorial Atlantic ocean over the past 125,000 yr, concluded that warm periods correlate with carbonate maximums, whereas cold periods correlate with carbonate minimums and an increase in the siliciclastic input to the bottom sediment. During the last interglacial period three high sea-level stands have been recognized, which correspond to three CaCO3 maxima, separated by low sea-level stands with corresponding low carbonate contents (Bé et al., 1976). These CaCO3 fluctuations occur with a frequency ranging between 18,000-20,000 yr. Also, Shackleton et al. (1984) found some correspondence between relatively lighter oxygen isotopes and high CaCO3 percentages over the last 2.5 Myr in sediments from the DSDP site 552A.

The model proposed by Hallock (1987) can be used to interpret the variations in carbonate contents in the marlstone-siliciclastic mudstone couplets of the Oligocene-Miocene succession of the Campos Basin. In this case the marlstones would represent more oligotrophic and warmer periods, while the siliciclastic mudstones more eutrophic and cooler periods. This is reinforced by the fact that in the siliciclastic mudstones the total organic carbon values are higher than those of the marlstones (respectively up to 2.1 and less than 0.5 weight%, see **Chapter 8**). This could reflect the greater organic productivity during the eutrophic periods combined with a better preservation potential for the organic matter. The transition from the underlying siliciclastic mudstones to the marlstones is characterized by a gradual increase in foraminifera and nannofossil content. Additionally, when the marlstones pass into chalk beds there is a relative decrease in foraminifera content and an increase in the nannofossil content. The latter situation was observed in the Braarudosphaera-rich chalk beds that form the Blue Marker (see **section 5.3.9** in **Chapter 5**). In these beds the planktonic foraminifera become scarce and sedimentation was dominated mainly by coccoliths. According to Hallock (1987) this type of sedimentation with a predominance of coccoliths represents highly oligotrophic

environments, established during major marine transgressions. As discussed in chapters 5 and 6, the Oligocene interval contains chalk beds (the Blue Marker) deposited approximately between 32 and 33 Myr ago (Shimabukuro, 1987), coinciding with a major highstand of sea level according to Haq et al. (1987). Based on this evidence it is possible to conclude that the marlstones represent sedimentation during transgressive periods while the siliciclastic sedimentation represents the regressive periods. This implies that during transgressions the coastal source areas were flooded and nutrients and siliciclastic sediments were not effectively transported into the more distal parts of the basin. Consequently the "trophic resource continuum" was very wide, and the converse occurred during regressions. Similarly, Posamentier et al. (1988) suggest that marlstone and siliciclastic mudstone intervals represent respectively highstands and lowstands of sea-level. However, this then poses the problem concerning the duration and the magnitude of such highstands and lowstands. Analysis of the frequencies of sedimentary cycles found in the Oligocene-Miocene succession of the Campos Basin may help to resolve this problem. The marlstone-siliciclastic mudstones couplets represent very high frequency alternations in the depositional conditions, while the bundles richer in marlstone would represent longer periods in which the deposition of marlstones was more important than that of siliciclastic mudstones. The converse would be true for those bundles richer in siliciclastic sediments. Using this as a working hypothesis it is possible to infer that the intervals richer in marlstones would represent highstands of the sea level, including periods of high frequency oscillations but of a low amplitude. The interval which embodies the chalk beds of the Blue Marker would represent a major transgression i.e. an event of much greater environmental change.

7.3 POSSIBLE CAUSES OF CYCLICITY

Fischer (1986) said "We live by rhythms, in a world of predictably recurring tides, suns, moons and seasons. This **calendar frequency band** reflects the rotational and orbital cycles of Earth and Moon." Other lower frequency events have also been discussed in the literature such as: 1) rhythmic tree growth (Zeuner, 1952; Pearson, 1978; Schove, 1983) and isotopic variations (Libby, 1983) which coincide with the **22-yr Hale cycle** in the solar polarity and its **11-yr sunspot hemicycle;** and 2) the **Milankovitch frequency band (10-500 Kyr)** which reflects cyclicity in the distribution of solar energy on Earth and consequently its climate (Milankovitch, 1941).

There is no doubt that the Earth's orbit is subjected to cyclic variations (Vernekar, 1972; Imbrie & Imbrie, 1979; Berger, 1978, 1988, 1989b). The annual energy receipt of solar radiation over the Earth as a whole does not change, but its distribution varies with latitude and season. This distribution of energy is controlled by:

1) **obliquity cycle (41 Kyr)** which corresponds to a change in the Earth's rotational axis by up to 3°;

2) **eccentricity cycles (100 Kyr and 413 Kyr)** which correspond to changes in the Earth's orbit from almost circular to more elliptical;

3) **precesses** with a period of **26 Kyr.**

When the Earth's rotation axis is nearly normal to the elliptical orbit, i.e **low obliquity,** more energy is delivered to the equator and less to the poles, with consequent increase in the mean annual latitudinal temperature and a decrease in seasonality.

Eccentricity and **precession of equinoxes** affect climate by interaction. The period of precession relative to the elliptical orbit varies as a result of a drag on the elliptical orbit and may be shortened to as little as 14 Kyr, and has two modes at 19 Kyr and 23 Kyr (Fischer, 1986). At such intervals, one of the hemispheres will face the Sun at midsummer and will experience exceptionally short, hot summers and long, cold winters, while the other hemisphere

enjoys long, cool summers and short, mild winters. In the opposite phase of the precessional cycle, the states of the hemispheres are reversed. The intensity of this precessional effect is proportional to the eccentricity of the orbit, it waxes and wanes with the cycles in orbital eccentricity (Fischer, 1986).

Despite strong statistical support for the astronomical theory (Hays et al., 1976), little is known about the real physical mechanism that links insolation with global climate. Denton and Hughes (1983) have proposed a mechanism based on the "interlocked variations of ice-sheet heat sinks in both polar hemispheres, amplified and transmitted Milankovitch summer half-year insolation changes between 45° and 75° N into the globally synchronous climate changes recorded in geologic records". Milankovitch summer insolation (precession and obliquity) in the Northern Hemisphere[3] drives the model of Denton and Hughes (1983) by controlling the melting margins, which in their turn control most of the variations in this system, because the advance or retreat of the melting margins initiated concurrent eustatic sea-level change. The precession effect dominates variations of the extensive terrestrial margins, which in turn initiate the sea-level changes that control all marine margins elsewhere on the globe. However, extreme glacial events occur only when tilt (every 41 Kyr) reinforces precession. This is because tilt affects ablation on the northern ice streams that control much of the interior downdraw. Therefore, simultaneous downswings and minima of these combined precession and tilt effects produce glacial extremes.

These models (Denton and Hughes, 1983) can explain the 23 Kyr and 41 Kyr frequency of oxygen-isotope changes observed in deep-sea sediments, which are related to ice volume (Hays et al., 1976). However, the astronomical theory of ice ages does not specifically predict the 100 Kyr cycle

---

[3] Variations in incoming Northern Hemisphere summer insolation depend largely on the 41 Kyr tilt cycle at high latitudes and on the 23 Kyr precession cycle at midlatitudes (Ruddiman and McIntyre, 1981b).

that dominates the late Quaternary climatic records (Broecker and van Donk, 1970; Hays et al., 1976; Imbrie and Imbrie, 1980). The essential features of this dominant cycle are the terminations that lead to full interglaciations spaced about 100 Kyr apart. In the model of Denton and Hughes (1983) terminations occur when simultaneous upswings in precession and tilt at critical Northern Hemisphere latitudes affect full-bodied ice sheets that have achieved a glacial maximum, triggering powerful feedback mechanism of accelerated downdraw (Denton and Hughes, 1981a), and resulting in self-starvation (Ruddiman and McIntyre, 1981a). This combination of necessary glacial and orbital conditions recurs only at 100 Kyr intervals in late Quaternary time, when Northern Hemisphere precession and tilt effects are in phase both for the termination and the preceding full glacial maximum. Additionally, eccentricity variations on a 96 Kyr cycle play an important role in terminations by amplifying precession and thus promoting full glaciations and interglaciations.

To apply the model of Denton and Hughes (1983) as a working hypothesis for this study it is necessary to know the global scenario of the Earth and whether or not there were ice caps at the poles during the deposition of the Oligocene-Miocene. According to Kvasov and Verbitsky (1981) a deep strait came into existence between Australia and Antarctica at the Eocene and Oligocene boundary (38 Myr ago), but the Drake Passage[4] between the Antarctic Peninsula and South America had not yet come into existence. As a result the waters of the Southern Ocean had to make an almost round-the-world trip, giving them enough time to cool considerably. This accounted for the remarkable development of Antarctic glaciation since Oligocene (**Fig.7.4**). The formation of the East Antarctic Ice sheet caused a drop in world sea level of about 60 m (Kvasov and Verbitsky, 1981).

---

[4]The passage did not open earlier than 23.5 ± 2.5 Myr ago, and only about 11-14 (ca. 12) Myr ago that the South Ring Stream must have overcome the last obstacle and encircled the whole of the Antarctic continent (Kvasov and Verbitsky, 1981).

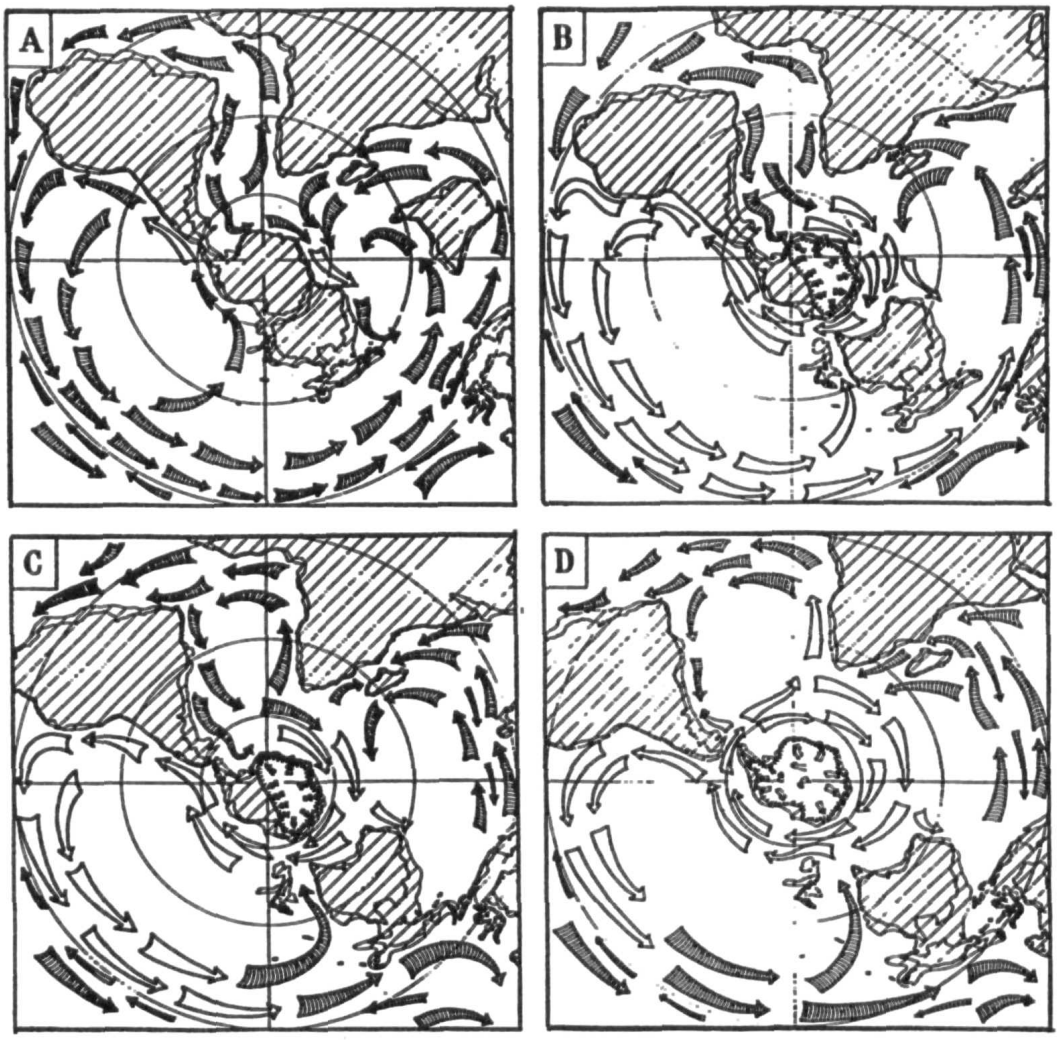


Fig. 7.4 Current in the oceans of the Southern Hemisphere. A) Palaeocene (60 Myr ago); B) beginning of Oligocene (35 Myr ago); C) beginning of Miocene (20 Myr ago); d) currents at present. (1) Continents with epicontinental seas; (2) ice sheets; (3) warm currents; (4) cold currents (Kvasov and Verbitsky, 1981; Fig.2).

In view of the presence of Antarctic ice caps in the Oligocene-Miocene the model of Denton and Hughes (1983) could be applied to explain cyclicities in the Oligocene-Miocene succession of the Campos Basin. The oscillations of the ice cap volumes (glaciations and interglaciations) would have influenced the eustatic sea level and the most important of these oscillations would have occurred within the Milankovitch band (i.e. 10-500 Kyr).

7.4 TIME SERIES OR SPECTRAL ANALYSIS OF SEDIMENTARY CYCLES

Time series analysis has been widely used to define frequencies of sedimentary cycles (see Terra Nova v.1 nº5, 1989). The STATGRAPHICS program was used for time series or spectral analysis of the core and wireline data. The frequencies were determined from periodograms and the types of data used were: 1) calcium carbonate percentages in core samples at every 10 cm in well 330, 2) visual estimations of marlstone and mudstone thicknesses from core photos, and 3) wireline logs (see **Chapter 4** for methodology).

Due to computing limitations (see Chapter 4) the CaCO3% core data from well 330 was divided into two parts and spectral analysis was carried out on each interval (**Fig 7.5 A, B** and **C**, respectively). As a result four groups of frequencies were obtained and their corresponding wave lengths calculated as: 20-25.5 cm, 28-43 cm, 93-130 cm and 230-470 cm (**Fig. 7.5 B** and **C**). The three groups of smaller wave lengths (i.e. higher frequencies) coincide with those found by Owen-Hughes[5] using a different type of computer program (**Fig. 7.6**). The variations in the wave lengths of these higher frequencies reflect changes in couplet thicknesses. This can be confirmed visually in the cores of this well (see **Fig. 5.15 in Chapter 5**). However, variations of larger wave lengths (1 - 4.7 m), i.e. lower frequencies, reflect a combination of couplet thickness variation and

---

[5] Mr. Matthew Owen-Hughes has used this CaCO3% data set and corresponding wireline logs of the wells 330 and MRL-4 in his undergraduate statistic project, carried out under the supervision of Dr. John Ferguson, to test whether the marlstone-mudstone cycles observed visually were statistically significant.

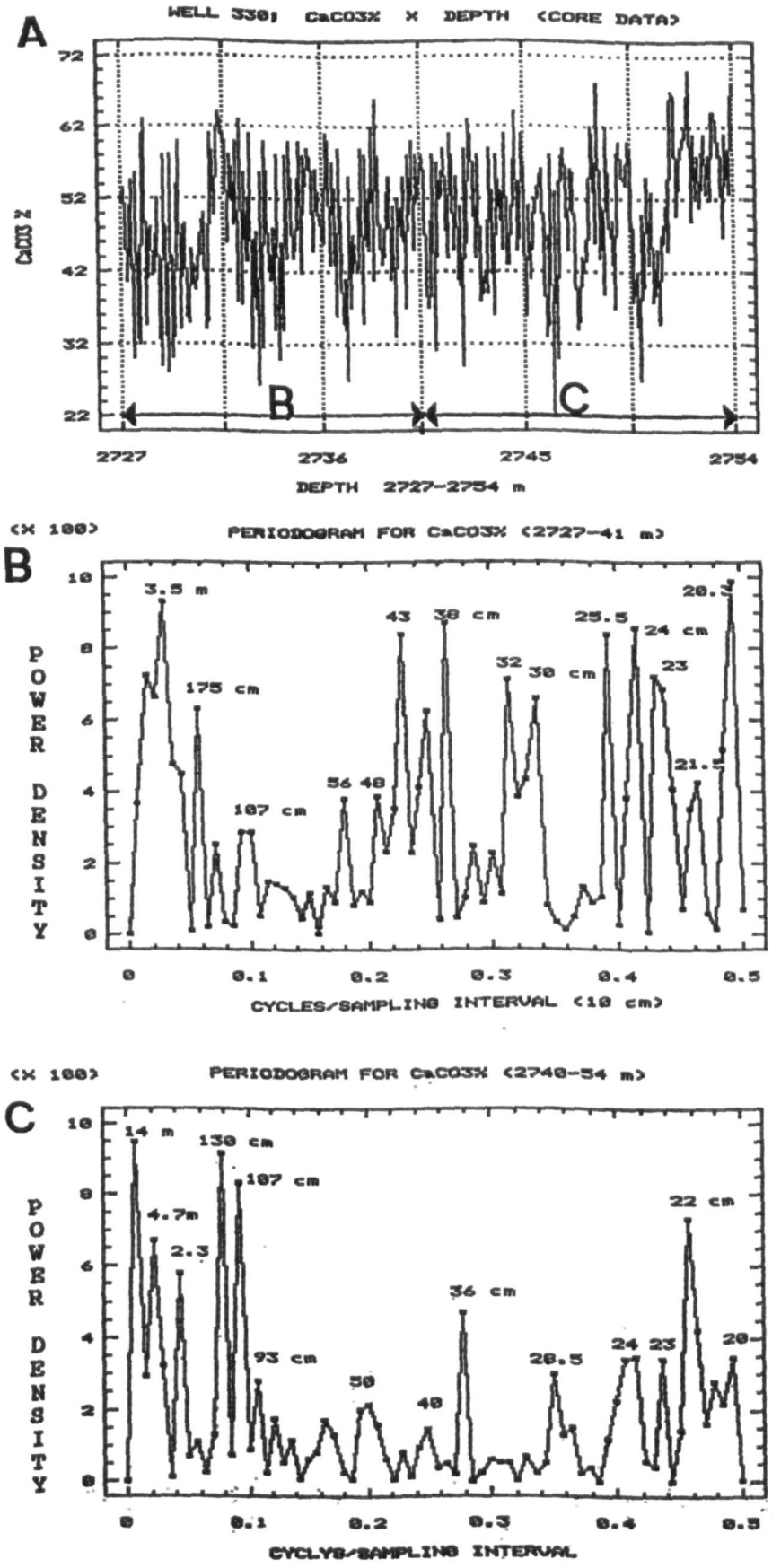
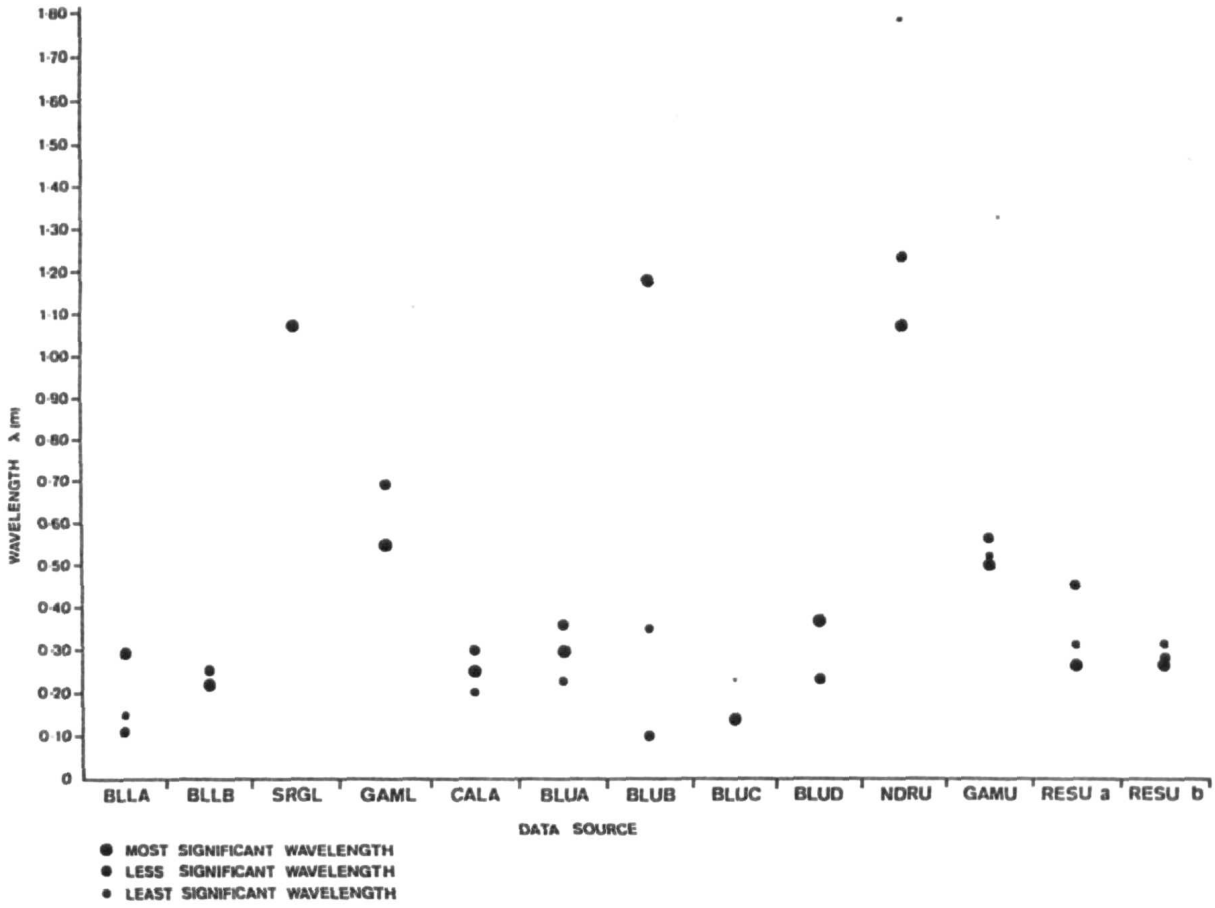


Fig. 7.5 (A) Variations of CaCO3% with depth. The frequencies and corresponding wavelengths (cm) of the CaCO3 variations shown in (A) are presented in (B) and (C).



Where: BLLA, BLLB, BLUA, BLUB, BLUC, and BLUD = data from core photographs; RESUa AND RESUb = dipmeter; CALA = CaCO3%; SRGL= sonic and gamma ray logs; NDRU = neutron/density/ resistivity logs; A = well 330; and B = well MRL-4.

Fig. 7.6 Wavelengths of the cyclicity obtained from cores and wireline logs of wells 330 and MRL-4.

different organization of bundles. To obtain a better understanding of these variations in couplet thickness the total cored interval (27 m) was divided into 7 equal intervals[6] and the results are shown in the **Fig. 7.7.** It can be seen that there are two very significant frequencies whose wave lengths vary between 20-30 cm and 95-190 cm, and a less important one with a wave length varying between 34-47 cm. Additionally, when these seven intervals are compared it is possible to see a general decrease in the wavelengths (i.e. couplet thickness) with increasing depth from 31.7 cm (2727.0-30.7 m) to 23-21 cm (2750.0-53.7 m). However, a local relative increase in the wavelength (i.e. 27 cm) in the interval 2742.4-46.1 m is also present (see **Fig. 7.7**), reflecting fluctuations in the accumulation rates.

Significant variations in the measured characteristics are needed for spectral analysis, consequently high frequencies with low amplitudes will not be shown clearly on the periodogram. However, it is possible to improve the results either by taking the differences between adjacent values with a lag of 1 or by cubing the values and then re-running the periodogram (see methodology in **Chapter 4**). On the other hand, if the lower frequencies are of interest a smoothing filter of the high frequencies needs to be used prior to the application of the periodogram (see **Chapter 4**).

The smoothed curve of the CaCO3% for the total cored interval of well 330 (**Fig. 7.8 A**) shows wavelengths of the same order (50-200 cm) as those on the neutron log over a corresponding stratigraphic interval in well MRL-4 (**Fig. 7.1**, see also **Table 7.1A** and **B**). This implies that the corresponding wireline frequencies and wave lengths of the logs provide an equivalent smoothed data set, even when the thicknesses of the couplets are below the tool resolution.

The wavelengths obtained for the CaCO3% with smoothed data have the following values: 93 cm, 104 cm, 217 cm, 320 cm and 433 cm (**Fig. 7.8 B**). Similar wavelengths for CaCO3%,

---

[6] It was chosen to divide this interval in seven equal parts because it would result in intervals of 3.8 m that are similar to the most important lower frequencies and because it would be easier to compare the results of equally spaced intervals.

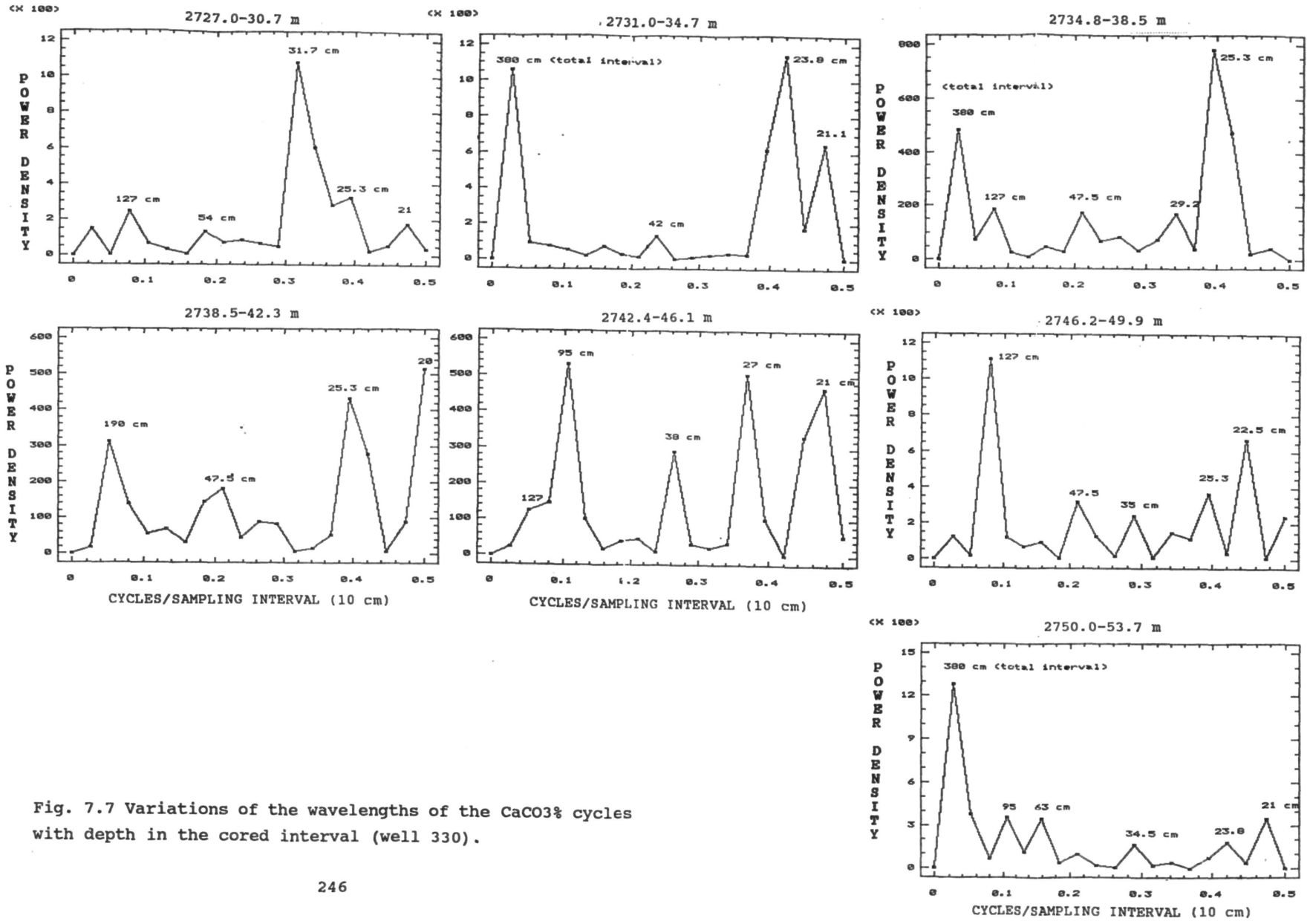
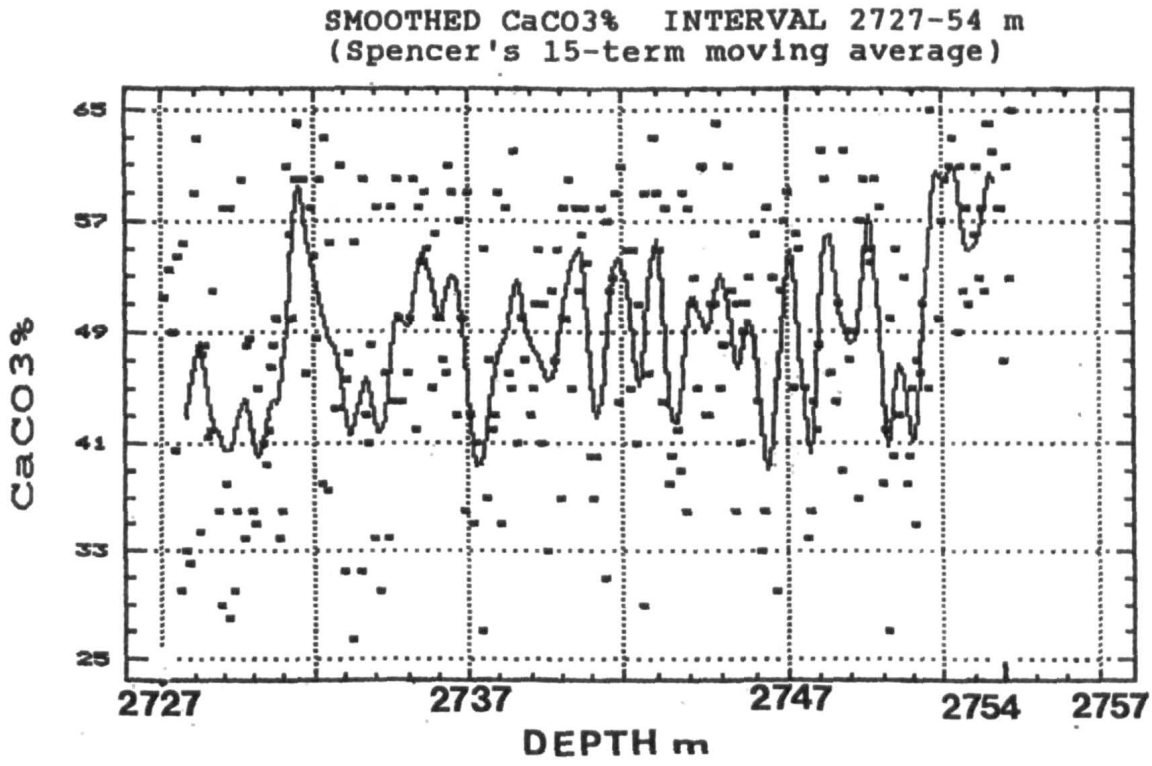


Fig. 7.7 Variations of the wavelengths of the CaCO3% cycles with depth in the cored interval (well 330).



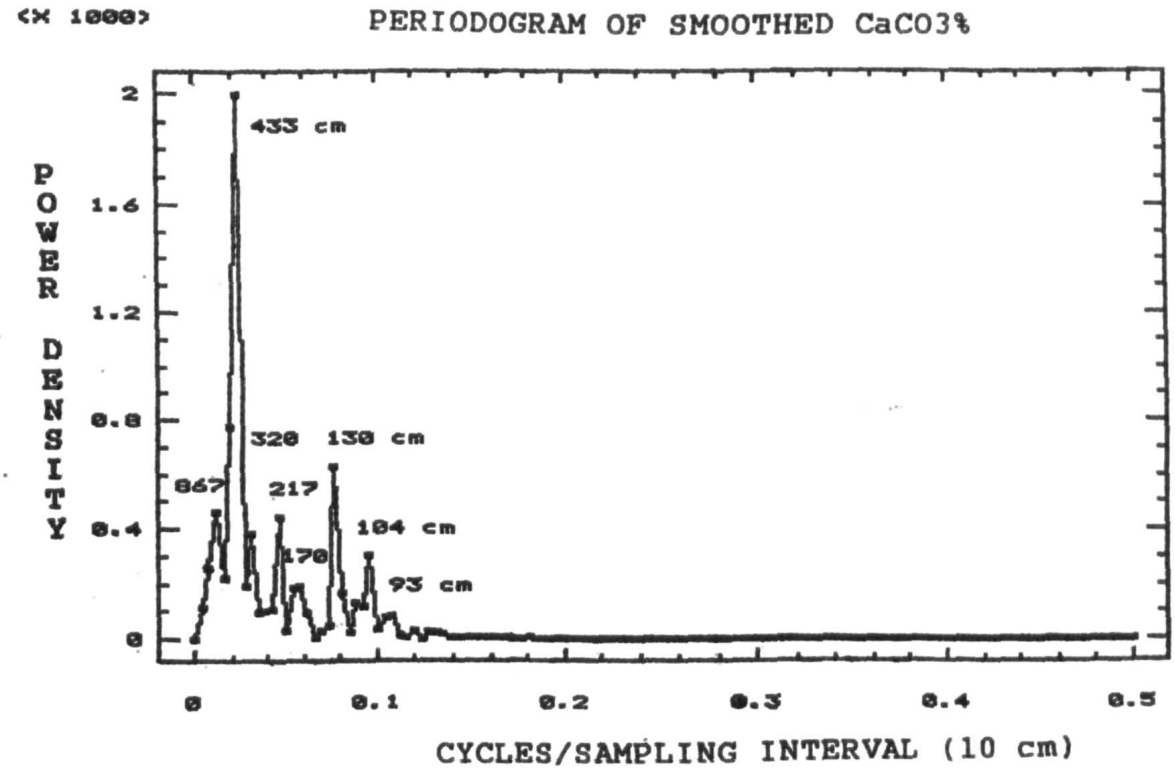


Fig. 7.8 (A) Smoothed curve for CaCO3% and (B) corresponding frequencies and calculated wavelengths.

derived from core and wireline log data, were obtained (25-26 cm, 37-53 cm, and 96-160-200 cm) from the same stratigraphic interval (zones N-530/N-540), from wells MRL-4 and 342, 40 Km to the south and 12 Km to the north respectively of well 330, when spectral analysis was applied (**Table 7.1**).

As the sediments deposited during zone N-540 have been cored totally in well MRL-4 (27.65 m) and its time span is 3.3 Myr (Beurlen et al., 1988) it is possible to estimate the average undecompacted sedimentation rate of this interval as 27.65 cm/3.3 Myr, i.e. 0.84 cm/Kyr. This assumes that there is no major hiatus in this stratigraphic record. Similar procedures were used for the other wells even in those without cores, but where palaeontological data were available from cuttings (see **Table 7.2**). The estimated average undecompacted sedimentation rate show similarities in different wells, especially for the zones N-520/530/540. However, zone N-530 is usually thinner in the majority of the wells (**Table 7.2**) which can be interpreted as result of a hiatus, probably due to erosion. The younger zones N-545, N-550, and N-560/570 have more variable average sedimentation rates.

It is possible to use these estimated sedimentation rates to establish the period of time for each wave length of the frequencies of the couplets or their bundles and determine whether they correspond or not to the band of orbital periodicities (e.g. climatic cycles or Milankovitch Band). If they are similar it will be possible to normalize the periods of these frequencies with those of the climatic cycles (e.g. 100 Kyr) and then to estimate the most probable rate of sedimentation for each stratigraphic interval.

As there are several frequencies present in the periodograms it is difficult to interpret which corresponds to the 400 Kyr, 100 Kyr, 41 Kyr and 19-23 Kyr Milankovitch periodicities. A way to solve this problem is to use the ratio between the Milankovitch periodicities (Cottle, 1989; see **Table 7.3**) as a correlation parameter combined with the average sedimentation rate and the thicknesses of the

marlstone-mudstone couplets (**Table 7.4**).

TABLE 7.1 A

WELL: 330 CaCO3% sampling at every 10 cm	
Interval	Main frequencies represented by their corresponding wavelengths in cm (* the most significant ones)
2727.0-54.4 m (27.4 m) Smoothed interval:	*433 325 217 173 *130 104 93
2727.0-41.0 m (14 m) Normal:	*350 *175 *44 *38 *25 *24 *20
Differencing	44 *38 32 30 *25 *24 *23 *20
2740.4-54.4 m (14 m) Differencing	466 233 *127 *107 93 *36 23 *22 36 29 24 23 *22 20
2727.0-30.7 m (3.7 m)	127 54 *32 25 21
2731.0-34.7 m (3.7 m)	42 *24 21
2734.8-38.5 m (3.7 m)	127 47 29 *25
2738.5-42.3 m (3.8 m)	190 47 *25 20
2742.4-46.1 m (3.7 m)	127 *95 41 *27 *21
2746.2-49.9 m (3.7 m)	*127 47 35 25 *22
2750.0-53.7 m (3.7 m)	95 63 35 24 *21

WELL: MRL-4 core photo; sampling 1 lithology per 10 cm; the lithologies were represented by codes[7].	
Interval	Wavelengths in cm
2632-2652 m (20 m)	117 77 57 *51 47 45 *43 36 35 31 29
2632-2642 m (10 m)	125 59 *53 *45 40 30 *26 24 21
2642-2652 m (10 m)	91 *48 *43 *37 28
2652-2672 m (20 m)	*166 *61 *41 *38 28 25 24 23 22
2652-2662 m (10 m)	*166 71 *45 *38 36*25
2662-2672 m (10 m)	166 111 67 45 *42 *37 29 24 23 22
2685-2694 m (9 m)	*200 *45 37 33 25 23 21

[7] Codes used: sandstone = -1; mudstone = 1; calcareous mudstone = 2; marlstone 3.

TABLE 7.1 B (continuation)

WELL: MRL-4	
NEUTRON LOG (ΦN p.u.); sampling: 1 value per 40 cm;	
Interval	Main frequencies represented by their corresponding wavelengths in cm (* the most significant ones)
2632-2712 m	
normal	364 333 296 216 160 154
differencing	296 216 *160 *154 114 96
2632-72 m	*667 500 308 *160 143 125 108 87
2632-52 m	333 *200 105 87
2652-2672 m	250 *200 143 125 111 87
2672-2712 m	
normal	444 364 308 235 160 114
differencing	356 302 231 *157 145 135 115 96
2672-2752 m	
normal	*2667 533 444 320 235 154 116 96
differencing	320 229 *151 136 127*116*96
2712-2752 m	
normal	667 400 250 210 190 129 114 95
differencing	218 196 *131 115 96
2633-2650 m using 20 cm for sampling: NEUTRON LOG	
normal	*860 287 215 *172 115*91 82
differencing	560 336 *210 *153 120 90 *80 70*60
DENSITY LOG	
normal	570 *344 246 172 132 91
differencing	560 *280 210 120 98 87 67
WELL: 342	
NEUTRON LOG (ΦN p.u.); sampling: 1 value per 40 cm;	
2735-2764 m	
normal:	*933 *560 *400 *311 245 155 140 127
differencing	543 388 *272 *170 113 104 94 85
DIPMETER LOG; sampling: 1 value per 10 cm.	
2735-50 m	*500 *300 *187 136 38 33 *28 26 22

TABLE 7.2

NANNOFOSSIL ZONES	N-520	N-530	N-540	N-545	N-550	N-560/70
TIME SPAN (Myr)	3.1	3.0	3.3	1.8	4.5	2.7
well 344 interval (m) sed. rate (cm/Kyr)	 72 2.3	 36 1.2	 36 1.1	 125 6.9	 775 17.2	 216 8.0
MRL-4 core interval (m) (cm/Kyr)	 0.87	 ~26 0.84	 27.6			
well 219 interval (m) (cm/Kyr)		 18 0.6	 34 1.03		 275 ? 6.1	 828 30.7
well 325 interval (m) (cm/Kyr)	 54 1.7	 36 1.2	 36 1.1			 990 36.7
well 330 interval (m) (cm/Kyr)		 ~10 0.33	 ~34 1.03			
well 356 interval (m) (cm/Kyr)	 72 2.3	 18 0.6	 36 1.1			
well 360 interval (m) (cm/Kyr)	 72 2.3	 36 1.2				
AVERAGE cm/Kyr	2.3	1.2	1.1	6.9 ?	6-17	8-36.7

TABLE 7.3

Orbital Periodicities in Kyr	413	100	41	23	19
413	1	4.13	10.1	18.0	21.7
100		1	2.44	4.35	5.26
41			1	1.78	1.21

As core availability is usually limited it is important to be able to do this kind of analysis using only wireline log data. The microresistivity curves of the dipmeter log in combination with the other wireline logs appear to the most satisfactory when core samples are not available provided the stratigraphic interval under study is already known.

TABLE 7.4 A

NANNOFOSSIL ZONE N-520 AV. SED. RATE 2.3 cm/Kyr	
WELL	Wavelengths cm & corresponding periodicities Kyr
344	NEUTRON
cm	380 340 317 173 137 117 112 106 93 86
Kyr	165 148 138 75 60 51 49 46 40 37
MILANK	< 100 Kyr > < 41 Kyr >
USING MILANKOVITCH BAND: AV. SED. RATE = 2.1-3.2 cm/Kyr	

NANNOFOSSIL ZONE N-530 AV. SED. RATE 1.2 cm/Kyr	
WELL	Wavelengths cm & corresponding periodicities Kyr
330	(CaCO3%)
cm	470 230 127 107 95 63 48 35 28 25 24 22.5 21
Kyr	391 191 105 89 79 52 40 29 23 21 20 19 18
MILANK	<400> < 100 > < 41> < 23 - 19 Kyr >
USING MILANKOVITCH BAND: AV. SED. RATE = 1.1-1.2 cm/Kyr	
344	NEUTRON
cm	700 440 290 180 150 139 124 89 85 70 66 59 49 40
Kyr	583 367 242 150 125 116 103 74 71 58 55 49 41 33
MILANK	< 400 > < 100 Kyr > < 41 >
USING MILANKOVITCH BAND: AV. SED. RATE = 1.2-1.4 cm/Kyr	
MRL-4	NEUTRON/CORE
cm	302 231 157 145 135 115 96 45 37 33 25 21
Kyr	252 193 131 121 113 96 80 38 31 28 21 18
MILANK	< 100 Kyr >< 41 > <23 -18>
USING MILANKOVITCH BAND: AV. SED. RATE = 1.23 cm/Kyr	

TABLE 7.4 B (continuation)

NANNOFOSSIL ZONE N-540 AV. SED. RATE 1.1 cm/Kyr	
WELL	Wavelengths cm & corresponding periodicities Kyr
330	CaCO3%
cm	350 190 127 95 47 43 38 32 30 27 25.5 24 23 21.5
Kyr	318 173 115 86 43 39 35 29 27 25 23 22 21 20
MILANK	<400> < 100> < 41 > < 23 - 19 Kyr >
USING MILANKOVITCH BAND: AV. SED. RATE = **1.1-1.3 cm/Kyr**	
344	NEUTRON
cm	*720 *400 327 280 200 170 *130 116 100 92 82
Kyr	655 364 297 255 182 155 118 105 91 84 75
MILANK	< 400 > < 100 Kyr >
USING MILANKOVITCH BAND: AV. SED. RATE = **1.0-1.3/Kyr**	
MRL-4	NEUTRON/CORE
cm	360 216 166 154 145 114 96 67 45 37 31 24 22
Kyr	327 196 151 140 132 104 87 61 41 34 28 22 20
MILANK	<400> < 100 Kyr> < 41 > < 23-19>
USING MILANKOVITCH BAND: AV. SED. RATE = **1.2 cm/Kyr**	
NANNOFOSSIL ZONE N-545 AV. SED. RATE 6.9 cm/Kyr	
WELL	Wavelengths cm & corresponding periodicities Kyr
344	NEUTRON
cm	907 820 600 480 410 380 270 247 170 130 120 113
Kyr	131 119 87 70 59 55 39 36 25 19 17 16
MILANK	< 100 Kyr > < 41 > < 23 - 19 >
USING MILANKOVITCH BAND: AV. SED. RATE = **7.0 cm/Kyr**	
	AV. SED. RATE 1) **6.9 cm/Kyr**; 2) **1.2 cm/Kyr**
MRL-4	NEUTRON/CORE
cm	560 336 210 153 120 99 80 70 60 51 47 43 35 29
1) Kyr	81 49 30 22 17 14 12 10 9 7 7 6 5 4
2) Kyr	467 280 175 128 100 83 67 58 50 43 39 36 29 24
MILANK	< 400 > < 100 Kyr > < 41 > < 23 >
USING MILANKOVITCH BAND: AV. SED. RATE = 1.2 cm/Kyr	

TABLE 7.4 C (continuation)

NANNOFOSSIL ZONE N-550 AV. SED. RATE 17.2 cm/Kyr									
Wavelengths cm & corresponding periodicities Kyr									
Well 344 interval: 1700 - 1800 m									
cm		330	250	233	189	179	149	123	115
Kyr	(too low)	19	15	14	11	10	9	7	7
MILANK.		<	23		-	19 (?)			>
option		<	41 Kyr			><	23 - 19		>
USING MILANKOVITCH BAND: AV. SED. RATE = 5.7-6.1 cm/Kyr									
interval: 1800 - 2400 m									
cm		870	769	741	600	555	541	417	370	333
Kyr		51	45	43	35	32	31	24	22	19
MILANK.		<		41	Kyr		>	<	23-19	>
USING MILANKOVITCH BAND: AV. SED. RATE = 16.6-20 cm/Kyr									

After matching the sedimentary cycles with the Milankovitch periodicities it is possible to use this type of data to determine the time span of a given sedimentary sequence just by counting how many peaks equivalent to (X) Kyr exist in the wireline logs of a sedimentary interval. This could also be used to determine the probable periodicity of turbidites. Further more, in those intervals with a very high rate of sedimentation such as the Miocene in the Campos Basin it should also be possible to estimate the time span between potential seismic reflectors (i.e. rocks with good impedance contrasts) and correlate them with seismic sections using synthetic seismograms.

Well 344 can be used to illustrate this practical approach (**Fig. 7.2**). There is a gradual upward increase in the sedimentation rate from the basal nannofossil zones N-520/530/540 to the zones N-545/550/560/570. This is represented in the wireline logs by an increase upwards in the thickness of the marlstone and mudstone beds. In the intervals corresponding to nannofossil zones N-530, N-540 and N-545 there are 5 relatively thin (<4 m) turbidite sandstones, which do not seem to be associated with much erosion (**Fig. 7.2**). To determine their periodicities

spectral analysis of these intervals were made (see **Table 7.5** and **Fig. 7.9**).

TABLE 7.5

INTERVALS BETWEEN TURBIDITES IN THE ZONE N-545; WELL 344										
NANNOFOSSIL ZONE N-545 AV. SED. RATE 6.9 cm/Kyr										
Main frequencies represented by their corresponding wavelengths **cm** and periodicities **Kyr** derived from the **NEUTRON LOG**										
interval										
2482-2520 m										
cm	630	480	380	270	210			120		
Kyr	91	70	55	39	30			17		
2525-2555 m										
cm	600	430		270		190	170	143	125	110
Kyr	87	62		39		28	25	21	18	16
2555-2580 m										
cm	620	410						130	120	110 99
Kyr	90	59						19	17	16 14
2580-2607 m										
cm		453			247					113 70
Kyr		66			36					16 10
MILANKOVITCH	< 100 Kyr >			< ?	41		><	23	- 19	>

In the interval 2482-2520 m (38 m) in well 344 there are 29 small peaks in the neutron log of ~1.3 m wavelength. Based on spectral analysis these are equivalent to a periodicity of ~19-23 Kyr. Additionally these 29 small peaks form 10 bundles each ~3.8 m thick, and their computed periodicities vary between ~41-100 Kyr (**Table 7.5**). However, only 9 of these 10 bundles can be seen in the RIL and sonic logs presented in **Fig. 7.2**, because of the scale of these logs. In the enlargement **Fig. 7.2 b**, it is possible to identify more easily the turbidite sandstone that occurs at the base of this interval and some of the individual marlstone-mudstone peaks in the neutron log below and above this turbidite. The probable time span between the turbidites from 2482 and 2520 m is **551-667 Kyr**. This was determined using the orbital periodicity of 19-23 kyr per cycle and an average sedimentation rate (undecompacted) of 6.9-5.7 cm/Kyr (**Table 7.5**).

PERIODOGRAM OF THE NEUTRON LOG POROSITIES FOR WELL 344

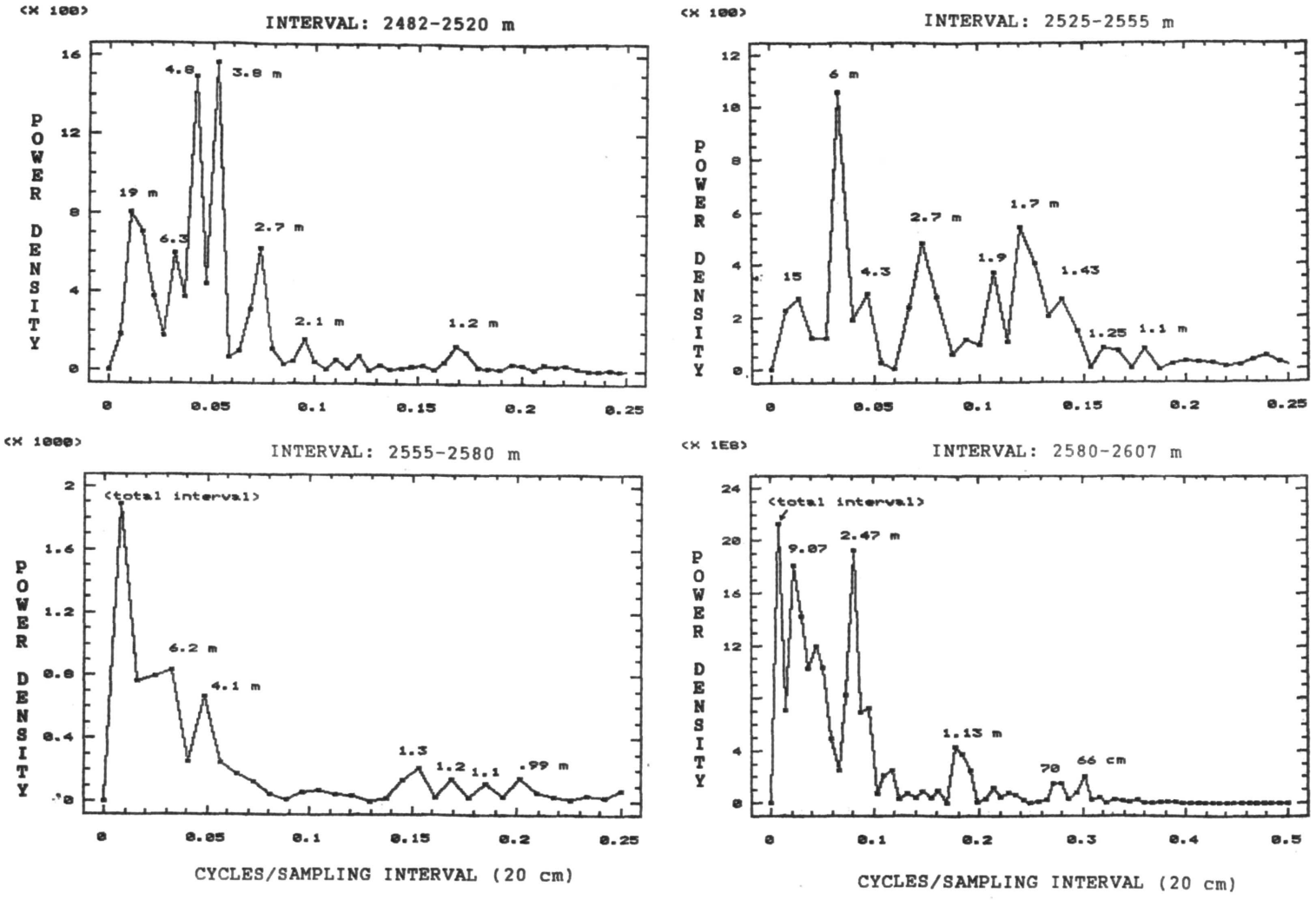


Fig. 7.9 Frequencies and corresponding wavelengths of the cycles between turbidites in the nannofossil zone N-545.

In the depth interval between the two turbidites between 2525-2555 m (30 m) there are 20 small cycles of ~1.5 m wavelength (19-23 Kyr) in the neutron log. The probable time span between these turbidites is **380-460 Kyr**, based on the orbital periodicity of 19-23 Kyr and average undecompacted sedimentation rate of 7.9-6.5 cm/Kyr. In the depth interval of 2555-2580 m (25 m) there are 20 small cycles of ~1.25 m wavelength (19-23 Kyr) in the neutron log. The probable time span between these turbidites is **380-460 Kyr**, based on orbital periodicities of 19-23 Kyr (6.6-5.4 cm/Kyr).

In the interval 2580-2607 m (27 m) there are 30 small cycles of ~0. 90 m wavelength, in the neutron log, from the turbidite body down to the base of the zone N-545 that would correspond to **~570-690** Kyr, based on orbital periodicity of 19-23 Kyr (4.7-3.9 cm/Kyr).

However, if the previous cycles are normalized in relation to the orbital periodicity of 41 Kyr instead of 19-23 Kyr the following values, for the time span between each turbidite sandstone, would be obtained: 2485-2520 m = 1189 Kyr; 2525-2555 m = 820 Kyr; 2555-2580 m = 820 Kyr; 2580-2607 m = 1230 Kyr. These time spans are equivalent to much lower average sedimentation rates (i.e., 3.2 cm/Kyr, 3.7 cm/Kyr, 3.0 cm/Kyr, and 2.2 cm/Kyr, respectively) compared to a general average sedimentation rate of 6.9 cm/Kyr for the whole interval. From this, it can be concluded that the 19-23 Kyr is best periodicity to be used to calculate the time span between these turbidite sandstones.

In zone N-540 of well 342 there are thin turbidite sandstones interbedded with marlstone-mudstone couplets. Spectral analysis of this interval indicates that these couplets have an average wavelength of ~28 cm (**Fig 7.3B** and **C, Table 7.1B** and **Fig. 7.10**). These couplets are also organized in bundles with a wavelength cycle of ~187 cm and they can be easily identified on the neutron log (**Table 7.1B** and **Fig 7.3**). It can be seen in the dipmeter log that the thin turbidites are separated by about 21 couplets over 6 m

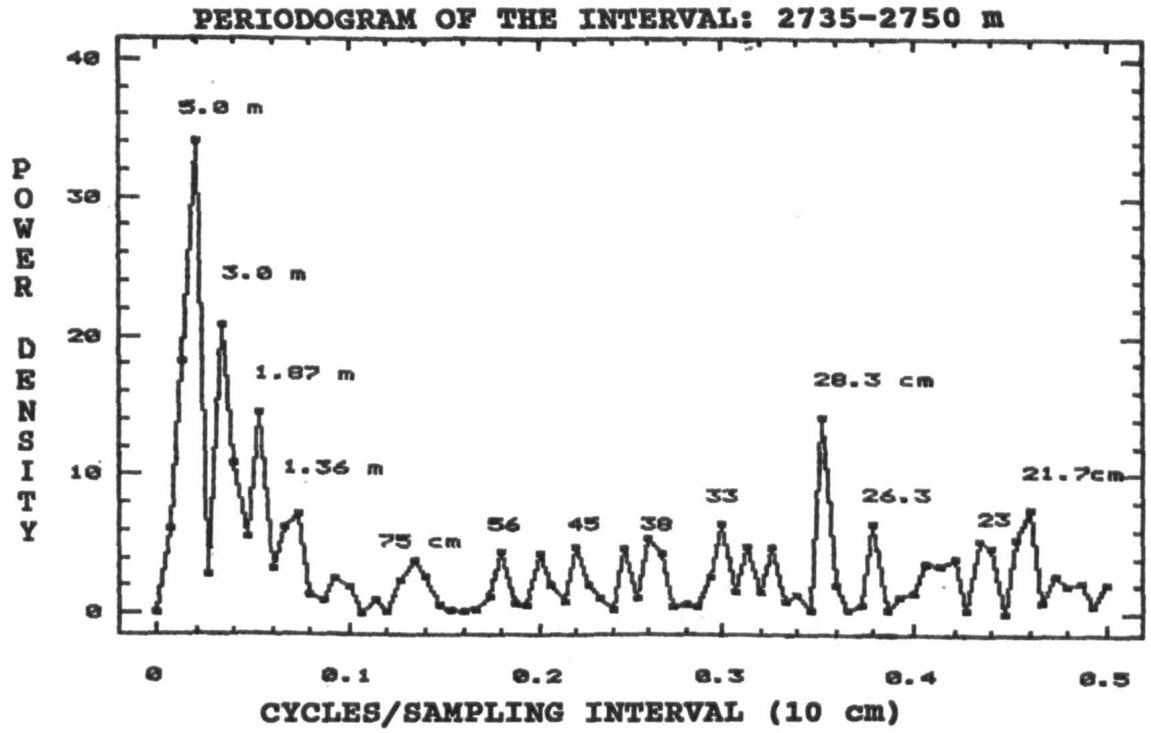


Fig. 7.10 Frequencies and corresponding wavelengths derived from dipmeter log of well 342.

(see **Fig. 7.3 B** and **C**). Assuming 1.1 cm/Kyr as the average sedimentation rate for this zone N-540, the 28 cm wavelength would have a periodicity of ~25 Kyr. This corresponds reasonably to the orbital periodicity of 19-23 Kyr. Consequently, when these cycles are normalized to this periodicity (19-23 Kyr) the total time span separating the turbidites would be **399-483 Kyr.** These results are very similar to those obtained for the time span between the turbidites within zone N-545 in well 344, despite their different sedimentation rates (i.e. 1.1 cm/kyr for zone the N-540 against 6.9 cm/Kyr for the zone N-545). This time span corresponds roughly to an orbital periodicity of 400 Kyr. The latter implies that these relatively thin turbidites (i.e. 4^{th} order minor events) would have had their periodicities controlled by climatic cycles.

In well 342, in addition to the thin turbidites interbedded with marlstones, there are also very thick turbidite sandstones (**Fig. 7.3**). Assuming previous calculations for the periodicities of the thin turbidites as **399-483 Kyr** to be correct, the major turbidite sandstones

(i.e. major events) would be separated by about 1200-1455 Kyr. This time span also coincides approximately with the 3rd order variation in eustatic changes determined by Haq et al. (1987) for the Cenozoic.

This kind of approach can also be used to refine the position and the occurrence in time of the main turbidite systems. This can be shown in well 344 where there is a turbidite sandstone within zone N-530 (**Fig. 7.2 C**), but because of the relative low resolution of the palaeontological tool (see Chapter 6), it is not possible accurately to know its age. Consequently, any attempt to correlate it with the "sea level" curves of Haq et al. (1987) can only be a rough estimation. However, as the Blue Marker has been interpreted as having been deposited between 33 and 32 Myr ago (Shimabukuro, 1987) it is possible to assume as a working hypothesis that the top of this marker has an age of 32 Myr. This can be used as a relative "absolute age" to estimate the time span up before the first occurrence of the turbidite in well 344. There are 24 m of marlstones between the Blue Marker and the base of the turbidite (**Fig. 7 2 C**). In this interval the neutron log shows 18 small peaks with an average wavelength of ~133 cm. The average sedimentation rate previously calculated for this interval was 1.2-1.3 cm/Kyr (**Table 7.4B**), giving a total time span for the interval of 2.0-1.8 Myr. Consequently, the estimated age for the base of this turbidite sandstone would be approximately 30.2-30.0 Myr. This is the age of the largest sea-level fall during the Oligocene (Haq et al. (1987), which occurred just after a major highstand period when the Blue Marker and these marlstones were deposited (see **Fig. 6.8** in Chapter 6).

Another practical application of spectral analysis is to correlate the contrasts in velocity and density between the mudstones, marlstones and dolomitized marlstones and their seismic responses. It is possible, for example, to use sedimentary cycles to establish the relative age of a seismic reflector by counting the number of marlstone peaks in the wireline logs between two reflectors, and then

multiply by the time span of the peaks. This is easier done when the sedimentation rate is high, i.e. over 10 cm/Kyr.

In the wireline logs of well 344, within the depth interval of 2300-2500 m, there are three levels (2350 m, 2400 m and 2475 m) which could be equivalent to potential seismic reflections (i.e good sonic velocity contrast) (see **Fig. 7.2**). Within the interval 2350-2475 m there are 20 main peaks in the sonic and RIL logs, 12 within the depth interval of 2400-2475 m and 8 between 2350-2400 m. The periodogram, derived from the neutron log, for the interval 2442-2477 m, indicates the dominance of the 8.2 m wavelength (**Fig. 7.11**). Additionally, the most significant wavelengths of the total interval (1700-2480 m) corresponding to the nannofossil zone N-550 vary between ~2 and 8.7 m. These wavelengths correspond approximately to the orbital periodicity of 41 Kyr (see **Table 7.4C**). Based on the 41 Kyr periodicity, the time span for the intervals containing 12 (2400-2475 m) and 8 peaks (2350-2400 m), mentioned above, would correspond respectively to **~492 Kyr** and **~328 Kyr**. This time span range coincides with those for the thin turbidites of well 342.

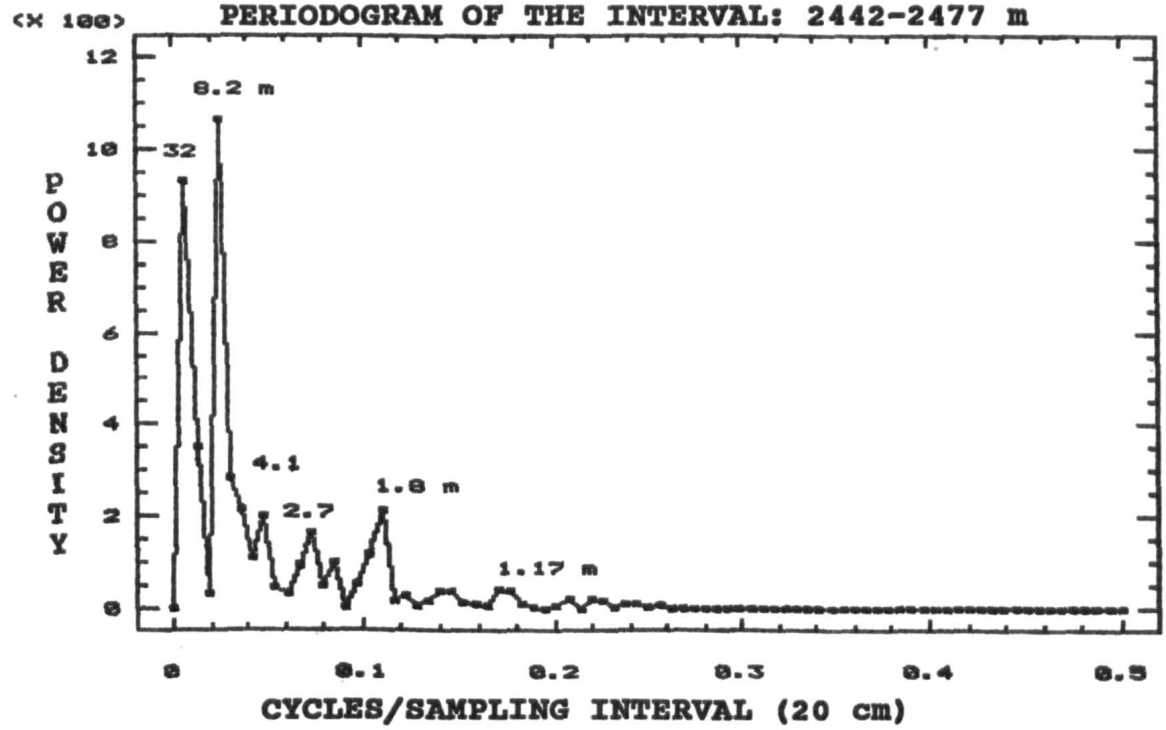


Fig. 7.11 Frequencies and corresponding wavelengths from the basal interval of the zone N-550, derived from neutron log.

As calculated from data of well 342, important turbidite sandstones occurred over a time interval of about ~1.2-1.5 Myr. From this it can be inferred that in an interval with an average sedimentation rate of 17 cm/Kyr (e.g. zone N-550 of well 344) important sedimentological changes would be expected to occur every 3 or 4 main sedimentary cycles (i.e. 200-250 m). These changes could also be the cause for important contrasts in the sedimentary rock characteristics (i.e impedance contrast) required to produce seismic reflectors. Using this approach, it should be possible to estimate the time span involved in the deposition of a sedimentary sequence by counting the number of its seismic reflectors. This procedure can lead to some errors but the degree of error can be predicted and will depend on the type and quality of the available data and the sedimentation rates. When the latter is very high the errors would be relatively small.

However, this assumption also implies that turbiditic sandstones should always occur about every 400, 800 or 1200-1500 Kyr, but this has not been observed in the study area. This suggests that the frequency of occurrence of these turbidites are probably superimposed on a lower frequency wave cycle which reflects more prolonged phenomenon. Such lower frequency wave cycles could well be the Tertiary eustatic changes of ~10 Myr (Haq et al., 1987) (**Fig. 6.8**). Using this frequency range as an example it can be said that the phenomenon (i.e. relative sea-level fall) that has triggered the formation of important sand-rich turbidites within the Oligocene-Lower Miocene succession of the Campos Basin would be the result of resonance i.e when all the favourable frequencies have been in phase and their combined amplitudes were enhanced causing a sea-level fall. However, this lower frequency wave cycle (i.e. ~10 Myr) instead of being eustatic (Haq et al., 1987) could be of tectonic origin. The occurrence of two intervals of sand-rich turbidites in the Tertiary succession of the Campos Basin (e.g. Middle Eocene and Oligocene/Lower Miocene, see **Fig. 3.5** and **3.6**) could therefore be related to the Tertiary

isostatic uplift of the source area (Mohriak, 1988).

In conclusion, the occurrence of sand-rich turbidites in the studied succession of the Campos Basin could have been either driven by a combination of a low frequency wave cycles of eustatic or tectonic origin superimposed by eustatic fluctuations related to orbital periodicities, i.e. Milankovitch band climatic cycles.

7.5 STABLE ISOTOPES

Oxygen and carbon stable isotopic compositions of foraminiferal tests have been widely used to determine variations in temperature of their marine environments and estimate variations in the total ocean volume during glacial and interglacial periods. An integration of the marine record of $\delta^{18}O$ for the Pleistocene and the orbital theory was presented by Imbrie et al. (1984). Their work represents an alternative approach to the one discussed above based on spectral analysis of lithological characteristics to determine the existence of the Milankovitch band periodicities.

The sampling interval used by Imbrie et al. (1984) varied from 1.5 cm (~1.1 Kyr) to 8 cm (~5.0 Kyr) for a total of 85 m of core. Such a large number of samples is necessary to fulfil the requirements for spectral analysis. However, in this study, due to the limitations of time, equipment and because this topic is not the main point of this research project, only 29 isotopic analyses of benthonic foraminifera, Cibicidoides sp. (25) and Florilus sp. (4) were made of core samples from well 330 (see Chapter 4 for methodology).

7.5.1 STABLE ISOTOPE RESULTS

The results show that the oxygen isotope values are all negative indicative of a "lighter" composition and an enrichment in ^{16}O. The $\delta^{13}C$ values are all slightly positive indicative of an enrichment in ^{13}C (**Table 7.6**).

There are significant variations in the $\delta^{18}O$ values from -0.730 to -2.291‰ over a vertical distance of only 120 cm

(**Table 7.6** and **Fig. 7.12A**). In a more closely sampled interval of only 10 cm the $\delta^{18}O$ values vary between -1.098 to -2.217‰ (**Table 7.6**). When the differences between adjacent values of $\delta^{18}O$ and $\delta^{13}C$ are plotted against depth significant oscillations in the values of the stable isotopes are clearly seen (**Fig. 7.12B**).

A plot of $\delta^{18}O$ and $\delta^{13}C$ versus corresponding percentages of CaCO3 against depth shows that the higher percentages of CaCO3 are commonly associated with less negative $\delta^{18}O$ and less frequently slightly positive $\delta^{13}C$ values (**Fig. 7.13A**). In a set of more closely spaced samples over the depth range 2795.5 to 2733.9 m, the % CaCO3 $\delta^{18}O$ values are highly variable (**Fig. 7.13B**). The variations in % CaCO3 and $\delta^{18}O$ show a similar pattern and again higher percentages of CaCO3 have less negative $\delta^{18}O$ values (**Fig. 7.13B** and **Table 7.6**). The plot of the percentages of CaCO3 against $\delta^{18}O$ and $\delta^{13}C$ clearly shows this trend of an increase in the CaCO3% associated with less negative $\delta^{18}O$ (**Fig. 7.14**).

7.5.2 INTERPRETATION AND DISCUSSION OF THE ISOTOPE SIGNATURE

The computed bottom temperatures (**Table 7.6**) using the oxygen stable isotopes of benthonic foraminifera for these samples are unrealistically high to be depositional temperatures (19.1°C and 26.2°C) using Cibicidoides sp., and even higher values using Florilus sp. (27.5°C and 31.0°C). These relatively high temperature values reflect mainly the influence of diagenesis related to the infilling of the foraminiferal chambers with calcite cements, which would shift the $\delta^{18}O$ towards "lighter" values. The cementation of foraminiferal chambers has been observed in thin-sections, especially in the deeper samples of the Oligocene succession (see Chapter 8). To compute these temperatures using the formulae of Epstein et al. (1953) & Craig (1965) it was also assumed that the $\delta^{18}O_{water}$ = 0‰ SMOW, based on modern sea-water values which is not necessarily true for the sea waters in the Oligocene. Consequently, these calculated temperatures do not represent the real temperatures at the time of deposition.

TABLE 7.6

Benthonic foraminifera: *Cibicidoides* sp.						
DEPTH	$\delta^{13}C‰_{PDB}$	DIFF	$\delta^{18}O‰_{PDB}$	DIFF	TEMP°C*	CaCO3%**
2727.7 m	+0.606		-1.341		21.8	33.0
2729.5 m	+0.015	.591	-0.730	.611	19.1	60.0
2730.8 m	+0.910	.895	-1.386	.656	22.0	34.0
2731.4 m	+0.891	.190	-0.851	.535	19.6	64.0
2732.7 m	+0.859	.032	-2.291	1.440	26.2	43.5
2733.1 m	+0.900	.041	-1.098	1.193	20.7	47.5
2733.2 m	+0.624	.276	-1.782	.684	23.8	26.5
2733.4 m	+0.521	.103	-1.689	.093	23.8	31.5
2733.5 m	+0.259	.262	-1.182	.507	21.1	60.0
2733.6 m	+0.290	.031	-1.990	.808	24.8	41.0?
2733.7 m	+0.550	.260	-1.567	.423	22.8	48.0?
2733.8 m	+0.264	.286	-2.217	.650	25.8	34.0?
2733.9 m	+0.813	.549	-1.440	.777	22.2	58.0?
2736.7 m	+0.757	.056	-1.080	.360	20.6	50.0
2737.6 m	+0.864	.107	-1.130	.050	20.8	47.0
2738.3 m	+0.469	.395	-1.470	.340	22.4	45.0
2739.3 m	+0.019	.450	-0.876	.594	19.8	51.0?
2740.9 m	+0.764	.745	-1.928	1.052	24.5	40.0
2741.9 m	+0.138	.626	-0.954	.974	20.1	60.0
2743.7 m	+0.370	.232	-1.539	.585	22.7	59.0
2744.7 m	+0.486	.116	-1.334	.205	21.8	51.0
2745.7 m	+0.653	.167	-1.522	.188	22.6	51.0
2746.6 m	+0.546	.107	-1.179	.343	21.1	52.0?
2747.7 m	+0.191	.355	-1.415	.236	22.1	44.0
2751.8 m	+0.883	.692	-1.928	.513	24.5	66.0
Florilus sp.						
2729.5 m	+0.937		-2.739		28.3	60.0
2729.7	+0.949	.012	-3.272	.533	31.0	48.0
2751.8 m	+0.564	.385	-2.515	.757	27.2	66.0?
2753.2 m	+0.588	.024	-2.569	.054	27.5	58.0

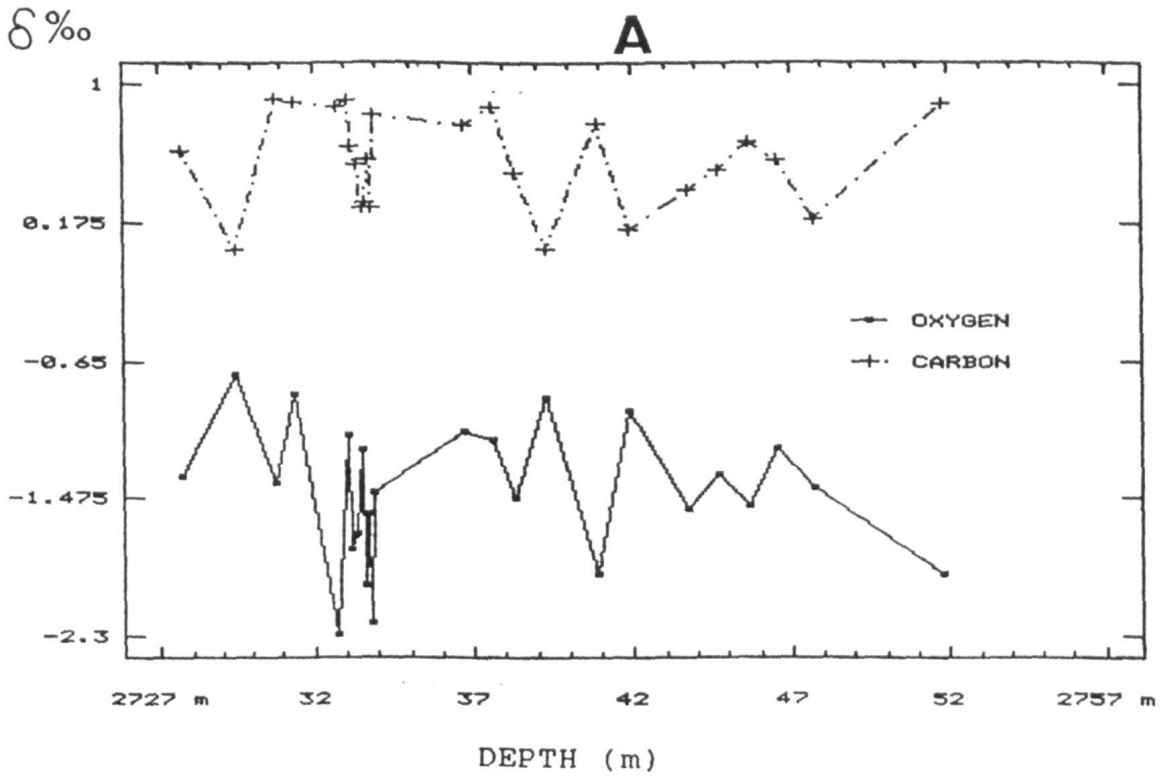
(?) These CaCO3 results have been adjusted, because the samples for CaCO3% and for isotopes were collected at different times and not necessarily has the same part of the core been sampled.

*The temperature was calculated based on Epstein et al. (1953) & Craig (1965) formulae:

Temp (°C) = 16 - 4.14 ($\delta c - \delta w$) + 0.13 ($\delta c - \delta w$)^2,

where $\delta c = \delta^{18}O$ of calcite ‰PDB; $\delta^{18}O$ of water ‰SMOW, it was assumed that the δw= 0‰SMOW.

** CaCO3% in total sediment



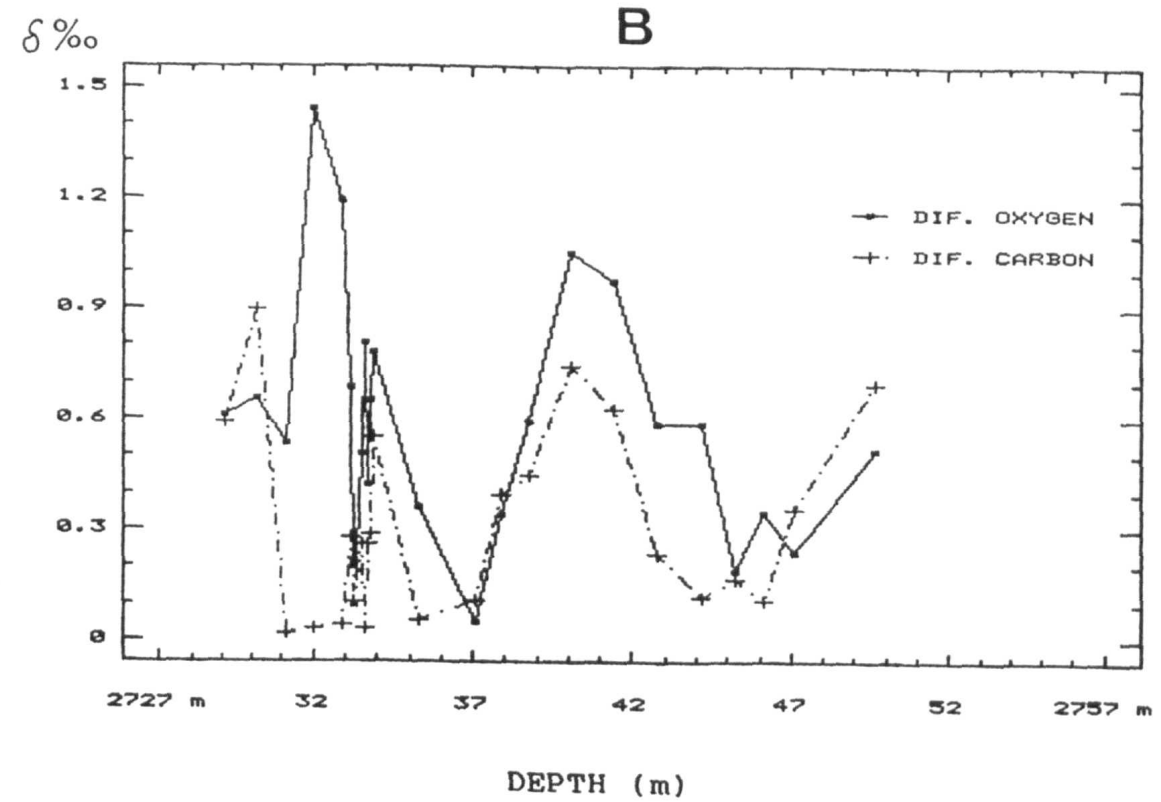


Fig. 7.12 (A) Oxygen and carbon stable isotopes of benthonic foraminifera (Cibicidoides sp.) from well 330; and (B) the difference between adjacent isotope values against depth.

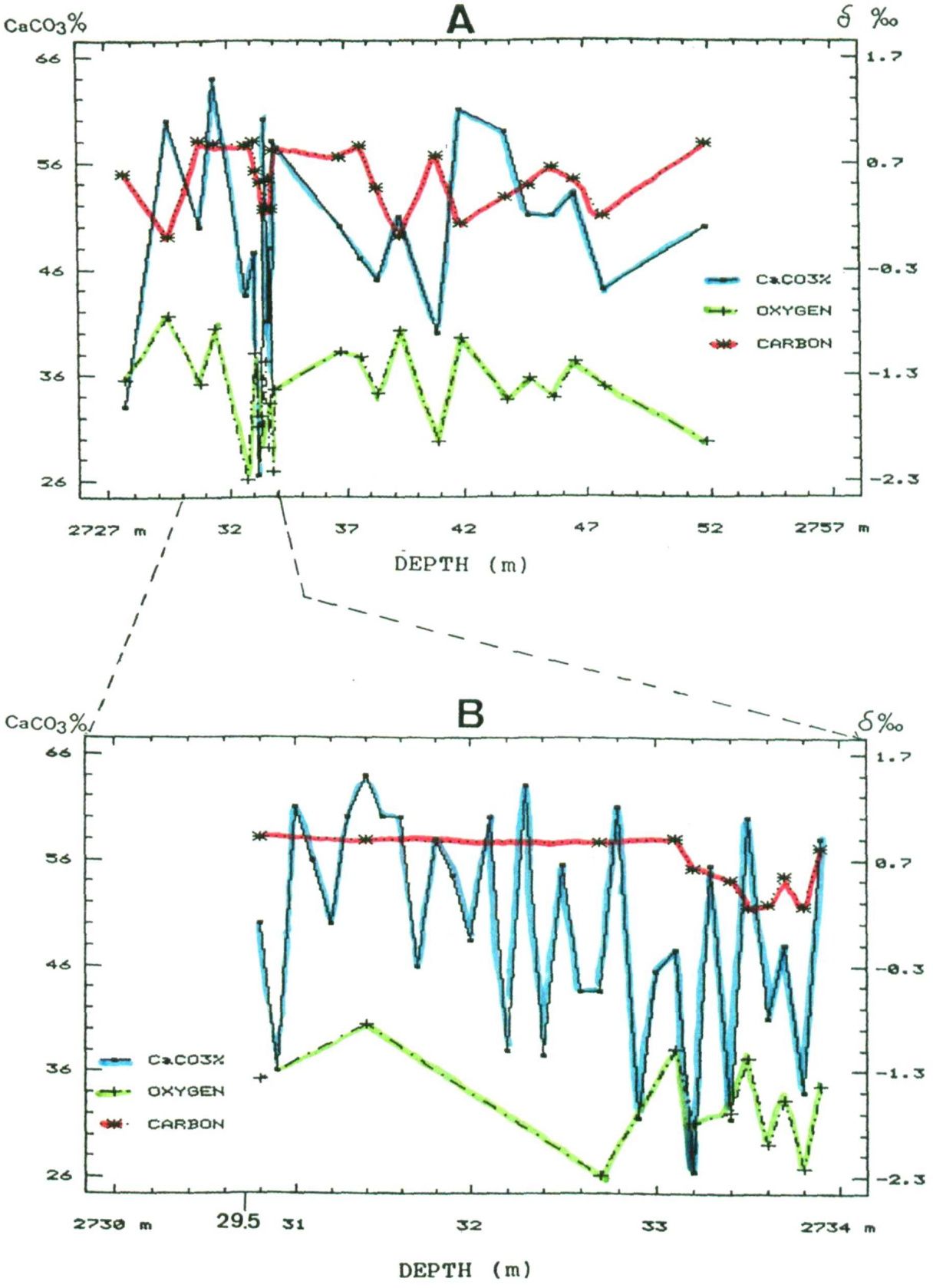


Fig. 7.13 (A) Oxygen, carbon isotopes and CaCO3% plotted against depth of total sampled interval (2727.7-51.8 m; in (B) is shown an enlargement of the interval more closely sampled i.e. 10 cm (2729.5-2733.9 m).

CaCO3% AND CORRESPONDING OXYGEN AND CARBON STABLE ISOTOPES OF BENTHONIC FORAMINIFERA

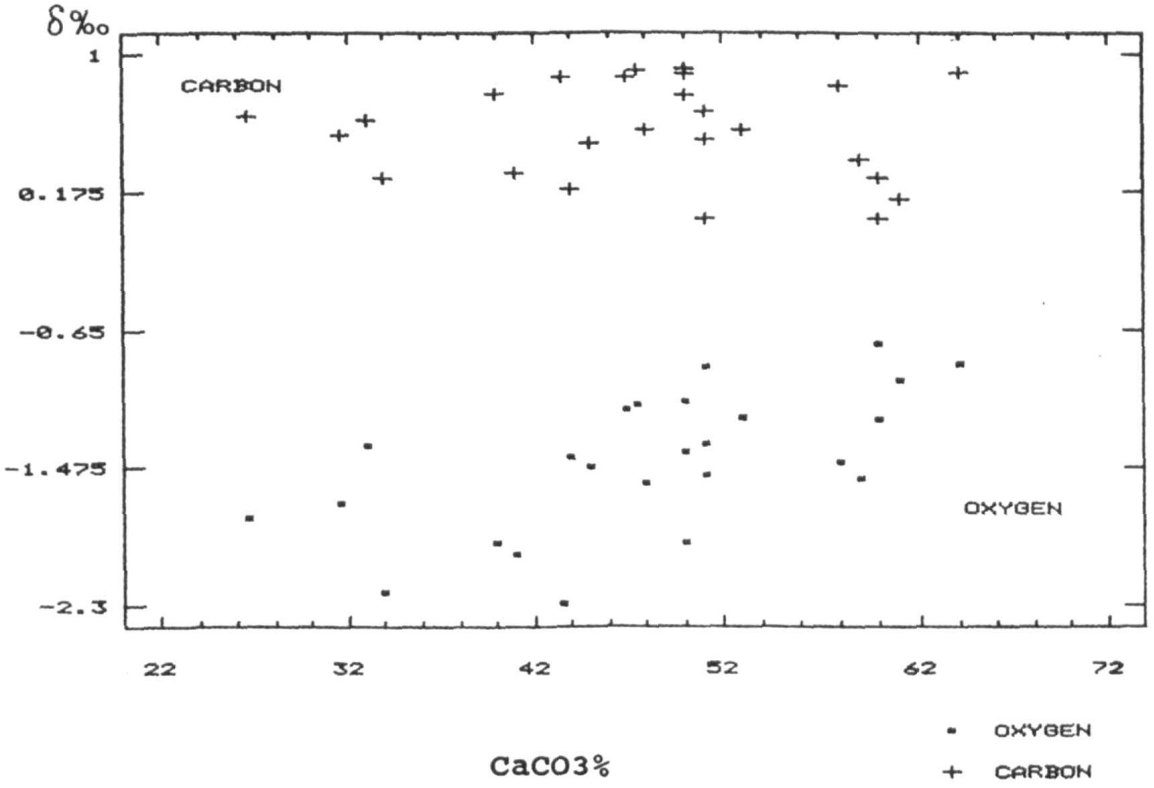


Fig. 7.14 Variations in the CaCO3% in relation to the oxygen and carbon stable isotopes in well 330.

In addition to possible diagenetic effects on the isotopic values, the differences between the results from Cibicidoides and Florilus are caused by a differential fractionation of the isotopes between the two species.

Provided the diagenetic effects have been uniform in all the samples oxygen and carbon isotopic data observed in the samples from well 330 probably reflect the relative variations in the sea-water temperature, salinity and also global isotopic variations in the oceans due to changes in the ice volume at the time of deposition. The distinction between these various factors would need a much larger number of samples from which the trend of diagenetic effects and other influences could be taken into account.

Following previous interpretations (see sections 7.2 and 7.3), the Oligocene marlstones and carbonate mudstones of the Campos Basin were probably deposited during transgressions or highstands of sea-level under a warm climate and the converse was probably true for the rhythmically interbedded mudstones (e.g. Bé et al., 1976). If the sea-level fluctuations were partially controlled by eustasy we would expect an enrichment[8] in the ocean waters of ^{18}O during the low sea levels and vice-versa during the highstands. Consequently, it would be expected that marlstones should be enriched in ^{16}O and siliciclastic mudstones in ^{18}O (e.g. Shackleton et al., 1984). However, the oxygen stable isotope results from well 330 show less negative $\delta^{18}O$ values associated with higher CaCO3% (marlstones), and the lighter ones associated with lower CaCO3% (mudstones), i.e. the opposite of what might be expected (**Table 7.6, Fig. 7.14**). This discrepancy could be partly explained by the fact that the analyzed samples are from upper bathyal sediments rather than the pelagic sediments, sampled in the majority of the DSDP wells, used to establish isotopic variations in the sea-waters (e.g. Shackleton et al., 1984). The DSDP sites are usually located on open ocean, abyssal environments, away from the influence of coastal/shelf processes.

Additionally, the oxygen isotopic composition is a function of both the ambient sea-water composition and temperature. Lower salinities and warmer temperatures would both result in lighter $\delta^{18}O$ values for the foraminifera (Fairbanks, 1989). The effect of these parameters can be inferred by studying the circulation patterns and temperatures of the Brazilian continental margin during the Oligocene-Miocene based on palaeogeographic reconstructions (Kvasov and Verbitsky, 1981, their Fig. 2, see **Fig. 7.4**). At the beginning of the Oligocene and Miocene the currents

---

[8] The enrichment in ^{18}O in the ocean waters during glacial periods (low stands of sea level) can be explained by the preferential evaporation of the ^{16}O and its precipitation in form of snow in the poles. The reverse occurring during the interglacial periods when there is melting of the ice caps with consequent liberation of large amounts of ^{16}O into the ocean.

along the Brazilian continental margin were dominated by warm waters flowing from north to south (**Fig. 7.5 C and D**). During the lowstands of sea level (glacial periods) the warmer coastal waters would have shifted towards offshore regions causing a rise in the water temperature and a relative increase in the influence of lower salinity waters due to the proximity of rivers. Consequently, the waters in the upper bathyal environment could have become warmer and had a lowered salinity. This would have been recorded in the foraminiferal tests as a relative enrichment in lighter oxygen isotopes, despite a general enrichment of the open oceans waters with the heavier ^{18}O. The reverse could have occurred during the highstands of sea level when the warmer waters could have been kept shorewards with a consequent increase in the salinity and decrease in the bottom water temperatures in this environment. Carbonate-rich sediments (marlstones) could have been deposited during these periods with relative enrichment in heavier oxygen isotopes in contrast to lighter oxygen isotopes of the mudstones. This seems the most reasonable explanation of the oxygen isotope data.

As seen in **Fig 7.13A**, there appears to be some slight preference for more positive carbon isotopes to be associated with more negative oxygen isotopes and lower CaCO3%, and vice-versa for the less positive carbon isotopes (**Fig. 7.13**). During periods of high productivity the ^{12}C is used in the photosynthesis and the ^{13}C remains in the water. This indicates that in general the deposition of marlstones with less negative oxygen and less positive carbon isotopes occurred during periods of low productivity (i.e. transgressions, according to Hallock, 1987). The opposite occurred during relative low sea-level stands and the deposition of mudstones with more negative oxygen and more positive carbon isotopes. This indicates that there was a more significant depletion of ^{12}C from the water during the deposition of the mudstones as a result of a higher organic productivity associated with an increase in nutrients. This can be in part confirmed by the higher percentages of total

organic carbon found in the mudstones compared with the marlstones (see **Chapter 8**).

Oxygen and carbon isotopes from DSDP sites 277, 279, and 281 (Shackleton and Kennett, 1974) show that there was a period of global cooling ($\delta^{18}O$ more positive, +0.5 to +1.8‰) and a tendency to more negative values of carbon ($\delta^{13}C$ = +1 to -0.4‰) during the Oligocene. These values are quite different from those obtained from the analysis in well 330 which reflect differences in temperature, mainly due to water depths and geographical locations compared to the samples analyzed by Shackleton and Kennett (1974), and also diagenetic effects.

Rodrigues and Takaki (1987) carried out isotopic studies on the Palaeocene-Middle Miocene carbonates from northeast Brazil. They used total carbonate samples and obtained similar but mirror-like trends for the carbon isotopes to those presented by Shackleton and Kennett (1974). Their oxygen curves also show a shift towards more negative values (e.g. $\delta^{18}O$ -6 to -2 ‰ PDB) during the Oligocene. This was interpreted as reflecting diagenetic effects associated with a vadose environment and could represent a period of general sea-level fall in the Oligocene.

Despite of the diagenetic effects mentioned above there is a good probability that the variations observed in the oxygen stable isotopes of the Oligocene of the Campos Basin also reflect orbital induced phenomenon at the time of sediment deposition, as suggested by Imbrie et al. (1984) for the Pleistocene, and are responsible for the variations in the percentage of CaCO3 in the sediments.

7.6 CONCLUSIONS

In conclusion it is possible to say that this study of cyclicity in the percentages of CaCO3 derived directly from analysis of core samples or indirectly from wireline logs and their calibration with the orbital periodicities has several applications in stratigraphic studies.

The occurrence of sand-rich turbidites in the studied

succession of the Campos Basin was probably controlled by a sea-level fall driven by a combination of a low frequency wave cycle of "eustatic" (e.g. 10 Myr according to Haq et al., 1987) or tectonic origin (e.g. Tertiary uplift of the Serra do Mar Mountains) superimposed by eustatic fluctuations related to climatic cycles of about ~400 Kyr and 1200-1500 Kyr.

The existence of significant variations in the oxygen isotope results (up to 1.561 ‰) and their coincidence with variations in the CaCO3%, could be related to orbital periodicities (~20-100 Kyr). However, it is difficult to reach well defined conclusions from the stable isotope data without more continuous and very closely spaced (~10 cm) sampling over a greater stratigraphic interval. This would allow any diagenetic influence to be removed and the real trends to be defined. This could then help identify the most important palaeogeographic events and estimate the influence of isotopic variations arising from shelf/coastal processes. These could have overprinted the oceanic isotopic signatures and also need to be discounted if the isotopic data are to be used to infer eustatic oscillations due to variations in the ice caps volumes. Such continuous isotopic profiles combined with the cyclic variations in the CaCO3%, could then be correlated with those derived from the DSDP open ocean sites and thus establish the signatures corresponding to sea-level variations. This in turn would help define the intervals in which sea-level variations would have been more significant and indicate potential time intervals most favourable for the occurrence of sand-rich turbidites. Additionally, correlations between wells, which are essential for any sequence stratigraphy study, could also be greatly improved by this type of approach.

CHAPTER 8

MUDROCK PETROLOGY

8.1 INTRODUCTION AND PREVIOUS WORK

The Campos Formation (3.2.1.4) consists predominantly of dark/grey mudstones/siltstones, greenish grey bioturbated marlstones, few chalky intervals and siliciclastic turbidites. This formation embodies two main episodes of sedimentation, one from the Coniacian to the Maastrichtian representing a progressively deepening marine environment (up to bathyal/abyssal) and the other from the Middle Eocene to the Recent representing a prograding shelf/slope environment with a condensed section during the Oligocene. The Palaeocene and the Lower Eocene successions are in general absent due to erosion.

The mineralogy of the Campos Formation has previously been studied by Anjos (1986) utilizing cuttings from one well that covered the stratigraphic interval from the Coniacian to the Upper Miocene, with a maximum sample depth of 3500 m and a maximum borehole temperature of 100 °C. The main conclusions of Anjos (1986) are: 1 - the general clay mineralogy of the Campos Formation is represented mainly by kaolinite and mica, illite-smectite is less abundant and chlorite occurs only as a minor constituent; 2 - the illite-smectite in all samples is randomly interstratified and has an X.R.D. pattern that suggests it is an Fe-rich dioctahedral illite-smectite and represents the weathering product of felsic rocks influenced by climatic conditions that favoured a high concentration of iron; 3 - there is an upward increase in the amount of quartz in the mudstones reflecting the progradational nature of the upper part of the Campos Formation; 4 - variations in the quartz, illite-smectite and kaolinite contents indicate that the mineralogy of the Campos Formation largely

reflects detrital depositional influences; 5 - there is only a slight increase in the percentage of illite layers in the illite-smectites with increasing depth; 6 - the kaolinite content shows no systematic increase or decrease with increasing depth, and seems to be detrital in origin; 7 - the total clay content varies non-systematically with depth and reflects changes in kaolinite content; 8 - the relatively large amount of kaolinite identified in an Oligocene sample (2600 m) possibly corresponds to a low sea-level stand for the Oligocene indicated by Vail et al. (1977); and 9 - the calcite content increases slightly with depth.

8.2 SAMPLING

The type and distribution of the samples examined in this study differ from those studied by Anjos (1986). In her work the samples (cuttings) came from a single well and covered the stratigraphic interval from the Upper Miocene down to the Coniacian, reaching a maximum depth of 3500 m and a maximum borehole temperature of 100°C. In the present study the core samples came from different wells and all were from Oligocene-Lower Miocene successions. Only in well 154 were cuttings used to sample the interval 2940-3850 m between the two cores.

The sample depths and corresponding burial temperatures vary from 2414 m to 3860 m and from 46°C to 123°C (**Fig.8.1**). The temperature variations mainly reflect variations in the water depth of the wells, varying from -91 m up to -1565 m. The relationship between the temperature at 2700 m and the water depth of the wells in the studied area shows that the lower temperatures are found in the wells from the greater water depths (**Fig. 8.2**). The mean geothermal gradient for the first 2600 m is relatively low, around 18°C/Km. It increases to over 30°C/km in the deeper intervals, especially in the Cretaceous parts of the succession. The mean geothermal gradient for the first 3000 m is 25°C/Km. The higher geothermal gradients in the Cretaceous succession can be partially explained by the proximity to the Rift

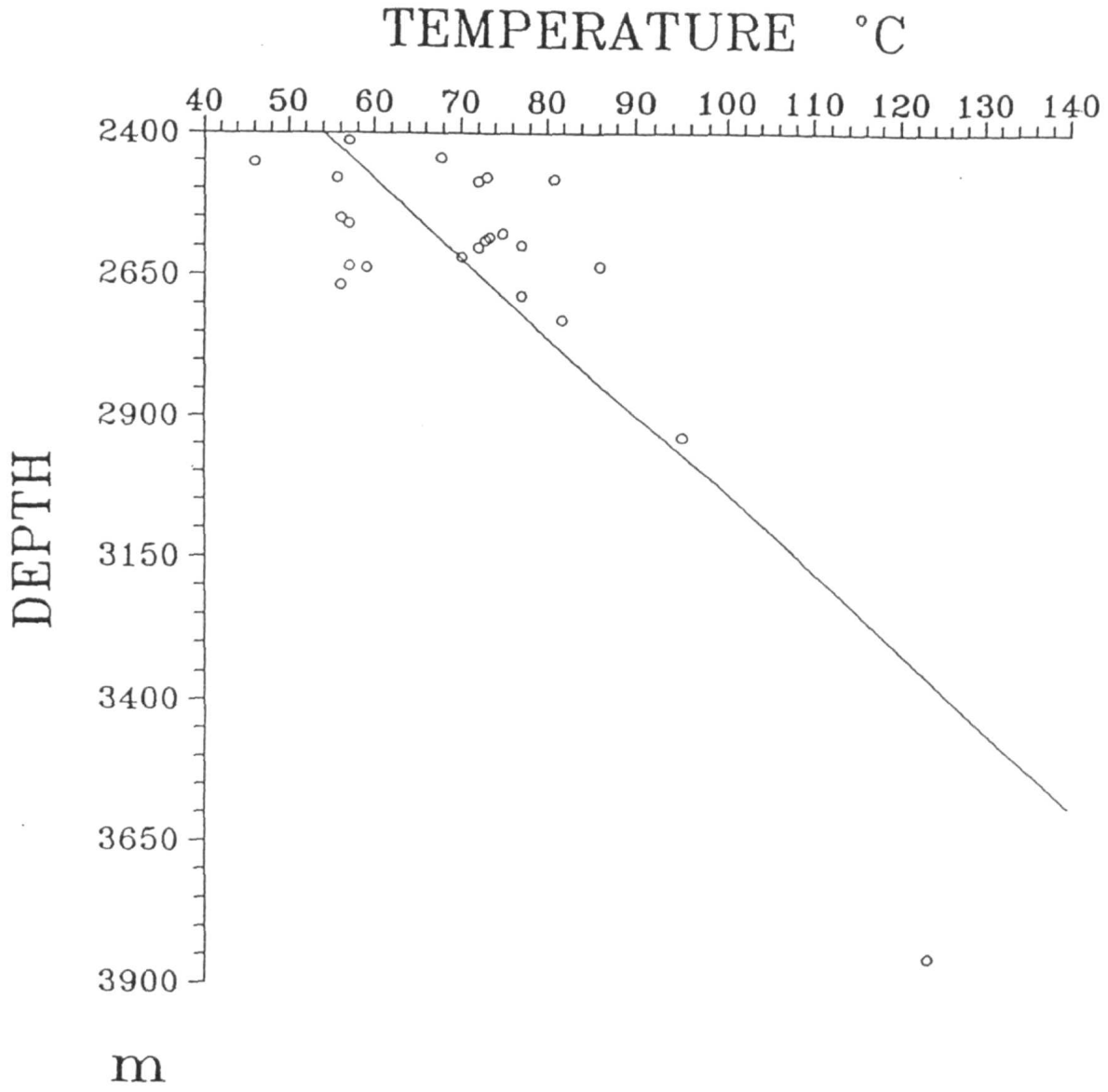


Fig. 8.1 - Relationship of the temperature with sample depth from the sea surface.

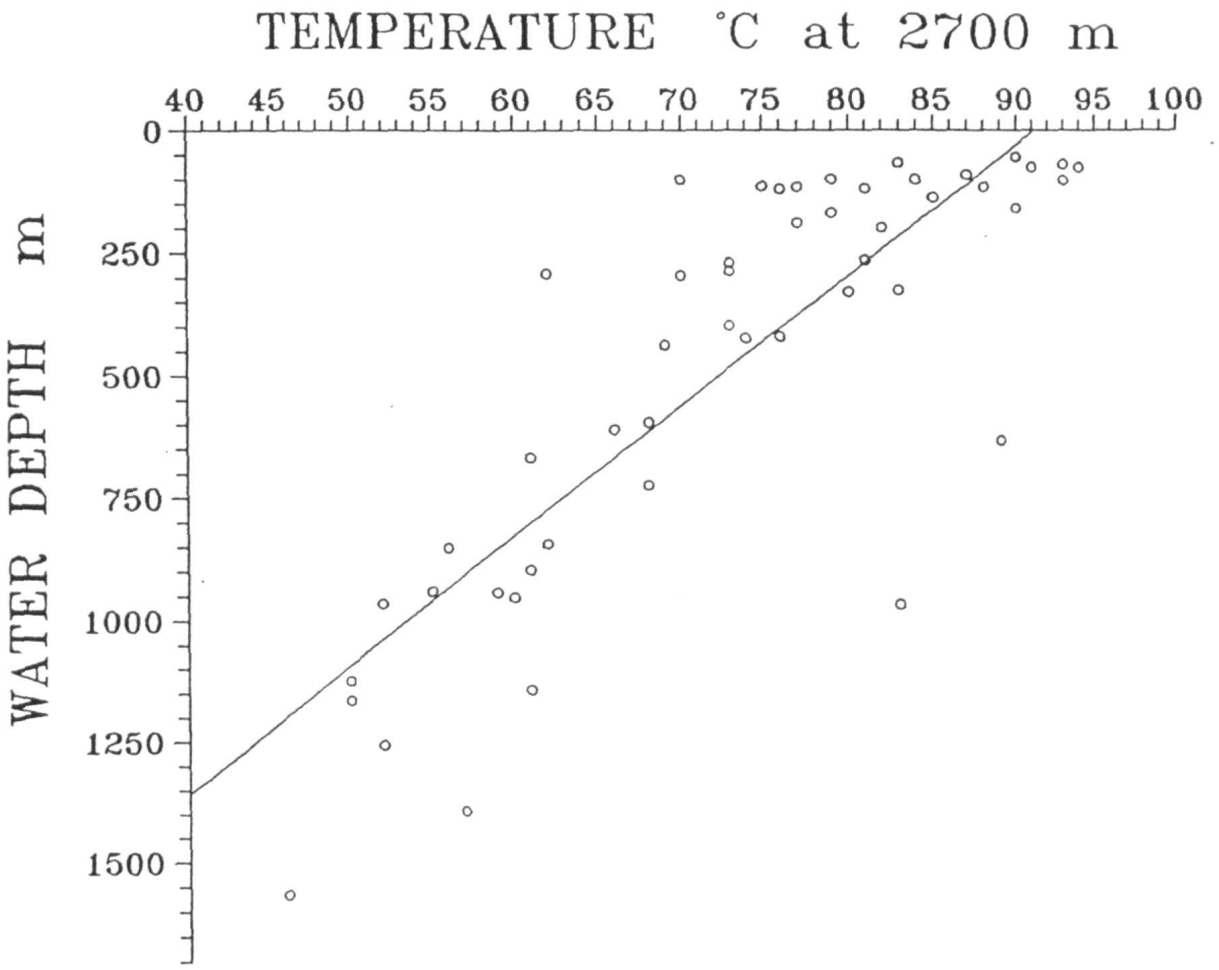


Fig. 8.2 - Variations of the temperature at 2700 m from the sea surface in relation to the water depth of the wells.

sequence and the existence of Aptianevaporites, that have relatively higher thermal conductivity compared to the mudstone sequences. This results in more effective heat transfer to the adjacent rocks.

8.3 COMPOSITIONS OF THE OLIGOCENE-LOWER MIOCENE MUDROCKS

The succession of Oligocene mudrocks in the studied area consists mainly of medium-bedded (10-30 cm) rhythmic dark grey/ greenish, poorly laminated, slightly bioturbated, hemipelagic calcareous mudstones and greenish grey, heavily bioturbated, massive foraminiferal-nanofossil marlstones.

The Oligocene succession had a low average sedimentation rate[1] (1.5 cm/1000 yr, undecompacted), while the Miocene succession had an average rate approximately ten times higher (15 cm/1000 yr). The higher accumulation rates in the Miocene reflect the nature of the progradational shallowing upward sequence, which consists of very thickly bedded (> 1 m) slightly calcareous dark grey, structureless/ poorly laminated silty mudstones interbedded with medium-thick (100 cm) greenish-grey bioturbated foraminiferal-nanofossil marlstones. Locally, due to growth faults, the mean rate of sedimentation was as high as 36 cm/Kyr. The calcium carbonate content of the mudrocks is directly related to the abundance of microfossils (nanofossil and foraminifera) and inversely proportional to the rate of sedimentation. The calcium carbonate content in the Oligocene mudrocks is much higher than in Miocene mudrocks.

The total organic carbon (T.O.C.) of the mudrocks is very low, usually less than 0.70% weight, though locally the values reached 2.10% weight in a radioactive[2] mudstone. According to the Geochemistry Lab of the Research Centre of Petrobrás the organic matter present in the mudstones can be classified as type III kerogen (Tissot et al., 1974).

---

[1] The average rate of sedimentation was calculated using the undecompacted thickness of the interval divided by its time span, assuming that there is no major hiatus in the analyzed interval.

[2] The term radioactive was used to differentiate those mudstones, that have GR log values around 118 ºAPI, compared to the mean GR values of around 90 ºAPI.

8.3.1 WHOLE-ROCK MINERALOGY

The mudrocks consist of quartz, calcite, K-feldspar, plagioclase, biotite, muscovite, clay minerals and some pyrite. Rutile, ilmenite and anatase commonly occur as minor constituents. The identification of these minerals was based on x-ray powder diffraction data (Brown and Brindley, 1980; and Brown, 1980). The relative amount of calcite is directly related to the lithofacies.

The mudrocks when analyzed under the S.E.M., show a very fine siliciclastic muddy matrix with variable amounts of calcareous microfossils (nannofossil and foraminifera) and very fine sand/silt sized-grains of quartz, K-feldspar, plagioclase, biotite, muscovite, and minor amounts of heavy minerals (rutile, ilmenite, zircon, apatite, and amphibole).

8.3.2 CLAY MINERALOGY

8.3.2.1 COMPOSITION OF THE CLAY GRADE FRACTIONS (< 2 μm) IN THE MUDROCKS

According to Rocha et al. (1975) the clay mineralogy of the sediments being deposited on the modern continental shelf of the Rio de Janeiro province consists of kaolinite, smectite and illite and represents the weathering products of the Precambrian coastal rocks under a tropical climate (see **Chapter 2** for the regional geology of the source area).

To examine the probable influence of the lithofacies on the clay composition the mudrocks were divided as follow (see Chapter 5 for lithofacies definition):

a) Marlstone Lithofacies G_2 (<2/3 $CaCO_3$ >1/3);
b) Mudstone Lithofacies G_4 (<1/3 $CaCO_3$);
c) Mottled Mudstones/siltstones, Lithofacies **MM**;
d) mudstones of the top part of the Bouma sequence characterized by the Lithofacies **FTde**;
e) additionally samples from the Diamictite Lithofacies **DMT** were analyzed to make comparisons with the other lithofacies.

The samples were grouped into two sets according to their depth and lithofacies. The relative abundance of the clay minerals in this study were estimated semi-

quantitatively from X.R.D. data using the relative intensities of the peaks and the methodology is described in **Chapter 4.**

The clay mineralogy of the mudrocks is dominated by smectite-rich (~90% of smectite) randomly interstratified mixed-layer illite-smectite with subordinate or similar percentages of illite and kaolinite (see **Table 8.1**). There is no vermiculite associated with the illite-smectites (see **Chapter 4**).

TABLE 8.1

samples from 2414 to 2941 m (<2μm fraction)	Average values					
lithofacies	K%	I%	I/S%	SM%	K/I	(I/S)/I
marlstone (G2)	19	23	58	87	0.82	2.52
mudstone (G4)	24	23	53	90	1.04	2.30
mottled mudstone (MM)	34	24	42	89	1.41	1.75
mudstone (FTde)	23	29	48	92	0.79	1.60
diamictite (DMT)	24	26	50	94	0.92	1.92
samples from 3852 to 3855 m (<2μm fraction)						
mudstones (G4)	24	38	38	10	0.63	1.00
mottled mudstone (MM)	21	33	46	11	0.64	1.39

Where **K** = kaolinite, **I** = illite, **I/S** = illite-smectite, and **SM** = smectite in the mixed-layer illite-smectite.

There is a significant difference in the illite content of the mixed-layer illite-smectites compared to those reported by Anjos (1986) determined using the method of Rettke (1981). The percentage of illite in the samples that she analyzed is 35% for the shallowest samples (2,000 m), much higher than the values (around 5%) determined in the

present work. Srodon (1981) found that the method of Rettke depends strongly on the domain size distribution and he found errors as much as 30% in the amount of smectite in the mixed-layer composition determined using this method. The discrepancies between the illite-smectite compositions from this study and those of Anjos (1986) are probably due to the different methodologies used to quantify the amount of smectite. Alternatively, they could be real compositional differences reflecting the different geographical positions of the wells from which the analyzed samples were collected in the basin.

Anjos (1986) suggested that the 10 Å mineral present in the samples that she analyzed is not true illite, because the 5 Å reflection is too weak. She concluded that it is more likely to be biotite because of the presence of flakes of biotite in the coarser sized fractions and the occurrence of an 060 peak of 1.54 Å. In the samples analyzed in this study biotite was also found in the coarser fractions and identified in the randomly oriented samples from its 060 reflection at 1.53 Å (see **Fig. 8.3**). A comparison between the two X.R.D. traces of solvated samples with ethylene glycol from similar depths, one from Anjos (1986, Fig. 6) and the other from the present data set show that the illite peak at 5 Å is present in both samples, although weaker in the Anjos sample (**Fig. 8.4**). In conclusion it is possible to say that the 10 Å peak, together with the 5 Å one, does represent illite as well as biotite.

According to Brown and Brindley (1980) the identification of dioctahedral smectites is based on the presence of a medium-strong reflection between 1.49-1.50 Å. Using this characteristic, it is possible to say that the presence of the 060 reflection at 1.503 Å in the analyses of the randomly oriented powder samples indicates that the mixed-layer illite-smectite is dioctahedral (see **Fig. 8.3**). Anjos (1986) came to the same conclusion from the analyzes of her samples and comparisons with a computer-simulated pattern for a dioctahedral Fe-rich dioctahedral illite-smectite.

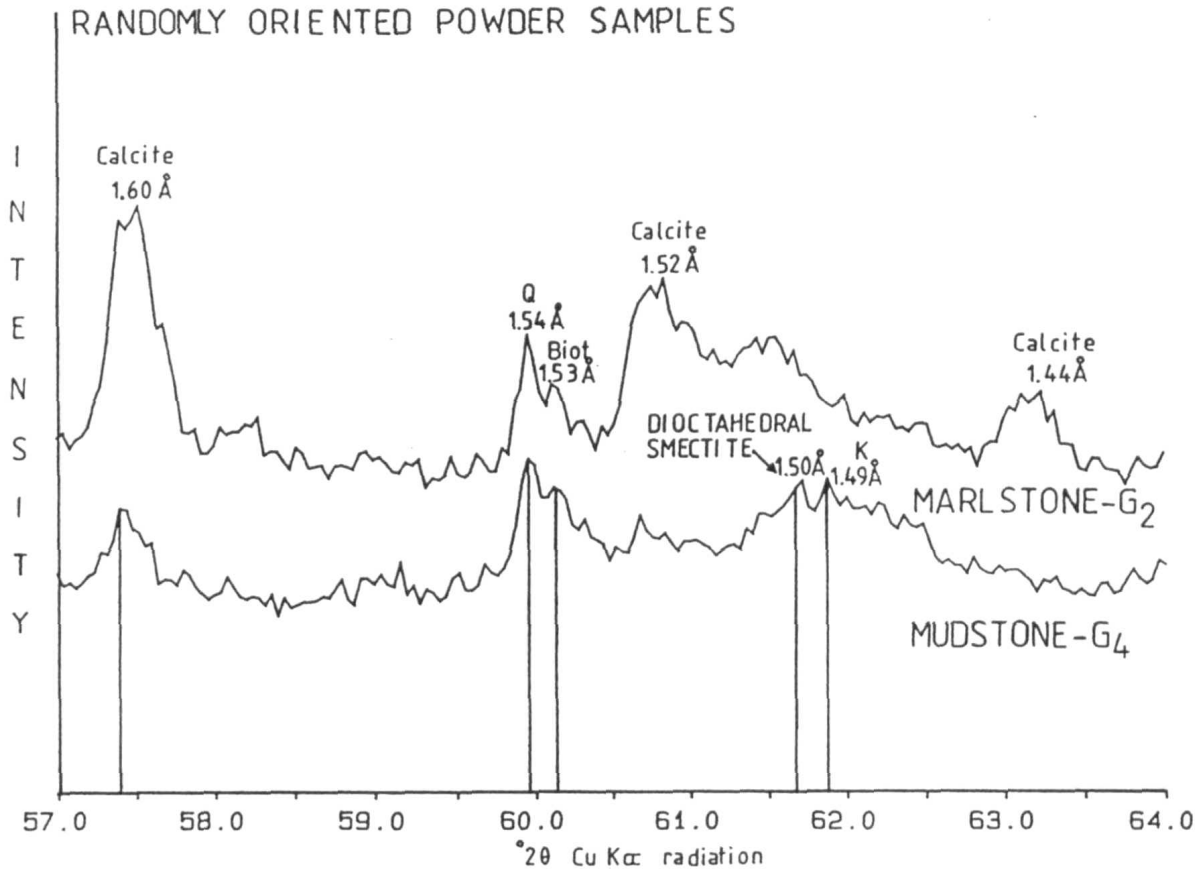


Fig. 8.3 - X.R.D. traces of the randomly oriented powder samples from marlstone G_2 and mudstone G_4 showing the 1.50 Å peak of the dioctahedral illite-smectite and also the 1.53 Å peak of the biotite.

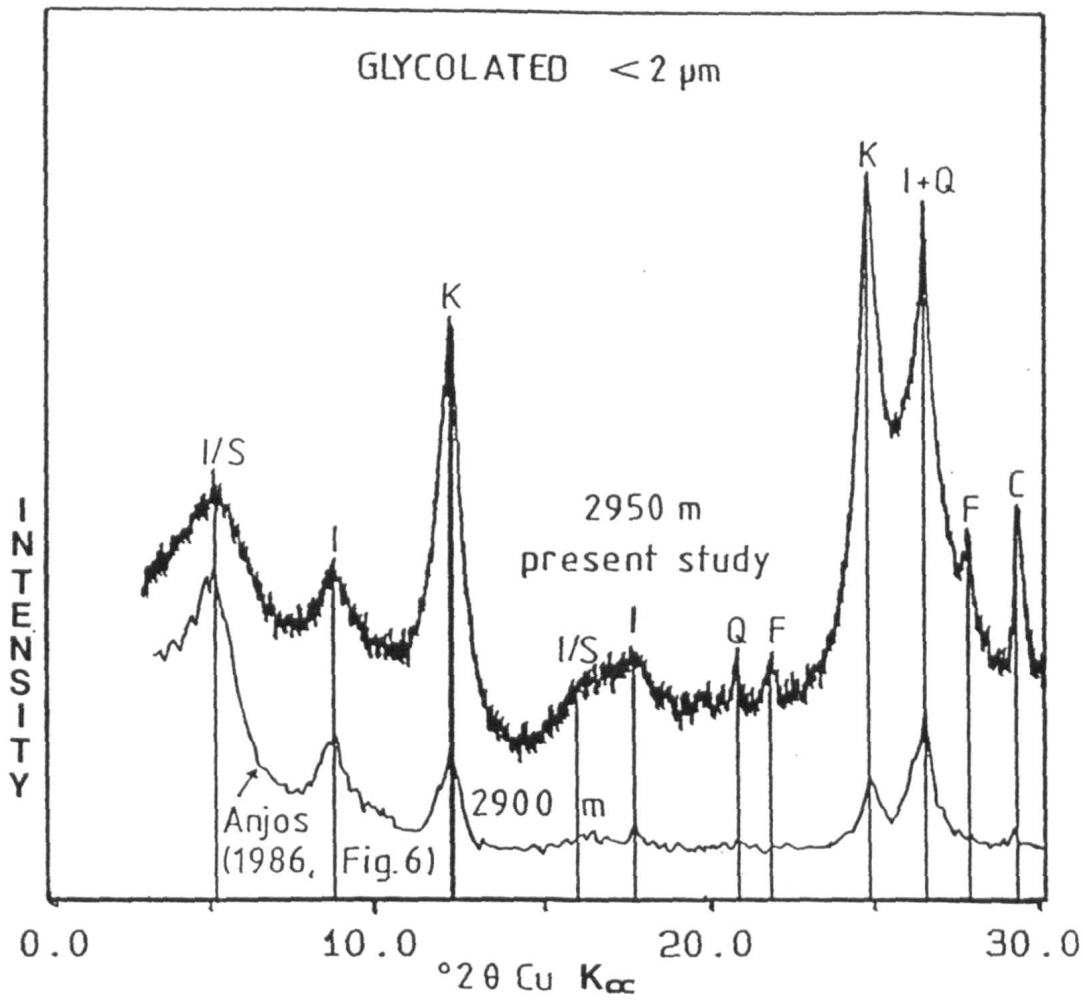


Fig. 8.4 - Comparison between X.R.D. glycolated traces of the oriented clay grade fraction (<2 µm) from similar depths, one from Anjos (1986, Fig. 6) and the other from the present study.

Using S.E.M. techniques chlorite, together with kaolinite, was identified in mudstones from a depth of 3852 m (well 154) growing diagenetically within foraminiferal chambers and infilling the secondary porosity created by the dissolution of the foraminiferal tests. However, when this sample was analyzed using X.R.D. no conclusive evidence of chlorite was found. The most likely reason for the absence of chlorite in the X.R.D. traces could be the relative low percentage, probably less than 5%, of this mineral in the sample (see **Fig. 8.5**).

8.3.2.2 CLAY MINERAL COMPOSITIONS OF THE MUDROCKS AND THE SANDSTONES

In order to make comparisons between the clay mineralogy of the mudrocks and the sandstones some analyses were carried out on the <2μm fractions of the very fine-grained sandstones and interlaminated mudstones of lithofacies **Rip, FTcd, Fla** and the fine- to coarse-sandstones, lithofacies **FTab, FTa, Amg** and **VcS**. The clay grade fractions of the sandstones are dominated by kaolinite with minor amounts of discrete illite and illite-smectite (see **Table 8.2** and **Fig. 8.6**).

Chlorite was also found in samples from two wells, 310 (2594 m = K + Chl 69%, and 2687 m = K + Chl 68%) and 154 (3852 m = Chl 35%). The chlorite in the sample from well 154 (3852 m) is characterized by the presence of the 14.4 Å, 7.09 Å, and 3.54 Å reflections in the air dry state. On heating at 550 ºC the 14.4 Å changes to 13.96 Å and the 7 Å and 3.5 Å reflections disappear (see **Fig. 8.7**). In the two samples from the well 310, the typical reflections for the kaolinite, (7.15 - 7.17 Å) in the other samples, are not differentiated but the 7.07 - 7.09 Å peak was clearly defined. The 14.6 Å reflection in the air-dried state is also present and collapses to 13.74 Å when heated to 550ºC. The 14 Å reflection cannot be differentiated in the glycolated samples, which may indicate that this chlorite could be interstratified with smectite (see **Fig. 8.8**). For more details about kaolinite and chlorite within the

sandstones see **sections 9.5.1, 9.5.9, 9.5.11, 9.6.3,** and **9.6.4.**

TABLE 8.2

a) samples from 2451 m to 2687 m (<2μm fractions)

lithofacies	K%	I%	I/S%	SM%	K/I	(I/S)/I
very fine-sandstone (Rip, FTcd, Fla)	58	21	21	89	2.76	1.0
fine/coarse-sandstone (FTab, FTa, AmS, VcS)	92	5	3	91	18.40	0.6
coarse/pebbly-sandstone (GvS/VcS): K + Chl=	(68)	12	20	88	(5.67)	1.6

b) sample from 3852 m (<2μm fraction)

fine/medium-sandstone (FTa): NO I/S

Chl = 35%, K = 63 %, I = 2 %, Chl/I = 17.5, K/I = 31.5

Where: **K** = kaolinite, **I** = illite, **I/S** = illite-smectite, **SM** = percentage of smectite in the interstratified illite-smectite, **Chl** = chlorite, **K/I** = ratio kaolinite/illite and (I/S)/I = ratio illite-smectite/illite.

Although the typical kaolinite peak (7.15 Å - 7.17 Å) was not detected in the X.R.D. analyses of these two samples from well 310, kaolinite was observed when the specimens of these rocks were analyzed under the S.E.M. (see **Chapter 9**).

The reflection that usually appears at 3.52 Å after the heating of the sample at 550 °C, corresponds to the anatase reflection. This was hidden by the stronger reflection of the chlorite or kaolinite when the samples were analyzed in air dry or glycolated state. This can be seen in a X.R.D. trace from a kaolinite-rich sandstone in the **Fig. 8.6.**

Fig. 8.5 - X.R.D. traces of the oriented clay grade fraction showing the main reflections present in the sample from 3855 m and 123°C of Lithofacies MM. The curves have different multiplication factors to avoid superposition.

FIG. 8.5

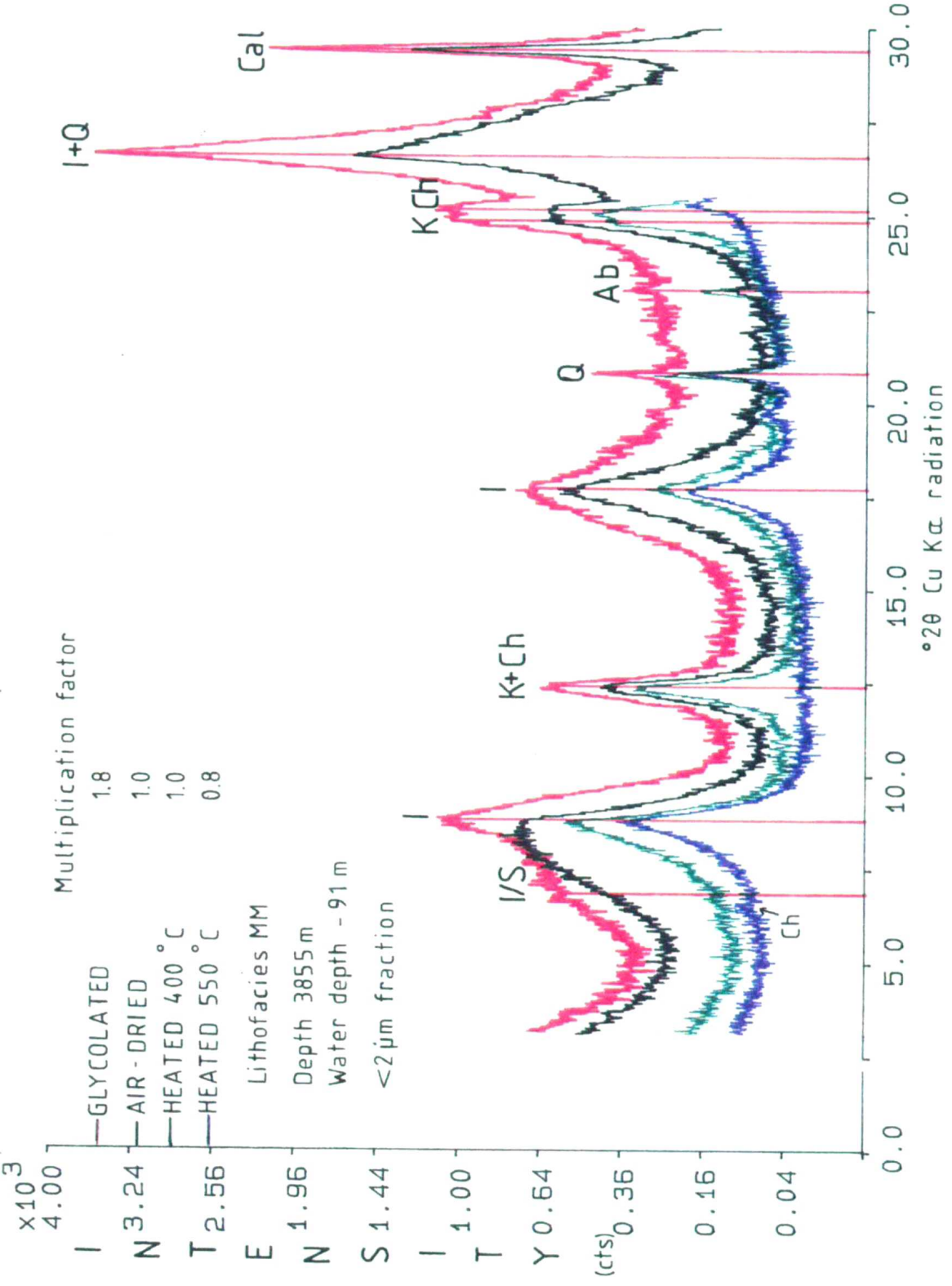

Multiplication factor
GLYCOLATED 1.8
AIR - DRIED 1.0
HEATED 400 °C 1.0
HEATED 550 °C 0.8
Lithofacies MM
Depth 3855 m
Water depth - 91 m
<2 µm fraction
INTENSITY (cts) x10^3
4.00
3.24
2.56
1.96
1.44
1.00
0.64
0.36
0.16
0.04
I+Q
Cal
K Ch
Ab
Q
I
K+Ch
I/S
I
Ch
0.0
5.0
10.0
15.0
20.0
25.0
30.0
°2θ Cu Kα radiation

Fig. 8.6 - X.R.D. traces of the oriented clay grade fractions (<2 μm) showing the main reflections of the lithofacies **FTab** (medium/fine sandstone) at 2463 m and 48°C. The curves have different multiplication factors to avoid superposition. Where: Q = quartz, I = illite, K = kaolinite, Pl = plagioclase, Ab = albite and Ant = anatase.

FIG.8.6

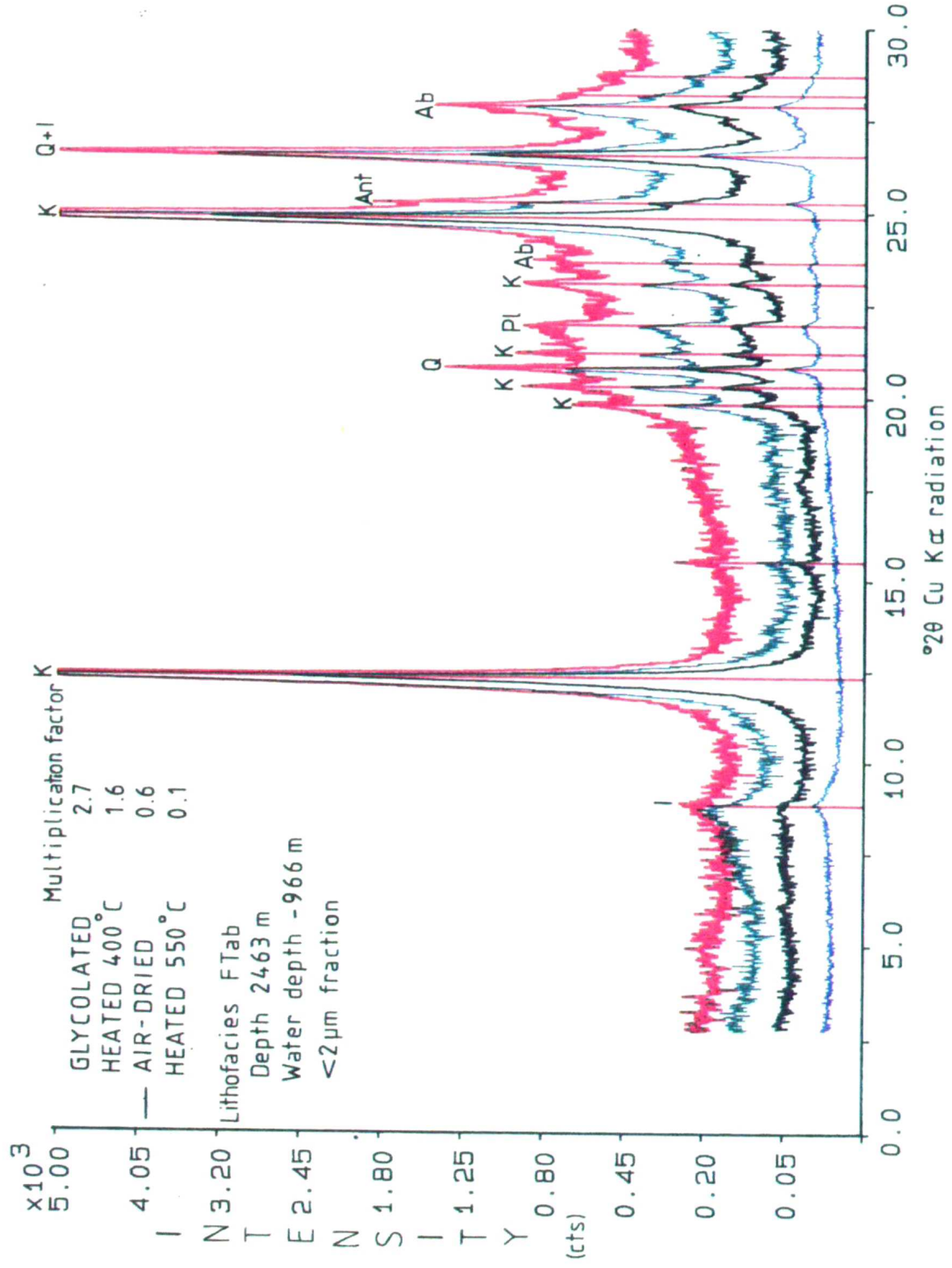

GLYCOLATED
HEATED 400°C
AIR-DRIED
HEATED 550°C
Multiplication factor
2.7
1.6
0.6
0.1
Lithofacies FTab
Depth 2463 m
Water depth -966 m
<2µm fraction
INTENSITY (cts)
x10 3
5.00
4.05
3.20
2.45
1.80
1.25
0.80
0.45
0.20
0.05
0.0
5.0
10.0
15.0
20.0
25.0
30.0
°2θ Cu Kα radiation
K
Q+I
K
Ant
Ab
Q
K
K
Pl
K
Ab
K
I

Fig. 8.7 - X.R.D. traces of the oriented clay grade fractions (<2 μm) showing the main reflections present in the sample from 3852 m and 123° C of Lithofacies FTab. Where: Ch = chlorite, I = illite, K = kaolinite, Q = quartz, Ab = albite, and Mi = microcline. The curves have different multiplication factors to avoid superposition.

FIG. 8.7

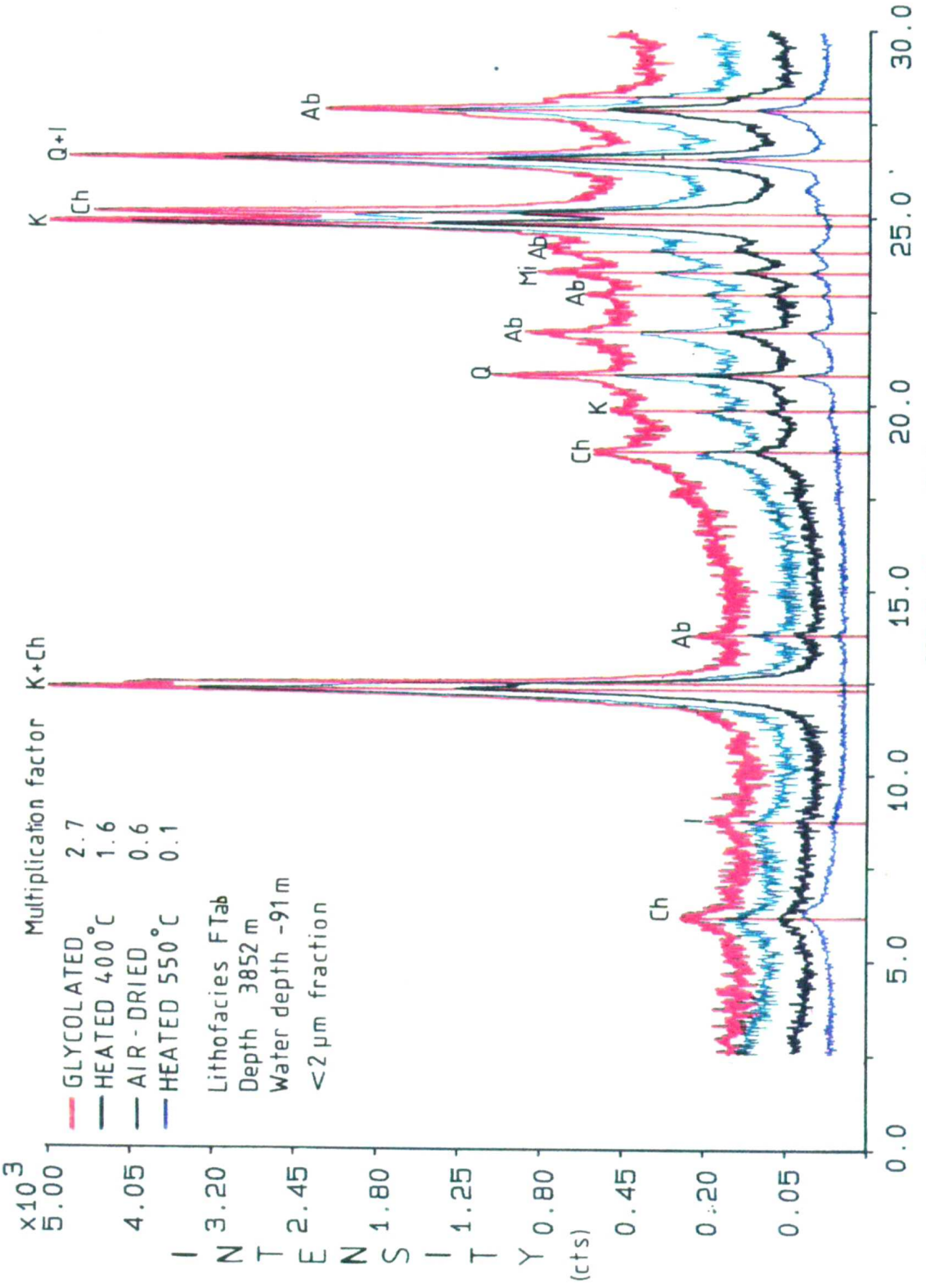
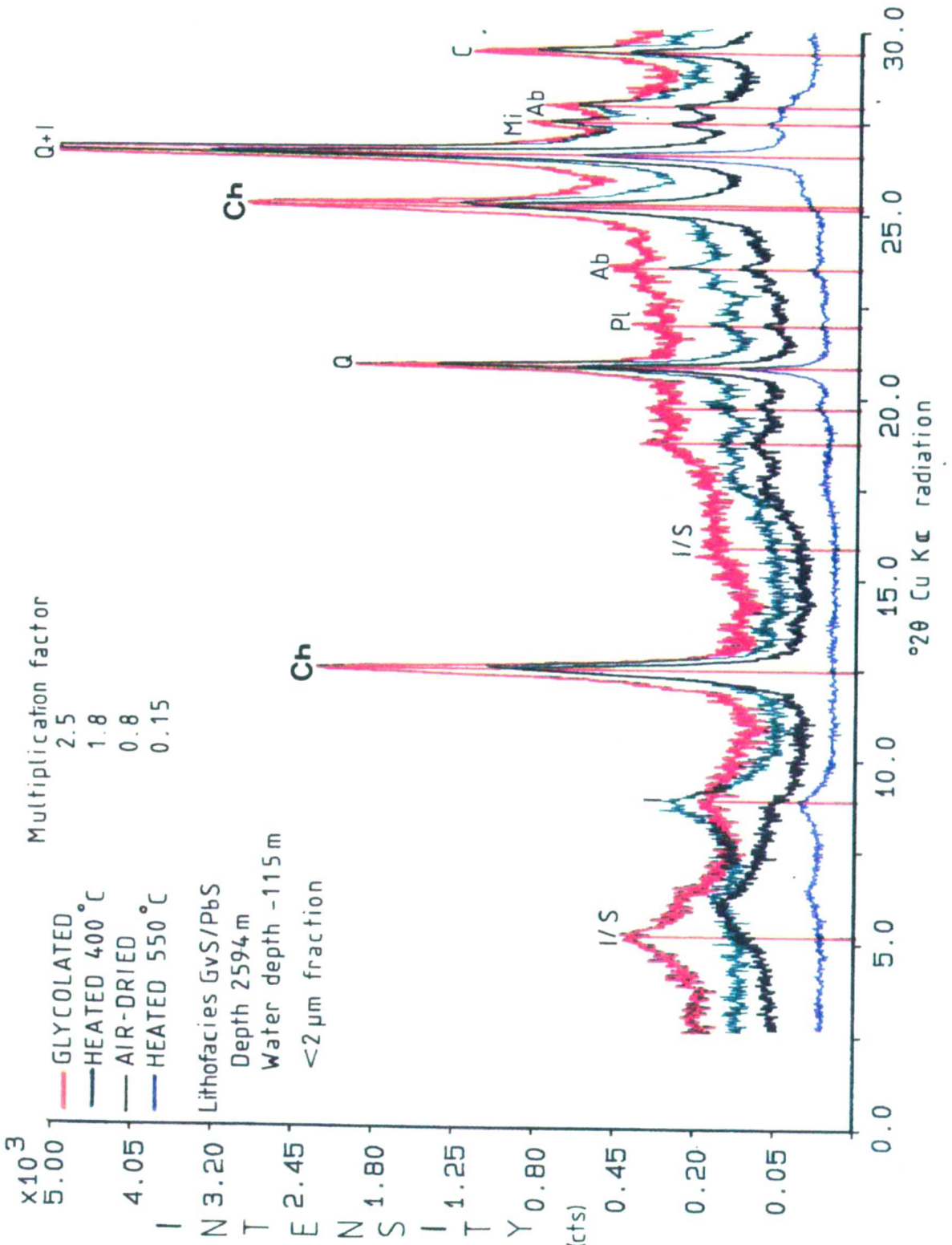

Multiplication factor
GLYCOLATED 2.7
HEATED 400°C 1.6
AIR-DRIED 0.6
HEATED 550°C 0.1
Lithofacies FTab
Depth 3852 m
Water depth -91 m
<2 µm fraction
INTENSITY (cts)
°2θ Cu Kα radiation
K+Ch
Ch
I
Ab
Q
K
Mi
Q+I

Fig. 8.8 - X.R.D. traces of the oriented clay grade fractions (<2 μm) showing the main reflections present in the sample from 2594 m and 75º C, of the lithofacies Pebbly Sandstone GvS/PbS. Where: Ch = chlorite, I/S = illite-smectite, I = illite, Q = quartz, Pl = plagioclase, Ab = albite, Mi = microcline, and C = calcite. The curves have different multiplication factors to avoid superposition.

FIG. 8.8


Multiplication factor
GLYCOLATED 2.5
HEATED 400°C 1.8
AIR-DRIED 0.8
HEATED 550°C 0.15
Lithofacies GvS/PbS
Depth 2594 m
Water depth -115 m
<2 µm fraction
x10^3
5.00
4.05
3.20
2.45
1.80
1.25
0.80
0.45
0.20
0.05
INTENSITY (cts)
Q+I
Ch
Q
Ch
I/S
I/S
Ab
Pl
Mi
Ab
C
0.0
5.0
10.0
15.0
20.0
25.0
30.0
°2θ Cu Kα radiation

8.4 CLAY MINERAL COMPOSITIONS OF THE VARIOUS LITHOFACIES

The pelagic/hemipelagic marlstones (G_2) have higher percentages of illite-smectite (see **Fig 8. 9, Fig. 8.10** and **Table 8.1**) compared to the other lithofacies (**Fig. 8.9**). The X.R.D. traces of the oriented clay grade fraction (< 2 μm) of the mudstones (G_4) show similar patterns to those of the marlstones (G_2), but with less illite/smectite (**Fig. 8.11**).

The turbiditic-mudstones (**FTde**), diamictites (**DMT**) and mottled mudstones (**MM**) have slightly higher percentages of kaolinite and illite compared to the hemipelagic lithofacies (G_2/G_4) (**Fig. 8.9**).

The very fine-sandstones (**Rip, FTcd** and **Fla**) have high percentages of kaolinite, and even higher values of kaolinite are found in the coarser sandstones, lithofacies **VcS, AmS, FTa, FTab** (**Table 8.1** and **8.2**).

Although there are variations in the proportions of the clay minerals between the different lithofacies a plot of the glycolated X.R.D. traces of the different mudrock lithofacies shows similar characteristics. The main differences are the higher relative concentrations of illite/smectite and calcite in the marlstones, and higher relative concentrations of quartz in the diamictites (**DMT**) and the turbiditic-mudstones (**FTde**) (see **Fig. 8.12**).

There is an inverse relationship between the percentages of kaolinite and illite-smectite and the relative amount of illite is almost constant for all the lithofacies (**Fig. 8.13**). The two extremes are the illite-smectite-rich marlstones, and the kaolinite-rich sandstones.

There is a decrease in the ratio of illite-smectite to illite from the marlstones (G_2) to the turbiditic-mudstones (**FTde**) (see **Fig. 8.14**).

The significant decrease in the ratio of illite-smectite/illite from the marlstones (G_2) to the turbiditic-mudstones (**FTde**) is readily seen in **Fig. 8.14**. This trend is more difficult to observe in **Fig. 8.9** because there are only small differences between the composition of the mudstones (G_4) and the turbiditic-mudstones (**FTde**).

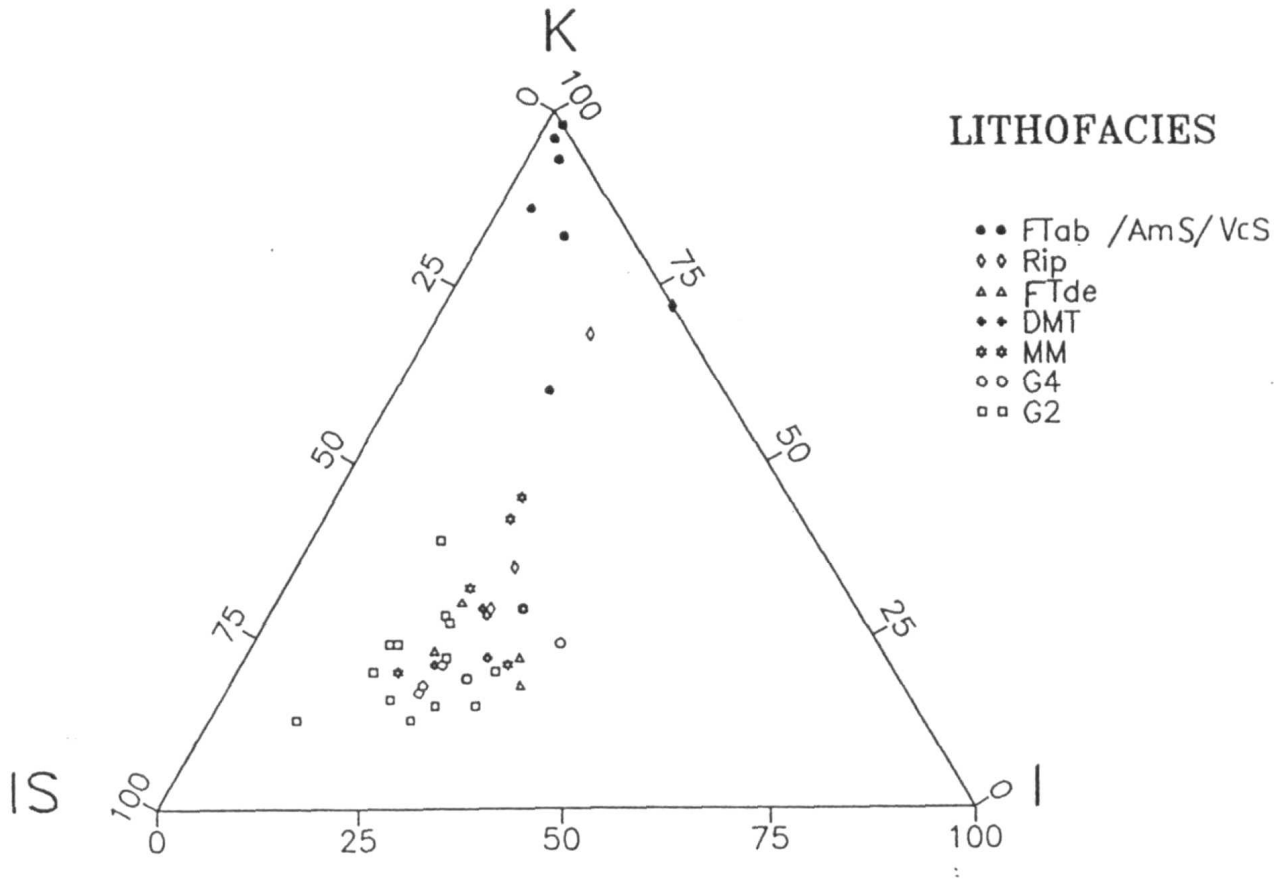


Fig. 8.9 - Relative percentages of the main clay minerals (K = kaolinite, I = illite, and I/S = illite-smectite) presented in the various lithofacies. Lithofacies: **FTab/AmS/VcS** = Fine/very coarse-sandstone; **Rip** = Very fine-sandstone; **FTde** = Mudstone of the top of Bouma sequence; **DMT** = diamictite; **MM** = Mottled mudstone; G_4 = Siliciclastic mudstone; G_2 = Marlstone. For more details of the lithofacies see **Chapter 5**.

Fig. 8.10 - X.R.D. traces of the oriented clay grade fractions (<2 μm) showing the typical reflections present in the Marlstone G_2 (2553 m and 57º C). The curves have different multiplication factors to avoid superposition.

FIG.8.10

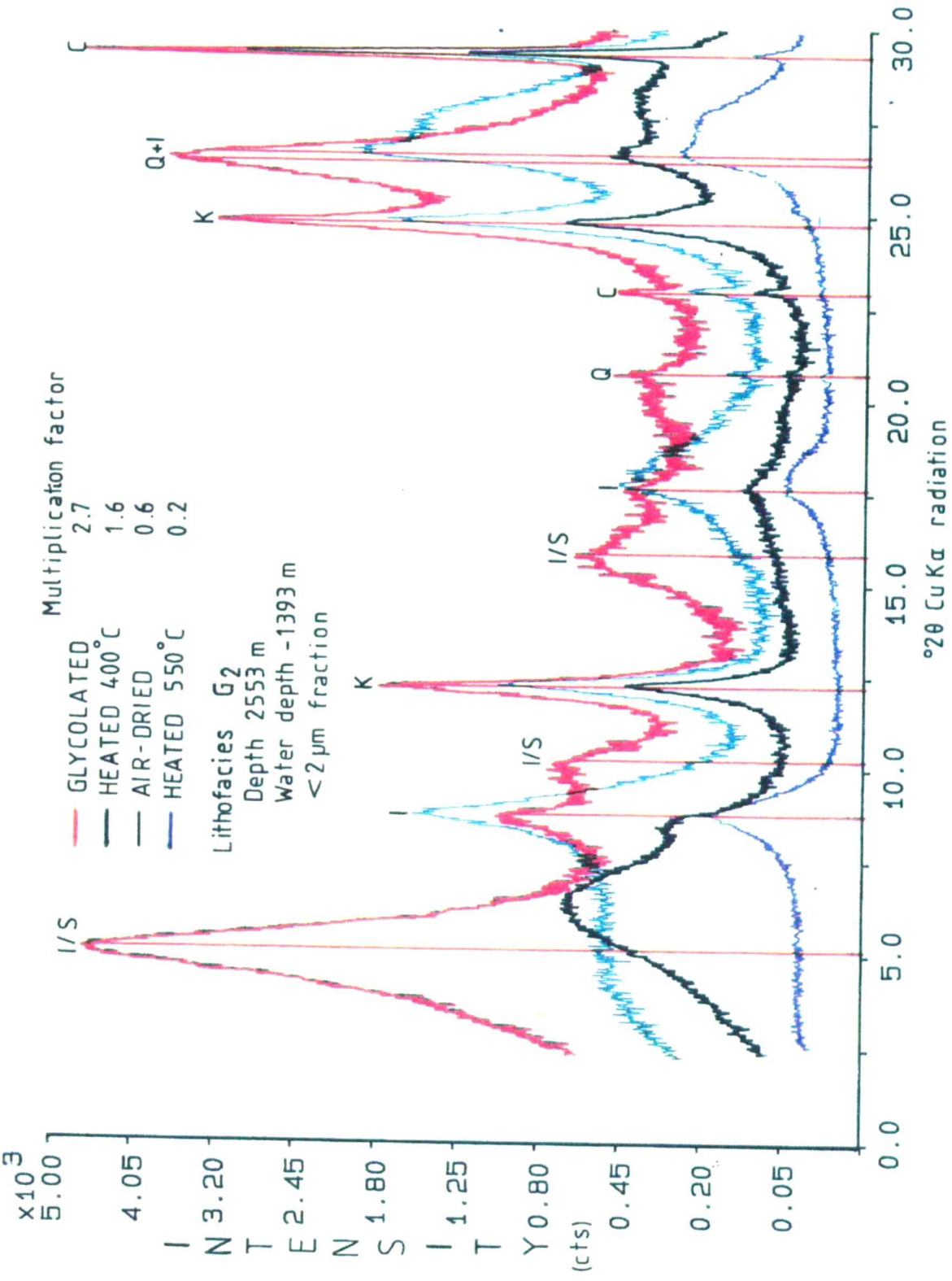
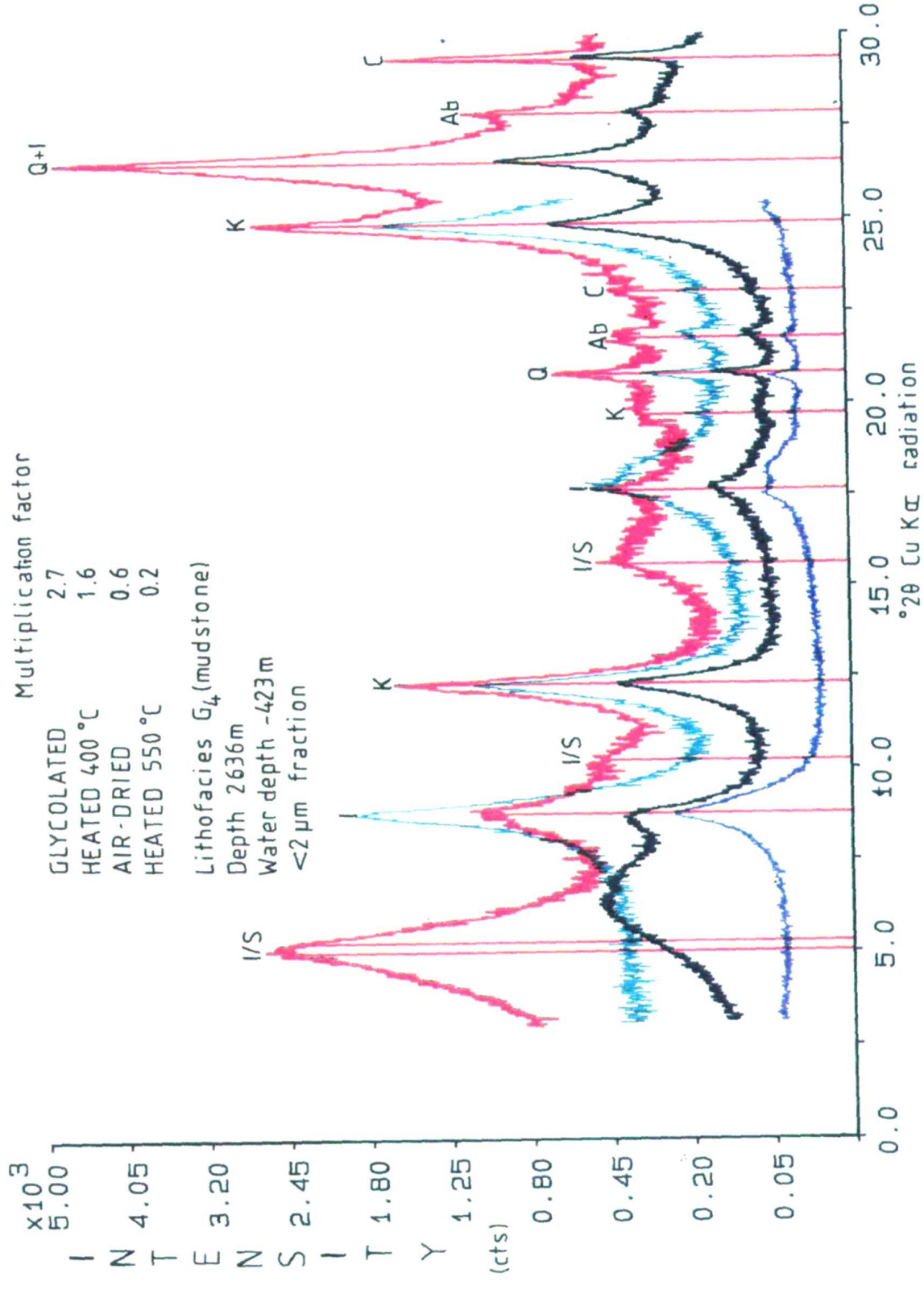

Multiplication factor
GLYCOLATED 2.7
HEATED 400°C 1.6
AIR-DRIED 0.6
HEATED 550°C 0.2
Lithofacies G2
Depth 2553 m
Water depth -1393 m
<2 µm fraction
I/S
K
I
Q+I
C
Q
INTENSITY (cts)
x10³
5.00
4.05
3.20
2.45
1.80
1.25
0.80
0.45
0.20
0.05
0.0
5.0
10.0
15.0
20.0
25.0
30.0
°2θ Cu Kα radiation

Fig. 8.11 - X.R.D. traces of the oriented clay grade fractions (<2 μm) showing the typical reflections present in the Mudstone G_4 (2636 m and 72° C). Where: I/S = illite-smectite, I = illite, K = kaolinite, Q = quartz, Ab = albite, C = calcite. The curves have different multiplication factors to avoid superposition.

FIG. 8.11


Multiplication factor
GLYCOLATED 2.7
HEATED 400 °C 1.6
AIR-DRIED 0.6
HEATED 550 °C 0.2
Lithofacies G4 (mudstone)
Depth 2636m
Water depth -423m
<2 µm fraction
INTENSITY (cts)
x10^3
5.00
4.05
3.20
2.45
1.80
1.25
0.80
0.45
0.20
0.05
0.0
5.0
10.0
15.0
20.0
25.0
30.0
°2θ Cu Kα radiation
I/S
I
K
Q+I
Q
Ab
C

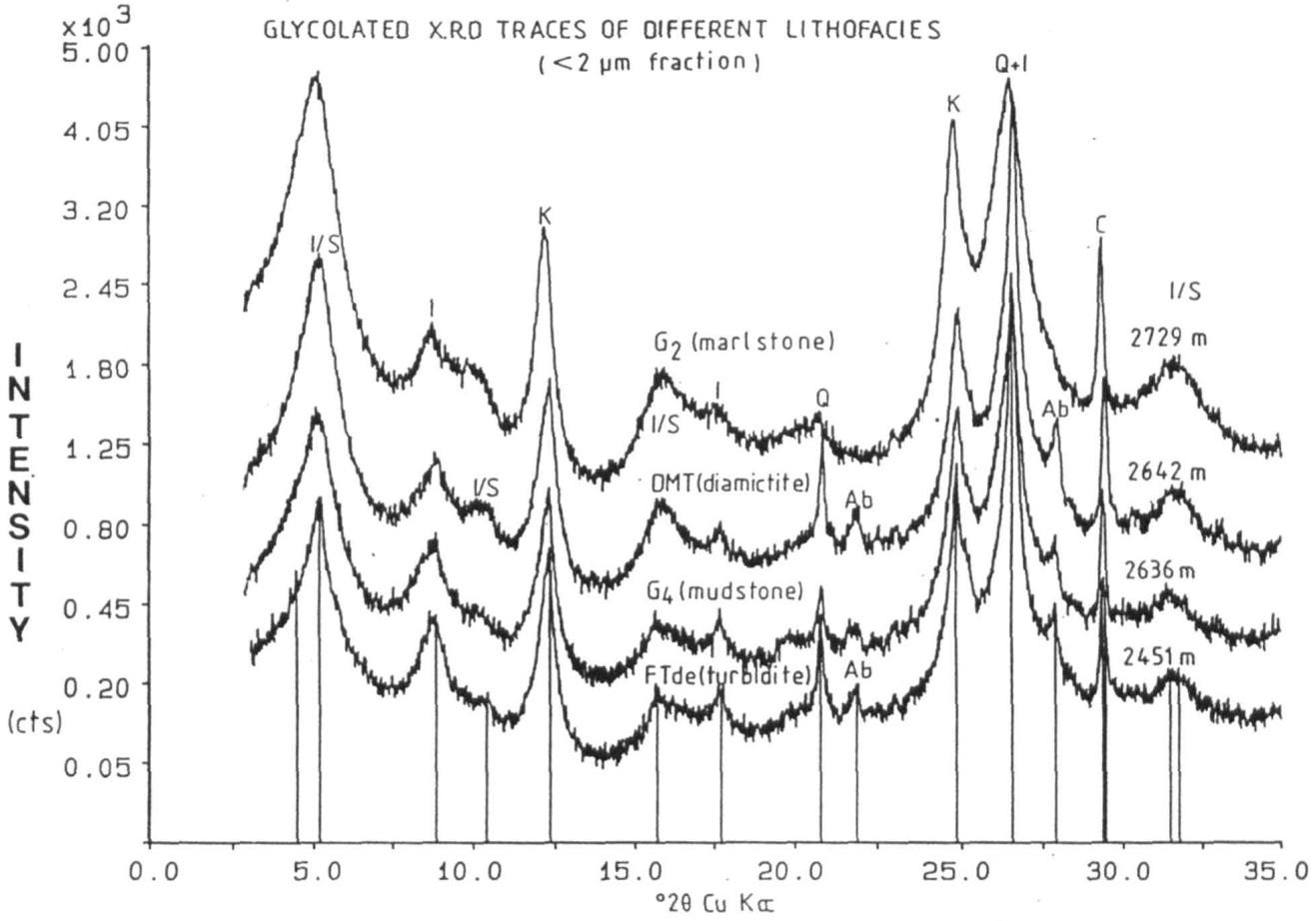


Fig. 8.12 - X.R.D. traces of the glycolated oriented clay grade fractions (<2 µm) showing the typical reflections present in the Marlstone G_2, Mudstone G_4, Diamictite **DMT**, and Turbiditic-mudstones **FTde**.

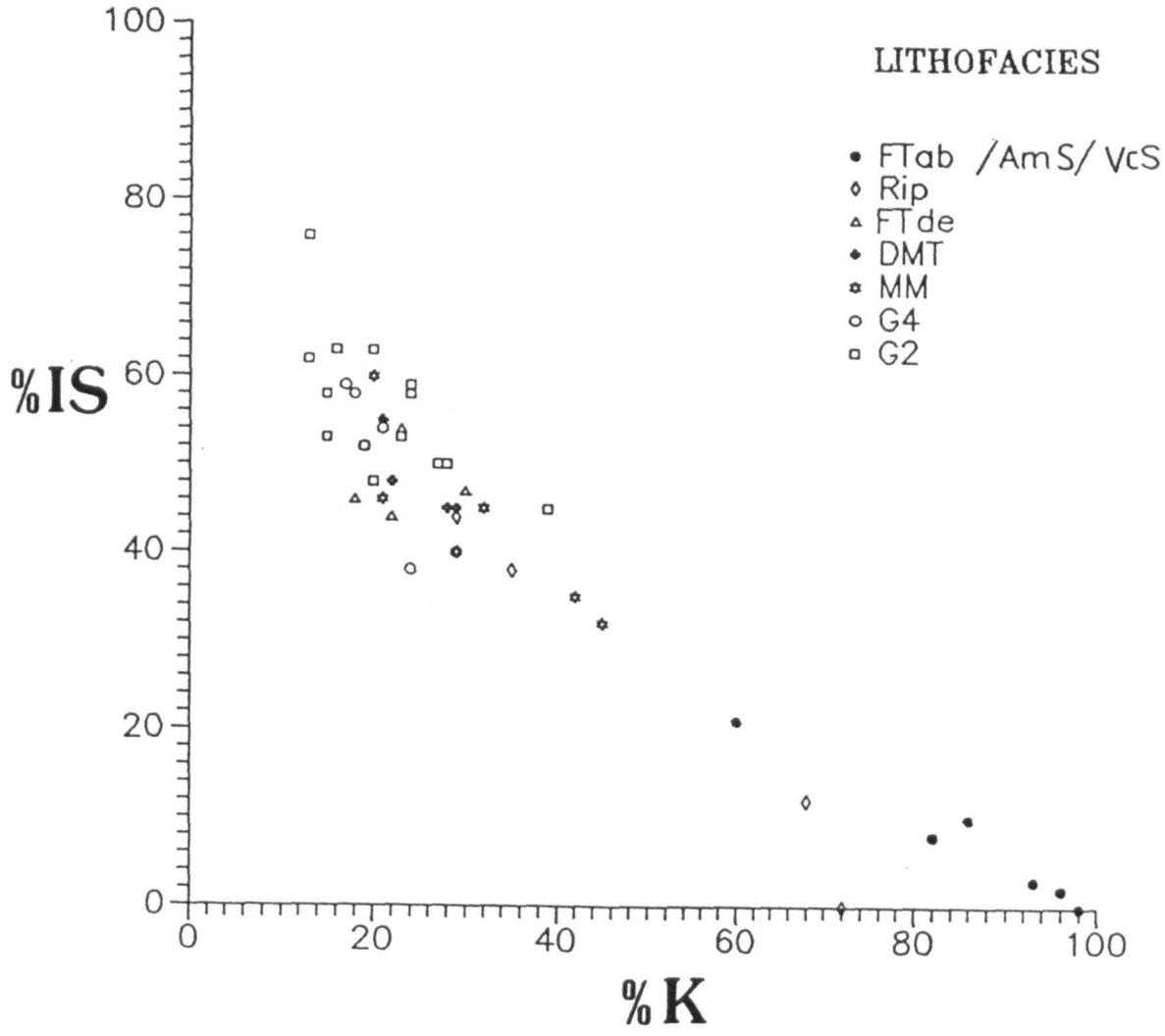


Fig. 8.13 - Relationship between the percentages of kaolinite versus illite-smectite in the different lithofacies (see Fig. 8.9 for key to lithofacies symbols).

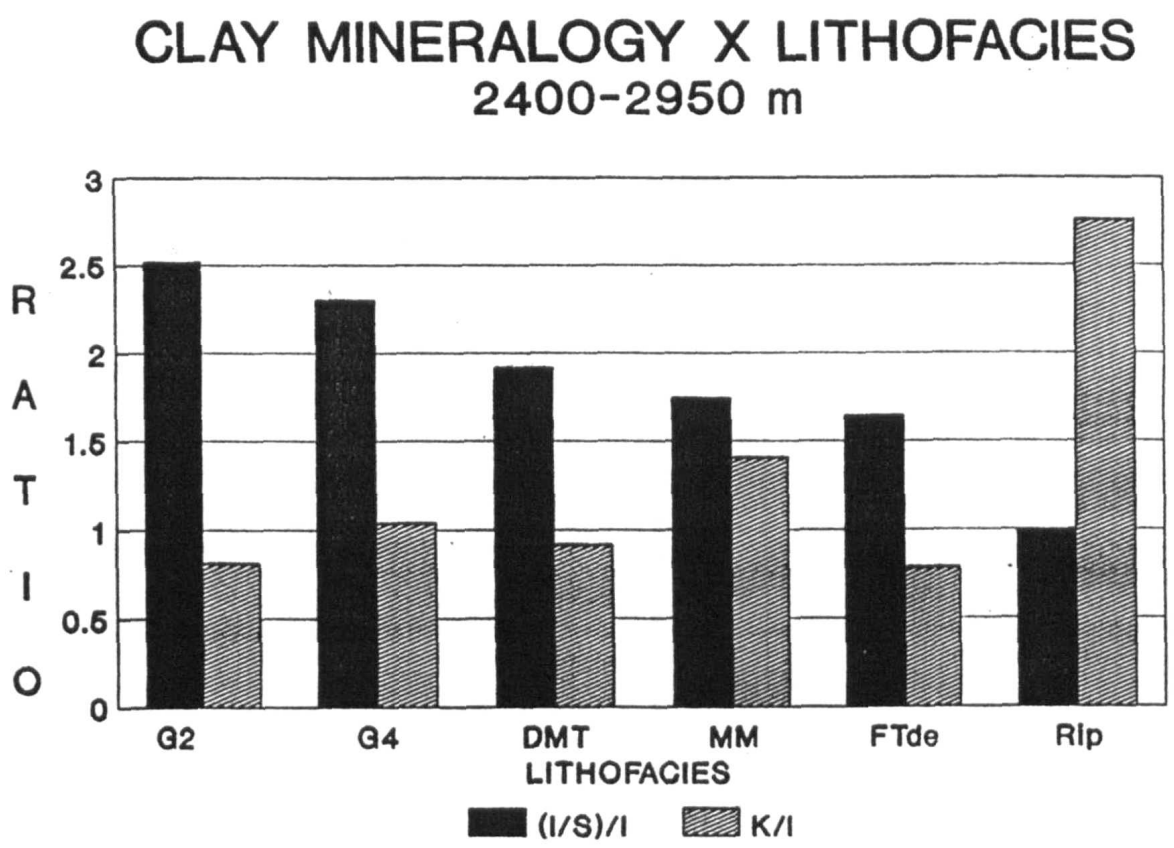


Fig. 8.14 - Relationship between the average illite-smectite/illite and kaolinite/illite ratios versus lithofacies.

The use of ratios has therefore proved to be a useful means of differentiating the hemipelagic sediments from the turbiditic mudstones. However, clay mineral compositions can only be used to differentiate depositional environments of different lithofacies if the analyzed intervals have not undergone much diagenesis. This was possibly the case in some of the studied samples. This problem can be examined in **Fig. 8.15** where the average ratios of K/I and (I/S)/I of two lithofacies from samples of different depth intervals (2400-2950 m and 3850-3860 m) have been plotted. The relative decrease of these ratios in the deepest interval could be a consequence of the illite increasing due to the diagenetic formation of illite with depth (see 8.5 below).

8.5 DIAGENESIS OF THE MUDROCKS

The effects of diagenesis on the composition of the mudrocks were observed from the X.R.D. analysis and more directly using S.E.M. techniques.

8.5.1 INTERSTRATIFIED ILLITE-SMECTITE

Although the core samples analyzed were not from regularly spaced depth intervals it was possible to observe mineralogical variations with burial.

The mixed-layer illite-smectite in the shallowest samples (2414-2941 m) is randomly interstratified, but in the deeper samples (3852-3855 m) the illite-smectite is regularly ordered and illite-rich of the IIS type, according to the methods described in Srodon (1980) and R=2 in the Reichweite System (I:SM >1, Allevardite-type). **Fig. 8.16** shows X.R.D. data of samples from the Mudstone Lithofacies (G_4), from two different depths and burial temperatures (2637 m and 71°C, 3852 m and 123°C). The shallower sample has randomly interstratified illite-smectite with 5% illite, while the deeper one contains ordered illite-smectite with 90% illite. Additionally, it should also be noted that calcite is not detected in the deeper sample, possibly as a consequence of dissolution of calcite with depth.

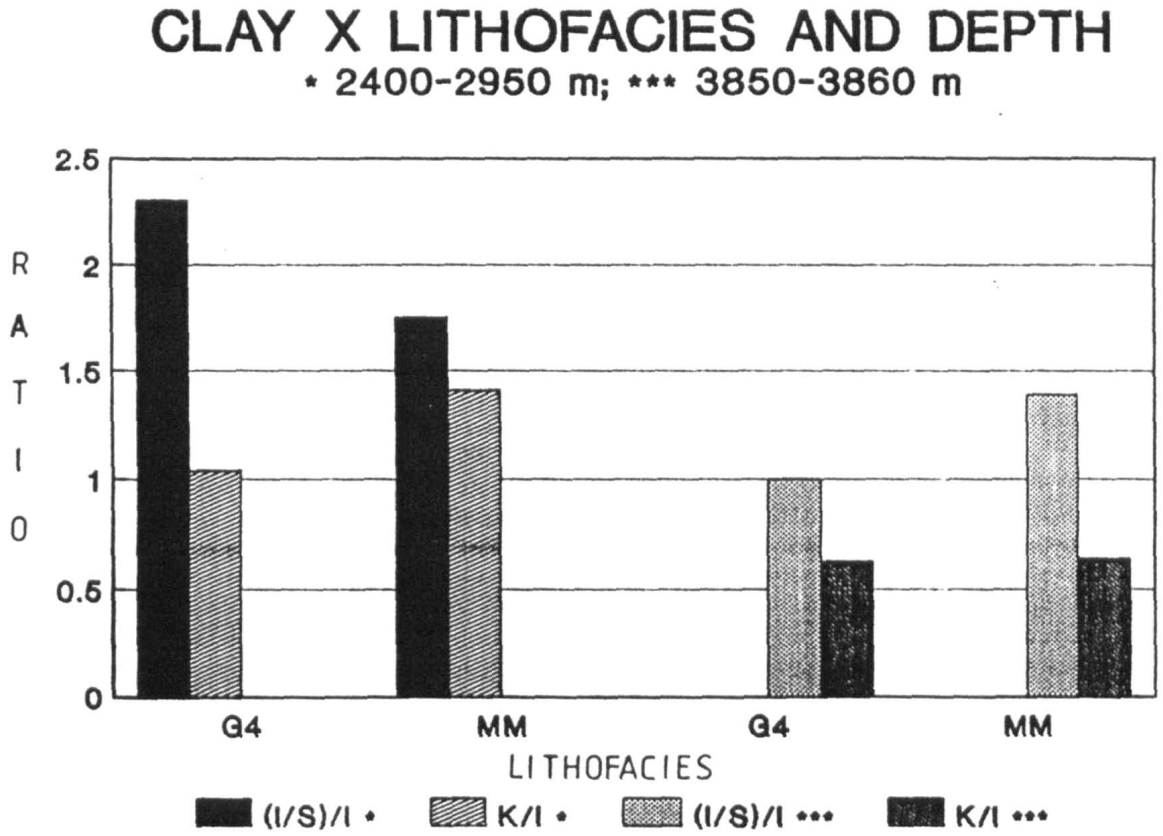


Fig. 8.15 - Relationship between the percentages of kaolinite versus illite-smectite in the different lithofacies from two depth intervals (2400-2950 m and 3850-3860 m).

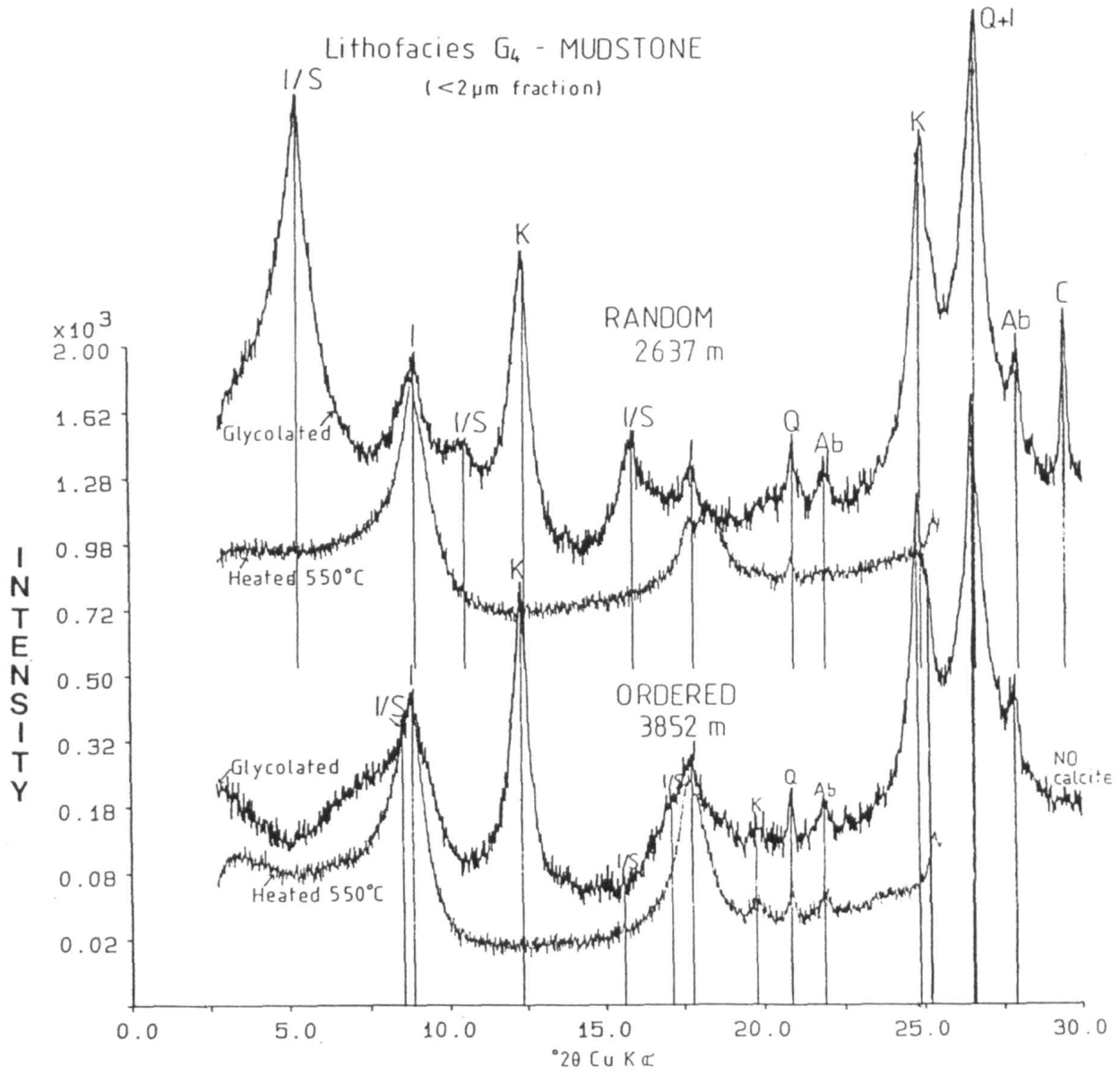


Fig. 8.16 - X.R.D. glycolated and heated 550º C traces of the oriented clay grade fractions (<2 µm) showing the variation of the illite-smectite with depth. Where:
I = illite, K = kaolinite, I/S = illite-smectite,
Q = quartz, Ab = albite, and C = calcite.

When the X.R.D. data for the present work are compared with those presented by Anjos (1986, her Fig. 6, respectively shown in the **Fig. 8.17 A** and **B**), there is no evidence of ordering in her data. At 3440 m she recorded random mixed-layer illite-smectites with 52% of smectite. A direct comparison between the two data sets is dangerous, because of the different methods[3] used to estimate the percentage of smectite in the mixed-layer illite-smectites. However, the X.R.D data from this study (**Fig. 8.17A**) indicates that the transformation of the random into ordered interstratified mixed-layer illite-smectite seems to have occurred at depths between 2950 m and 3850 m in well 154. However, further X.R.D. analyses of cuttings samples taken between 2950 m and 3850 m show no evidence of ordered illite-smectite found in the core sample at 3855 m (**Fig. 8.18**). However, the decrease in intensity of the 17 Å reflection can be indicative of increasing amounts of illite in random mixed-layer illite-smectite (Brindley and Brown, 1980). From these analyses of cuttings it was not possible to determine with any accuracy the illite-smectite composition in terms of %illite and %smectite. An alternative explanation, but less convincing, for the very high amounts of illite in the mixed-layer illite smectite of the core sample from 3855 m could be due to changes in the provenance. However, this would not explain the variations in the intensity of the 17 Å reflection with depth observed in **Fig. 8.18** as discussed above. Therefore there appears to have been a relatively rapid illitization of the illite-smectites over an interval of about 900 m (2950-3850 m) with a corresponding increase in the burial temperature of 28°C in the samples from well 154 (**Fig 8.18** and **8.19**). The calculated geothermal gradient for this interval is 31 °C/Km, which is significantly higher than the 23°C/Km used by Anjos (1986). This enhanced geothermal could help to explain the relatively rapid illitization of the illite-smectites that seems to have occurred in the mudrocks

[3] Anjos (1986) has used the method described in Rettke (1981) and I have used the methods describe in Chapter 4.

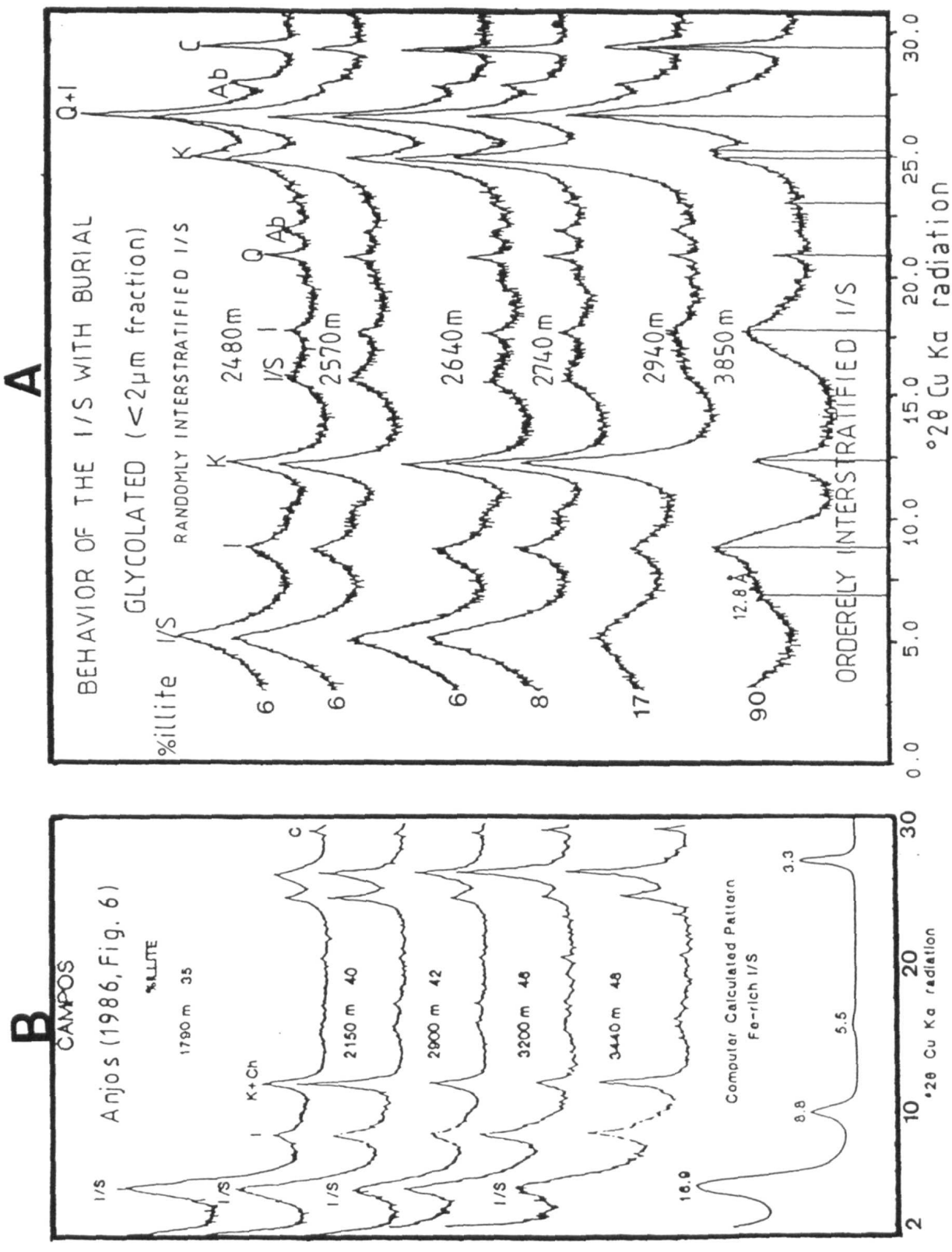


Fig. 8.17 - Behaviour of the illite-smectite X.R.D. glycolated traces of the oriented clay grade fractions (<2 µm) (**A**) of this study and (**B**) those presented in Anjos (1986, her Fig 6).

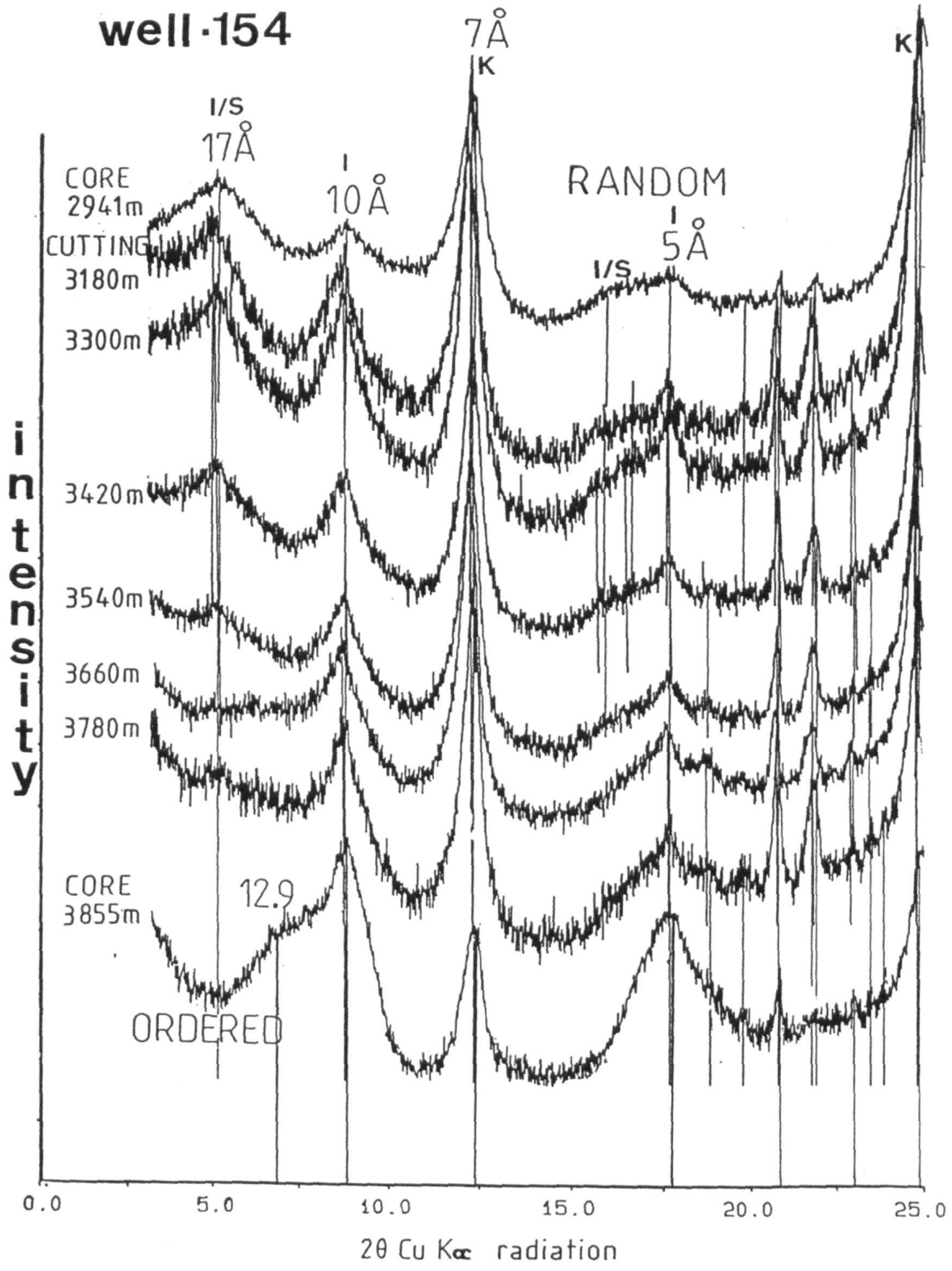


Fig. 8.18 - X.R.D. glycolated traces of the oriented glycolated clay grade fractions (<2 μm) of core and cutting samples showing the variation of the mixed-layer illite-smectite with depth, from random to ordered interstratified. Where: I/S = illite-smectite, I = illite, K = kaolinite.

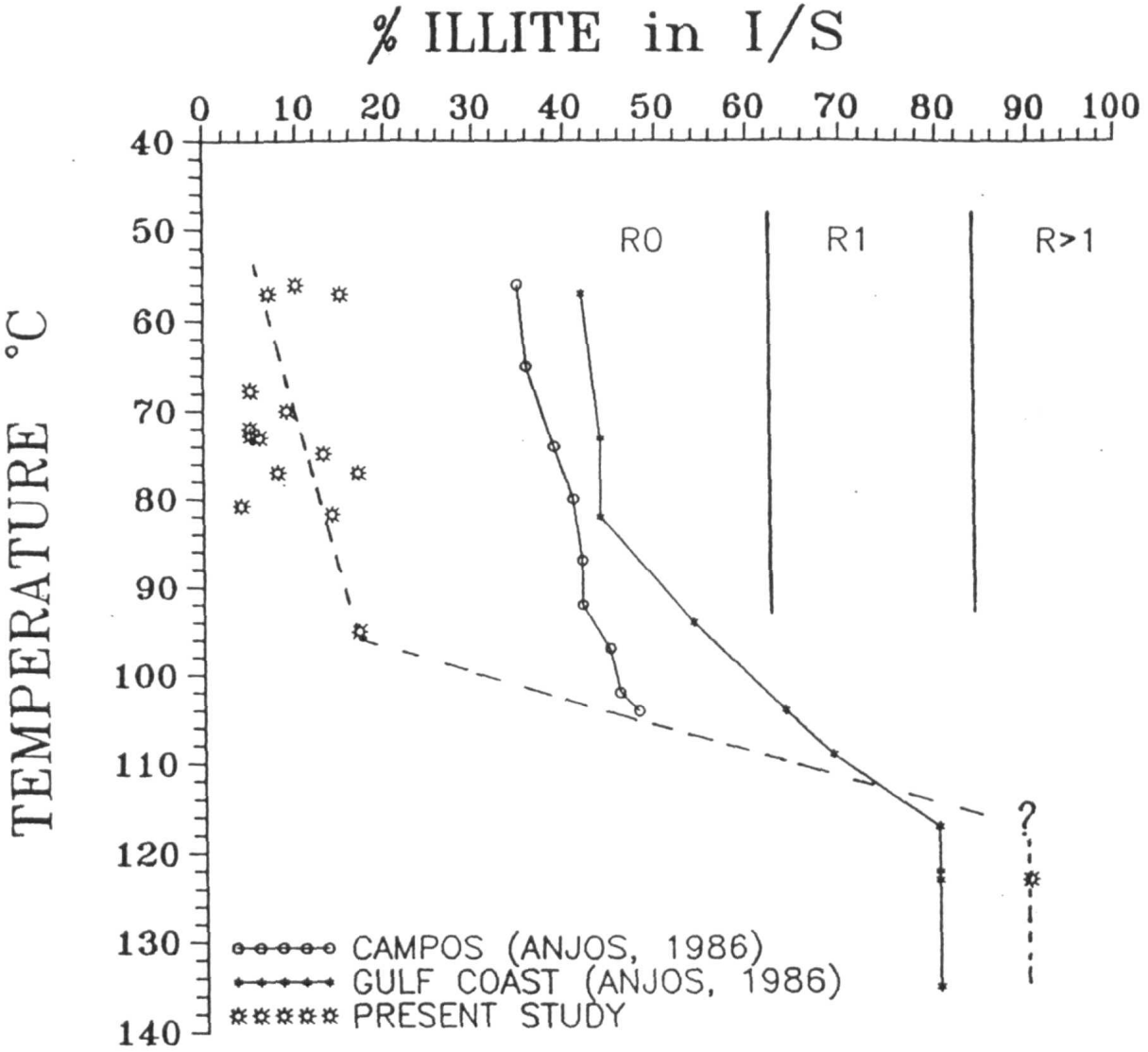


Fig. 8.19 - Variations of the percentage of illite-smectite with temperature °C. Data from the present work are compared with those from Anjos (1986, her Fig. 7).

of well 154, which was not observed by Anjos in her samples from the Campos Basin (**Fig. 8.19**).

One of the possible causes for the relatively high geothermal gradient in well 154 is its structural position in a downthrown block of a growth fault that places the Miocene succession in contact with the Aptian evaporites. This might have caused a rapid increase in temperature over a relatively short time, when about 2,000 m of Lower Miocene sediments were deposited in ~6 Myr (i.e 36 cm/Kyr).

The illitization of illite-smectites during burial diagenesis of mudrocks has been widely documented. It is a mineralogical reaction that can be summarized as smectite + K^{+} + Al^{3+} --> illite + Si^{4+} with loss of iron and magnesium from smectite layers (Hower et al., 1976), and temperature is an important factor controlling this reaction. Additionally, the presence of ordered illite-smectite in well 154 at burial temperature of about 120°C accords well with the presence of ordered illite-smectites at similar burial temperatures elsewhere (e.g. Gulf Coast Tertiary mudrocks, **Fig. 8.19**).

8.5.2 EARLY DIAGENESIS: FRAMBOIDAL PYRITE AND DOLOMITE

Early diagenesis in modern organic-rich marine muds is controlled by microbial oxidation of the organic matter and can be differentiated in descending order as aerobic respiration, sulfate reduction, and carbonate reduction/ methane generation (**Table 8.3**). This depth zonation reflects the effects of progressively less efficient modes of metabolism within the sediment column (Claypool & Kaplan, 1974). The most energetically favourable or efficient reactions occur first (Stumn & Morgan, 1970; Claypool & Kaplan, 1974).

The most common early diagenetic products are pyrite, in the sulfate reduction zone, and carbonate cements in the methanic zone.

8.5.2.1 FRAMBOIDAL PYRITE

S.E.M. analyses of the Oligocene mudrocks of the Campos Basin have shown the presence framboidal pyrite mainly within the foraminiferal chambers (**Plate 8.1 A**).
Framboidal pyrite in the Miocene mudrocks is more common and occurs not only inside foraminiferal chambers but also in the siliciclastic matrix, replacing organic matter and in biotite (see **Plate 8.1 B, C, D**).

In terrigenous or hemipelagic sediments the sulfide (H_2S) reacts rapidly and completely with ferric iron to form pyrite. The presence of framboidal pyrite provides clear evidence for diagenetic processes that involved sulfate reduction (Gautier, 1985).

TABLE 8.3 (From Berner, 1980)

REACTION	FREE ENERGY (KJ/mol of CH_2O)
Aerobic respiration:	
$CH_2O + O_2 \rightarrow CO2 + H_2O$	- 475
Nitrate reduction:	
$5CH_2O + 4NO_3 \rightarrow 2N_2 + 4HCO_{3-} + CO_2 + 3H_2O$	- 448
Sulfate reduction:	
$2CH_2O + SO_{4=} \rightarrow H_2S + 2HCO_3^-$	- 77
Methanogenesis:	
$2CH_2O \quad CH_4 + CO_2$	- 58

The zonation shown in the **Table 8.3** reflects the degree of oxygenation of the bottom waters, the rate of accumulation of organic matter versus siliciclastic and biogenic carbonate and the consequent degree of bioturbation. When the rate of sedimentation is low and the bottom waters are well oxygenated almost all the organic matter is destroyed by the aerobic organisms and little is

left for the sulfate-reducing bacteria and methanogens (Gautier, 1985).

The differences in the type of occurrence and abundance of pyrite in the Oligocene and Miocene rocks are probably due to the relatively lower sedimentation rates and better oxygenation from greater bioturbation during the deposition of the Oligocene mudrocks, compared with the Miocene. As a result the majority of the organic matter in the Oligocene rocks was oxidized and destroyed, while in the Miocene mudrocks some organic matter has been preserved in the siliciclastic matrix. This could explain the relatively higher percentages of pyrite in the Miocene rocks. The presence of pyrite preferentially inside the foraminiferal tests indicates the presence of favourable microenvironments for pyritization and must have occurred during the very early stages of diagenesis.

8.5.2.2 DOLOMITE

S.E.M. analyses have shown that dolomite in the studied mudrocks occurs as sparse or abundantly distributed rhombs **(Plate 8.2)**. The dolomite has grown replacing calcareous microfossils (foraminifera and coccoliths) or in the matrix **(Plate 8.2)**. The sparse dolomite occurs most often in the siliciclastic matrix, although it can also be found infilling large planktonic foraminifera and between biotite cleavages **(Plate 8.2 B, D)**. The zonation observed in the dolomite rhombs **(Plate 8.2)** (B.S.I.) is the result of variations in the iron contents (probe data). Usually there is an increase of the iron content towards the borders of the crystals indicating an initially low iron content, that may be related to the early formation of framboidal pyrite. Compactional features such as fracturing of the rhombs indicate that the dolomite is a pre-compaction diagenetic phase **(Plate 8.2 C)**.

The relationship between the relative timing of the pyrite and dolomite generation can be seen in the **photomicrograph D (Plate 8.2)**, where the pyrite has grown first between the cleavages of the biotite and was then

enclosed by the later dolomite.

There are a few examples of intensely dolomitized intervals and these are always associated with marlstones (G_2) interbedded with relatively thick (> 3 m) siliciclastic mudstones. This preferential dolomitization is illustrated in **Plate 8.3** (well 329). The S.E.M. **photomicrographs A** and **B** were taken from samples a few centimetres above the dolomitized marlstone, while the **photomicrographs C** and **D** were taken from samples in the middle and below this bed, respectively. There is no evidence of dolomite in the samples below (**D**) and above (**A** and **B**) the dolomitic bed. In another well (AB-1), only sparsely zoned ferroan dolomite was found about 1.5 m below another dolomitized marlstone interval.

The presence of thick siliciclastic mudstones interbedded with marlstones could have provided the necessary conditions for the development of a methanic zone. This assumes that the sulfate has been removed from the pore waters to form pyrite allowing further organic reactions to have produced methane. In open-marine environments dominated by terrigenous sediments, two processes are mainly responsible for microbial methane generation: acetate fermentation (Sansone and Martens, 1981) and CO_2 reduction (Mechalas, 1974).

$CH_3COOH = CH_4 + CO_2$ (acetate fermentation)

$CO_2 + 8H^+ = CH_4 + 2H_2O$ (CO_2 reduction)

In general, biogenic methane is generated in significant amounts from the base of the sulfate reduction zone (few meters below the water-sediment interface) to depths of about 1,000 m (Rice and Claypool, 1981). When sulfide concentrations have become very low (i.e. in the methanic zone) dolomite is apparently commonly found phenomenon (eg. Piscotto and Mahoney, 1981, Kelts and Mackenzie, 1982). According to Baker and Kastner (1981) sulfate reduction promotes dolomitization in three ways: a) by removal of the dissolved $SO_{4=}$ inhibitor; b) production of alkalinity; and c) production of NH_4^+, which subsequently exchanges with absorbed Mg^{++}.

PLATE 8.1

A - S.E.M. (B.S.I. = backscattered electron imaging) photomicrograph showing framboidal pyrite (py) inside planktonic foraminifera. Mudstone Lithofacies G_4 (2564 m and 57 °C).

B - S.E.M. (B.S.I.) photomicrograph showing framboidal pyrite (py) growth in the matrix. Mottled Mudstone Lithofacies MM (2942 m and 95 °C).

C - S.E.M. (B.S.I.) photomicrograph showing framboidal pyrite (py) replacing organic matter. Mudstone Lithofacies G_4 (2627 m and 72 °C).

D - S.E.M. (B.S.I.) photomicrograph showing framboidal pyrite (py) and dolomite rhombs (d) between the biotite cleavages. Diamictite Lithofacies DMT (2487 m and 76 °C).

PLATE 8.1

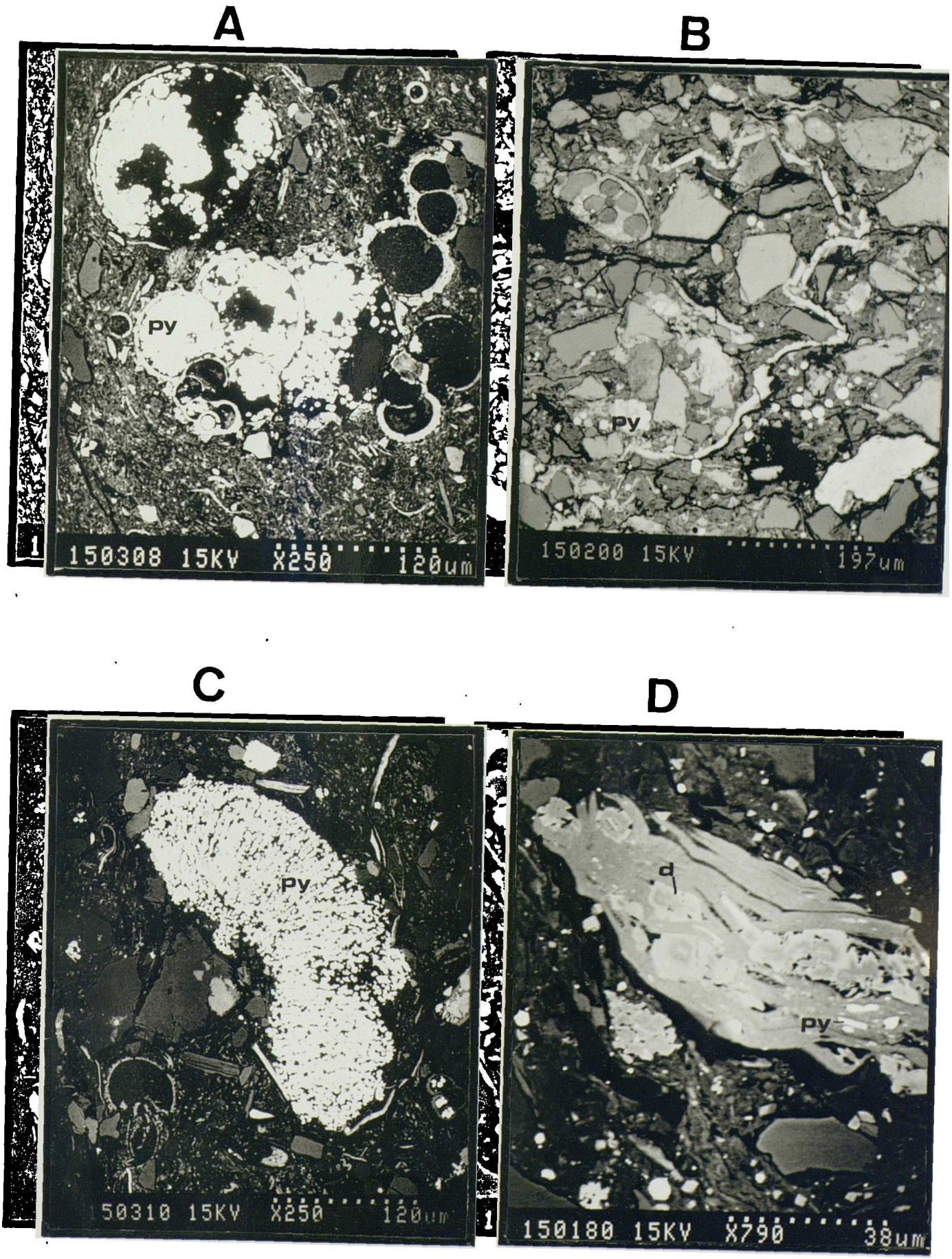

A
B
py
150308 15KV X250 120um
py
150200 15KV 197um
C
D
Py
50310 15KV X250 120um
d
py
150180 15KV X790 38um

PLATE 8.2

A - S.E.M. (B.S.I.) photomicrograph showing isolated or scattered dolomite (d) in a coccolith-rich mudstone. The large dark grain showing evidence of dissolution is a K-feldspar (Kf). Calcareous Mudstone Lithofacies G_3 (2737 m and 82 °C).

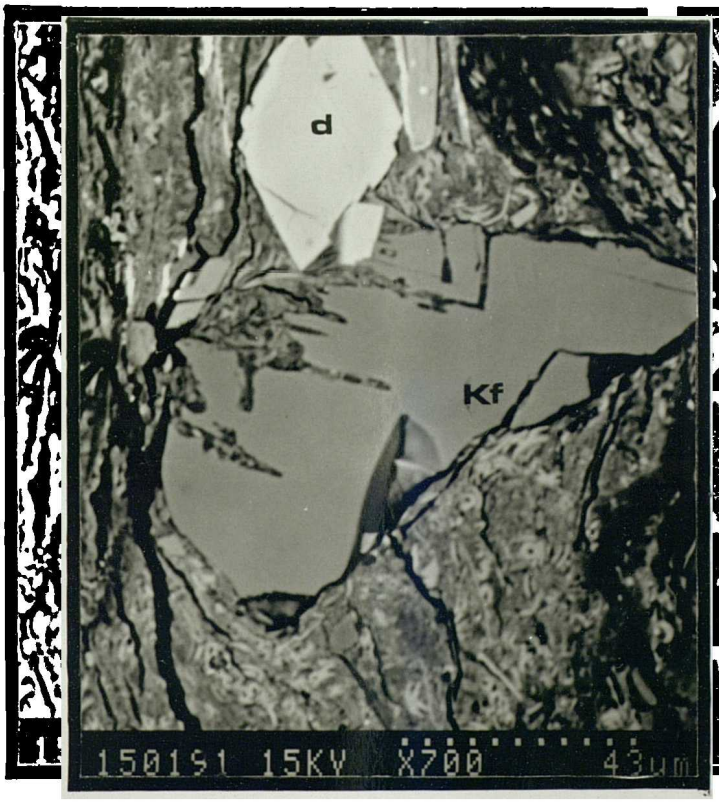
B - S.E.M. (B.S.I.) photomicrograph showing zoned rhombs of dolomite (d) and calcite (c) inside a planktonic foraminifera. Mudstone Lithofacies G_2 (2633 m and 71°C).

C - S.E.M. (B.S.I.) photomicrograph showing pervasive dolomitization of a marlstone, lithofacies G_2, with zoned ferroan dolomite (d) rhombs and compaction features represented by fractured crystals (2647 m and 72°C).

D - S.E.M. (B.S.I.) photomicrograph showing pyrite (py) and dolomite (d) growths between the biotite (bi) cleavages, and subsequent evolved by dolomite. Calcareous Mudstone Lithofacies G_3 (2737 m and 82°C, the same sample as in the photomicrograph A).

PLATE 8.2

A



B



C



D

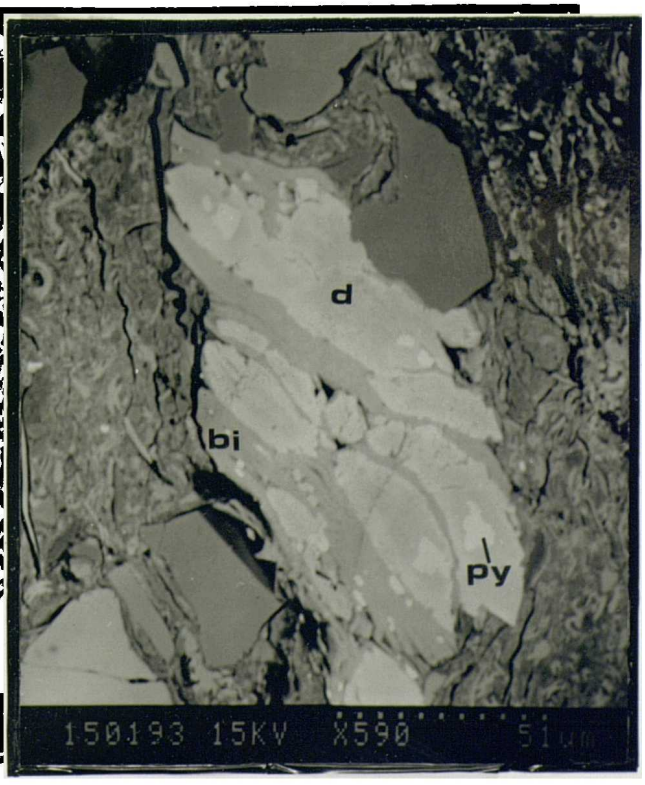


PLATE 8.3

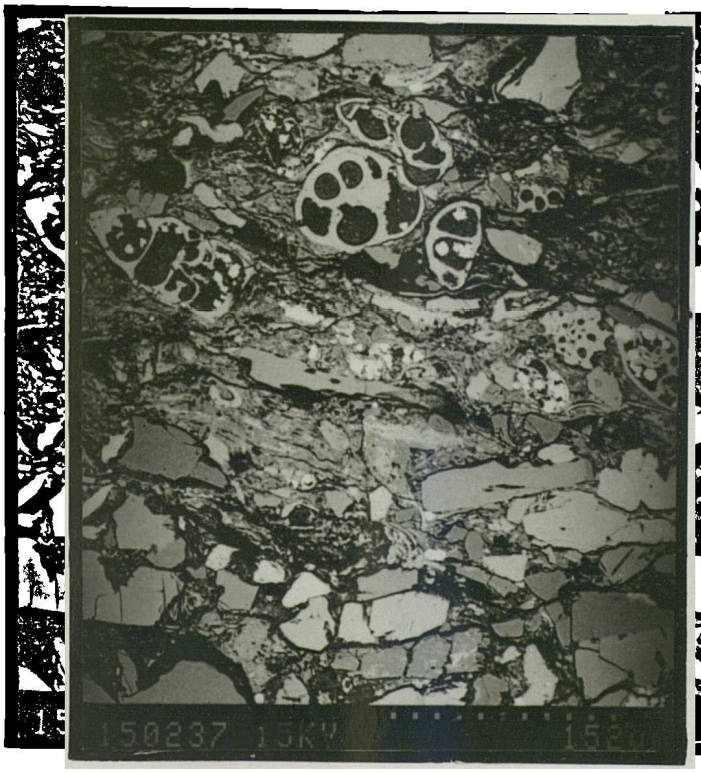
A and **B** - S.E.M. (B.S.I.) photomicrographs showing the absence of dolomite in a sample from above the dolomitized marlstone. The foraminiferal chambers are completely infilled with kaolinite (K) cement and some framboidal pyrite (py). Mudstone Lithofacies G_4 (well 329, 2646 m and 72°C).

C - S.E.M. (B.S.I.) photomicrograph showing the ferroan dolomite (d) rhombs with zonation due to the variation in the iron content. The interpenetration of the crystals resulted from compaction, indicating an early dolomite generation. Marlstone Lithofacies G_2, dolomitized (2647 m and 72°C).

D - S.E.M. (B.S.I.) photomicrograph of a mudstone G_4 showing the absence of dolomite below the dolomitized bed (2648 m and 72°C).

PLATE 8.3

A



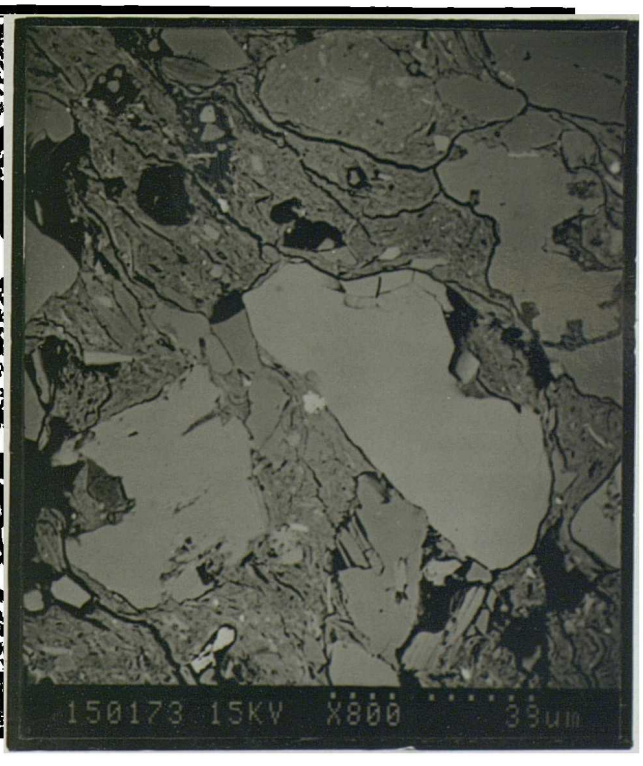
B



C



D



The lack of dolomitization in the thinly interbedded marlstones/mudstones of the studied succession could have been due to the presence of sulfate in the pore waters. Baker and Kastner (1981) showed that dolomitization is effectively inhibited by aqueous $SO_{4=}$ in concentrations as low as 5% of normal sea water concentration. The inferred existence of relatively high concentrations of sulfate in the pore waters of the thinly interbedded marlstones/ mudstones could be explained by intense bioturbation together with the low rates of sedimentation, thus favouring the mixture of the connate waters with the bottom sea waters. In this way the formation of dolomite could have been inhibited. In those cases where scattered rhombs of dolomite were formed locally favourable conditions (i.e. low sulfate) might have existed.

The exploratory importance of these dolomitized beds lies in their potential as seismic reflectors. The higher density and velocity values of the dolomitized beds compared to the adjacent mudstones produce a good impedance contrast. This does not mean that all dolomitic beds will appear as seismic reflectors. However, the widespread distribution of the marlstones and their subsequent dolomitization, enhancing the density contrast with the interbedded siliciclastic mudstones, will have generated high amplitude and continuous reflectors.

8.5.3 FELDSPAR DIAGENESIS

The majority of the analyzed mudrock samples came from relatively low burial temperature intervals, ranging from 55ºC to 87ºC, and three from depths of intermediate (95ºC) and higher (123ºC) temperatures (see **Fig 8.1**).

Feldspar alteration and dissolution has occurred in the investigated samples, but the percentage of altered feldspar is relatively low (see **Plate 8.4**). Higher percentages of altered feldspar were found in the deeper samples and also in those with relatively higher contents of organic matter.

Although the **photomicrographs A** and **B** (**Plate 8.4**) are from the same sample (57ºC and 1.7% of T.O.C.) it is

possible to see that the plagioclase in **A** was partially leached, leaving a secondary microporosity, while the plagioclase in **B** is also altered but kaolinite has formed in situ as an alteration product (**Plate 8.4**). The probable cause for this contrast is the differential mobility of aluminium in the two microdiagenetic environments. In the case where kaolinite is present the aluminium remained immobile and in the other it was removed.

One of the deepest (3850 m, 123°C) analyzed samples shows evidence of plagioclase dissolution but with no associated kaolinite (**Plate 8.4 C, D**). The polyphase feldspar grain (plagioclase darker and K-feldspar brighter) in **photomicrograph C** shows differential resistance to alteration with plagioclase seeming to have been altered first. Additional diagenetic phenomenon characterized by later quartz and feldspar overgrowths also occurred (**photomicrograph D**). There is also in the same photomicrograph a fractured quartz grain cemented by TiO_2 (very bright). This kind of cement (TiO_2) was seen in other samples, always associated with relatively high organic matter, but usually only in very low quantities.

The present data can be compared with the model proposed by Surdam and Crossey (1985a and 1985b) to try to explain the alteration and dissolution of the feldspars shown in **photomicrographs A** and **B** (**Plate 8.4**).

Surdam and Crossey (1985a and 1985b) proposed a model in which the carboxylic acids (CH_3COO^-) act as transport agents for aluminium after the dissolution of the feldspar. These organic acids increase aluminosilicate and also carbonate solubilities and can be generated either by thermal or oxidative cracking of carboxylic or phenolic groups from kerogen in the adjacent source rocks. Carothers and Kharaka (1978a) have demonstrated that the peak concentrations of the carboxylic acids typically occur from 80°C to 120°C and they act as the main buffer[4] in this temperature range. Carboxylic acids can also be generated by

[4] Buffer: a measure of the ability of the solution to resist to pH changes when titrated with acid or base (Morel, 1983).

oxidation reactions via the reduction of the ferric iron released during clay diagenesis. Approximately 60% of the iron in the mixed-layer clay phases may be released over the burial depths and temperatures when the mixed-layer illite-smectites are likely to become illitized and ordered (Surdam and Crossey, 1985a).

The major problem for the application of Surdam and Crossey model in this study is that dissolved plagioclase is found in a sample with a burial temperature of 57°C (**Plate 8.4**), and 90% smectite in the random mixed-layer illite-smectite. Thus the temperatures are too low and there is no evidence of illitization of mixed-layer clays required by the Surdam and Crossey model. There is therefore either another mechanism causing feldspar dissolution and transformation of feldspars to kaolinite or the kind of process mentioned by Surdam and Crossey (1985a and 1985b) might have started in the Campos Basin mudrocks at lower temperatures (i.e. < 80-120°C).

Bourdou et al (1984) studied organic matter from the Mahakam delta and demonstrated that the carboxyl groups were being generated prior to 80°C. Carothers and Kharaka (1978a, 1980) stated that most of the carboxylic acids would be destroyed by bacteria in organic-rich rocks at temperatures below 80°C. However, relatively low concentrations of bacteria could mean that carboxylic acids produced at temperatures of <80°C could be preserved and thus cause dissolution of the feldspars at relatively low temperatures. One possible reason for the low bacterial production could be the presence of sulfate in the pore waters (see **section 8.5.2.2**).

At greater depths (3852 m) and higher temperatures (123°C) there is further evidence of plagioclase and k-feldspar dissolution (**Plate 8.4, C** and **D**). In the same sample quartz and albite overgrowths also occur. This suggests that this rock has already passed through a period when the feldspar was partially dissolved followed by a period when the conditions were favourable for quartz and feldspar generation. This reinforces that the diagenetic

PLATE 8.4

A and **B** - S.E.M. (B.S.I.) photomicrographs from a mudstone G_4 with 1.7% weight of T.O.C. showing altered plagioclase (pl). The alteration products are absent in **A**, but are present in **B** as kaolinite (K). (2563 m and 57ºC).

C - S.E.M. (B.S.I.) photomicrograph showing a composed feldspar grain (Kf = K-feldspar, brighter; and pl = plagioclase, darker) with differential alteration. The plagioclase was more susceptible to alteration and leaching. There is no alteration product present. Mottled Mudstone Lithofacies (MM) (3855 m and 123ºC).

D - S.E.M. (B.S.I.) photomicrograph showing quartz (qz) (darker) and plagioclase (pl) overgrowths (o), Additionally near the right bottom corner there is a fractured quartz cemented with TiO_2 (t), the brightest. Mottled Mudstone Lithofacies (MM) (3855 m and 123ºC).

PLATE 8.5

A



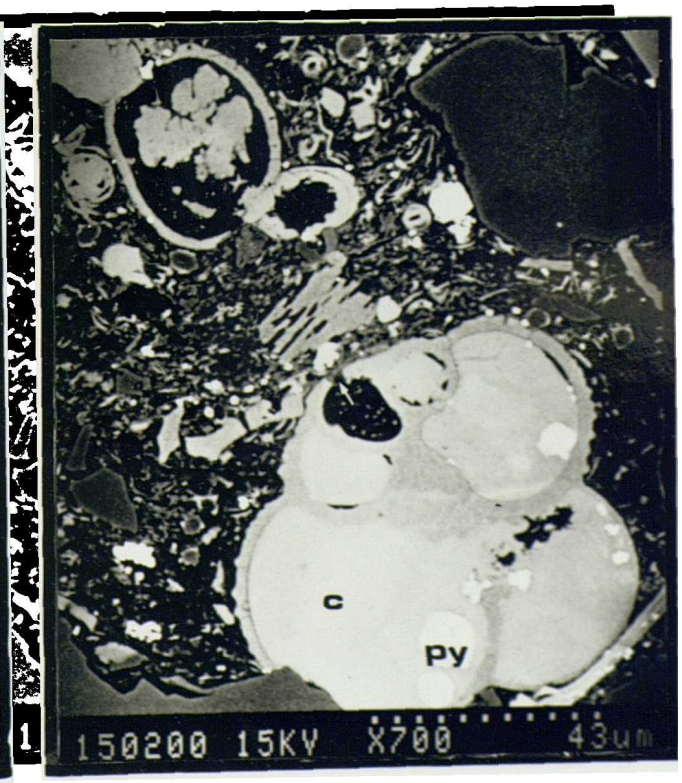
B



C



D



processes in the mudrocks of the Campos Basin involving feldspars and kaolinite occurred relatively early in the diagenetic history of the Basin.

8.5.4 AUTHIGENIC CLAY MINERALS

The chambers of the foraminifera from the shallowest mudstones (2400-2500 m) are generally empty or only partially infilled with framboidal pyrite. Calcite or in some cases ferroan dolomite, also infills some of the foraminifera, usually in the marlstones or the mottled mudstones (see **Plate 8.5**). These authigenic phases are usually early diagenetic in origin. However, with increasing depth there is an infilling of the chambers of the foraminifera with clay cements such as kaolinite and less frequently illite-smectite and chlorite (**Plate 8.6** and **Fig 8.20**). The illite-smectite crystals show a random growth and their morphology differs from the booklets of the kaolinite (see **Plate 8.6**, and **plates 8.3 B, 8.7 C D, 8.8 A, B** and **C**). Notice that not necessarily all the chambers were infilled, frequently the inner and smaller ones remain empty. This is possibly related to the inaccessibility of these innermost chambers to the influence of reactive diagenetic fluids.

The pervasive bioturbation found in the Mottled Mudstone Lithofacies **MM**, would have caused an increase in the amount of coarser grains (very fine- sand/coarse-silt grains) producing locally burrows and lenses of very fine-sandstone within the mudstones. This created more porous and permeable conditions and enhanced the diagenetic effects, especially calcite cementation, feldspar and mica alteration and kaolinite cementation (**Plate 8.7**). This can be seen in a sample of a Mottled Mudstone (**MM**) (2941 m and 95°C) containing altered plagioclase (**Plate 8.7A** and **B**) and biotite (**8.7C**), and microfossils cemented by kaolinite (**Plate 8.7C** and **D**). The coexistence, in the same sample, of kaolinite cements within foraminiferal chambers and altered feldspars without kaolinite is very puzzling and indicates the variety of diagenetic micro environments in the mudrocks.

PLATE 8.5

A - S.E.M. (B.S.I.) photomicrograph showing benthonic foraminifera which are empty or are filled with framboidal pyrite (py, top right corner) and dolomite (d) in the planktonic foraminifera (bottom right). Mudstone Lithofacies G_4 (2414 m and 53°C).

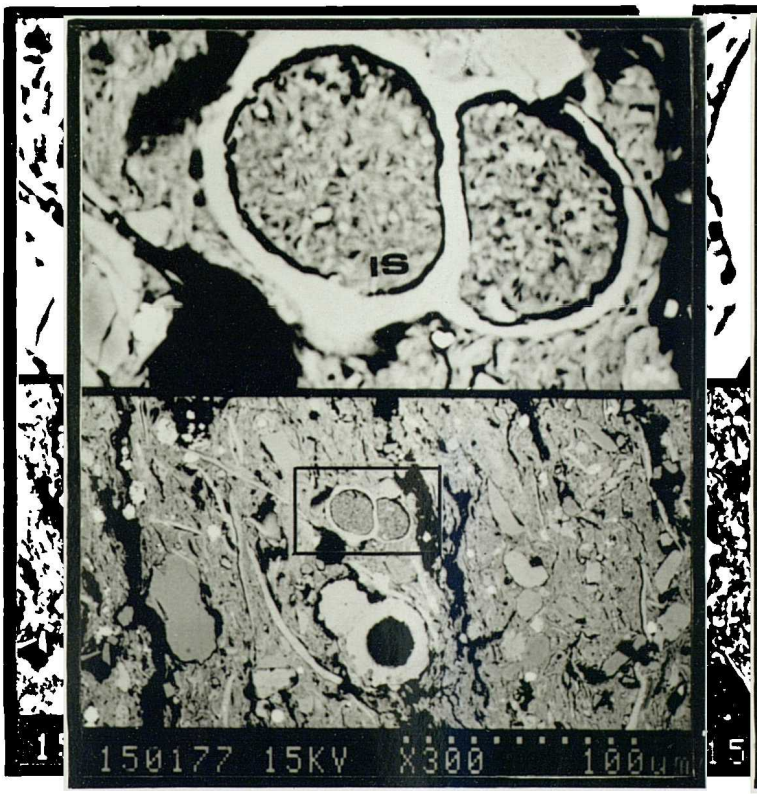
B - S.E.M. (B.S.I.) photomicrograph showing empty benthonic and planktonic foraminifera. At the top of the photo there is a benthonic foraminifera with framboidal pyrite (py). Turbiditic-mudstone, Lithofacies FTde (2445 m and 67°C).

C - S.E.M. (B.S.I.) photomicrograph showing planktonic foraminifera with small euhedral calcite (c). At the left bottom corner there is a broken ferroan dolomite (d). Marlstone Lithofacies G_2 (2618 m and 77°C).

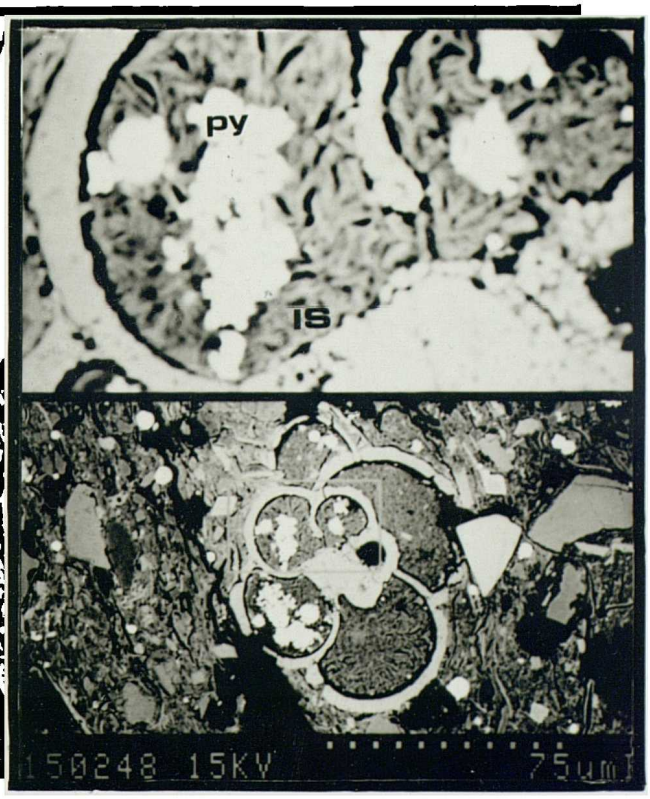
D - S.E.M. (B.S.I.) photomicrograph showing a planktonic foraminifera infilled with calcite cement (C). The innermost chamber had remained non-cemented by calcite, but was later cemented by kaolinite, probably due to an opening developed in the test due to fracturing during compaction. Observe a fracture (arrow) in this inner chamber. Marlstone Lithofacies G_2 (2639 m and 72°C).

PLATE 8.6

A



B



C



D

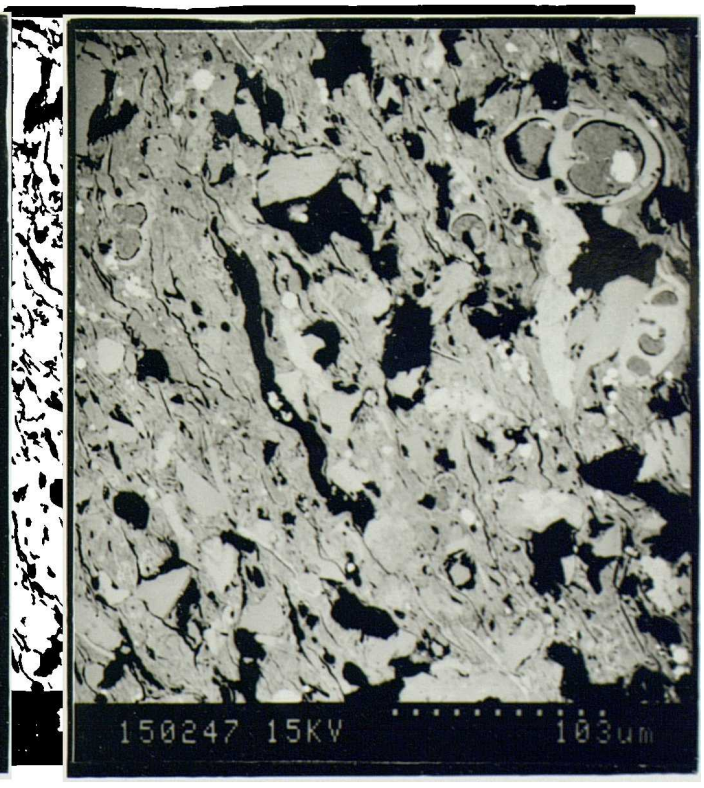


PLATE 8.6

A - S.E.M. (B.S.I.) photomicrograph showing foraminiferal chambers infilled with illite-smectite (IS). Mudstone Lithofacies G_4 (2636 m and 72°C).

B - S.E.M. (B.S.I.) photomicrograph showing chambers of planktonic foraminifera with illite-smectite (IS) and framboidal pyrite (py, brighter). Mudstone Lithofacies G_4 (2637 m and 72°C).

C - S.E.M. (B.S.I.) photomicrograph showing chambers of planktonic foraminifera cemented by kaolinite (K). Observe the vermicular forms of the kaolinite booklets. Diamictite Lithofacies DMT (2481 m and 72°C).

D - S.E.M. (B.S.I.) photomicrograph showing several chambers of planktonic foraminifera infilled with kaolinite and framboidal pyrite. Observe the compaction features associated with quartz and feldspar grains. Observe the general texture which shows the orientation of the elongated and plate-like grains. Mudstone Lithofacies G_4 (2638 m and 72°C).

PLATE 8.4

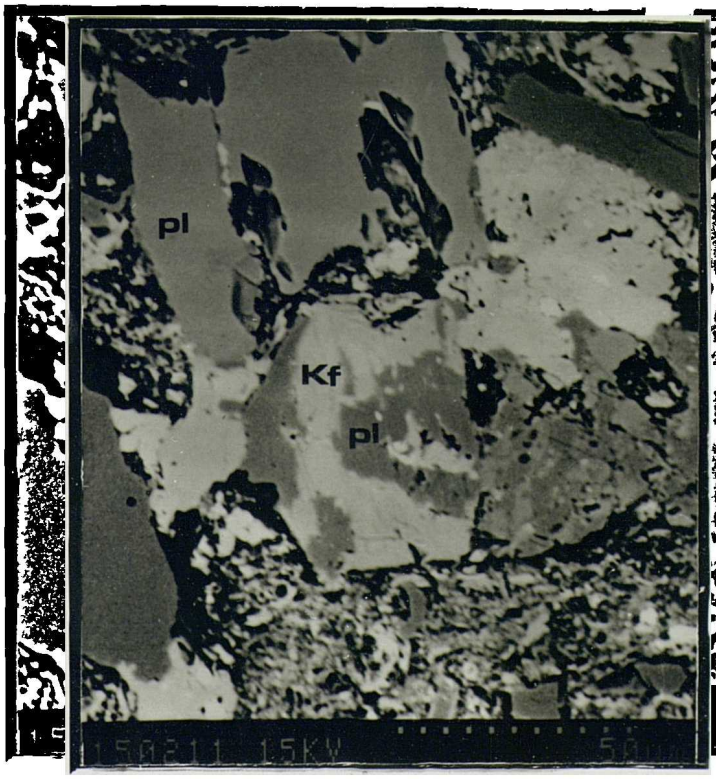
A



B



C



D



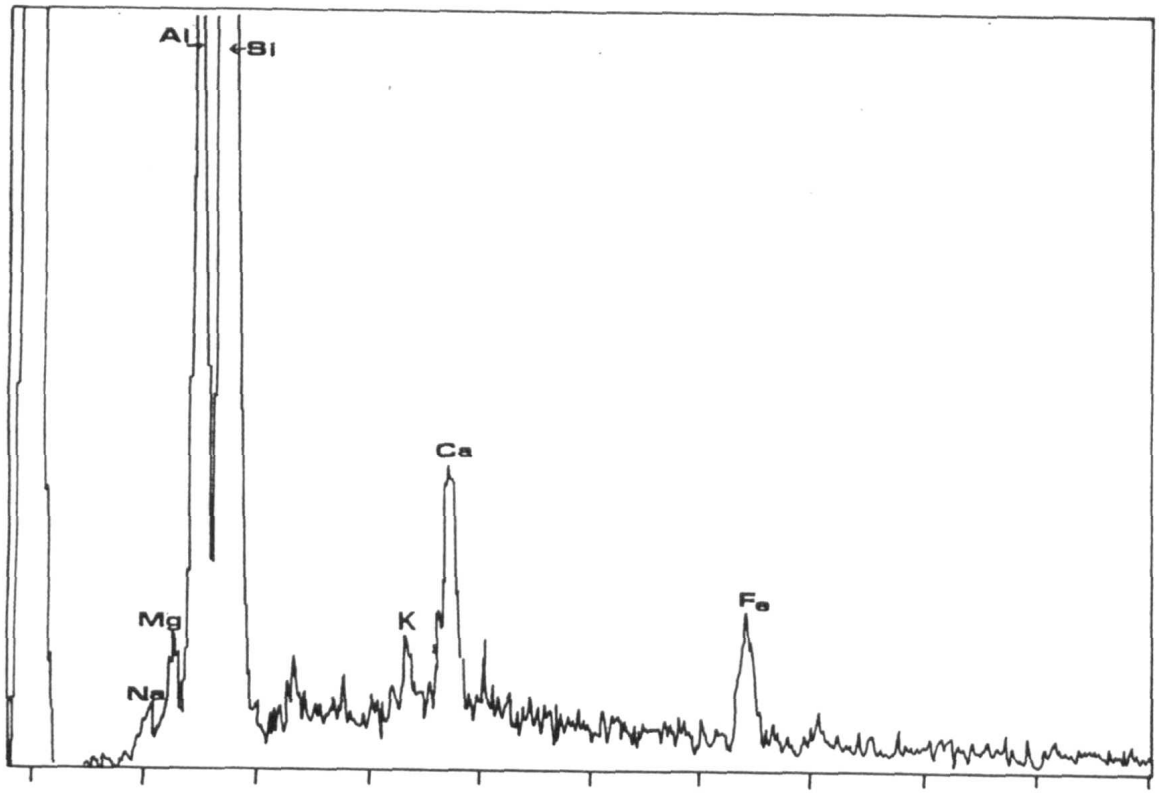


Fig. 8.20 - "Finger print" showing the composition o the illite-smectite cement inside the foraminifera, from the **Plate 8.6 A.** (20 EV/CHAN, live time = 65 secs, spectrum length = 1024 CHAN).

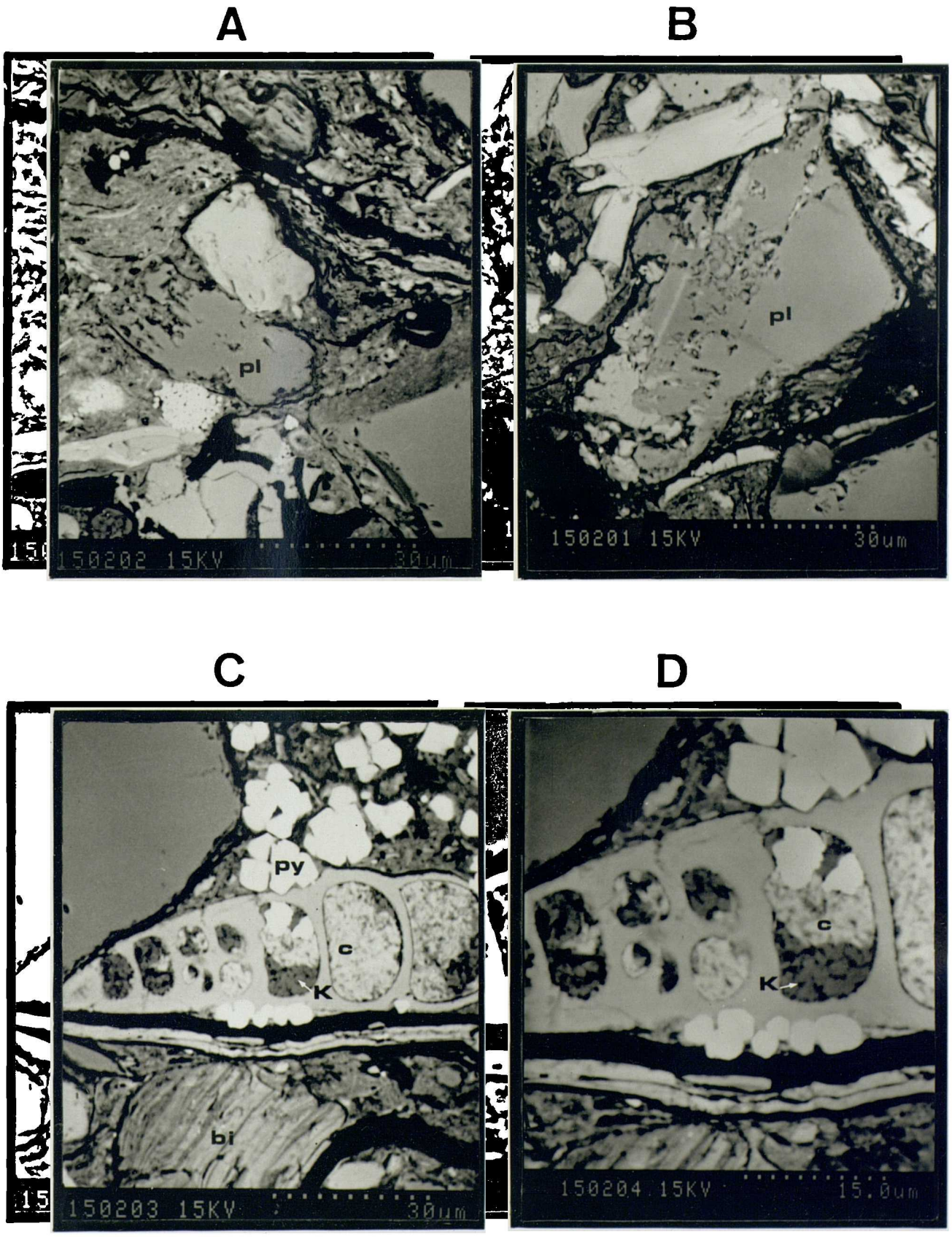
PLATE 8.7

These S.E.M. photomicrographs are from the same sample of Mottled Mudstone Lithofacies MM (2941 m and 95°C).

A and **B** S.E.M. (B.S.I.) photomicrograph show partially altered and leached plagioclase (pl).

C and **D** S.E.M. (B.S.I.) photomicrograph show the chambers of a benthonic foraminifera infilled with kaolinite (K) and pyrite (py). The brighter zones associated with the kaolinite, inside the chambers of the foraminifera are the result of the growth of late calcite (c).

PLATE 8.7


A
B
pl
pl
150202 15KV 30um
150201 15KV 30um
C
D
py
c
K
bi
c
K
150203 15KV 30um
150204 15KV 15.0um

According to MacGowan and Surdam (1988) the stability of organic complexes with aluminium is very pH dependent. A change in pH from say 6 to 7 can cause the complexes to destabilize and precipitate an Al-mineral phase such as kaolinite. This could explain, at least partially, the coexistence of kaolinite and altered feldspar as seen in the **Plate 8.7.**

Using S.E.M. analysis chlorite was found in a deep sample (3852 m, and 123°C). The chlorite occurs associated with kaolinite inside foraminiferal chambers, and infilling the space left following the dissolution of the calcite of the foraminiferal tests (**Plate 8.8 A, B, C**). Biotite has also been altered to chlorite mainly along the cleavage planes (**Plate 8.8 D**).

To explain the detectable amounts of chlorite observed only in the deepest set of samples and its association with kaolinite within foraminiferal tests the following type of reactions may be applicable (Hower et al., 1976; Boles & Franks, 1979):

smectite + Al^{+3} + K^{+} ---(illitization)--> **illite** + Si^{+4} with additional loss of iron and magnesium from smectite layers;

Fe^{+2} + Mg^{+2} + **kaolinite** ----> **chlorite.**

This implies that the illitization of the smectites may have contributed iron and magnesium for the chloritization (i.e. replacement) of kaolinites and also biotites, that may also have previously been altered to kaolinite (**Plate 8.8**).

8.5.5 CALCITE DISSOLUTION

There is some evidence of calcite dissolution within the mudstones with increasing depth of burial. This can be seen in X.R.D. traces when two samples of the same lithofacies from different depths are compared (see **Fig. 8.16**). There is also evidence of calcite dissolution from S.E.M. analyses. This is illustrated in the **Plate 8.8** (**A, B** and **C**) where the foraminiferal tests have been replaced by chlorite.

The variation of the calcium carbonate with depth and with facies are illustrated in **Fig. 8.21.** The two shallower samples (2560 m and 2570 m) are from the Mudstones Lithofacies (G_4), but have different calcite contents. The X.R.D. analysis of the sample from 2560 m does not show any detectable calcite. In this sample only agglutinated benthonic foraminifera were found, suggesting poorly oxygenated bottom waters (Eduardo Koutsoukos personal communication, 1989). This environment could have restricted the formation and preservation of calcareous microfossils, which are the principal source of calcite.

In the X.R.D. analyses of the two samples from different lithofacies at the same burial depth (3852-55 m, **Fig 8.21**) the mudstone (G_4) sample contains no detectable calcite, due to dissolution of the microfossils and replacement by chlorite (**Plate 8.8**). Conversely, the mottled mudstone (**MM**) sample, shows some calcite dissolution (S.E.M. analysis) but it still contains abundant calcareous microfossils, usually recrystallized, and thus calcite is detected in the X.R.D. analysis. If only the samples of lithofacies G_4 were compared the interpretation would be that the calcite disappears with depth. The importance of these examples is to show how dangerous it can be to draw conclusions from data using only one method and without knowing the factors that could influence the variables.

Anjos (1986) reported a slight increase in calcite with depth in samples from a Campos Basin well. Based on data from the present study it is possible to interpret the slight increase in calcite with depth observed by Anjos (1986) as the result of a facies change rather than diagenetic transformations. There is direct evidence of calcium carbonate dissolution in the Campos Basin with depth, but the calcite lost may be relatively small compared with changes due to facies variation. There are variations of the order of 40% in the $CaCO_3$ contents between the marlstones and the mudstones and reflecting variations in the amounts of calcareous microfossils (**Table 7.6**).

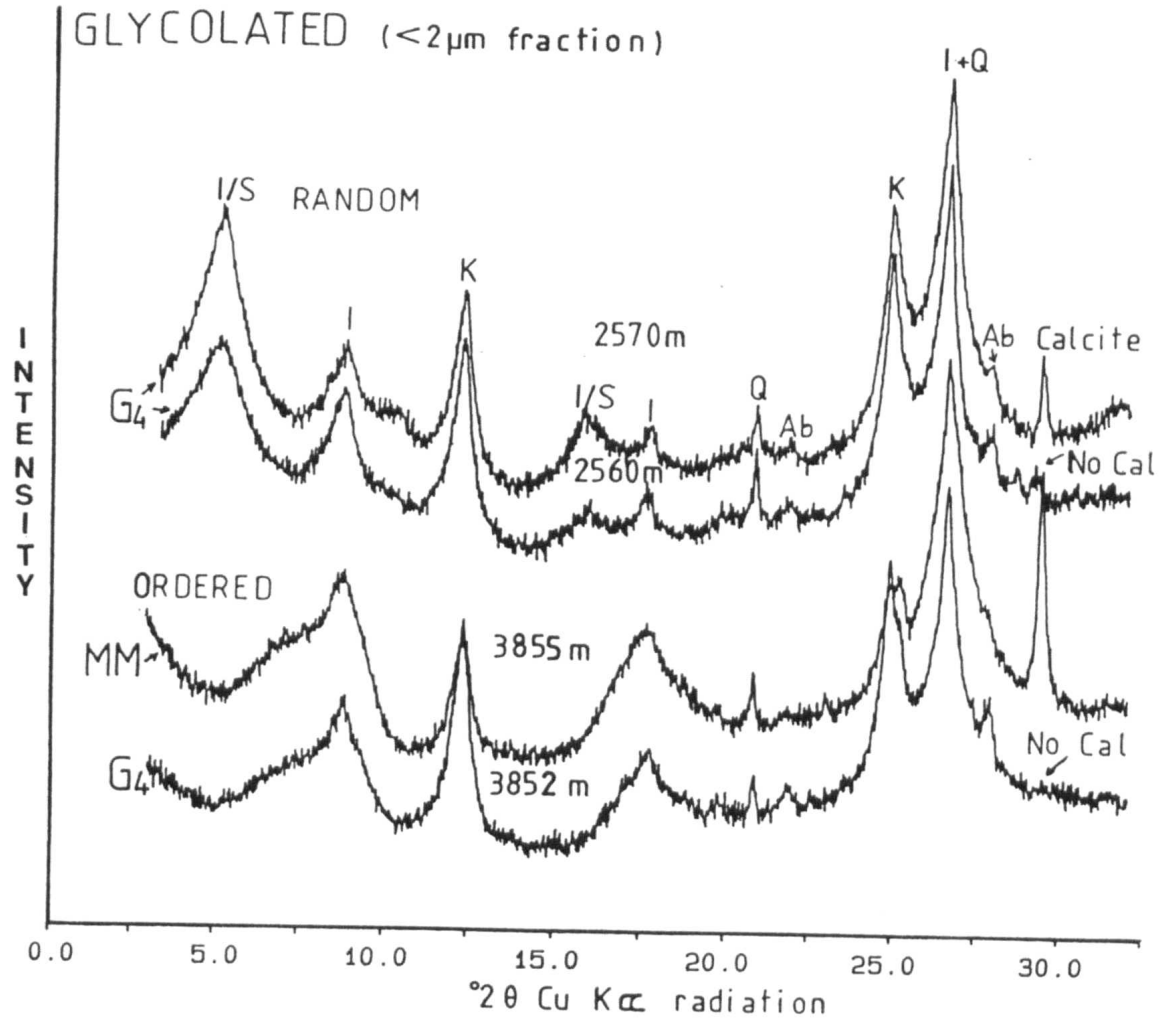


Fig. 8.21 - Glycolated X.R.D. traces of the oriented clay grade fractions (<2 μm) showing the behaviour of the calcite in relation to lithofacies and depth.

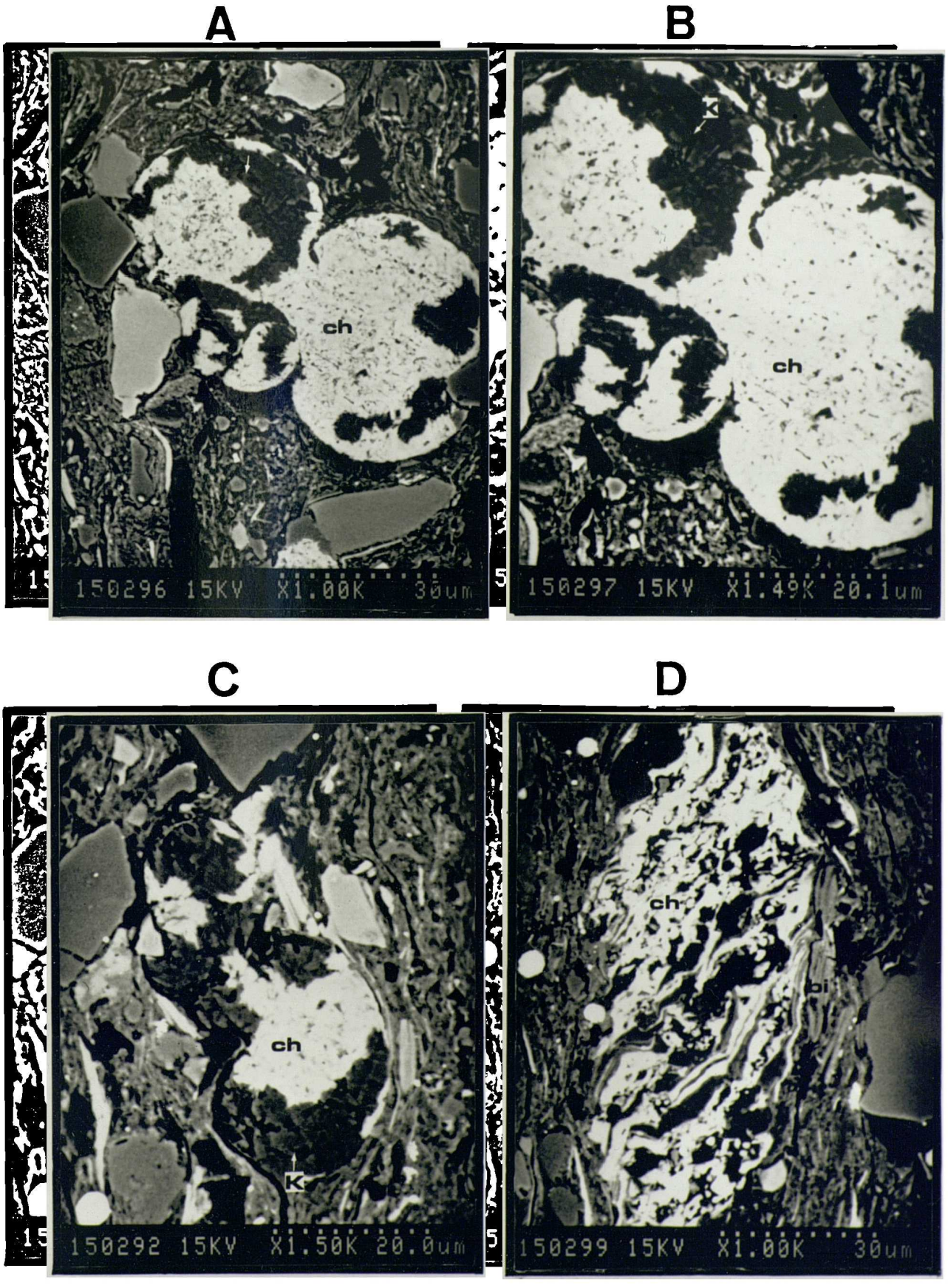
PLATE 8.8

This plate shows examples of the replacement of kaolinite and biotite by chlorite from the same sample, a Mottled Mudstone Lithofacies MM (3852 m and 123°C).

A, **B** and **C** S.E.M. (B.S.I.) photomicrograph show examples of kaolinite (K) cement inside of the chambers of a planktonic foraminifera partially replaced by chlorite (ch). Observe specially in **A** and **B** that the foraminiferal test has been dissolved and completely replaced by chlorite.

D - S.E.M. (B.S.I.) photomicrograph showing biotite (bi) altered to chlorite (ch), brighter, and to kaolinite (K), darker, along the cleavages. The chlorite appears as brighter areas under B.S.I. due to its relatively higher iron content.

PLATE 8.8


A
B
C
D
ch
K
bi
150296 15KV X1.00K 30um
150297 15KV X1.49K 20.1um
150292 15KV X1.50K 20.0um
150299 15KV X1.00K 30um

8.6 DISCUSSION AND CONCLUSIONS

The mudrocks of the Oligocene-Miocene succession of the Campos Basin consist of marlstones, siliciclastic mudstones and mud-rich diamictites. Although there are differences in the relative percentages of clay minerals (**Table 8.1**), the overall composition of mudrocks of the different lithofacies are very similar. The most significant variations are the relatively higher proportions of illite-smectite in the Marlstone (G_2), quartz in the diamictites (**DMT**), and kaolinite in the mottled mudstones/siltstones (**MM**) (see **Fig. 8.13**). The marlstones have higher percentages of illite-smectite than the other mudrocks at similar depths and temperatures (**Fig. 8.9**, and **8.14**).

Anjos (1986) found that kaolinite and discrete illite were the most abundant clay minerals in the samples from the well that she analyzed. This is the opposite to what has been observed in this study, where the most abundant clay mineral is illite-smectite. These discrepancies could be due to different analytical methods or differences in the depositional environment of the two sample sets. The samples analyzed here are from environments further offshore then those analyzed by Anjos (1986).

As discussed by Weaver (1961), and Millot (1964), because of its larger grain size and different flocculation rates, kaolinite may be expected to be deposited closer to the shore line while the smaller particles of smectite and illite-smectite would be transported further from the shore. This discrimination in the relative percentage of the clay minerals could help explain the higher percentage of illite-smectite observed in the marlstones and explain the differences with the data of Anjos (1986).

Additionally, Anjos (1986) attributed the high amount of kaolinite found in an Oligocene sample (2600 m) as reflecting a drop in sea-level and corresponding to the low-sea level in the sea-level chart of Vail et al. (1977). This assumes that the high percentages of kaolinite in deep-water mudstones in general would represent regression. If this assumption was correct, higher values of kaolinite

could be used as an indicator for the periods of low-sea level and be potential tool for predicting the presence of turbidites. However, the only significant difference between the clay mineralogy of the hemipelagic mudstones and the turbiditic-mudstones (top of the Bouma sequence = Tde) of the studied succession is a relatively lower ratio of I/S:I and K:I in the latter (see **Fig. 8.14**). It is important to point out that this kind of differentiation can only be applicable to those samples from shallow depths (2400-2950 m), where the effects of diagenesis are minimal and the clay minerals can be considered to be prodominantly detrital.

The mineralogy of the shallower buried mudrocks (2400-2950 m, 48-95°C) in the studied succession is characterized by the following mean clay mineral composition: 55% smectite-rich (90% SM) random illite-smectite, 25% illite and 20% kaolinite, which are predominantly detrital in origin. In contrast the more deeply buried mudrocks (3850-3860 m, 123°C) contain 50% illite-rich (10% SM) ordered illite-smectite, 30% illite and 20% kaolinite, suggesting that illitization of the illite-smectite has occurred over the narrow temperature range of 95° to 123°C (**Fig. 8.18**).

Based on X.R.D. and S.E.M. analyses of the mudrocks the following paragenetic sequences of the diagenetic phases, techniques, have been identified: a) (2400-2950 m) framboidal pyrite, ferroan dolomite, calcite, local feldspar alteration, kaolinite and smectite infilling foraminiferal chambers; b) (3850-3860 m) partial calcite dissolution, chlorite replacing kaolinite in foraminiferal chambers, quartz/feldspar overgrowths and ordering of interstratified illite-smectites.

The association of the strongly illitized samples with growth faults, such as in well 154, suggests that the faults could be an important potential source for fluids that may have migrated into the shallower sand-rich reservoirs. The release of fluids associated with the illitization of the illite-smectites and possible replacement of kaolinite by chlorite in the downthrown blocks regions of the growth

faults and their subsequent migration into shallower reservoirs located in adjacent blocks, would have probably been an intermittent but relatively continuous process as the faults developed. These fluids may therefore have contributed to diagenetic reactions in these reservoirs (see Chapter 9). The seismic pumping multiflow mechanism (Sibson et al., 1975) describes fluid expulsion associated with faults and could be used here to explain fluid migration from depth into shallower reservoir rocks. Another interesting aspect of this problem is the relative short geologic time that would be involved in this type of situation where illitization of the illite-smectites appears to have occurred over a period of a few million years. Additionally, if hydrocarbon migration is linked with the illitization of the illite-smectites, as many authors suggest, it would be possible to roughly estimate the probable period for hydrocarbon migration by comparing the sedimentation rates associated with faulted blocks and the degree of illitization of the illite-smectites in these sites.

CHAPTER 9

SANDSTONE COMPOSITION AND DIAGENESIS

9.1 INTRODUCTION

In this chapter will be described the sandstone framework compositions, their diagenetic products and the most probable paragenetic sequence for the diagenetic phases and their possible mechanisms of generation.

The provenance of the sandstones has been established by comparing their petrographic characteristics with those described in the literature, the modern sediments of the southern Brazilian coastal areas (Kowsmann & Costa, 1974 and 1980; Savage et al., 1988; and Muehe, 1989), and the Upper Cretaceous-Eocene turbidites of the Campos Basin (Freitas, 1987; and Moraes, 1989). Additionally, their diagenetic products and paragenetic sequences have also been compared with the latter.

9.2 SANDSTONE COMPOSITION

9.2.1 FRAMEWORK COMPOSITION

The determination of the sandstone composition was based on petrological analyses of 70 samples using thin-section, S.E.M. and X.R.D. techniques (see **Chapter 4, section 4.3**, for more details of these methodologies). The averaged composition of the framework of the sandstones can be divided into three main groups, according to their grain sizes: a) gravelly-sandstones Q_{50} F_{15} RF_{35} $(L_{26} + B_9)$; b) very coarse/fine-grained sandstones Q_{73} F_{22} RF_5 $(L_1 + B_4)$; c) fine/very fine-grained sandstones Q_{65} F_{17} RF_{18} $(L_4 + B_{14})$; where Q = quartz, F = feldspar and RF = rock fragments (RF = L + B, where L = lithic, mica and heavy minerals; and B = bioclast; see below for more details).

The composition and textural characteristics of the sandstones are described below in a decreasing order of mineral abundance.

QUARTZ The quartz is usually monocrystalline, although polycrystalline and chert grains are also present in the coarse/very coarse sand-sized fractions. The average percentage of quartz in the sandstone is 73%, but this figure decreases to around 60% when the grain size decreases to very fine-sand or when it increases to pebbly/gravelly-sand. This mainly reflects increases in the bioclastic and lithic contents of these sandstones. The average grain size of the quartz is lower medium (350-250 μm) to upper fine (250-177 μm) sand grade. The grains are usually subangular/subrounded, but locally rounded/well-rounded grains are also found, indicating the different nature and duration of varying depositional processes. The surfaces of the grains frequently show evidence of corrosion, specially when associated with calcite cements (see **Plate 9.1 A**). The quartz grains frequently have microscopic mineral inclusions, some of the largest consisting of biotite, apatite and rutile.

FELDSPAR The majority of the sandstones have an average feldspar content of around 22% (7- 39%). It varies, in a similar way to the quartz contents, as a function of the bioclastic and lithic contents in the coarsest and the finest sandstones. However, when the percentage of feldspar is measured only relative to the quartz content their relative proportions are almost constant (23-21% of feldspar). The most abundant type of feldspar is microcline, whilst orthoclase and plagioclase usually comprise about 10% of the total feldspar. The K-feldspar and plagioclase exhibits different degrees of alteration, partly inherited from the source area and partly as a result of diagenetic alterations. This distinction between inherited altered feldspars and those altered during diagenesis is possible to observe when the feldspar in tightly cemented calcareous zones (early poikilotopic calcite) are compared

with those of the adjacent non-calcareous porous sandstones. When granitic rock fragments are analyzed plagioclase usually seems to be more altered than microcline. Quartz and microcline in some of these rock fragments have poikiloblastic textures what can be related to their metamorphic origin and consequently some of the observed alterations in the plagioclase, associated with usually fresh microcline, could in part be the result of previous metamorphism rather than due entirely to weathering (see **Plate 9.1**).

ROCK FRAGMENTS As these sandstones contain variable amounts of bioclasts they have been included in the rock fragments component for classification purposes (see **section 9.3**). The rock fragments component was divided into two main groups: 1) **lithic** = igneous/metamorphic and sedimentary rock fragments, mica (biotite and muscovite), heavy minerals (excluding mica), and glauconite; and 2) **bioclast** = of shallow- and deep-water origin; see their descriptions below.

1) Lithic (including mica and heavy minerals)

a) The igneous/metamorphic rock fragments consist of granitic/gneissic fragments, meta-siltstones and very rare basic volcanic rocks. All these rock fragments are relatively rare and only found in the very coarse/gravelly-grained sandstones (see **Plate 9.1 D**).

b) The sedimentary rock fragments are very abundant in the gravelly-sandstones, making up more than 50% of the framework grains. They consist mainly of fragments of mudstones, siltstones, carbonaceous siltstones normally replaced by siderite/ankerite, marlstones, dolomitic marlstones, wackestones and packstones[1], and tight calcite cemented fine/medium-sandstones with abundant glauconitic pellets and bioclasts (mainly of shallow-water species like echinoids, bivalves, macro-foraminifera, ostracods, and bryozoa), see **Plate 9.2 A-C**.

[1]According to the classification of Dunham, (1962).

PLATE 9.1

A) Quartz (QZ) grains with inclusions and evidence of corrosion by calcite cement (C). Associated tests of planktonic (P) and benthonic (B) foraminifera are also present. Sample depth 2661 m. XP. Scale bar 75 μm.

B) K-feldspars (K) and plagioclase (P) with different degrees of alteration in the tight calcite cemented zones. Sample depth 2579 m. XP. Scale bar 300 μm.

C) The different degrees of alteration in the tight calcite (C) cemented and porous zones. Observe that in the porous zone there are relicts of a feldspar (F) grain that has been almost totally leached. The blue colour is the result of resin impregnation and represents porosity. Sample depth 2600 m. PPL. Scale bar 300 μm.

D) K-feldspar (K) and plagioclase (P) with different degrees of alteration in a granitic rock fragment. Sample depth 2582 m. XP. Scale bar 300 μm.

PLATE 9.1

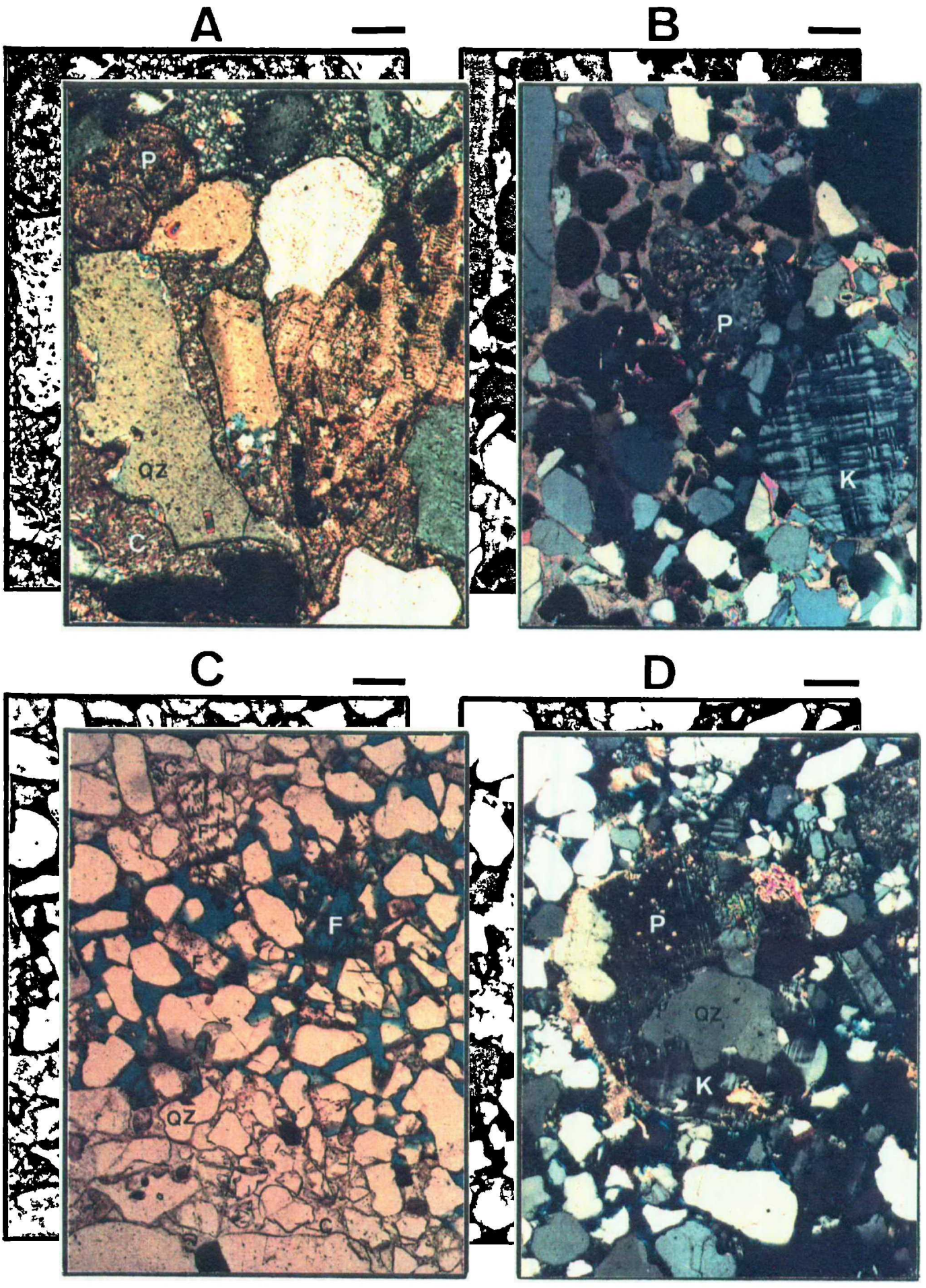


PLATE 9.2

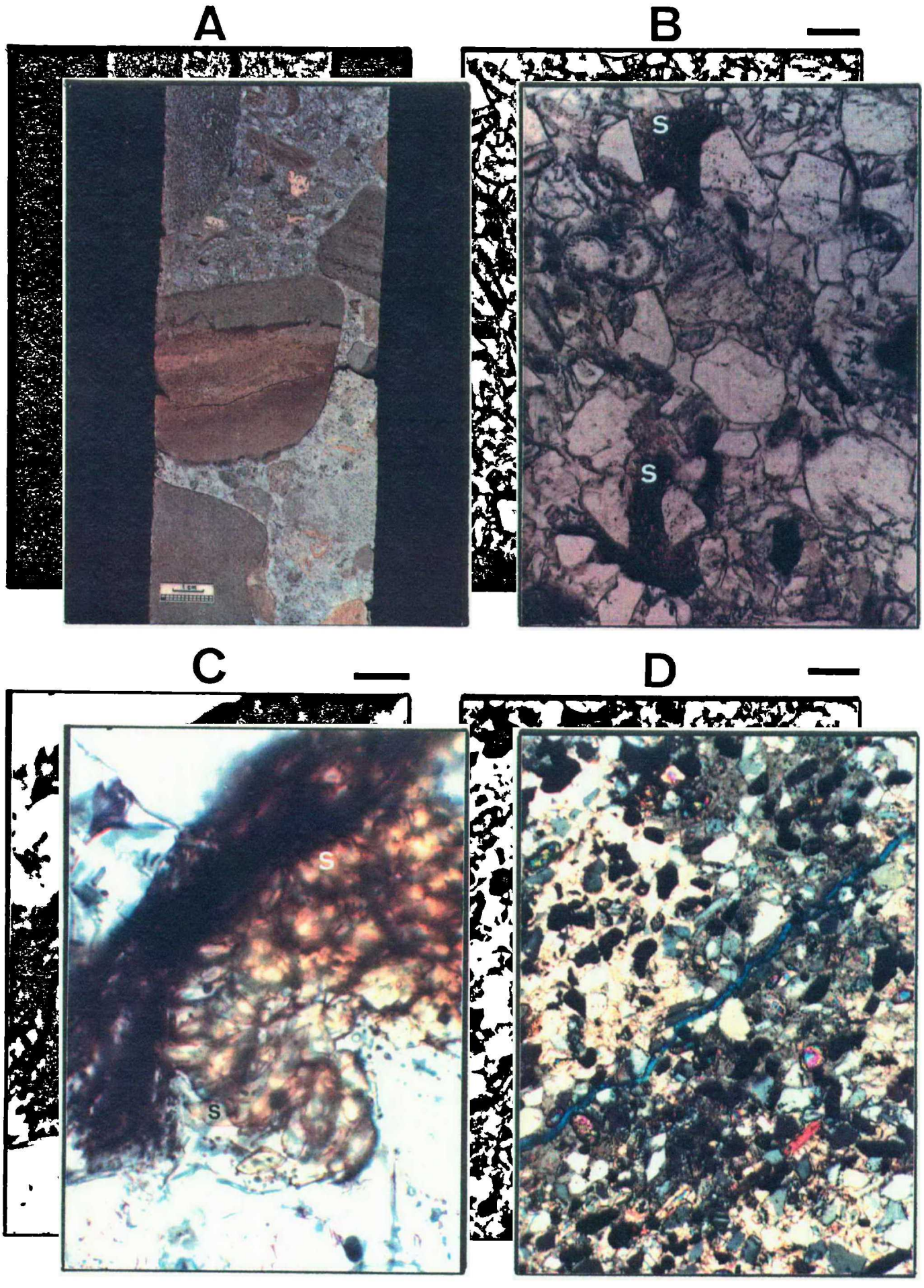
A) A core sample showing the composition of some lithic fragments in the Gravelly-Sandstone Lithofacies. Scale bar 1 cm.

B) The characteristics of the carbonaceous siltstone fragments with siderite (S). Observe the dark brownish colours and the compaction features associated with these detrital grains. Sample depth 2639 m. PPL. Scale bar 120 μm.

C) A close view of the siderite (S) crystals being partially enclosed by the calcite cement. Sample depth 2639 m. PPL. Scale bar 20 μm.

D) The heavy minerals in the fine-grained sandstone, mainly represented by opaques (black grains) and zircon (colourful). Sample depth 2583 m. XP. Scale bar 120 μm.

PLATE 9.2



The carbonaceous siltstones fragments, extensively replaced by siderite/ankerite, occur in sandstones of all grain-sizes but usually are of similar size to the average grain-size of the individual sandstones. These fragments consist of microscopic aggregates of brown rhombs of ankerite/siderite that have grown in a muddy carbonaceous matrix.

Usually the softer sedimentary rock fragments are platy and angular, while the harder ones tend to be more spherical and well-rounded (**Plate 9.2**).

c) The biotite and muscovite percentages are higher in the fine/very fine-grained sandstones, although they also occur associated with other grain sizes. In the fine-grained sandstones mica occurs together with the silt-sized grains in the leeside of the ripples and in the mud drapes between the sandy laminae.

d) The heavy mineral assemblage consists of rutile, ilmenite, zircon, epidote, tourmaline, garnet, and apatite. They occur in all sandstone lithofacies, but usually only as traces. However, anomalous amounts of heavy minerals, locally more than 5%, were observed in some fine/very fine-sandstones. These sandstones are in general thin-bedded (<15 cm) and interbedded with mudstones/marlstones (see **Plate 9.2 D** and **section 9.6.1** for discussion about their possible origin).

2) **Bioclast:**

The term "bioclast" is being used generally to include both fragmental and whole sand-sized calcareous organisms. The bioclasts present in the analyzed sandstones can be divided into shallow- and deep-water types. The "shallow-water" bioclasts for the purpose of this work are of those organisms most commonly derived from inner/middle neritic (<100 m of water depth) environments, and "deep-water" ones those derived from the middle neritic/bathyal (>100 m of water depth) environments.

a) The most common shallow-water bioclasts found were bivalves, echinoids, red algae (encrusting and branching), bryozoa, milliolids, macro-foraminifera, and some other benthonic and planktonic foraminifera (see **Plate 9.3 A-C**).

b) The deep-water assemblage is characterized by small benthonic and planktonic foraminifera, and the lack of massive bioclasts like red algae (see **Plate 9.3 D**).

The limits of these groups are not rigid, but they appear to be adequate for the practical purpose of differentiating the bioclasts in the sandstones. As can be seen in the **Table 9.1** and in the **Figure 9.1**, there is a preference for the shallower assemblages to be concentrated in the coarser-grained sandstones, and the deep-water bioclasts in the finer-grained sandstones.

9.2.2 SANDSTONES MATRIX

The majority of the rocks of the sandy lithofacies has less than 5% of matrix. The only two lithofacies that have more than 15% of matrix were the diamictites (lithic graywacke, according to Pettijohn et al., 1973) and some gravelly-sandstones. The matrix of the latter consists mainly of rip-up-mudclasts that were deformed during the compaction (see **Plate 9.4**). The fine-grained material found in the sandstones can be divided into two groups: a) detrital in origin or the result of compaction, including pseudomatrix; b) diagenetic in origin by alteration of grains into clay minerals or by direct precipitation of clay minerals in the sandstones pores. The first group (detrital) is mainly found in the very fine-grained sandstones (true matrix) and in the gravelly/pebbly-sandstones where it can be true matrix or pseudomatrix (compaction of mudclasts, see **Plate 9.4 and section 9.5.1**). The second group (diagenetic) is found more frequently in the fine/coarse-grained sandstones. They have very little detrital matrix and the majority of the clay grade fractions, when present, is represented by diagenetic kaolinite mainly due to feldspar alteration (see **Plate 9.5 A and section 9.5.9**).

TABLE 9.1

LITHOFACIES	AVERAGE COMPOSITION							
	QTZ	FELD = K-F + Plag			RF = SWB + DWB + L			
GvS *	50	15	13	2	35	7	2	26
**	33-68	7-19	7-19	0-6	15-60	1-15	0-5	3-58
VcS/Amg	73	22	20	2	5	5	<1	<1
	60-84	14-32	11-31	0-9	0-16	0-16	0-1	0-2
FTab	71	23	20	3	6	1	4	1
	59-81	12-39	10-36	0-6	0-17	0-4	0-11	0-3
FTb	74	21	19	2	5	0	4	1
	66-84	13-27	13-22	0-5	1-9	0	1-9	1-5
Fla/Wav	66	19	17	2	15	0	12	3
	50-75	13-24	10-22	0-3	6-32	0	5-25	1-7
Rip	64	14	14	<1	22	0	17	5
	61-67	9-19	9-18	0-1	14-27	0	8-24	3-7

* average value; ** values' variation. QTZ=quartz; FELD=feldspar; K-F=potash feldspar, Plag=plagioclase; RF= "rock fragment"; RF = [SWB=shallow-water bioclast; DWB = deep-water bioclast; L = lithic (rock fragments, shale clast, mica, heavy minerals, organic matter)]. Where, shallow water = inner/middle neritic (<100 m); and deep water = middle neritic/bathyal (>100 m).

Where, **GvS** = gravelly sandstone; **VcS/Amg** = very coarse/amalgamated sandstone; **FTab** = fine/medium sandstone with Tab, **FTb** = fine sandstone with Tb, **Fla/Wav** = very fine/fine sandstone with either flaser or wavy bedding; **Rip** = very fine/fine sandstone with ripple-cross-lamination (for more details see **Chapter 5**).

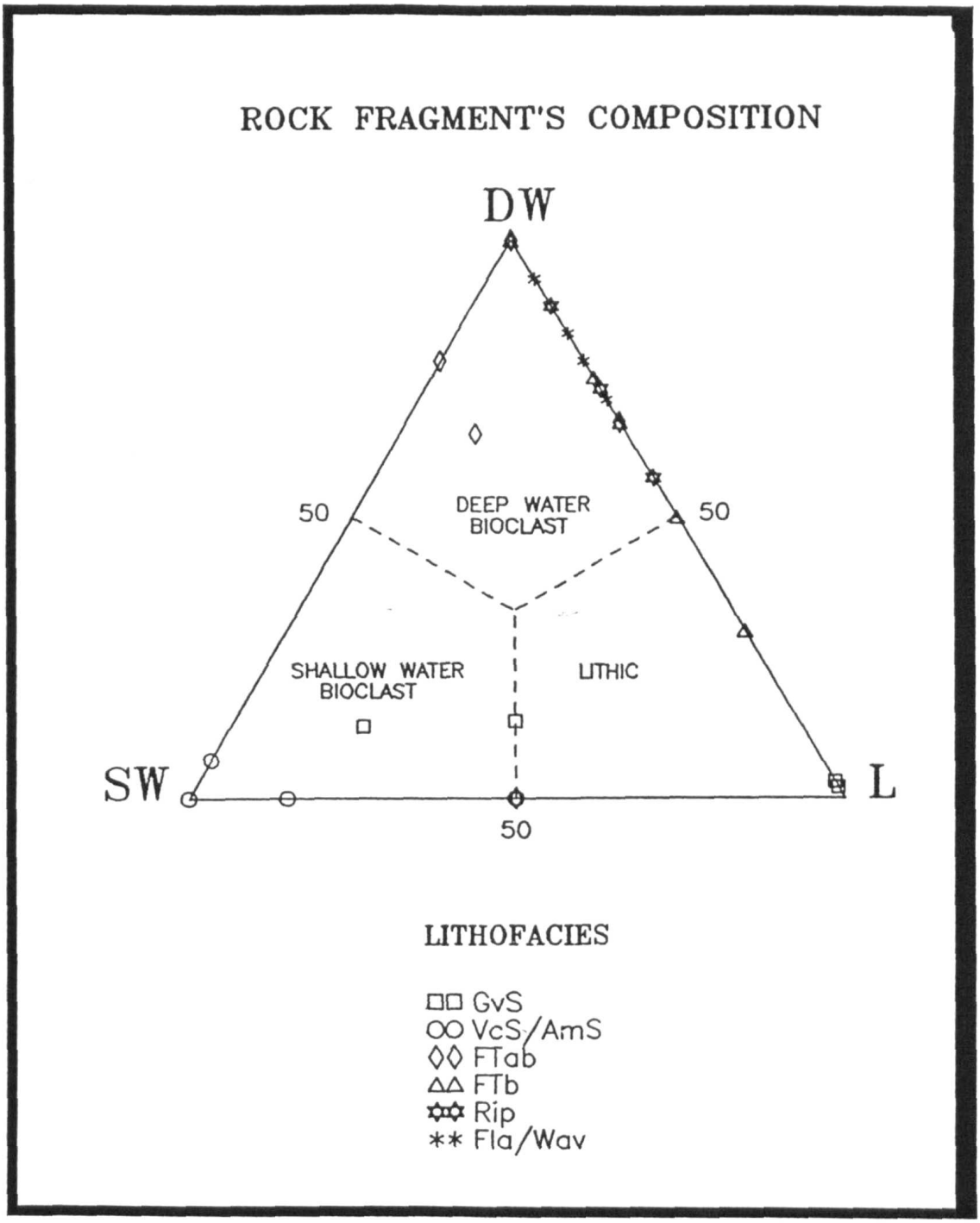


Figure 9.1 - Relative composition of the Rock Fragment components in the sandstone lithofacies.

PLATE 9.3

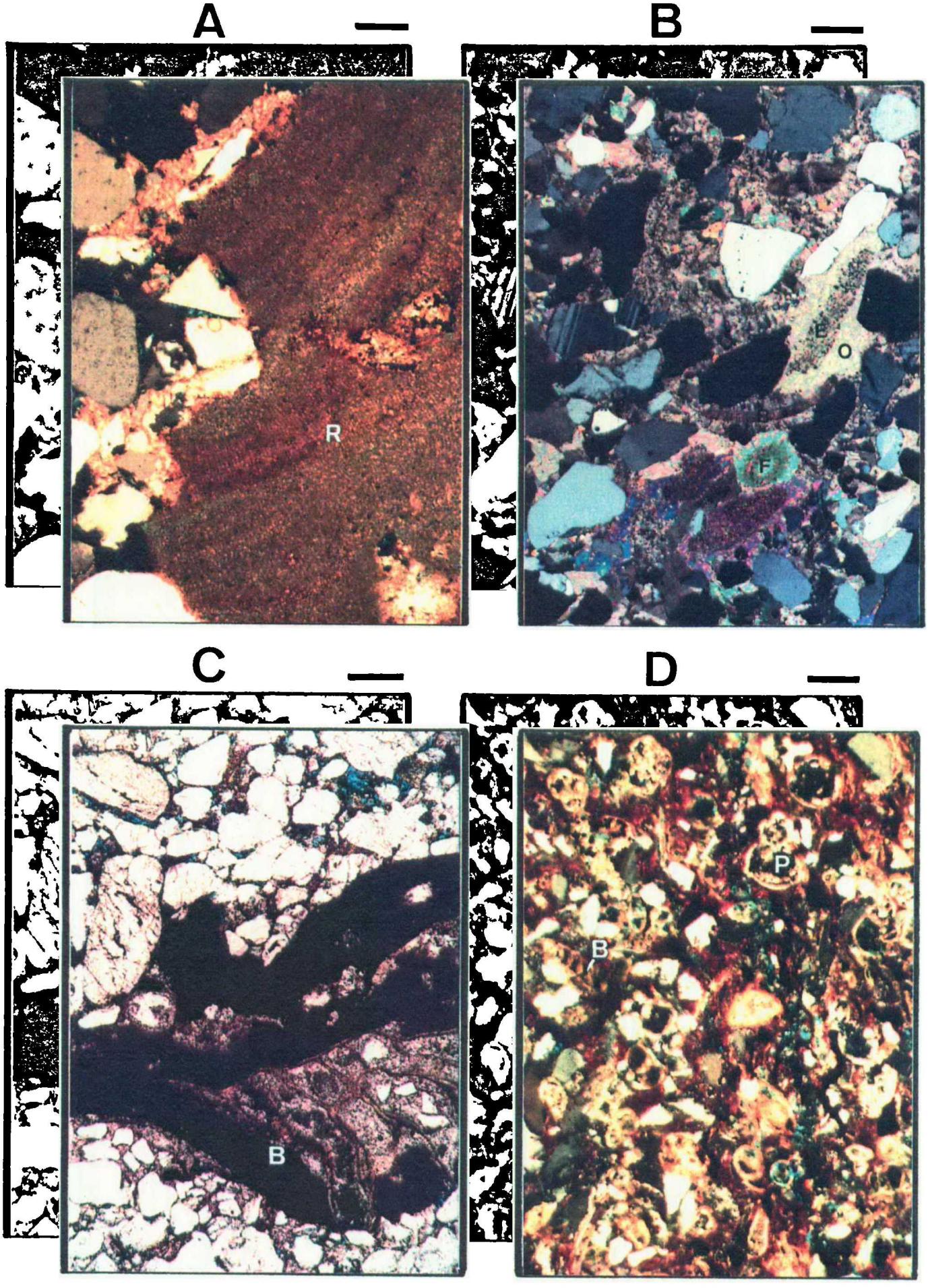
A) A shallow-water bioclast represented by red algae (R). Sample depth 2579 m. XP. Scale bar 300 μm.

B) A shallow-water bioclast represented by echinoid (E) and bivalve (B). Observe the syntaxial calcite overgrowth (O) on the echinoids. Sample depth 2551 m. XP. Scale bar 300 μm.

C) A shallow-water bioclast represented by a bryozoa (B). Sample depth 2579 m. PPL. Scale bar 300 μm.

D) The deep-water bioclast assemblage represented by tests of planktonic (P) and small benthonic (B) foraminifera. Sample depth 2447 m. XP. Scale bar 120 μm.

PLATE 9.3



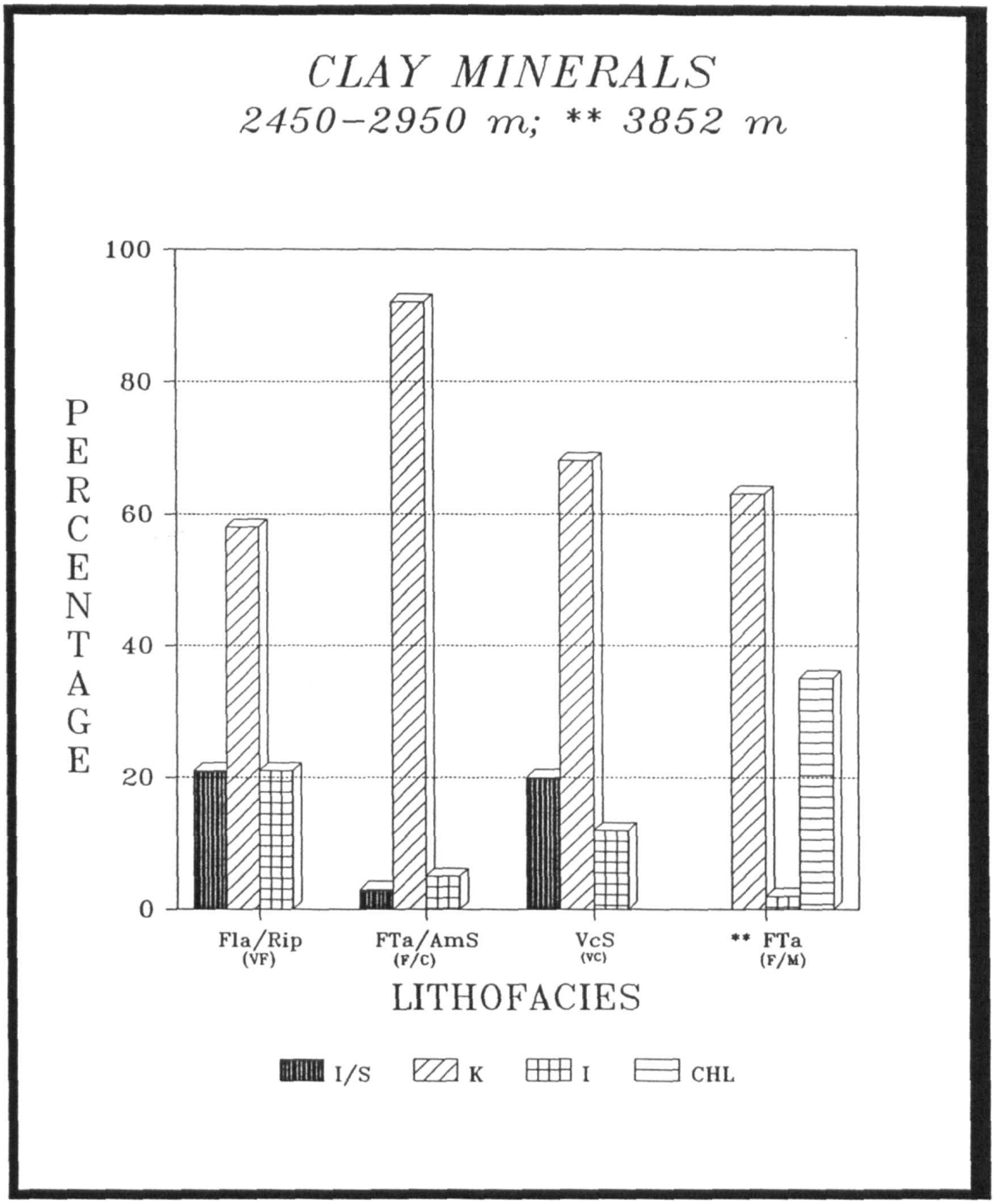


Figure 9.2 - Relative percentages of clay minerals in the clay grade fractions of the rocks of the sandy lithofacies. (VF) = very fine sand-size; (F/C) = fine/coarse; (VC) = very coarse; and (F/M) = fine/medium sand.

X.R.D. analyses of the clay grade fractions show that kaolinite is the most abundant clay mineral in all rocks of the sandy lithofacies (**Fig. 9.2**). The second-most abundant clay mineral in the sandstones, from 2400-2950 m depth interval, is the smectite-rich (90% SM) mixed-layer illite-smectite, and the least abundant is the illite. The reason for the relatively higher amounts of kaolinite in the fine/coarse-sandstones is the relative lack of detrital matrix. The composition of the detrital matrix is dominated by illite-smectite, and it reflects the composition of the adjacent mudrocks (see **Chapter 8, sections 8.3.2.1** and **8.3.2.2**). In the sandstone sample from 3852 m mainly kaolinite and chlorite are found, and both are diagenetic in origin (see the **section 9.5.11**).

9.3 SANDSTONE CLASSIFICATION

The adopted classification was that of Pettijohn et al. (1973) after Dott (1964), see **Fig. 9.3**. As stated earlier it was necessary to modify the definition of the rock fragment (RF) component of the Pettijohn et al. (1973) classification to include both lithic fragments (inclusive mica and heavy minerals) and bioclasts (RF = L + B) (**Fig. 9.4**). The sandstones that have more than 10% of bioclast in the total framework composition have been described as "bioclastic". The names of the Pettijohn et al. (1973) classification have therefore been altered to: bioclastic arkosic arenite (or bioclastic arkose), bioclastic subarkose, bioclastic quartz arenite, bioclastic sublitharenite, and bioclastic lithic arenite, when applicable (see **Fig. 9.5**). The composition of the sandstones in relation to their lithofacies is shown in **Fig. 9.4**. The majority of the lithofacies plots near to the boundary between subarkose and arkose. The gravelly-sandstone and the very fine-sandstone lithofacies have higher proportions of lithic + bioclastic components (RF) in relation to the other lithofacies and consequently they plotted in the sublitharenites and lithic arenites fields (see **Table 9.1**).

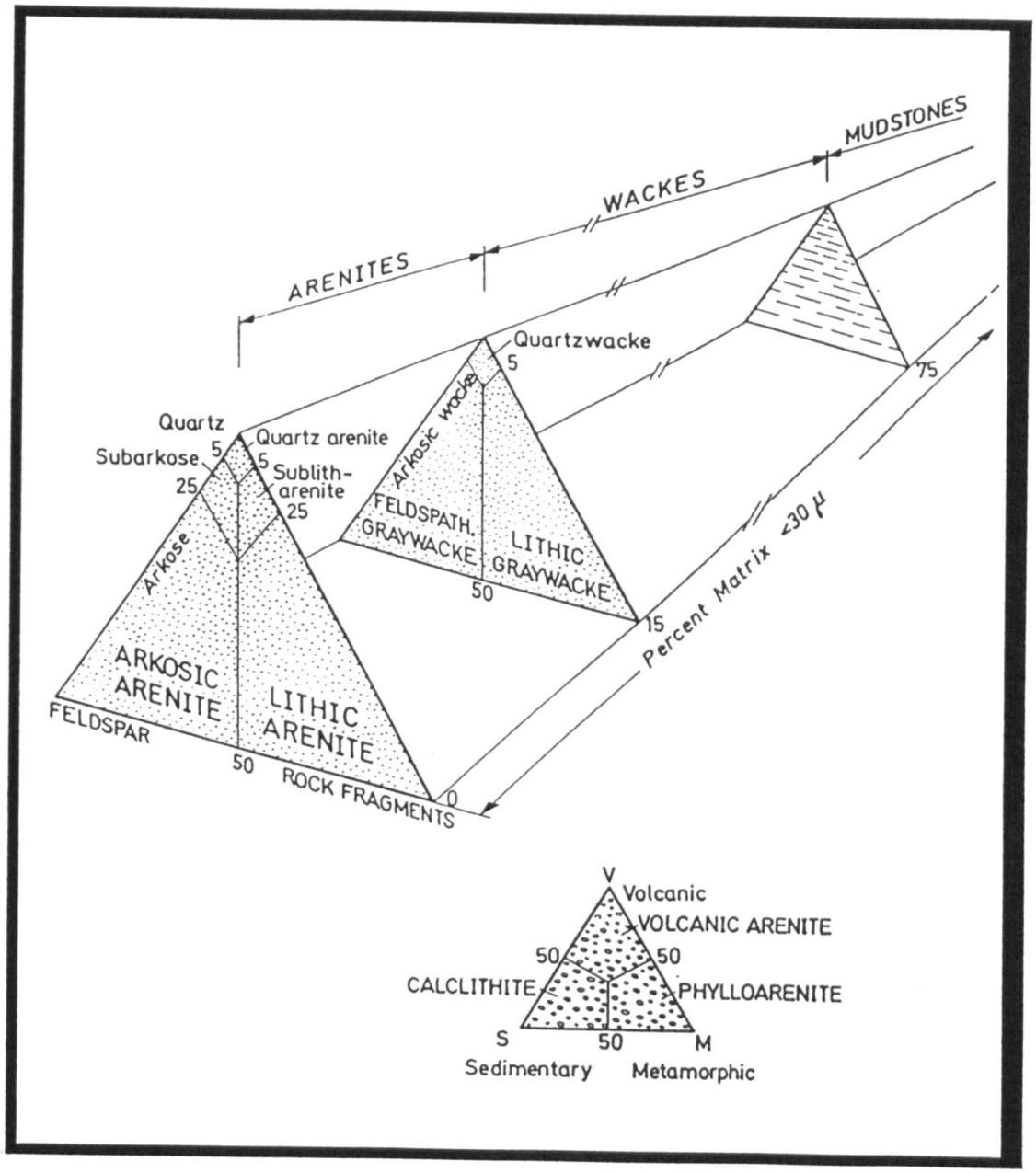


Figure 9.3 - Classification of terrigenous sandstone from Pettijohn et al. (1973, modified from Dott, 1964).

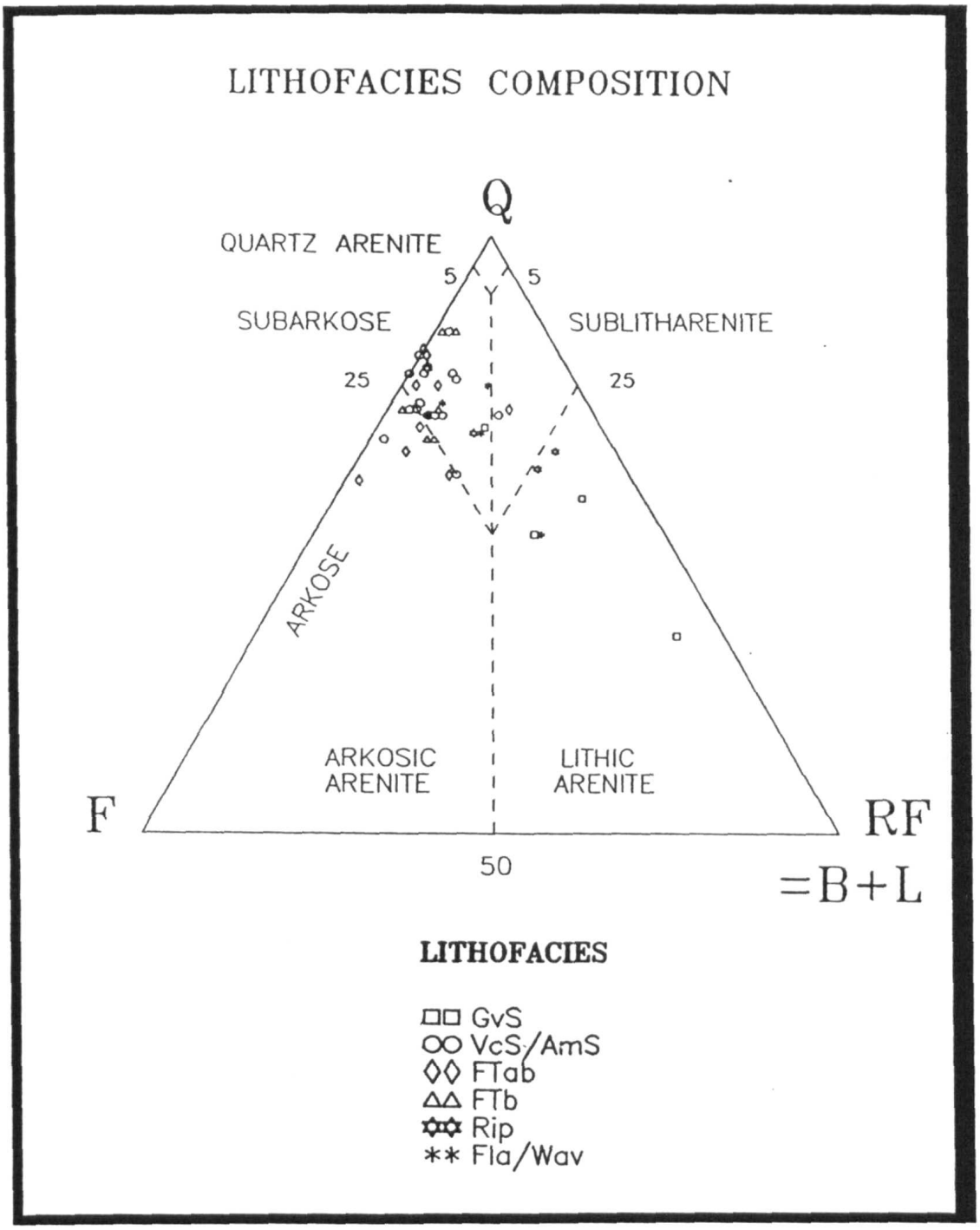


Figure 9.4 - Composition of the various sandstones lithofacies plotted on a modified classification triangle from Pettijohn et al. (1973), where the RF = bioclast + lithic.

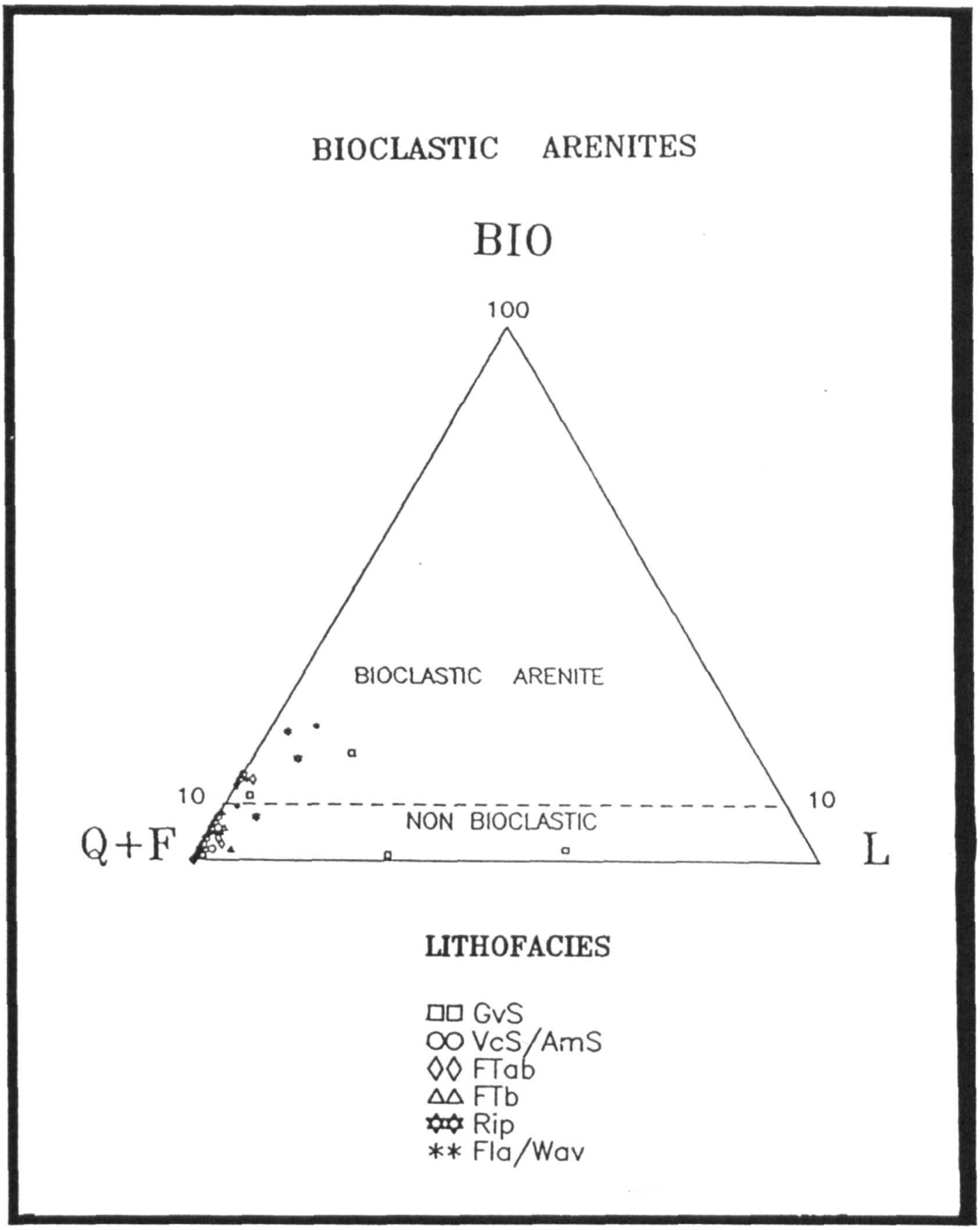


Figure 9.5 - Classification of the sandstone lithofacies in relation to their bioclastic content.

The lithofacies represented by the diamictites can be classified mainly as lithic-graywackes.

Sandstones of the Gravelly-Sandstone Lithofacies **Gvs** contain sedimentary rock fragments (siltstone, mudstones, marlstones and packstones), some fragments of granitic composition, and bioclasts (the latter mainly derived from shallow-water environments = inner/middle neritic. The Fine/Very fine-Sandstone Lithofacies (**Fla/Wav/Rip**), at the other end of the grain-size distribution, also have relatively high percentages of bioclasts in the RF component. However, the bioclasts consist mainly of benthonic and planktonic foraminifera derived from deeper water environments (middle neritic/bathyal), or incorporated into these sandstones after deposition by bioturbation. The composition of the RF component, in these very fine/fine-grained sandstones, consists mainly of mica, heavy minerals, small shale fragments, and some organic matter.

9.4 PROVENANCE OF THE SANDSTONES

The composition of the Oligocene-Miocene turbidites of the Campos Basin in the studied area reflects their provenance area plus modifications arising during transport, deposition and resedimentation.

Adjacent to the modern Campos Basin are the Serra do Mar mountains, up to 2,000 m high which consist mainly of granitic-gneissic rocks composed dominantly of quartz, feldspar (especially microperthitic microcline) and biotite (see **Chapter 2**). Today, the general climate of the region is tropical with an average temperature range of 20°C to 25°C and an average annual rainfall of 1.5 meters (Savage et al., 1988). The major river in the area is the Paraíba do Sul over 950 Km in lengths and a drainage area of 57,000 Km^2 (Ribeiro Filho, 1948). The area has two distinct contrasting topographies the steep mountains and the flat coastal plain, made up of Cenozoic sediments. During the Cenozoic the climate oscillated between humid and semi-arid conditions with periods of erosional/depositional followed by stable

phases (Meis & Amador, 1977; Muehe, 1983 and 1989). The data available from the onshore part of the modern Campos Basin describe a coastal region dominated by fan deltas and wave dominated deltas with associated lagoonal and beach environments (Bacoccoli, 1971; Mohriak, 1984; Dominguez et al., 1987, and see **Chapter 3**).

Sedimentological studies of the modern coastal and continental shelf areas of the Rio de Janeiro state can provide suitable comparisons regarding provenance and sedimentary processes at the time of deposition of the analyzed turbiditic sandstones.

Savage et al. (1988) studied the sediments of a Holocene regressive beach sequence in an embayment to the southwest of Rio de Janeiro (Baixada de Jacarepagua), surrounded by Precambrian granites of the Serra do Mar mountains. They defined four main depositional environments: a) fluvial, represented by angular arkosic arenites (Pettijohn et al., 1973) Q_{63} F_{27} RF_{10} (RF = rich in clay coated grains); b) ancestral Holocene beaches, represented by subarkoses Q_{69} F_{17} RF_{14} ; c) beach ridges, represented by quartz arenites Q_{100} F_0 RF_0 ; d) modern beaches, represented by quartz arenites Q_{97} F_3 RF_0 (see **Fig. 9.6 A**). The average compositions of the Holocene sediments of the Baixada de Jacarepagua and data from the present study are presented respectively in the **Fig. 9.6A** and **9.6B**. When comparing the two data sets it is important to note that Savage et al. (1988) did not include bioclasts, mica and heavy minerals in the rock fragment (**RF**) component whereas these are included in the **RF** component for this study. The average compositions of the sandstones from the present work are approximately intermediate between the ancestral beach and fluvial sands of Savage et al. (1988).

Savage et al. (1988) interpreted the presence of relatively unaltered plutonic rock fragments, large amounts of feldspar, mica, clay aggregates and coats in the alluvial fans and fluvial sediments as an indication of moderate tropical weathering conditions during the Holocene.

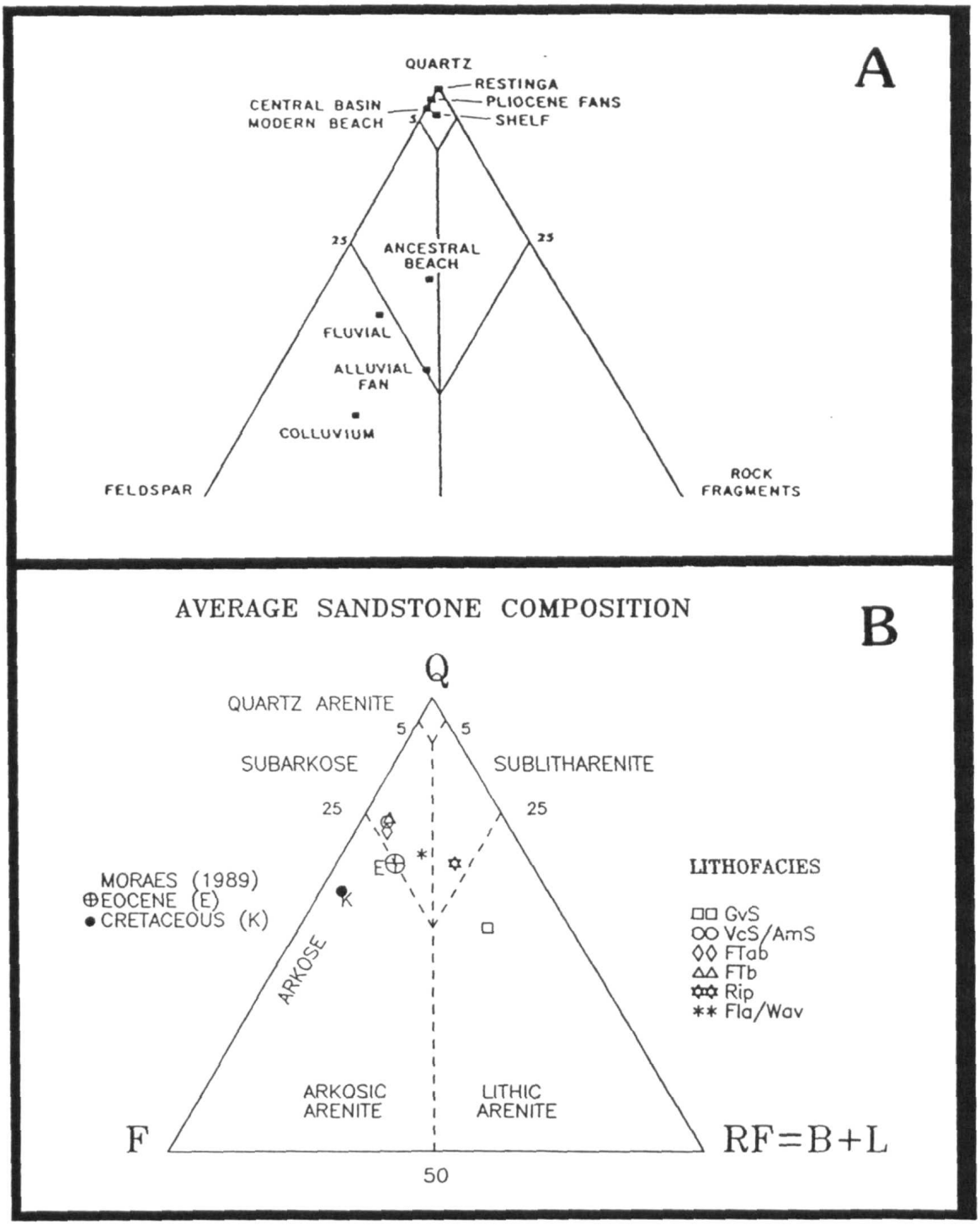


Figure 9.6 - Average sandstone compositions: A) of the modern coastal sediments from the southeast of Brazil (Savage et al., 1988); B) of the Oligocene-Miocene (present study) and of the Eocene and Upper Cretaceous turbidites (Moraes, 1989) of the Campos Basin.

According to Krynine (1935) the amount of detrital feldspar in sandstones reflects the balance between the rate of decomposition and the rate of erosion. The provenance area for the modern Campos Basin is characterized by a high relief, rapid erosion and a tropical climate. Consequently both fresh and partially weathered feldspars would be expected to be incorporated into the sediments, as confirmed by Savage et al. (1988). However, in cases where weathering has acted for longer periods of time feldspar-poor, quartz-rich sediments would be produced, as found in the Pleistocene alluvial fans, southeast of Rio de Janeiro. This provides striking evidence of the importance of tropical weathering on the composition of the sands (Savage et al., 1988; see **Fig. 9.6 A**). This indicates that feldspar alteration, under tropical weathering, is also time dependent, confirming the observations of Krynine (1935). Consequently, feldspar-rich sediments subjected to longer weathering periods would undergo substantial relative enrichment in quartz.

Similar processes would be expected to have occurred in alluvial fans sediments subjected to subaerial exposure for long periods; for example, during major highstands of sea level, when coastal onlaps[2] would be generated. Although during low-stands of sea level greater areas would be subaerially exposed, the time span involved is usually relatively short (Haq et al., 1987) and erosion would prevail. Consequently the most effective period for feldspar alteration would be during the highstands of sea level. In the succeeding lowstands those sediments from the alluvial fans and coastal plain would then be eroded and resedimented into offshore and deep-water areas of the basin. As a result, the composition of the offshore sediments would be enriched in quartz compared to the composition of the modern alluvial and fluvial sediments. The latter were deposited over a relatively short period, the Holocene highstand, and

[2]Vail et al. (1977), and Posamentier et al. (1988).

were not exposed long enough to weathering (see **Fig. 9.6**). However, other parameters such as grain size and recycling must also be taken into account when comparisons are made. The coarse-grained sands found in the modern Brazilian continental margin are part of relict palaeoshorelines that are presently at water depths deeper than 50 m (Kowsmann & Costa, 1974; and Kowsmann, 1980), while the medium-grained sands at water depths shallower than 30 m represent the reworking of the sand fraction of the hinterland regolith (Muehe, 1989).

In **Fig. 9.6 B** are also plotted the compositions of the upper Cretaceous and Eocene turbidites from the Campos Basin determined by Freitas (1987) and Moraes (1989). The Cretaceous turbidites consist of conglomeratic to very coarse/medium sand-sized arkosic arenites while the Eocene turbidites are medium/very coarse sand-size arkose/subarkose arenites, with relatively high percentages of bioclasts (9%) compared to the bioclast-poor (1%) Cretaceous turbidites.

The rocks of the present study have variable amounts of marine derived grains such as bioclasts and glauconitic pellets (**Fig. 9.5** and **9.6B**) reflecting a winnowing of the alluvial and fluvial derived sediments on coastal and shelf regions accompanied by increasing concentrations of these marine derived grains in the sediments.

The composition (coarser grained, more arkosic and less bioclastic) of the Cretaceous turbidites in the Campos Basin may be the result of a narrower shelf during their deposition. This is in contrast with the younger Eocene and Oligocene-Miocene turbidites, which occur progressively more offshore and have finer grain sizes reflecting a wider depositional shelf, in which carbonate grains were more abundant and the siliciclastic grains subjected to a more intense reworking.

Based on the data presented above and previously it is possible to conclude that the studied turbidites were the result of a mixture of relatively well sorted sediments formed by wave and current action in coastal and shelf

environments where large amounts of benthonic and planktonic foraminifera would have been added to the siliciclastic sediments. The resedimentation of these sediments into deep-water settings of the Basin probably occurred during storm periods, at low sea-level stands, when the combined effect of longshore currents and fluvial out-flows would have driven the sediments into the heads of canyons inducing gravity flows to form the turbidites. The Oligocene canyons on the shelf edge of the Campos Basin (Gamboa et al., 1986) have acted as efficient sediment traps during the lowstands of sea-level as demonstrated by the large volumes of sandy-turbidites found at their terminations (see **Chapter 6, Fig. 6.13**). The concentration of deep-water microfauna in the very fine sand/coarse silt-sized fractions of the turbidites reflects their small grain size and low densities, allowing the microfossils to behave hydrodynamically as grains effectively smaller than their actual size. Conversely, the massive shallow-water bioclasts, such as red algae, bivalves, echinoids and bryozoa, tend to be concentrated in the coarse/very coarse sand fractions of the turbidites.

9.5 SANDSTONE DIAGENESIS

The analyzed sandstones were sampled mainly from depths between 2450-2750 m and burial temperature range of 48-87°C (Oligocene-Lower Miocene in age), with only one sample coming from 3852 m and a temperature of 123°C (Lower Miocene in age). In spite of the relatively shallow depths of burial and their relatively low temperatures the majority of these sandstones have undergone significant diagenesis. The most common diagenetic events are early poikilotopic calcite cementation, calcite dissolution and the generation of kaolinite. However, other diagenetic phases have also been identified and will be described below.

9.5.1 PSEUDOMATRIX OR COMPACTION MATRIX

The term pseudomatrix (Dickinson, 1970) or compaction matrix (McBride, 1985; Moraes, 1989) is here used to describe the fine-grained material found infilling the interstitial pore space of the sandstones as a result of the mechanical deformation of ductile grains such as mudclasts. In the analyzed samples this kind of matrix is usually via the deformation of rip-up mudclasts. They are most commonly found associated with the coarser sandstones, but also can occur in fine/medium-grained sandstones and is particularly common in basal sequences of these sandstones. The nature of this pseudomatrix is shown in the core **photo A** and the **photomicrograph B** in the **Plate 9.4**. The mineralogical composition of these mudclasts is similar to those of the interbedded mudstones (see **Chapter 8**), with a clay mineral assemblage of randomly interstratified smectite-rich (± 90% of smectite) illite-smectites, kaolinites and illites, with variable amounts of silt-sized quartz and feldspar.

In well 310, the matrix has different characteristics. It is difficult to establish whether it is a true or pseudomatrix. However, the presence of mudclasts in the core is an indication that at least part of the matrix has been generated by compaction. Another complicating factor is the presence of calcite cement replacing this matrix (see **Plate 9.5 B and C**). The S.E.M. analysis of this material indicates that it consists of a mixture of illite-smectite, microquartz and some chlorite, the latter occurring generally as groups of small rosettes. This matrix appears to be the result of a diagenetic alteration with a later enclosing calcite cement (see **Plate 9.6 S.E.M. photomicrographs A** and **B**). The X.R.D. analysis of this fine-grained material revealed that it consists of smectite-rich (88% of smectite) mixed-layer illite-smectite, chlorite and kaolinite. The S.E.I. observations indicate that at least part of this kaolinite, if not all, is the result of feldspar alteration (see **section 9.5.3**), while the chlorite seems to be an alteration product of the matrix.

PLATE 9.4

A) A gravelly-sandstone with rip-up-mudclasts, which after compaction have produced pseudomatrix or compactional matrix. Core photo. Scale bar 1 cm.

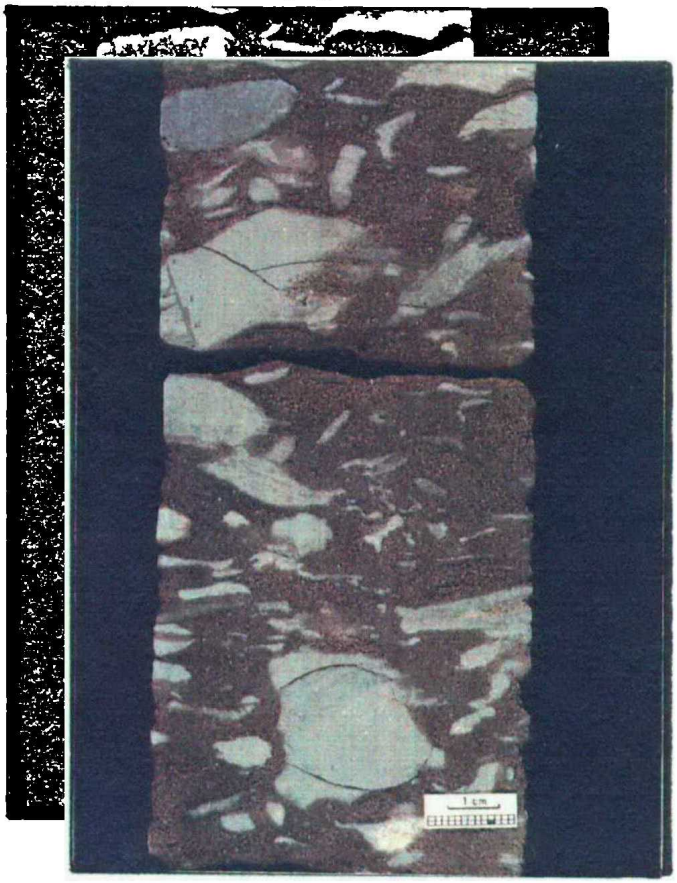
B) The previous sample under the optical microscope. Observe the behaviour of the mudclasts (M) under compaction. The blue colour represent porosity. Sample depth 2481 m. PPL. Scale bar 660 μm.

C) The composition of the Diamictite Lithofacies (lithic graywacke). Core photo. Scale bar 1 cm.

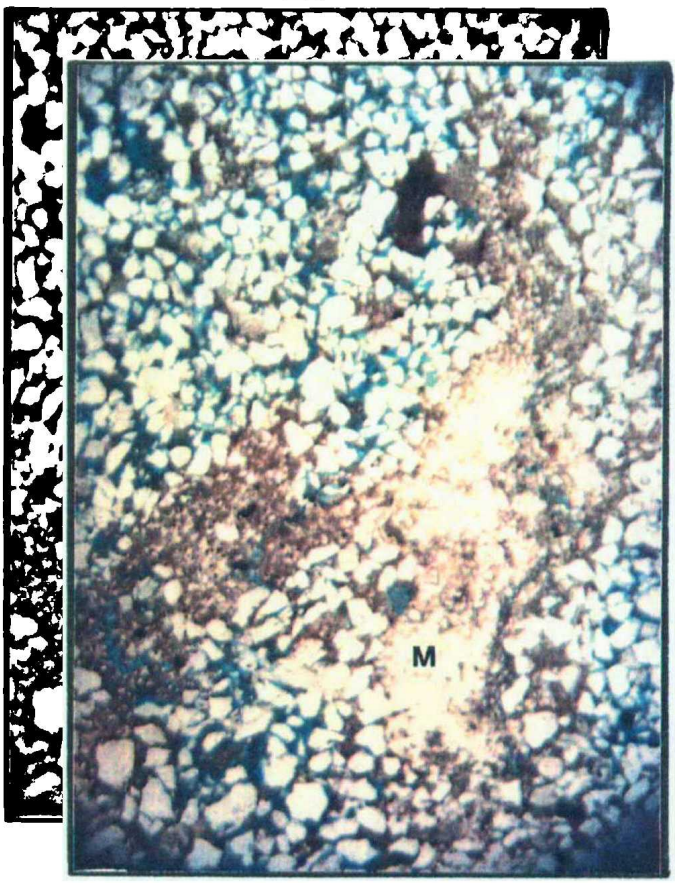
D) The previous sample under the optical microscope. The matrix consists of illite-smectite mixed layer, kaolinite and illite. Sample depth 2654 m. PPL. Scale bar 300 μm.

PLATE 9.4

A



B



C



D



PLATE 9.5

A) Kaolinite (K) as result of feldspar alteration. This type of clay mineral is a cement and not a detrital matrix. Sample depth 2585 m. PPL. Scale bar 120 μm.

B) The characteristics of the detrital matrix (M) found in the well 310. Sample depth 2687 m. PPL. Scale bar 120 μm.

C) The previous sample in XP. Observe the calcite (C) cement partially replacing the matrix (M). Sample depth 2687 m. Scale bar 120 μm.

D) The characteristics of the microquartz cement under PPL in a fine-grained sandstone. The brownish colour that gives a "dirty" aspect to the thin-section is a mixture of microscopic quartz grains and clay minerals. Sample depth 2601 m. PPL. Scale bar 120 μm.

PLATE 9.5

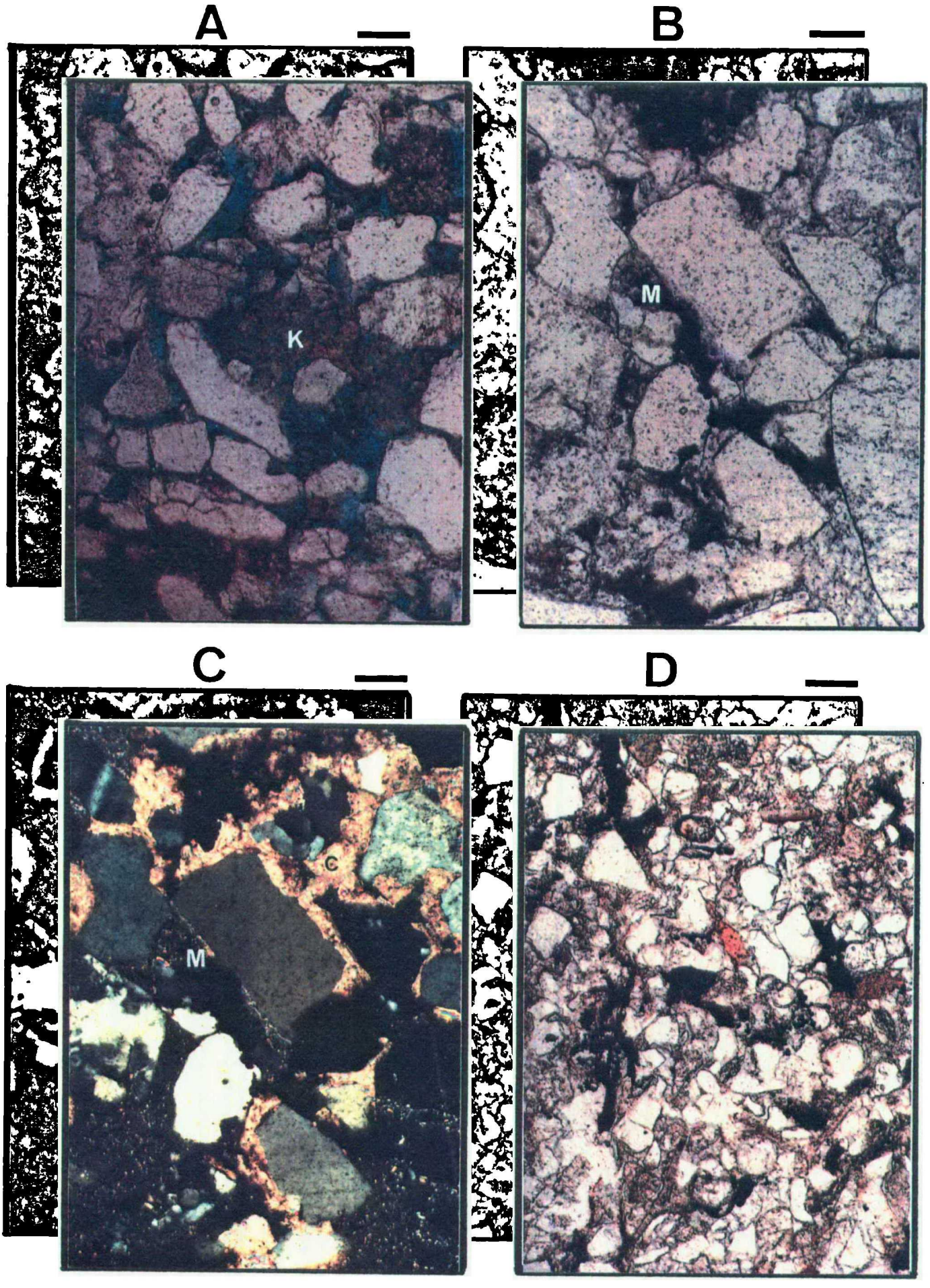


PLATE 9.6

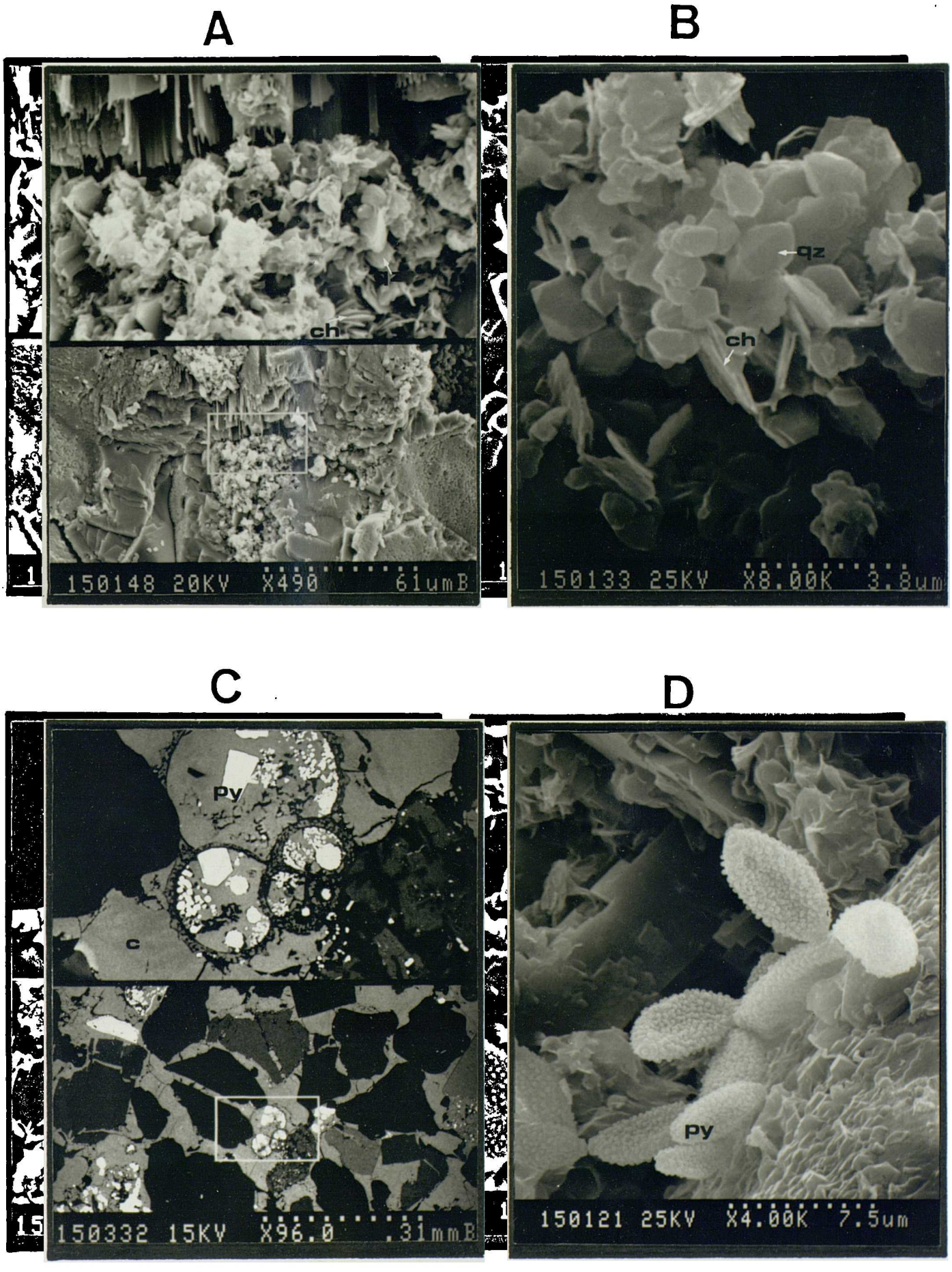
A) S.E.I. photomicrograph of the sandstone in well 310 showing the characteristics of the matrix in two different magnifications, the lower half has a magnification of ~ 680 X (photo/negative enlargement = 1.4 x 490 X) and the upper half has 5 X the lower one (~3,400 X). Observe the presence of microquartz (qz) and chlorite (ch) rosettes in the higher magnification. The scale bar is represented by a line of dots at the right bottom corner of the photo.

B) S.E.I. photomicrograph showing a close view of the matrix from the previous photo, with euhedral microquartz (qz) and small rosettes of chlorite (ch). Magnification ~11,200 X (photo/negative = 1.4 x 8,000 X).

C) B.S.I. photomicrograph showing framboidal and euhedral pyrite (py) inside a planktonic foraminifera in a very extensively calcite (c) cemented sandstone. The magnification of the upper half of the photo is 5 X the lower half, ~670 X and ~134 X respectively (photo/negative = 1.4 x 96 X).

D) S.E.I. photomicrograph showing framboidal pyrite (py) in the pore of a very coarse-grained sandstone. Magnification ~5,600 (photo/negative = 1.4 x 4,000 X).

PLATE 9.6


A
B
ch
qz
ch
150148 20KV X490 61umB
150133 25KV X8.00K 3.8um
C
D
Py
c
py
150332 15KV X96.0 .31mmB
150121 25KV X4.00K 7.5um

9.5.2 FRAMBOIDAL PYRITE

Framboidal pyrite occurs as a minor component in the sandstones. It consists of small framboidal aggregates, usually spherical or elliptical, occurring inside foraminiferal tests, replacing organic matter or even, but less commonly, in the sandstone pore spaces (see **plates 9.5 D, 9.6 C** and **D**). The predominant association of the framboidal pyrite with the foraminifera indicates that its generation probably has taken place during early diagenesis, with the organic matter of the foraminifera or other sources of organic matter helping to generate a reducing environment in the sulphate reduction zone (see **Chapter 8, section 8.5.2**, for comparison with the pyrite in the mudrocks). This process typically occurs at very shallow depths of burial (Gautier, 1985).

9.5.3 MICROQUARTZ

Very early chert/microquartz cements were found in thin-bedded fine-grained and pebbly/coarse-grained sandstones. The microquartz in the former appears to have been precipitated directly into primary pores such as foraminiferal chambers (**Plate 9.7A**), but in the latter the microquartz shows evidence of being generated by alteration of the matrix or pseudomatrix (**Plate 9.8B**).

The chert/microquartz in the thin-bedded fine-grained sandstones, under optical microscope, is characterized as an almost isotropic, "dirty", microcrystalline siliceous cement (**Plate 9.5 D**). This cement has a very characteristic texture when thin-sections are viewed in backscattered imaging mode (SEM), with its darker appearance contrasting with the brighter calcite and the detrital quartz and feldspar grains (see **Plate 9.7A**). When this cement was examined using the S.E.I. (fractured surface) it was shown to consist of euhedral microquartz crystals that vary from 1 to 5 μm. Between the microquartz crystals there is also often a diagenetic smectitic clay material with an imperfect honeycomb-like morphology (**Plate 9.7 B** and **C**).

The presence of this smectitic-clay gives the "dirty" appearance observed optically. The microquartz cement besides infilling pores, also occurs as a drusiform overgrowth on detrital quartz. Where the chert has been partially dissolved larger microquartz crystals have grown into the secondary pore spaces (see **Plate 9.7D**).

The association of chert/microquartz with a matrix/pseudomatrix was found only in the thinly bedded pebbly/coarse-grained sandstones of well 310. This siliceous material when analyzed under the S.E.M. (S.E.I.) appears as euhedral microquartz crystals (1-5 μm) within a matrix of a smectite-rich illite-smectite and chlorite. In this case there is much more clay material than was observed in the fine-grained sandstone. The microquartz also occurs as drusiform overgrowths, coating detrital quartz grains as found in the fine-grained sandstones. In spite of the general similarities between the occurrences of the microquartz in the two mentioned examples (**plates 9.7** and **9.8**), there were significant differences between them. In the fine-grained sandstones no detrital clay was observed and only small amounts of authigenic smectite occur between the quartz crystals (**Plate 9.7**). In the pebbly/coarse-grained sandstones detrital clay material is common, mainly represented by illite-smectite, as well as authigenic chlorite and kaolinite. Freitas (1987) and Moraes (1989) studying the turbidites from the upper Cretaceous of the Campos Basin have also found opal/microquartz as cements in sandstones. They related their origin to the alteration and replacement of the clay minerals of the matrix.

Based on the evidence shown above it is suggested that in the fine-grained sandstones the chert/microquartz precipitated as cements in the pore space of these sandstones, whilst in the pebbly-sandstones it was the result of alteration of the matrix or pseudomatrix, as proposed by Freitas (1987) and Moraes (1989).

PLATE 9.7

A) B.S.I. photomicrograph showing the characteristics of the siliceous (s) cement under backscattered imaging. Observe its very dark microcrystalline texture in contrast to the detrital grains (quartz and feldspar) and the very bright calcite (c) cement. Magnification of ~840X (photo/negative = 1.4 x 600 X).

B) S.E.I. photomicrograph, fractured surface, showing the shape of those siliceous microcrystals observed with the B.S.I. using thin-section in the previous photo (A). They consist of euhedral microquartz (qz). As reference for the size of these crystals note the coccolith (cc) present on the top left corner of the photo. Magnification ~9,800X (photo/negative = 1.4 x 7,000).

C) S.E.I. photomicrograph showing a detail of the clay particles associated with the microquartz (qz), they consist mainly of smectite (sm). Magnification ~9,660X (photo/negative = 1.4 x 6,900 X).

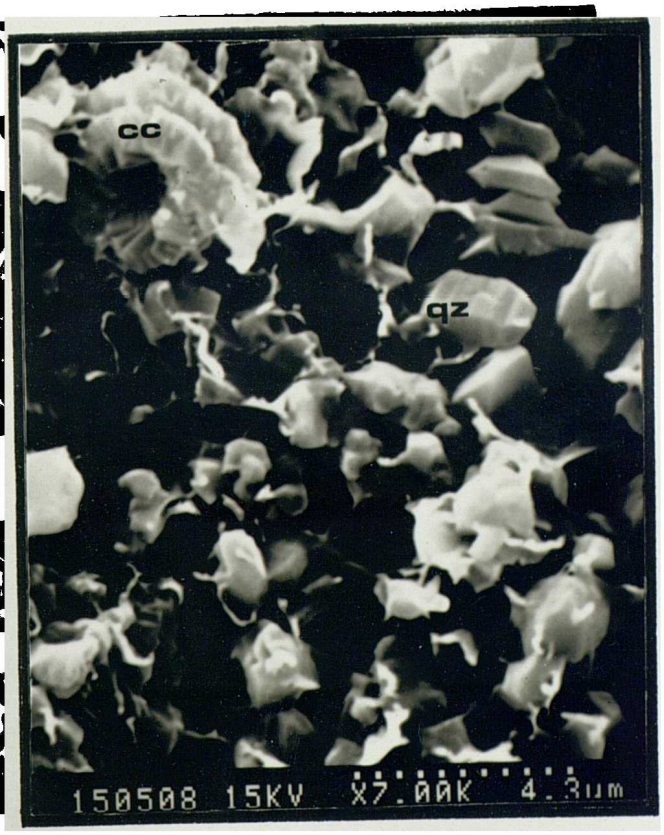
D) B.S.I. photomicrograph showing a detail of a secondary pore generated by partial dissolution of the siliceous (s) cement. Observe that the quartz (qz) crystals that have grown into these pores are larger than those found in the crystallized chert cement. Magnification ~2,380X (photo/negative = 1.4 x 1,700 X).

PLATE 9.7

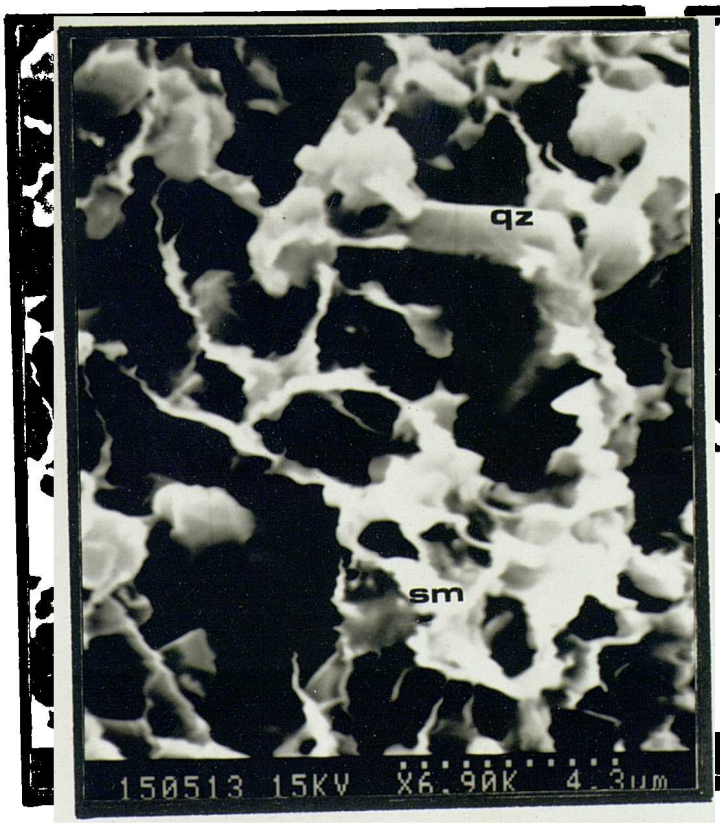
A



B



C



D

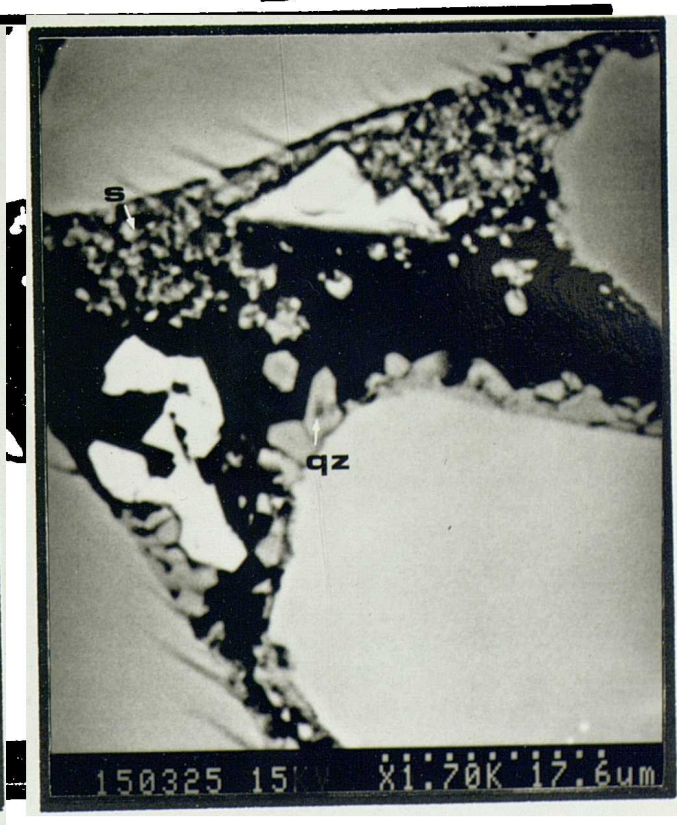


PLATE 9.8

A) S.E.I. photomicrograph showing a detail of the microquartz (qz) coating the grains. In the close up it is possible to observe the calcite (c) partially enveloping the microquartz. The upper half of the photomicrograph is 10 X the magnification of the lower half, respectively ~ 345 X and ~ 3,450 X (photo/negative = 1.4 x 247 X).

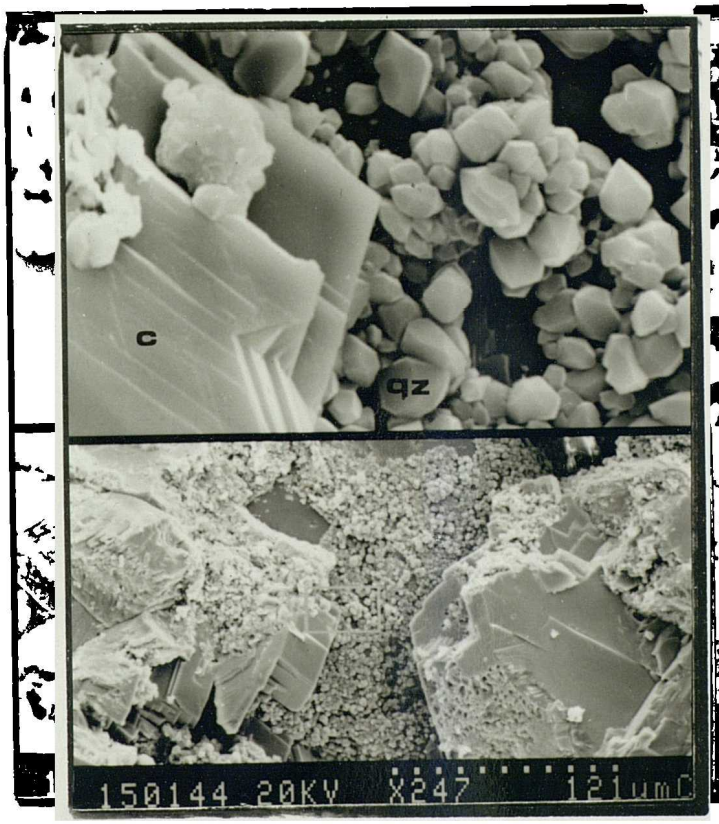
B) S.E.I. photomicrograph showing the same material as the previous photo where it is possible to observe the microquartz and some booklets of kaolinite (K). The latter, in spite of being associated with this matrix, is most likely to be a product of feldspar alteration. Magnification ~ 4,200 X (photo/negative = 1.4 x 3,000 X).

C) B.S.I. photomicrograph showing a K-feldspar overgrowth (o), but with a different composition, on a detrital K-feldspar (Kf) grain previously to the generation of the calcite (c) cement. The upper half of the photomicrograph is 5 X the magnification of the lower half, respectively ~ 560 X and ~ 112 X (photo/negative = 1.4 x 80 X).

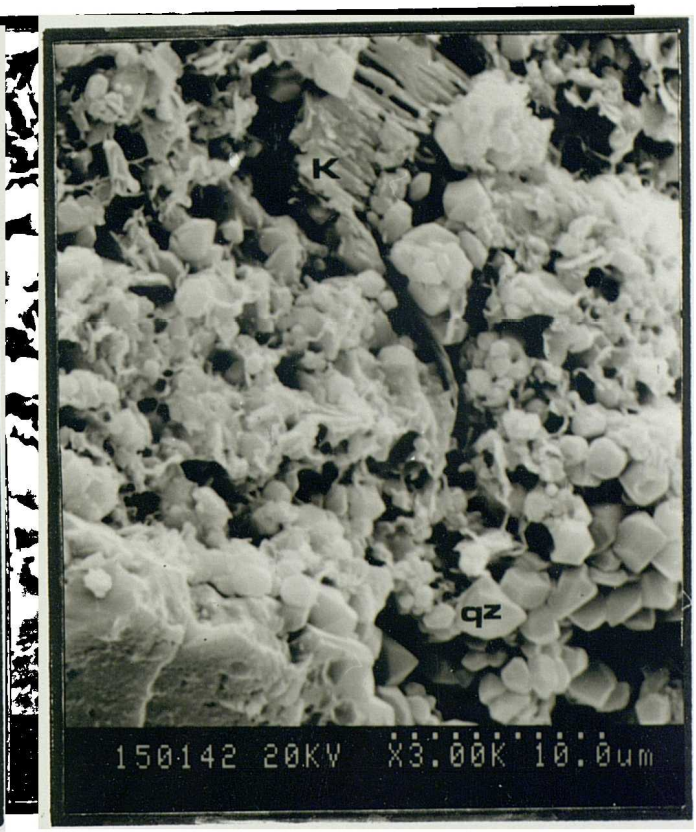
D) S.E.I. photomicrograph showing K-feldspar overgrowth (o) with a later smectite (sm) coating. Observe that the detrital K-feldspar has dissolved almost completely but that diagenetic K-feldspar overgrowth remains indicating that the latter is stable under the diagenetic conditions. The magnification of the upper half is 5 X the lower half, respectively ~ 1,715 X and ~ 343 X (photo/negative = 1.4 x 245 X).

PLATE 9.8

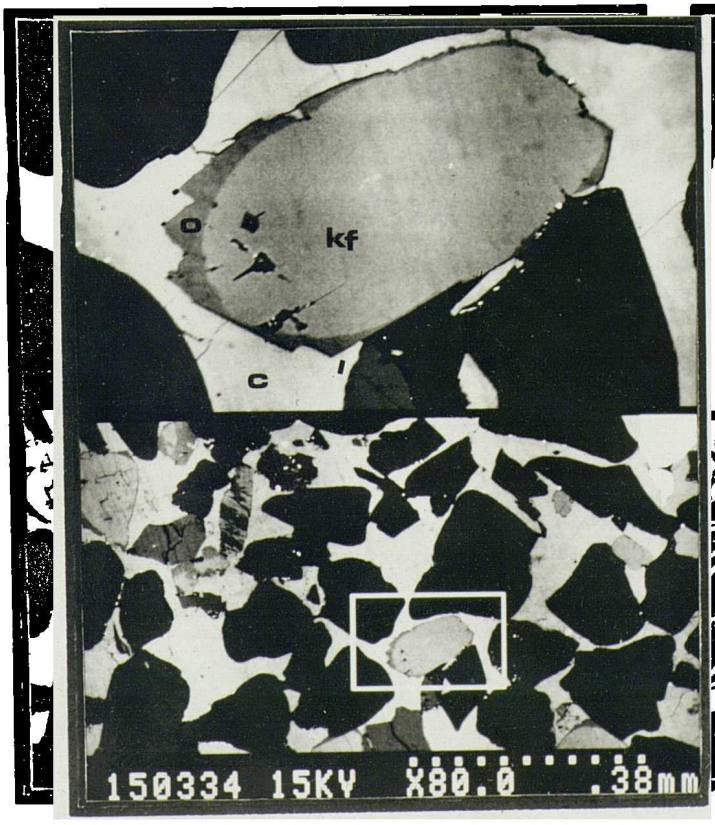
A



B



C



D



9.5.4 EARLY FELDSPAR OVERGROWTHS

Early feldspar overgrowths are rare in the analyzed sandstones. but sometimes good examples of this kind of early cement are seen (**Plate 9.8C**). The overgrowth have a K-feldspar composition on a K-feldspar detrital grain, but the overgrowth has less potassium than the detrital grain as shown by its darker appearance under backscattered imaging. This feldspar overgrowth was interpreted as early because of its relationship with the early poikilotopic calcite (see **section 9.5.7**). This relationship is different from later phases of feldspar overgrowths, that have occurred elsewhere following the dissolution of the poikilotopic calcite (see **section 9.5.12**). Another example of early K-feldspar overgrowths can be seen in the **Plate 9.8D**, where it occurs before the generation of the diagenetic smectite coating.

9.5.5 SMECTITE COATING

Diagenetic smectite coatings are characterized by a microscopic clay film with a cellular/honeycomb morphology. Although widespread in one of the analyzed samples, where it covers all the detrital grains, this kind of cement has been mainly found only in the samples from one well (334) and then usually as patches. This clay coating in terms of its effect in porosity reduction is insignificant. However, it could have helped to prevent some precipitation of later quartz overgrowth cements. This smectite coating (**plates 9.8, 9.9,** and **9.10**) clearly postdates the early K-feldspar overgrowth and predates the dissolution of detrital feldspars, the kaolinite cement and the later quartz and feldspar overgrowths. In spite of not having found a direct relationship between this clay coating and the early calcite cement it is probable that the former has precipitated first.

PLATE 9.9

A) S.E.I. photomicrograph showing the thin smectite (sm) coating on the detrital grains. Observe that it is earlier than the dissolution of the plagioclase (pl). Magnification ~ 826 X (photo/negative = 1.4 x 590 X).

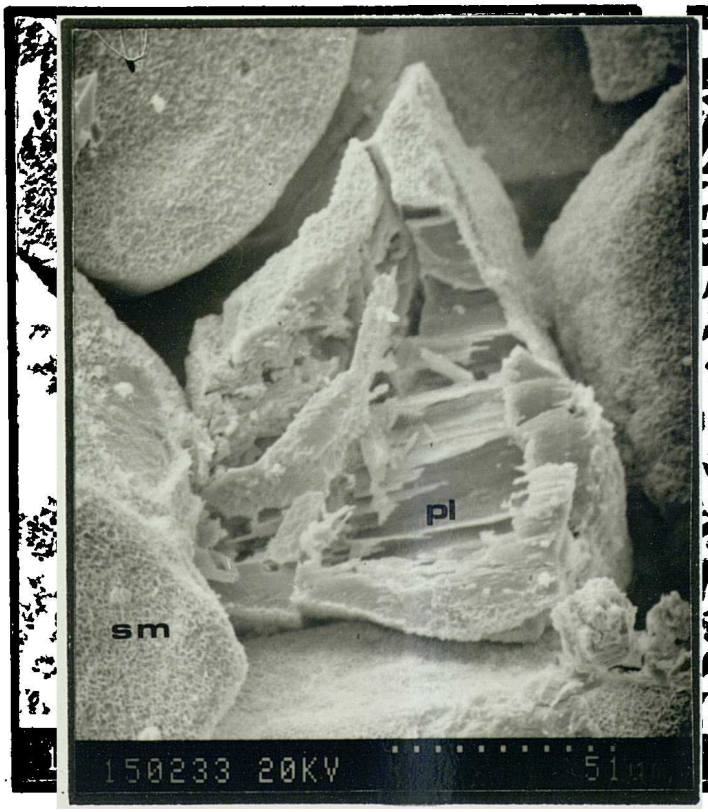
B) S.E.I. photomicrograph showing the cellular/honeycomb structure of the smectite coating. Magnification ~ 6,860 X (photo/negative = 1.4 x 4,900 X).

C) S.E.I. photomicrograph showing an example of a patchy coating of smectite. Magnification ~3,500 X (photo/negative = 1.4 x 2,500 X).

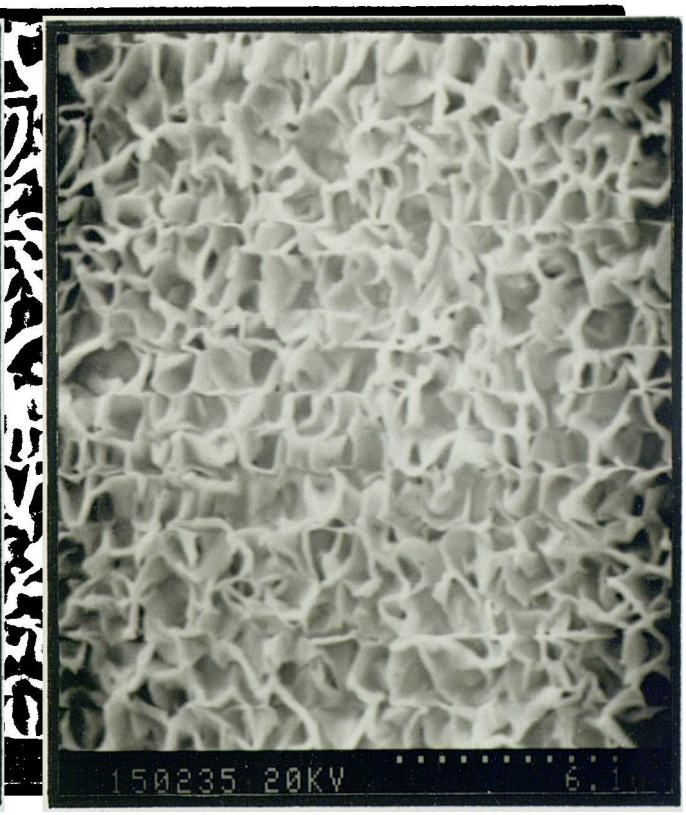
D) S.E.I. photomicrograph showing the kaolinite (K) post-dating the smectite (sm) coating. Magnification of the upper half is 10 X the lower part, respectively ~ 3,060 X and ~ 306 X (photo/negative = 1.4 x 219 X).

PLATE 9.9

A



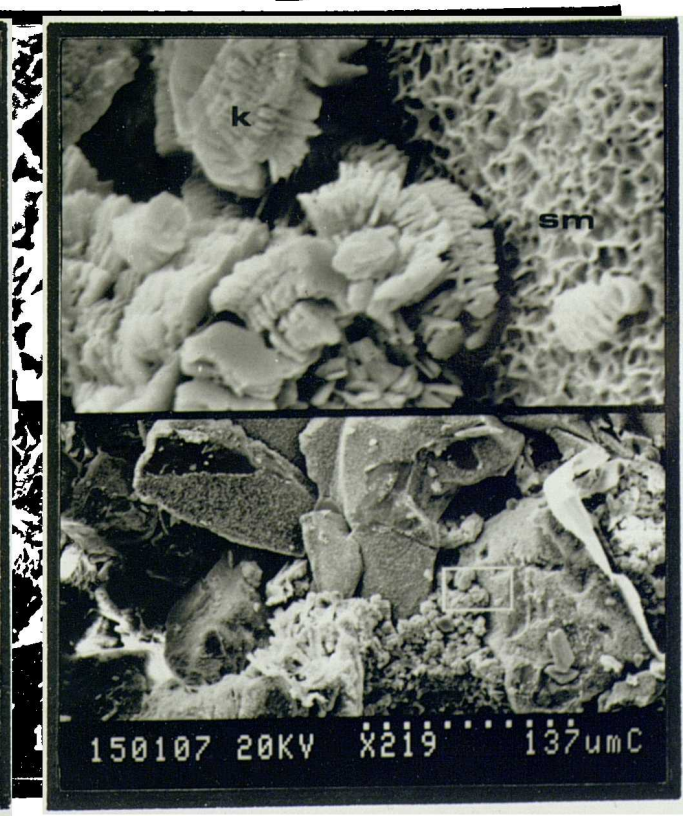
B



C



D



9.5.6 ANKERITE

Locally, and in only a very few sandstones, ankerite was found enveloped by early poikilotopic calcite. The ankerite crystals occur as small rhombs (50 μm), with more magnesium in the centre of the crystal and more iron (brighter under B.S.I.) towards the edges (**Plate 9.10 B**).

There is a probability that of some of these rhombs are detrital in origin and associated with the clasts of carbonaceous siltstones containing early diagenetic siderite/ankerite, that are frequently found as clasts in some sandstones (see **section 9.2.1**). The distinction between detrital and diagenetic is difficult when the calcite cementation is pervasive and encloses this material (see **Plate 9.2 B, C**).

9.5.7 EARLY CALCITE

The most important and abundant cement found in the sandstones consists of equant and/or poikilotopic calcite cement. The abundance of this type of calcite cement varies from only traces to more than 35% of the rock volume. In spite of having this wide variation there is a discernible bimodal distribution of the cement. The most abundant mode of occurrence of the calcite is only as trace amounts, and the other less abundant mode is as very high percentages of calcite, between 20 and 35% of the rock volume. The position of the calcite cement in the paragenetic sequence of the diagenetic phases clearly postdates the early feldspar overgrowth and the microquartz cements (see **Plate 9.8 A** and **Plate 9.10 C** and **D**). There are also two main associations between this type of calcite cement and the grain size. Poikilotopic and/or coarse equant calcite is associated mainly with the pebbly/medium-grained sandstones, in which there are relatively large amounts of shallow-water bioclasts (see **section 9.2**). The smaller calcite cement crystals are associated with deep-water bioclasts in the fine/very fine-grained sandstones and bioturbated siltstones.

PLATE 9.10

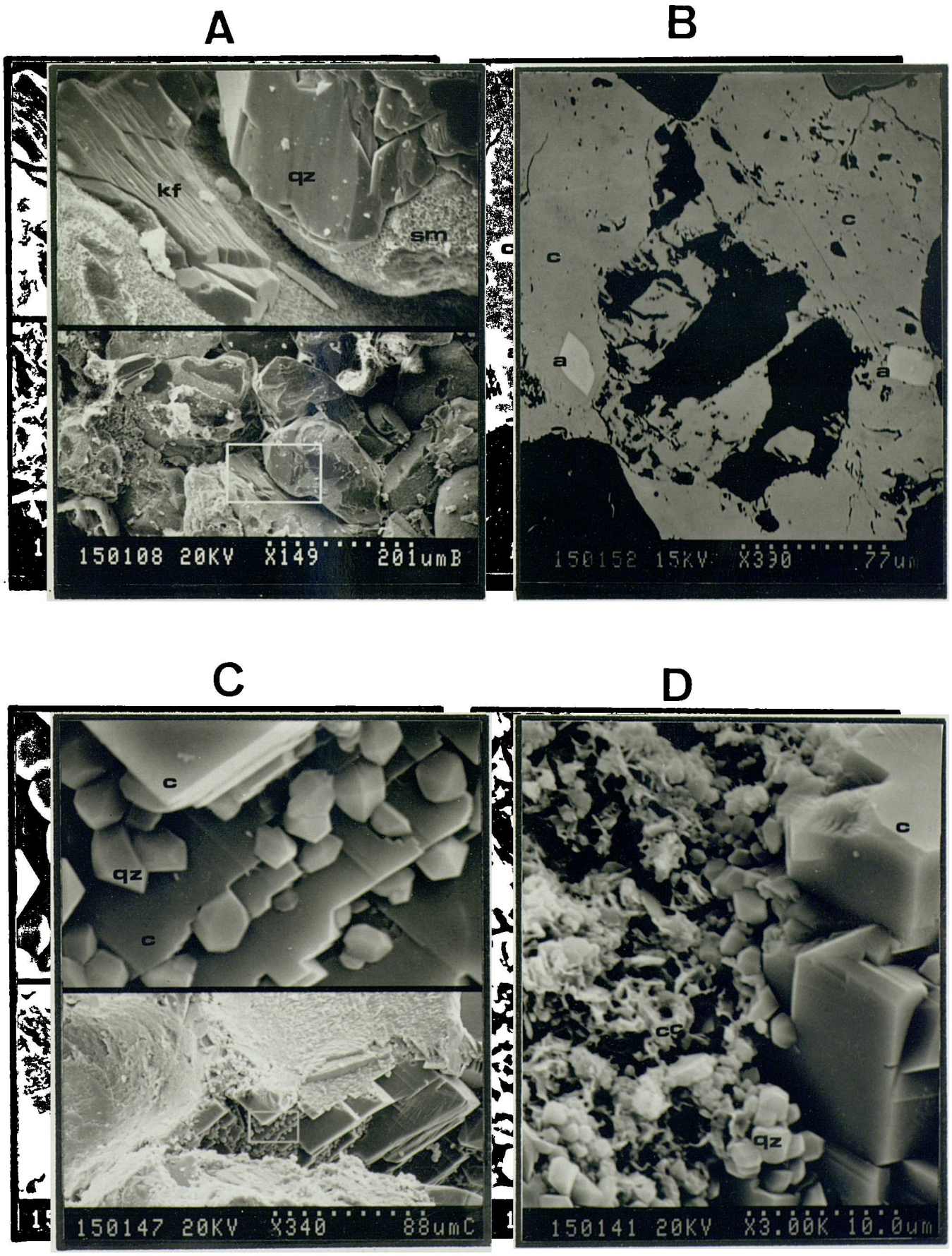
A) Quartz (qz) and K-feldspar (Kf) overgrowths over detrital grains. Their development has occurred after the precipitation of the smectite (sm) coating as can be seen by the absence of the coating over these overgrowths. Magnification of the upper half is 5 times the lower half of the photo, respectively ~ 1050 X and ~ 210 X (S.E.I. photo/negative = 1.4 x 149 X).

B) Sandstone cemented by poikilotopic calcite (c) and rhombs of ankerite (a) with brighter B.S.I. contrast. These ankerite rhombs have more magnesium in their centre and more iron content towards the crystal edges again giving a brighter B.S.I. contrast. Magnification of ~ 546 X (B.S.I. photo/negative = 1.4 x 390 X).

C) Calcite (c) cement enveloping microquartz (qz) cements. The magnification of the upper half of the photo is 10 times the lower one, respectively ~ 4,760 X and ~ 476 X (S.E.I. photo/negative = 1.4 x 340 X).

D) Calcite (c) crystals enveloping the matrix (illite-smectite, microquartz, chlorite and coccoliths) indicating that the calcite has been precipitated later than the alteration of the matrix (well 310). Magnification of ~4,200 X (S.E.I. photo/negative = 1.4 x 3,000 X).

PLATE 9.10


A
B
C
D
kf
qz
sm
150108 20KV X149 201umB
c
a
150152 15KV X390 77um
qz
150147 20KV X340 88umC
cc
150141 20KV X3.00K 10.0um

The poikilotopic/equant calcite cement is usually iron-rich, whilst the small calcite crystals are poorer in iron (based on staining with potassium ferricyanide). However, the equant calcite associated with the echinoid overgrowths do not stain.

The sandstone grain framework in the tight calcite cemented zones is quite open, with grains showing mainly point contacts or even "floating" in the calcite cement. The latter is more commonly associated with the poikilotopic cement. The "floating" grains that are locally observed are mainly the result of intense or total replacement of bioclasts, and are most frequently observed in those sandstones rich in echinoids. The calcite is replacive of the bioclasts and also corrosive to detrital feldspar and quartz grains. Where the cementation has been pervasive even the microfractures of the grains have been infilled with the calcite and the walls of the microfractures pushed apart. The occurrence of tight calcite cemented intervals in the thickly-bedded and amalgamated sandstones are associated with the presence of relatively large amounts of shallow-water bioclasts and with the very coarse/coarse-grained sandstones. The bioclasts have probably acted as nucleation sites for the calcite cement (i.e. overgrowths on the echinoid fragments) as well as source of calcium carbonate. From the characteristics discussed above, it is very likely that this cementation has taken place at relatively shallow burial depths (see **plates 9.3 B, 9.11 A-D**). Consequently, this phenomenon must have created early diagenetic permeability barriers.

The higher percentages of calcite cement in the fine/very fine-grained sandstones were found in those beds with higher amounts of deep-water bioclasts (see **section 9.2**). The bioclasts, both in the fine-sandstones and in the bioturbated zones, show evidence of recrystallization and the calcite cement occurs as very small crystals, probably as consequence of the presence of many nucleation points such as the bioclasts (see **Plate 9.12**). The fine-grained

thin-bedded sandstones are usually tightly cemented with calcite when they are: 1) interbedded in thick marlstone sequences; 2) contain relatively high amounts of deep-water bioclasts; 3) are heavily bioturbated and associated with siltstones.

The calcite in the bioturbated siltstones occurs in the burrows, with their relatively coarser grain size (very fine sand-sized grains) rather than in the matrix. The cementation appears to have occurred early in the evolution of these siltstones because it is possible to see that burrows have preserved their circular cross sections and there is evidence of differential compaction around the cemented burrows (see **Plate 9.12 C**). Tightly cemented burrows were also observed in the sandstones while the remaining parts of the rock were uncemented. Bioturbation appears to have encourage calcite cementation probably due to the presence of organic products left by the burrowing organisms and/or permeability contrasts between the burrow and the host rock.

9.5.8 SECONDARY POROSITY

Secondary porosity was identified using the textural features described by Schmidt and Mcdonald (1979) using thin-sections and fractured surface samples (S.E.I.). The most commonly found characteristic features of secondary porosity were: corroded grains, dissolution of calcite cement, oversized pores and intragranular porosity due to total or partial dissolution feldspar or bioclasts. The most abundant type of secondary porosity is intergranular and is related to calcite dissolution. Feldspar alteration/dissolution, in general, has caused only a small real increase in the porosity and is preserved mainly as microporosity due to the later replacement of feldspar by kaolinite. However, there are some sandstones where the feldspar grains have been dissolved partially or completely creating intragranular or moldic macroporosity, respectively, but kaolinite has not precipitated in the

PLATE 9.11

A) Tightly calcite cemented sandstone where it is possible to see scattered red (R) algae fragments, beige spots. See Plate 3 A for the detail in thin-section. Core photo. Scale bar 1 cm.

B) Characteristics of the poikilotopic calcite cement (C). Observe that the grains have mainly point contacts and a single calcite crystal extends around many grains. Sample depth 2661 m. XP. Scale bar 300 μm.

C and D) Characteristics of a tight cemented bioclastic (echinoid (E), bivalve (B) and milliolid (M)) sandstone showing the replacive habit of the calcite. The impression of the existence of "floating" grains is mainly due to the total replacement of the bioclasts (mainly echinoids) by calcite. This can lead to an overestimation of the amount of the calcite cement and its relationship with the initial pore size/framework packing.
(C) Sample depth 2637 m; XP; Scale bar 120 μm. (D) Sample depth 2637 m; XP; Scale bar 300 μm.

PLATE 9.11

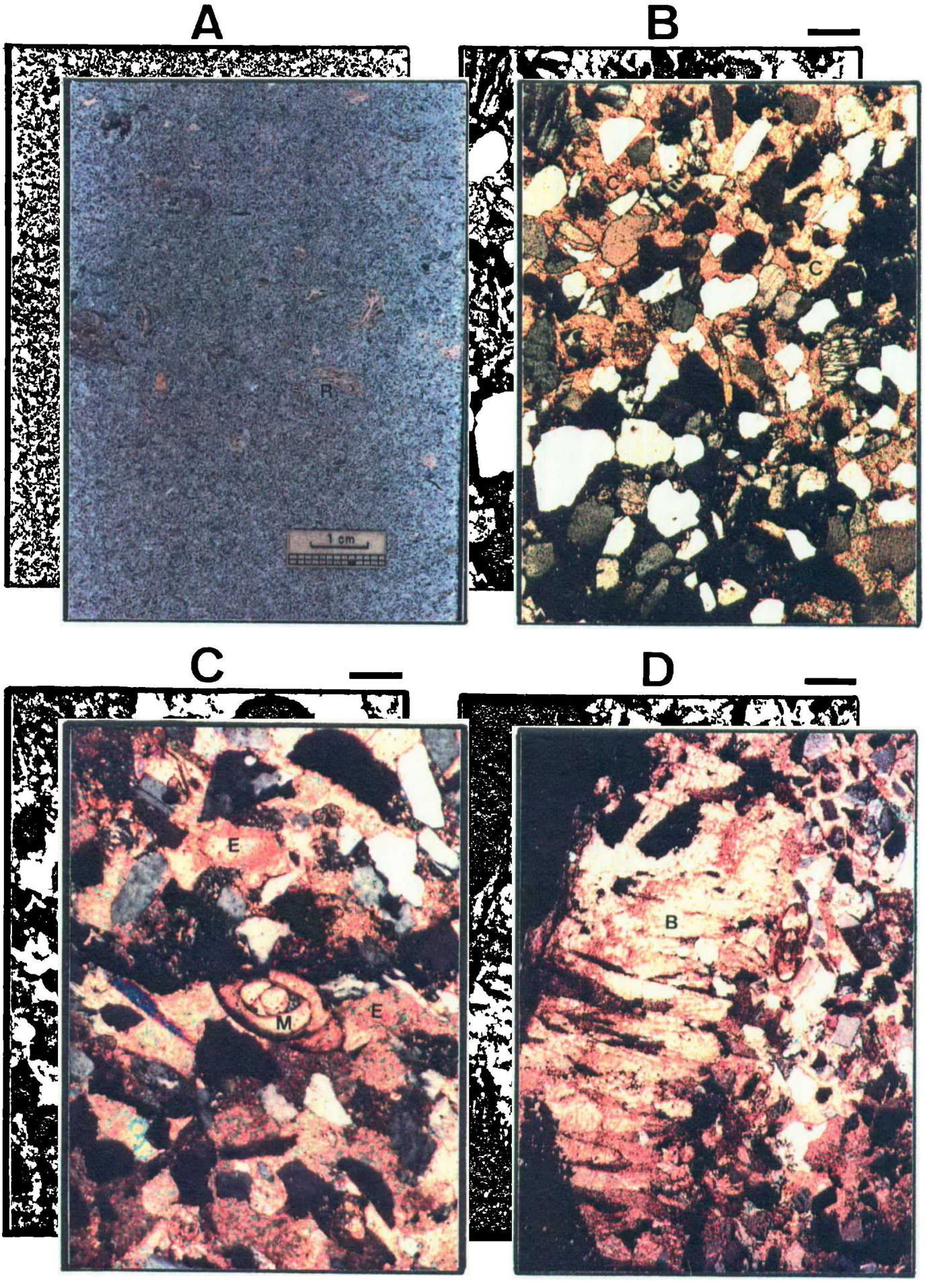


PLATE 9.12

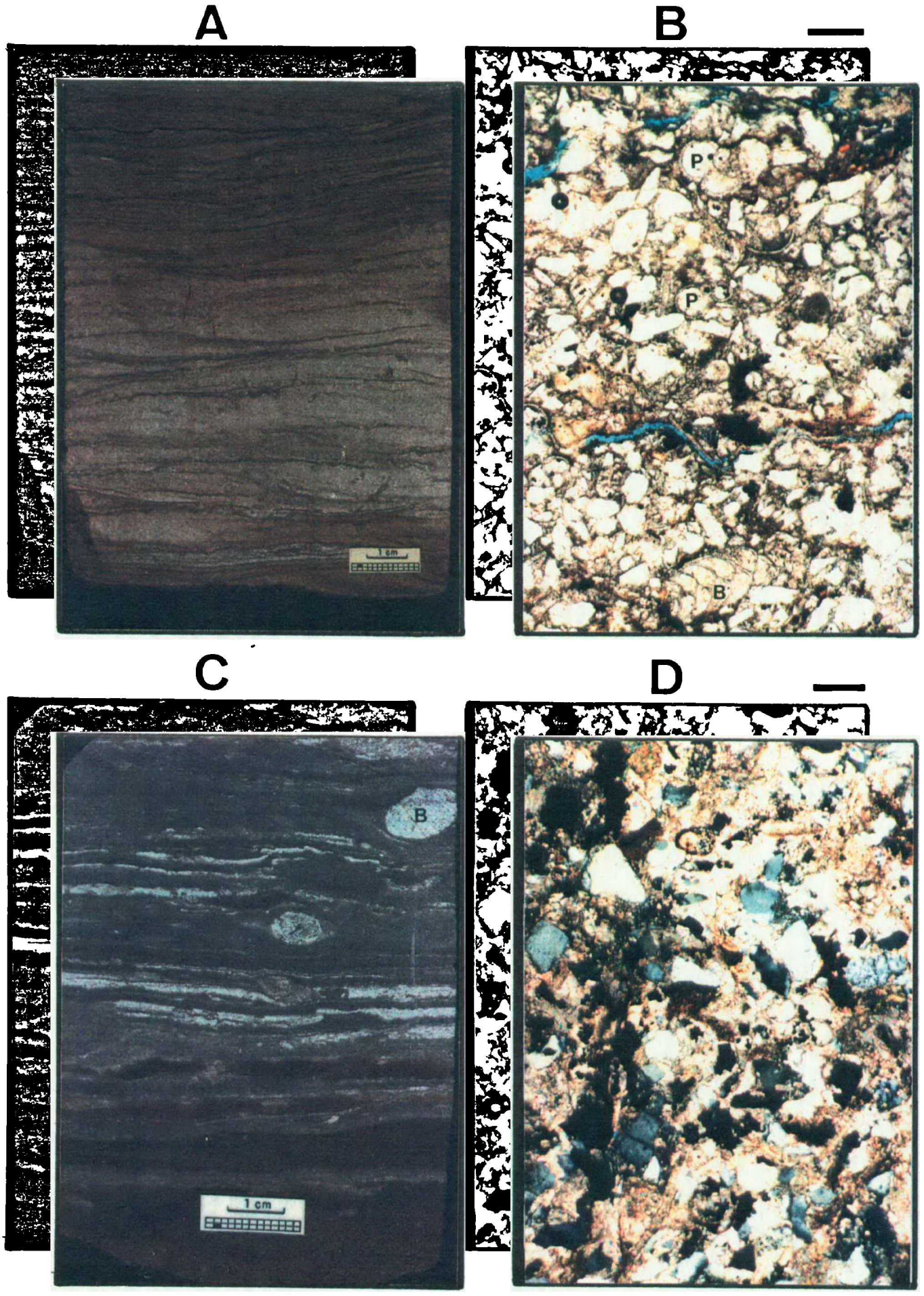
A) Very fine/fine-grained sandstone (Ripple Sandstone Lithofacies **Rip**) where it is possible to observe cementation variations as a function of the bioclastic content. The dark brown colour is more porous and it is impregnated with oil, while the grey rock is tight. Core photo. Scale bar 1 cm.

B) Sandstone shown in the previous photo showing the deep-water bioclasts, planktonic (P) and benthonic (B) foraminifera, and the calcite infilling almost all the porosity (represented by the blue resin). Sample depth 2601 m. Photomicrograph PPL. Scale bar 120 μm.

C) Control of cementation by bioturbation (B). As the burrows in the mudrock have been infilled with sand-sized grains the cementation by calcite is greater in the burrows because of their better local poro-permeabilities. Additionally, it can be seen that this calcite cementation must have occurred quite early because the burrows are almost circular and the mudrock shows evidence of differential compaction due to the more resistant characteristics of the cemented burrow. Core photo. Scale bar 1 cm.

D) Fine-grained sandstone with deep-water bioclasts acting as nucleation points for the small calcite crystals. Sample depth 2601 m. Photomicrograph XP. Scale bar 120 μm.

PLATE 9.12



secondary pore space (see **plates 9.13 A-D** and **9.14 A** and **B**).

Early calcite cementation has occurred preferentially in the coarse- and fine-grained bioclast-rich sandstones. The converse is true for the dissolution of the calcite. In other words, when the fluids that caused the dissolution of the calcite started to flow through the reservoirs they followed the most porous and permeable (less cemented) pathways and calcite dissolution has therefore been more efficient and significant in these less well cemented zones. As the most intensively cemented intervals have become almost impermeable zones, the dissolving fluids could only corrode them around their borders or, if present, through permeable pathways such as fractures (**Plate 9.14 C** and **D**).

The quantity of calcite that has been precipitated and later removed by dissolution is very difficult to quantify, in spite of the evidence that these two events have occurred (see **Plates 9.13** and **9.14**).

The analyses using the S.E.I. have shown that there are two main stages of residual calcite: one where the crystals are still well defined, and only with corrosive features on their surfaces; and the other where most of the calcite has already been dissolved leaving only a "sugar-like" residual texture (see **Plate 9.15 A** and **B**). The bioclasts have also undergone dissolution and recrystallization, to different degrees. Locally, in the tightly cemented zones, they have been preserved from dissolution, although they have been partially or totally replaced by calcite cements (see **Plates 9.11** and **9.12**).

9.5.9 KAOLINITE

The alteration/dissolution of feldspars and the generation of kaolinite is the third most important diagenetic phenomenon observed in the majority of the sandstones. This phase was found in sandstones from depths and temperatures varying from 2450 to 3852 m and from 48º to 123ºC, respectively. The most common feature of this diagenetic phase is the replacement of feldspar by

kaolinite. This can be clearly seen in thin-sections and even better in the S.E.I., where the kaolinite occurs commonly as isolated "nests of booklets", characterizing its association with the framework grains (see **Plate 9.15 photomicrographs C** and **D**). The amount of kaolinite varies from 0% to up to 10%, but on average it is around 2%. There are sandstones where no kaolinite is seen, but the feldspar grains show dissolution features, whilst in others kaolinite occurs abundantly.

The feldspar alteration/dissolution has been differential, the most common altered grains are those that have already been partially altered prior to deposition. This distinction is possible by comparing the feldspar grains in the tight calcite cemented intervals, where the framework composition was "frozen" and preserved from further alterations, with the feldspars in adjacent porous intervals (see **Plate 9.1**).

Additionally to the alteration of feldspar, muscovite and biotite have also been partially altered to kaolinite. The alteration into kaolinite has usually started at the edges of the mica flakes, through the cleavage planes, generating the characteristic split edges of the mica flakes (see **Plate 9.16 A**).

The kaolinite is very abundant in the deepest sandstone sample (3852 m) and shows evidence of initial replacement by albite and chlorite, as well as being enveloped by later albite and quartz overgrowths (see **Plate 9.17 photomicrographs A, B** and **D**).

9.5.10 DOLOMITE

Rare small rhombs (~40 μm) of ferroan dolomite were found infilling secondary pores associated with kaolinite (see **Plate 9.17 C**). There is no direct evidence of its position in the diagenetic sequence in relation to quartz and feldspar overgrowths, but it clearly postdates the dissolution of calcite.

PLATE 9.13

A and B) Pebbly-sandstone showing evidence of dissolution of the calcite (C) cement. The blue areas represent porosity. Sample depth 2679 m. Scale bar 75 μm. Photomicrographs (A) PPL and (B) XP.

C) Secondary porosity (P) formed by the dissolution of calcite cement and feldspar grains, the latter as moldic porosity. Some kaolinite is also present (K). Sample depth 2447 m. Photomicrograph PPL. Scale bar 75 μm.

D) Intragranular secondary porosity associated with partial feldspar (F) dissolution. Sample depth 2575 m. Photomicrograph PPL. Scale bar 75 μm.

PLATE 9.13

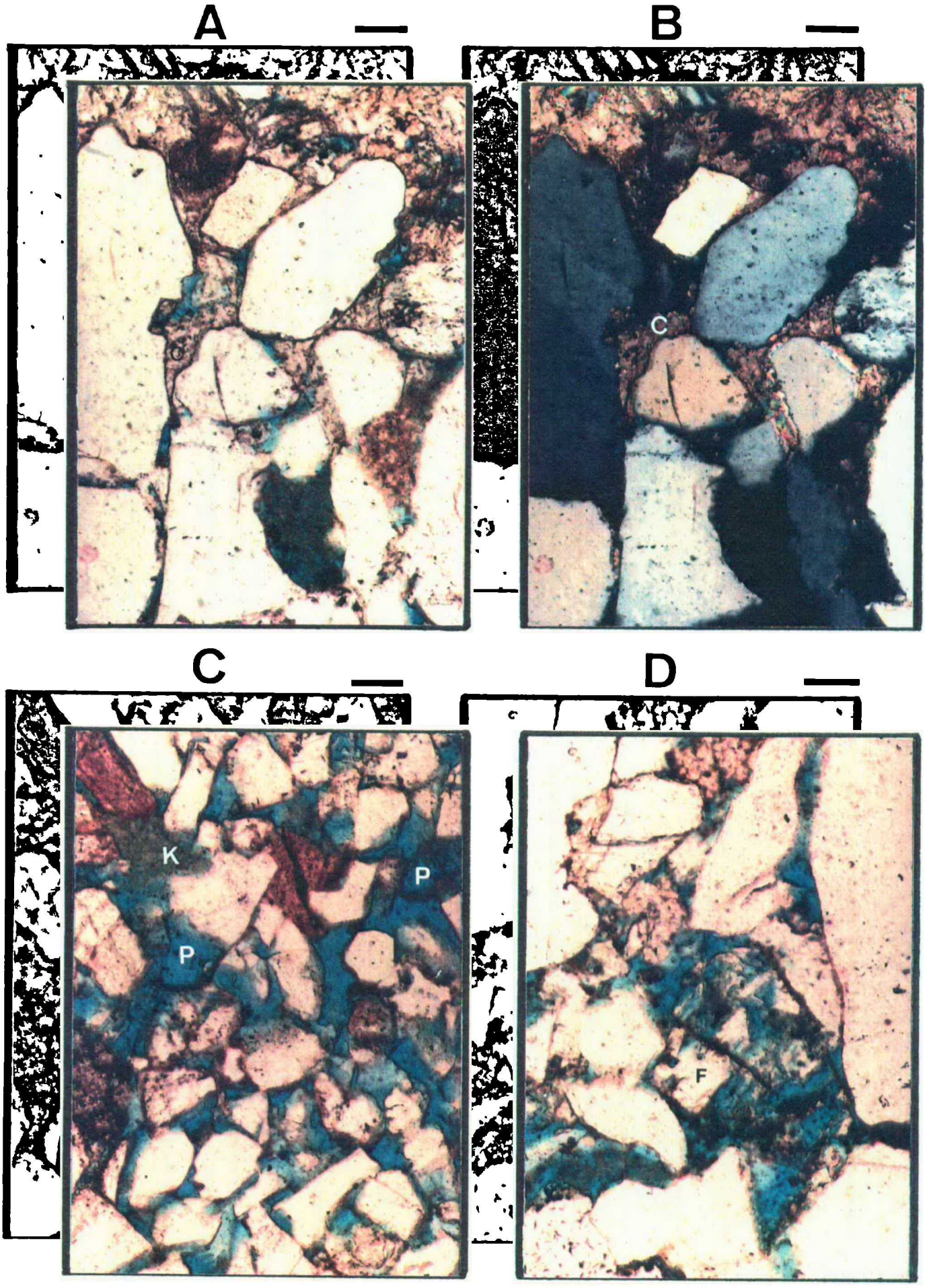


PLATE 9.14

A and **B)** Partial and differential dissolution of plagioclase (PL). Observe the presence of fractures (F) and intragranular porosity in the plagioclase at the left top corner of the photo. Sample depth 2585 m. Photomicrographs **(A)** PPL and **(B)** XP. Scale bar 120 μm.

C) Tight calcite cemented coarse/very coarse-grained sandstone showing secondary porosity, due to partial dissolution of the calcite, infilled by oil, the region stained in dark brown. Core photo Scale 1 cm.

D) Tight calcite cemented coarse sandstone showing the control on the dissolution of the calcite by fractures, porous pathways allowing the dissolving fluids to penetrate these tight zones. The horizontal fracture in the middle of the photo is due to core handling. Core photo. Scale bar 1 cm.

PLATE 9.14

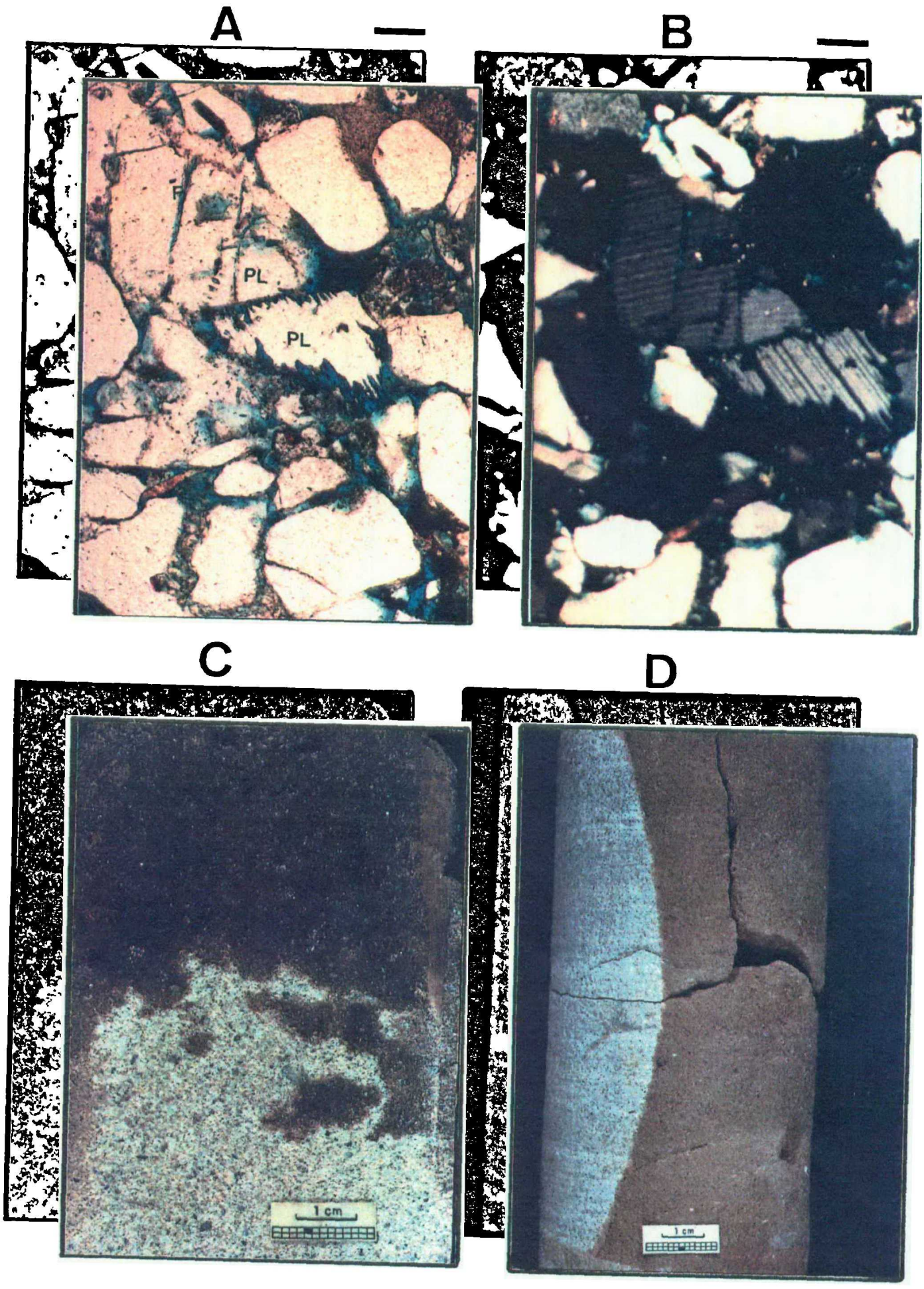


PLATE 9.15

A) Features associated with partial dissolution of the calcite (c) cement. The magnification of the upper half of the S.E.I. photo is 10 X the one of the lower half, respectively ~4,200 X and ~420 X (photo/negative = 1.4 x 300 X).

B) "Sugar like" aspect of the partial dissolved calcite (c). The magnification of the upper half of the S.E.I. photo is 5 X the one of the lower half, respectively ~4,900 X and ~980 X (photo/negative = 1.4 x 700 X).

C) "Nests" of kaolinite (K) booklets as result of in situ feldspar alteration. The magnification of the upper half of the S.E.I. photo is 10 X the one of the lower half, respectively ~1,820 X and ~182 (photo/negative = 1.4 x 130 X).

D) Close up of kaolinite (K) booklets. Magnification of ~3,500 X (S.E.I. photo/negative = 1.4 x 2,500 X).

PLATE 9.15

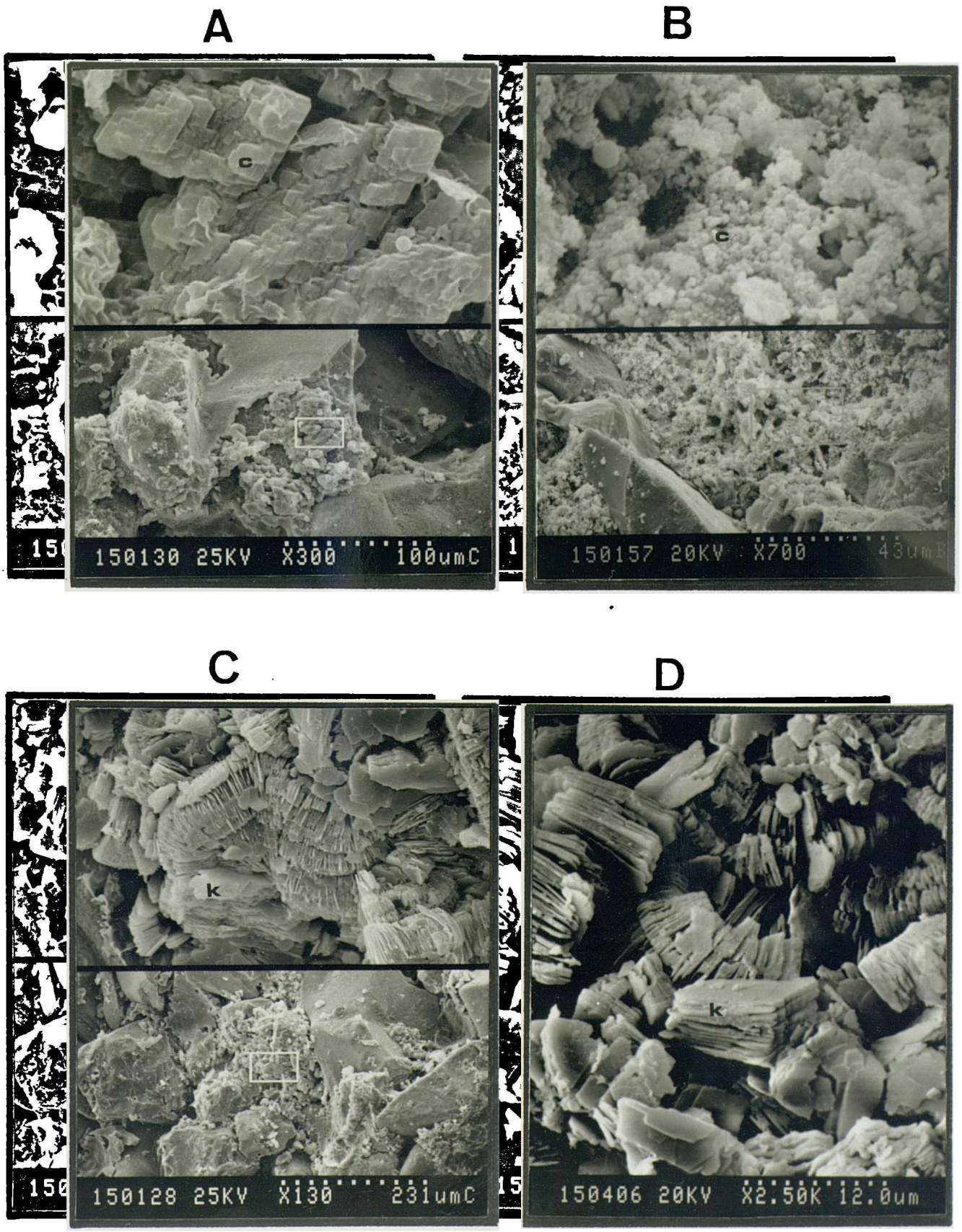

A
B
C
D
c
c
k
k
150130 25KV X300 100umC
150157 20KV X700 43umB
150128 25KV X130 231umC
150406 20KV X2.50K 12.0um

PLATE 9.16

A) Muscovite (M) being altered into kaolinite (K), along its cleavages causing an expansion of the muscovite. Sample depth 3852 m. Photomicrograph XP. Scale bar 75 μm.

B) A rim of albite overgrowth (O) around an altered and partial leached feldspar (F) grain. This type of late overgrowth could have acted as a mechanism to delay the reduction of the porosity by compaction. Sample depth 3852 m. Photomicrograph PPL. Scale bar 120 μm.

C) Moldic porosity (P) due to the leaching of feldspar grains and later the development of quartz overgrowth (O), which probably have prevented some porosity reduction by compaction. Sample depth 3852 m. Photomicrograph PPL. Scale bar 120 μm.

D) Euhedral calcite (C) growing into a secondary pore where there is some kaolinite. Sample depth 3852 m. Photomicrograph PPL. Scale bar 75 μm.

PLATE 9.16

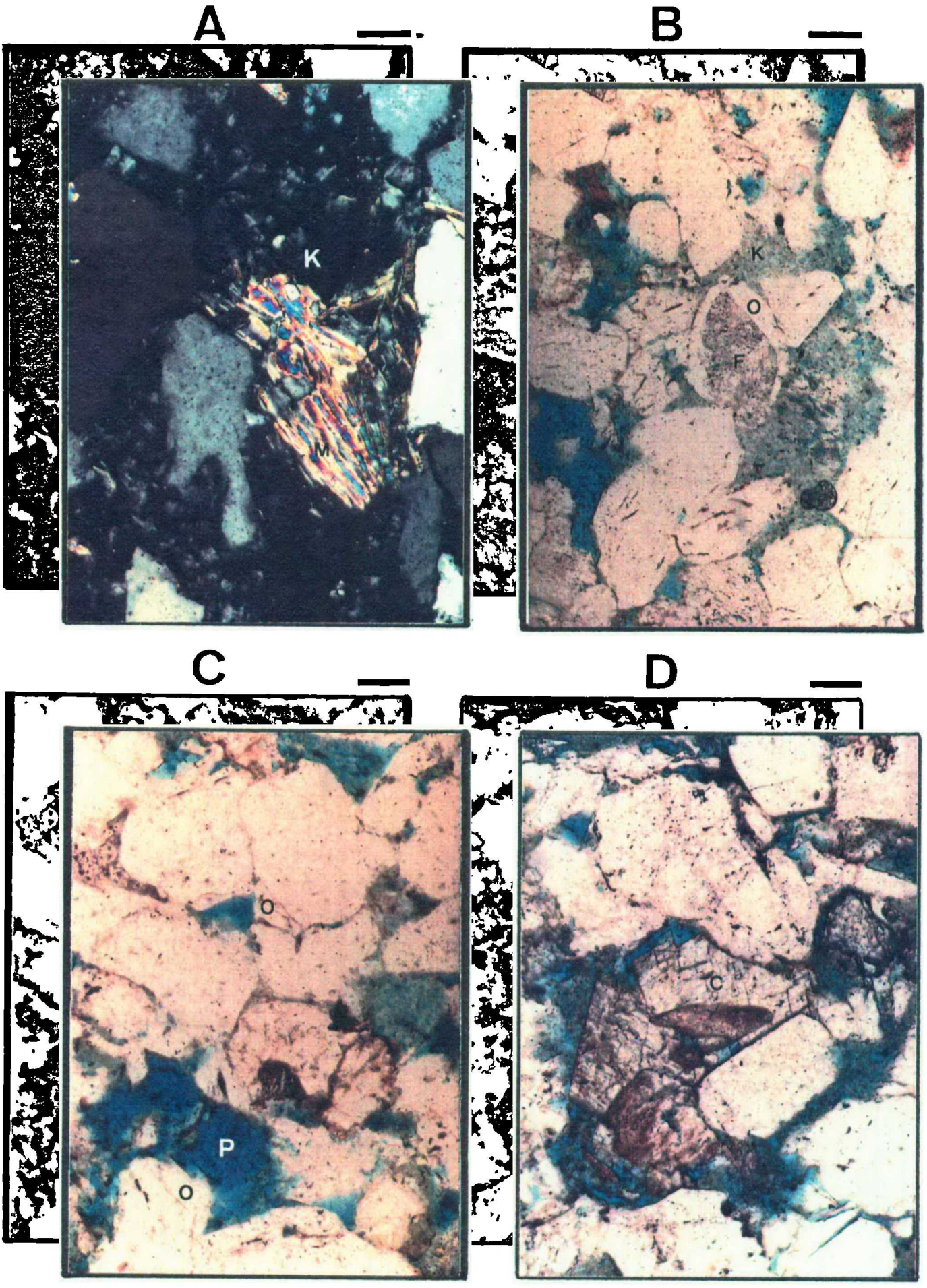


PLATE 9.17

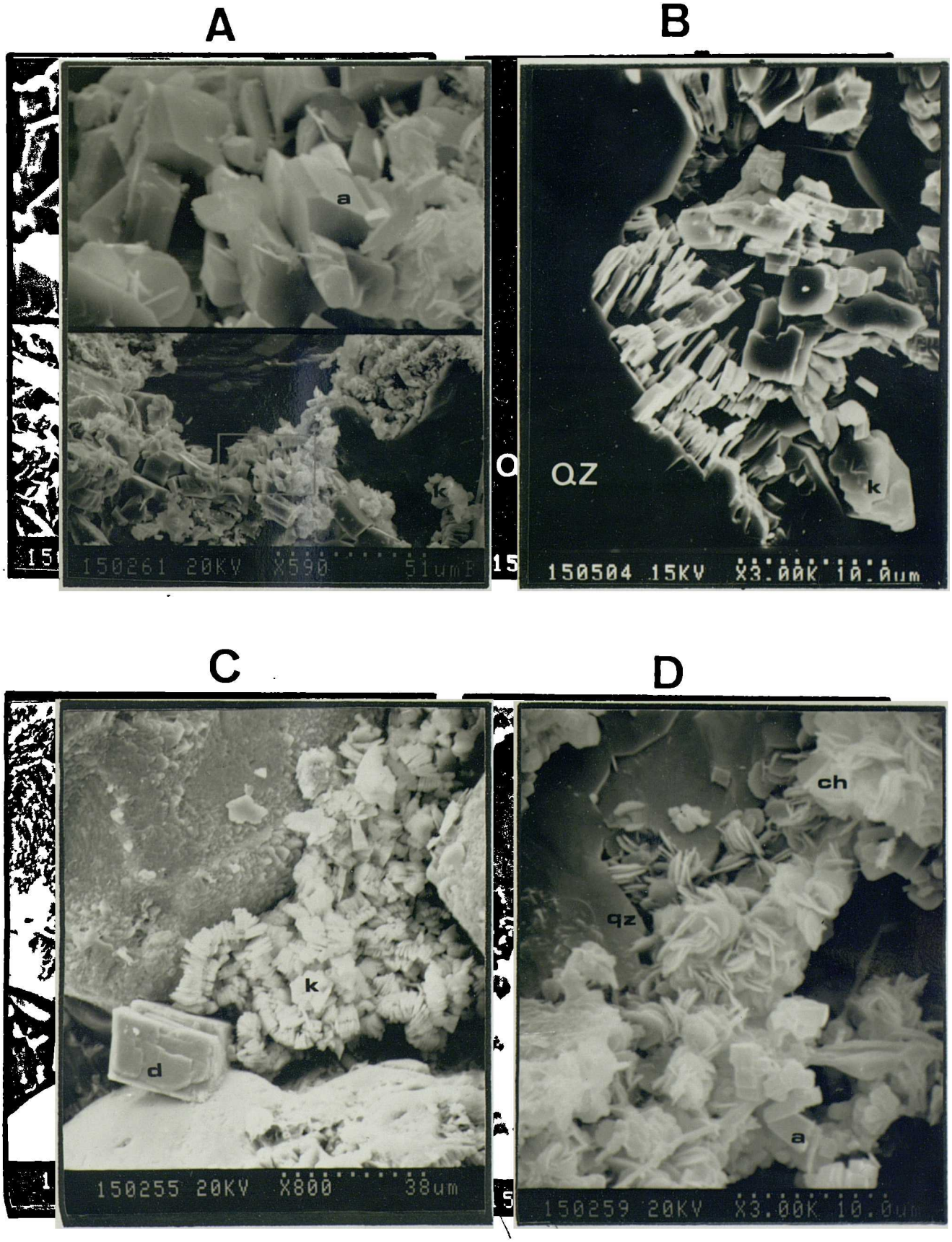
A) Small albite crystals (a) growing and enveloping the kaolinite (K). The magnification of the upper half of the S.E.I. photo is 5 X the lower half, respectively ~4,130 X and ~826 X (photo/negative = 1.4 x 590 X).

B) Quartz (qz) overgrowth enveloping the kaolinite (K). Magnification of ~4,200 X (S.E.I. photo/negative = 1.4 x 3,000 X).

C) Dolomite (d) rhomb associate with kaolinite (K) in a pore. Observe that the crystal faces are not perfectly smooth, indicating that it could have been partially dissolved (transition zone). Magnification of ~1,120 X (S.E.I. photo/negative = 1.4 x 800 X).

D) quartz (qz) overgrowth enveloping chlorite (ch) rosettes. Magnification of ~4,200 X (S.E.I. photo/negative = 1.4 x 3,000 X).

PLATE 9.17


A
a
k
150261 20KV X590 51um
B
QZ
k
150504 15KV X3.00K 10.0um
C
k
d
150255 20KV X800 38um
D
ch
qz
a
150259 20KV X3.00K 10.0um

9.5.11 CHLORITE

Diagenetic chlorite in the sandstones occurs associated with the alteration of the pseudomatrix in well 310 at relatively shallow depths (2600-2700 m) and also in the deepest sandstone sample (3852 m) in well 154. The chlorite in the shallower samples occurs associated with illite-smectite, microquartz, and kaolinite (see **section 9.5.1** and **9.5.3**). This type of chlorite forms as an early diagenetic phase in the paragenetic sequence as one of the products of the alteration of the pseudomatrix together with microquartz.

The relationship between microquartz and early calcite cementation is very clearly seen in S.E.I., the microquartz predates the calcite and so does the chlorite (see **sections 9.5.1** and **9.5.3** and respective plates).

The second type of chlorite in a sample from 3852 m forms larger crystals. This chlorite was found closely associated with kaolinite, and predates the later feldspar and quartz overgrowths (see **Plate 9.17 D**). In a sample from a mudrock adjacent to this sandstone was also seen chlorite associated with kaolinite in foraminiferal chambers and possible replacing it (see **Chapter 8, section 8.54** and **Plate 8.8**).

9.5.12 QUARTZ AND FELDSPAR OVERGROWTHS

Late quartz and feldspar overgrowths are common but volumetrically insignificant in terms of porosity reduction. In the **Plate 9.18 A** and **B** are shown examples of incipient quartz overgrowth on detrital quartz and albite overgrowths on partially dissolved plagioclase. However, in the deepest sample (3852 m) quartz and feldspar overgrowths are better developed. Here the overgrowths have probably prevented some porosity reduction by compaction as can be seen in **Plate 9.16 B** and **C**.

The quartz/feldspar overgrowths occur both in the water and in the oil zone, indicating that this diagenetic phase has occurred prior to migration of hydrocarbon into these

reservoirs. This is also true for nearly all the other diagenetic phases already described.

9.5.13. PYRITE

A late phase of development of pyrite is restricted in occurrence and appears commonly as irregular forms mainly associated with organic matter, biotite, or infilling secondary porosity. This type of pyrite differs from the early framboidal phase in size, shape, and mode of occurrence. It is more commonly found in the thin-bedded fine-grained sandstones. The reason for this could be that this kind of sandstone frequently has more organic matter than the coarser-grained sandstones. This diagenetic phase seems to have formed after the dissolution of the early formed calcite. The latter was observed in a gravelly-sandstone where the pyrite occurs in a secondary pore that was later infilled with euhedral calcite (late phase) (see **Plate 9.19 A** and **B**).

9.5.14 EUHEDRAL CALCITE

Euhedral calcite cement was found in some sandstones as a late diagenetic phase. This calcite contains less iron than the early calcite (section 9.5.7) and occurs usually as small euhedral crystals infilling secondary pores (see **plates 9.16 D, 9.18 C** and **D**). However, in a gravelly-sandstone this type of calcite has occurred as very coarse euhedral crystals. Under cathodoluminescence this coarse calcite has brighter colours than the early ferroan calcite that has dim and darker red C.L. colours. The euhedral calcite has well defined zoning with an increase in the luminescence toward the edges of the crystals, probably as result of oscillations in the fluid characteristics during its growth (see **plates 9.19 A-D** and **9.20 A**). This cement is restricted to the water or transitional oil/water zones. Implying that its generation postdates the main oil migration.

PLATE 9.18

A) Quartz (qz) overgrowth on a detrital quartz grain and a partially dissolved calcite (c) cement. Magnification of ~1,106 X (S.E.I. photo/negative = 1.4 x 790 X).

B) A detail showing dissolution of plagioclase and the subsequent albite (a) overgrowth. The magnification of the upper half of the S.E.I. photo is 10 X the lower half, respectively ~980 X and ~98 X (photo/negative = 1.4 x 70X).

C) Late euhedral calcite (c) cement. Observe as well the presence of an illite (?) fibre making a bridge in the pore. The magnification of the upper half of the S.E.I. photo is 5 X the one of the lower half, respectively ~2,380 X and ~476 (photo/negative = 1.4 x 340 X).

D) Small euhedral calcite (c) crystal growing in the intragranular secondary porosity, due to partial K-feldspar (Kf) dissolution, indicating the this calcite is a late phase in relation to the generation of the secondary porosity. Magnification of ~1,106 X (S.E.I. photo/negative = 1.4 x 790 X).

PLATE 9.18

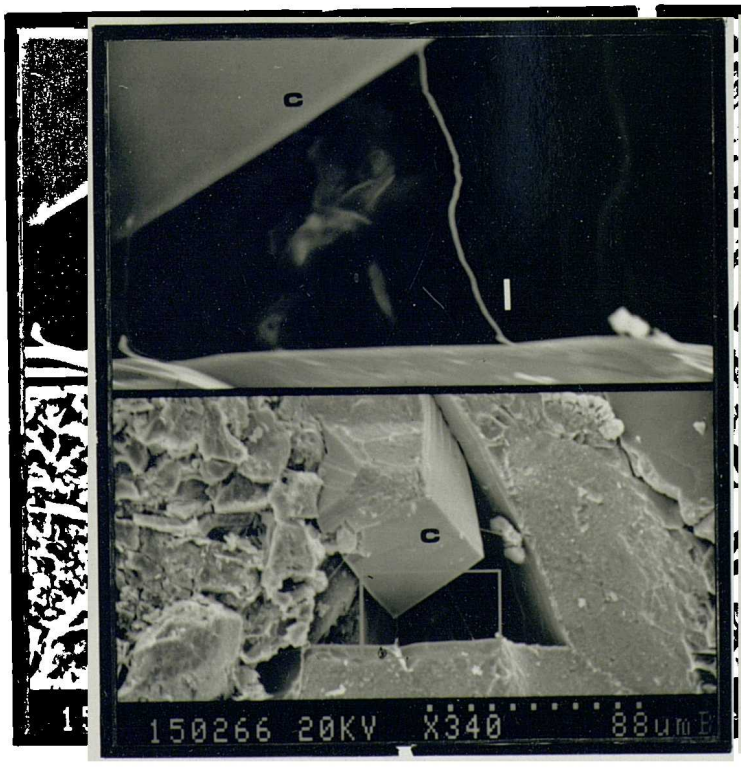
A



B



C



D



PLATE 9.19

A and **B**) Secondary pore in a gravelly-sandstone infilled with large euhedral calcite (EC) crystals. Observe the absence of grains in the zone cemented by this calcite. The area cemented with the early ferroan calcite (FC) is replete with grains. In the left top corner of the photo, at the transition of the two zones there is a rim of pyrite (PY) that has been precipitated after the formation of the secondary porosity. Another interesting feature in this thin-section is the presence of a nearly rectangular pore (P) at the right top corner of the photo characterized by the blue resin in natural light. In the bottom left corner of the photo **A** is marked the area shown by the photo **C**. Sample depth 2680 m. Photomicrographs (**A**) PPL and (**B**) XP. Scale bar 660 μm.

C) Cathodoluminescence photomicrograph showing an enlargement of the field marked on the photo **A**. Observe the brighter colours towards the edge of the euhedral calcite crystals, possible due to compositional variations. Bar scale 220 μm.

D) Cathodoluminescence photomicrograph showing the border between the secondary pore that has been infilled with the zoned euhedral calcite (EC), brighter region, and the region with grains of quartz (QZ), darker, and feldspar, blue, that has been cemented with the early ferroan (FC) calcite, dark area between the grains. Observe the local dissolution features characterized by the black sector with a reddish rim in the darker zone. The black rim on the euhedral calcite shown at the top right corner of the photo consists of pyrite (PY) that has been precipitated in this secondary pore prior to the precipitation of the euhedral calcite. Bar scale 55 μm.

PLATE 9.19

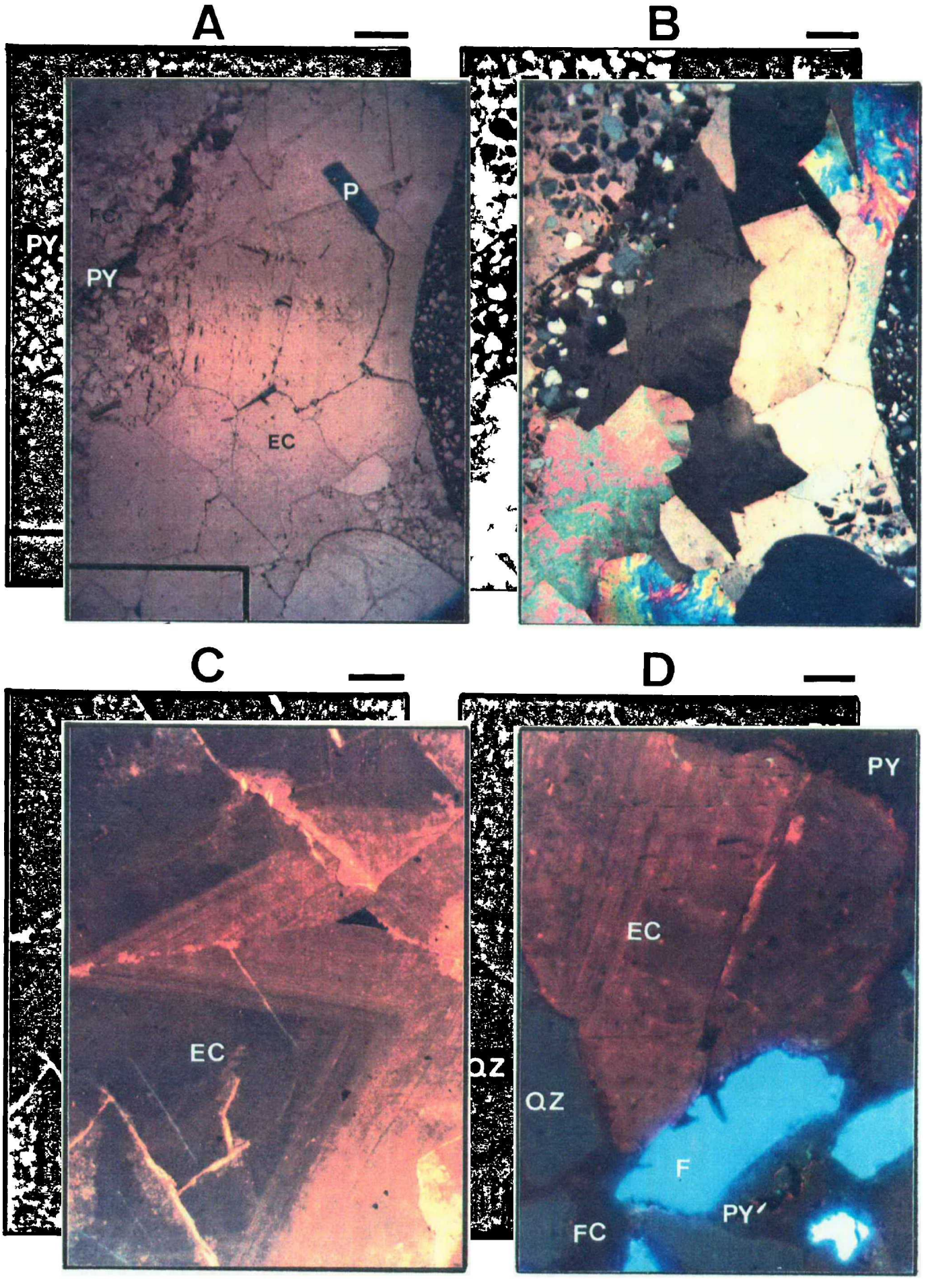


PLATE 9.20

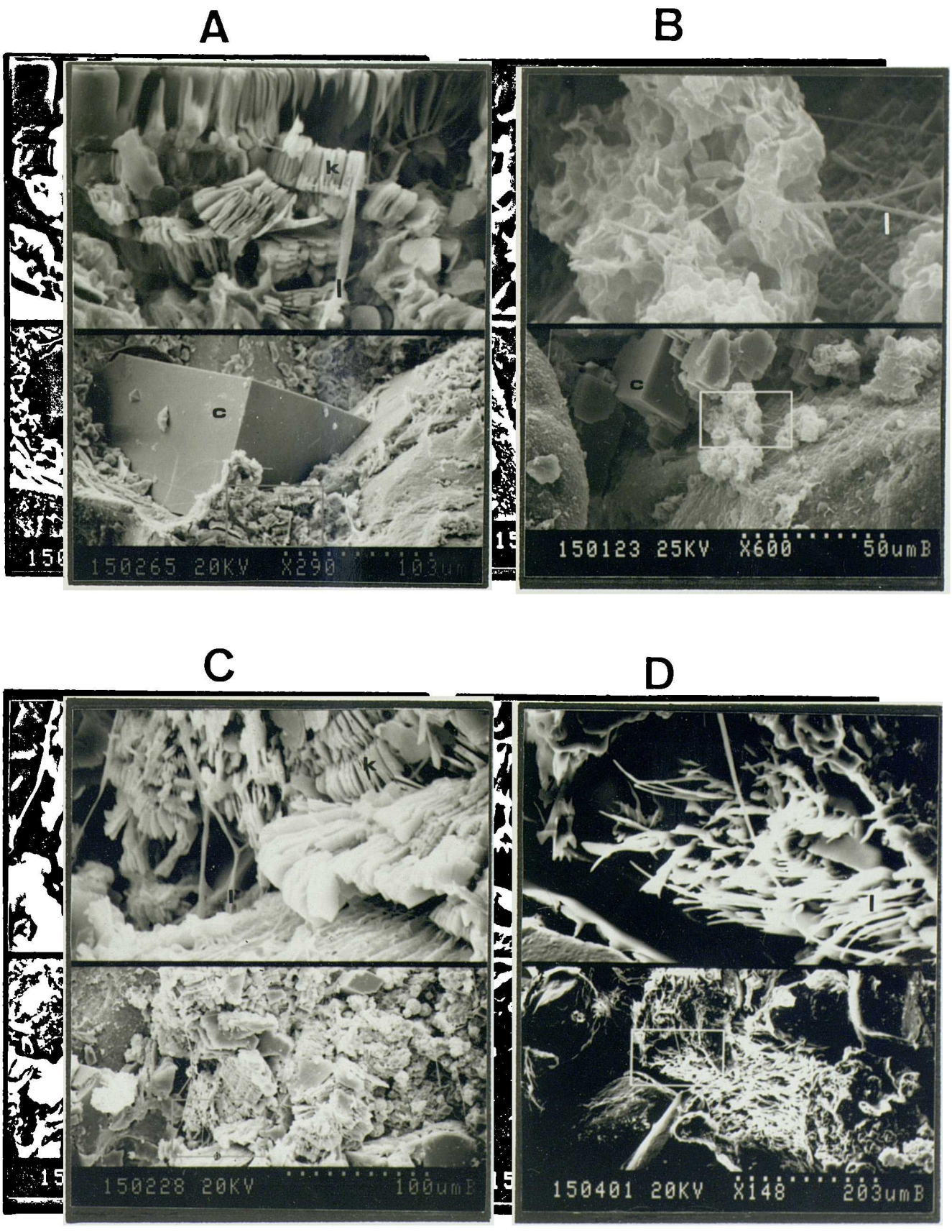
A) Euhedral calcite (c) associated with kaolinite and a few illite (I) fibres (?). The magnification of the upper half of the photo is 5 X the lower half, respectively ~2,030 X and ~406 (S.E.I. photo/negative = 1.4 x 290 X).

B) Illite (I) fibres (?) making a bridge between a detrital grain and a matrix particle. The magnification of the upper half of the photo is 5 X the lower half, respectively ~4,200 X and ~840 (S.E.I. photo/negative = 1.4 x 600 X).

C) Illite (I) fibres (?) associated with kaolinite. The magnification of the upper half of the photo is 5 X the lower, respectively ~2,100 X and ~420 X (S.E.I. photo/negative = 1.4 x 300 X).

D) Illite (I) fibres growing from a mudclast. The magnification of the upper half of the photo is 5 X the lower half, respectively ~1,036 X and ~207 X (S.E.I. photo/negative = 1.4 x 148 X).

PLATE 9.20


A
B
C
D
k
l
c
150265 20KV X290 103um
150123 25KV X600 50umB
150228 20KV 100umB
150401 20KV X148 203umB

9.5.15 FIBROUS ILLITE

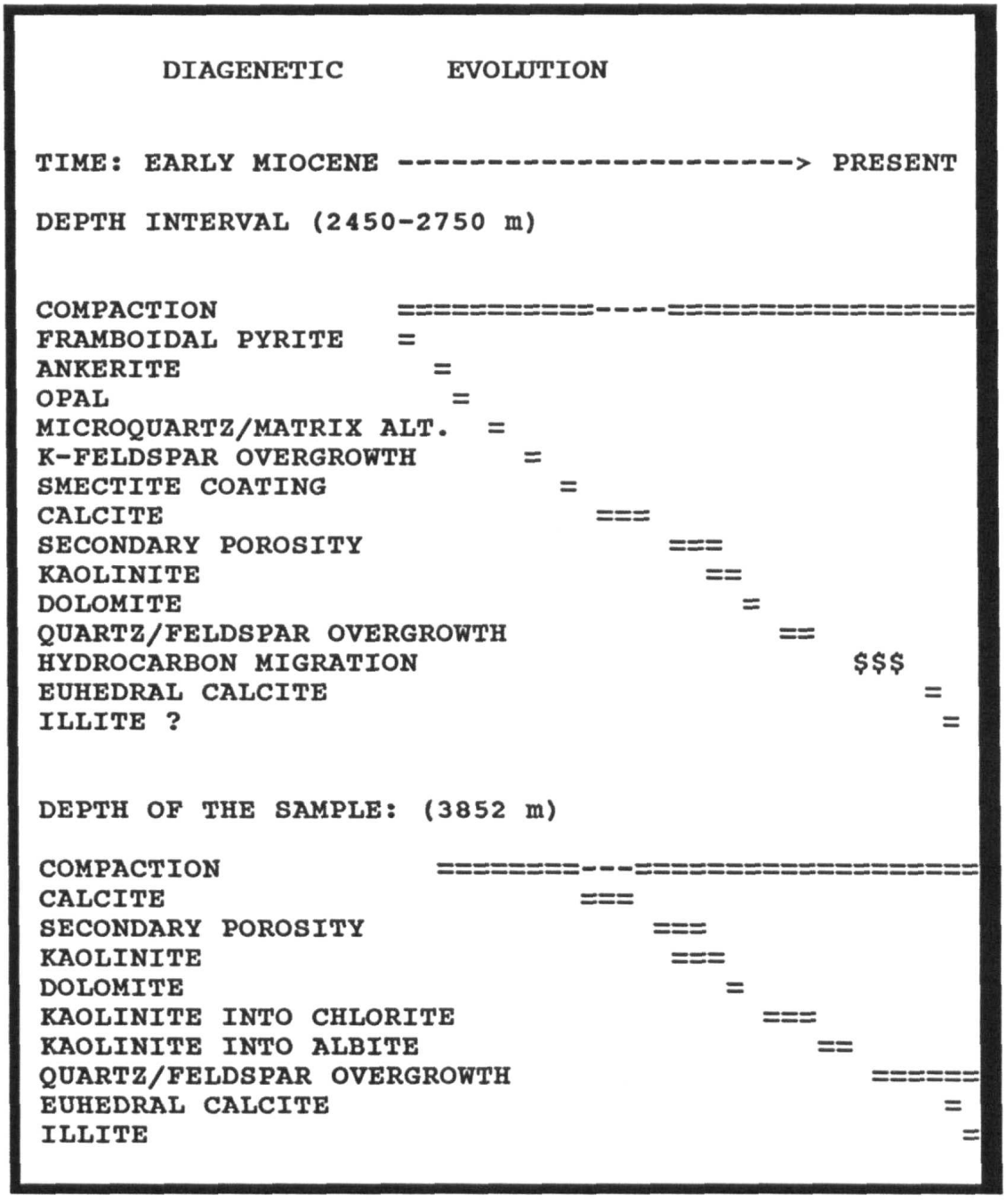
Minor amounts of illite are the last observed paragenetic phase of the diagenetic sequence. It occurs only as isolated fibres on kaolinite and feldspar/quartz overgrowths, and even on the euhedral calcite confirming its position as the latest diagenetic product (**plates 9.18 C** and **9.20 A-D**). It also has been developed as a recrystallization product of mudclasts in some sandstones (see **Plate 9.20 D**).

This form of illite has been found only in those sandstones that are presently in the water zone and as consequence it does not have any influence in the poro-permeability of the reservoirs containing hydrocarbons.

9.6 PARAGENESIS-DISCUSSION

The most probable paragenesis for the observed diagenetic phases of the Oligocene-Lower Miocene sandstones of the Campos Basin are summarized in below:

TABLE 9.2



In the next sections will be discussed some of the possible generative mechanisms for the major diagenetic phases.

generative mechanisms for the major diagenetic phases.

9.6.1 MICROQUARTZ CEMENT

Microquartz cements only occur in the Mottled Thin-bedded Very fine/fine-grained Sandstone (**MS** Lithofacies) interbedded with marlstone/mudstone and in the Gravelly/very coarse-grained Sandstone (Lithofacies **GvSm**). In the gravelly/very coarse-sandstones microquartz is associated with detrital matrix/pseudomatrix which has been diagenetically altered to a mixture of illite-smectite, authigenic chlorite and kaolinite. A similar situation has been described by Freitas (1987) and Moraes (1989).

In the very fine/fine-grained thin-bedded sandstones, the microquartz appears to be an early cement with only small amounts of associated authigenic smectite.

As described in Chapter 5, this Lithofacies **MS** was found within marlstone intervals occurring as isolated thin-beds (3-15 cm) of very fine/ fine-grained sandstone, commonly heavily bioturbated and in some cases with relatively large amounts (>5%) of heavy minerals (see **Plate 9.2 D**). These thin-bedded sandstones are usually interbedded within relatively thick sequences of mudrocks and the initial source of silica could have come from these mudrocks, probably via dissolution of siliceous organisms such as diatoms and radiolaria as suggested for the opaline cements of the Cretaceous turbidites of the Campos Basin by Freitas (1987).

9.6.2 CALCITE CEMENT

As was shown above (sections 9.5.7 and 9.5.14), there are two types of calcite cement, the more abundant ferroan variety with early diagenetic poikilotopic/equant crystal textures and the later diagenetic one with euhedral crystals and less iron infilling secondary pores, found only in the water zones.

The possible sources for the abundant early calcite in the studied succession could be: 1) surrounding marlstones; 2) partial dissolution of bioclasts in the sandstones; or 3)

example the Macaé Formation (see **Fig. 3.3** of the **Chapter 3**). The possible sources for the CO_2 could be from the mudrocks during thermal decarboxylation or fermentation of organic matter.

In some of the models presented in the literature (e.g. Curtis, 1978, 1983; and Gautier, 1985) part of the iron (Fe^{3+}) present in the mudrocks, adjacent to the sandstones, is consumed in the sulphate reduction zone to form framboidal pyrite. With further diagenesis the methanogenesis occurs, the available Fe^{3+} continues to be reduced and iron-rich carbonate is precipitated.

Associated with the methane-producing bacteria zone there is an important carbon isotopic fractionation with the generation of very light methane δ^{13} C values (-50 to -100 ‰), leaving residual pore water TDC (total dissolved carbon) enriched in δ^{13} C (Claypool and Kaplan, 1974; Nissenbaum et al., 1972; Deines, 1981; and Anderson & Arthur, 1983). Thus, as the bacterial methane production continues, the pore water TDC evolves to heavier δ^{13} C values. An example of this situation is shown in the **Figure 9.7** (from the Fig. 1-49 of Anderson & Arthur, 1983) where data from five sites of the Deep Sea Drilling Project were plotted. Note the initial excursion to negative δ^{13} C values, during the sulphate reduction zone, followed by an enrichment in δ^{13} C during the methanogenesis.

In theory, with increasing burial and compaction the waters enriched in δ^{13} C would migrate into adjacent porous sandstones and precipitate ferroan calcite at potential nucleation sites, such as bioclasts, if the conditions were favourable. As a result those intervals richer in these nucleation sites (bioclasts) would be the preferentially cemented zones and the calcite cement would be ferroan with predominantly positive carbon isotopic values (**Fig 9.7**).

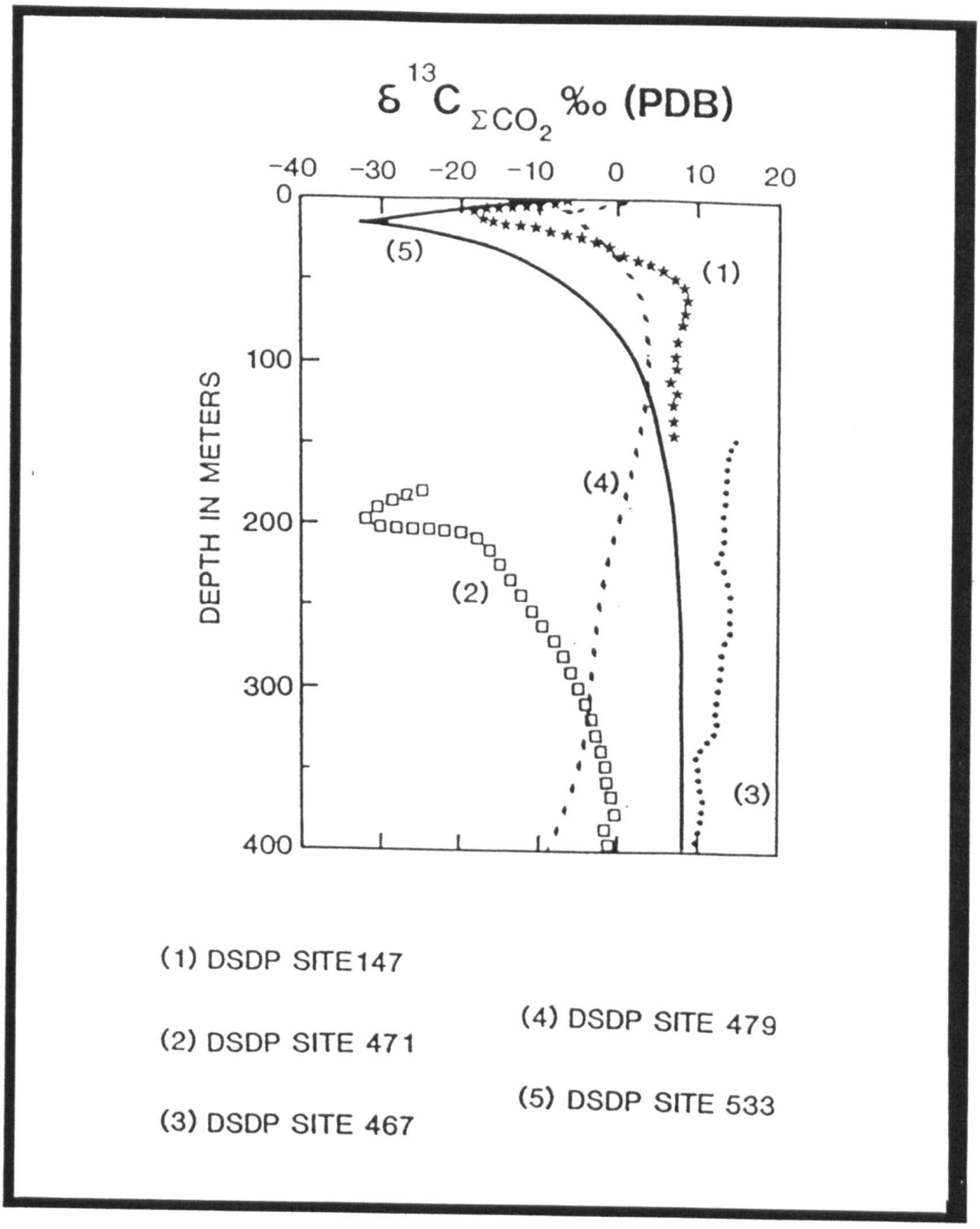


Figure 9.7 - δ^{13} C profiles of total CO_2 from pore waters of anoxic sediments recovered in five sites of the Deep Sea Drilling Project DSDP (Anderson & Arthur, 1983 Fig. 1-49).

The results of stable isotope analyses of the calcite[3] in seven sandstones samples are shown in the **Table 9.3.** Five of the calcite samples from coarse- and fine-grained sandstones had positive carbon isotopic values indicating an enrichment in δ^{13} C similar to that expected from the carbon generated in the methanic zone (Curtis, 1978; and Anderson & Arthur, 1983). The value of - 0.92 δ^{13} C $‰_{PDB}$ can be considered associated with this group of positive values, but contaminated by small amounts of calcite of a different origin.

The calcite sample from the gravelly/coarse-grained sandstone (**GvS** Lithofacies) has a strong negative value of -12.11 δ^{13} C $‰_{PDB}$ indicates a genesis not associated with the methanogenic zone. There was also a late diagenetic euhedral calcite infilling secondary porosity created by partial dissolution of the early ferroan calcite (**Plate 9.19**). This negative carbon isotopic value therefore represents a mixture of values from the early ferroan calcite and the late euhedral cement. The euhedral calcite cement must have had more negative carbon values to produce an average value of -12.11 δ^{13} C $‰_{PDB}$, when mixed with the likely positive carbon values of the early ferroan calcite. These negative carbon isotope values are probably the result of CO_2 liberated during the hydrocarbon generation. The isotopic composition of the oil found in these reservoirs has an average value of -24.7 δ^{13} C $‰_{PDB}$ (Mello, 1988; Trindade et al., 1987).

The oxygen isotopes values for the calcite cement were converted into equivalent formation temperatures using the formulae of Epstein et al. (1953) and Craig (1965), where δ^{18}Ow was assumed to be that of normal marine waters i.e. 0‰ SMOW (see **Table 9.3**). The estimated temperatures vary from 31°C to 46.5°C, respectively corresponding to -3.29 ‰ PDB and -6.17 ‰ PDB. As the lowest calculated temperature value is associated with the sample that has the late

[3] The isotopic analyses have been carried out using the bulk calcite, without differentiating its origin.

TABLE 9.3:

SOURCE OF THE DATA	$\delta^{13}C$ ‰ PDB	$\delta^{18}O$ ‰ PDB	$\delta^{18}O$ ‰ SMOW*
WELL: AB-1; 2606.70 m (O/W)	- 0.92	- 6.17	+ 24.04
fine-sand, early calcite		Temp = + 46.5°C	
WELL: 329; 2680.70 m (WATER)	- 12.11	- 3.29	+ 27.01
gravelly sandstone with		Temp = + 31.0°C	
early and euhedral calcite		*T = + 46.6 °C	
WELL: 329; 2686.10 M (WATER)	+ 8.62	- 5.83	+ 24.57
coarse-sand, early calcite		Temp = + 44.5°C	
WELL: 328; 2590.10 M (WATER)	+ 1.68	- 4.70	+ 25.56
fine-sand, early calcite		Temp = + 38.3°C	
WELL: 334; 2611.35 M (OIL)	+ 7.90	- 3.99	+ 26.29
coarse-sand, early calcite		Temp = + 34.5°C	
WELL: 335; 2657.25 M (OIL)	+ 2.80	- 4.75	+ 25.50
coarse-sand, early calcite		Temp = + 38.6°C	
WELL: 358; 2551.04 M (WATER)	+ 4.20	- 3.60	+ 26.69
coarse-sand, early calcite		Temp = + 32.6°C	

$\delta^{18}O‰_{SMOW} = 1.03\ \delta^{18}O‰_{PDB} + 30.4$ (Hudson, 1977).

WATER = sample in the water zone; O/W = sample in the transitional zone. The temperature was calculated based on Epstein et al (1953) & Craig (1965) formulae: $Temp = 16 - 4.14\ (\delta c - \delta w) + 0.13\ (\delta c - \delta w)^2$, where $\delta c = \delta^{18}O$ of calcite ‰PDB; $\delta^{18}O$ of water ‰SMOW, it was assumed that the δw= O‰SMOW. Additionally for the sample -3.29‰, with euhedral calcite, the temperature *T was calculated using δw= +2.3‰ from Franks & Forester, (1984).

diagenetic euhedral calcite a second temperature was calculated using an isotopic water value of +2.3 ‰ SMOW found in formation waters of a sandstone reservoir at 900 m from the Gulf Coast (Franks & Forester, 1984). The temperature calculated in this second way gives a value of 46.6°C.

The oxygen isotope derived temperatures indicate that the precipitation of the early ferroan calcite cement has probably occurred between 31°C and 46.5°C.

The interpretation of the paragenetic sequence of the diagenetic phases indicates that the euhedral calcite is a late phase that occurs only in the water zones, postdating the main oil migration. However, it is not possible to determine its likely temperature of formation from the isotopic data because of the presence of the early formed calcite in the sample analyzed.

In conclusion, it is possible that the early ferroan poikilotopic calcite was generated within the methanogenic fermentation zone. The later euhedral calcite was formed under the influence of the thermal decarboxylation of organic matter in the source rocks. That could explain the more negative values found in the sample with this late cement.

Moraes (1989) presented isotopic data for calcite cements from Cretaceous and Eocene turbidites of the Campos Basin that vary from + 0.4 to -20.1 δ^{13} C ‰ $_{PDB}$ with an average of -10 δ^{13} C ‰ $_{PDB}$, and +20.1 to 26.3 δ^{18}O ‰ $_{SMOW}$ with an average of + 23.29 δ^{18} O ‰ $_{SMOW}$. He interpreted these values as the result of precipitation of calcite generated during the decarboxylation of organic matter in the adjacent mudstones with the calcium coming from the underlying Macaé Formation, at temperatures between 40 to 75 °C.

By comparing the present isotopic data with those of Moraes (1989) it is very likely that his results are also the product of calcite cement generated in more than one phase, though he did not comment on this. The analyses were carried out on total calcite samples that could include

calcites of different origins. This could in part explain the differences in the iron content that he found in the calcite cements. The early calcite would be ferroan with positive carbon isotopic values, whilst the later would be poorer in iron and with more negative carbon isotopic values.

9.6.3 SECONDARY POROSITY

The dissolution of the calcite cement, bioclasts and some detrital feldspars were the main causes of secondary porosity in the analyzed sandstones. It is difficult to calculate how much secondary porosity was created during this process, and how much of the present porosity is primary or secondary. It appears that primary porosity is dominant, but there are some sandstones associated with the tight calcite cemented intervals in which the porosity is mainly secondary and it is possible to observe the transition between the tight and the porous sandstones. In spite of this evidence, it is difficult to be sure to what extent the sandstone have been more intensely cemented by calcite and then later dissolved, especially in those that have high porosity values of ~30%. Dissolution of the calcite has occurred but the degree of cementation/dissolution is still difficult to assess.

Many models have been proposed to explain secondary porosity phenomena, and amongst them the following are worthy of citation: Schmidt & McDonald (1979), Hayes (1979), Pittman (1979), Bjorlykke (1983), Curtis (1983), Surdam and Crossey (1985a and 1985b), Giles & Boer (1989), Burley et al. (1989), Smith & Ehrenberg (1989) and many others.

A model that has lately received much attention was the one published by Surdam and Crossey (1985a and 1985b). In their model the principal agents responsible for the generation of secondary porosity are the carboxylic and carbonic acids. Carboxylic acids are found in oil field brines and have their production peak in the temperature interval between 80º to 120ºC, mainly from type III organic

matter (Tissot et al., 1974 classification). As bacteria are destroyed above 80°C and the thermocatalytic degradation of kerogen increases with temperature, producing carboxylic acids ($CH_3\ COO^-$), the concentration of these acids can cause the dissolution of carbonate in the adjacent sandstones. One of the proposed ways to generate carboxylic acids in the model of Surdam and Crossey (1985a and 1985b) involves the transformation of smectite into illite. When mixed-layer illite-smectite becomes ordered there is possible mobilization of Fe^{+3}, which is then reduced by the organic matter ($CH_2O + 2Fe_2O_3 \rightarrow CO_2 + H_2O + 4FeO$). As a consequence of the oxidation of the kerogen the peripheral organic acid groups like phenolic and carboxylic would be released.

Other authors like Schmidt and Mcdonald (1979), Hayes (1979), and Curtis (1983) considered that the only critical parameter for the generation of the secondary porosity is the partial pressure of CO_2, produced during the thermal decarboxylation of the kerogen. However, on the other hand authors like Bjorlykke (1983) and Giles & Marshall (1986) do not consider the CO_2 and the carboxylic acids from the maturation of organic matter is likely to be sufficient to generate significant volume of secondary porosity. In the model of Bjorlykke (1983) the ingress of meteoric water is the principal mechanism responsible for secondary porosity. This appears to be applicable for continental, shallow water deposits or to rocks subject to subaerial erosion, but is not likely to be important for deep-water reservoirs such turbidites that have never been exposed subaerial.

In spite of all the controversies in the literature there is agreement that in one way or the other temperature, pH, CO_2 and organic acids play variably important roles in causing secondary porosity.

In the analyzed sandstones the depths and burial temperatures are relatively shallow and low, respectively 2450-2750 m and 48-87°C. Those wells that are located in water depths over 500 m have lower temperatures ~55°C (**Fig. 9.8**). This implies that the majority of the analyzed

succession is not in the temperature interval for peak generation of carboxylic acids (80-120°C) in the model of Surdam and Crossey (1985a and 1985b). In the adjacent mudrocks the most common type of organic matter is of type III, but is only present in small amounts (usually <0.7 weight%). In **Chapter 8** it was shown that in the analyzed mudrocks there is some alteration and dissolution of feldspars and kaolinite cementation in foraminiferal chambers, but the amount of diagenetic products observed in the shallower mudstones does not seems to be enough to explain all the diagenetic phases observed in the interbedded sandstones. Additionally the ordering and illitization of the smectite-rich (90% SM) illite-smectite have not occurred, in the analyzed succession, until depths and temperatures greater than 3,000 m and 95°C, respectively. In the Surdam and Crossey's (1985a and 1985b) model the transformation of smectite into illite with liberation of Fe^{+3} and consequent oxidation of the kerogen with generation of carboxylic acids could only have occurred in the deeper and hotter parts of the Campos Basin, such as the large downthrown blocks bounded by growth faults. The majority of the present temperatures in the studied succession (48-88°C) falls under the influence of bacterial fermentation at less than 80°C. This is well exemplified by the type of oil found in these sandstones, low A.P.I. degree (18-22°) and biodegraded (data from the Geochemical laboratory of Petrobrás). Probably, if reasonable amounts of carboxylic acids have been generated in the surrounding mudrocks part of it could have been involved in mudrock reactions and the remainder would probably have been largely destroyed by the bacterial activity at these low temperatures.

The general subsidence curve of the Campos Basin (**Fig. 9.9**) presented by Mohriak (1988) shows clearly that the major increase in subsidence after the deposition of the analyzed succession (Oligocene-Lower Miocene), has occurred in the last 10 million years. This indicates that the burial

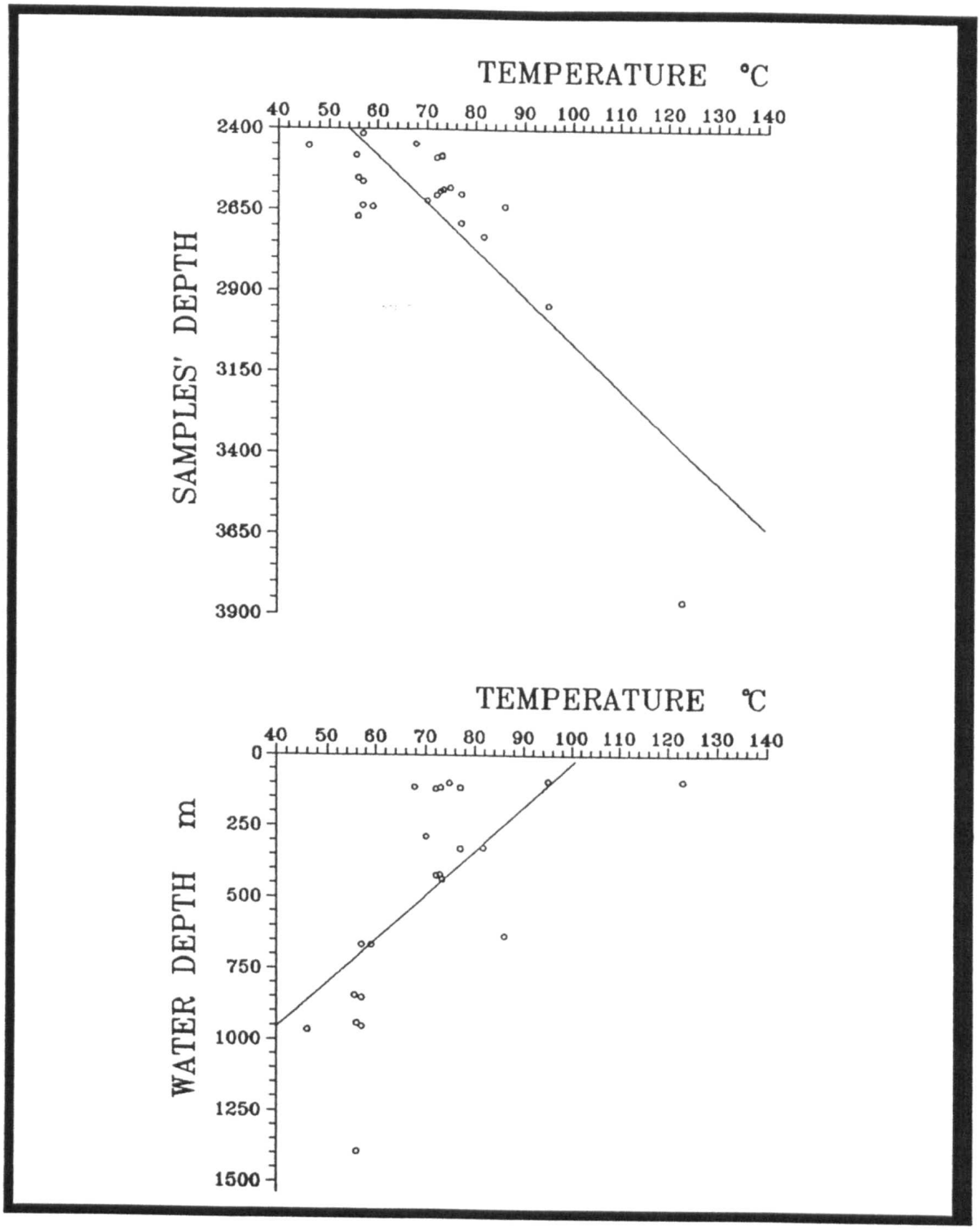


Figure 9.8 - Distribution of the temperatures of the samples in the analyzed sandstones.

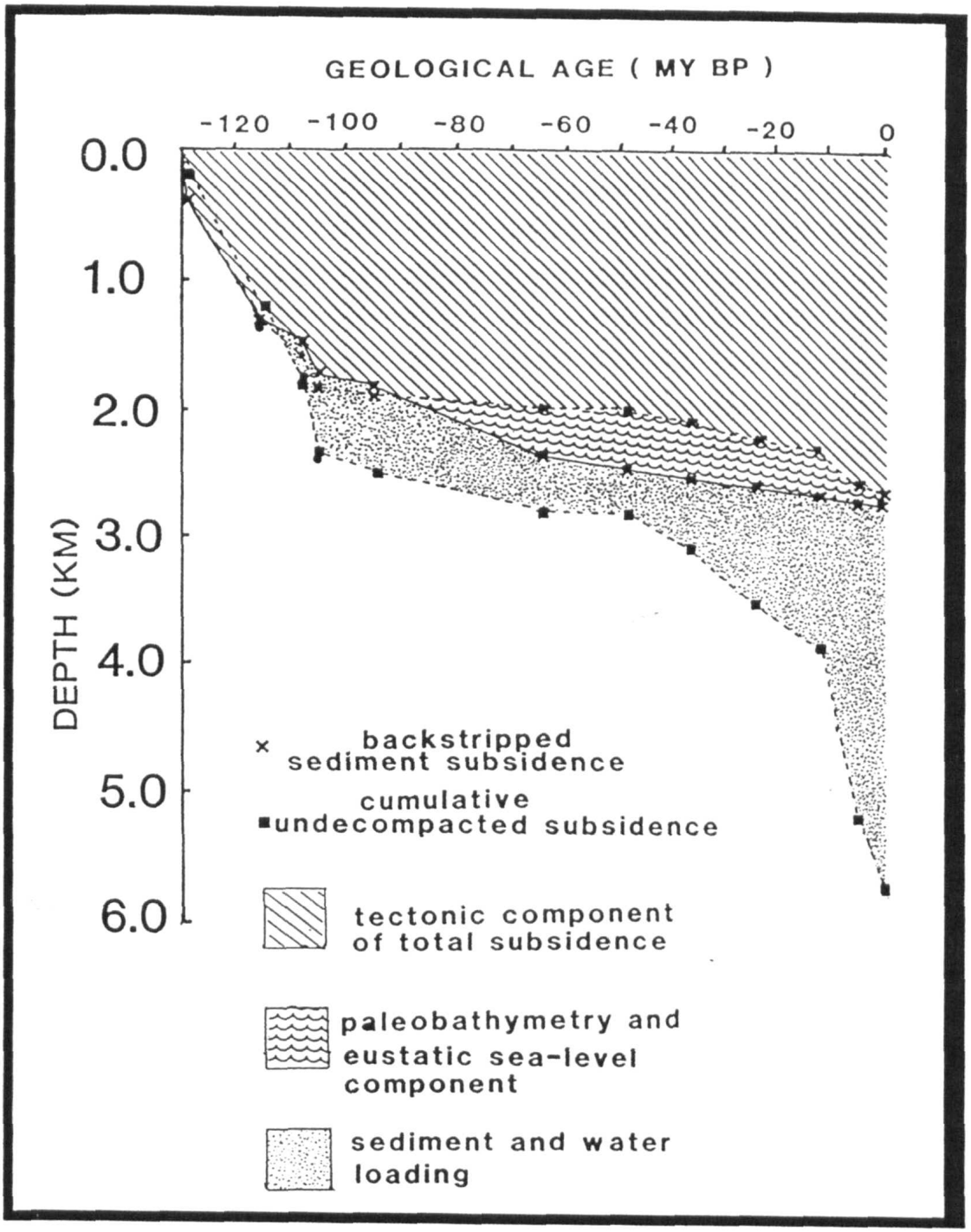


Figure 9.9 - General model of the subsidence curves obtained by backstripping the boreholes in the Campos Basin (Mohriak, 1988, Fig. 6.8).

temperatures affecting the studied succession, until a few millions years ago, were much lower than they are today.

Based on the data discussed above, it becomes very difficult to apply the Surdam and Crossey (1985a and 1985b) model if the source for the carboxylic acids came from the adjacent mudrocks.

A model that is more likely to explain the observed diagenetic phases and the generation of secondary porosity in these reservoirs is the one described by Giles and Boer (1989) and Burley et al (1989), in which migrating fluids, from deeper parts of the basin, moving along fault zones (seismic pumping mechanism: Sibson et al., 1975; and Sibson, 1981) generating secondary porosity and causing various diagenetic reactions.

The mechanism described by Giles and Boer (1989) is mainly concerned with the cooling of fluids when they migrate up through the basin succession via a fault or an aquifer. They have shown that the capacity for cementation or dissolution in an aquifer will depend on the initial pH of the fluids and the difference in temperature between the source of the fluid and the host reservoir. For pH values between 6.9 and 8.1 the cooling of the fluid causes oversaturation in relation to calcite and for values of pH below 6.9 the cooling causes undersaturation and as has a significant leaching potential.

As the sedimentary load has been increased by the progradation with a high sedimentation rate (15 cm/kyr) during the Miocene, the reactivation of faults has also increased and the seismic pumping mechanism (Sibson et al., 1975) could also be applied here. The mudrocks from the deeper sections could already have entered the hydrocarbon generation window with liberation of great volumes of CO_2 into the associated waters, and a possible lowering of the pH of the solution. When these fluids with lower pH have entered and cooled in the shallower reservoirs undersaturation in relation to calcite could have been reached, causing intense calcite leaching. Carboxylic acids

could also have migrated upward into these shallow reservoirs thus possibly providing, in part, the explanation for the leaching of some feldspar grains (Surdam and Crossey, 1985a), with the mobilization of aluminium and the absence of kaolinite in the vicinities of these leached grains. However, as the majority of the altered feldspars contain their alteration product, kaolinite, in situ it is very likely that any mobilization and transport of aluminium was only very limited.

Curtis (1983) has suggested that acid solutions encountering calcite in sandstones would dissolve it and as consequence the pH would rise. If these acidic fluids have also affected or dissolved the feldspars this increase in the pH would then encourage kaolinite supersaturation. The kaolinite precipitation would then be favoured by the change from more acidic to less acidic pore-waters. The evidence found in the analyzed sandstones seems to fit in with this kind of model in which hot fluids migrating along fault planes have entered the sandstones causing calcite dissolution and alteration of the feldspars, and as the pH changed to higher values, favoured the precipitation of kaolinite. Giles and Boer (1989) have also mentioned that hot fluids with lower pH can also be oversaturated in relation to silica, and by decreasing the fluid temperature quartz can be precipitated because its solubility decreases with decreasing temperature. This mechanism could also be used to explain the presence of quartz and feldspar overgrowths observed after the generation of the secondary porosity (**Table 9.2**).

Another possible application of this model could explain the presence of chlorite associated with the alteration products of the matrix in the sandstones of well 310. Fractures and slickensides were observed in the cored section indicating that this well crossed a fault zone and that hot fluids could have ascended along it causing the formation of the observed chlorite and other diagenetic events.

9.6.4 LATE DIAGENETIC PHASES IN THE DEEPEST SAMPLE

The diagenetic phases observed in the deepest sample (3852 m), within the water zone, were the generation of chlorite, albite and overgrowths of quartz and feldspar. Locally euhedral calcite and fibrous illite are also seen, but only as traces. Although there is little direct evidence, it is possible that part of the kaolinite in the deepest analyzed sandstone has been replaced in part by albite (**Plate 9.17**) and chlorite. In the deepest mudrock samples adjacent to this sandstone, chlorite was found replacing kaolinite (**Chapter 8, Plate 8.8**) and it is possible that a similar transformation could have also occurred in the adjacent sandstones. These kinds of transformations (**KAOLINITE** + ankerite + water = **CHLORITE** + quartz + calcite + CO_2 and **KAOLINITE** + quartz + NaCl + calcite = **ALBITE** + water + $CaCl_2$ + CO_2), at similar depths and temperatures have been reported from previous studies (Boles and Franks, 1979; Curtis, 1983; Smith and Ehrenberg, 1989).

Quartz and feldspar overgrowths appear to be the last diagenetic phase in this sample (see **Plate 9.17**)

9.7 CONCLUSIONS

The main diagenetic events observed in the sandstones from 2450-2750 m were calcite precipitation, secondary porosity generation via dissolution of bioclasts, calcite cement and feldspars (with associated precipitation of kaolinite). Other minor diagenetic products and phases were also observed but they have little volumetric importance. Nevertheless some of them can be locally important, such as the microquartz cement. In the deepest sandstone analyzed chlorite, albite and significant quartz/feldspar overgrowths were additionally found.

Two kinds of calcite cement were identified. An early diagenetic ferroan poikilotopic/equant calcite with positive δ^{13} C values generated probably from the carbon produced during the fermentation of the organic matter

(methanogenesis) in the adjacent mudstones during the early burial stages. The second is a late euhedral calcite that appears infilling secondary pores and only occurs in the water zone. This has negative δ^{13} C values, probably formed with the carbon produced during the thermal decarboxylation of the organic matter in deeper parts of the Basin.

Euhedral calcite and fibrous illite were observed only in the water zone and do not influence the properties of the hydrocarbon-bearing reservoirs, as their amounts in terms of effecting porosity reduction are insignificant.

The relatively small amounts of cements following the generation of secondary porosity in the shallow reservoirs is probably related to the rapid subsidence that has occurred in the Campos Basin during the last few millions years. This has meant that there has been a relatively short period of time between the generation of secondary porosity and subsequent infilling with hydrocarbon.

CHAPTER 10

SUMMARY AND CONCLUSIONS

The Oligocene-Lower Miocene succession of the Campos Basin in the studied area consists of upper bathyal foraminiferal-nannofossil marlstones, siliciclastic mudstones and sand-rich turbidites. Eight main depositional sequences have been identified. The sequences that embody the sand-rich turbidites are **1** (local nannofossil zone N-530/550-560) **2** (N-560), and **3** (N-570). Within these three sequences five main turbidite systems were identified, but locally up to eight systems can be recognized. They were deposited respectively during zones N-530 (Fan **a**), N-540 (Fan **b**), N-545 (Fans **c** and **d**)/N-550 (Fan **e**), N-560 (Fan **f**) and N-570 (Fans **g** and **h**).

The turbidite systems are characterized by:
a) hemipelagic sediments (Electrofacies Association **I**), b) channels (Electrofacies Association **II**); c) channel-lobe transition (Electrofacies Association **III**); d) and proximal lobes (Electrofacies Association **IV**), and e) localized contourite deposits (Electrofacies Association **V**).

The rocks of the Hemipelagite Electrofacies Association (**I**) are characterized by a cyclic interbedding of pelagic/hemipelagic Carbonate Mudstone/Marlstone Electrofacies (**G1/G2**) and the Mudstone Electrofacies (**G3/G4**). It represents the highstand deposits with the sedimentary cycles reflecting climatic cyclicity. The chalk/marlstones of the "BLUE MARKER", which is the effective basement of the studied succession, is an example of this type of electrofacies association.

The Channel Electrofacies Association (**II**) is characterized by (~30 m) channel-fill electrofacies (Gravelly Sandstones **GvS**, Diamictites **DMT**, Chaotic **F**, Amalgamated Sandstone **AmS**, Thick-bedded **FTab** and Muddy thin-

bedded **FTb-e** sand-mud couplets) and channel-margin/overbank electrofacies (Sandy Thin-bedded Sand-mud Couplets Electrofacies **E** and Mudstone Electrofacies **G3/G4**), whose thickness is around 5 m.

The Channel-Lobe Transition Electrofacies Association (**III**) is characterized by thick (~50 m) amalgamated (Amalgamated Sandstone Electrofacies **AmS**), and relatively continuous turbidite sandstones showing a characteristic "blocky" pattern in the wireline logs.

The Proximal Lobes Electrofacies Association (**IV**) is characterized by thick (30-120 m) and continuous (several Km) sandstone bodies, represented mainly by the Amalgamated Sandstone Electrofacies (**AmS**).

The Contourites Electrofacies Association (**V**) is characterized by Mottled Mudstones Electrofacies (**MM/MS**) which is the result of local reworking of fine-grained sediments by bottom currents and intense contemporaneous bioturbation.

The sand-rich turbidites systems (N-530, N-540 and N-545/N-550) of the Basal sequence (**1**) occur in seismic sections as high amplitude reflectors, which frequently show hummocky-clinoform patterns. These basal turbidite systems show an onlapping evolutional pattern (locally enhanced when associated with faults) that can be interpreted as a depositional environment controlled partially by the intermittent fall and rise of sea level from a maximum low position at about 30 Myr, within the zone N-530 (~31.5-28.5 Myr), to a high position in zone N-545/N-550 (~24-19 Myr). The upper turbidite systems (N-560/N-570), which occur in the depositional sequences **2** and **3**, are located at the base of the progradation of Lower Miocene slope sediments and relatively more offshore than the basal ones.

The lack of well developed levee-like features in the seismic sections, the condensed nature of the Oligocene succession, the very high sand:mud ratio and the relatively high proportion of shallow water bioclasts indicate that these turbidite sandstones were generated by high concentration turbidity currents, probably induced primarily

by littoral drift cells at the head of the Oligocene canyons during periods of relatively low sea-levels. These gravity flows are considered to have been deposited into broad lows created by the collapse of the underlying Aptian evaporites. The confinement of high density gravity flows in these lows together with the starved sediment conditions for the Basin, during the deposition of the basal part of this succession, were the main factors controlling the formation of these sand-rich turbidites. Additionally, the existence of a high relief source area due to the uplift of the Serra do Mar Mountains, a wave-dominated shelf and probably the absence of a major river would also have contributed to the concentration of sand in the coastal/shelf depositional environments during the highstands prior to their resedimentation into deep-water settings.

There were three main depocentres for the sand-rich turbidites: two in the northern and northern-most parts of the area and one in the south. The structural lows associated with the collapse of the underlying Aptian evaporites seem to have partially controlled the location of these depocentres. The Oligocene canyons mapped by Gamboa et al. (1986) coincide with the position of possible feeders for these turbidite depositional centres.

The characteristics of the Oligocene/Lower Miocene turbidite complex is similar to those of sand-rich fan systems models such as the "suprafan" lobes of Normark (1970) or the "poorly efficient"/Type II of Mutti (1979; 1985). Their seismic characteristic also resemble those of the basin-floor fan model of Vail (1987) and Posamentier & Vail (1988).

The turbidite systems appear to have been generated as a single depositional stage, characterized by sudden deposition of sand with a sharp termination. This is expressed as a box-like wireline log pattern. Subsequently, each system was overlain by deposition of pelagic/ hemipelagic sediments represented by cycles of marlstone/mudstones. The study of these sedimentary cycles using spectral analysis indicates that they represent

periodicities of ~19-23 Kyr, ~41 Kyr, ~100 Kyr and ~400 Kyr, compatible with the Milankovitch theory of climatic cycles. Additionally it was possible to establish that minor turbidite events, interbedded within marlstone/mudstones, occurred with a periodicity of about 400-500 Kyr, while the major turbidite sandstone events occurred within time intervals of the order of ~1.2-1.5 Myr.

Oxygen and carbon stable isotope analyses of benthonic foraminifera also show significant cyclical variations of the same order as those of the carbonate cycles (marlstone/mudstone couplets). However, it was not possible to define precisely their relationship with global sea-level variations because of the small number of isotopic determinations (29) and the influence of diagenetic effects and coastal/shelf depositional environment on the isotopic values.

The preference for the occurrence of sand-rich turbidites in only some stratigraphic intervals in the Campos Basin, such as Middle Eocene and Oligocene/Lower Miocene, indicates that the periodicities of these turbidites were probably linked with lower frequency phenomena such as major falls in relative sea-level. The latter could have been either eustatic or tectonic in origin or even a combination of these two. The eustatic curve presented by Haq et al. (1987), for the Tertiary, shows that major sea-level variations have periodicities of about 10 Myr. However, tectonic activity such as the Tertiary uplift of the source area could also have produced similar relative sea-level falls. Consequently, the phenomenon which has triggered the important sand-rich turbidites in the Campos Basin during the Oligocene-Lower Miocene could have been the result of resonance of climatic frequencies (e.g. Milankovitch band) superimposed on a lower frequency wave of either eustatic or tectonic origin, causing important sea-level falls during this period.

The determination of 30 Myr as the age for the base of the first turbidite system (Fan a) above the Blue Marker was based on spectral analysis using the Milankovitch theory and

assuming 32 Myr as the "absolute" age for the top of this marker. Accurate dating for the younger fans (**b, c, d, e, f, g, h**) was not possible, and will require more specific palaeontological studies, 3D seismic data and further spectral analysis. However, it is possible to say that they have been deposited most probably within the following age ranges: **b** = 26.5-25 Myr; **c** and **d** = 25-23 Myr; **e** = 23-19 Myr; **f** = 19-18 Myr; **g** and **h** = 18-16.5 Myr.

The age of 30 Myr for the base of the first fan above the Blue Marker sea-level coincides with the major Oligocene sea-level fall proposed by Haq et al. (1987). However, the estimated ages for the other turbidite systems (**b** to **h**) do not coincide very well with the eustatic sea-level curve of Haq et al. (1987). As there are still uncertainties about the absolute ages of these younger turbidite systems no final conclusion can be reached at this stage concerning the relationship between these younger events and the eustatic curves of Haq et al. (1987).

Detailed petrological analyses have been made of both mudrocks and sandstones to gain a more detailed understanding of the depositional and diagenetic environments.

The overall clay mineral compositions of the clay fractions of the mudrock lithofacies are very similar and reflect a predominantly detrital origin. The most significant variations are the relatively higher proportions of the illite-smectite in the Marlstone (G_2), the kaolinite in the Mottled Mudstone (MM). The only significant difference between the clay mineralogy of the mudstones and the turbiditic mudstones (top of the Bouma sequence = Tde) is a relatively lower ratio of I/S:I and K:I in the latter. However, this difference only applies to the shallow samples (2400-2950 m), because with increasing burial the illite-smectite appears to be illitized.

The mean clay mineral compositions of the shallower buried mudrocks (2400-2950 m and 48-95°C) consists of 55% of smectite-rich (90% SM) random illite-smectite, 25% illite and 20% kaolinite. In contrast, more deeply buried mudrocks

(3850-3860 m, 123°C) contain 50% illite-rich (10% SM) ordered illite-smectite, 30% illite and 20% kaolinite. This suggests that illitization of the illite-smectites probably has occurred over the narrow temperature range of 95° to 123°C. However, more samples of other deep buried mudstones are needed to confirm this illitization of the illite-smectites.

Based on X.R.D. and S.E.M. analyses the following diagenetic phases have been identified in the mudrocks: a) (2400-2950 m) framboidal pyrite, ferroan dolomite, calcite, local feldspar alteration, kaolinite and smectite infilling foraminiferal chambers; b) (3850-3860 m) partial calcite dissolution, chlorite replacing kaolinite in foraminiferal chambers, quartz/feldspar overgrowths and a probably ordering of the interstratified illite-smectites.

The turbidite sandstones are predominantly subarkoses and arkoses (Pettijohn et al., 1973) and the feldspar is mainly microcline. Bioclasts are common (average 5%), with coarse-grained sandstones enriched in shallow water species (echinoid, red algae and bryozoa), whilst the fine/very fine-grained sandstones contain deeper-water species of mainly benthonic and planktonic foraminifera.

The diagenetic phases and processes identified in the sandstones, based on XRD, electron and optical microscopy data, are as follows in approximate order of formation: a) (samples from 2450-2750 m, 45°C-85°C) framboidal pyrite, ankerite, microquartz, K-feldspar overgrowths, smectite coatings, widespread ferroan calcite either as a coarse equant mosaic or poikilotopic cements, generation of secondary porosity by dissolution of calcite and feldspars, replacement of feldspar and mica by kaolinite, growth of small rhombs of ferroan dolomite, K-feldspar/albite and quartz overgrowths, euhedral pyrite, euhedral calcite and illite (euhedral calcite and illite were only found in the water zone); b) (3850 m, 123°C) equant or poikilotopic calcite cements, secondary porosity (dissolution of calcite and feldspars) kaolinite, dolomite, chlorite, albite replacing kaolinite, significant quartz and feldspar

overgrowths, and minor amounts of euhedral calcite and illite.

The early diagenetic calcite has positive δ^{13} C values and it has probably been generated from the carbon produced during the fermentation of the organic matter in the adjacent mudstones during the early burial stages. The euhedral calcite, that appears infilling secondary pores and only occurs in the water zone, has negative δ^{13} C values and probably formed with the carbon derived from deeper parts of the Basin during the thermal decarboxylation of the organic matter.

The generation of the diagenetic phases and the secondary porosity in the sandstones appears to have been associated with formation fluids which originated in deeply buried successions such as those from the downthrown-block regions of the growth faults. The migration of fluids into shallower reservoirs, located in adjacent blocks related to such faults, would have probably been an intermittent but relatively continuous multiflow process, via seismic pumping as the faults developed. This mechanism seems to best explain the presence of several diagenetic phases in the shallow reservoirs within relatively low burial temperatures (45º - 85ºC).

The relatively small amounts of cements following the generation of secondary porosity in the shallow reservoirs is probably related to rapid subsidence which occurred in the Campos Basin during the last few million years. This indicates that there has been a relatively short period of time between the generation of secondary porosity in the reservoirs and their subsequent infilling by hydrocarbons. This was followed by a less active diagenetic and possibly shorter period indicated by the insignificant percentages of cements (illite and euhedral calcite) found in samples from the water zone.

REFERENCES

ALMEIDA, F. F. M., HASUI, Y., NEVES, B. B. B. (1976). The Upper Precambrian of the South America. Boletim IG, Instituto de Geociências da USP, v. 7, p. 45-80.

_____, et al. (1981). Brazilian structural provinces: an introduction. Earth Science Reviews, v. 17, p. 1-29.

AMARAL, G., et al. (1966). Potassium-argon dates of basaltic rocks from southern Brazil. Geochimica et Cosmochimica Acta, v. 30, p. 159-189.

ANDERSON, T. F. & ARTHUR, M. A. (1983). Stable isotopes of oxygen and carbon and their application to sedimentologic and paleoenvironmental problems. S.E.P.M. Short Course nº 10, Dallas, p. 1-151.

ANJOS, S. C. (1986). Absence of clay diagenesis in Cretaceous-Tertiary marine shales, Campos Basin, Brazil. Clay and Clay Minerals, v. 34, n. 4, p. 424-434.

APPI, C. J. & KOWSMANN, R. (1987). Modelo deposicional quaternário do cone do Amazonas. Rio de Janeiro, PETROBRAS/CENPES, Internal report, 56 p.

ARAUJO, M. B. and BEURLEN, G. (1975). Projeto Rio Paraíba do Sul - sedimentaçao deltaica Holocênica: Petrobrás Internal Report, DEXPRO/DIVEX, Rio de Janeiro.

ASMUS, H. E. and PORTO, R. (1972). Classificaçao das bacias sedimentares brasileiras segundo a tectonica de placas. In: Anais do XXVI Congresso Brasileiro de Geologia, v. 2, p. 67-90.

_____ (1975). Controle estrutural da deposiçao Mesozóica nas bacias da margem continental brasileira. Rev. Bras. Geoc. v. 5, p. 160-175.

_____ and PORTO, R. (1980). Diferenças nos estágios iniciais da evoluçao da margem continental brasileira: possíveis causas e implicaçoes. In: Anais do XXXI Congresso Brasileiro de Geologia, v. 1, p. 225-239.

_____ and Guazelli, W. (1981). Descriçao sumária das estruturas da margem continental brasileira e das áreas oceanicas e continentais, adjacentes. In: Projeto Remac, v. 9, p. 187-269.

_____ (1982). Significado geotectonico das feiçoes estruturais das bacias marginais brasileiras e áreas adjacentes. In: Anais do XXXII Congresso Brasileiro de Geologia, v. 4, p. 1547-1557.

AZAMBUJA FILHO, N. C. de & KOUTSOUKOS, E. A. M. (1990). Palaeoecology of the Oligocene-Lower Miocene turbidites and associated facies of the Campos Basin, offshore Brazil. In preparation.

BACOCCOLI, G. (1971). Os deltas marinhos holocênicos brasileiros - uma tentativa de classificaçao. Boletim Técnico Petrobrás, Rio de Janeiro, v. 14 (1/2) p. 5-38.

_____, G. & MORALES, R. G. (1973). Bacia do Espirito Santo: geologia e perspectivas petrolíferas. Rio de Janeiro, PETROBRAS, Internal report.

BAILEY, S. W. (1980). Structures of layer silicates. In: BRINDLEY, G. N. & BROWN, G., eds., Crystal structure of Clay Minerals and their x-ray identification, Min. Soc. Lond. 495 p., p. 1-123.

BAKER, P. A. and KASTNER, M. (1981). Constrains on the formation of sedimentary dolomite. Science, v. 213, p. 214-216.

BARROS, M. C. (1980). Geologia e recursos petrolíferos da Bacia de Campos. In: Anais do XXXI Congresso Brasileiro de Geologia, v. 1, p. 254-265.

BE, A. W. H., DAMUTH, J., LOTT, L., and FREE, R. (1976). Late Quaternary climatic record in western equatorial Atlantic sediment. Geol. Soc. of Am. Memoir 145, p. 165-200.

BEERBOWER, J. R. (1964). Cyclothems and cyclic depositional mechanisms in alluvial plain sedimentation. Kans. State Geol. Surv. Bull. v. 169, nº 1, p. 31-42.

BEIN, A. & WEILER, Y. (1976). The Cretaceous Talme Yale Formation, a contour current shaped sedimentary prism of carbonate debris at the continental margin of the Arabian

craton. Sedimentology, v. 23, p. 511-532.

BERGER, A. (1978). Long-term variations of caloric insolation resulting from the Earth's orbital elements. Quaternary Research, v. 9, p. 139-167.

_____, (1988). Milankovitch theory and climate. Rev. Geophys. v. 26 nº 4, p. 624-657.

_____, (1989b). Astronomical frequencies for pre-Quaternary palaeoclimate studies. Terra Nova, v. 1, nº 5, p.474-479.

BERNER, R. A. (1980). Early diagenesis - A theometrical approach. Princeton Univ. Press, 241 p.

BERTANI, R. T. & CAROZZI, A. V. (1984). Microfacies, depositional models and diagenesis of Lagoa Feia Formation (Lower Cretaceous), Campos Basin, Offshore Brazil. Ciência Técnica Petróleo, seçao: Exploraçao de petróleo nº 14, CENPES-PETROBRAS, 104 p.

BEURLEN, G. (1981). Correlaçao das unidades geocronológicas e biostratigráficas com os ciclos globais de variaçao do nível do mar. Petrobrás - Rio de Janeiro, Tabela Interna, DEPEX/LABOR/SEPALE.

_____, SHIMABUKURO, S., AZEVEDO, R., and UESUGUI, E. N. (1988). Carta bioestratigráfica da Bacia de Campos. Petrobrás.

BJORLYKKE, K. (1983). Diagenetic reactions in sandstones. In: Sediment Diagenesis, PARKER, A. and SELLWOOD, B. W. eds., Reidel, Dordecht, p. 169-213.

BOLES, J. R. & FRANKS, S. G. (1979). Clay diagenesis in Wilcox Sandstones of southwest Texas: implications of smectite diagenesis on sandstone cementation. Jour. Sed. Petrol. v. 49, p. 55-70.

BOUMA, A. H., (1962). Sedimentology of some Flysch Deposits; a Graphic Approach to Facies Interpretation. Elsevier, Amsterdam, 168 p.

_____ (1964). Ancient and recent turbidites. Geol. Mijnb., v. 43, p. 375-379.

_____, STELTING, C. E. and COLEMAN, J. M. (1985). Mississippi Fan, Gulf of Mexico. In: Submarine Fans and Related Turbidite Systems, 1985. (Edited by A. H. Bouma,

W. R. Normark, N. E. Barnes). p. 143-150. Frontiers in Sedimentary Geology, Spring-Verlag.

BOUDOU, J. P., DURAND, B., and OUDIN, J. L. (1984). Diagenetic trends of a Tertiary low-rank coal series. Geochimica et Cosmochimica Acta, v. 48, p. 2005-2010.

BREHME, I. (1984). Vales submarinos entre o Banco dos Abrolhos e Cabo Frio. Msc. Thesis. Universidade Federal do Rio de Janeiro -Instituto de Geociências. 116 p.

BRENNER, T. C., FERRARI, A. L., and PENHA, H. M. (1980). Lineamentos estruturais do nordeste do Estado do Rio de Janeiro. In: Anais do XXXI Congresso Brasileiro de Geologia, v. 5, p. 2551-2564.

BRINDLEY, G. W. (1980). Quantitative x-ray analysis of clays. In: BRINDLEY, G. N. & BROWN, G., eds., Crystal structure of Clay Minerals and their x-ray identification, Min. Soc. Lond. 495 p., p. 411-438.

BROECKER, W. A. aND VAN DONK, J. (1970). Insolation changes, ice volumes, and O^{18} record in deep-sea cores. Reviews of Geophysics v. 8, p. 169-198.

BROWN, G. (1980). Associated Minerals. In: BRINDLEY, G. N. & BROWN, G., eds., Crystal structure of Clay Minerals and their x-ray identification, Min. Soc. Lond. 495 p., p. 361-410.

BROWN, G. and BRINDLY, G. W. (1980). X-ray diffraction procedures for Clay Mineral identification. In: BRINDLEY, G. N. & BROWN, G., eds., Crystal structure of Clay Minerals and their x-ray identification, Min. Soc. Lond. 495 p., p. 305-359.

BURLEY, S. D., MULLIS, J., and MATTER, A. (1989). Timing diagenesis in the Tartan Reservoir (UK North Sea): constrains from combined cathodoluminescence microscopy and fluid inclusion studies. Marine and Petroleum Geology, v. 6, nº 2, p. 98-120.

CAMPOS, C. W. M. (1980). Estudo de um modelo para subsidência térmica da crosta terrestre. Boletim Técnico da Petrobrás, v. 23, p. 341-360.

CARMINATTI, M. (1987). Relaçoes entre a evoluçao estrutural e a ocorrência de campos gigantes na área nordeste da

Bacia de Campos. Rio de Janeiro, PETROBRAS, Internal report, 13 p.

CAROTHERS, W. W. and KHARAKA, Y. K. (1978a). Aliphatic acid anions in oil-field waters - implications for origin of natural gas. A.A.P.G. Bull., v. 62, p. 2441-2453.

_____ and _____ (1980). Stable carbon isotopes of HCO_3 in oil field waters-implication for the origin of CO_2. Geochim. et Cosmochim. Acta, p. 323-332.

CARSTENS, H., and FINSTAD, K.G. (1981). Geothermal gradients of the Northern North Sea Basin, 59-62ª N. Petroleum Geology of the Continental Shelf of North-West Europe, Institute of Petroleum, London, p. 152-161.

CASTRO, J. & AZAMBUJA FILHO, N. C. (1980). Fácies, análise estratigráfica e reservatórios da Formaçao Lagoa Feia, Cretáceo inferior da bacia de Campos. Rio de Janeiro, PETROBRAS, Internal report, 110 p.

_____, AZAMBUJA FILHO, N. C. & XAVIER, A. A. P. G. (1981). Fácies e análise estratigráfica da Formaçao Lagoa Feia, Cretáceo inferior da bacia de Campos, Brasil. In: Anais do VIII Congresso Geológico Argentino. San Luis, Actas II, p. 567-576.

CHATFIELD, C. (1984) The analysis of time series, an introduction. 3rd edition, London Chapman and Hall. 286 p.

CHOUGH, S. K. and HESSE, R. (1985). Contourites from Eirik ridge, south Greenland. Sedimentary Geology., v. 41, p. 185-199.

CLAYPOOL, G. E. and KAPLAN, I. R. (1974). The origin and distribution of methane in marine sediments. In: I. R. KAPLAN, ed., Natural gases in marine sediments. New York, Plenum Press, p. 99-139.

CORDANI, U. G. and BITTENCOURT, I. (1967). Determinaçoes de idades Potássio-Argonio em rochas do Grupo Açungui. In: Anais do XXI Congresso Brasileiro de Geologia, p. 159-165.

_____, and KAWASHITA, K. (1971). Estudo geocronológico pelo método Rb/Sr de rochas graníticas intrusivas no Grupo Açungui. In: Anais do XXV Congresso Brasileiro de Geologia, v. 1, p. 105-110.

_____, et al. (1972). Idades Potássio-Argonio da regiao leste brasileira. In: Anais do XXVI Congresso Brasileiro de Geologia, p. 71-75.

COTTLE, R A. (1989). Orbitally mediated cycles from the Turonian of southern England: their potential for high-resolution stratigraphic correlation. Terra Nova, v. 1, nº 5, p. 426-431.

COUTO , C. P. and MEZZALIRA, S. (1971). Nova Conceituaçao geocronológica de Tremembé, Estado de Sao Paulo, Brasil. In: Anais da Academia Brasileira de Ciências, v. 43 (sup), p. 473-488.

COX, R. E. (1984). Early Tertiary submarine clastic fans of the North Sea. In Course Notes Nº 29, Part 2 of Joint Association for Petroleum Exploration Courses (JAPEC-UK), 132 p.

CRADDOCK, J. M. (1968). Statistic in the computer age. Unibooks, English Universities Press, 214 p.

CRAIG, H. (1957). Isotopic standards for carbon and oxygen and correction factors for mass spectrometric analysis of carbon dioxide. Geochim. Cosmochim. Acta, v. 12, p. 133-49.

_____, (1965). The measurement of oxygen isotope paleotemperatures. In: TONGIORGI, E. ed. Stable isotopes in oceanographic studies and paleotemperatures. Consiglio Nazionale delle Richerche, Laboratorio de Geologia Nucleare, Pisa, p. 161-182.

CRIMES, T. P. (1973). From the limestones to distal turbidites: a facies and trace fossil in the Zumaya flysch (Palaeocene-Eocene), North Spain. Sedimentology, v. 20, p. 105-131.

_____ (1976). Sand fans, turbidites, slumps and the origin of the Bay of Biscay: A facies analysis of the Guipuzcoan flysch. Palaeogeography, Palaeoclimatology, Palaeoecology, v. 19, p. 1-15.

CURTIS, C. D. (1978). Possible links between sandstone diagenesis and depth-related geochemical reactions occurring in enclosing mudstones. J. Geol. Soc. Lond., v. 135, p. 107-117.

_____ (1983). Geochemistry of porosity enhancement and reduction in clastic sediments. In: Petroleum Geochemistry and Exploration of Europe. Brooks (ed.), Blackwell Scientific/Geological Society, London, p. 113-125.

DAMUTH, J. E. et al. (1983). Distributary channel meandering and bifurcation patterns on the Amazon deep-sea fan as revealed by long-range side-scan sonar (GLORIA). Geology, v. 11 (2), p. 94-98.

DEINESS, P. (1981). The isotopic composition of reduced organic carbon. In: Handbook of environmental isotope geochemistry, P. FRITZ and J. C. FONTES (eds.), v. 1, Elsevier, p. 329-406.

DELLA FAVERA, J. C. et al. (1975). Projeto Carapebus. Rio de Janeiro, PETROBRAS-CENPES, Internal report.

DENTON, G. H. and HUGHES, T. J. (Eds.) (1981a). The Latest Great Ice Sheets. Wiley-Interscience, New York.

_____, _____ (1983). Milankovitch theory of Ice Ages: Hypothesis of ice-sheet linkage between regional insolation and global climate. Quaternary Research, v. 20, p. 125-144.

DEWEY, J. F. and BIRD, J. M. (1970). Mountain belts and the new global tectonics. Journal of Geophysical Research, v. 75, p. 2625-2647.

DIAS, J. L., GUAZELLI, W., CATTO, A. J. and VIEIRA, J. C. (1987). Integraçao do arcabouço estrutural da Bacia de Campos com o embasamento pré-cambriano adjacente. In: Anais do I Simp. Geol. RJ-ES, Rio de Janeiro, v. 1, p. 189-197.

DIAS BRITO, D. (1987). A bacia de Campos no Meso-Cretáceo: uma contribuiçao a paleoceanografia do Atlantico Sul primitivo. Revista Brasileira de Geociências, v. 17 (2), p. 162-167.

DICKINSON, W. R. (1970). Interpreting detrital modes of greywacke and arkose. Jour. Sed. Pet., v. 40, p. 695-707.

DNPM (1978). Carta Geológica do milionésimo. Ministério das Minas e Energia, Brasil.

DOMINGUEZ, J. M. L., MARTIN, L. and BITTENCOURT, A. C. S. P. (1987). S.E.P.M. Special Publ., nº 41, p. 115-128.

DOTT, R. H. Jr. (1964). Wacke, graywacke and matrix - what approach to immature sandstone classification ? Jour. Sed. Pet. v. 34, p. 625-632.

DUNHAM, R. J. (1962). Classification of carbonate rocks according to depositional texture. A.A.P.G. Memoir nº 1, p. 108-121.

EPSTEIN, S., BUCHSBAUM, H. A., and UREY, H. C. (1953). Revised carbonate water isotopic temperature scale. Geol. Soc. Am. Bull., v. 64, p. 1315-1326.

ESLINGER, E. and PEVEAR, D. (1988). Clay Minerals for petroleum geologists and engineers. S.E.P.M. Short Course nº 22. Tulsa, U.S.A., 215 p.

FAIRBANKS, R. G. (1989). A 17,000-year glacio-eustatic sea level record: influence of glacial melting rates on the Younger Dryas event and deep-ocean circulation. Nature v. 342, 7 December, p. 637-642.

FALKENHEIN, F. U. H. , FRANKE, M. R., and CAROZZI, A. V. (1981). Petroleum geology of Macaé Formation (Albian-Cenomanian), Campos Basin, Brazil (Carbonate microfacies-deposicional and diagenetic models - natural and experimental porosity): Petrobras, CENPES, Ciência Técnica Petróleo, seçao exploraçao de petroleo nº 11, 140 p.

FEELEY, M. H. , MOORE JR, T. C., LOUTIT, T.S. and BRYANT, W. R. (1990). Sequence stratigraphy of Mississippi Fan related to oxygen isotope sea level index. A.A.P.G. Bull., v. 74, p. 407-424.

FERTL, W. H. and WICHMANN. P. A. (1977). How to determine static BHT from well log data. World Oil, v. 184, nº 1, p. 105-106.

FIGUEIREDO, A. M. F. & GABAGLIA, G. P. R. (1986). Sistema classificatório aplicado às bacias sedimentares brasileiras. Revista Brasileira de Geociências, v. 16, nº 4, p. 350-369.

FISCHER, A. G. (1986). Climatic rhythms recorded in strata. Ann. Rev. Earth Planet. Sci. v. 14, p. 351-376.

FOLK, R. L. and WARD, W. C. (1957). Brazos River Bar: A study in the significance of grain size parameters. Jour. Sed. Petrology, v. 27, p. 3-27.

FRANCHETEAU, J. and LE PICHON (1972). Marginal fracture zones as structural framework of continental margins in South Atlantic ocean. A.A.P.G. Bull., v. 56, p. 991-1007.

FRANKS, S. G. and FORESTER, R. W. (1984). Relationships among secondary porosity, pore-fluid chemistry and carbon dioxide, Texas Gulf Coast. In: Mcdonald, D. A. and Surdam, R. C. (eds.), Clastic diagenesis, A.A.P.G. Memoir 37, p. 63-79.

FREITAS, L. C. S. de (1987). Estudo de reservatório do Membro Carapebus (Cretáceo) no Campo de Carapeba, Bacia de Campos, Estado do Rio de Janeiro, Brazil. Msc. thesis, Universidade Federal de Ouro Preto, Brazil, 130 p.

GAMBOA, L. A. P., ESTEVES, F. R., SHIMABUKURO, S., CARMINATTI, M., PERES, W. E., SOUZA CRUZ, C. E. (1986). Evidências de variaçoes do nível do mar durante o Oligoceno e suas implicaçoes faciológicas. In: Anais do XXXIV Congresso Brasileiro de Geologia, 23 p.

GAUTIER, D. L. (1985). Interpretation of early diagenesis in ancient marine sediments. In: D. L. GAUTIER et al. eds., Relationships of organic matter and mineral diagenesis. Lecture notes, S.E.P.M. Short Course nº 17, p. 6-78.

GILES, M. R. and MARSHALL, J. D. (1986). Constrains on the development of secondary porosity in the subsurface: re-evaluation of processes. Marine and Petrol. Geol., v. 3, p. 243-255.

_____ and BOER, R. B. de (1989). Secondary porosity: creation of enhanced porosities in the subsurface from the dissolution of carbonate cements as a result of cooling formation waters. Marine and Petroleum Geology, v. 6, nº 6, p. 261-269.

GOLDSTEIN, J. I., NEWBURY, D. E., ECHLIN, P.: JOY, D. C. FIORIC, D., LIFSHIN, E. (1981). Scanning electron microscopy and x-ray microanalysis. Plenum Press, London.

GONTHIER, E. G., FAUGERES, J. -C., and STOW, D. A. V. (1984). Contourite facies of the Faro Drift, Gulf of Cadiz. In: Fine-grained sediments: Deep-water processes and facies, STOW, D. A. V. and PIPER, D. J. W. (eds.),

Geological Society Special Publication nº 15, p. 275-292.
GUARDADO, L. R. & ARSO, L. R. (1985). Cenário regional e expressao sísmica dos turbiditos da Bacia de Campos. Rio de Janeiro, PETROBRAS/DEPEX, Internal report.
_____, GAMBOA, L. A. P. and LUCCHESI, C. S. (1990). Petroleum Geology of the Campos Basin, Brazil; A model for a production atlantic type basin. In: J. D. EDWARDS and D. A. SANTAGROSSI (eds.), Divergent/passive margin basins, A.A.P.G. Memoir 48, p. 3-81.
HALLOCK, P. (1987). Fluctuations in the trophic resource continuum: A factor in global diversity cycles? Paleoceanography, v. 2, nº 5, p. 457-471.
HAQ, B. U. , HARDENBOL, J. , VAIL, P. R. (1987). Chronology of fluctuating sea level since the Triassic. Science, v. 235, p. 1156-1167.
HARALYI, N. and HASUI, Y. (1982). Compartimentaçao geotectonica do Brasil oriental com base na informaçao geofísica. In: Anais do XXXII Congresso Brasileiro de Geologia.
HARBAUGH, J. W. & MERRIAM, D. F. (1968). Computer applications in stratigraphic analysis. John Wiley & Sons, Inc., London, 282 p.
HARMS, J. C. & FAHNESTOCK, R. K. (1965). Stratification, bed forms and flow phenomena (with an example from the Rio Grande). In: Primary sedimentary structures and their hydrodynamic interpretation, G. V. Middleton , ed., Soc. Econ. Paleont. Mineral. Spec. Publ. nº 12, p. 84-115.
HASUI, Y. and PONÇANO, W. L. (1978). Organizaçao estrutural da bacia de Taubaté. In: Anais do XXX Congresso Brasileiro de Geologia, v. 1, p. 368-381.
_____ and OLIVEIRA, M. A. F. (1984). Província Mantiqueira -Setor Central. In: O Precambriano do Brasil, eds. Almeida, F. F. M. and Hasui, Y., p. 308-344.
HAYES, J. B. (1979). Sandstone diagenesis - the hole truth. In: SCHOLLE, P. A. & SCHLUGER, P. R. eds., Aspects of Diagenesis. Spec. Publ. nº 26, S.E.P.M., Tulsa, Oklahoma, p. 127-139.

HAYS, J. D., IMBRIE, J. and SHACKLETON, N. J. (1976). Variations in the earth's orbit: Pacemaker of the ice ages. Science, v. 194, p. 1121-1132.

HEEZEN, B. C., HOLLISTER, C. D. & RUDDIMAN, W. F. (1966). Shaping of the continental rise by deep geostrophic contour currents. Science, v. 152, p. 502-8.

HOWER, J., ESLINGER, E. V., HOWER, M. E., and PERRY, E. A., Jr. (1976). Mechanism of burial metamorphism of argillaceous sediments: Mineralogical and chemical evidence. Geol. Soc. Amer. Bull., v. 87, p. 725-737.

HUDSON, J. S. (1977). Stable isotopes and limestone lithification. Journal of the Geological society of London, v. 133, p. 637-660.

IMBRIE, J. & IMBRIE, K. P. (1979). Ice Ages: Solving the Mistery. Short Hills, Nj: Enslow, 224 p.

_____, and IMBRIE, J. Z. (1980). Modelling the climatic response to orbital variations. Science, v. 207, p. 943-53.

_____, HAYS, J. D., MARTINSON, D. G., McINTYRE, A., MIX, A. C., MORLEY, J. J., PISIAS, N. G., PRELL, W. L., and SHACKLETON, N. J. (1984). The orbital theory of Pleistocene climate: support from a revised chronology of marine $\delta^{18}O$ record. In: A. L. BERGER et al. (eds.), Milankovitch and Climate, Part I, D. Reidel Publishing Company, p. 269-305.

JENKINS, G. M. and WATTS, D. G. (1968). Spectral Analysis and its Applications. San Francisco: Holden-Day.

JOPLING, A. V. and WALKER, R. G., (1968). Morphology and origin of ripple-drift cross lamination with examples from the Pleistocene of Massachussetts. J. Sediment. Petrol., v. 38, p. 971-984.

KELTS, K. and MacKENZIE, J. A. (1982). Diagenetic dolomite formation in Quaternary anoxic diatomaceous muds of the DSDP Leg 64, Gulf of California. In: Initial Reports of the Deep Sea Drilling Project, v. 64, pt. 2, p. 553-569.

KIGSTON, D. R. , DISHROON, C. P. , WILLIAMS, P. A. (1983). Global basin classification system. A.A.P.G. Bull., v. 67, p. 2175-2193.

KLEMME, H. D. (1971). The giants and the super giants - Part 1, What giants and their basins have in common: The Oil and Gas Journal, March 1, p. 85-90.

KOLLA, V. & COUMES, F. (1987). Morphology, internal structure, seismic stratigraphy, and sedimentation of Indus Fan. A.A.P.G. Bulletin, v. 71, nº 6, p. 650-677.

KOUTSOUKOS, E. A. M. (1984). Evoluçao paleoecológica do Albiano ao Maastrichtiano na área noroeste da Bacia de Campos, Brasil, com base em foraminíferos. In: Anais do XXXIII Congresso Brasileiro de Geologia, v.2, p. 685-698.

_____ (1985). Evoluçao paleoecológica do Albiano ao Maastrichtiano na área noroeste da Bacia de Campos. Petrobrás/CENPES, Internal report.

_____ (1987). A área noroeste da Bacia de Campos, Brasil, do Mesocretáceo ao Neocretáceo: evoluçao paleoambiental e paleogeográfica através de estudos de foraminíferos. In: Anais do IX Congresso Brasileiro de Paleontologia.

_____ & DIAS-BRITO, E. (1987). Paleobatimetria da margem continental do Brasil durante o Albiano. In: Anais do IX Congresso Brasileiro da Paleontologia.

KOWSMANN, R. O. & COSTA, M. P. de A. (1974). Paleolinhas de costa na plataforma continental das regioes sul e norte brasileira. Revista Brasileira de Geociências, v. 4, p. 215-222.

_____ (1980). Bancos arenosos holocênicos da plataforma continental brasileira: Gênese e potencial mineral. Notícia Geomorfológica v. 20 nº 39-40, p. 3-20.

KRUIT, C., BROUWER, J. & EALEY, P. (1972). A deep-water fan in the Eocene Bay of Biscay. Nature, Physical Science, v. 240, p. 59-61.

KRUIT, C., BROUWER, J., KNOX, G., SCHOLLNBERGER, W., Van VLIET, A. (1975). Une excursione aux cones d'alluvion en eau profonde d'age Tertiaire pre de San Sebastian. Guide pour l'excursion Z-23. IXe Congres International de Sédimentologie, Nice, France, 50 p.

KRYNINE, P. D. (1935). Arkose deposits in the humid tropics, a study of sedimentation in the southern Mexico. Am. Jour. Sci., v. 29, p. 353-363.

KVASOV, D. D. and VERBITSKY, M. YA. (1981). Causes of Antarctic Glaciation in the Cenozoic. Quaternary Research, v. 15, p. 1-17.

LEYDEN, R. (1976). Salt distribution and crustal models for the eastern Brazilian margin. In: Anais da Academia Brasileira de Ciências, v. 48, sup., p.159-168.

_____ et al. (1976). South Atlantic diapiric structures. A.A.P.G. Bulletin, v. 60, p. 196-212.

LIBBY, L. M. (1983). Past Climates. Austin, Univ. Tex. Press. 143 p.

LLOYD, M. G. and HALL, G. E. (1981). The S.E.M. examination of geological samples with a semi-conductor back-scattered electron detector. Amer. Mineral, v. 66, p. 362-368.

LOUTIT, T. S., HARDENBOL, J., VAIL, P. R., and BRAUM, G. R. (1988). Condensed sections: The key to age determination and correlation of continental margin sequences. In: Sea-Level Changes - An integrated Approach, S.E.P.M. Special Publication nº 42, p. 183-213.

MacGOWAN, D., and SURDAM, R. C. (1988). Difunctional carboxylic acid anions in oil-field waters. Organic Geochemistry, v. 12, p. 245-259.

MARTINI, E. (1971). Standard tertiary and quaternary calcareous nanoplankton zonation. In: FARINACCI, A. , ed. Proc. II Plankt. Conf. Roma, Rome, Edizioni Tecnoscienza. v. 2, 739-785.

McBRIDE, E. E. (1985). Sandstone diagenesis. Soc. Econ. Paleont. (Lec. notes for short course), 33 p.

MECHALAS, B. J. (1974). Pathways and environmental requirements for biogenic gas production in the ocean. In: KAPLAN, I. R. ed., Natural gases in marine sediments. Plenum Press, p. 11-25.

MEIS, M. R. M. & AMADOR, E. S. (1977). Contribuiçao ao estudo do Neocenozoico da baixada da Guanabara - Formaçao Macacu. Revista Brasileira de Geociências, v. 7 nº 2, p. 150-174.

MELLO, M. R. (1988). Geochemical and molecular studies of the depositional environments of source rocks and their derived oils from the Brazilian Marginal Basins. PhD

thesis, Bristol University, 273 p.

_____, GAGLIANONE, P. C., BRASSELL, S. C., MAXWELL, J. R. (1988c). Geochemical and biological marker assessment of depositional environment using Brazilian offshore oils: Marine and Petroleum Geology, v. 5, n. 3, p. 205-223.

MIDDLETON, G. V. (1967). Experiments on density and turbidity currents: III. Deposition sediment. Can. Journ. Earth Sci., v. 4, p. 475-505.

MILANKOVITCH, M. (1941). Kanon der Erdbestrahlung und seine Anwendung auf das Eiszeitenproblem. Akad. Royale Serbe 133, 633 p.

MILLOT, G. (1964). Géologie des argiles; altérations, sédimentologie geochimie. Paris, Masson et Cie.

MITCHUM, R. M. Jr. (1977). Seismic stratigraphy and global changes of sea level, part II: Glossary of terms used in seismic stratigraphy. In: Clayton, C. E., ed., Seismic Stratigraphy-Applications to Hydrocarbon Exploration. Tulsa. A.A.P.G. Memoir nº 26, p. 205-212.

_____, VAIL, P. R., AND SANGREE, J. B. (1977). Seismic stratigraphy and global changes of sea levels, part 6: stratigraphic interpretation of seismic reflection patterns in depositional sequences. In: Clayton, C. E., ed., Seismic Stratigraphy-Applications to Hydrocarbon Exploration. Tulsa. A.A.P.G. Memoir nº 26, p. 117-133.

_____, VAIL, P. R. and THOMPSON III, S. (1977). Seismic stratigraphy and global changes of sea level, part 2: The depositional sequence as a basic unit for stratigraphy analysis. In: Clayton, C. E., ed., Seismic Stratigraphy-Applications to Hydrocarbon Exploration. Tulsa. A.A.P.G. Memoir nº 26, p. 53-62.

_____, (1985). Seismic stratigraphy expression of submarine fans. In: BERG, O. R. and WOOLVERTON, D. G., eds., Seismic stratigraphy II: An interpretation approach to hydrocarbon exploration, A.A.P.G Memoir 39, Tulsa.

MOHRIAK, W. U. (1984). Geologia da borda oeste da Bacia de Campos. Petrobrás Internal Report, DEPEX/DIRSUL/SECASU.

_____ (1988). The tectonic evolution of the Campos Basin, offshore Brazil. D. Phil. thesis, Oxford University, 369p.

_____, HOBBS, R. and DEWEY, J. F. (1990). Basin-forming processes and the deep structure of the Campos Basin, offshore Brazil. Marine and Petroleum Geology, v. 7, nº 2, p. 94-122.

MORAES, M. A. S. (1989). Diagenetic evolution of Cretaceous-Tertiary turbidite reservoirs, Campos Basin, Brazil. A.A.P.G. Bull. v. 73, nº 5, p. 598-612.

MUEHE, D. (1983). Conseqüências higroclimáticas das glaciaçoes quaternarias no relevo costeiro a leste da Baía de Guanabara. Revista Brasileira de Geociências, v. 13 nº 4, p. 245-252.

_____ (1989). Distribuiçao e characterizaçao dos sedimentos arenosos da plataforma continental interna entre Niterói e Ponta Negra, RJ, Brazil. Revista Brasileira de Geociências, v. 19 nº 1, p. 25-36.

MUTTI, E. and RICCI LUCCHI, F. (1972). Le torbibiti dell' Alppennine settentrionale: introduzione all' analisi di facies. Memorie Societa Geologica Italiana, v. 11, p. 161-199. (Translated into English by T. H. Nilsen (1978), International Geology Review, v. 20, nº 2, p. 125-166.

_____, _____ (1975). Turbidite facies and facies associations. In: E. Mutti et al. (Editors). Examples of Turbidite Facies and Associations from Selected Formations of the Northern Apennines. Field Trip Guidebook A-11, 9th International Association of Sedimentologists Congr., Nice, p. 21-36.

_____ (1977). Distinctive thin-bedded turbidite facies and related depositional environments in the Eocene Hecho Group (South-Central Pyrenees, Spain). Sedimentology, v. 1, p. 107-131.

_____, BARROS, M. C. , POSSATO, S. , GUARDADO, L. R. (1979). Distribuiçao estratigráfica e modelo deposicional das areias eocênicas do membro Carapebus, Bacia de Campos. Rio de Janeiro, PETROBRAS/DEPEX, Internal report.

_____ (1979). Turbidites et cones sous-marins profonds, in Peter Homewood (ed.), Sédimentation détritique (fluviatile, littorale et marine), Institut de Géologie, Université de Fribourg, Suiss, p. 353-419.

_____ (1980). Deep-sea fan turbidite sediments winnowed by bottom currents in the Eocene of the Campos Basin, Brazilian offshore (abs), Bochum, 1st European Meeting, International Association of Sedimentologists, p. 114.

_____ (1985). Turbidite Systems and Their Relations to Depositional Sequences. In: G. G. Zuffa (ed.) Provenance of Arenites, by D. Reidel Publishing Company. p. 65-93.

_____, REMANCHA, E., SGAVETTI, M., ROSELL, J., VALLONI, R., ZAMORANO, M. (1985). Stratigraphy and facies characteristics of the Eocene Hecho Group Turbidite Systems, south-central Pyrenees. Excursion guidebook nº12, 6th European Regional Meeting, Lleida-Spain, p. 521-576.

_____ and NORMARK, W. R. (1987). Comparing examples of modern and ancient turbidite systems: Problems and concepts. In: LEGGET, J. K. and ZUFFA, G. G., eds., Marine Clastic Sedimentology: Concepts and Case Studies. Graham and Trotman, London, p. 1-37.

NAIRN, A. E. M. and STEHLI,F. G. (1973). A model for the South Atlantic. In: NAIR, A. E. M. and STEHLI, F. G., eds, The South Atlantic, p. 1-24, Plenum Press, New York.

NISSENBAUM, A., PRESLEY, B. J., KAPLAN, I. R. (1972). Early diagenesis in a reducing fjord, Saanich Inlet, British Columbia - I. Chemical and isotopic changes in major components of seawater. Geochim. Cosmochim., Acta, v. 36, p. 1007-1027.

NORMARK, W.R. (1970). Growth patterns of deep sea fans. A.A.P.G. Bull., v. 54, p. 2170-2195.

NWACHUKWU, S. O. (1976). Approximate Geothermal Gradients in Niger Delta Sedimentary Basin. A.A.P.G. Bull., v. 60, p. 1073-1077.

O'CONNELL, S., STELTING, C. E., BOUMA, A. H., COLEMAN, J. M., CREMER, M., DROZ, L., MEYER-WRIGHT, A. A., NORMARK, W. R., PICKERING, K. T., STOW, D. A. V., and DSDP Leg 96 Shipboard Scientists (1985). Drilling results on the lower Mississippi Fan. In: Submarine Fans and Related Turbidite Systems, 1985. (Edited by A. H. Bouma, W. R. Normark, N. E. Barnes), p. 291-298. Frontiers in Sedimentary Geology, Spring-Verlag.

OJEDA Y OJEDA, H. (1982). Structural framework, stratigraphy and evolution of Brazilian Marginal Basins. A.A.P.G. Bul., v. 77, p. 732-749.

PEARSON, R. (1978). Climate and Evolution. London/New York/San Francisco. Academic, 244 p.

PEREIRA, M. J., TRINDADE, L. A. F., and GAGLIANONE, P. C. (1984). Origem e evoluçao das acumulaçoes de hidrocarbonetos na Bacia de Campos. In: Anais do XXXIII Congresso Brasileiro de Geologia, v. 10, p. 4763-4777.

PETTIJOHN, F. J., POTTER, P. E., and SEIVER, R. (1973). Sand and Sandstone. Springer-Verlag, New York, 618 p.

PICKERING, K. T., STOW, D. A. V., WATSON, M. and HISCOTT, R. (1986). Deep-water facies, process and models: A review and classification scheme for modern and ancient sediments. Earth-Sci. Rev., v. 23, p. 75-174.

_____, HISCOTT, R. N. & HEIN, F. J. (1989). Deep marine environments, London, Unwin Hyman, 416 p.

PISCOTTO, K. A. and MAHONEY, J. J. (1981). Isotopic survey of diagenetic carbonates. Deep Sea Drilling Project Leg 63. Initial Reports of the DSDP, v. 63, p. 595-609.

PITTMAN, E. D. (1979). Porosity, diagenesis and production capability of sandstone reservoirs. In: SCHOLLE, P. A. & SCHLUNGER, P. R. eds., Aspects of Diagenesis. Special Publication nº 26, S.E.P.M., Tulsa, Oklahoma, 159-173.

PONTE, F. C. & ASMUS, H. E. (1978). Geological framework of the Brazilian Continental Margin. Geol. Rundsch, v. 68, p. 201-235.

_____; FONSECA, J. dos REIS & CAROZZI, A. V. (1980). Petroleum habitats in the Mesozoic-Cenozoic of the continental margin of Brazil. In: Canadian Society of Petroleum Geologists. Facts and principles of world petroleum occurrence. Calgary, Memoir 6, p. 857-86.

POSAMENTIER, H. W., JERVEY, M. T., and VAIL, P. R. (1988). Eustatic controls on clastic deposition I - conceptual framework. In: Sea-Level Changes - An integrated Approach, S.E.P.M. Special Publication nº 42, p. 109-124.

POSAMENTIER, H. W. and VAIL, P. R. (1988). Eustatic controls on clastic deposition II - Sequence and system tract

models. In: Sea-Level Changes - An integrated Approach, S.E.P.M. Special Publication nº 42, p. 125-154.

POWERS, M. C. (1953). A new roundness scale for sedimentary particles. Jour. Sed. Pet., v. 23, p. 117-119.

RADAMBRASIL (1983). Folhas SF-23/24 - Rio de Janeiro/Vitória, v. 32, p. 27-304.

READING, H. G. (1986). Facies. In: READING, H. G., ed., Sedimentary environments and facies. Second edition. Blackwell Scientific Publications, Oxford. p. 4-19.

RETTKE, R. C. (1981). Probable burial diagenetic and provenance effects on Dakota Group clay mineralogy, Denver Basin. Jour. Sed. Pet., v. 51(2), p. 541-552.

REYNOLDS, R. C. (1980). Interstratified clay minerals. In: BRINDLEY, G. W. and BROWN, G. eds. Crystals structures of Clay Minerals and their x-ray identification. Min. Soc. of Lond, p. 249-304.

_____ and HOWER, J. (1970). The nature of interlayering in mixed-layer illite-montmorillonite. Clay & Clay Minerals, v. 18, p. 25-36.

REZENDE, W. M. (1978). O sistema de falhas transformantes da placa sul-americana e eventos relacionáveis na margem continental brasileira. Rio de Janeiro, PETROBRAS, Internal report, 21 p.

RIBEIRO FILHO, R. (1948). Caracteres físicos e geológicos da Bacia do Paraíba. Departamento Nacional da Produção Mineral, Boletim nº 127, Rio de Janeiro.

RICCI LUCCHI, F. (1984). Fan sedimentation with emphasis on the North Sea Tertiary. Course Notes nº 29, Part 1, Joint Association for Petroleum Exploration Courses (UK), 73 p.

RICCOMINI, C., PELOGGIA, A. U. G., SALONI, J. C. L., KOHNKE, M. W., and FIGUEIRA, R. M. (1989). Neotectonic activity in the Serra do Mar rift system (southeastern Brazil). Jour. of South American Sciences, v. 2, nº 2, p. 191-197.

RICE, D. D. and CLAYPOOL, G. E. (1981). Generation, accumulation, and source potential of biogenic gas. A.A.P.G. Bull., v. 67, p. 5-25.

RICHTER, A. J. (1985). Aplicaçao de nanofósseis calcários no mapeamento da discordancia pré-eocénica na Bacia de

Campos Col. Trab. Paleont. Brasília. Ministério de Minas e Energia, DNPM, Série Geológica, nº 27, p. 471-480.

RILEY, J. P. & CHESTER, R. (1971). Introduction to Marine Chemistry. Academic Press, London. 465 p.

ROBERTSON, A. H. F. & OGG, J. G. (1986). Palaeoceanographic setting of the Callovian North Atlantic. In: North Atlantic palaeoceanography, C. P. Summerhayes & N. J. Shackleton, eds., Geol. Soc. (London) Spec. Publn 21. Oxford: blackwell Scientific, p. 283-98.

ROCHA, J., MILLIMAN, J. D., SANTANA, C. I., and VICALVI, M. A. (1975). Upper Continental margin sedimentation off Brazil, Southern Brazil. In: Contribution to Sedimentology, MILLIMAN, J. D. and SUMMERHAYS, C. P. eds., Stuttgart, 4, p. 117-150.

RODRIGUES, R. and TAKAKI, T. (1987). Isotope stratigraphy of cenozoic carbonate sequences of Brazilian northern coast. B. Geoci. Petrobrás, Rio de Janeiro, v. 1(2), p. 177-182.

RUDDIMAN, W. F. and McINTYRE, A. (1981a). The mode and mechanism of the last deglaciation: Oceanic evidence. Quaternary Research, v. 16, p. 125-134.

_____, _____ (1981b). Oceanic mechanisms for amplification of the 23,000 year ice-volume cycle. Science v. 212, p. 617-627.

SANSONE, F. J. and MARTENS, C. S. (1981). Methane production from acetate and associated methane fluxes from anoxic coastal sediments. Science, v. 211, p. 707-709.

SAVAGE, K. M., DE CESERO, P., and POTTER, P. E. (1988). Mineralogic maturity of modern sand along a high-energy tropical coast: Baixada de Jacarepaguá, Rio de Janeiro, Brazil. Journal of South American Earth Sciences, v. 1, nº 4, p. 317-328.

SCHALLER, H. (1973). Estratigrafia da Bacia de Campos. In: Anais do XXVII Congresso Brasileiro de Geologia, v. 3, p. 247-258.

SCHLUMBERGER LIMITED (1981). Dipmeter interpretation. New York, v.1, 61 p.

SCHMIDT, V. and McDONALD, D. A. (1979). The role of secondary porosity in the course of sandstone diagenesis. In: SCHOLLE, P. A. and SHLUNGER, P. R. (Eds) Aspects of diagenesis. Special Publication n ° 26, S.E.P.M., Tulsa, Oklahoma, p. 175-207.

_____,_____ (1979). Texture recognition of secondary porosity in sandstones. In: SCHOLLE, P. A. and SHLUNGER, P. R. (Eds) Aspects of diagenesis. Special Publication n ° 26, S.E.P.M., Tulsa, Oklahoma, p. 209-225.

SCHOLLE, P.A. (1979). An illustrated guide to the constituents, textures, cements and porosities of sandstones and associated rocks. A.A.P.G., Memoir 28, 201 p.

SCHOVE, D. J. (1983). Sunspot Cycles. Stroudsburg, Pa: Hutchinson-Ross. 397 p.

SCHWARZACHER, W. (1975). Sedimentation models and quantitative stratigraphy. Developments in sedimentology nº 19, Elsevier, 382 p.

SECASU (1980). O campo de Pampo e áreas adjacentes. Rio de Janeiro, PETROBRAS/DEPEX, Internal Report, 31 p.

SELLEY, R. C. (1978). Ancient sedimentary environments. 2n ed., Chapman and Hall, London, 287 p.

_____ (1979). Dipmeter and log motifs in North Sea submarine-fan sands. Bull. A.A.P.G., v. 63, P. 905-917.

SHACKLETON, N.J. and KENNETT, J. P. (1974). Paleotemperature history of the Cenozoic and the initiation of Antarctic glaciation: oxygen and carbon isotope analyses in DSDP sites 277, 279, and 281. In: DSDP sites 277, 279, 291 Initial Reports, v. 29, p. 743-755.

_____, et al. (1984). Oxygen isotope of the onset of ice-rafting and history of glaciation in the North Atlantic region. Nature, v. 307, p. 620-623.

SHANMUGAM, G., MIOLA, R. J. (1988). Submarine fans: Characteristics, models classification, and reservoir potential. Earth-Sci. Rev., v. 24, p. 383-428.

_____, _____, McPHERSON, J. G., O'CONNELL, S. (1988). Comparison of turbidite facies associations in modern passive-margin Mississippi fan with ancient active-margin

fans. Sedimentary Geology, v. 58, p. 63-77.

SHAW, H. F. (1970). The preparation of oriented clay mineral discs. Geol. Soc. London v. 39, p. 371-405.

_____ (1987). Clays and their effects in source & reservoir rocks. Joint Association for Petroleum Exploration Courses, Course notes nº 61, 166 p.

SHIMABUKURO, S. , RICHTER, A. J. , GOMIDE, J. (1985). Nanofósseis calcáreos: Bioestratigrafia do Mioceno ao Pleistoceno na plataforma brasileira. Col. Trab. Paleont. Min. Minas Energia, DNPM. Série Geológica n. 27. Seçao Paleont. Estrat., v. 2, p. 491-502.

_____ (1987). Caracterizaçao paleobiológica do "Marco Azul" : Um importante marco estratigrafico oligocênico na Bacia de Campos, Brasil. Anais do Congresso Brasileiro de Paleontologia, Rio de Janeiro, Brazil. p. 1043-53.

_____, MESQUITA, A. C. F., CRUZ, C. E. S., APPI, C. J.,GAMBOA, L. A. P., ESTEVES, F. R., CARMINATTI, M., PERES, W. E. (1987). "BRAARUDOSPHAERA CHALK", Um evento oligocênico na Bacia de Campos. In: Anais do X Congresso Brasileiro de Paleontologia, Rio de Janeiro, abstract.

SIBSON, R. H., MOORE, J. McM. and RANKIN, A. H. (1975). Seismic pumping - a hydrothermal fluid transport mechanism. J. Geol. Soc. London, v. 131, p. 653-659.

_____ (1981). Fluid flow accompanying faulting: field evidence and models. In: D. W. Simpson and P. G. Richards, eds., Earthquake Prediction: An International Review. American Geophysical Union, Maurice Ewing Series 4, p. 593-603.

SMITH, J. T. and EHRENBERG, S. N. (1989). Correlation of carbon dioxide abundance with temperature in clastic hydrocarbon reservoirs: relationship to inorganic chemical equilibrium. Marine and Petroleum Geology, v. 6, nº 2, p. 129-135.

SONOKI, N. T. (1987). Contribuiçao ao conhecimento geológico da evoluçao do Canyon de Enchova, Bacia de Campos. Msc. thesis, UFOP, Ouro Preto, Brazil, 111 p.

SOUZA CRUZ, C. E. de, BARROCAS, S. L. S. and APPI, C. J. (1987). Modelo deposicional dos reservatórios turbidíticos oligocênicos/eomiocênicos do Campo de Albacora, Bacia de Campos, Brasil. Boletim de geociências da Petrobrás v. 1, nº 2, p. 215-223.

SRODON, J. (1980). Precise identification of illite/smectite interstratifications by x-ray powder diffraction. Clays and Clay Minerals, v. 28, nº 6, p. 401-411.

_____, (1981). X-ray identification of randomly interstratified illite-smectite in mixtures with discrete illite. Clay Minerals, v. 16, p. 297-304.

_____, (1984). X-ray powder diffraction identification of illitic materials. Clays and Clay Minerals, v. 5, p. 337-349.

STATGRAPHICS (1988). Statistical Graphics System. Statistical Graphics Corporation user's guide. STSC. USA. 766 p.

STELTING, C. E., PICKERING, K. T., BOUMA, A. H., COLEMAN, J. M., CREMER, M.,DROZ, L., MEYER-WRIGHT,A.A., NORMARK, W. R., O'CONNELL, S., STOW, D. A. V., and DSDP Leg 96 Shipboard Scientists (1985). Drilling Results on the Middle Mississippi Fan. In: Submarine Fans and Related Turbidite Systems, 1985. (Edited by A. H. Bouma, W. R. Normark, N. E. Barnes). p. 275-282. Frontiers in Sedimentary Geology, Spring-Verlag.

STEWART, I. J. (1987). A revised stratigraphic interpretation of the Early Palaeogene of the Central North Sea. In: BROOKS, J. & GLENNIE, K. W. eds. (Graham & Trotman, 1987), Petroleum Geology of North West Europe, v.1, p. 557-576.

STOW, D. A. V. and BOWEN, A, J. (1980). A physical model for the transport and sorting of fine-grained sediments by turbidity currents. Sedimentology v. 27, p. 31-46.

_____, and PIPER, D. J. W. (1984). Deep-water fine-grained sediments: facies models. In: Fine-grained sediments: Deep-water processes and facies, eds., Geological Society, Special Publ., nº 15, p. 611-646.

STUMN, W. and MORGAN, J. J. (1970). Aquatic chemistry. New York, John Wiley and Sons, 583 p.

SURDAM, R. C. and CROSSEY, L. J. (1985a). Organic-inorganic reactions during progressive burial: Key to porosity/ permeability enhancement and/or preservation. The Philosophical Transactions of the Royal Society of London, Series A, v. 315, p. 135-156.

_____,_____ (1985b). Mechanisms of organic/inorganic interactions in sandstone/shale sequences. In: Relationship of organic matter and mineral diagenesis, SEPM Short Course Notes nº 17, p. 177-232.

TISSOT, B. P., DURAND, B., ESPITALIE, J., and COMBAZ, A. (1974). Influence of nature and diagenesis of organic matter in formation of petroleum. A.A.P.G. Bull., v. 58, p. 499-506.

_____, DEMAISON, G., MASSON, P., DETEIL, J. R., COMBAZ, A. (1980). Paleoenvironments and Petroleum potential of middle Cretaceous black shales in Atlantic basins. A.A.P.G. Bull. v.64 nº 11, p. 2051-63.

TOMKEIEFF, S. I. (1983). Dictionary of Petrology. Eds.: E. K. Walton, B. A. O. Randall, M. H. Battey, and O. Tomkeieff, 680 p.

TRINDADE, L. A. F. & CARMINATTI, M. (1987). Estudo da migraçao secundária de hidrocarbonetos nas áreas dos Campos de Albacora e Marlim, Bacia de Campos. Petrobrás-DEPEX, Internal report.

VAIL, P. R., MITCHUM, R. M. Jr., TOOD, R. G., WIDMIER, J. M. THOMPSON, S. III, SANGREE, J. B., BUBB, J. N., and HATELID, W. G., (1977). Seismic stratigraphy and global changes of sea level. In: Clayton, C. E., ed., Seismic Stratigraphy- Applications to Hydrocarbon Exploration. Tulsa. A.A.P.G. Memoir nº 26, p. 49-212.

_____ and TODD, R. G. (1981). Northern North Sea Jurassic unconformities, chronostratigraphy. In: Petroleum Geology of the Continental Shelf of North-West Europe. Phila. PA., Heyden & Son, Inc., p. 216-235.

_____, KARDENBOL, J. and TODD, R. G. (1984). Jurassic unconformities, chronostratigraphy and sea-level changes

from seismic stratigraphy and biostratigraphy. In: SCHLEE, J. S., ed., Interregional unconformities and hydrocarbon accumulation. A.A.P.G. Memoir 36.

_____, (1987). Seismic stratigraphy interpretation using sequence stratigraphy, part 1: Seismic stratigraphy interpretation procedure, In: BALLY, A. W., ed., A.A.P.G. Atlas of Seismic Stratigraphy.

_____, (1988). Sequence stratigraphy workbook, fundamentals of sequence stratigraphy. 1988 A.A.P.G. Annual Convention Short Course: Sequence stratigraphy interpretation of seismic well and outcrop data, presented by P. R Vail and J.B. Sangree, March 19, 1988, Houston, Texas.

VAN WAGONER, J. C., POSAMENTIER, H. W., MITCHUM, R. M., VAIL, P. R., SARG, J. F., LOUTIT, T. S., AND HARDENBOL, J. (1988). An overview of the fundamentals of the sequence stratigraphy and key definitions. In: Sea-Level Changes - An integrated Approach, S.E.P.M. Special Publication nº 42, p. 41-45.

VERNEKAR, A. (1972). Long-period global variations of incoming solar radiation. Meteorol. Monogr. v. 12, nº 34.

WALKER, G. F. (1957). Differentiation of vermiculites and smectites in clays. Clay Miner. Bull., v. 3, p. 154-163.

_____, (1958). Reactions of expending lattice minerals with glycerol and ethylene glycol. Clay Miner. Bull., v.3, p. 302-313.

WALKER, R. G. (1965). The origin and significance of the internal sedimentary structures of turbidites. Proc. Yorkshire Geol. Soc. v. 35, p. 1-32.

_____, (1978). Deep-water sandstone facies and ancient submarine fans: Models for exploration for stratigraphic traps. A. A. P. G. Bull., v. 62, p. 932-966.

WALTON, E. K. (1967). The sequence of internal structures in turbidites. Scottish Journal Geology, v. 3, p. 306-317.

WEAVER, C. E. (1958). Geologic significance of argillaceous sediments, 1. Origin and significance of clay minerals in sedimentary rocks; 2. Clay petrology of Upper Mississippian-Lower Pennsylvanian sediments of central

United States. A.A.P.G. Bull., v. 42, p. 254-309.

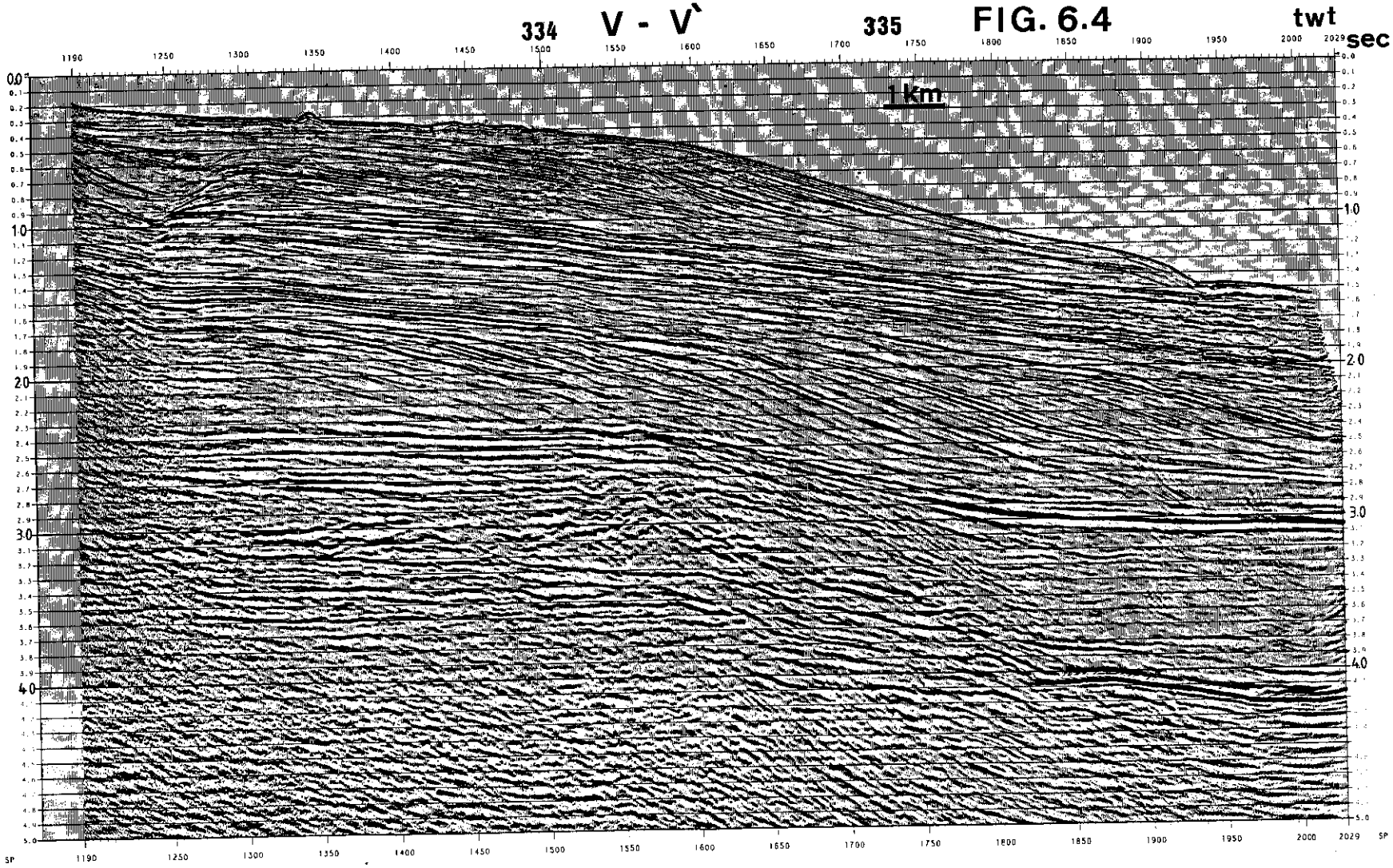
_____ (1961). Clay mineralogy of the Late Cretaceous rocks of the Washakie basin. In: Wyominig Geol. Assoc. Guidebook, 16th Ann. Field Conf., p. 148-154.

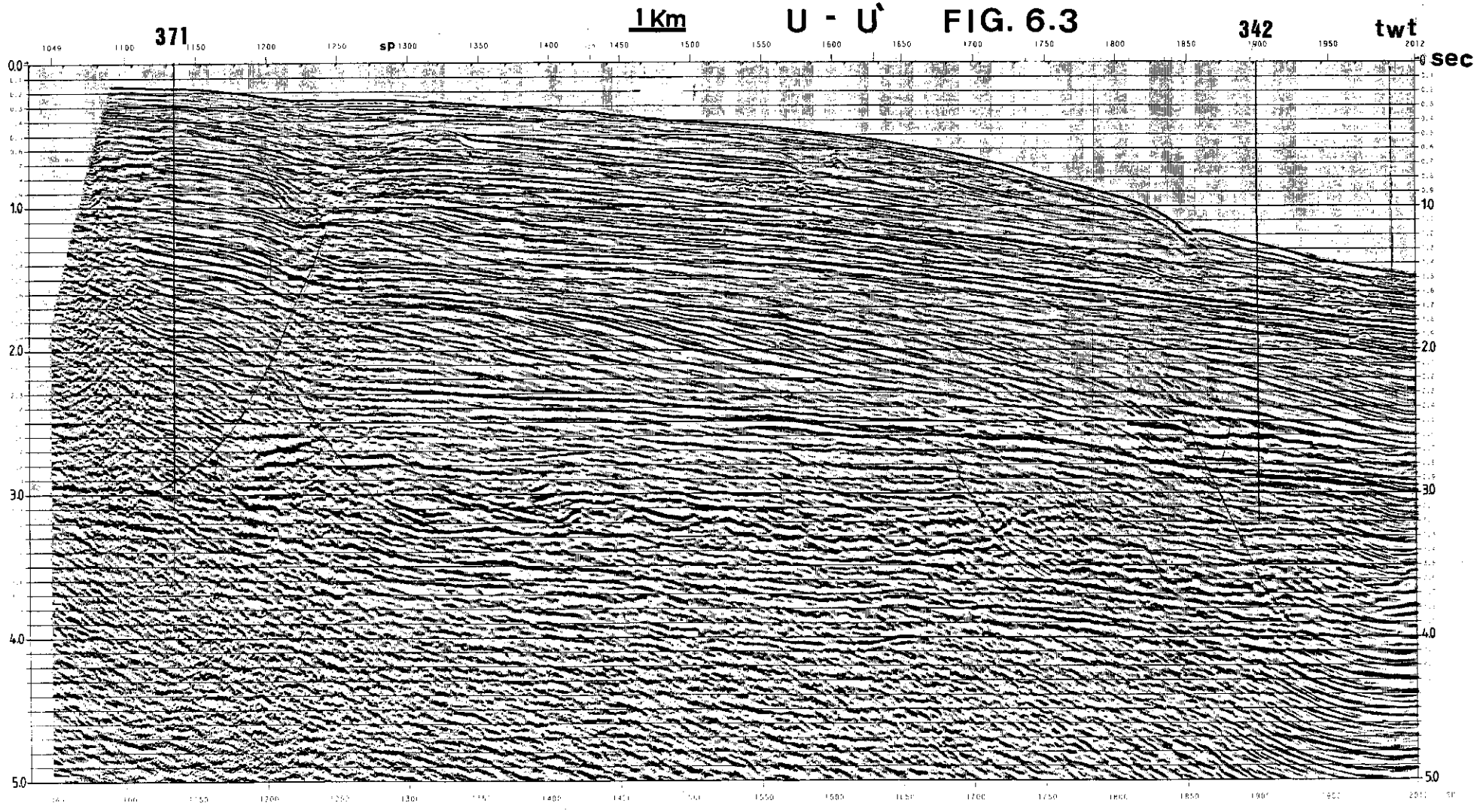
WETZEL, A. (1984). Bioturbation in deep-sea fine-grained sediments: influence of sediment texture, turbidite frequency and rates of environmental change. In: Fine-grained sediments: Deep-water processes and facies, STOW, D. A. V. & PIPER, D. J. W., eds., Geological Society, Special Publication nº 15, p. 595-608.

WHITE, S. H. , GRANT, P. R. and BRODIE, K. (1980). Scanning electron microscopy. Unpublished course notes. Imperial College of Science and Technology.

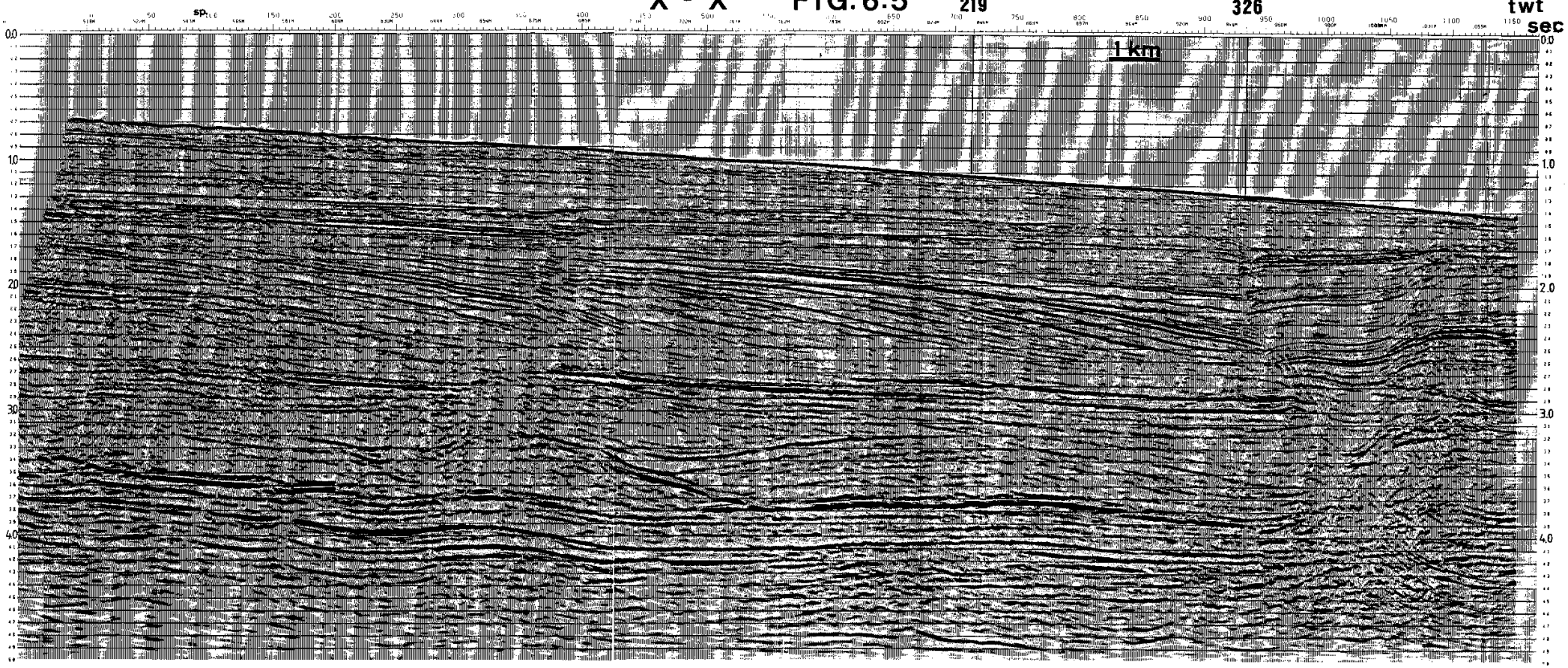
WILGUS, C. K.; HASTINGS, B. S.; KENDALL, C. G. St. C.; POSAMENTIER, H. W.; ROSS, C. A. R.; and VAN WAGONER, J. C. (1988). Sea-level changes: an integrated approach, editors of S.E.P.M. Special Publication 42, 407 p.

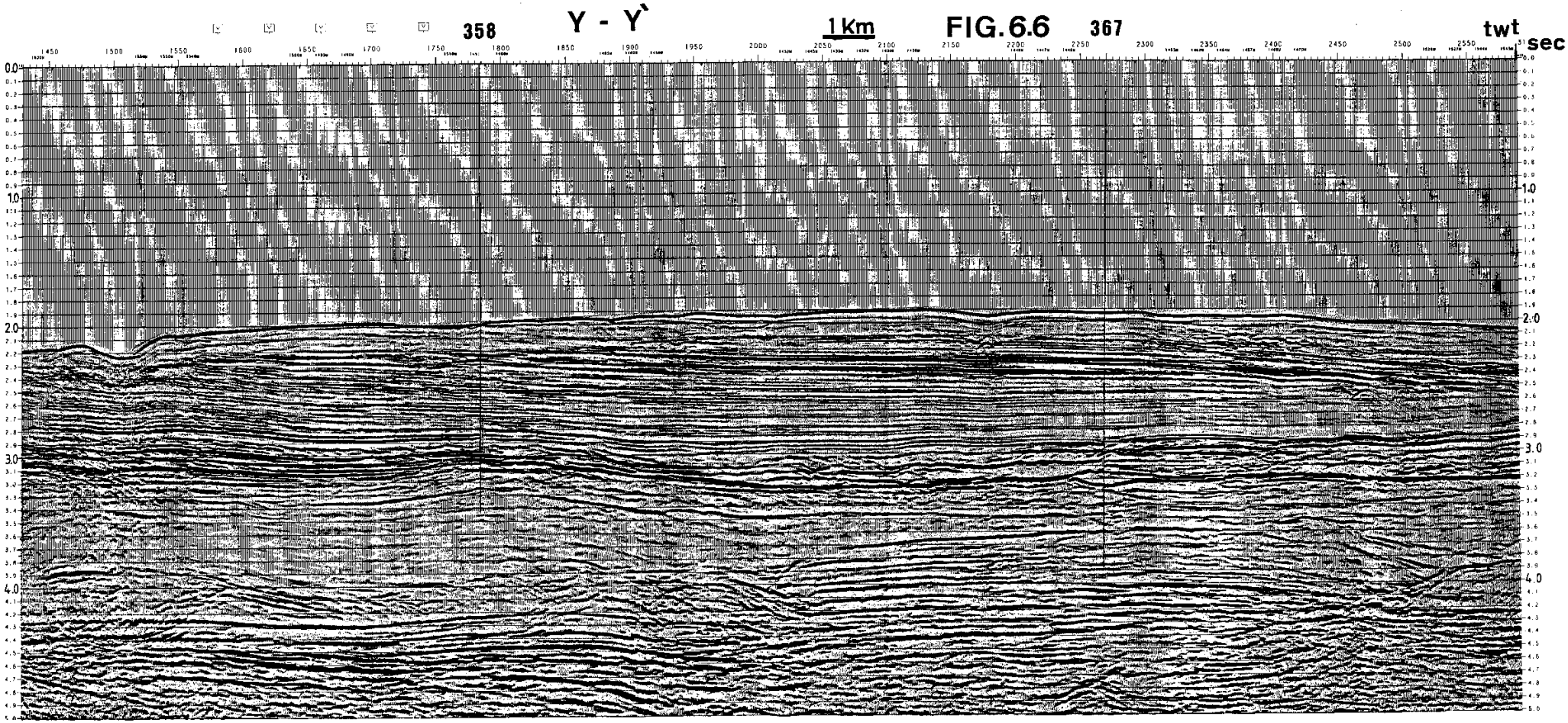
ZEUNER, F, E, (1952). Dating the Past. London: Methuen 3rd ed., 495 p.


334
V - V`
335
FIG. 6.4
twt
sec
1 km
SP

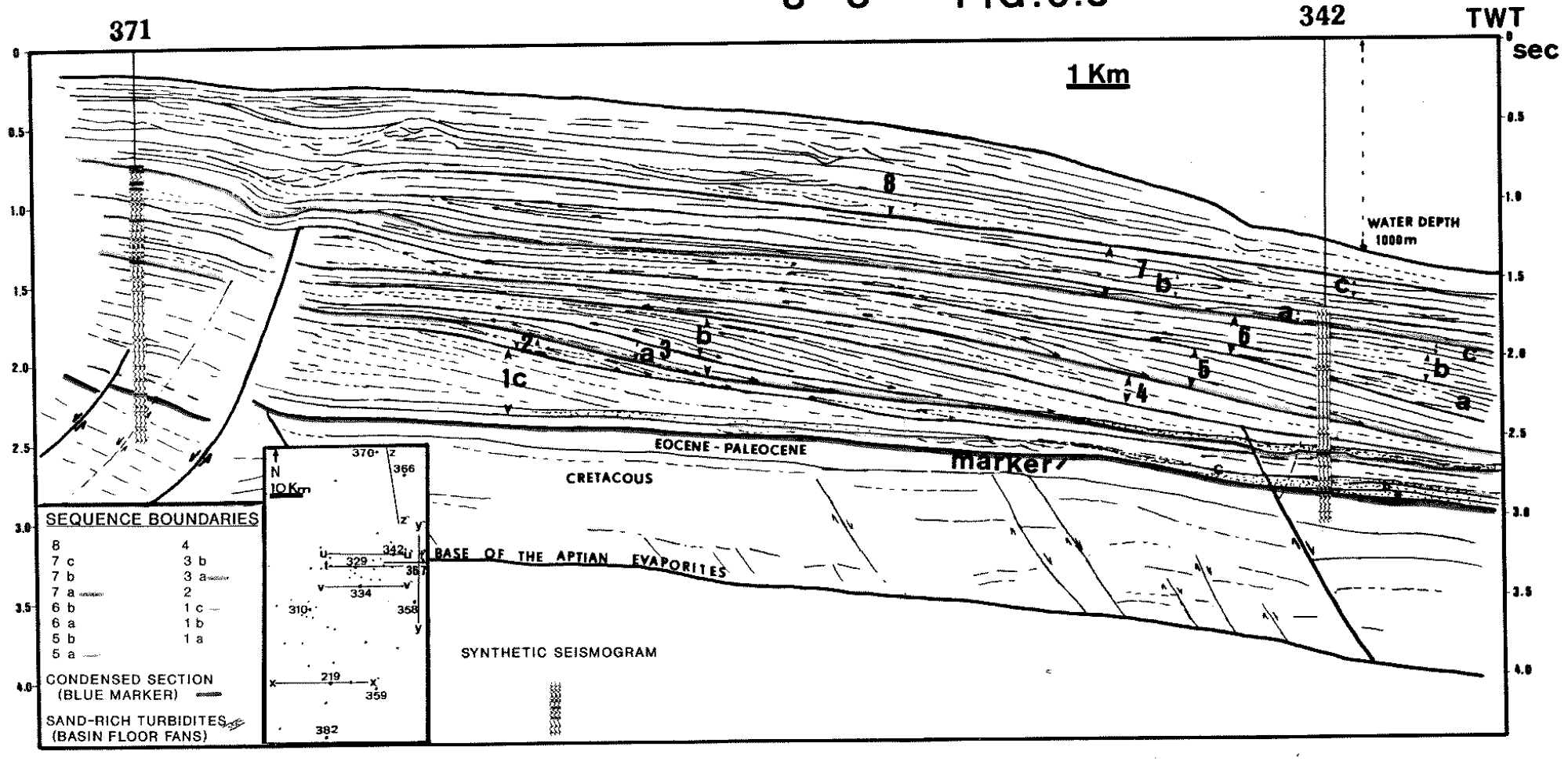

1Km
U - U`
FIG. 6.3
371
342
twt
sec
sp
0.0
1.0
2.0
3.0
4.0
5.0

X - X` FIG. 6.5




358
Y - Y`
1Km
FIG.6.6
367
twt sec

U - U` FIG.6.3


371
342
TWT
sec
1 Km
WATER DEPTH
1000m
EOCENE - PALEOCENE
marker
CRETACOUS
BASE OF THE APTIAN EVAPORITES
SYNTHETIC SEISMOGRAM
SEQUENCE BOUNDARIES
8
7 c
7 b
7 a
6 b
6 a
5 b
5 a
4
3 b
3 a
2
1 c
1 b
1 a
CONDENSED SECTION
(BLUE MARKER)
SAND-RICH TURBIDITES
(BASIN FLOOR FANS)
N
10Km
370
366
342
329
367
334
310
358
219
359
382

V - V`

FIG. 6.4

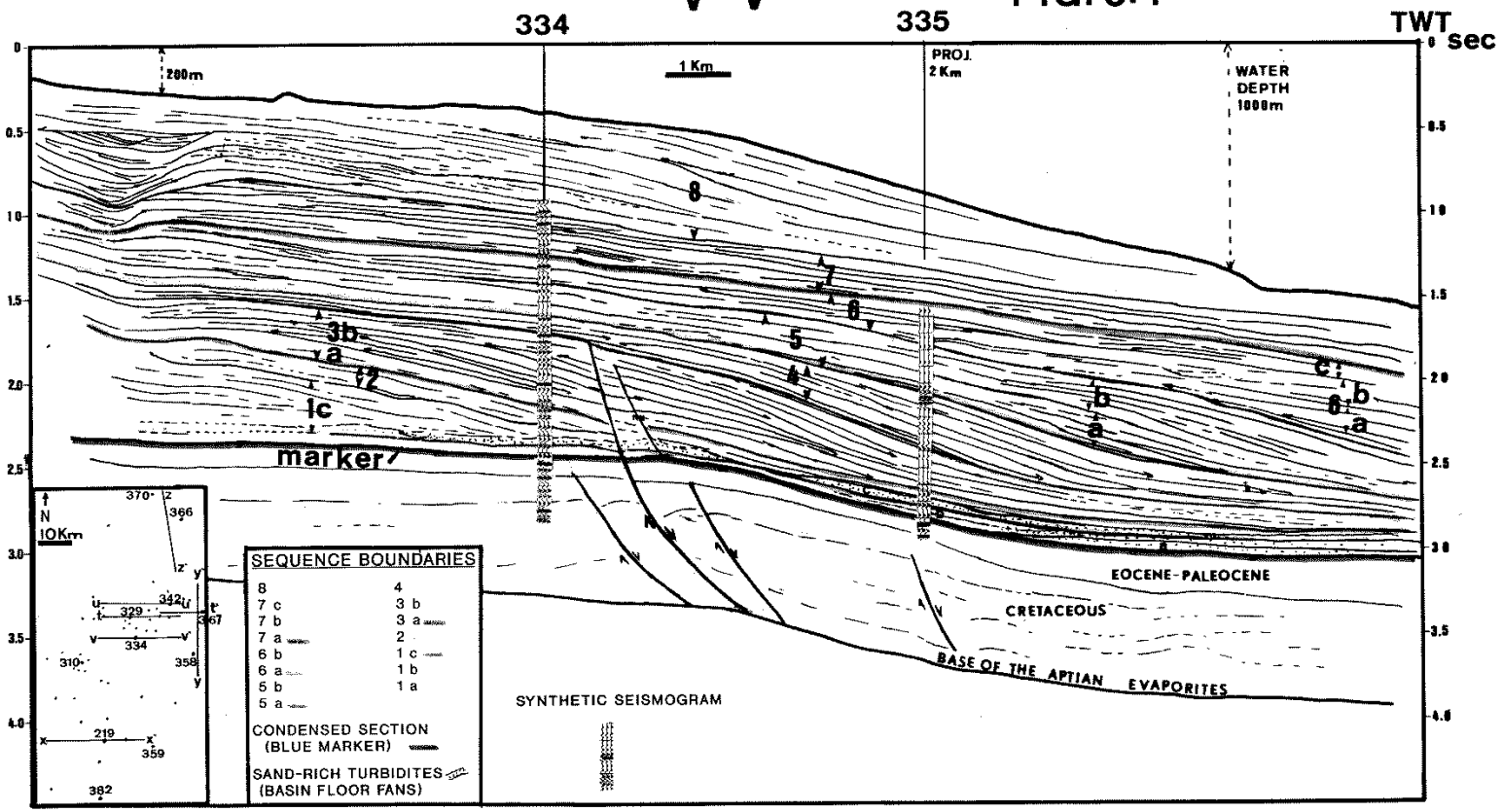
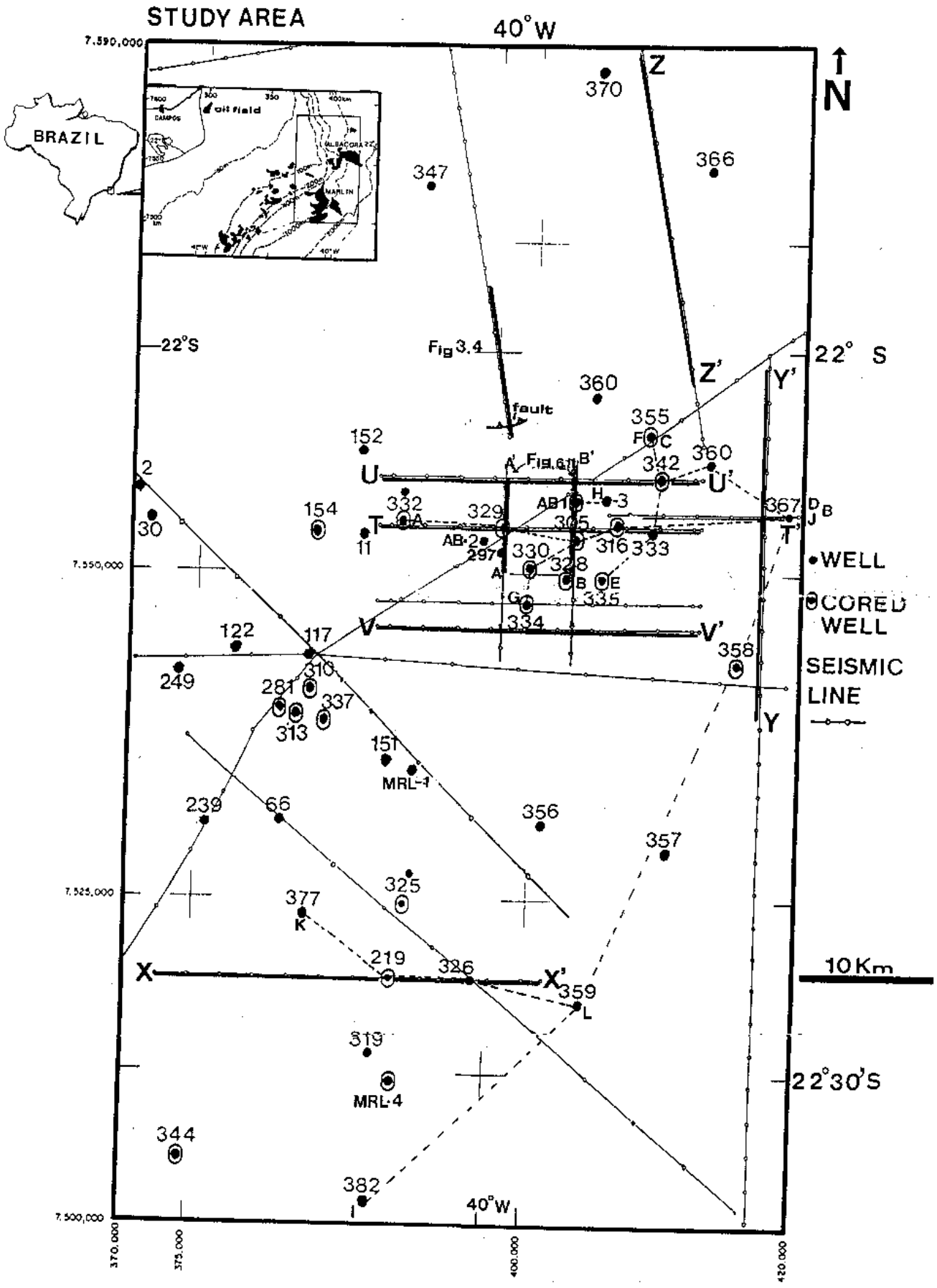

334
335
TWT sec
200m
1 Km
PROJ.
2 Km
WATER
DEPTH
1000m
8
7
6
5
4
3b
a
2
1c
marker
b
a
c
b
a
N
10Km
370
366
342
329
367
334
310
358
219
359
382
SEQUENCE BOUNDARIES
8
7 c
7 b
7 a
6 b
6 a
5 b
5 a
4
3 b
3 a
2
1 c
1 b
1 a
CONDENSED SECTION
(BLUE MARKER)
SAND-RICH TURBIDITES
(BASIN FLOOR FANS)
SYNTHETIC SEISMOGRAM
EOCENE-PALEOCENE
CRETACEOUS
BASE OF THE APTIAN EVAPORITES

TABLE 5.1

ELECTROFACIES	LITHOFACIES	LITHOLOGY-STRUCTURES	THICKNESS	GR°API	ΔT µsec/ft	RHOB g/cc	ØN u.p.
A	(GvS) GRAVELLY-SANDSTONE	GvS	Disorganized poorly sorted gravelly-sandstone; litharenite	<1 m up to a few m	46	59	2.62	17
	(GvSm) GRAVELLY SANDSTONE with MUDCLASTS	GvSm	Mudstone pebbles in a medium/fine sandy matrix; disorganized; litharenite	<1 m up to a few m	65	114	2.22-30 average= 2.25	36-39
	(DMT) DIAMICTITE	DMT	Disorganized gravelly mudstone/muddy gravelly sandstone (lithic graywacke)	60 cm up to 30 m	65-70	76-90	2.37	19-20
B	(AmS) AMALGAMATED SANDSTONE	AmS	Amalgamated coarse/fine-sandstone, massive; subarkose	40 cm up to > 10 m	45 45	120 cemented = 80	2.10-15 2.40	27-29 7-21
		VcS	Very coarse-sandstone amalgamated, poorly sorted, coarse tail; bioclastic subarkose	50 cm up to 7 m	38-45 40-55	96-98 cemented = 60-70	2.13-15 2.25-52	27-29 7-21
C	(FTab) THICK-BEDDED SAND-MUD COUPLETS	FTab	Thick-bedded medium/fine-sandstone with Tab and locally Tabc; subarkose	40 cm up to a few m	SGR=60 CGR=46	110-112	2.15-20	29-31
		FTb	Parallel-laminated fine-sandstone, loc. with Tbc, amalgamated subarkose	10-20 cm up to 4 m	50-63	93-103	2.17-27	29-35
D	(FTb-e) MUDDY THIN-BEDDED SAND-MUD COUPLETS	FTb-e	Thin-bedded fine-sandstone with Tbcde Tbc, Tcde, locally with Tacde; subarkose	av. beds of 5 cm interval 10 m	95	96	2.31	30-31
		FTde	Millimetric rhythmic siltstone, interbed. with coarse silt	interval with a few m	90-95	107-109	2.25-30	30-35
E	(E) SANDY THIN-BEDDED SAND-MUD COUPLETS	Fla	Thin-bedded fine/v.f. sandstone with flaser-bedding and faint ripple-cross-laminat. subarkose	av. beds of 4 cm interval 4 m	SGR=85 CGR=44	117-120	2.14-20	27-30
		Wav	Fine/very fine-sandstone with thin-wavy-bedding, ripple-cross-laminations; subarkose	av. beds of 3 cm interval 5 m	50-68	105-110	2.18-30	26-32
		Rip	Very fine-sandstone with lenticular-bed. and climbing- or ripple-drift; subark.	av. beds of 2 cm interval 4 m	70-76	86-123	2.24-35	26-33
F	(F) "CHAOTIC"	F	Contorted coherent/semi-coherent, balled brecciated siltstones mudstones	from a few cm up to > 7 m	70-90	76-106	2.25-46	15-33
G	(G1/G2) CHALK/MARLSTONE	G1	Chalk/carbonate mudst rich in coccoliths	av. bed of 60 cm	15	57	2.57	4
		G2	Marlstones rich in foraminifera/coccoliths	av. bed of 30 cm	50	100	2.36-37	28-30
	(G3/G4) MUDSTONE	G3	Calcareous mudstone with foraminifera	beds of a few cm	65-75	90	2.40-45	27-30
		G4	Siliciclastic mudstones	a few cm > 10 m	85	110-120	2.28-40	39-40
H	(MM/MS) MOTTLED MUDSTONE/SANDSTONE	MM	Medium/thick-bedded mottled sandy mudstones	50 cm up to 50 m	75-80	100-103	2.20-24	31-40
		MS	Medium/thin-bedded mottled muddy bioclastic sandstones with heavy minerals	5 cm up to a few m	57	65		
	(BS1) BIOTURBATED SANDY SILTSTONE	BS1	Medium-bedded bioturbated sandy siltstone	a few cm up to 1-2 m	50-80	105-110 87-88 = cemented	2.19-23	33-39

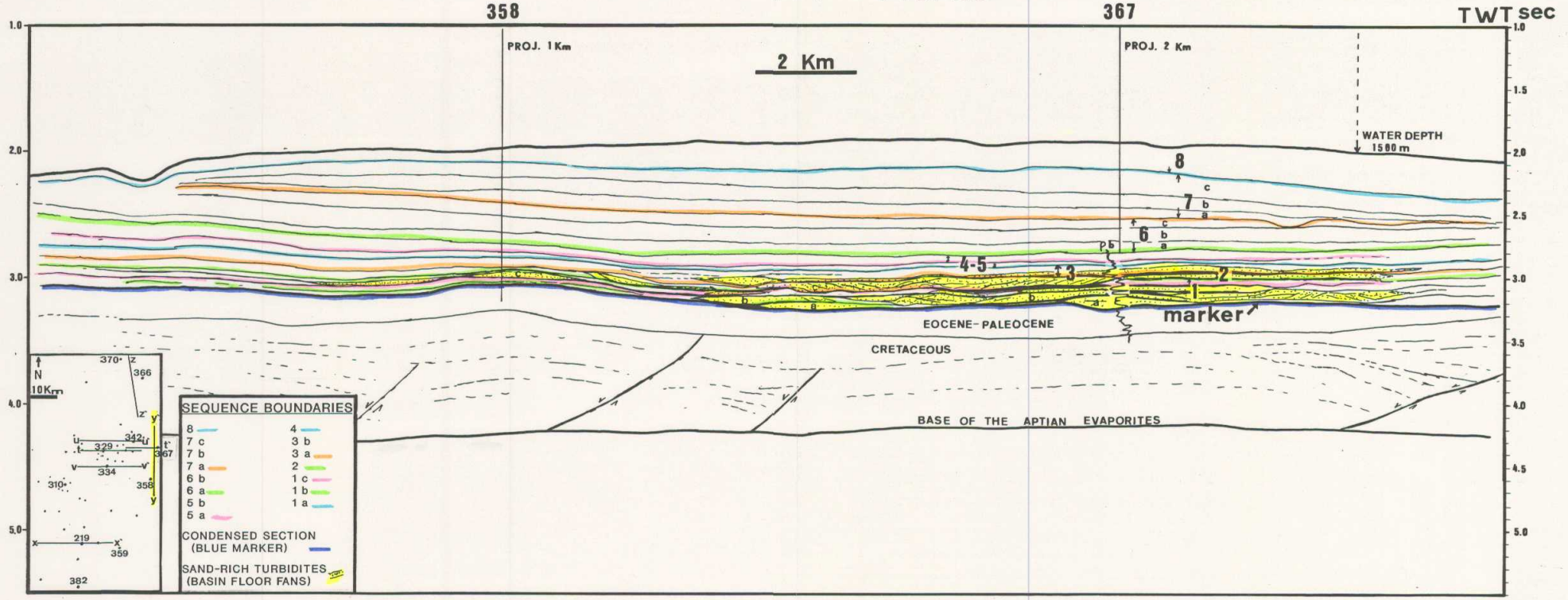
FIG. 4.1



STRATIGRAPHIC SECTIONS: A-B, C-D, E-F, G-H, I-J, K-L respectively FIG.: 5.11, 5.12, 5.13, 5.14, 5.15, 5.16

SCHEMATIC SECTIONS: T-T', U-U', V-V', X-X', Y-Y', Z-Z' respectively FIG.: 6.2, 6.3, 6.4, 6.5, 6.6, 6.7

Y - Y` FIG. 6.6


358
367
TWT sec
PROJ. 1 Km
2 Km
PROJ. 2 Km
WATER DEPTH
1560 m
8
7 c
7 b
7 a
6 c
6 b
6 a
4-5
3
2
1
marker
EOCENE-PALEOCENE
CRETACEOUS
BASE OF THE APTIAN EVAPORITES
N
10Km
370
366
342
329
334
310
358
367
219
359
382
SEQUENCE BOUNDARIES
8
7 c
7 b
7 a
6 b
6 a
5 b
5 a
4
3 b
3 a
2
1 c
1 b
1 a
CONDENSED SECTION
(BLUE MARKER)
SAND-RICH TURBIDITES
(BASIN FLOOR FANS)